ASME
SETTING THE STANDARD

Transactions of the ASME, Journal of Fluids Engineering (ISSN 0098-2202) is published bimonthly (Jan., Mar., May, July, Sept., Nov.) by The American Society of Mechanical Engineers, Three Park Avenue, New York, NY 10016. Periodicals postage paid at New York, NY and additional mailing offices.
POSTMASTER: Send address changes to Transactions of the ASME, Journal of Fluids Engineering, c/o THE AMERICAN SOCIETY OF MECHANICAL ENGINEERS, 22 Law Drive, Box 2300, Fairfield, NJ 07007-2300.
CHANGES OF ADDRESS must be received at Society headquarters seven weeks before they are to be effective. Please send old label and new address.
STATEMENT from By-Laws. The Society shall not be responsible for statements or opinions advanced in papers or ... printed in its publications (B7.1, Par. 3).

Journal of Fluids Engineering

Published Bimonthly by ASME

VOLUME 128 • NUMBER 6 • NOVEMBER 2006

TECHNICAL PAPERS

(Contents continued on inside back cover)

This journal is printed on acid-free paper, which exceeds the ANSI Z39.48-1992 specification for permanence of paper and library materials. ♾™
♻ 85% recycled content, including 10% post-consumer fibers.

TECHNICAL BRIEFS

ERRATUM

The ASME Journal of Fluids Engineering is abstracted and indexed in the following:

Applied Science & Technology Index, Chemical Abstracts, Chemical Engineering and Biotechnology Abstracts (Electronic equivalent of Process and Chemical Engineering), Civil Engineering Abstracts, Computer & Information Systems Abstracts, Corrosion Abstracts, Current Contents, Ei EncompassLit, Electronics & Communications Abstracts, Engineered Materials Abstracts, Engineering Index, Environmental Engineering Abstracts, Environmental Science and Pollution Management, Excerpta Medica, Fluidex, Index to Scientific Reviews, INSPEC, International Building Services Abstracts, Mechanical & Transportation Engineering Abstracts, Mechanical Engineering Abstracts, METADEX (The electronic equivalent of Metals Abstracts and Alloys Index), Petroleum Abstracts, Process and Chemical Engineering, Referativnyi Zhurnal, Science Citation Index, SciSearch (The electronic equivalent of Science Citation Index), Shock and Vibration Digest, Solid State and Superconductivity Abstracts, Theoretical Chemical Engineering

Electro-Osmotic Flow in Reservoir-Connected Flat Microchannels With Non-Uniform Zeta Potential

S. A. Mirbozorgi
Mechanical Engineering Department,
Ferdowsi University,
Mashhad, Iran

H. Niazmand
Mechanical Engineering Department,
Ferdowsi University,
Mashhad, Iran
and
Mechanical Engineering Department,
University of Waterloo,
Waterloo, Ontario, Canada N2L 3G1

M. Renksizbulut
Professor
Mechanical Engineering Department,
University of Waterloo,
Waterloo, Ontario, Canada N2L 3G1
e-mail: metin@uwaterloo.ca

The effects of non-uniform zeta potentials on electro-osmotic flows in flat microchannels have been investigated with particular attention to reservoir effects. The governing equations, which consist of a Laplace equation for the distribution of external electric potential, a Poisson equation for the distribution of electric double layer potential, the Nernst-Planck equation for the distribution of charge density, and modified Navier-Stokes equations for the flow field are solved numerically for an incompressible steady flow of a Newtonian fluid using the finite-volume method. For the validation of the numerical scheme, the key features of an ideal electro-osmotic flow with uniform zeta potential have been compared with analytical solutions for the ionic concentration, electric potential, pressure, and velocity fields. When reservoirs are included in the analysis, an adverse pressure gradient is induced in the channel due to entrance and exit effects even when the reservoirs are at the same pressure. Non-uniform zeta potentials lead to complex flow fields, which are examined in detail. [DOI: 10.1115/1.2353261]

Keywords: electro-osmotic flow, zeta potential, micro-channel flow, reservoir effects

1 Introduction

Generating fluid motion in micro-scale channels, such as those found in "lab-on-chip" devices, is of considerable challenge and interest. Mechanical micropumps utilize moving parts, which complicate the fabrication and sealing of associated systems as well as controlling their operation. On the other hand, electro-osmotic pumps with no moving parts can effectively transport liquids through microchannels by means of externally applied electric fields, making them ideally suited for microelectromechanical systems applications.

The need to understand and control electro-osmotic flows has stimulated many fundamental studies over the years. It is well known that most dielectric surfaces acquire an electrical charge when exposed to an electrolyte solution. As expected, the surface charge influences nearby ions in the solution such that those with the opposite charge to that of the surface (counter ions) are attracted to the surface, while ions of the same charge (co ions) are repelled. The resulting counter-ion rich region near the wall is called the electric double layer (EDL), and the associated electric potential at the "surface" is called the zeta potential [1]. Here, the surface is identified as a plane approximately one ionic diameter away from the actual wall where the no-slip boundary condition is applied. The charged particles in the EDL can be moved by the application of an external electric field, which in turn set the surrounding liquid into motion due to viscous drag. Thus, an electro-osmotic flow (EOF) is generated.

A survey of the relevant literature indicates that most investigations have been confined to electro-osmotic flows with *uniform* zeta potentials at the walls: e.g., Rice and Whitehead [2], Andreev et al. [3], Patankar and Hu [4], Santiago [5], Yang et al. [6–8], Ren and Li [9], Lin et al. [10], Zhang et al. [11], and Kang et al. [12], among others. As intuitively expected, these studies show that the EOF characteristics depend strongly on the value of the zeta potential. However, *non-uniform* zeta potential distributions are commonly encountered in micro-channel flows. For example, typical fluids driven electro-osmotically in the channels of medical microdevices contain biological particles, which often stick to the walls and thus cause non-uniform wall surface charge distributions. Other factors like impurities in the wall material, manufacturing defects, wall-adsorbed species, and variations in the solution *p*H may also lead to non-uniform zeta potential distributions.

The effects of non-uniform zeta potentials distributions on electro-osmotic flows have been examined by several researchers. Anderson and Idol [13] investigated EOF in cylindrical microchannels with periodic zeta potential distributions. Their solution is based on Fourier transformations for the zeta potential with respect to the channel length, and shows that the classical Helmholtz-Smoluchowski equation together with the average value of the zeta potential predicts the mean electro-osmotic velocity accurately. Herr et al. [14] experimentally investigated electro-osmotic flows in microchannels with a step change in zeta potential. They also derived an analytical velocity distribution for the limit of a thin EDL, which is only valid for regions sufficiently far away from the discontinuity in the zeta potential. Ren and Li [15] numerically studied EOF in circular microchannels with axial variations in the zeta potential and showed that non-uniform zeta potentials can cause different types of velocity profiles. They also showed that the form of the zeta potential distribution has no effect on the flow rate, and that the average value of the zeta potential can be used to evaluate the electro-osmotic flow rate accurately. Fu et al. [16] numerically studied the effects of a step change in the zeta potential distribution. They used the Nernst-Planck equation to model the changes in EOF characteristics. Yang et al. [17] proposed an analytical model to describe the effects of non-uniform zeta potential in electro-kinetic flows. They considered the continuities of electric current and flow rate simultaneously which lead to a non-uniform electric field.

The abovementioned studies have all ignored the effects of fluid reservoirs on the flow within the channel, but as Zhang et al. [11] and Yang et al. [8] showed for the case of a constant zeta poten-

Contributed by the Fluids Engineering Division of ASME for publication in the JOURNAL OF FLUIDS ENGINEERING. Manuscript received February 9, 2006; final manuscript received March 24, 2006. Assoc. Editor: Dimitris Drikakis.

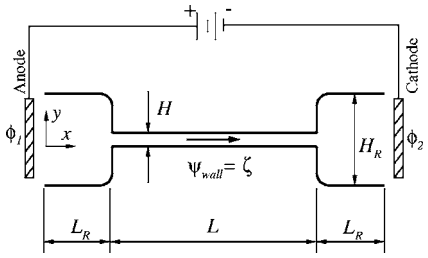

Fig. 1 Electro-osmotic flow between parallel plates with two identical reservoirs

tial, there is an induced pressure gradient due to the presence of reservoirs. Also, all except Fu et al. [16] assumed that the net charge density in the fluid is constant during the movement of the electrolyte solution through the channel, and applied the Boltzmann distribution for the ionic concentration. Strictly speaking, the Boltzmann distribution is applicable only when the fluid is at rest. The ionic concentration distributions are affected by the presence of the fluid motion, especially secondary motion perpendicular to the walls. Therefore, the general Nernst-Planck equation should be used to describe the ionic concentration distributions in EOF.

In the present work, numerical techniques are used to study the effects of non-uniform zeta potentials on electro-osmotic flow between parallel plates (flat channel) with particular attention to reservoir effects and variable ionic concentration due to flow. The working fluid is a constant-property Newtonian liquid. To investigate the effects of a non-uniform zeta potential, a variety of distributions are considered at the walls such as increasing, decreasing, parabolic, and patchy distributions along the channel. The governing equations consist of a Laplace equation for the distribution of external electric potential ϕ, a Poisson equation for the distribution of the EDL potential ψ, the Nernst-Planck equation for the distribution of the charge density in the fluid, and the modified Navier-Stokes equations for the flow field, which are solved numerically using a finite-volume method in a generalized coordinate system.

2 Mathematical Model

Most microchannels encountered in practical applications have large cross-sectional aspect ratios, and therefore, fluid flows in such flat channels can be realistically modeled as 2D flows between parallel plates. In the present study, the electro-osmotic flow is created in a straight finite-length channel positioned between two liquid reservoirs, which are equipped with electrodes to produce an electric field tangential to the EDL. The system geometry and the associated nomenclature are as shown in Fig. 1.

2.1 Electric Field. In electro-osmotic flows, two types of electric field can be identified with respect to their origin. The first one is an applied or external field generated by the electric charge on the anode and cathode. The distribution of electrical potential between the electrodes is represented by $\phi(x,y)$, and the resulting electric field is given by $-\nabla\phi$. The second electric field is due to the net charge distribution in the EDL. The variation of electrical potential in this region is represented by $\psi(x,y)$, and the associated electric field is given by $-\nabla\psi$. The total electric field is simply a linear superposition of these two parts.

2.1.1 External Electric Potential, ϕ. The required external electric field is created by placing electrodes in the reservoirs and applying a voltage difference across them. Here, as shown in Fig. 1, the constant potentials on the anode and cathode are specified to be ϕ_1 and ϕ_2, respectively, and the distribution of electric potential across the system is obtained by solving the following Laplace equation:

$$\frac{\partial^2\phi}{\partial x^2}+\frac{\partial^2\phi}{\partial y^2}=0 \tag{1}$$

Introducing $\bar{x}=x/H$, $\bar{y}=y/H$, $\bar{\phi}=\phi/(E_{\text{ref}}H)$ where $E_{\text{ref}}=(\phi_1-\phi_2)/(L+2L_R)$ is the characteristic electric field strength, and after dropping the superscripts, the dimensionless form of this equation is found to be identical to itself. For boundary conditions, ϕ_1 and ϕ_2 are specified, and the normal gradient of ϕ is set equal to zero at the walls. It is worth noting that inside the microchannel (sufficiently far from the entrance and exit) ϕ varies linearly with axial position.

2.1.2 Electric Potential in the EDL, ψ. The electric double layer forms due to the interaction of the ionized solution with the static charges on the surfaces. The electric potential of ions in the EDL is related to the net electric charge density, ρ_e, via the following Poisson equation:

$$\frac{\partial^2\psi}{\partial x^2}+\frac{\partial^2\psi}{\partial y^2}=-\frac{\rho_e}{\varepsilon_r\varepsilon_0} \tag{2}$$

where ε_r is the dielectric constant of the solution, and ε_0 is the permittivity of vacuum. For a symmetric electrolyte i.e., the co-ions and the counter-ions have the same charge valance, $(z^+=-z^-=z)$, the net electric charge density is given by:

$$\rho_e=ze(n^+-n^-) \tag{3}$$

where n^+ and n^- are the concentrations of the positive and negative ions, respectively, and e is the elementary electric charge. Introducing $\bar{\psi}=\psi/(k_bT/ze)$, $(\bar{n})^+=n^+/n_0$, $(\bar{n})^-=n^-/n_0$, $\bar{\rho}_e=\rho_e/(zen_0)$, and after dropping the superscripts, Eq. (2) and Eq. (3) are written in dimensionless form as:

$$\rho_e=n^+-n^- \tag{4}$$

$$\frac{\partial^2\psi}{\partial x^2}+\frac{\partial^2\psi}{\partial y^2}=-\frac{k^2\rho_e}{2} \tag{5}$$

where $n_0=CN_A$ is the bulk number concentration of ions in the electrolyte solution, C is the molar concentration of ions, N_A is Avogadro's number, T is the absolute temperature, and k_b is the Boltzmann constant. The parameter $K=[2z^2e^2n_0/(\epsilon_r\epsilon_0k_bT)]^{1/2}$ is called the Debye-Huckel parameter, and its reciprocal represents the characteristic EDL thickness. The coefficient $k=KH$ in Eq. (5) is referred to as the double-layer thickness parameter. This equation is subject to the following dimensionless boundary conditions: $\psi=\zeta$ at the walls, where ζ is the zeta potential, and $\partial\psi/\partial x=0$ at the inlet and outlet.

2.2 Distribution of Ionic Concentration. In order to find the net charge density ρ_e, the distributions of ionic concentrations (n^+ and n^-) must be determined. This is achieved by solving the following transport equation, known as the Nernst-Planck equation:

$$\frac{\partial(un^+)}{\partial x}+\frac{\partial(vn^+)}{\partial y}=\frac{\partial}{\partial x}\left(D^+\frac{\partial n^+}{\partial x}\right)+\frac{\partial}{\partial y}\left(D^+\frac{\partial n^+}{\partial y}\right)+\frac{\partial}{\partial x}\left[D^+n^+\left(\frac{ze}{k_BT}\right)\left(\frac{\partial\phi}{\partial x}+\frac{\partial\psi}{\partial x}\right)\right]+\frac{\partial}{\partial y}\left[D^+n^+\left(\frac{ze}{k_BT}\right)\left(\frac{\partial\phi}{\partial y}+\frac{\partial\psi}{\partial y}\right)\right] \tag{6a}$$

$$\frac{\partial(un^-)}{\partial x}+\frac{\partial(vn^-)}{\partial y}=\frac{\partial}{\partial x}\left(D^-\frac{\partial n^-}{\partial x}\right)+\frac{\partial}{\partial y}\left(D^-\frac{\partial n^-}{\partial y}\right)-\frac{\partial}{\partial x}\left[D^-n^-\left(\frac{ze}{k_BT}\right)\left(\frac{\partial\phi}{\partial x}+\frac{\partial\psi}{\partial x}\right)\right]-\frac{\partial}{\partial y}\left[D^-n^-\left(\frac{ze}{k_BT}\right)\left(\frac{\partial\phi}{\partial y}+\frac{\partial\psi}{\partial y}\right)\right] \tag{6b}$$

where u and v are the velocity components in the x and y directions, and D^+ and D^- are the diffusion coefficients of the positive and negative ions, respectively. The first two terms on the right hand side of these equations are the familiar diffusion terms due to concentration gradients, while the last two terms represent diffusion due to electric potentials. Usually, the latter are referred to as the migration terms [18]. In non-dimensional form, these equations become:

$$\frac{\partial(un^+)}{\partial x}+\frac{\partial(vn^+)}{\partial y}=\frac{1}{\mathrm{ReSc}^+}\left\{\frac{\partial^2 n^+}{\partial x^2}+\frac{\partial^2 n^+}{\partial y^2}+\frac{\partial}{\partial x}\left[n^+\left(A\frac{\partial\phi}{\partial x}+\frac{\partial\psi}{\partial x}\right)\right]+\frac{\partial}{\partial y}\left[n^+\left(A\frac{\partial\phi}{\partial y}+\frac{\partial\psi}{\partial y}\right)\right]\right\} \tag{7a}$$

$$\frac{\partial(un^-)}{\partial x}+\frac{\partial(vn^-)}{\partial y}=\frac{1}{\mathrm{ReSc}^-}\left\{\frac{\partial^2 n^-}{\partial x^2}+\frac{\partial^2 n^-}{\partial y^2}-\frac{\partial}{\partial x}\left[n^-\left(A\frac{\partial\phi}{\partial x}+\frac{\partial\psi}{\partial x}\right)\right]-\frac{\partial}{\partial y}\left[n^-\left(A\frac{\partial\phi}{\partial y}+\frac{\partial\psi}{\partial y}\right)\right]\right\} \tag{7b}$$

where $\mathrm{Sc}^{\pm}=\mu/\rho D^{\pm}$ is the Schmidt number, $\mathrm{Re}=\rho U_{\mathrm{ref}}H/\mu$ is the Reynolds number, $U_{\mathrm{ref}}=-\varepsilon_r\varepsilon_0 E_{\mathrm{ref}}\zeta/\mu$ is the characteristic EOF velocity, ρ is the density, μ is the dynamic viscosity, and $A=E_{\mathrm{ref}}H/(k_bT/ze)$ is a non-dimensional parameter representing the ratio of the externally applied voltage to the elementary voltage. It is useful to note that the elementary voltage is 25 mV at ambient temperature (293 K). These equations are subject to the following dimensionless boundary conditions: at the inlet $n^+=n^-=1$, at the outlet $\partial n^+/\partial x=\partial n^-/\partial x=0$, and at the walls, local thermodynamic equilibrium prevails such that $n^+|_{\mathrm{walls}}=\exp(-\zeta)$ and $n^-|_{\mathrm{walls}}=\exp(\zeta)$ based on the Boltzmann probability distribution.

2.3 Modified Navier-Stokes Equations. In electro-osmotic flows, an electric field is externally applied to an electrolyte solution which has been affected by the static charges existing on the walls, and the resulting electric body force must be incorporated into the momentum equations. In micro-scale flows, particularly for liquids, the flow field can still be modeled by continuum mechanics. Thus, the modified Navier-Stokes equations for the steady electro-osmotic flow of a constant-property Newtonian fluid are:

$$\frac{\partial u}{\partial x}+\frac{\partial v}{\partial y}=0 \tag{8}$$

$$\frac{\partial(\rho uu)}{\partial x}+\frac{\partial(\rho vu)}{\partial y}=-\frac{\partial P}{\partial x}+\mu\left(\frac{\partial^2 u}{\partial x^2}+\frac{\partial^2 u}{\partial y^2}\right)-\rho_e\left(\frac{\partial\phi}{\partial x}+\frac{\partial\psi}{\partial x}\right) \tag{9a}$$

$$\frac{\partial(\rho uv)}{\partial x}+\frac{\partial(\rho vv)}{\partial y}=-\frac{\partial P}{\partial y}+\mu\left(\frac{\partial^2 v}{\partial x^2}+\frac{\partial^2 v}{\partial y^2}\right)-\rho_e\left(\frac{\partial\phi}{\partial y}+\frac{\partial\psi}{\partial y}\right) \tag{9b}$$

where P is pressure, and the last terms in Eq. (9*a*) and Eq. (9*b*) represent the electric body force acting on the fluid. In the above equations, $\partial\phi/\partial x$ and $\partial\phi/\partial y$ are the components of the externally applied electrical field, both of which have finite values at the entrance and exit of the microchannel. However, $\partial\phi/\partial y=0$ in regions sufficiently far from the entrance and exit in the present geometry.

The momentum equations can be nondimensionalized using $\bar{u}=u/U_{\mathrm{ref}}$, $\bar{v}=v/U_{\mathrm{ref}}$, $\bar{P}=P/\rho U_{\mathrm{ref}}^2$, and after dropping the superscripts, Eq. (9*a*) and Eq. (9*b*) become:

$$\frac{\partial(uu)}{\partial x}+\frac{\partial(vu)}{\partial y}=-\frac{\partial P}{\partial x}+\frac{1}{\mathrm{Re}}\left(\frac{\partial^2 u}{\partial x^2}+\frac{\partial^2 u}{\partial y^2}\right)-B\rho_e\left(A\frac{\partial\phi}{\partial x}+\frac{\partial\psi}{\partial x}\right) \tag{10a}$$

Table 1 Constants and thermo-physical properties

Variable	Value [unit]
D	2×10^{-9} [m^2/s]
e	1.602×10^{-19} [C]
k_b	1.381×10^{-23} [J/K]
N_a	$6.022\times10^{+23}$ [1/mol]
ϵ_r	80
ϵ_0	8.854×10^{-12} [C/V m]
ρ	$1\times10^{+3}$ [kg/m^3]
μ	1×10^{-3}[Pa s]

$$\frac{\partial(uv)}{\partial x}+\frac{\partial(vv)}{\partial y}=-\frac{\partial P}{\partial y}+\frac{1}{\mathrm{Re}}\left(\frac{\partial^2 v}{\partial x^2}+\frac{\partial^2 v}{\partial y^2}\right)-B\rho_e\left(A\frac{\partial\phi}{\partial y}+\frac{\partial\psi}{\partial y}\right) \tag{10b}$$

where $B=n_0k_bT/\rho U_{\mathrm{ref}}^2$ is a dimensionless parameter representing the ratio of ionic pressure to dynamic pressure. These equations are subject to the following dimensionless boundary conditions: at walls of the microchannel, all components of velocity are zero and the boundary condition for pressure is:

$$\nabla^2 P=Bk^2\rho_e^2/2 \tag{11}$$

This equation has been derived by taking the divergence of the incompressible momentum equation at the wall where the advection terms are zero, $\nabla^2\phi=0$ and $\nabla^2\psi=-k^2\rho_e/2$. Everywhere in the microchannel, except in the entrance and exit regions, the pressure gradient in the flow direction is constant or changes very slowly, and therefore, Eq. (11) can be simplified to:

$$\partial^2 P/\partial n^2=Bk^2\rho_e^2/2 \tag{12}$$

where n is the direction normal to the wall. At the inlet and outlet of the problem domain: $\partial u/\partial x=0$, $v=0$. With due attention to electro-osmotic pumping requirements, the present work is confined to cases with a specified electric body force and zero pressure difference between the reservoirs. It should be noted that using a zero pressure gradient as a boundary condition for one end of the microchannel while the other end has a specified pressure will not lead to a unique solution unless the mass flow rate is specified.

2.4 Input Data. In the present study, it is assumed that the microchannel is made of silicon with the zeta potential at the wall varying in the range $-100\ \mathrm{mV}\le\zeta\le-25\ \mathrm{mV}$. The working fluid is water with KCl in solution, where the bulk ionic molar concentration is specified as $C=10^{-6}$ kmol/m^3. Hence, the bulk ionic number concentration is $n_0=6.022\times10^{20}$ ions/m^3. It is further assumed that the temperature of the solution is constant at 293 K, and the mass diffusion coefficient of K^+ and Cl^- ions are approximately equal, $D=D^+\cong D^-$.

All other constants and thermo-physical properties used in the computations are listed in Table 1 [19]. With these values, the Schmidt number is $\mathrm{Sc}=\mu/(\rho D)=500$ and, the Debye-Huckel parameter becomes $K=3.284\times10^6$ m^{-1}. In the present work, the height of the micro-channel H is not an input parameter, but rather, it is calculated using the specified non-dimensional EDL thickness parameter k, that is $H=k/K$. Furthermore, the Reynolds number $\mathrm{Re}=\rho U_{\mathrm{ref}}H/\mu$ is an input parameter from which the reference velocity U_{ref} is calculated. Note that U_{ref} is directly related to the reference external electric field E_{ref} and, therefore, the corresponding applied potential difference $(\phi_1-\phi_2)$ is known from $E_{\mathrm{ref}}=(\phi_1-\phi_2)/(L+2L_R)$. Numerically, ϕ_2 is set to zero, and ϕ_1 is simply determined from $\phi_1=E_{\mathrm{ref}}(L+2L_R)$. For cases involving a variable zeta potential, U_{ref} is based on the average value of the zeta potential along the channel.

In all numerical cases considered here, Re and k are specified as 0.02, and 32, respectively. These values correspond to H

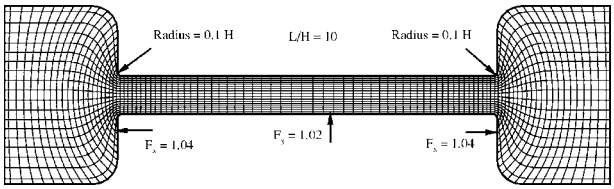

Fig. 2 A typical algebraically generated mesh

$\cong 10$ μm and $U_{\text{ref}} \cong 2$ mm/s, associated with a reference electric field strength of $E_{\text{ref}} \cong 28$ V/mm for $\zeta = -100$ mV.

3 Numerical Method

The governing equations are solved numerically using the well known finite-volume method with collocated variables in a body fitted coordinate system. The SIMPLEC [20] scheme handles the linkage between velocity and pressure fields. However, to avoid the checkerboard effect in the pressure field due to the use of collocated variables, the interpolation scheme of Rhie-Chow [21] is used to calculate the convecting mass flow rates. The diffusive and convective terms are evaluated using a central differencing scheme, and thus, the method is second order accurate in space. The resulting algebraic system of equations is then solved using a line-by-line iterative method with the tri-diagonal matrix algorithm [22].

The computations begin by solving Eq. (1) to obtain the distribution of the externally applied electrical potential (ϕ) and the associated electric field. Initially, the electric potential in the EDL (ψ) is assigned a zero value everywhere, while at the walls $\psi = \zeta$. Once Eq. (5) is solved with initially zero n^+ and n^-, the ψ field develops, and subsequently the Nernst-Planck equations [Eqs. (7*a*) and (7*b*)] give finite values for n^+ and n^-. The net electrical charge density (ρ_e) then follows from Eq. (4). Thus, the electric body force needed to move the fluid is developed, and the next iterative stages start. In stage 1, the computations of flow field begin with a guessed pressure field, and the modified momentum equations [Eqs. (9*a*) and (9*b*)] are solved to obtain the velocity field. Using this velocity field, the continuity equation (Eq. (8)) is solved to correct the pressure and velocity fields as described by Van Doormaal and Raithby [20]. The flow field affects the distribution of the net electrical charge density, and therefore, in stage 2, the Nernst-Planck equations are solved again to obtain the distribution of the ionic concentrations. Subsequently, the distributions of the net electrical charge density and EDL potential are recalculated with Eq. (4) and Eq. (5), respectively. Using the new ρ_e and ψ fields, the iterations are continued until convergence is achieved. The convergence criteria for the residuals of all equations are set to 1×10^{-16} and double precision is used for all variables.

A typical algebraically generated non-orthogonal mesh used in the present work is shown in Fig. 2, where a coarse grid is displayed for clarity. The radii of corners at the intersection of reservoirs with the microchannel are $0.1H$ and F_x is the grid expansion factor at these locations, while F_y is another expansion factor near the walls. These expansion factors, especially F_y, must be selected with care such that there will be a sufficient number of grid points within the EDL to capture the distribution of the associated potential ψ. It should be noted that for a given k, although the EDL thickness is fixed, the number of grid points required within the EDL varies depending on the value of the zeta potential. An EDL with a larger zeta potential requires more grid points near the walls due to associated steeper ψ gradients there.

To verify the accuracy of the code, the numerical results are compared with the classical analytical solution for an *ideal* electro-osmotic flow between parallel plates (*uniform zeta potential and no reservoirs*). Here, the important assumption is that the axial pressure gradient is zero, which is a reasonable assumption for fully developed EOF in very long microchannels without any reservoirs. The external electric potential ϕ is found from Eq. (1), which in this case has a simple linear solution, $\phi \sim x$. In the Nernst-Planck equation, the advection term becomes negligible as compared to the diffusion and migration terms, and the solution yields the Boltzmann distribution: $n^{\pm} = \exp(\mp\psi)$. Thus, the net electrical charge density is given by $\rho_e = n^+ - n^- = -2\sinh(\psi)$, and Eq. (5) is reduced to the Poisson-Boltzmann equation:

$$\frac{d^2\psi}{dy^2} = k^2 \sinh(\psi) \tag{13}$$

The Debye-Huckel approximation, $[\psi/(k_bT/ze)] \ll 1$, may be used to further simplify this equation. With this approximation, the absolute value of the zeta potential should be less than 25 mV; however, zeta potentials up to 100 mV can be used with reasonable accuracy. The simplified equation becomes:

$$\frac{d^2\psi}{dy^2} = k^2\psi \tag{14}$$

It can be easily shown that the solution of this equation with $\psi|_{y=0} = \zeta$ and $\partial\psi/\partial y|_{y=H/2} = 0$ as the boundary conditions is:

$$\frac{\psi}{\zeta} = \frac{\cosh[k(y/H - 1/2)]}{\cosh(k/2)} \tag{15}$$

In Fig. 3(*a*), the numerical results are compared with the analytical solution given above for $k = 15$, $k = 32$, and $k = 100$ with excellent agreement. Similarly, excellent agreement is observed in Fig. 3(*b*) between the present numerical results for the ionic concentrations (n^+ and n^-) and those obtained from the Boltzmann distribution $n^{\pm} = \exp(\mp\psi)$. The associated flow field is determined using the momentum equations [Eqs. (10*a*) and (10*b*)], which reduce to:

$$\frac{1}{\text{Re}}\frac{d^2u}{dy^2} + A\rho_e\left(-\frac{d\phi}{dx}\right) = 0 \tag{16a}$$

$$-\frac{dP}{dy} + B\rho_e\left(-\frac{d\psi}{dy}\right) = 0 \tag{16b}$$

Clearly, in this flow, the net electric body force is in balance with the friction at the walls and, while the axial pressure gradient is zero, there is a significant transverse pressure gradient induced by the EDL potential. The solution of Eq. (16*a*) and Eq. (16*b*) yields:

$$\frac{u}{U_{\text{ref}}} = 1 - \frac{\cosh[k(y/H - 1/2)]}{\cosh(k/2)} \tag{17}$$

$$\frac{P}{P_{\max}} = \left(\frac{\cosh[k(y/H - 1/2)]}{\cosh(k/2)}\right)^2 \tag{18}$$

where $U_{\text{ref}} = -\varepsilon_0\varepsilon_r\zeta E/\mu$ with $E = -d\phi/dx = (\phi_1 - \phi_2)/(L + 2L_R)$, and $P_{\max} = z^2e^2\zeta^2n_0/(k_bT)$ which occurs at the walls. Note that in this case the actual applied electric field is equal to E_{ref} defined previously as the characteristic electric field strength. As shown in Figs. 4(*a*) and 4(*b*), the agreement between the present numerical predictions and this analytical solution is excellent.

A grid-size study with $k = 32$, $L/H = 5$, $\text{Re} = 0.02$ and $\zeta = -25$ mV shows that $N_i \times N_j$ and F_y should be at least 101×61 and 1.02, respectively. Here, N_i is the number of grid points in the flow direction, and N_j is the number of points in the transverse direction. As can be seen in Fig. 5, for a numerical grid with 151×91 points, the velocity profile has excellent agreement with the analytical solution.

The analytically predicted mass flow rate per unit depth of channel is given by:

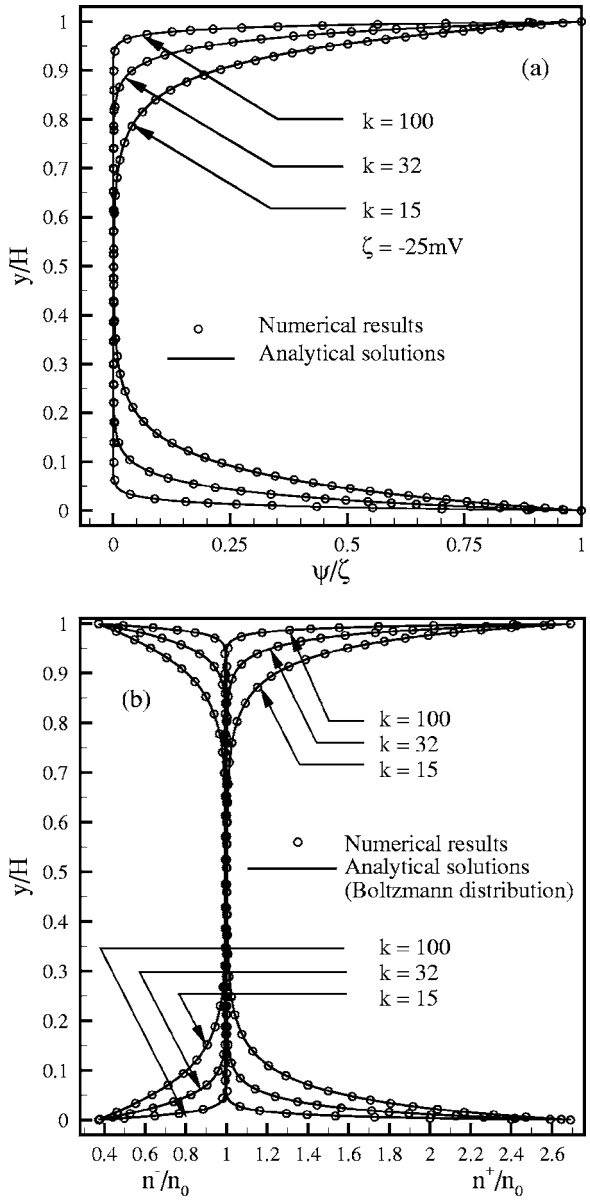

Fig. 3 (*a*) **EDL potential, and** (*b*) **the ionic concentrations** n^+ **and** n^- **distributions for an ideal EOF with Re=0.02,** $\zeta=-25$ **mV,** $k=15$, $k=32$, **and** $k=100$

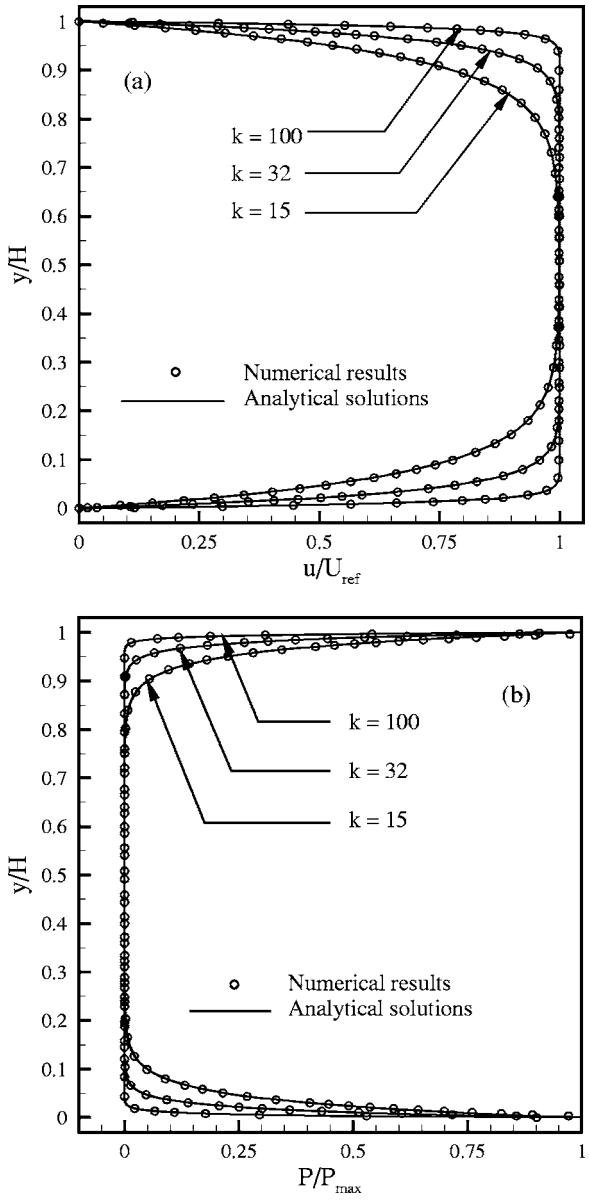

Fig. 4 (*a*) **Velocity, and** (*b*) **pressure distributions in an ideal EOF with Re=0.02,** $\zeta=-25$ **mV,** $k=15$, $k=32$, **and** $k=100$

$$\dot{M} \equiv \frac{\dot{m}}{\rho U_{\text{ref}} H} = 1 - \frac{\tanh(k/2)}{k/2} \tag{19}$$

For a grid with 51×31 points, the numerically calculated flow rate per unit depth of channel is $\dot{M}=0.91725$. For grids with 101×61 and 151×91 points, the corresponding flow rates are $\dot{M}=0.93540$ and $\dot{M}=0.93725$, respectively, while the exact flow rate based on Eq. (19) is $\dot{M}=0.93750$. Consequently, using a set of grid points around 151×101 for $\zeta=-25$ mV produces a grid-independent solution. As mentioned above, the number of grid points and the expansion factors depend on the value of the zeta potential. For example, $N_i\times N_j$ and F_y should be at least 151×141 and 1.05, respectively, when $\zeta=-100$ mV for the same case of $k=32$.

4 Results and Discussion

In this section, results are presented for electro-osmotic flows in finite-length flat channels connected to fluid reservoirs. Cases involving prescribed uniform, continuously variable, and patchy zeta potential distributions at the walls will be examined.

4.1 Uniform Zeta Potential. In applications (such as a lab-on-chip device), the microchannels have finite lengths and communicate with fluid reservoirs. Obviously, the flow passes through regions with abrupt contraction and expansion at the channel inlet and exit, and therefore, the problem cannot be realistically analyzed based on the ideal EOF model presented in the preceding section. In other words, the entrance and exit effects may significantly affect the whole flow pattern, especially in the case of relatively short length channels.

The geometry of the problem under consideration is shown in Fig. 1. As an initial case, it is assumed that the microchannel and the reservoirs are made of different materials such that only the channel walls have a finite zeta potential, while $\zeta=0$ for the reservoir walls. Figures 6 and 7 show the numerical results for the

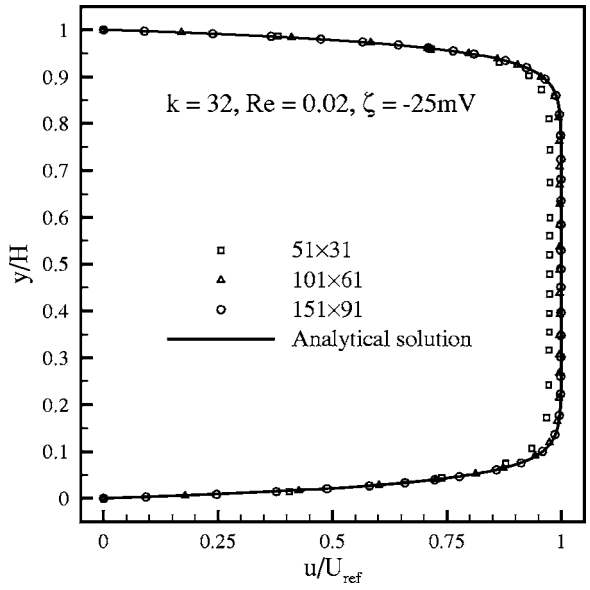

Fig. 5 The effect of grid size on the velocity profile in an ideal EOF with Re=0.02, ζ=−25 mV, k=32, L/H=5 and F_y=1.02

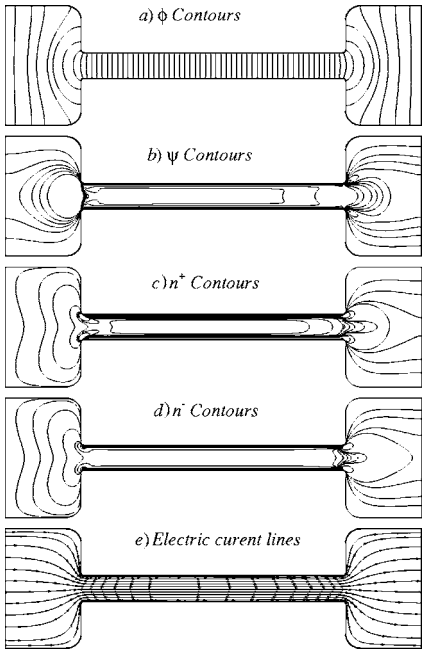

Fig. 7 EOF with constant zeta potential at micro-channel walls; ζ=−50 mV, L/H=10, Re=0.02, and k=32

flow and electric fields for an EOF with ζ=−50 mV, L/H=10, Re=0.02, k=32, and equal reservoir pressures. Although the zeta potential in the flow direction is constant, Fig. 6(*a*) confirms that the pressure contours are changing throughout the microchannel, which will be discussed in detail in the next section. Figure 6(*b*) shows that, in contrast to the corresponding ideal case (Fig. 5), the velocity profiles do not have "plug profiles" even in the fully developed regions of the flow, but rather, display concavity in the core flow. This behavior is due to a lack of body force on the electrically neutral core fluid, and the existence of an adverse pressure gradient across the entire channel (see Fig. 8). Figures 6(*c*) and 6(*d*) show the velocity contours, and it is observed that fully developed conditions (v=0, $\partial u/\partial x$=0) are attained within a distance of about $H/2$ from the entrance, and persist to within a similar distance from the exit of the channel. Given the large and sudden flow contraction, such a short entrance length is remarkable. It appears that the negative effects of sudden contractions and expansions on the flow development are largely offset by the electric body force acting on the fluid particles in the EDL parallel to the walls. Figure 6(*e*) shows the streamlines, and as expected, flow separation is observed in the corner regions of the reservoirs. Later, it will be demonstrated that these recirculation zones are eliminated in the presence of electric body forces in the reservoirs.

Figure 7(*a*) shows the distribution of the externally applied electric potential ϕ in the system. It is important to note that the

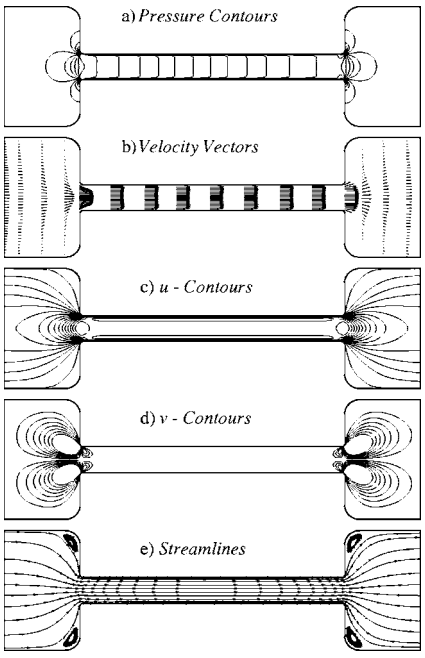

Fig. 6 EOF with constant zeta potential at micro-channel walls; ζ=−50 mV, L/H=10, Re=0.02, and k=32

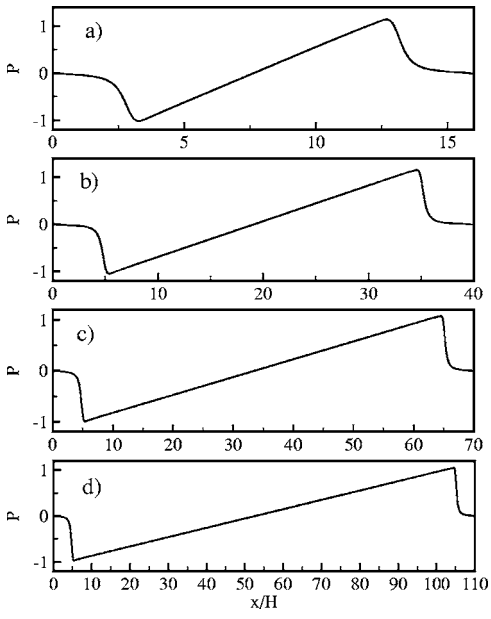

Fig. 8 Pressure distribution on the center plane of a micro-channel between two identical reservoirs. EOF with ζ=−50 mV, Re=0.02, k=32; (*a*) L/H=10, (*b*) L/H=30, (*c*) L/H=60, (*d*) L/H=100.

solution of the Laplace equation [Eq. (1)] in this domain has a great effect on the other results. Since the domain has a slender section in the micro-channel region, and because the only boundary condition in this region is a Neumann-type of condition ($d\phi/dn=0$ at the micro-channel walls), the specified boundary potentials ϕ_1 and ϕ_2 at the inlet and outlet of the problem domain cannot easily affect the midsection, and therefore, obtaining an accurate solution for the applied electric field becomes computationally very intensive. This difficulty becomes more acute when the L/H ratio is increased. Since non-converged results for the external electric field will lead to an incorrect flow pattern, a very accurate solution of the ϕ field is essential.

Figure 7(b) shows that the distribution of the EDL potential ψ near the ends of the microchannel is completely different from that in the middle section. At the inlet and exit regions of the channel, the nonaxial or secondary motion of the flow affects the distribution of positive and negative ions via the advection terms in the Nernst-Planck equation. Figures 7(c) and 7(d) show the distribution of positive and negative ions, respectively. These ionic fields are quite complex and cannot be obtained from the Boltzmann distribution. Figure 7(e) shows the electric current lines. In view of the significance of bulk fluid motion on ion transport, it is not surprising to see much similarity between the electric current lines and the flow stream lines.

Despite the zero pressure difference prescribed between the reservoirs, an adverse pressure gradient develops in the system as shown in Fig. 8. The trends observed in this figure are consistent with key features of flows through abrupt geometric contractions and expansions (Kays and London [23]). In general, the pressure drop at the entrance of the channel has both reversible and irreversible components. The reversible component is simply due to the abrupt reduction in the flow area, while the irreversible losses are associated with shear friction and free expansion following the formation of a vena contracta inside the channel due to flow separation at its entrance. Also, the evolution of the velocity profile leads to changes in the momentum rate and associated pressure losses. The underlying physics is the same at the channel exit, but in contrast to the inlet conditions, the reversible and irreversible contributions are in the opposite direction such that a pressure increase occurs due to flow area expansion, while the irreversible free expansion, shear friction, and momentum rate changes result in pressure losses. Hence, the pressure at the exit may increase or decrease depending on the relative magnitude of these reversible and irreversible components.

In the case of an EOF in a microchannel, the electric body force acting on the EDL prevents flow separation at the sharp entrance to the channel (see Fig. 6), and therefore, the inlet pressure losses are smaller as compared to an ordinary pressure-driven flow. In the very low Reynolds number environment of a typical EOF, the irreversible pressure losses at the exit of a channel are greater than the pressure recovery due to flow area expansion, and therefore, there is a net pressure drop at the exit as well. Step changes in the zeta potential at the entrance and exit of the channel also affect these pressure changes, which will be discussed in the next section. Since the reservoirs are at the same pressure, the applied body force must then not only maintain the momentum balance along the channel, but also ensure that the fluid builds up sufficient pressure to overcome the irreversible losses at the exit. Thus, an adverse pressure gradient develops along the channel as shown in Fig. 8. This figure also shows that an adverse pressure gradient exists everywhere in the channel regardless of its length, which is in agreement with the observations of Zhang et al. [11]. However, there is a contradiction with Yang et al. [8], whose numerical results indicate a zero pressure gradient along the channel except at the inlet and exit regions. The reason for this discrepancy can be traced directly to the accuracy of the solution for the external electric field, which is of critical importance as mentioned earlier.

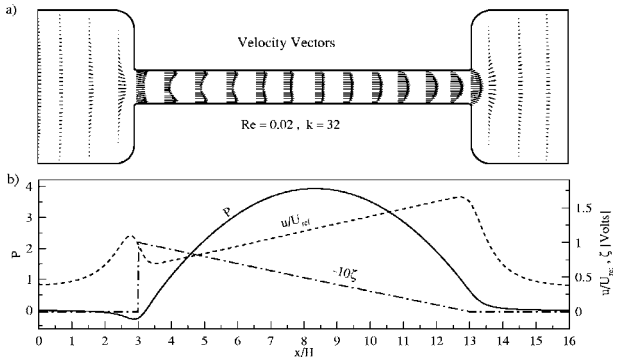

Fig. 9 EOF with a linear change in zeta potential. $L/H=10$, $\mathrm{Re}=0.02$, $k=32$; (a) velocity vectors, (b) velocity and pressure distributions on center plane.

The present authors have also obtained such erroneous results with partially converged numerical solutions of the external electric field.

4.2 Non-Uniform Zeta Potentials. As mentioned earlier, quite often, the zeta potential varies along the micro-channel walls for a variety of reasons ranging from manufacturing defects to adsorption of organics at the walls. In order to investigate the effects of non-uniform zeta potentials, a number of problems involving decreasing, increasing, parabolic, and patchy zeta potential distributions are considered in this section. Clearly, a variable zeta potential distribution along the channel is accompanied by corresponding axial variations in the electrical body force, resulting in a non-uniform electro-osmotic pumping effect. Considering the continuity requirements, this non-uniform pumping effect leads to a non-linear induced pressure distribution, and therefore, a fully developed flow region cannot develop in this type of EOF.

For the first problem considered, Fig. 9 shows the specified zeta potential distribution and the predicted velocity vector field as well as the mid-plane pressure and velocity variations. In this case, the prescribed zeta potential distribution leads to a decreasing electro-osmotic pumping effect in the flow direction. Pressure attains a minimum value at the inlet (due to entrance losses explained earlier) and a maximum value approximately midway through the channel before approaching smoothly the prescribed zero pressure level in the discharge reservoir. In the first half of the channel, decreasing pumping effects along with continuity requirements are responsible for the observed trend in the adverse pressure gradient. With higher upstream pressure and rapidly weakening zeta potentials, the flow in the second half of the channel begins to resemble a typical pressure driven laminar flow as seen in Fig. 9(a).

The velocity profiles go through a rather complex evolution along the channel while the mid-plane velocity u/U_{ref} shown in Fig. 9(b) increases linearly except near the entrance and exit. This behavior of the flow can be explained with the help of Fig. 10 which shows the forces acting on the fluid along the channel. The terms shown in this figure are the components of the integral momentum balance given below [Eq. (20)] where the terms have been normalized using the average wall shear stresses $\tau_{w,\mathrm{avg}} = \int_{L_R}^{L+L_R} (\tau_{\mathrm{wall}}/L)dx$:

$$\left[\tau \int_0^H \rho_e E_{\mathrm{tot},x} dy\right] - \frac{d}{dx}\left[\int_0^H \rho u^2 dy\right] - \tau_{\mathrm{walls}} - \frac{d}{dx}\left[\int_0^H P dy\right] = 0 \tag{20}$$

In this equation, τ_{walls} represents friction forces at both the upper and lower plates, and $E_{\mathrm{tot},x} = (A\,\partial\phi/\partial x + \partial\psi/\partial x)$ is the local total electric field. In Fig. 10, the sign of each term in the momentum balance is also included in the plot to highlight the opposing na-

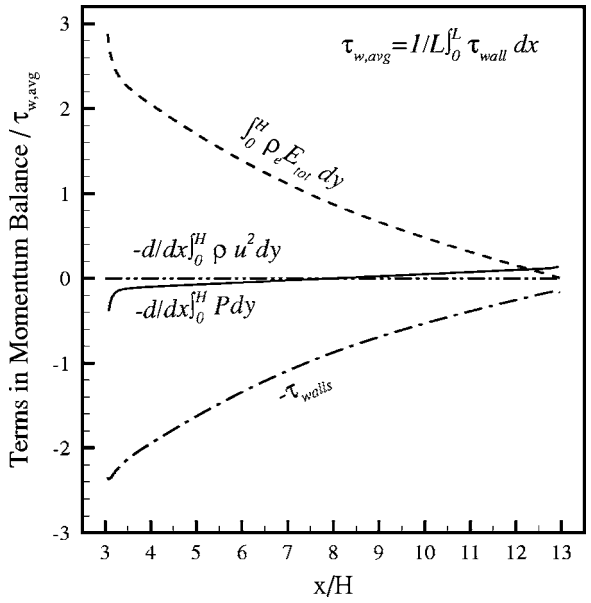

Fig. 10 Comparison of terms in the momentum balance for the case described in Fig. 9

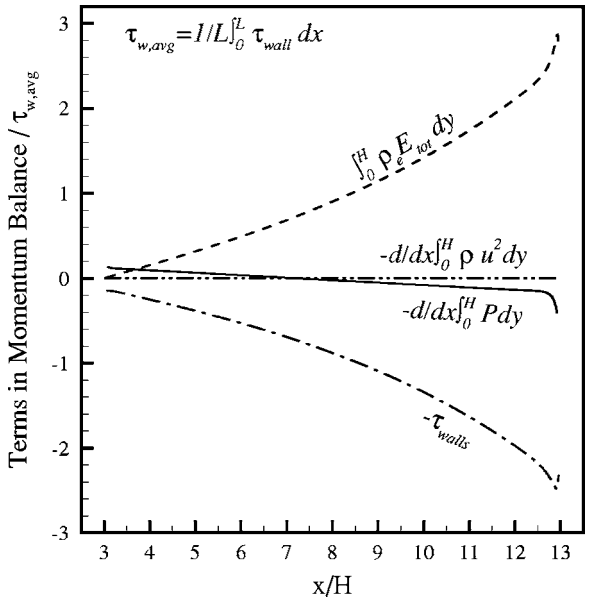

Fig. 12 Comparison of terms in the momentum balance for the case described in Fig. 11

ture of the forces acting on the fluid. This figure indicates that, although the velocity profile goes through significant changes, the acceleration term is essentially zero everywhere. Consistent with the prescribed zeta potential distribution, the electric body force decreases in the flow direction. The observed rapid change in the body force at the entrance of the channel is due to the specified step change in the zeta potential at this location (see Fig. 9). The pressure forces are observed to increase linearly in the flow direction except at the entrance where a rapid rise occurs, again due to the step change of zeta potential there. It is also seen that the pressure forces oppose the electric body force at first, but later ($x/H \geq 7.9$) act as a driving force. In fact, pressure becomes the main driving force for $x/H \geq 12.3$. While this integral analysis is very useful in describing the overall flow behavior along the channel, it should be kept in mind that in the core region of the channel, the electric body force is essentially zero, and therefore, the fluid motion is controlled by the pressure and viscous forces alone. Hence, a direct result of the adverse pressure gradients existing in the first half of the channel is a concave velocity profile in the core region, and the favorable pressure gradients in the second half leads to the parabolic velocity profile at the exit, as seen in Fig. 9.

Figure 11 describes a problem identical to the one defined earlier in Fig. 9 except that in this case, the prescribed zeta potential distribution leads to an increasing electro-osmotic pumping effect in the flow direction rather than a decreasing one. As expected, the velocity and pressure fields now show an inverse pattern as compared to those in Fig. 9, and the predicted flow behavior can be explained with the help of Fig. 12 in a manner similar to the previous problem, which will not be repeated.

The next problem studied involves a parabolic zeta potential distribution along the micro-channel as shown in Fig. 13. In this case, both near the entrance and exit, parabolic velocity profiles are observed as a consequence of weak electric body forces and favorable pressure gradients there. In the middle section of the channel, strong body forces exist near the walls due to the prescribed zeta potential distribution, and these forces coupled with the local adverse pressure gradients result in the observed convex velocity profiles. It is worth noting that the cross-sectional average pressure behaves similar to the mid-plane pressure, and therefore, describing the cross-sectional velocity profile based on the mid-plane pressure is justified. The contribution of each term in the integral momentum balance [Eq. (20)] along the channel is shown in Fig. 14. Again, the acceleration term is found to be negligibly small. Since the electric body force acts mainly near the wall, its behavior affects the wall shear stress very strongly, and therefore,

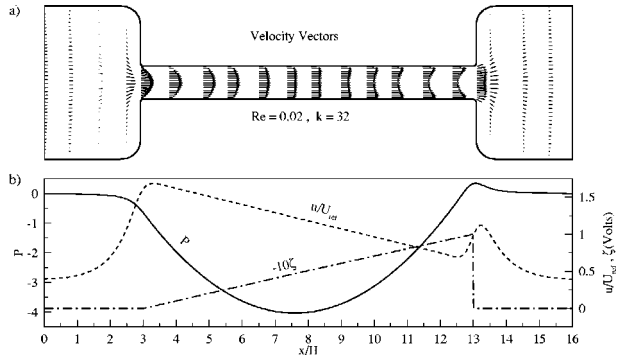

Fig. 11 EOF with a linear change in zeta potential. $L/H=10$, $Re=0.02$, $k=32$; (*a*) velocity vectors, (*b*) velocity and pressure distributions on center plane.

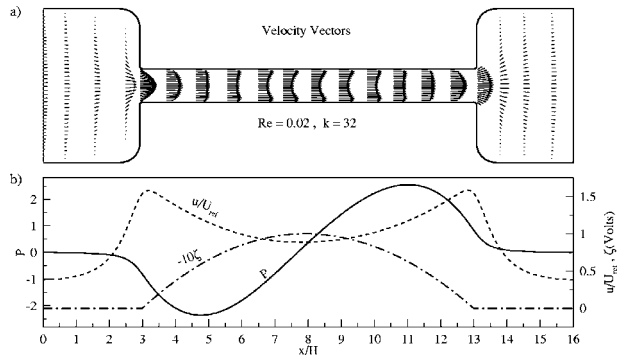

Fig. 13 EOF with a parabolic change in zeta potential. $L/H=10$, $Re=0.02$, $k=32$; (*a*) velocity vectors, (*b*) velocity and pressure distributions on center plane.

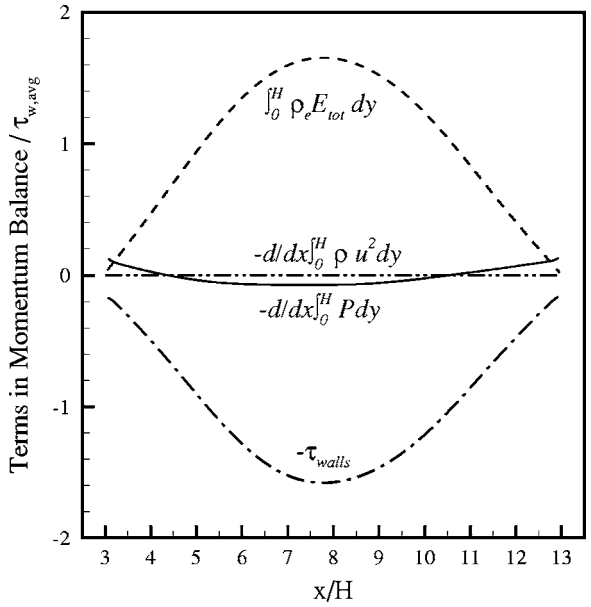

Fig. 14 Comparison of terms in the momentum balance for the case described in Fig. 13

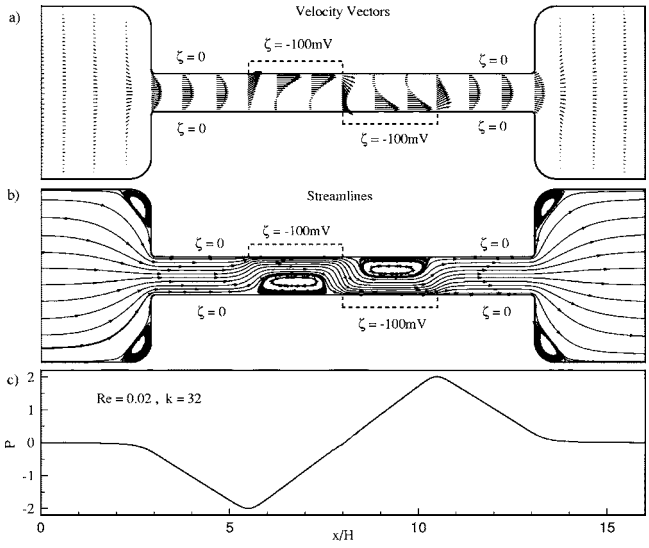

Fig. 16 EOF with a patchy distribution of zeta potential such that $\zeta=-100$ mV on patches and zero elsewhere. $L/H=10$, Re $=0.02$, $k=32$; (*a*) velocity vectors, (*b*) streamlines, (*c*) pressure distribution on center plane.

the latter resisting force essentially mirror images the former driving force. The cross-sectional pressure forces undergo variations consistent with the mid-plane pressure distribution (Fig. 13(*b*)) such that, for a large portion of microchannel ($4.4<x/H<10.6$), the pressure forces oppose the flow. Clearly the adverse pressure gradients prevent the strong body force from forming a plug-flow velocity profile in this region.

In previous cases, it was assumed that the zeta potential variations have continuous distributions. However, patchy distributions are also encountered in electro-osmotic flows where the zeta potentials in one or more regions (here referred to as *patch zones*) are very different from other parts of the channel. First, a distribution with one patch zone located on the upper wall of the microchannel is studied. As identified in Fig. 15, this patch zone is arbitrarily located at $5.5\leq x/H\leq 8$ and assigned a zeta potential of -100 mV while $\zeta=0$ elsewhere. The velocity vectors and the

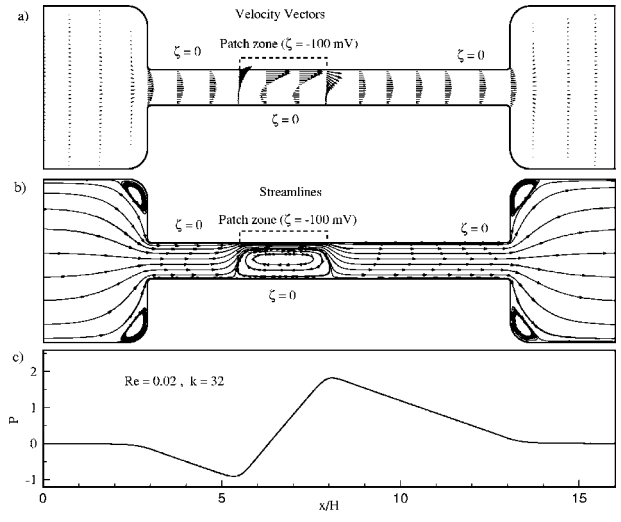

Fig. 15 EOF with a patchy distribution of zeta potential such that $\zeta=-100$ mV in the patch zone and zero elsewhere. $L/H=10$, Re$=0.02$, $k=32$; (*a*) velocity vectors, (*b*) streamlines, (*c*) pressure distribution on center plane.

streamlines clearly show the development of a rather large recirculation region below the patch zone. The adverse pressure gradient observed in this part of the channel (Fig. 15(*c*)) is due to the fact that the localized electric body force creates a flow there, which in turn induces a low pressure region upstream in order to pull fluid from the corresponding reservoir into the channel and a high pressure region downstream for discharge into the outlet reservoir. As can be seen from the velocity vectors (Fig. 15(*a*)), near the upper wall in the patch zone, the electric body force is dominant, resulting in a much increased mass flow rate there. On the other hand, the electrical body force is essentially zero for fluid particles sufficiently far away from the upper wall. Thus, mass conservation requirements together with the presence of an adverse pressure gradient are responsible for the formation of the observed recirculation zone over the lower wall.

With multiple patch zones, more complicated flows emerge in the microchannel. Clearly, the resulting flow pattern is influenced by the location and strength of the patch zones as well as the channel height. Figure 16 shows a case with two patch zones; one located on the upper wall at $5.5\leq x/H\leq 8$, and the other on the lower wall at $8\leq x/H\leq 10.5$. The prescribed zeta potential in both of these zones is -100 mV while it is set to zero for the rest of the system. In this case, two recirculation zones are formed resulting in a highly non-uniform velocity field inside the channel. This configuration is in essence that of two electro-osmotic pumps in tandem, and the resulting pressure distribution across the channel follows the trends explained earlier.

Since reservoirs and channels in a typical microfluidic device (such as a lab-on-chip device) are manufactured from the same material, a more realistic or practical problem involves the presence of patch zones when the zeta potential in the rest of the system is finite as well. Figure 17 shows a case which is identical to the problem defined earlier in Fig. 16 except that in this case, a zeta potential of -25 mV is prescribed everywhere (including the reservoirs) while $\zeta=-100$ mV in the patch zones. In contrast to Fig. 16, the velocity profiles and streamlines in Fig. 17 show that the presence of electrical forces in the channel (especially in the patched zones) can overcome the adverse pressure gradients, thereby preventing the formation of recirculation zones. However, depending on the channel height, and patch strength and location, different flow patterns may emerge. Finally, it is useful to note that the recirculation zones previously present inside the reser-

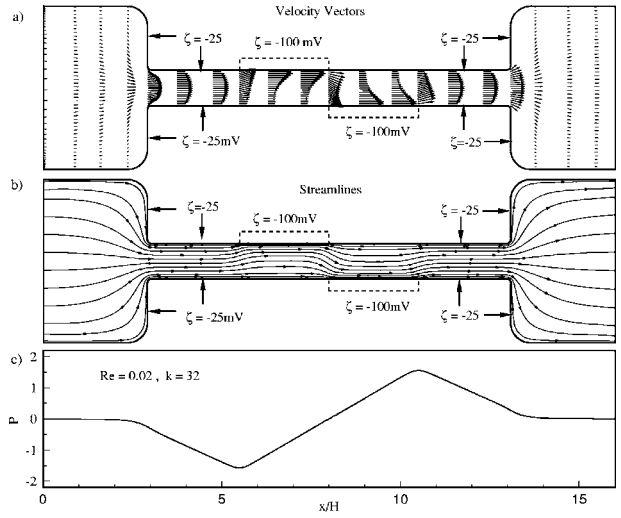

Fig. 17 EOF with a patchy distribution of zeta potential such that ζ=−100 mV on patches and −25 mV elsewhere. L/H=10, Re=0.02, k=32; (*a*) velocity vectors, (*b*) streamlines, (*c*) pressure distribution on center plane.

voirs (Fig. 16) disappear when the fluid acquires additional momentum near the walls in the presence of an electric body force.

5 Conclusions

The effects of non-uniform zeta potentials on electro-osmotic flows in reservoir-connected flat microchannels have been investigated. In the present work, particular attention has been given to reservoir effects, which have been largely ignored in the literature. The flow in the flat microchannel has been modeled realistically as flow between parallel plates, and the associated governing equations have been solved using numerical techniques based on the well-known control-volume method. A new boundary condition has been developed for pressure at the walls, significantly improving the accuracy of the results.

During this study, it has been observed that the flow field predictions are very sensitive to the numerical solution of the Laplace equation for the external electric field with partially converged results leading to erroneous conclusions, particularly for the pressure distribution along the microchannel. The present results show clearly that there is an adverse pressure gradient throughout the channel with pressure drops at both ends of the duct due to irreversible entrance and exit losses associated with the presence of reservoirs. Several cases of electro-osmotic flows involving increasing, decreasing, parabolic, and patchy zeta potential distributions have been investigated, resulting in rather complex flow patterns. The interaction of different forces acting on the fluid along the channel has been examined in detail, showing that no fully developed velocity field may develop in this type of EOF. The present study also demonstrates clearly that patchy zeta potential distributions, which may arise from a variety of sources such as the adsorption of organics in biochips or simply from manufacturing defects, can lead to even more complicated flows with recirculation zones inside microchannels.

Acknowledgment

This research was supported by the Natural Sciences and Engineering Council of Canada, and the Ministry of Science, Research and Technology of Iran. Seyed Ali Mirbozorgi thanks Professors Mohammad Reza Modarres Razavi and Mohammad Moghiman of Ferdowsi University for their help.

Nomenclature

A = ratio of the externally applied voltage to the elementary voltage, $A=E_{\text{ref}}H/(k_bT/ze)$
B = ratio of ionic pressure to dynamic pressure, $B=n_0k_bT/\rho U_{\text{ref}}^2$
D = diffusion coefficient
e = elementary charge of an electron
E_{ref} = Reference applied electric field strength
H = microchannel height
K = Debye-Huckel parameter, $K=(2z^2e^2n_0/\varepsilon_r\varepsilon_0k_bT)^{1/2}$
k = EDL thickness parameter, $k=HK$
k_b = Boltzmann constant
L = microchannel length
L_R = reservoir length
$\dot{m}$ = mass flow rate per unit depth of channel
N_a = Avogadro's number
n^+ = concentration of positive ions
n^- = concentration of negative ions
n_o = bulk ionic concentration
P = pressure
Re = Reynolds number, $\text{Re}=\rho U_{\text{ref}}H/\mu$
Sc = Schmidt number, $\text{Sc}=\mu/\rho D$
u, v = velocity components
U_{ref} = reference velocity, $U_{\text{ref}}=-\varepsilon_r\varepsilon_0E_{\text{ref}}\zeta/\mu$
x, y = Cartesian coordinates
z = valance number of positive and negative ions

Greek Symbols

ε_o = permittivity of vacuum
ε_r = dielectric constant of the electrolyte solution
ϕ = applied electric potential
μ = dynamic viscosity of the working fluid
ρ = density of the working fluid
ρ_e = net electric charge density
ζ = zeta potential
ψ = EDL potential

References

[1] Hunter, R. J., 1981, *Zeta Potential in Colloid Science: Principles and Applications*, Academic, London, pp. 4–7.
[2] Rice, C. L., and Whitehead, R., 1965, "Electrokinetic Flow in a Narrow Cylindrical Capillary," J. Phys. Chem., **69**, pp. 4017–4023.
[3] Andreev, V. P., Dubrovsky, S. G., and Stepanov, Y. V., 1997, "Mathematical Modeling of Capillary Electrophoresis in Rectangular Channels," J. Microcolumn Sep., **9**, pp. 443–450.
[4] Patankar, N. A., and Hu, H. H., 1998, "Numerical Simulation of Electroosmotic Flow," Anal. Chem., **70**, pp. 1870–1881.
[5] Santiago, J. G., 2001, "Electroosmotic Flows in Micro-Channels With Finite Inertial and Pressure Forces," Anal. Chem., **73**, pp. 2353–2365.
[6] Yang, R. J., Fu, L. M., and Lin, Y. C., 2001, "Electroosmotic Flow in Microchannels," J. Colloid Interface Sci., **239**, pp. 98–105.
[7] Yang, R. J., Fu, L. M., and Hwang, C. C., 2001, "Electroosmotic Entry Flow in a Microchannel," J. Colloid Interface Sci., **244**, pp. 173–179.
[8] Yang, R. J., Tseng, T. I., and Chang, C. C., 2005, "End Effects on Electroosmotic Flows in Microchannels," J. Micromech. Microeng., **15**, pp. 254–262.
[9] Ren, L., and Li, D., 2002, "Theoretical Studies of Microfluidic Dispensing Processes," J. Colloid Interface Sci., **254**, pp. 384–395.
[10] Lin, J. Y., Fu, L. M., and Yang, R. J., 2002, "Numerical Simulation of Electrokinetic Focusing in Microfluidic Chips," J. Micromech. Microeng., **12**, pp. 955–961.
[11] Zhang, Y., Gu, X. J., Barber, R. W., and Emerson, D. R., 2004, "An Analysis of Induced Pressure Fields in Electroosmotic Flows Through Microchannels," J. Colloid Interface Sci., **275**, pp. 670–678.
[12] Kang, Y., Yang, C., and Huang, X., 2002, "Dynamic Aspects of Electro-Osmotic Flow in a Cylindrical Microcapillary," Int. J. Eng. Sci., **40**, pp. 2203–2221.
[13] Anderson, J. L., and Idol, W. K., 1985, "Electroosmosis Through Pores With Non-Uniformly Charged Walls," Chem. Eng. Commun., **38**, pp. 93–106.
[14] Herr, A. E., Molho, J. G., Mungal, M. G., and Kenny, T. W., 2000, "Electroosmotic Capillary Flow With Non-Uniform Zeta Potential," Anal. Chem., **72**, pp. 1053–1057.
[15] Ren, L., and Li, D., 2001, "Electroosmotic Flow in Heterogeneous Micro-Channels," J. Colloid Interface Sci., **243**, pp. 255–261.

[16] Fu, L. M., Lin, J. Y., and Yang, R. J., 2003, "Analysis of Electroosmotic Flow With Step Change in Zeta Potential," J. Colloid Interface Sci., **258**, pp. 266–275.
[17] Yang, J., Masliyah, J. H., and Kwok, D. Y., 2004, "Streaming Potential and Electroosmotic Flow in Heterogeneous Circular Microchannels With Non-Uniform Zeta Potential: Requirements of Flow Rate and Current Continuities," Langmuir, **20**, pp. 3863–3871.
[18] Masliyah, J. H., 1994, *Electrokinetic Transport Phenomena*, Alberta Oil Sands Technology and Research Authority, Edmonton, pp. 71–97.
[19] Weast, R., Astle, M. J., and Beyer, W. H., 1983, *CRC Handbook of Chemistry and Physics*, CRC, Boca Raton, FL, pp. E-49, F-11, F-38, F-46.
[20] Van Doormaal, J. P., and Raithby, G. D., 1984, "Enhancement of the SIMPLE Method for Predicting Incompressible Fluid Flows," Numer. Heat Transfer, **7**, pp. 147–163.
[21] Rhie, C. M., and Chow, W. L., 1983, "Numerical Study of the Turbulent Flow Past an Airfoil With Trailing Edge Separation," AIAA J., **21**, pp. 1525–1532.
[22] Patankar, S. V., 1980, *Numerical Heat Transfer and Fluid Flow*, McGraw-Hill, New York, pp. 52–54.
[23] Keys, W. M., and London, A. L., 1984, *Compact Heat Exchangers*, McGraw-Hill, New York, pp. 108–110.

Ejection Process Simulation for a Piezoelectric Microdroplet Generator

An-Shik Yang[1]
Associate Professor
e-mail: asyang@mail.dyu.edu.tw

Wei-Ming Tsai
Graduate Student

Department of Mechanical and Automation Engineering,
Da Yeh University,
Chang Hwa, 515, Taiwan

The purpose of this work is to investigate the liquid ejection process of a novel microdroplet generator applying a computational approach. In simulations, the theoretical model is based on the unsteady three-dimensional conservation equations of mass and momentum with the treatment of surface tension effect at the gas-liquid boundary by the continuous surface force scheme. The volume-of-fluid method along with the piecewise linear interface construction technique is implemented to describe the interfacial movements. The time evolution of droplet meniscus shape is predicted and compared to Shield's microphotographed images for the computer code validation. To explore the practicability of the proposed new microdroplet generator, the flow behavior during the stages of liquid ejection and droplet formation are examined with water as the baseline test fluid for a full ejection cycle of 50 μs. *In addition, 12 numerical experiments were conducted to determine droplet ejection characteristics by systematically varying the ejection time period as well as surface tension and viscosity of liquids. Simulations reveal that a liquid strand with a shorter breakup time and a longer breakup length could be achieved by reducing the ejection time and decreasing the liquid surface tension and viscosity. For the ejection time greater than* 4.0 μs, *the ejection velocity is too low to render a sufficient momentum for droplet breakup. The feasibility studies have demonstrated the potential of this proposed microdroplet generator in dispensing diverse liquids with the surface tension and the viscosity up to* 0.08 N/m *and* 3.0 cps.
[DOI: 10.1115/1.2353275]

Keywords: piezoelectric microdroplet generator, droplet ejection process

1 Introduction

Since the rapid progress of microelectromechanical systems (MEMS) technologies, micro droplet generators have turned out to be one of the essential fluid-handling devices for delivering tiny liquid droplets (with a diameter typically on the order of a micrometer) in precise dosing control. The applications of microdroplet generators are increasingly widespread on various fields, for instance, inkjet printing, biochemical sample transport and screening, direct writing/packaging for deposition of light emitting polymer displays, and integrated circuit cooling [1,2]. Commonly, a microdroplet generator contains a fluid chamber with a nozzle from where liquid is impelled out under mechanical actuation. If the liquid jet gains sufficient momentum to surmount the restoring effects of surface tension and viscous forces, the liquid strand is broken up and proceeds with the droplet formation. The geometric design configurations, fluid properties, and operational principles can substantially affect the size and the velocity of droplets ejected from a generator [3].

There are two major mechanisms for producing microdroplets: the thermal bubble and the piezoelectric systems. In a thermal bubble droplet generator, the pulse current is applied to heat up liquid in the chamber, leading to a growing bubble on the surface of a heater. Working as a pump, the bubble impels liquid out of the nozzle for forming a droplet [4]. The chamber design of thermal droplet generators could be small for high-resolution requirements. Moreover, the fabrication cost is low, since the manufacturing processes are compatible with the accessible IC industry. However, the disadvantages of the generated high temperature on the heater and the requisite evaporation of liquid make it less reliable for droplet control and highly selective to fluids. In contrast, the piezoelectric microdroplet generators employ a piezo disk or tube with an electrical pulse utilized for droplet ejection [5]. The piezoelectric droplet generators are relatively expensive due to the involvement of the micromachining practices and the high-voltage driving system required for operation. Concerning the reliability and the applicability for various kinds of liquids, the piezoactuated droplet generators could provide much more potential for liquid dispensing purpose.

Extensive efforts have been made to examine the droplet ejection process for generating controllable microdroplets. Asai et al. [6,7] and Asai [8] performed both experimental and computational investigations on determining the unsteady droplet length for a thermal bubble jet. Fromm [9] derived an axisymmetric stream-function equation to describe the droplet flow structure with respect to variations of the square-wave pressure history imposed on the nozzle inlet. Shield et al. [10] predicted free surface contours by one-dimensional jet equations with consideration of the surface tension force. The computed droplet formation development was in a qualitative agreement with experimental observations, revealing that the theoretical model needs further improvement to achieve better prediction accuracy. With a one-dimensional theoretical model, Pimbley [11] inspected the drop expelled in a stream for identifying the region of allowable droplet formation. Chen et al. [12,13] set up an optical apparatus to visualize the evolution of droplet under different heating conditions. Moreover, triangular-shaped electrical profiles were employed in a piezo droplet generator to prevent the detachment of satellite droplets from the main droplet. The liquid ejection length grew linearly with the operating voltage.

Previous models were not able to predict the transient flow properties of velocity, shape, and trajectory of the liquid droplet primarily due to their deficient modeling for the surface tension

[1]Corresponding author.

Contributed by the Fluids Engineering Division of ASME for publication in the JOURNAL OF FLUIDS ENGINEERING. Manuscript received June 2, 2005; final manuscript received January 29, 2006. Assoc. Editor: Theodore Heindel.

effect and interface movements with continuing topology changes. The volume-of-fluid (VOF) method has been proven successful in simulating the gas-liquid interfacial flow motions in recent years. By adapting various volume-tracking techniques [14–16] with the sophisticated treatment of interfacial dynamics [17–19], the up-to-date models can achieve satisfactory predictions for the droplet ejection process. For instance, Feng [20] utilized a computer code FLOW3D® to perform a fluid dynamic analysis of droplet ejection from an axisymmetric liquid chamber for predicting the volume and speed as well as shape evolution of ejected drops with the VOF method. Wu et al. [21] also solved the ejection, formation, and impact of a liquid droplet by a solution algorithm (SOLA) scheme in conjunction with VOF and piecewise linear interface construction (PLIC) techniques in a simplified squeeze-mode piezoelectric inkjet printing device. The effects of surface tension and viscosity on the liquid droplet stability were numerically examined in this study.

A novel piezoelectric microdroplet generator has been developed at the Micro-electro-mechanical System Laboratory of Da-Yeh University, Taiwan [22]. Based on the shear-type actuating concept, the current piezoactuator design has the advantages of better structure integrity with inexpensive fabrication cost, enhanced electromechanical coupling properties for lower electrical operating voltages during droplet producing, and minimization of liquid contact with the piezoceramic material. The present work aims to determine the droplet formation characteristics of this novel microdroplet generator before the finalization of detailed design configuration. To conduct simulations of complex interfacial flow phenomena involving fluid inertia, capillarity, and free-surface movements, a commercial computational fluid dynamics package CFD-ACE(U)® is employed as the framework for numerical calculations [23]. Various effects including the ejection time interval and liquid physical properties on the ejection performance are also examined for achieving better understanding in the design of innovative piezo microdroplet generators.

2 Theoretical Formulation of Interfacial Flows

The computer software CFD-ACE(U) has been used to analyze the droplet ejection process for a piezoelectrically driven microdroplet generator [23]. In order to simulate the complicated mixture flow behavior of two incompressible and immiscible fluids with consideration of the effects of surface tension and gravitational force, the model in the CFD-ACE(U) computer code is based on the time-dependent, three-dimensional conservation equations of mass and momentum as follows:

$$\frac{\partial u}{\partial x}+\frac{\partial v}{\partial y}+\frac{\partial w}{\partial z}=0 \tag{1}$$

$$\frac{\partial}{\partial t}(\rho u)+\nabla\cdot\rho\vec{V}u=-\frac{\partial p}{\partial x}+\frac{\partial}{\partial x}\left[2\mu\frac{\partial u}{\partial x}\right]+\frac{\partial}{\partial y}\left[\mu\left(\frac{\partial v}{\partial x}+\frac{\partial u}{\partial y}\right)\right]+\frac{\partial}{\partial z}\left[\mu\left(\frac{\partial u}{\partial z}+\frac{\partial w}{\partial x}\right)\right]+\mathbf{F}_x^{\sigma}+\rho\mathbf{g}_x \tag{2}$$

$$\frac{\partial}{\partial t}(\rho v)+\nabla\cdot\rho\vec{V}v=-\frac{\partial p}{\partial y}+\frac{\partial}{\partial x}\left[\mu\left(\frac{\partial v}{\partial x}+\frac{\partial u}{\partial y}\right)\right]+\frac{\partial}{\partial y}\left[2\mu\frac{\partial v}{\partial y}\right]+\frac{\partial}{\partial z}\left[\mu\left(\frac{\partial v}{\partial z}+\frac{\partial w}{\partial y}\right)\right]+\mathbf{F}_y^{\sigma}+\rho\mathbf{g}_y \tag{3}$$

$$\frac{\partial}{\partial t}(\rho w)+\nabla\cdot\rho\vec{V}w=-\frac{\partial p}{\partial z}+\frac{\partial}{\partial x}\left[\mu\left(\frac{\partial u}{\partial z}+\frac{\partial w}{\partial x}\right)\right]+\frac{\partial}{\partial y}\left[\mu\left(\frac{\partial v}{\partial z}+\frac{\partial w}{\partial y}\right)\right]+\frac{\partial}{\partial z}\left[2\mu\frac{\partial w}{\partial z}\right]+\mathbf{F}_z^{\sigma}+\rho\mathbf{g}_z \tag{4}$$

where $\vec{V}$ is the velocity vector with components of u, v, and w in the x-, y-, and z-axes, while p, ρ, and μ represent the pressure, density, viscosity of mixture fluid, respectively. The terms $\rho\mathbf{g}$ and $\mathbf{F}^{\sigma}$ denote the gravitational force and the surface tension at the liquid-gas interface.

The surface tension terms in the momentum equation (Eqs. (2)–(4)) are treated using the continuous surface force (CSF) model [17–19]. Instead of considering interfacial dynamics with a complicated geometric configuration, the CSF model simulates the surface phenomenon as a localized volumetric force $\mathbf{F}^{\sigma}$ over a computational cell. Thus,

$$\mathbf{F}^{\sigma}=\mathbf{f}^{\sigma}\delta^{\sigma} \tag{5}$$

where $\mathbf{f}^{\sigma}$ is the surface tension force per unit interfacial area. δ^{σ} represents a surface δ function, which exists only in the interfacial transition regions with the variable f (defined as the volume fraction of each computational cell taken by liquid) varying from 0 to 1. Hence, δ^{σ} is denoted as

$$\delta^{\sigma}=|\nabla f| \tag{6}$$

The symbol $\mathbf{f}^{\sigma}$ can be expressed as

$$\mathbf{f}^{\sigma}=\sigma\kappa\vec{n} \tag{7}$$

where κ is the mean interfacial curvature, given by

$$\kappa=-\nabla\cdot\vec{n} \tag{8}$$

The term $\sigma\kappa\vec{n}$ indicates that $\mathbf{f}^{\sigma}$ is proportional to the curvature κ with the force acting along the normal direction of the interface.

In exploring the transient gas-liquid flow behavior with a volume tracking technique, the VOF method is employed to describe interfacial movements by a scalar field variable f. In practice, the isocontour of $f=0.5$ is typically applied to identify the interfacial location for computation and visualization purposes. The volume fraction f is evolved by the integration of f field over volume throughout the calculation domain as follows:

$$\int\frac{\partial f}{\partial t}dV+\int\nabla\cdot(\vec{V}f)dV=0 \tag{9}$$

For those physical properties in a computational cell, the values of the mixture density and the mass-weighted mixture viscosity can be determined using the following mixing rule with the known volume fraction f

$$\rho=f\rho_L+(1-f)\rho_G \tag{10}$$

$$\mu=\frac{f\rho_L\mu_L+(1-f)\rho_G\mu_G}{\rho} \tag{11}$$

here ρ_L, μ_L, ρ_G, and μ_G refer to the density and viscosity for the liquid and gas phase. The mass and momentum conservation equations are discretized by the finite control volume approach. For the convective terms, the second-order accurate central difference scheme is adopted with the adaptive damping for treating nonphysical oscillations in the numerical solutions. The typical second-order accurate central difference scheme is used for evaluating the diffusion terms. For the transient term, the Crank-Nicolson scheme is applied to provide the second-order accuracy in time. The iterative semi-implicit method for pressure-linked equations consistent (SIMPLEC) numerical scheme is used for velocity-pressure coupling [24–26].

In evaluating the liquid volume fluxes from the target cell to all close adjacent cells, the multidimensional piecewise linear interface construction (PLIC) method is employed for the free surface reconstruction [15,17,18]. In each cell containing the interface, the liquid-gas boundary is shaped to be piecewise linear (or planar) with the following form:

$$\vec{x}\cdot\vec{n}-\eta=0 \tag{12}$$

where $\vec{x}$ is the position vector of any point on the interface, $\vec{n}$ is the interfacial outward-pointing unit normal vector, and η is the interface constant. In exercise, the normal $\vec{n}$ is calculated through

the unit gradient of f ($\nabla f/|\nabla f|$), directing out of the liquid phase for indicating the orientation of the interface plane. With the known f value in each cell holding an interface, the interface constant η is also computed via matching the interface truncation volume (V_{TR}) to the actual liquid volume ($V_L = fV_c$). Thus,

$$V_{TR} = fV_c \tag{13}$$

In the end, the shape and orientation of an interface plane for the corresponding interface cell can be readily reconstructed utilizing Eqs. (12) and (13). The interfacial liquid volume flux for a given velocity field can be determined through flow advection ($\delta V = \vec{V} \cdot \vec{n} dA \delta t$). As volumes (also volume fractions) advance in time with the propagation of planar interfaces by the flow, the f value at the cell (with the index of i, j, k) is updated through the volume evolution equation.

$$f_{i,j,k}^{n+1} = f_{i,j,k}^{n} - \frac{\delta V_{i+1/2,j,k}^{n} - \delta V_{i-1/2,j,k}^{n}}{V_{i,j,k}} - \frac{\delta V_{i,j+1/2,k}^{n} - \delta V_{i,j-1/2,k}^{n}}{V_{i,j,k}} - \frac{\delta V_{i,j,k+1/2}^{n} - \delta V_{i,j,k-1/2}^{n}}{V_{i,j,k}} \tag{14}$$

The surface advection calculation in the time evolution of liquid volume is explicit and has an inherent stability requirement on the allowable time-step magnitude. In each numerical cell, the stability limit is restricted by the CFL number (defined as (the local velocity magnitude) $\times$ (the maximum timestep) / (the characteristic length of a local cell)), which must satisfy the condition CFL <1 via the setting of the automatic time-step option in the CFD-ACE(U) code. In practice, values as low as 0.1 are often required to ensure that the free surface crosses less than a cell during that time step. In this analysis, the normalized residual errors of the flow variables (u, v, w, and p) of each time step converge to the order of 10^{-5} for both cases with the CFL number=0.1 and 0.05. The impact of a finer time step on the droplet breakup length and time is insignificant.

3 Results and Discussion

Numerical calculations were conducted using the computational fluid dynamics software CFD-ACE(U) to validate the present theoretical model by comparing the predictions to Shield et al.'s experimental observations [10]. Figure 1 illustrates the schematic diagram and numerical grids of a test squeeze-type cylindrical microinjector with the corresponding temporary displacement profile of the piezo diaphragm. Using the electrical voltage of 90 V and the pulse length of 20 μs, the droplet ejection and formation micrographs of ethylene glycol as working fluid were taken by an oscilloscope camera for measuring the size, shape, and velocity of droplets. As shown in Fig. 2(*a*), the liquid protrusion near to the nozzle exit is moderately underpredicted. This could be attributed to the vibration effect in the movements of the piezo diaphragm. Figure 2(*b*) indicates that the ejection length (defined by the distance from the leading edge of liquid ligament or droplet to the nozzle exit) increases linearly with time roughly after the liquid breakup. During the droplet flight stage, the visualized droplet size is 65 pl with the diameter of 50 μm, while the calculated droplet volume is $\sim$62 pl (49.1 μm dia) with the terminal flight velocity of 1.0 m/s. The difference between the predicted droplet volume and the experiments is 4.62%, demonstrating that the simulations can predict the time sequence of droplet shape with a reasonable accuracy.

Figure 3 demonstrates the schematic diagram and computational mesh of the current novel microdroplet generator. The plateshaped piezoactuator possesses two symmetrically poled regions with an oppositely lateral polarization direction. For the induced shear-type design, the piezo diaphragm is deformed against liquid to eject droplets as an external field is applied to the actuator. The thin thickness of diaphragm (<8 μm) could substantially improve the volume sweep of the piezo diaphragm. In addition, the round corner at the bottom side would eliminate the potential stress concentration for enhancing the structure integrity. The current microdroplet generator module adopts the platform approach, which can be modified to accommodate a varying number of nozzles, orifice sizes, and nozzle locations. As the first step toward the simulation of multiple droplet generators, this work focuses on exploring the droplet deformation behavior for a single droplet generator. The numerical grids of the present microdroplet generator consist of three sections, including the liquid chamber, the nozzle, and the area out of the nozzle. Finer grids have been arranged in the regions adjacent to the nozzle exit as well as near the moving and fixed solid wall boundaries with the smallest spacing of 1.2 μm for resolving steep variations of flow properties. The planned physical dimensions of the liquid chamber are

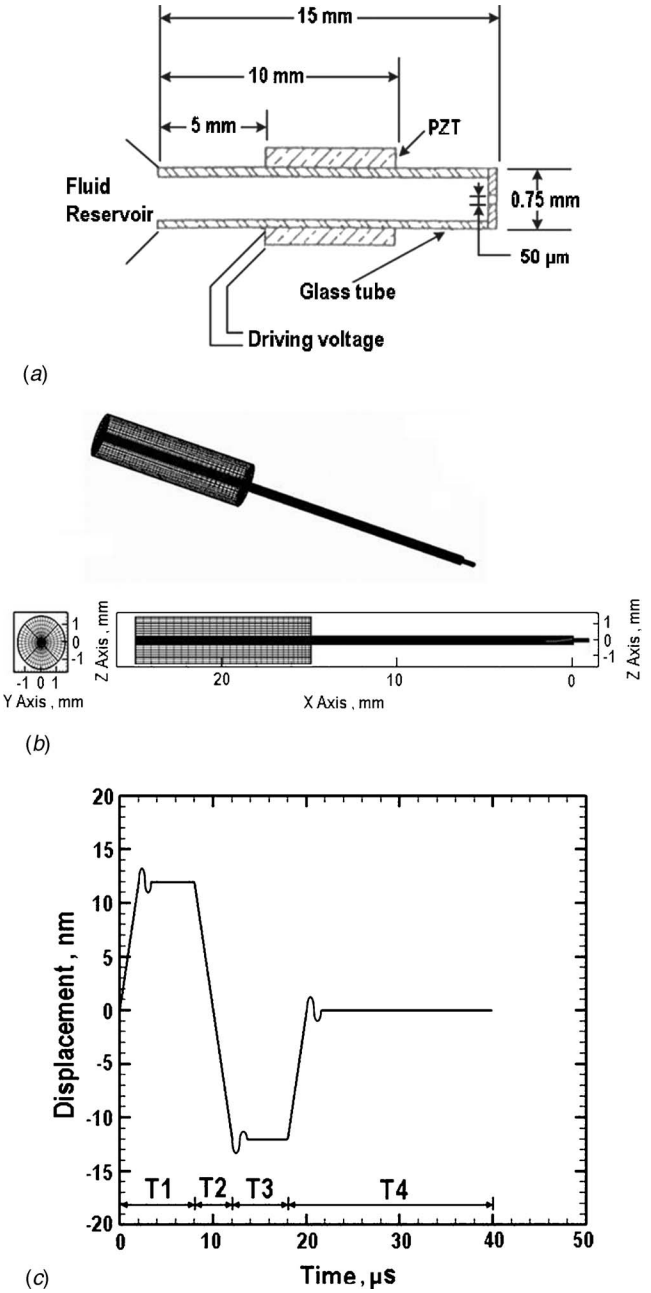

Fig. 1 (*a*) Schematic diagram of a test squeeze-type cylindrical microinjector from Ref. [10] (not to scale); (*b*) numerical grids of a test squeeze-type cylindrical microinjector with stereogram as well as end and side views; and (*c*) time-dependent displacement profile of the piezo diaphragm from Ref. [10]

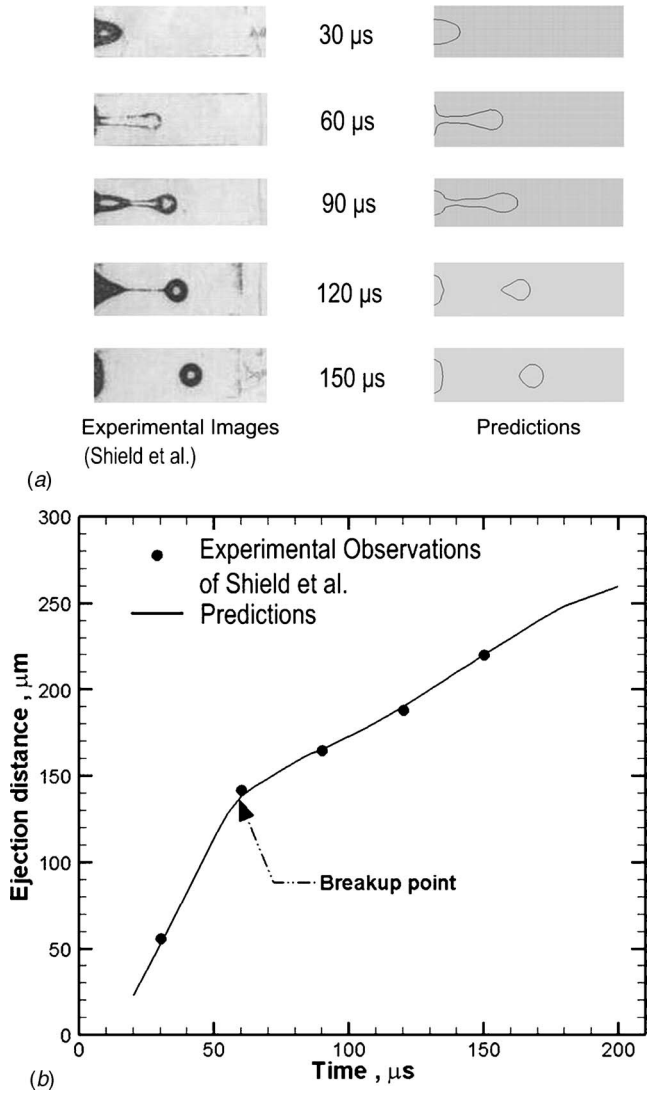

Fig. 2 (*a*) Comparison between the calculated results and visualized microimages of the time evolution of liquid shape, and (*b*) time history of the computed and measured injection length

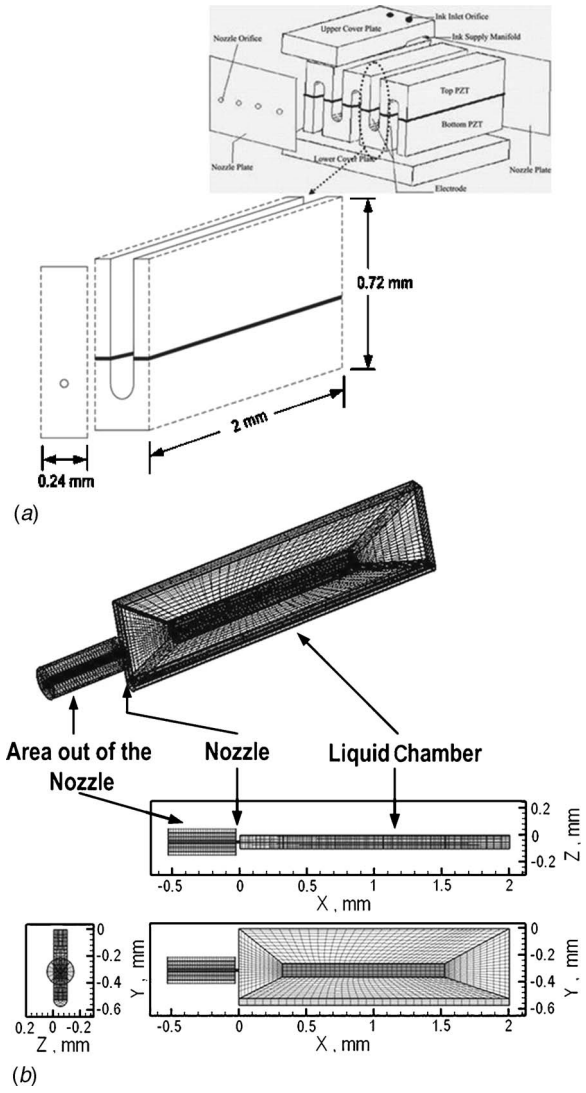

Fig. 3 (*a*) Schematic diagram of a novel micro-droplet generator, and (*b*) numerical grids of a full-size micro-droplet generator with stereogram as well as bottom, end, and side views

2000 μm in length, 100 μm in width, and 570 μm in height, while the diameter of nozzle exit is 20 μm with a circular cross section. Using water for the baseline calculation, the related density, viscosity, and surface tension are 10^3 kg/m^3, 1.0×10^{-3} N s/m^2 (1.0 cps), and 7.25×10^{-2} N/m. In a common practice of electroforming the nozzle plate with nickel on metal substrate, the contact angle is set to be 7.1 deg for water on the plate nickel nozzle wall.

Under the proposed driving voltage pulse, the temporary displacement representing the motion of the piezo diaphragm is determined by the finite element computer code ANSYS® by setting the typical values of piezoceramic material as Young's modulus of 5.0×10^{14} N/m^2, Poisson's ratio of 0.209, and density of 2070 kg/m^3, respectively. The specified displacement mainly considers the primary vibration of the diaphragm with the secondary and higher-order vibration ripples ignored. Figure 4 displays the transient displacement function of the piezo diaphragm with a trapezoid shape separated into three regions. The corresponding peak displacement is 30 nm. In T1, the piezo diaphragm deflects outward in accordance with the electric energizing for the duration of 0–6 μs and remains still until $t=14$ μs, leading to liquid flowing into the chamber during this filling stage. For the time period of T2 from 14 μs to 17 μs, the operating voltage of the electric pulse drops to 0 V. The rapid inward movement of the piezo diaphragm in this ejection time stage causes the sudden decrease of the chamber volume and, in turn, pushes droplets outside the nozzle opening. In the end, the piezo diaphragm holds stationary in T3 time interval (17–50 μs) for the completion of the droplet ejection. Acting as the prescribed moving boundary condition, the detailed displacement profile of the piezo diaphragm with a full cycle period of 50 μs is programmed to be the customized user subroutine, which is readily linked with the CFD-ACE(U) computer code for the droplet ejection analysis.

To investigate the practicability of the proposed new micro-droplet generator, water inside the chamber is considered to be initially immobile in simulations with an equilibrium liquid meniscus at the nozzle opening. In response to an electrical command, the liquid is driven for ejecting a droplet, and restores to the original rest state finally after refilling from the liquid reservoir. The pressures at the liquid inlet and the surrounding area out of the nozzle are 1 atm. The no-slip condition and zero normal gradient of pressure are enforced on the solid walls. Numerical computations have been performed on total grids of 79,372, 110,088, and 149,548 points. Figure 5 shows simulations of water ejection for different grids of 79,372, 110,088, and 149,548 points. During the droplet flight, the corresponding calculated droplet volumes

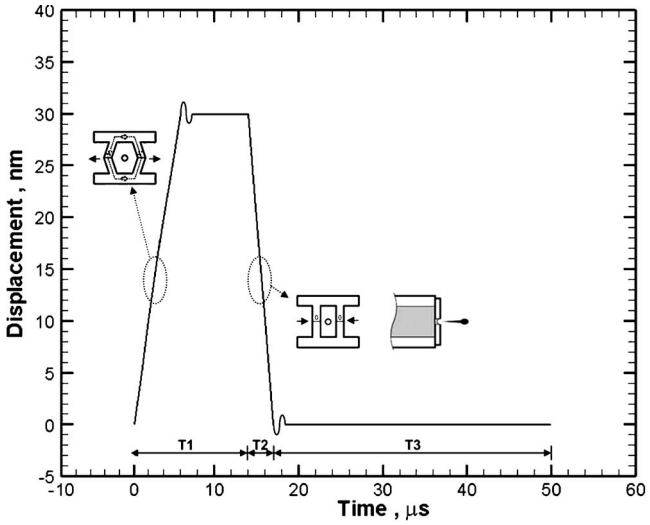

Fig. 4 Time-dependent displacement function of the piezo diaphragm

are 3.6, 4.9, and 5.0 pl (~18.9, 21.0, and 21.2 μm dia), respectively. The difference of the predicted droplet volume for 79,372 and 149,548 grids is 28.0%. However, the droplet volume difference reduces to 2.0% if the total grid number increases from 110,088 to 149,548. For the CFL values of 0.1 and 0.05, the corresponding time steps range on the order from 10^{-7} to 10^{-9} s. The time evolution of droplet ejection remains nearly identical when the CFL value is changed from 0.1 to 0.05. The predicted droplet breakup times for the CFL of 0.1 and 0.05 are 21.3 and 21.5 μs, respectively. The above results indicate that a satisfactory independence of the grid and the time step can be attained using the mesh setup of 110,088 grids with CFL=0.1. For calculations of each time step, the normalized residual errors of flow variables converge to 10^{-5} with the mass balance check within 0.5%. It normally needs ~110 h of central processing unit (CPU) time on a Pentium P4-2.8 GHz personal computer for a full-cycle simulation.

During the ejection phase, the piezo diaphragm moves backward rapidly for impelling water out of the chamber. As the liquid meniscus is progressively protruding with a bulge in the core region, the protrusion length at the end of ejection (t=17 μs) is ~51.6 μm with the forward velocity of 7.7 m/s. The corresponding Reynolds number (Re) is 155 based on the nozzle exit diameter. Figure 6 reveals the droplet ejection sequence for the current new piezoactuated microdroplet generator. The results from simulations show that the interfacial flow phenomenon involves four major circumstances, specifically, lengthening of the liquid protrusion, breakup of the liquid strand, convergence of the tailing droplet, and completion of the droplet formation. The x-y cut-view velocity vector fields are also shown instantly before and after the droplet breakup. At t=21 μs, the flow in the nozzle is reversed for protracting the liquid strand. Moreover, it is clearly observed that the liquid strand is encircled by the induced donut-shaped recirculating eddies, which could facilitate the enduring breakup process. As the forward momentum of liquid prevails over the resistance of surface tension and viscous forces; the liquid jet is thus broken up. The predictions also reveal that a clean droplet breakup is accomplished with a tailing droplet nearby the nozzle opening at t=22 μs. During the droplet flight course, the cohesive force due to the surface tension propels the change of droplet shape from a tailing body to a spheroid. The resultant droplet volume is ~4.9 pl at t=40 μs, and the related droplet diameter is 21.0 μm with the flight velocity of 4.0 m/s heading downstream. In the end of droplet formation, the flow in the chamber is ceased with the initial condition restored.

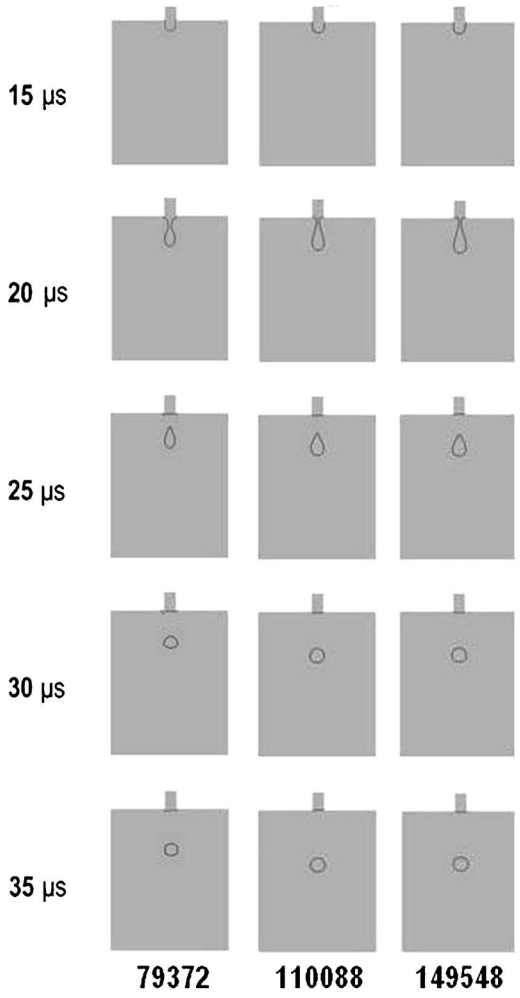

Fig. 5 Simulations of water ejection for different grids

In the design of piezoelectric microdroplet generators, the variations of ejection time period (T2) and fluid properties could substantially change the droplet ejection and formation behaviors. With the test matrix given in Table 1, a series of 12 numerical experiments were conducted to determine droplet ejection characteristics under specified simulation conditions. Figure 7 presents the time evolution of droplet ejection and the associated breakup length/time at different ejection time periods (cases 1–5). As the ejection time T2 reduces in the sequence of 3.5, 3.0, 2.5, and 2.0 μs, the ejection velocities at the end of ejection stage increase accordingly with 0.5, 4.0, 7.8, and 10.0 m/s. In general, a smaller T2 would produce a higher ejection velocity and, in turn, lead to an ejected liquid strand with a shorter breakup time but a longer breakup length. For T2=4.0 μs, the restoring effects of liquid surface tension and viscosity surmount the momentum. Consequently, the droplet could not be formed even if nearly the same liquid volume is displaced by the piezo diaphragm. Shortly, the liquid is retracted back to the nozzle.

Since a variety of liquid materials have launched their prospective applications in many industrial areas, the present study also investigates the effect of working fluid properties on the ejection performance. Figure 8 exhibits the time evolution of droplet ejection with the breakup length and time attached at different liquid surface tensions (cases 6–9). Based on the identical displacement profile of the piezo diaphragm in a full ejection cycle of 50 μs, an equal amount of liquid volume is driven out from the nozzle to achieve nearly same sizes of liquid spheroid in the end with the calculated droplet volume of 5.6 pl. As given in Table 2, the

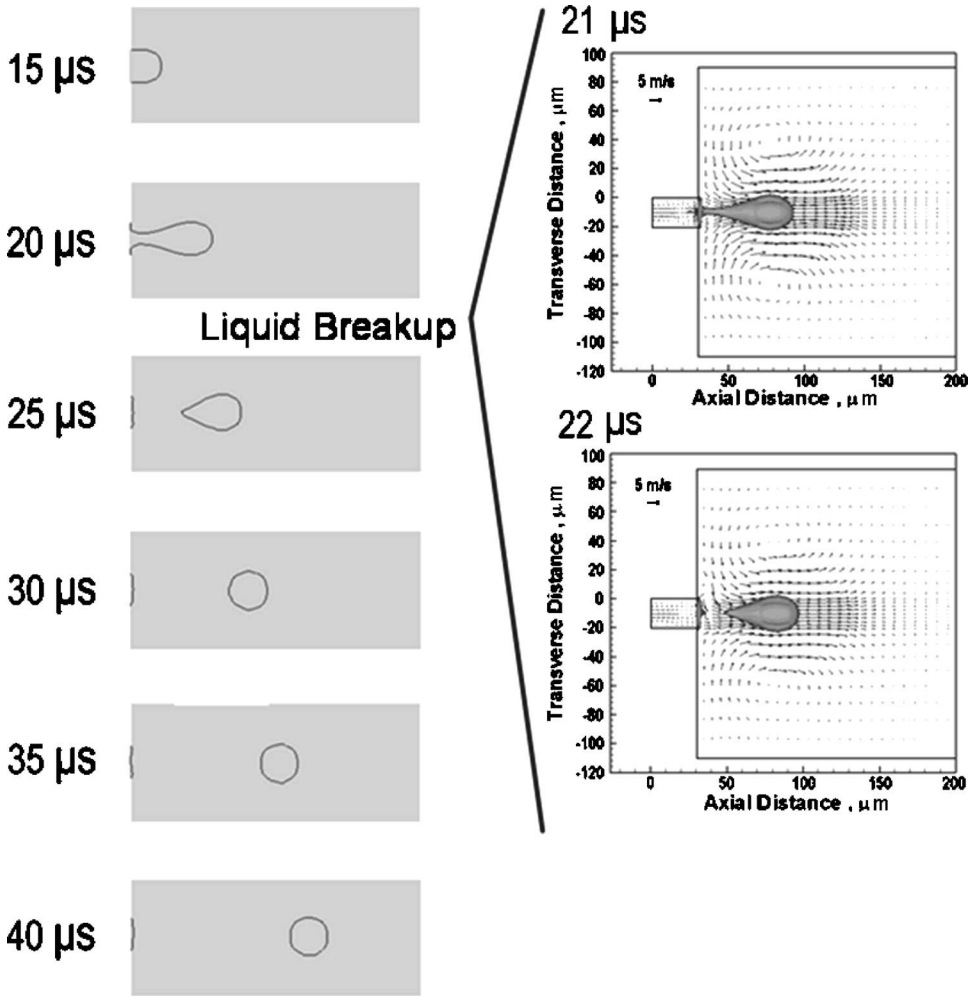

Fig. 6 Progression of the droplet ejection process with the velocity vector fields attached during the droplet breakup stage

breakup lengths and times are 55.2, 58.6, and 66.4 μm and 22.5, 21.5, and 21.0 μs for the liquid surface tensions of 0.08, 0.0725, and 0.05 N/m, respectively. To inspect the droplet formation behavior, the ejected liquid with low surface tensions is likely to create a slender liquid strand due to a weaker cohesive force with a longer breakup length and a relatively shorter breakup time. Meanwhile, it can take more time to attain the contraction of a spherical droplet, and end up with a faster droplet flight velocity.

Table 1 Test matrix for simulation conditions

Case	Viscosity (cps)	Surface tension (N/m)	Ejection time (μs)
1	1.0	0.0725	2.0
2	1.0	0.0725	2.5
3[a]	1.0	0.0725	3.0
4	1.0	0.0725	3.5
5	1.0	0.0725	4.0
6	1.0	0.05	3.0
7[a]	1.0	0.0725	3.0
8	1.0	0.08	3.0
9	1.0	0.09	3.0
10	0.5	0.0725	3.0
11[a]	1.0	0.0725	3.0
12	2.0	0.0725	3.0
13	3.0	0.0725	3.0
14	4.0	0.0725	3.0

[a]Those cases correspond to the baseline condition.

Conversely, for the case of σ=0.09 N/m, the high surface tension effect could result in the failure of droplet breakup. Figure 9 discloses the droplet ejection progression as well as the breakup length and time at different viscosities (cases 9–14). For liquid viscosities of 0.5, 1.0, 2.0, and 3.0 cps displayed in Table 2, the corresponding breakup lengths and times are 62.0, 57.0, 52.0, and 47.0 μm and 19.0, 21.5, 25.0, and 28.0 μs. The corresponding terminal velocities are 5.0, 4.0, 1.5, and 0.8 m/s in the droplet flight course. The calculated results indicate high viscous liquids are disposed to cause a relatively longer breakup time, a shorter breakup length, and a slower droplet flight velocity on account of strongly viscous dissipation. It is observed that the piezo generator fails to inject droplets for the liquids with viscosities over 4.0 cps. Based on the above calculated results, the ejection simulations have demonstrated the capability of this novel piezoelectric microdroplet generator in dispensing a broad range of liquids.

Conclusions

Numerical simulations are performed using the computational fluid dynamics computer package CFD-ACE (U)® to explore the droplet ejection phenomena for a novel piezoelectric microdroplet generator. In the analysis, the theoretical model considers the time-dependent three-dimensional conservation equations of mass and momentum, with incorporation of the continuous surface force (CSF) model for treating the interfacial surface tension effect. The behavior of interfacial movements is characterized by the volume-of-fluid (VOF) method in conjunction with the piece-

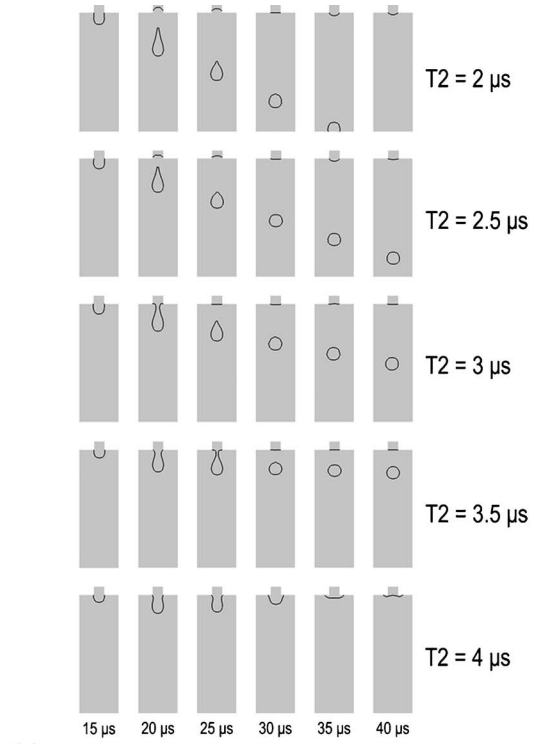

(*a*)

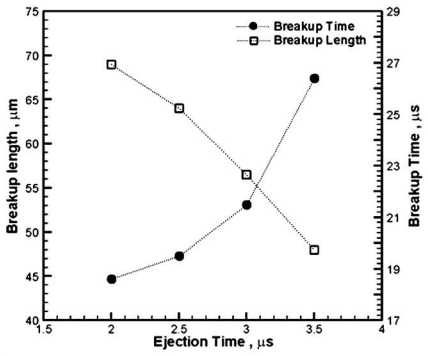

(*b*)

Fig. 7 (*a*) Time evolution of droplet ejection and (*b*) breakup length/time at different ejection time periods

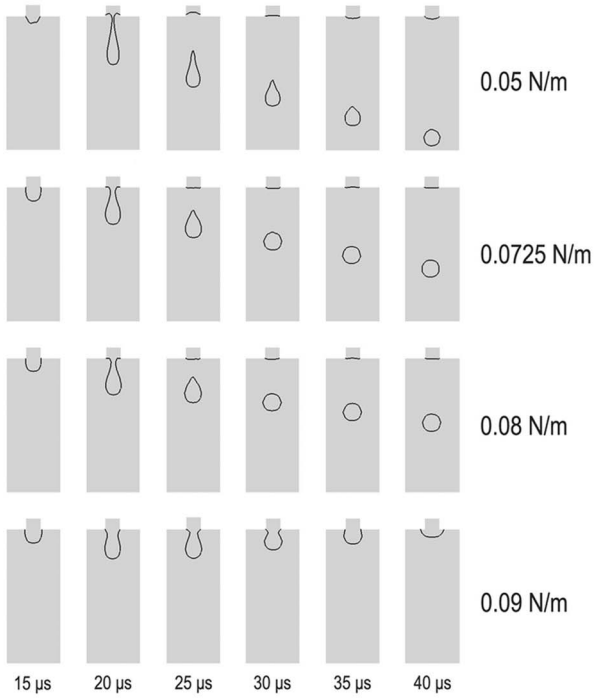

(*a*)

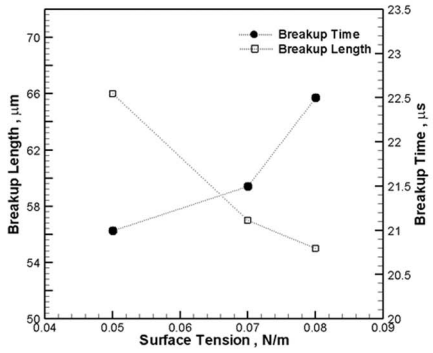

(*b*)

Fig. 8 (*a*) Time evolution of droplet ejection and (*b*) breakup length/time at different liquid surface tensions

wise linear interface construction (PLIC) technique. For the model validation, the predicted droplet shape contours were rather consistent with Shield's microphotographed images. In the system integrity and function check of current new piezo microdroplet generator, the ejection process of water droplet is evolved in the sequence of liquid protrusion, liquid strand breakup, convergence of tailing droplet, and droplet formation. The predicted droplet volume is 5.6 pl (21.0 μm dia) with the flight velocity of 4.0 m/s traveling downstream.

To respond to the design needs in probing the influence of important factors on the droplet ejection performance, 12 numerical experiments were carried out by varying the ejection time, liquid surface tension, and viscosity within the ranges of 2.0–4.0 μs, 0.05–0.09 N/m, and 0.5–4.0 cps. As the ejection time is reduced, a higher ejection velocity is attained and results in an ejected liquid strand with a shorter breakup time but a longer breakup length. In case the ejection time is $>$4.0 μs, the droplet could not be generated due to the lacking of frontward momentum. Owing to a weaker cohesive force, low surface-tension liquids tend to produce a slender liquid strand with a longer breakup length and a shorter breakup time. It can also take more time to contract into a spherical droplet with a faster droplet flight velocity. For $\sigma \geqslant 0.09$ N/m, the strong surface tension could end in the breakdown of droplet breakup path. Meanwhile, high viscous liquids are likely to cause a relatively longer breakup time, a shorter breakup length, and a slower droplet flight velocity on account of the strongly viscous dissipation. In calculations, the piezo generator could not generate droplets for the liquids with viscosities over 4.0 cps. Based on the above calculated results, the ejection simulations have demonstrated the capability of this novel piezoelec-

Table 2 Breakup lengths and times at different surface tensions and viscosities

Surface tension (N/m)	Viscosity (cps)	Breakup length (μm)	Breakup time (μs)
0.05	1.0	66.4	21.0
0.0725	1.0	58.6	21.5
0.08	1.0	55.2	22.5
0.0725	0.5	62.0	19.0
0.0725	1.0	57.0	21.5
0.0725	2.0	52.0	25.0
0.0725	3.0	47.0	28.0

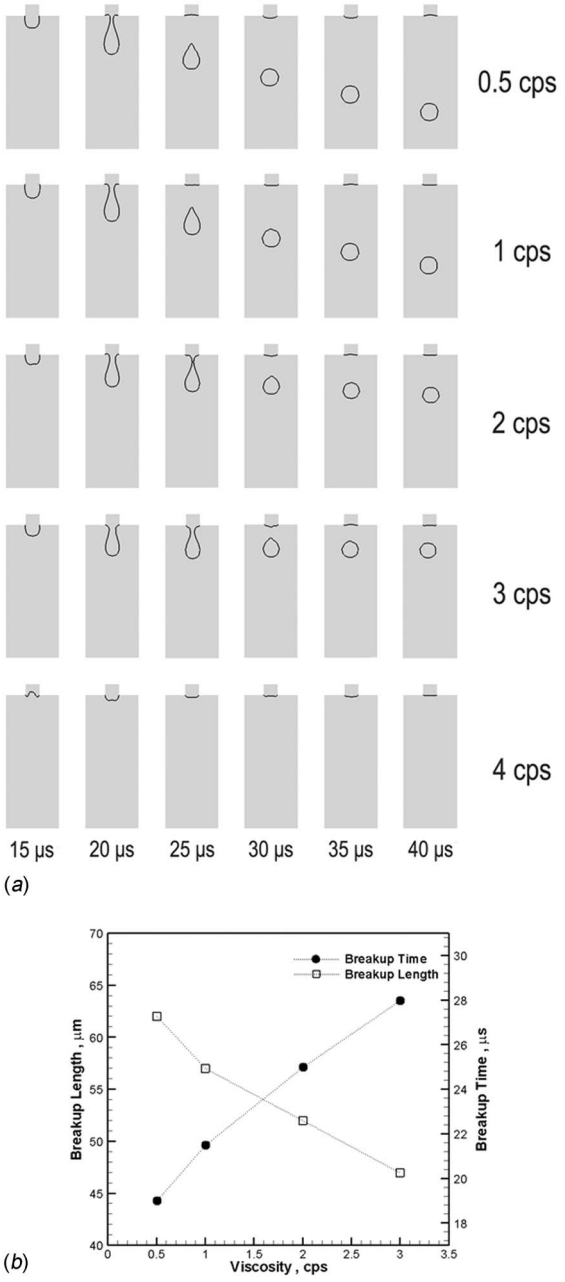

Fig. 9 (*a*) Time evolution of droplet ejection and (*b*) breakup length/time at different liquid viscosities

tric microdroplet generator in dispensing different liquids, with the surface tension and the viscosity in the ranges of 0.05–0.08 N/m and 0.5–3.0 cps, respectively.

Acknowledgment

This study represents part of the results obtained under Contract NSC 92-2218-E-212—005, sponsored by the National Science Council, Taiwan, Republic of China.

Nomenclature

f = volume fraction
f^σ = surface tension force per unit interfacial area
F^σ = volumetric force of surface tension
g = gravitational acceleration
$\vec{n}$ = interface unit normal vector
p = pressure
t = time
u, v, w = velocities in x, y, z direction
V = volume
$\vec{V}$ = velocity vector
$\vec{x}$ = position vector of any point on the interface
x, y, z = coordinates
δ^σ = surface delta function
η = interface constant
κ = mean interfacial curvature
μ = viscosity
ρ = density
σ = liquid surface tension coefficient

Superscripts

$n+1$ = new time step
n = old time step

Subscripts

L = liquid phase
G = gas phase
Tr = truncation
c = cell

References

[1] Tseng, F. G., 2001, "Micro-Droplet Generators," *MEMS Handbook*, M. Gad-el-Hak, ed., CRC Press, Boca Raton, pp. 30-1–30.
[2] Krestschmer, J., Tille, C., and Ederer, I., 1997, "A Drop-on-Demand Inkjet Printhead for a Wide Range of Applications," IS&Ts NIP 14: 1997 International Conference on Digital Printing Technologies, Seattle, pp. 343–347.
[3] Le, H. P., 1998, "Progress and Trends in Ink-jet Printing Technology," J. Imaging Sci. Technol., **42**(1), pp. 49–62.
[4] Allen, R. R., Meyer, J. D., and Knight, W. R., 1985, "Thermodynamics and Hydrodynamics of Thermal Ink Jets," Hewlett-Packard J., **36**, May, pp. 21–27.
[5] Lee, F. C., Mills, R. N., and Talke, F. E., 1984, "The Application of Drop-on-Demand Ink Jet Technology to Color Printing," IBM J. Res. Dev., **28**(3), pp. 307–313.
[6] Asai, A., Hara, T., and Endo, I., 1987, "One Dimensional Model of Bubble Growth and Liquid Flow in Bubble Jet Printers," Jpn. J. Appl. Phys., **20**(10), pp. 1794–1 801.
[7] Asai, A., Hirasawa, S., and Endo, I., 1988, "Bubble Generation Mechanism in the Bubble Jet Recording Process," J. Imaging Technol., **14**, pp. 120–124.
[8] Asai, A., 1992, "Three-Dimensional Calculation of Bubble Growth and Drop Ejection in a Bubble Jet Printer," ASME J. Fluids Eng., **114**, pp. 638–641.
[9] Fromm, J. E., 1984, "Numerical Calculations of the Fluid Dynamics of Drop-on-Demand Jets," IBM J. Res. Dev., **28**(3), pp. 322–333.
[10] Shield, T. W., Bogy, D. B., and Talke, P. E., 1987, "Drop Formation by DoD Ink-jet Nozzles: A Comparison of Experiment and Numerical Simulation," IBM J. Res. Dev., **31**(1), pp. 96–110.
[11] Pimbley, W. T., 1976, "Drop Formation From a Liquid Jet: A Linear One-Dimensional Analysis Considered as a Boundary Value Problem," IBM J. Res. Dev., **20**, pp. 148–156.
[12] Chen, P. H., Chen, W. C., and Chang, S. H., 1997, "Bubble Growth and Ink Ejection Process of a Thermal Inkjet Printhead," Int. J. Mech. Sci., **39**(6), pp. 683–695.
[13] Chen, P. H., Peng, H. Y., Liu, H. Y., Chang, S. L., Wu, T. I., and Cheng, C. H., 1999, "Pressure Response and Droplet Ejection of a Piezoelectric Inkjet Printhead," Int. J. Mech. Sci. **41**(2), pp. 235–248.
[14] Rider, W. J., Kothe, D. B., Mosso, S. J., Cerutti, J. H., and Hochstein, J. I., 1995, "Accurate Solution Algorithms for Incompressible Multiphase Flows," AIAA 95–0699, Reno, NV.
[15] Gueyffier, D., Li, J., Nadim, A., Scardoovelli, R., and Zaleski, S., 1999, "Volume-of-Fluid Interface Tracking with Smoothed Surface Stress Methods for Three-Dimensional Flows," J. Comput. Phys. **152**, pp. 423–456.
[16] Delnoij, E., Kuipers, J. A. M., and Swaaij, W. P. M., 1997, "Computational Fluid Dynamics Applied to Gas-Liquid Contactors," Chem. Eng. Sci. **52**(21), pp. 3623–3638.
[17] Kothe, D. B., Rider, W. J., Mosso, S. J., Brock, J. S., and Hochstein, J. I., 1996, "Volume Tracking of Interfaces Having Surface Tension in Two and Three Dimensions," AIAA 96–0859, Reno, NV.
[18] Meier, M., Yadigaroglu, G., and Smith, B. L., 2002, "A Novel Technique for Including Surface Tension in PLIC-VOF Methods," Eur. J. Mech. B/Fluids, **21**, pp. 61–73.
[19] Brackbill, J. U., Kothe, D. B., and Zemach, C., 1998, "A Continuum Method for Modeling Surface Tension," J. Comput. Phys., **100**, pp. 335–354.
[20] Feng, J. Q., 2002, "A General Fluid Dynamics Analysis of Drop Ejection in Drop-on-Demand Ink Jet Devices," J. Imaging Sci. Technol., **46**5, pp. 398–408.
[21] Wu, H. C., Hwang, W. S., and Lin, H. J., 2004, "Development of a Three-Dimensional System for Micro-Inkjet and its Experimental Verification,"

Mater. Sci. Eng., A, **373**, pp. 268–278.
[22] Cheng, C. H., Hu, R. C., Yeh, D. C., and Lin, Y. P., 2004, "Structure and Fabrication of a Novel Piezoelectric Micro-Droplet Generator," Taiwan ROC Patent No.: 194947 (in Chinese).
[23] ESI-CFD, 2004, *CFD-ACE(U)® V2004 User's Manual*, ESI-CFD Inc., Huntsville, AL; www.cfdrc.com.
[24] Patankar, S. V., 1980, *Numerical Heat Transfer and Fluid Flow*, Hemisphere, Washington, DC.
[25] Van Doormaal, J. P., and Raithby, G. D., 1984, "Enhancements of the SIMPLE Method for Predicting Incompressible Fluid Flows," Numer. Heat Transfer **7**, pp. 147–163.
[26] Jang, D. S., Jetli, R., and Acharya, S., 1986, "Comparison of the PISO, SIMPLER, and SIMPLEC Algorithms for the Treatment of the Pressure-Velocity Coupling in Steady Flow Problems," Numer. Heat Transfer **10**, pp. 209–228.

DSMC Simulation of Subsonic Flows in Parallel and Series Microchannels

M. Le

I. Hassan[1]
e-mail: IbrahimH@alcor.concordia.ca

N. Esmail

Department of Mechanical and Industrial Engineering,
Concordia University,
Montreal, QC, H3G 1M8 Canada

Flows in uniform, parallel, and series microchannels have been investigated using the direct simulation Monte Carlo (DSMC) method. For the uniform microchannel cases, at higher pressure ratio, mixed Kn-regime flows were observed, where the Knudsen number (Kn) varies from below 0.1 to above 0.1. Also, the higher pressure ratio makes the flow accelerate more as the flow develops through the uniform microchannel. In order to examine the heat transfer characteristics between the wall and the bulk flow, a linear temperature distribution was imposed on the wall. Most of the wall heat flux occurs within the channel entrance region while it remains a constant with a slight magnitude along the rest of the channel wall. For the series microchannel cases, the computational domain was established by adding three surfaces and excluding one region from the rectangular domain. Diffuse effects were observed near the interface of the two segments, where the flow upstream the interface can be either heated or cooled by the flow downstream depending on their temperature difference. In addition, the effect of the gas species was investigated by conducting the simulation using helium and argon respectively. It can be found that the speed of the gas with lighter molecular mass is much higher than that of the heavier gas. The computational domain of the parallel microchannel was established similarly to that of the series microchannel. Under a certain pressure ratio, more pressure drop occurs in the parallel parts as the gap height increases. The recirculation phenomenon was observed after the gap wall between the two parallel parts and was evaluated quantitatively in the present study by defining a parameter called the developing coefficient. The gap height between the two parallel parts has only slight effect of the flow development. [DOI: 10.1115/1.2354525]

Keywords: DSMC, microchannel heat transfer, parallel and series microchannels

1 Introduction

The progression of fabrication techniques has made it possible to manufacture microdevices with characteristic sizes comparable to the gas mean free path and, as a result, the flow is not necessarily in the continuum flow regime. Currently, the characteristic sizes of microdevices can be considerably small and even has the same order of one micrometer. Hence, for the flow at standard condition (STP), it becomes possible to obtain a Knudsen number (Kn) varying in the range of approximately 0.001–1 [1]. This indicates that the flow can fall into not only the continuum flow regime but also the slip or transition flow regime. In the continuum flow model ($Kn < 0.01$), the Navier-Stokes equations are the governing equations as long as the flow can be assumed infinitely divisible. When the flow becomes more rarefied, for example, when the Kn is of the order of 0.1, the continuum model may fail to predict the flow even with the slip boundary condition, making the Navier-Stokes equations no longer valid [2]. In order to study rarefied flows, the Boltzmann equation involving the motions of molecules rather than the macroscopic quantities must be employed in the flow prediction. However, it is very expensive to solve the Boltzmann equation either analytically or numerically; therefore, an alternative method, the direct simulation Monte Carlo (DSMC) method, is adopted in order to solve the problem. During the past decades, DSMC has been mainly used in atmospheric dynamics. However, in recent years, the DSMC method is chosen to model the micro flows in MEMS.

High-speed microchannel flow was simulated by Mavriplis et al. [1], Oh et al. [3], and Liou et al. [4]. From the practical point of view, more effort has been attributed to the subsonic microchannel flows. Fundamental works have been conducted for flows in two dimensional uniform microchannels [5–12], as well as for micro-Couette flow [7,13]. Flows in both the slip regime and the transition regime were taken into account. Specifically, Hadjiconstantinou [14–16] did a very comprehensive work in understanding the heat transfer characteristics of the flow in uniform microchannel. Some significant flow features due to the compressibility and the rarefaction of the flow, such as the flow acceleration along the channel, the nonlinear pressure distribution, and the velocity slip near the wall, were specified. As for the heat transfer characteristics between the wall and the bulk flow, imposing a higher wall temperature, the wall heat flux can only occur in the channel entrance region. Furthermore, the Nusselt number decreases with the increasing flow rarefaction.

In addition, microflows in other simple geometries were also examined; for example, straight microchannel with solid core inside [1], three-dimensional rectangular channel with a moving surface [10], straight microchannel with a rectangular orifice inside [12], bended microchannel [12], two-dimensional (2D) duct with a cavity [17], and T-shape micromanifold [18] have been employed in the DSMC simulation. The dynamic flow properties of the microflow differ somehow from those observed in the continuum flow.

To the best of our knowledge, the parallel and series microchannels, being the most typical configurations in microfluidic systems, have not been thoroughly investigated using the DSMC. In the current study, the diffuse effect will be investigated by applying different wall temperatures to the two uniform segments of the series microchannel. Also, helium and argon will be employed in

[1]Author to whom correspondence should be addressed.

Contributed by the Fluids Engineering Division of ASME for publication in the JOURNAL OF FLUIDS ENGINEERING. Manuscript received September 6, 2005; final manuscript received May 8, 2006. Assoc. Editor: Kenneth Breuer.

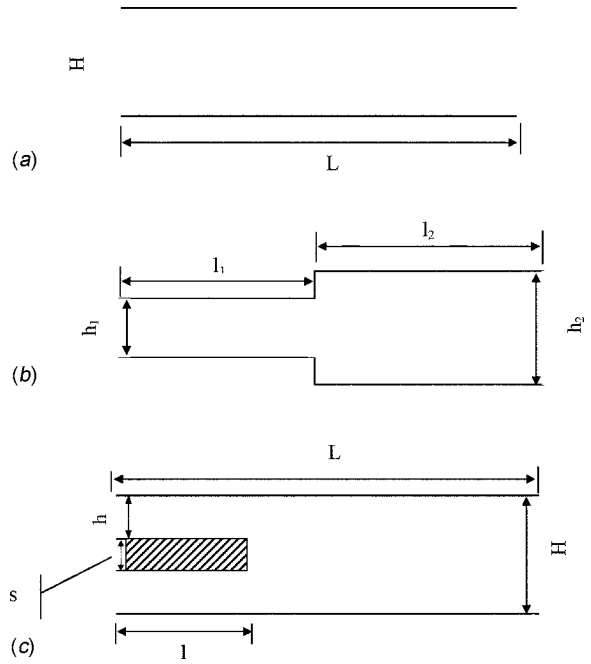

Fig. 1 (*a*) Schematic of the uniform microchannel geometry, (*b*) Schematic of the series microchannel geometry, and (*c*) Schematic of the parallel microchannel geometry

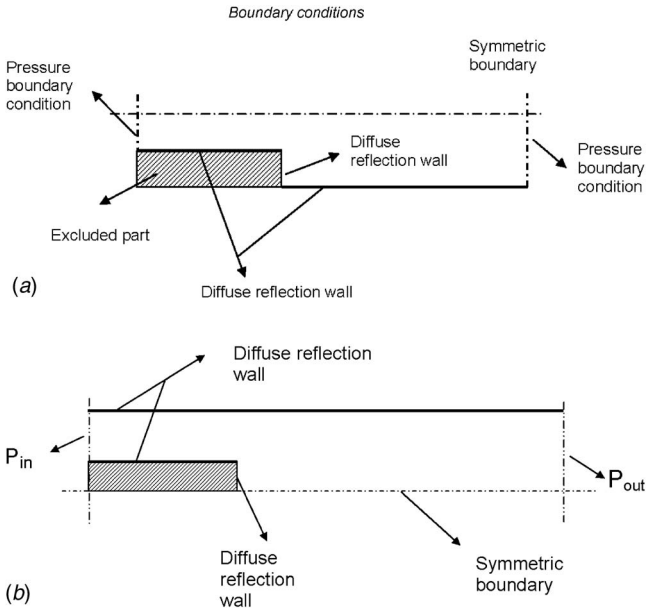

Fig. 2 (*a*) Boundary conditions for the series microchannel flow and (*b*) Boundary conditions for the parallel microchannel flow

simulation respectively to examine the effect of the gas species. In the parallel channel cases, the flow recirculation phenomenon will be evaluated quantitatively by defining a parameter named the developing coefficient. The accuracy of the results will be achieved by repeating the base cases with different mesh sizes and with different number of simulated particles per cell, respectively. Moreover, the verification of the current code will be implemented by comparing our results with some available analytical solutions in the base cases.

2 Problem Description

2.1 Testing Geometries. Figure 1 schematically shows the microchannels concerning the present work. Figure 1(*a*) shows the 2D uniform microchannel with the height H and the length L. Figure 1(*b*) depicts the 2D series microchannel, which consists of two uniform segments. The lengths of the two uniform segments are l_1 and l_2, respectively, corresponding to the heights, h_1 and h_2. The computational domain of the parallel channel is established as shown in Fig. 2(*a*). Three surfaces are added and treated as diffuse reflect walls, a rectangular part at the lower left corner is excluded while a symmetric boundary is imposed at the upper edge. Figure 1(*c*) shows the 2D parallel microchannel, which contains a main channel connected by two parallel uniform parts. The two parallel parts have the same length l and the height h and are separated by a gap with the height s, while the main channel height is H. The simulation is carried out in the computational domain established similarly to that of the parallel channel as shown in Fig. 2(*b*).

2.2 Modeling. The DSMC method introduced by Bird [19] is used in the current work to simulate the microchannel flow applying a particle-based model. The macroscopic properties in the flow field, such as the velocity, temperature, and density, are determined by sampling the microscopic quantities of the simulated particles based on each cell within the computational domain. The whole computational domain is divided into rectangular cells, each of which contains four subcells with a 2×2 subcell structure. According to Bird [19], the cell size should be 1/3 of the mean free path in order ascertain absence of large gradients of macroscopic properties within a cell. The simulation work is accomplished by modeling the evolution of the simulated particles, each of which represents a number of real molecules.

First, a number of particles are placed into each cell and start to move within a very short time interval, which is set to be smaller than the mean collision time in order to discretize the molecular motions. Once a particle reaches either the channel wall or the I/O boundary, its position and velocities are adjusted according to the imposed boundary conditions. In the present work, the pressure boundary conditions applied at the I/O boundary was developed by Wang and Li [12]. The theory of characteristics is adopted at both of the I/O boundaries based on each boundary cell. Hence, the cell-based inflow velocity and the temperature at either the upstream inlet boundary or the downstream outlet boundary can be determined. Furthermore, the velocity components of each molecule entering the domain can be calculated according to the Maxwellian equilibrium distribution function. As regarding the gas-surface interaction, the most common models concern the generalization of the diffuse or specular reflection model, which may cause the temperature of the incident molecules to differ from that of the reflected ones. In the present study, with the given wall temperatures, the diffuse reflection model is used. Thus, the upper and lower plates are considered as diffuse reflectors with full thermal accommodation. The outgoing velocity of a reflected particle is randomly assigned according to a half-range Maxwellian distribution determined by the wall temperature.

Second, the location of each particle is indexed by recording

Table 1 Test cases in straight uniform microchannels

	Straight uniform channels				
Quantity	case 1	case 2	case 3	case 4	case 5
$Kn_{in}(\lambda/H)$		0.0547		0.110	0.547
$H(\mu m)$		1		0.5	0.1
$L(\mu m)$	5	10	20	5	1
λ (μm)			5.47×10^{-2}		
Mesh size	50×50	50×100	50×200	50×50	25×50
T_∞ (K)			300		
P_{in} (Pa)			2.0×10^5		

Table 2 Test cases in parallel and series microchannels

	Parallel channel				Series channel		
Quantity	case 6	case 7	case 8	case 9	Quantity	case 10	case 11
Kn_{in}	0.137	0.182	0.273	0.547	Species	Helium	Argon/helium
$H(\mu m)$			1		$h_1/2$ (μm)	0.3	0.3
$L(\mu m)$			20		$h_2/2$ (μm)	0.5	0.5
$s(\mu m)$	0.2	0.4	0.6	0.8	l_1 (μm)	6.0	3.0
l (μm)			6		l_2 (μm)	10.0	5.0
λ (μm)				5.47×10^{-2}			
Mesh size			50×200			50×160	
T_∞				300			
P_{in} (Pa)				2.0×10^5			

the subcell number and the cell number where the particles are located. Third, collision partners are randomly selected from particles with the restriction that during a time step, the binary collisions are permitted only between the particles within the same cell. The no-time-counter (NTC) scheme introduced by Bird [19] is used to determine the collision pairs within a cell. This scheme makes the computational time proportional to the number of the simulated particles N. Within a cell of volume V_c, the collision probability P between two simulated particles, each of which representing F_N real molecules, over a time step, Δt, is given by Bird [19] as

$$P = \frac{F_N \sigma_T C_r \Delta t}{V_c} \tag{1}$$

and the corresponding maximum value is

$$P_{\max} = \frac{F_N (\sigma_T C_r)_{\max} \Delta t}{V_c} \tag{2}$$

where σ_T is the total cross section, C_r is the relative speed, and $P_{\max}$ is the maximum collision probability.

The average number of real molecules in the cell is nV_c and the average number of simulated molecules is

$$N = \frac{nV_c}{F_N} \tag{3}$$

Using the NTC scheme, $(1/2)N\bar{N}F_N(\sigma_T C_r)_{\max}\Delta t/V_C$ pairs are chosen from the cell at each time step, where N denotes the fluctuating quantity and $\bar{N}$ denotes the average value. The collision procedure is counted cell by cell. As mentioned before, the collision pair of molecules is chosen randomly within the same cell. Then, for a certain pair, the collision is determined by the probability

$$\frac{\sigma_T C_r}{(\sigma_T C_r)^{\max}} \tag{4}$$

According to the post-collision molecular velocity, the simulated particles will move in the next time step. The distance covered by the molecules in each direction is equal to the time step multiplied by the corresponding velocity components.

The post-collision state of the involved pair is determined stochastically, conserving momentum and energy with the post-collision angles selected from kinetic theory distribution. The variable hard sphere (VHS) model introduced by Bird [19] is used to model the intermolecular potential between collision pairs and to calculate the post-collision velocities from the precollision state. The VHS model was widely used because of its simplicity and also its good approximation to real intermolecular potential. Afterward, the macroscopic properties are sampled by the weighting average of the microscopic properties based on each cell. The whole procedure is repeated for the appropriate number of iterations until the steady state is achieved.

As shown in Table 1, the maximum channel length used in the current simulations is up to 20 μm; still, it is not as long as those in real experimental works, such as 3000 μm [20], 4000 μm [21], and 4500 μm [22]. This is due to the limitation in computational capability. For a typical case in the current work, the sample size is above 8×10^5 and the number of simulated molecules is over 1×10^5, which takes over 96 hours for a computer with a CPU of 3.6 GHz to complete. It should be emphasized that the Kn is varied by adjusting the channel height and that helium is used as the test species unless indicated otherwise. The test matrix according to the current work is described in detail in Tables 1 and 2. The channel length, pressure ratio, wall temperature distribution are also varied to investigate the effects of each factor on the flow properties and heat transfer characteristics.

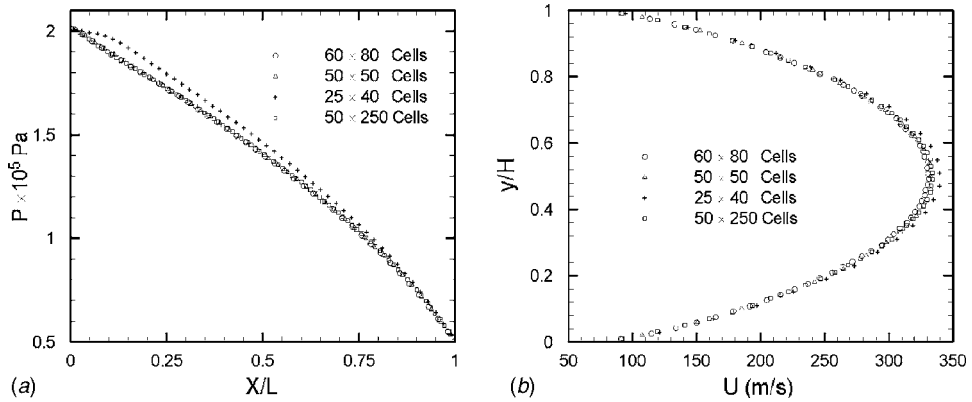

Fig. 3 Mesh size effect on (*a*) the pressure distribution along the uniform channel and (*b*) the streamwise velocity profiles at the channel midspan

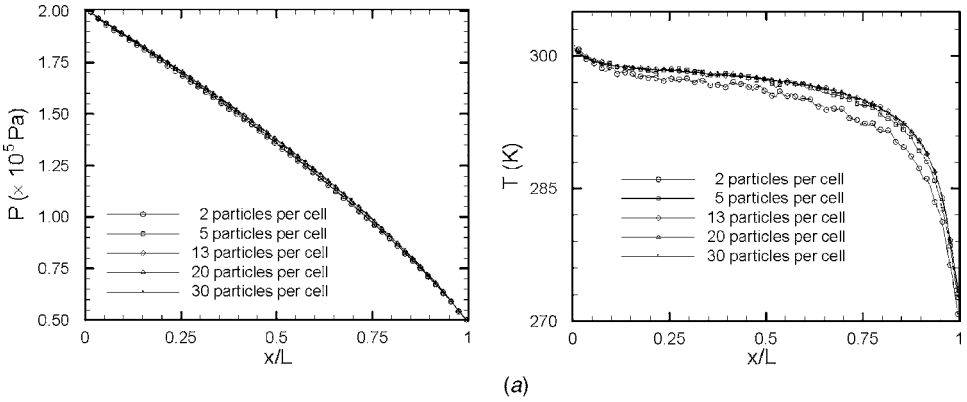

(*a*)

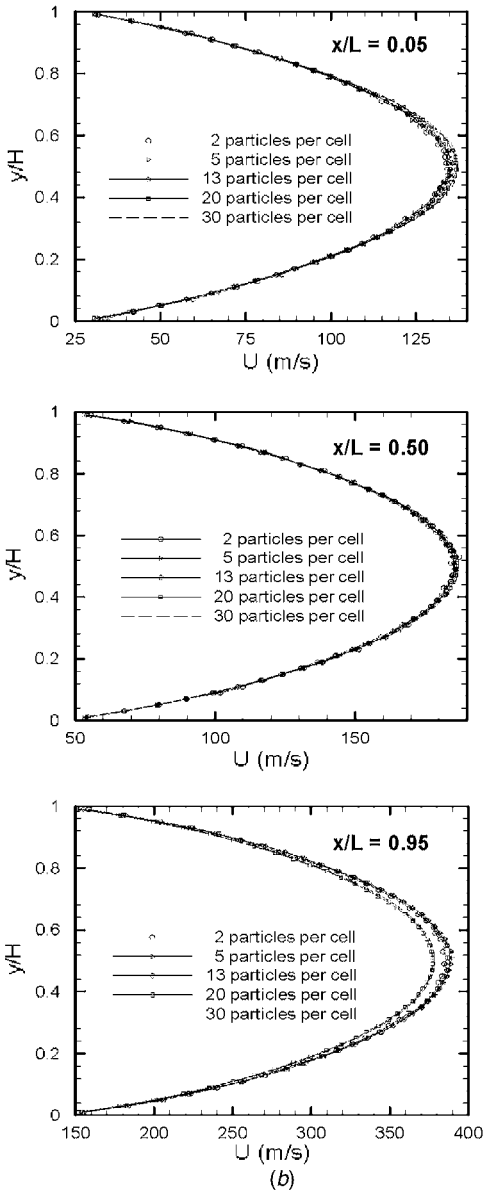

(*b*)

Fig. 4 (*a*) **Effect of the average number of simulated particles per cell on the pressure and centerline temperature distributions and** (*b*) **Effect of the average number of simulated particles per cell on velocity profiles at channel inlet, midspan, and outlet**

2.3 Accuracy of the Numerical Results. Unlike the conventional CFD solvers, there are three factors which can affect the accuracy of the simulation results, the number of cells in the computational domain, which is referred as the mesh size, the number of particles per cell, and the number of real molecules represented by each simulated particle, which is also called "scaling factor".

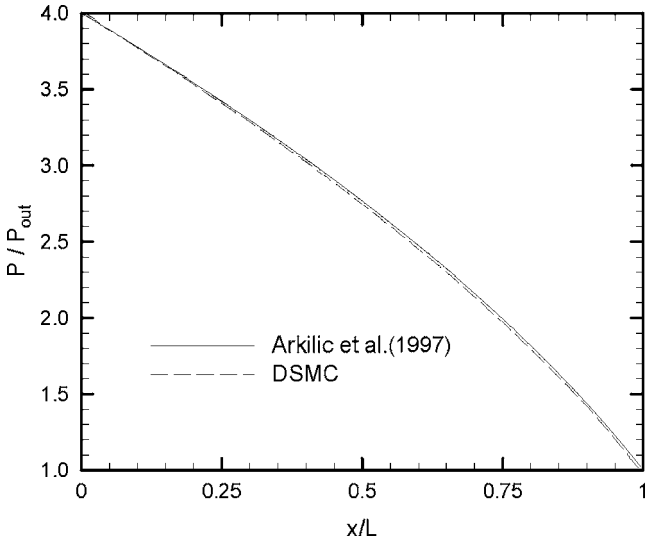

Fig. 5 Pressure distribution along the uniform microchannel for $Kn_{in}=0.0547$ and $P_{in}/P_{out}=4$

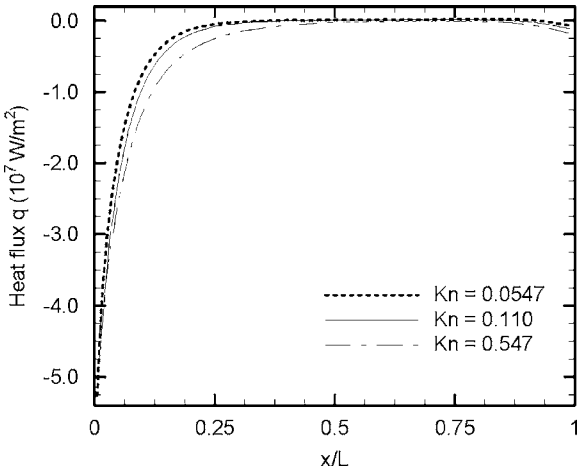

Fig. 7 Wall heat flux distribution for flow in uniform microchannels with $T_w=500$ K

The mesh size should be big enough to satisfy the accuracy requirement without exceeding the computer capacity. In addition, for a given problem the total number of molecules is fixed, which means that increasing the number of particles per cell will cause the scaling factor to decrease, fortunately, both of which lead to a more accurate solution. Therefore, the dependence of these two factors will be tested at the same time.

First, the mesh size independence was implemented by repeating the simulation with different cell dimensions in a short uniform microchannel, while sufficient number of simulated particles is involved for each case according to the work by Shu et al. [23]. In the present study, the cell dimension was set to be less than the inlet gas mean free path, since the mean free path increases along the whole channel due to the pressure drop. Therefore, if the cell dimension is appropriate compared with the inlet mean free path, the requirement of accuracy will be automatically satisfied along the rest of the entire channel.

For the channel with the height of 1 μm and the length of 5 μm, computations were first carried out with mesh size of 25×40, 50×50, and 60×80 respectively, corresponding to cell dimension of 0.305, 0.366, and 0.731 times the inlet mean free path in the direction normal to the flow. Furthermore, it was declared [24] that the cell dimension can be much greater than the local mean free paths in directions where the gradients of the flow properties are small, and while the time step could also been enlarged accordingly. This statement was proved in the present work by conducting a case with the mesh size of 50×250, which gives the cell dimension equal in both directions. Figures 3(*a*) and 3(*b*) show the comparison of the pressure distribution along the channel and the streamwise velocity profiles at the channel's mid-span based on different mesh sizes. It can be found that the mesh size (50×50) with the corresponding cell dimension in both directions is adequate to meet the accuracy requirement and the large cells in the flow direction do not affect the solution.

For the cases with the channel height of 0.5 μm and 0.1 μm, the mesh sizes 50×50 and 25×50 were selected, which correspond to the cell dimensions much smaller than the required ones. Apparently, these mesh sizes make the computation process more expensive. In fact, the coarser mesh (10×20) can also provide a good prediction of the velocity of the bulk flow with less computation effort; however, it is unable to capture the velocity information near the wall. Therefore, it should be specified that the number of grids needs to be sufficient not only to obtain high accuracy but also to prevent the information missing in predicting the flow. For the parallel and the series microchannel cases, the cell dimension was selected based on the grid independence test for the uniform microchannel.

Independence of the number of simulated particles was checked

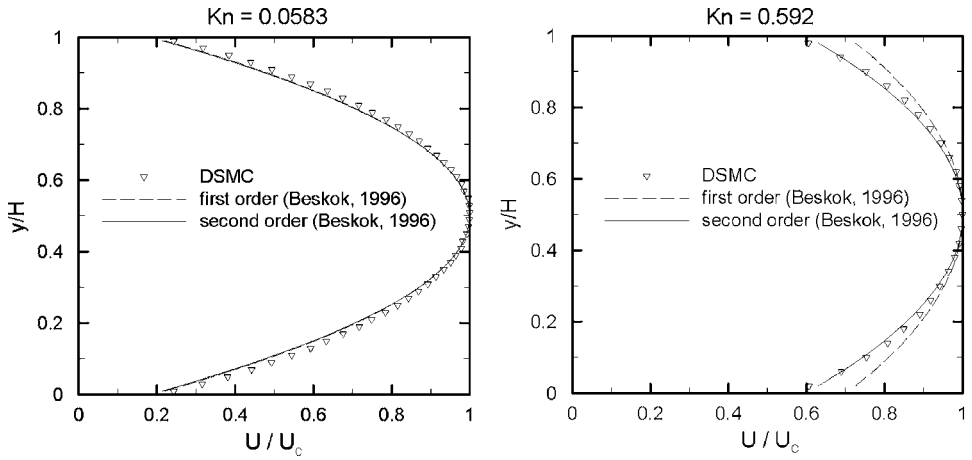

Fig. 6 Velocity profiles corresponding to different local Knudsen numbers in uniform microchannel

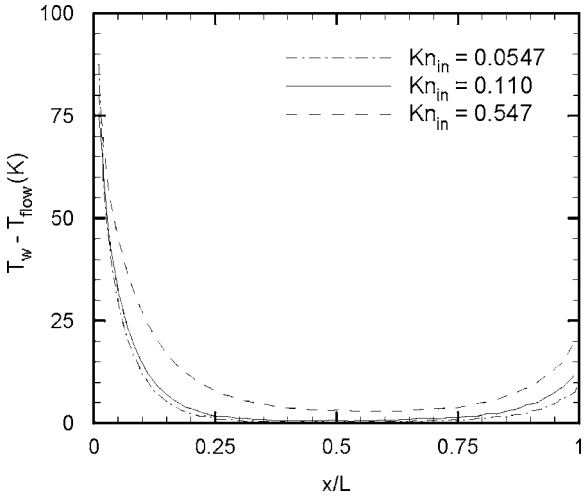

Fig. 8 Wall temperature jump for flow in uniform microchannels

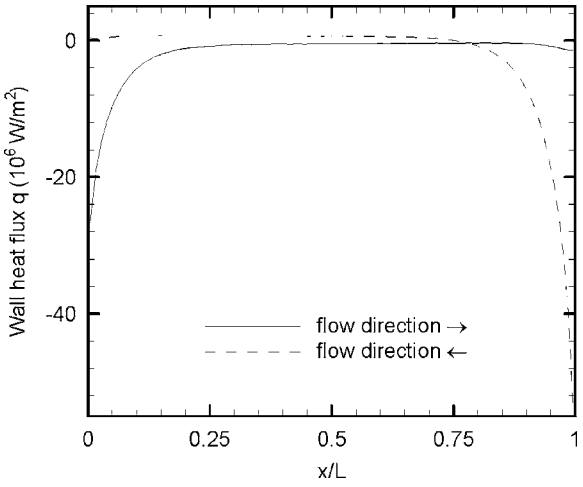

Fig. 11 Wall heat flux for cases with linear wall temperature distribution

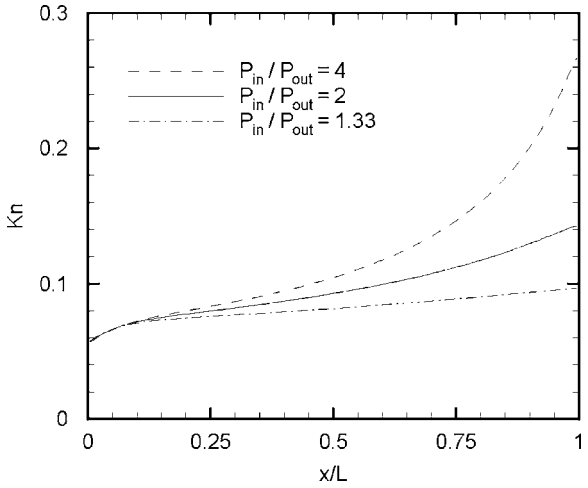

Fig. 9 Kn number distribution along the uniform channel for P_{in}/P_{out}=4, 2, and 1.33

also in the uniform microchannel. Four cases were carried out with averagely 2, 5, 13, 20, and 30 simulated particles in each cell, corresponding to the fixed scaling factor of 3.2×10^{10}, 1.2×10^{10}, 5.0×10^{9}, 3.0×10^{9}, and 2.0×10^{9}. Figures 4(*a*) and 4(*b*), shows the effect of the number of simulated particles on the pressure distribution and centerline temperature distribution along the channel, and the velocity profiles at different cross sections respectively. It can be noted that the centerline temperature is more sensitive to the number of particles especially near the channel exit. Similarly, deviation can be observed from the velocity profiles near the channel outlet obviously as shown in Fig. 4(*b*). This can be explained that as the pressure decreases along the channel, the flow becomes more rarefied; few molecules are contained in the cell near the channel exit. Therefore, when the scaling factor is fixed, the number of simulated particles contained in one cell decreases along the channel causing the significant difference near the channel exit. Similar tests have also been conducted in the parallel and series microchannels although the results are not presented here. It can be concluded that 20 simulated particles per cell used in the current work as well as the corresponding scaling factor, which has the order of 10^9, is appropriate to achieve the accuracy of the numerical results, which is also consistent to the conclusion presented in Shu et al.'s work [23].

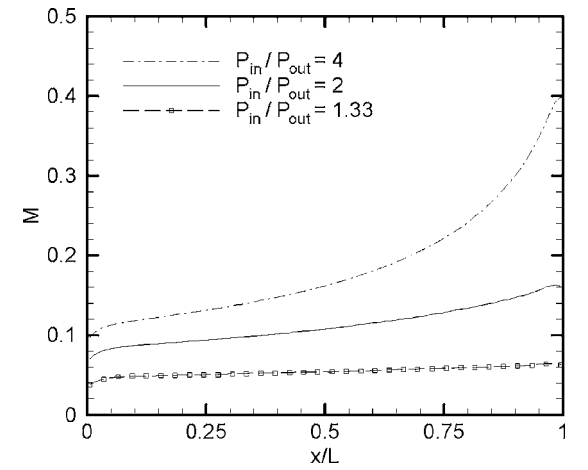

Fig. 10 Mach number distribution along the centerline of the uniform microchannel for P_{in}/P_{out}=4, 2 and 1.33

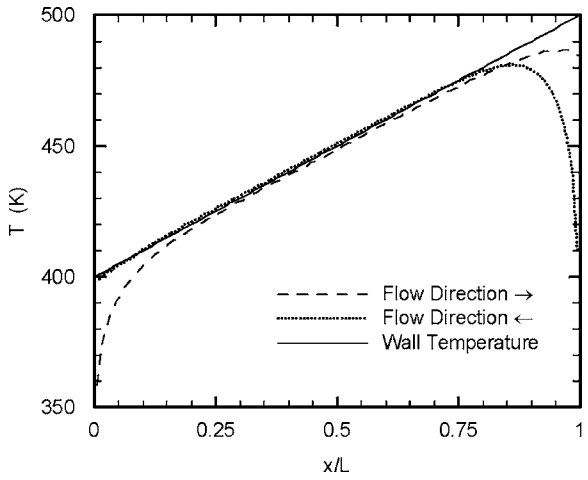

Fig. 12 Temperature distribution of the flow close to the wall

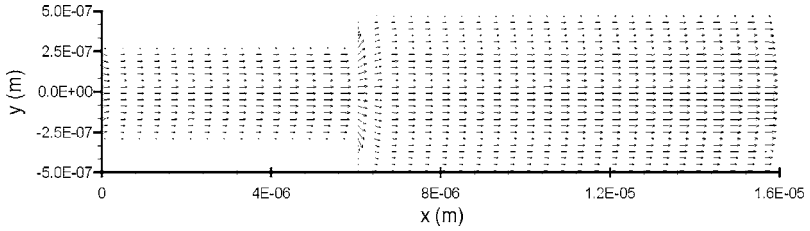

Fig. 13 Velocity vectors for series microchannel flow at $P_{in}/P_{out}=4$ and $Kn_{in}=0.0912$

3 Results and Discussion

3.1 Uniform Microchannels. The DSMC code used in the current work was first verified by comparing the results to analytical solutions. Figure 5 shows a good agreement between the DSMC result and the analytic solutions in the pressure distribution [25]. Moreover, Fig. 6 depicts the comparison of the normalized velocity profiles obtained from the DSMC modeling and the analytical solver by Beskok [26]. When the local Kn is equal to 0.0583, corresponding to the flow in the slip regime, the three curves agreed well with each other with a maximum deviation of $<8\%$. As the flow goes into the transition regime for Kn=0.592, the first-order approximation can no longer predict the flow accurately with an unexpected higher velocity slip occurring near the wall, while the second-order solution can still work properly. One can find that the DSMC is able to predict the flow not only in the slip regime but also in the transition regime successfully.

In order to investigate the Kn effect on the heat transfer characteristics for subsonic microchannel flows, the wall temperature was set as 500 K for the base case, case 2, case 4, and case 5, respectively, while the freestream gas temperature was 300 K. Figure 7 shows that for all the three cases most of the wall heat flux occurs at the channel entrance region, within 25% of the entire channel from the inlet. The magnitude of the wall heat flux in the higher Kn case is slightly greater than that in lower Kn cases. The negative sign indicates that the heat transfer direction is from the hot wall to the bulk flow. This may be caused by the higher wall temperature jump occurring in the more rarefied case as shown in Fig. 8.

In order to examine the pressure effect on the flow behavior, the pressure ratio 1.33, 2, and 4 were obtained by fixing the inlet pressure at 2.0×10^5 Pa while the outlet pressure varied from 0.5×10^5 Pa to 1.5×10^5 Pa. Figure 9 shows that when $P_{in}/P_{out}=2$ or 4 the local Kn increases from below 0.1 to above 0.1, which indicates that it is possible to have flow in mixing Kn regimes. Hence, DSMC becomes the uniform valid tool to predict this type of flow. The effect of the pressure ratio on the flow velocity is shown in Fig. 10. The flow velocity increases along the channel, and at a given position, the Mach number is larger with a higher pressure ratio. In addition, the Mach number increases more rapidly in a higher pressure ratio case than that in lower pressure ratio cases, especially in the lower half of the channel. Imposing a higher pressure ratio, the compressibility of the gas flow becomes more significant as it develops along the microchannel: a rapid decrease in the flow density occurs. Therefore, in order to satisfy mass conservation, the flow has to accelerate more accordingly. The pressure ratio has almost no effect on the wall heat flux (not shown here), since most of the heat transfer occurs at the first quarter length of the channel, where the pressure ratio has only slight effects on the flow.

Figure 11 shows the effect of the wall temperature distribution on the wall heat flux while Fig. 12 shows the resulting flow temperature distributions close to the walls. In the present work, a linear wall temperature distribution between 400 K and 500 K is applied to the base case 2. Figure 11 shows that when the flow enters from the cold side, where $T_w=400$ K, most of the wall heat flux occurs at the entrance region and maintains a slightly negative value along the rest of the channel. When the flow enters from the hot side, where $T_w=500$ K, downstream the entrance region where the flow was wholly heated (don't make sense), the heat flux is reversed from the bulk flow to the wall with a constant downstream the entrance region. This phenomenon can be explained by the wall temperature distribution depicted in Fig. 12. For the first case, after the flow was mainly heated within the entrance region the flow temperature was always slightly lower than the wall temperature since the wall temperature kept increasing. However, for the other case, as the flow becomes entirely heated by the high temperature at the entrance the wall, the wall temperature decreases along the channel, and as a result, the flow temperature is always slightly higher than the wall.

3.2 Series Microchannels. Figure 13 shows the velocity vectors for case 10 under the pressure ratio of 4. The streamwise velocity profiles at each cross section are parabolic as expected except for those close to the interface between the two channel segments. The Kn for this case varies from 0.0957 to 0.230. Hence, apparent velocity slip can be observed near the wall with the magnitude of about 20 m/s at the inlet and 60 m/s at the outlet. In Fig. 14, the dashed line represents the pressure distribution of the flow coming from the narrow section while the solid line refers to the flow coming from the wide section. As the gas stream enters the narrow segment, the collision rate between the molecules and the wall increases and enhances the wall friction. As a result, larger pressure drop can be always found within the narrow segment.

The heat transfer characteristic is investigated by setting the wall temperatures higher than the incoming flow temperature. For the first case, T_{w1} (the narrow-section wall temperature) and T_{w2} (the wide-section wall temperature) are kept at 400 K and 600 K, respectively. Accordingly, for the second case the wall tempera-

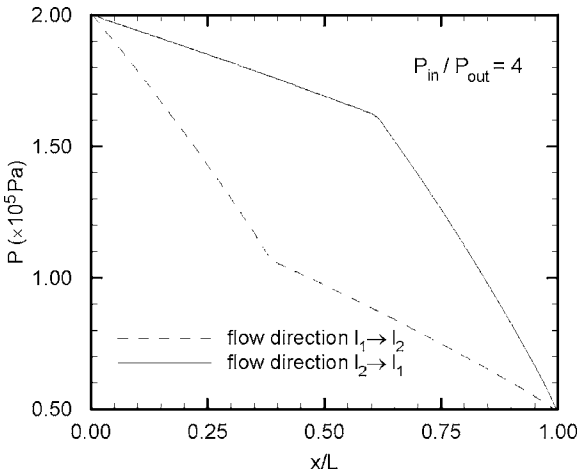

Fig. 14 Pressure distribution for the series microchannel flow coming from difference edges at $P_{in}/P_{out}=4$

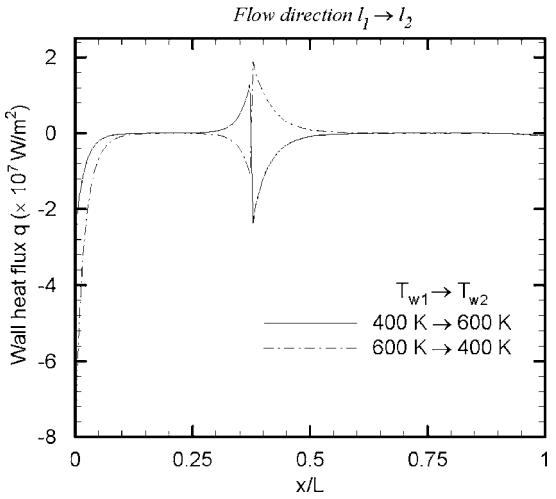

Fig. 15 Wall heat flux for the series microchannel flows with different wall temperature distributions

ture settings are reversed. Figure 15 shows that most of the wall heat flux occurs at the beginning of each section, thus warming up or cooling down the flow right away depending on the temperature difference, which in turn, is consistent to the results observed from the uniform channel cases. Unlike the uniform channel cases, a wall heat flux jump can be observed right before the interface for the first case, while a wall heat flux drop occurs in the same position for the second case.

Since the interface of the two channel segments is located at x/L=0.375, then Figs. 16(*a*) and 16(*b*) refer to the temperature profiles before the interface while Figs. 16(*c*) and 16(*d*) identify the temperature profiles after. For both cases, the flow temperature increases to the wall temperature at $x/L=0.25$ as shown in Fig. 16(*a*). However, in Fig. 16(*b*), it is interesting to find that at $x/L=0.36$ the flow temperature increases and becomes even higher than the local wall temperature for the first case. While for the second case, the flow temperature starts decreasing. This may be due to the diffusion effect of the rarefied flow, which allows the upstream flow to be warmed up or cooled down by the downstream flow near the interface. In the first case, the upstream flow from the interface is heated by the warmer downstream flow, which increases the flow temperature higher than the wall temperature. As a result, heat is transferred from the flow to the wall, which causes the wall heat flux jump as mentioned. In the second case, the flow in a small region upstream from the interface, which is already cooled by the downstream flow, needs to gain more heat from the wall and hence a heat drop occurs accordingly.

Case 11 is conducted to investigate the effect of the gas species, where argon gas flows is simulated. The velocity profiles in Figs. 17(*a*)–17(*d*) show that at $x/L=0.431$ the speed of the helium gas flow is greater than that of the argon flow; also, the velocity difference increases as the pressure ratio increases. The molecular mass of argon is 6.63×10^{-26} kg, almost ten times the molecular mass of helium, which is equal to 6.65×10^{-27} kg. The lighter gas is more sensitive to pressure drop throughout the channel and gains more acceleration as the pressure drop increases, which gives the larger difference in velocity yielding a higher velocity.

3.3 Parallel Microchannels. The velocity vectors are plotted out in Fig. 18, which schematically shows the development of the flow. The flow recirculation phenomenon can be found down-

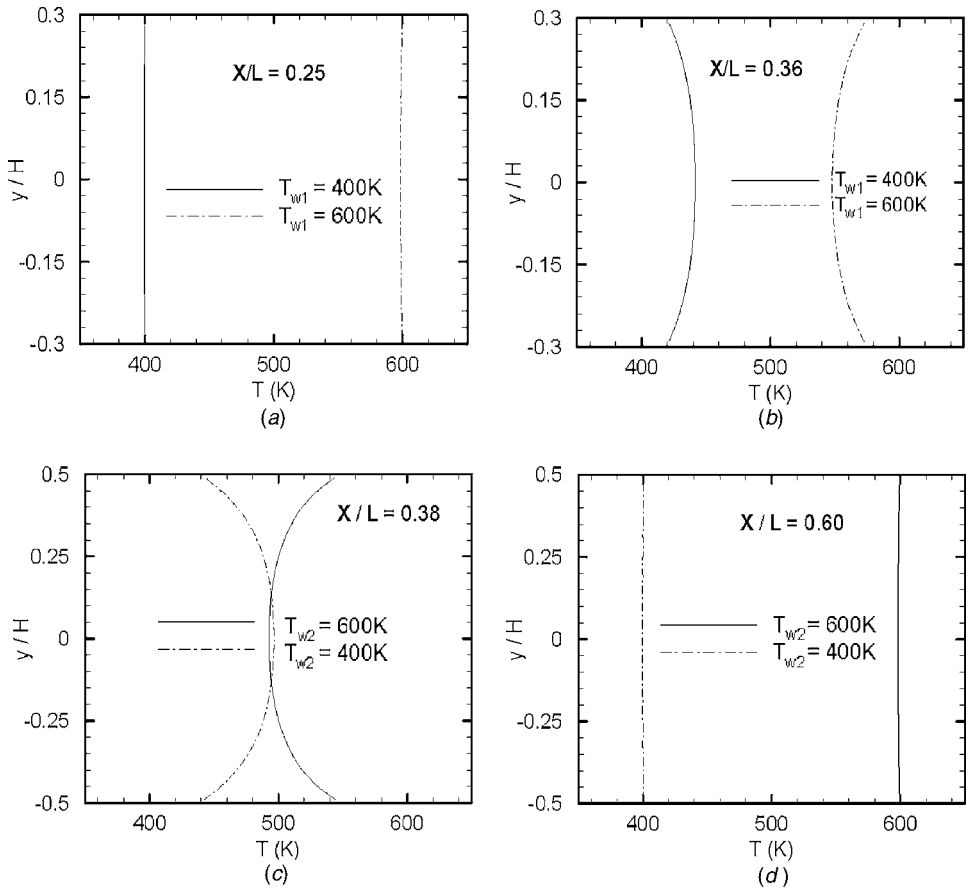

Fig. 16 Temperature profiles at (*a*) $x/L=0.25$, (*b*) $x/L=0.36$, (*c*) $x/L=0.38$, and (*d*) $x/L=0.60$

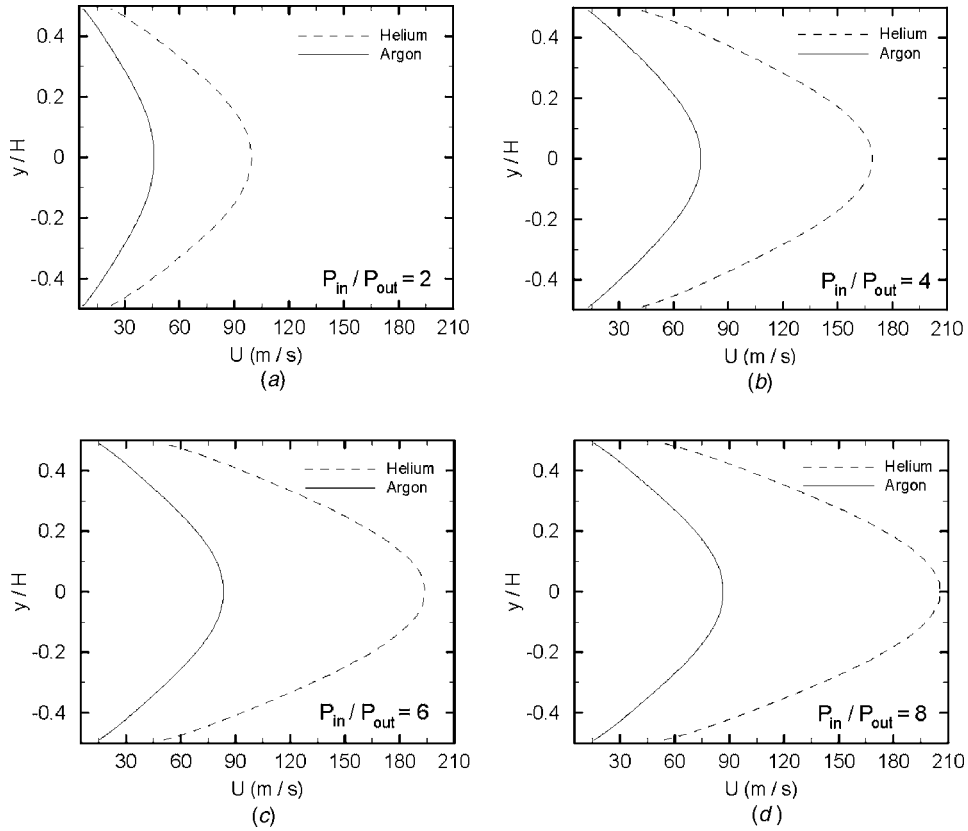

Fig. 17 Velocity profiles at $x/L=0.431$ for (*a*) $P_{in}/P_{out}=2$, (*b*) $P_{in}/P_{out}=4$, (*c*) $P_{in}/P_{out}=6$, and (*d*) $P_{in}/P_{out}=8$

stream from the gap which separates the two incoming flows. This is caused by a reversed pressure drop in the region where the parallel channel flows start to merge. After the flow was fully developed, the velocity profiles are parabolic as expected.

In the present work, the parameter, L_D/H, is introduced as a developing coefficient to evaluate the recirculation behavior in a quantitative manner, where L_D defines the developing length and H is the main channel height. The developing length is determined by introducing a relative density difference [27]

$$\xi = \frac{\Delta\rho}{\rho} = \frac{\rho_w - \rho_c}{\rho_w} \tag{5}$$

where ρ_w refers to the density close to the wall, and ρ_c refers the density at the channel centerline. The evolution of the relative density difference, ξ along the channel is shown in Fig. 19. A critical value 0.3% is selected to judge whether the recirculation is over. As the flow goes further downstream, the fluctuation of ξ is within ±0.3% after a certain length. Afterwards, the flow is considered to be well developed with a relative flat density distribution along the cross section. Thus the developing length L_D can be determined as shown in Fig. 19.

Case 7–9 are carried out by varying the gap size between the two parallel channels while keeping the domain size constant. The value of $s/H=0$ represents the situation where there is no gap to separate the parallel flows, while $s/H=1$ represents the situation where the gap blocks the channel completely. As the gap height increases, the height of each of the parallel parts decreases.

Figure 20 shows the effect of the gap size on the developing coefficient. As the gap size increases, the flow in the main channel becomes fully developed sooner. In fact, this effect is negligible. Figure 21 shows the effect of the gap size on the pressure distribution near the channel wall. It is apparent that as the gap size increases, more pressure drop occurs within the parallel parts due

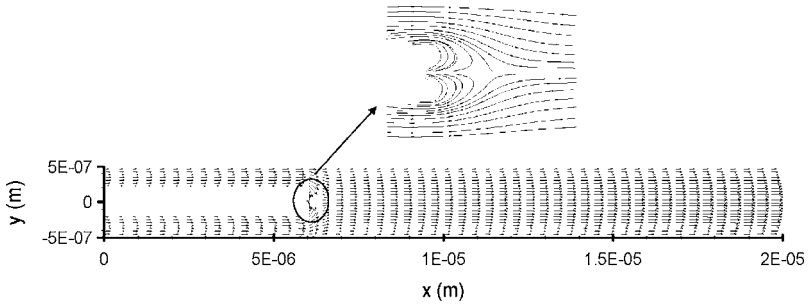

Fig. 18 Velocity vectors of the parallel microchannel flow at $P_{in}/P_{out}=4$ and $Kn_{in}=0.182$

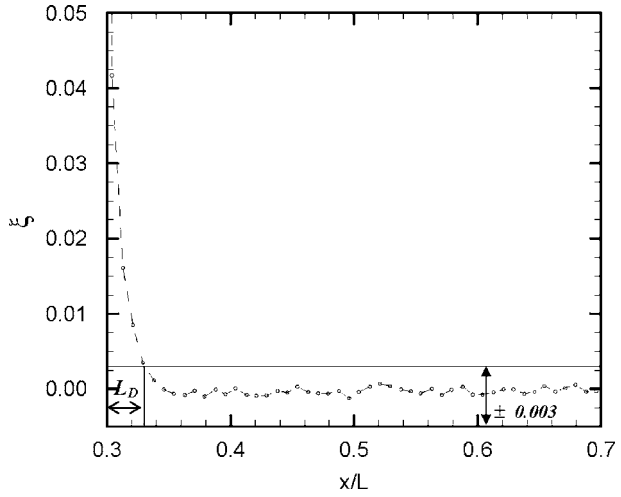

Fig. 19 Evolution of the relative density difference

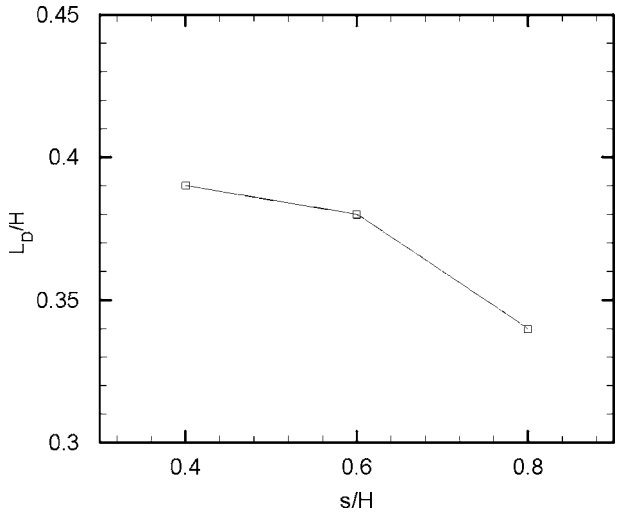

Fig. 20 Effect of the gap size on the developing coefficient

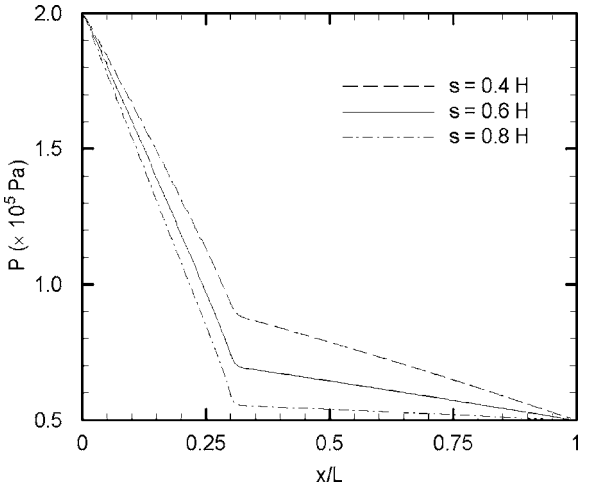

Fig. 21 Wall pressure distribution along the parallel microchannel with different gap sizes

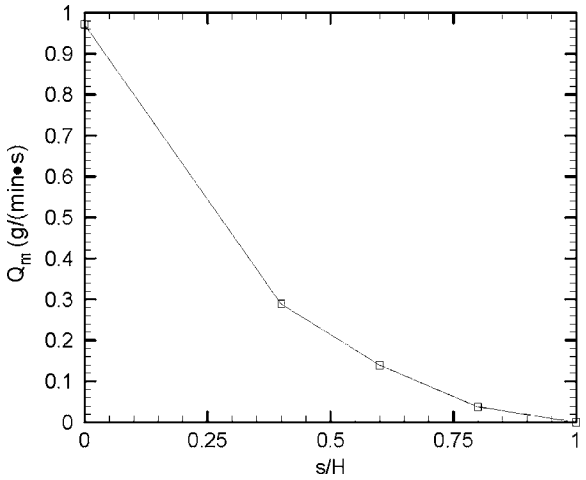

Fig. 22 Effect of the gas size on the mass flow rate at $P_{in}/P_{out}=4$

to the enhanced wall resistance, which is explained in the uniform channel section. The mass flow rate with respect to the nondimensional gap size is shown in Fig. 22.

4 Conclusion

In the present work, subsonic flows in the uniform microchannel, the series microchannel and the parallel microchannel, were investigated using DSMC. For the uniform microchannel flow, DSMC code with pressure boundary conditions was verified by comparing results with the analytical solutions. The nonlinear pressure distribution and the velocity slip near the wall were obtained as expected. Different inlet Kn corresponding to the slip regime and the transition regime were employed in uniform channel cases. As a higher pressure ratio is imposed, it is possible to have the flow in mixing Kn regimes, which makes DSMC the most powerful tool to predict the flow. Moreover, by applying a linear wall temperature distribution, a constant heat flux can be obtained downstream from the entrance region.

Series and parallel microchannel cases were conducted by modifying the original Bird's code and a successful modeling has been achieved. Instead of using the whole rectangular domain, a part of the domain was excluded. The new computational domain for series or parallel microchannel was established by adding three surfaces and applying one symmetric boundary along the channel centerline. For series microchannel flow, larger pressure drop occurs in the narrow segment as the flow enters from either of the channel edges. Imposing different wall temperatures on the two channel segments, the diffusion effect can be observed from the temperature profiles near the interface. As a result, a heat flux jump or heat flux drop within the interface region is obtained. Simulations were also performed for different gas species: helium and argon. Helium is much easier to be accelerated due to its light molecular mass. In parallel channel cases, a parameter named as developing coefficient is defined to evaluate the recirculation flow behavior quantitatively. The gap size has slight effect on the recirculation phenomenon.

Nomenclature

C_r = relative speed of two molecules
d = molecular diameter
F_N = number of real molecules represented by a simulated particle
h_1 = channel height of the first segment of the series microchannel
h_2 = channel height of the second segment of the series microchannel

H = channel height of the uniform microchannel
Kn = knudsen number
l_1 = channel length of the first segment of the series microchannel
l_2 = channel length of the second segment of the series microchannel
L = channel length of the uniform microchannel
L_D = developing length
M = mach number
n = number density
N = number of the simulated particles
$\bar{N}$ = average number of the simulated particles
P = probability of collision between two simulated particles
$P_{\max}$ = maximum probability of collision between two simulated particles
P_{in} = inlet pressure
P_{out} = outlet pressure
q = wall heat flux
Q_m = mass flow rate
S = gap size between the two parallel parts of the parallel microchannel
T_{flow} = flow temperature
T_{in} = inlet flow temperature
T_w = wall temperature
T_{w1} = wall temperature of the first segment of the series microchannel
T_{w2} = wall temperature of the second segment of the series microchannel
Δt = time step
U/U_c = dimensionless velocity
V_c = cell volume
VHS = variable hard sphere model
X = coordinate along the axis of the channel
Y = coordinate along the vertical direction of the channel

Greek Letters

λ = mean free path
σ = cross-section
α = thermal accommodation coefficient
ξ = relative density difference
ρ_w = flow density close to the wall
ρ_c = flow density at the channel center
ρ_{out} = outlet flow density
σ_T = total collision cross section

References

[1] Mavriplis, C., Ahn, J. C., and Goulard, R., 1997, "Heat Transfer and Flowfields in Short Microchannels Using Direct Simulation Monte Carlo," J. Thermophys. Heat Transfer, **11**, pp. 489–496.
[2] Karniadakis, G., and Beskok, A., 2002, *Micro Flows: Fundamentals and Simulation*, Springer-Verlag, Berlin.
[3] Oh, C. K., Oran, E. S., and Sinkovits, R. S., 1997, "Computations of High-Speed, High Knudsen Number Microchannel Flows," J. Thermophys. Heat Transfer, **11**, pp. 497–505.
[4] Liou, W. W., and Fang, Y., 2001, "Heat Transfer in Microchannel Devices Using DSMC," J. Microelectromech. Syst., **10**, pp. 274–279.
[5] Piekos, E. S., and Breuer, K. S., 1995, "DSMC Modeling of Micromechanical Device," FDRL-TR-95-5, Fluid Dynamics Research Laboratory.
[6] Fan, Q., Xue, H., and Shu, C., 1999, "DSMC Simulation of Gaseous Flows in Microchannels," *Proceedings of 5th ASME/JSME Joint Thermal Engineering Conference* March 15-19, San Diego, ASME, New York, ASME Paper No. AJTE99–6519.
[7] Liou, W. W., and Fang, Y. C., 2000, "Implicit Boundary Conditions for Direct Simulation Monte Carlo Method in MEMS Flow Predictions," Comput. Model. Eng. Sci., **1**, pp. 119–128.
[8] Xue, H., Fan, Q., and Shu, C., 2000, "Prediction of Micro-channel Flows Using Direct Simulation Monte Carlo," Probab. Eng. Mech., **15**, pp. 213–219.
[9] Fang, Y. C., and Liou, W. W., 2002, "Computations of the Flow and Heat Transfer in Microdevices Using DSMC With Implicit Boundary Conditions," ASME J. Heat Transfer, **124**, pp. 338–345.
[10] Fang, Y., Farouk, B., and Johnson, J., 2002, "Direct Simulation Monte Carlo Calculations of Three Dimensional Non-continuum Gas Flows," ASME, *Heat Transfer Division* (Publication) HTD, 372, pp. 33–40.
[11] Qunwu, H., Qiuwang, W., Xian, W., and Ozoe, H., 2004, "Computational Investigation of Low-Speed Gas Flow and Heat Transfer in Micro-Channel Using DSMC With Pressure Boundary Condition," Adv. Heat Transfer, **46**, pp. 463–469.
[12] Wang, M., and Li, Z., 2004, "Simulations for Gas Flows in Microgeometries Using the Direct Simulation Monte Carlo Method," Int. J. Heat Fluid Flow, **25**, pp. 975–985.
[13] Xue, H., Ji, H., and Shu, C., 2003, "Prediction of Flow and Heat Transfer Characteristics in Micro-Coutte Flow," Microscale Thermophys. Eng., **7**, pp. 51–68.
[14] Hadjiconstantinou, N. G., 2000, "Convective Heat Transfer in Micro and Nano Channels: Nusselt Number Beyond Slip Flow," *Proceedings of ASME Heat Transfer Division*, ASME, New York, Vol. 2, pp. 13–22.
[15] Hadjiconstantinou, N. G., and Simek, O., 2002, "Constant-Wall-Temperature Nusselt Number in Micro and Nano-Channels," ASME J. Heat Transfer, **124**, pp. 356–364.
[16] Hadjiconstantinou, N. G., 2003, "The Effect of Viscous Heat Dissipation on Convective Heat Transfer in Small-Scale Slipping Gaseous Flows," *First International Conference on Microchannels and Minichannels*, April 24–25, Rochester, ICMM2003-1029, pp. 269–273.
[17] Ikegawa, M., and Kobayashi, J., 1990, "Development of a Rarefied Gas Flow Simulator Using the Direct-Simulation Monte Carlo Method (2-d Flow Analysis with the Pressure Conditions Given at the Upstream and Downstream Boundaries)," JSME Int. J., Ser. II, **33**, pp. 463–467.
[18] Wu, J.-S., and Tseng, K.-C., 2001, "Analysis of Micro-scale Gas Flows With Pressure Boundaries Using Direct Simulation Monte Carlo Method," Comput. Fluids, **30**, pp. 711–735.
[19] Bird, G. A., 1994, *Molecular Gas Dynamics and the Direct Simulation of Gas Flows*, Oxford Engineering Science, Oxford University Press, New York.
[20] Pong, K.-C., Ho, C.-M., Liu, J., and Tai, Y.-C., 1994, "Non-linear Pressure Distribution in Uniform Microchannels," *Application of Microfabrication to Fluid Mechanics*, ASME, 197, pp. 51–56.
[21] Cheng, K. B., Wong, M., and Zohar, Y., 2003, "Parallel and Series Multiple Microchannel Systems," *Proceedings of IEEE Micro Electro Mechanical Systems (MEMS)*, IEEE, New York, pp. 291–294.
[22] Liu, J., Tai, Y.-C., and Ho, C.-M., 1995, "MEMS for Pressure Distribution Studies of Gaseous Flows in Microchannels," *Proceedings of IEEE Micro Electro Mechanical Systems (MEMS)*, IEEE, New York, pp. 209–215.
[23] Shu, C., Mao, X. H., and Chew, Y. T., 2005, "Particle Number Per Cell and Scaling Factor Effect on Accuracy of DSMC Simulation of Microflows," Int. J. Numer. Methods Heat Fluid Flow, **15**, pp. 827–841.
[24] Ilgaz, M., and Çelenligil, M. C., 2003, "DSMC Simulation of Low Density Choked Flow in Parallel-Plate Channel," *23rd International Symposium, AIP Conference Proceedings*, AIP, New York, Vol. 663, pp. 831–840.
[25] Arkilic, E. B., Schmidt, M. A., and Breuer, K. S., 1997, "Gaseous Slip Flow in Long Microchannels," J. Microelectromech. Syst., **6**, pp. 167–178.
[26] Beskok, A., 1996, "Simulations and Models for Gas Flows in Microgeometries," Ph.D. dissertation, Princeton University, Princeton.
[27] Wang, Moran, and Li, Z., 2006, "Gases Mixing in Microchannels Using the Direct Simulation Monte Carlo Method," Int. J. Heat Mass Transfer, **49**, 1696–1702.

Experimental Determination of Geometric Parameters for an Annular Injection Type Supersonic Ejector

Sehoon Kim
Senior Researcher
3-Hynmoo-3,
Agency for Defense Development,
Jochiwongil 462, Yuseong,
Daejeon, Republic of Korea

Sejin Kwon[1]
Division of Aerospace Engineering,
Department of Mechanical Engineering,
Korea Advanced Institute of Science and Technology,
373-1 Guseong-dong, Yuseong-gu,
Daejeon, 305-701, South Korea
e-mail: trumpet@kaist.ac.kr

The effects of four geometric parameters of an annular injection supersonic ejector, namely, the primary nozzle exit-to-throat area ratio, the contraction angle of the mixing chamber, the cross-sectional area and L/D ratio of the second-throat on the performance parameters including the secondary flow pressure, the starting pressure and unstarting pressure were investigated experimentally. The starting pressure exhibits linearly proportional dependence on the throat area ratio when the mixing chamber length is less than a certain critical value. For a longer mixing chamber, the starting pressure is proportional to the mixing chamber length while the unstarting pressure depends on the throat area ratio only. The geometric parameters of the second-throat do not affect the static pressure of the secondary flow. This implies that the secondary flow is aerodynamically choked in the mixing chamber and the static pressure of the secondary flow is determined by the choking condition since the mixing chamber of the annular injection ejector is relatively long. Based on the findings by the experiment, a simplified analytical model was proposed to predict the secondary flow pressure. The predicted secondary flow pressure agrees reasonably well with the measurement for a small contraction angle of the mixing chamber. [DOI: 10.1115/1.2353264]

Keywords: annular injection supersonic ejector, second-throat, aerodynamic choking, hysteresis

1 Introduction

An ejector is a device in which the momentum of the primary flow with high kinetic energy is transferred to the secondary flow. The momentum transfer takes place as the high-speed primary flow is injected into the secondary flow that is stagnant or moving slowly. When the primary flow is supersonic, the ejector effectively generates a secondary flow that is in near-vacuum condition [1].

The injection of the primary flow can be either central or annular; assuming the cross section of the secondary flow passage is cylindrical. In a central injection ejector, the primary flow is injected along the centerline of the secondary flow. The ejector of this type is easy to manufacture and has a simple structure. Most practical applications of ejectors have adopted central injection [1]. Existing theories and experimental data on ejectors are mostly concerned with central injection type. However, central injection is not adequate when the ejector is to be used for pumping chemical lasers, because the passage of the primary flow is directly exposed to the hot stream of secondary gas that is frequently caustic [2–4]. When maximizing the momentum of the secondary flow is critical as in rocket based combined cycle (RBCC) engines, the protrusion of primary flow passage into the secondary flow can lead to excessive momentum loss [5,6].

Annular injection of the primary flow is an alternative in these cases. By injecting primary flow through an annular nozzle at the internal wall of the secondary flow duct, the secondary flow passes the primary nozzle without severe disturbance. Figure 1 is a schematic of an annular injection type supersonic ejector with a second-throat. The primary flow is injected through an annular nozzle and mixed with the secondary flow in a mixing chamber. There is no blockage due to the primary flow in the secondary flow. The primary flow is deflected by a contraction angle, α, entering the mixing chamber. The contraction of the flow passage in the mixing chamber is desirable for better penetration of the primary flow into the stream of the secondary flow. However, the contraction angle should be moderate not to incur excessive pressure loss that may results from an oblique shock wave originating at the mixing chamber inlet. As a result, the mixing chamber in an annular injection ejector is significantly longer than that of a central injection ejector.

Figure 2 is a typical performance curve of an annular injection supersonic ejector [7,8]. The normalized primary stagnation pressure was plotted against the normalized secondary pressure. As the stagnation pressure of the primary flow increases, the fore part of the diverging section of the primary nozzle becomes supersonic and aft part becomes subsonic with a normal shock demarcating these two flow regions. As a result, subsonic mixing occurs between the primary and secondary flows in the entire mixing chamber. This condition corresponds to region (1) in the figure. As the stagnation pressure of the primary flow increases further, the shock wave is pushed outside of the primary nozzle. Therefore, supersonic mixing takes place in part of the mixing chamber as shown in region (2). When the primary stagnation pressure increases beyond starting pressure in region (3), the whole mixing chamber is filled with supersonic primary flow and the shock is swallowed by the second-throat. At this condition, the design static pressure of the secondary flow is established. Once the ejector is started, the supersonic ejection is in operation even at a primary pressure that is below the starting pressure of the primary flow. The supersonic ejection terminates when the stagnation pressure of the primary flow decreases further down to the unstarting point in Fig. 2. This is a unique feature of an annular injection ejector that is connected to a second-throat downstream. Taking

[1]Corresponding author.

Contributed by the Fluids Engineering Division of ASME for publication in the JOURNAL OF FLUIDS ENGINEERING. Manuscript received March 15, 2005; final manuscript received May 14, 2006. Assoc. Editor: Phillip M. Ligrani.

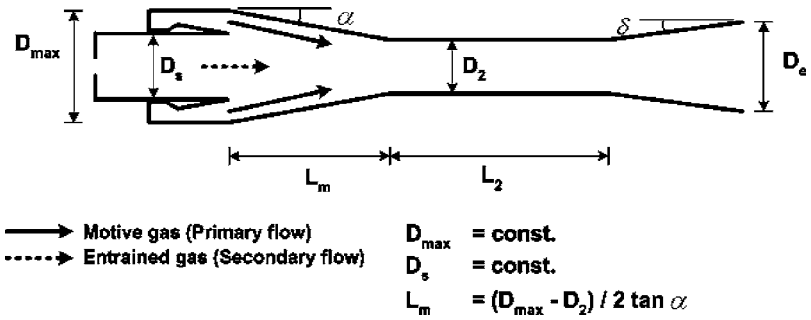

Fig. 1 Schematic of an annular injection type supersonic ejector with a second-throat

advantage of this hysteresis behavior, the steady operating stagnation pressure of the primary flow can be reduced significantly to a value that is slightly higher than the unstarting pressure after the ejector is started.

The gap between the starting and unstarting pressures becomes larger as the mixing chamber length increases. This behavior is not observed in a central injection ejector because its mixing chamber is relatively short [9,10].

In the present study, we investigated the effects of the primary nozzle shape and geometric configuration of the flow passage downstream the primary flow injection on the performances of an annular injection ejector, namely, static pressure of the secondary pressure and the primary stagnation pressure at the starting and unstarting conditions. By doing so, we intend to understand the performance characteristics and provide a baseline data for ejector sizing. The specific parameters we tested in the present study are; the nozzle of the primary flow, the throat area of the second-throat, the extended length of the second-throat, L_2, and the contraction angle that are all listed in Fig. 1.

Following the finding of experiments, a simple analytic model to estimate the secondary flow pressure for a given geometry and inlet condition was developed under the assumption that the secondary flow is choked aerodynamically in the middle of the mixing chamber [11–18]. Using the analysis, the compression ratio, Mach number of the secondary flow, and the aerodynamic choking point of the secondary flow were calculated.

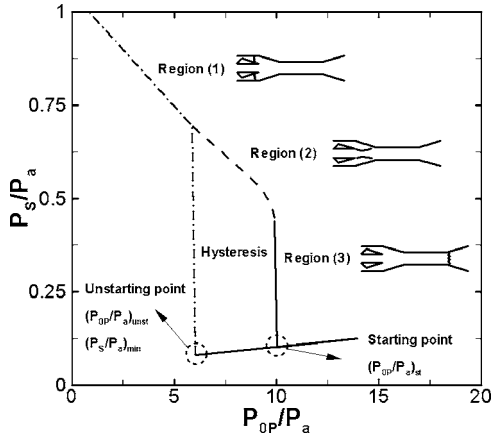

Fig. 2 A performance curve of a typical annular injection supersonic ejector with a second-throat

2 Experiments

2.1 Experimental Setup. The schematic of the test facility is illustrated in Fig. 3. The supersonic primary flow is injected annually downstream the inlet of the secondary flow. Low-pressure region is induced inside the mixing chamber due to the expanding primary flow and the secondary flow is sucked into the flow passage from the ambient via a mass flow controller (MFC). Mixing between the primary and secondary flows takes place in the mixing chamber that is a part of the flow passage between the primary nozzle exit and the second-throat inlet. Therefore, the primary nozzle, the mixing chamber, and the second-throat indirectly affect the secondary flow and determine the performance of the ejector by producing a low pressure region in the mixing chamber. The four geometric parameters that determine the flow field in the mixing chamber and other configurations are listed in Table 1. We experimentally determined the effects of these parameters on the ejector performance in the present study.

Three different values were tested for each geometric parameter, resulting in 81 shapes of the flow passage. The exit area of the primary nozzle (A_{Pe}) was fixed at $(\pi/4)$ (44^2-34^2) mm^2. The variation of the expansion ratio of the primary was made by changing the throat area (A_P^*) of the primary nozzle.

The experiment begins with gradually opening the valve of the primary flow line so that the stagnation pressure of the primary

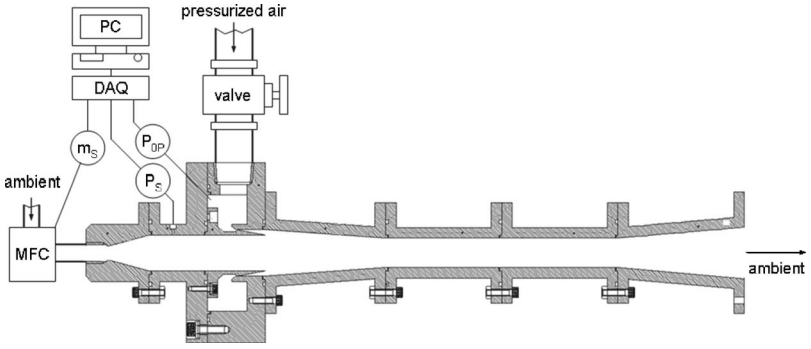

Fig. 3 Test installation of the annular injection supersonic ejector

Table 1 Configurations of the ejector

Primary nozzle area ratio, A_{Pe}/A_P^* (M_{Pe})	8.97 (3.8)	10.78 (4.0)	12.95 (4.2)
Second-throat area, $A_2^*=(\pi/4)D_2^2$	$(\pi/4)27^2$ mm^2	$(\pi/4)28^2$ mm^2	$(\pi/4)29^2$ mm^2
Second-throat L/D ratio, $(L/D)_2$	6	8	10
Contraction angle of mixing chamber, α	4 deg	7 deg	10 deg
Outer diameter at primary nozzle exit, D_{max}		44 mm	
Inner diameter at primary nozzle exit, D_S		34 mm	
Diameter at diffuser exit, D_e		50 mm	
Diverging angle of diffuser		5 deg	

flow steadily builds up. The valve is left open so that the stagnation pressure of the primary flow rises well beyond the starting pressure and then is closed gradually. The stagnation pressure of the primary flow drops steadily. The ambient air is sucked into the passage of the secondary flow. A predetermined air flow rate enters the secondary flow passing the mass flow rate controller. For each geometric configuration, three different secondary mass-flow rates, namely, 1, 2, 3 g/s were tested in addition to a case with zero secondary mass flow.

The performance of the ejector was experimentally determined by measuring the primary stagnation pressure (P_{0P}) and the static pressure of the secondary flow (P_S) simultaneously. The locations of the pressure measurements are shown in Fig. 3. The primary stagnation pressure was measured using a piezo-transducer with an operating range of 1–30 bar and accuracy of 0.08%, while a transducer with a range of 0–400 mbar and accuracy of 0.06% was used for measurement of the static pressure of the secondary flow. The data rates of both pressure measurements were 100 Hz.

2.2 Results and Discussion. Figure 4 shows the effect of the primary nozzle area ratio on the performance curve. Area ratios of 8.97, 10.78, and 12.95 correspond to the primary nozzle exit Mach number of 3.8, 4.0, and 4.2, respectively. The starting stagnation pressure of the primary flow increases with the Mach number in Fig. 4. The increased stagnation pressure is to compensate the reduction of the throat area of the primary nozzle (A_P^*) while the exit area is fixed and to accommodate the same mass flow rate that is required to choke the second throat. For a given primary stagnation pressure, the secondary flow pressure (P_S) slightly decreases as the primary exit Mach number increases. The lower static pressure at the primary exit for higher Mach number induces lower secondary flow pressure.

The effect of the contraction angle of the mixing chamber on the ejector performance is shown in Fig. 5. The contraction angle is inversely proportional to the length of the mixing chamber. As the angle increases, the mixing chamber becomes shorter and the starting pressure decreases since the distance that the exit flow of the primary nozzle should travel in supersonic speed before encountering the inlet of the second-throat decreases. The unstarting pressure is invariant at the change of the contraction angle, because both the second-throat area and the throat area of the primary nozzle are unchanged even if the length of the mixing chamber changes. With a bigger contraction angle, the oblique shock at the exit of the primary nozzle becomes stronger and results in higher static pressure in the shock downstream that induces higher static pressure of the secondary flow. This means that larger contraction angle reduces the starting stagnation pressure of the primary flow when the desired vacuum pressure for the secondary pressure is modest.

Figure 6 illustrates the effect of the second-throat area (A_2^*) on the ejector starting performance. As A_2^* increases, the starting pressure decreases while the unstarting stagnation pressure of the primary flow increases, resulting in a narrower hysteresis in the

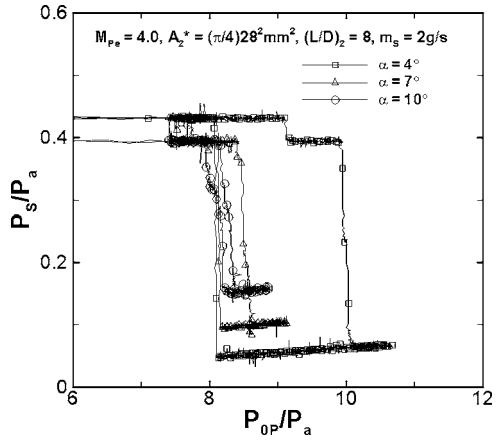

Fig. 5 Effect of mixing chamber contraction angle

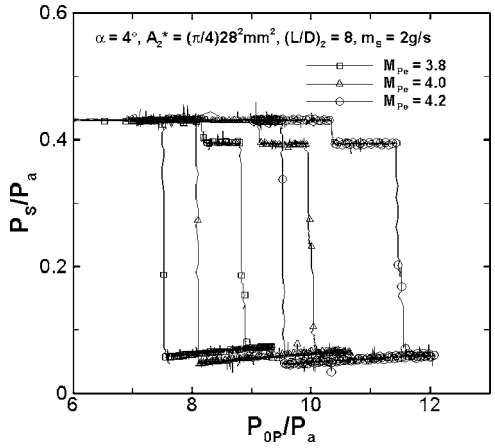

Fig. 4 Effect of Mach number at primary nozzle exit

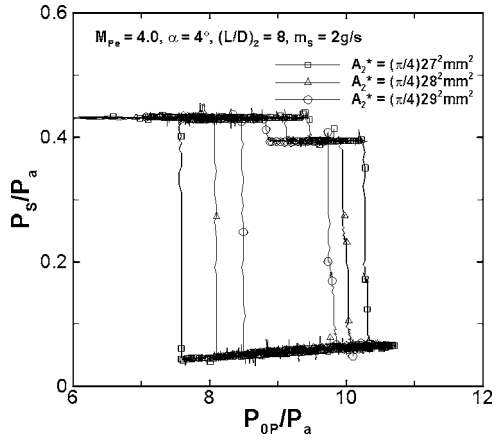

Fig. 6 Effect of second-throat cross-sectional area

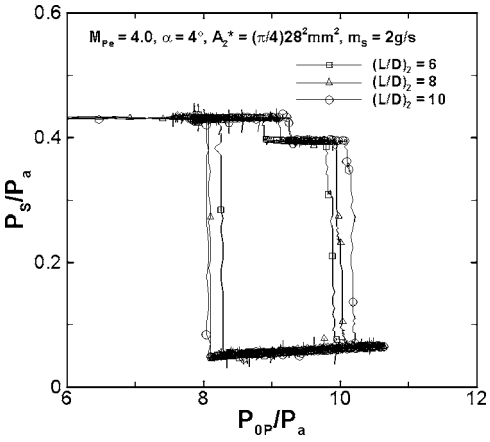

Fig. 7 Effect of second-throat L/D ratio

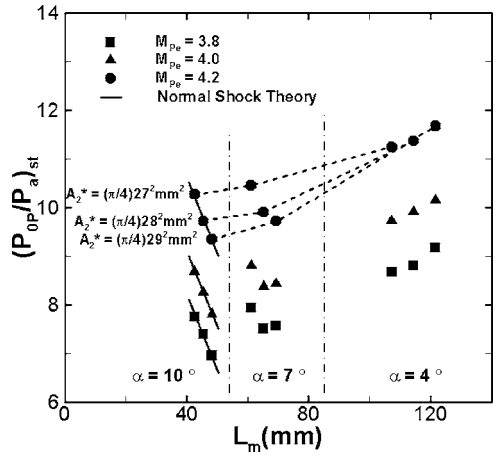

Fig. 9 Starting pressure with mixing chamber length

plot. The starting pressure decreases as a result of shorter mixing chamber following the discussion of Fig. 5. The unstarting stagnation pressure of the primary flow increases with A_2^* because the shock that is pushed downstream the second-throat returns to the mixing chamber at higher primary stagnation pressure when the second-throat area is large. If the second-throat is replaced with a constant area duct, the hysteresis behavior will disappear. While the ejectors remain in the "started" condition, the secondary flow pressure for all three cases of the second-throat area collapses on the same line. This means that the second-throat area, A_2^*, does not affect the secondary flow pressure as much as geometric parameters of the mixing chamber and the primary nozzle.

The effect of $(L/D)_2$ on the ejector performance curve is plotted in Fig. 7. For a larger $(L/D)_2$, the starting pressure increases and the unstarting pressure decreases slightly. Extending the length of the second-throat has an effect similar to reducing the second-throat in the discussion of Fig. 6 because relatively thicker boundary layer in the second-throat for larger L_2 results in a smaller effective flow passage at the end of the second-throat. Nevertheless, the effect of $(L/D)_2$ is modest for $(L/D)_2$ in the range from 6 to 10. The static pressure of the secondary flow does not depend on $(L/D)_2$ while the ejector remains in the "started" mode. This is the result of aerodynamic choking of the secondary flow inside the mixing chamber by interacting with the primary flow. Fabri et al. (Refs. [11,12]) also observed similar choking process in a central injection ejector. The static pressure of the secondary pressure upstream of aerodynamic choking, therefore, is insensitive to the changes in the second-throat.

In Fig. 8, the unstarting pressures from Figs. 4–7 are plotted against prediction by the normal shock theory (Ref. [19]) as a function of the area ratio of the second-throat to the primary nozzle throat. The symbols in the plot represent measured unstarting pressure with confidence level of 95% and 0.75% scatter. In the normal shock theory, it is assumed that the unstarting pressure is the stagnation pressure of the primary flow that sustains the normal shock wave at the second-throat. The figure shows that the prediction and measurement show a good agreement despite the diversity of the geometric configurations used in the measurements that result in Figs. 4–7.

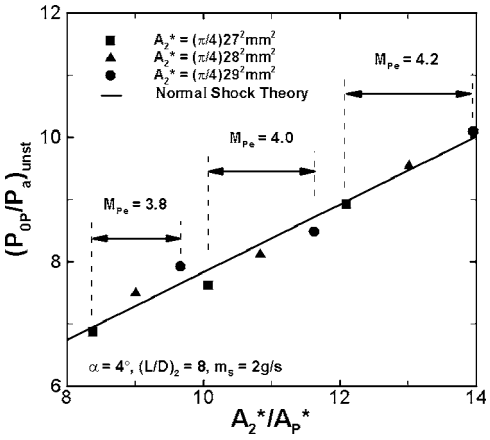

Fig. 8 Unstarting pressure with throat area ratio

The starting pressures of Figs. 4–7 are plotted with respect to the mixing chamber length, L_m in Fig. 9. The scatter of the measured starting pressure is within 0.53% with confidence level of 95% in this figure. For a contraction angle of 10 deg, the starting pressure increases with increasing A_2^*. For this angle, the starting and unstarting stagnation pressures of primary flow are almost the same as shown in Fig. 5 and this pressure is predictable by the normal shock theory. This is similar to the case of a central injection type ejector where hysteresis behavior is not observed. For a contraction angle of 4 deg, however, the starting pressure decreases with increasing A_2^*, which means that the starting pressure becomes more dependent on the length of the mixing chamber than A_2^*. This part is more relevant to the behavior of an annular injection ejector, since a relatively long mixing chamber is required for high vacuum secondary flow.

Around the mixing chamber length of 60–80 mm, a critical length can be defined so that the starting stagnation pressure depends neither on the second-throat area nor on the mixing chamber length near this value. When the mixing chamber is shorter than the critical length, the starting stagnation pressure depends not on the mixing chamber length but on the second-throat area. When the mixing chamber is longer than this length, the trend becomes reversed. The critical length of the mixing chamber is the maximum distance that the undisturbed primary flow would reach into the mixing chamber at a supersonic speed for a given inlet conditions.

3 Theoretical Analysis

Figure 10 is a schematic of the flow field in concern. Since the mixing chamber of an annular injection ejector is normally long, the aerodynamic choking of the secondary flow occurs in the mixing chamber and the secondary flow pressure (P_S) is determined by the choking as shown in our experiments and presented by Fabri et al. [11,12]. It means that the flow field within the mixing chamber is divided into two regions. In the subregion between *i* and *f*, mixing of the two flows is negligible. They actively begin to mix each other after the choking and a complete mixing is accomplished in the second-throat. In the subregion between *i* and

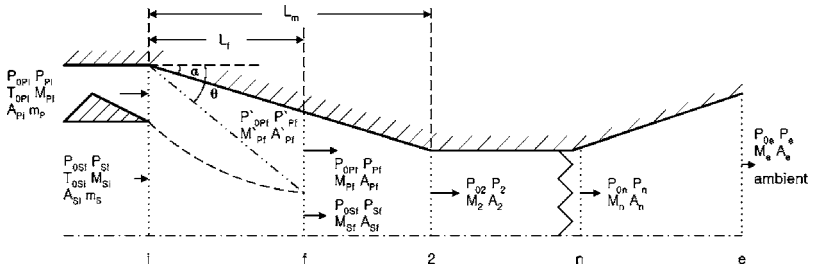

Fig. 10 Diagram of stations and nomenclature used in the theoretical analysis

f, a nonmixing model is used with an aerodynamic choking condition of the secondary flow at "f" [15]. After choking, in the region f-2, a mixing model is employed to obtain a completely mixed flow at the inlet of the second-throat, location "2" [20]. A normal shock relations are used for subregion 2-n and subsonic calculation recovers pressure at "e."

Assumptions and idealizations for the flow inside the ejector are summarized as follows:

(1) The working fluids are ideal gases with constant specific heat ratio, γ;
(2) the flow inside the ejector is steady and one-dimensional;
(3) condensation and friction are negligible;
(4) secondary flow is accelerated isentropically and choked within the mixing chamber;
(5) the oblique shock standing at the exit of primary nozzle affects only the properties of the primary flow at the choking point;
(6) the primary and secondary flow pressures at the choking point are identical;
(7) the two flows are completely mixed at the second-throat inlet and this uniform flow passes a normal shock within the extended throat;
(8) the walls are adiabatic and the wall drag forces are negligible.

3.1 Nonmixing Region (i-f). In the region i-f, the primary and secondary flows are accelerated without mixing. Subscript i is used for the primary nozzle exit (also the inlet of the mixing chamber) and f is for the location of aerodynamic choking of the secondary flow. The primed quantities of the primary flow refer to properties without consideration of an oblique shock. Nonmixing calculation of this subregion results in secondary flow properties for given primary flow conditions. As the two flows are assumed nonmixing, mass conservation is applied separately for primary and secondary flows, while the momentum equation is applied for the whole control volume of the region i-f. These equations are listed below

$$P_{Pi}A_{Pi} + P_{Si}A_{Si} - P'_{Pf}A'_{Pf} - P_{Sf}A_{Sf} = -v_{Pi}(\rho_{Pi}A_{Pi}v_{Pi}) - v_{Si}(\rho_{Si}A_{Si}v_{Si}) + v'_{Pf}(\rho'_{Pf}A'_{Pf}v'_{Pf}) + v_{Sf}(\rho_{Sf}A_{Sf}v_{Sf}) \quad (1)$$

$$m_P = \rho_{Pi}A_{Pi}v_{Pi} = \rho'_{Pf}A'_{Pf}v'_{Pf} \quad (2)$$

$$m_S = \rho_{Si}A_{Si}v_{Si} = \rho_{Sf}A_{Sf}v_{Sf} \quad (3)$$

For simplicity, we introduce three functions of Mach number following Mikkelsen et al. [15]

$$F_1(M) = 1 + \gamma M^2 \quad (4)$$

$$F_2(M) = M\left\{\gamma\left[1 + \frac{\gamma-1}{2}M^2\right]\right\}^{1/2} \quad (5)$$

$$F_3(M) \equiv \frac{F_1(M)}{F_2(M)} = \frac{1+\gamma M^2}{M\left\{\gamma\left[1+\frac{\gamma-1}{2}M^2\right]\right\}^{1/2}} \quad (6)$$

From Eqs. (1)–(3) expressed in terms of abbreviated form of Eqs. (4)–(6), we obtain the following equation to solve for M'_{Pf}, with the choking condition, $M_{Sf}=1$:

$$F_3(M'_{Pf}) = \frac{1}{F_2(M_{Pi})}\left\{\frac{P_{Si}}{P_{Pi}}\cdot\frac{A_{Si}}{A_{Pi}}[F_1(M_{Si}) - F_2(M_{Si})\cdot F_3(1)] + F_1(M_{Pi})\right\} \quad (7)$$

To solve Eq. (7), we first guess the secondary flow pressure, P_{Si}. If $F_3(M'_{Pf})$ is obtained, M'_{Pf} can be calculated from the quadratic Eq. (6). Among the two M'_{Pf}, we take a supersonic solution. With M'_{Pf} known, the pressure at the choking location is calculated.

From the assumption (5), the properties of the primary flow at location f are adjusted by the shock wave originating from the exit of the primary nozzle through oblique shock relations. Equation (7) is solved iteratively until static pressures of the primary and secondary flows are identical at the choking location.

3.2 Mixing Region (f–2). At the choking location, the only property that is balanced between primary and secondary flows is the static pressure. Other properties are still unbalanced. These unbalanced properties between the primary and secondary flows become homogenized in the mixing region, f-2. A modified Emanuel's mixing model is used to obtain the following formulation [20]:

$$M_2 = \left\{\frac{1}{(\gamma-1)(\beta-1)}\right\}^{1/2} \quad (8)$$

$$\beta = \left(1+\frac{m_S}{m_P}\right)\cdot\left(1+\frac{m_S}{m_P}\cdot\frac{h_{0S}}{h_{0P}}\right)\cdot\left\{\left[\frac{M_{Pf}^2}{M_{Pf}^2+\frac{2}{\gamma-1}}\right]^{1/2} + \frac{m_S}{m_P}\cdot\sqrt{\frac{h_{0S}}{h_{0P}}}\cdot\left[\frac{M_{Sf}^2}{M_{Sf}^2+\frac{2}{\gamma-1}}\right]^{1/2}\right\}^{-2} \quad (9)$$

$$P_2 = \frac{P_{Pf}A_{Pf}F_1(M_{Pf}) + P_{Sf}A_{Sf}F_1(M_{Sf})}{A_2F_1(M_2)} \quad (10)$$

A nondimensional parameter, β, is calculated by Eq. (9) using the flow properties at the choking location. With β known, Eq. (8) gives M_2 at the inlet of the second-throat. Then the pressure at the inlet of the mixing chamber is obtained from Eq. (10).

3.3 Normal Shock and Diffuser Relations (2-n-e). From the assumption (7), we apply the normal shock relations to obtain the flow properties downstream the shock. The Mach number and

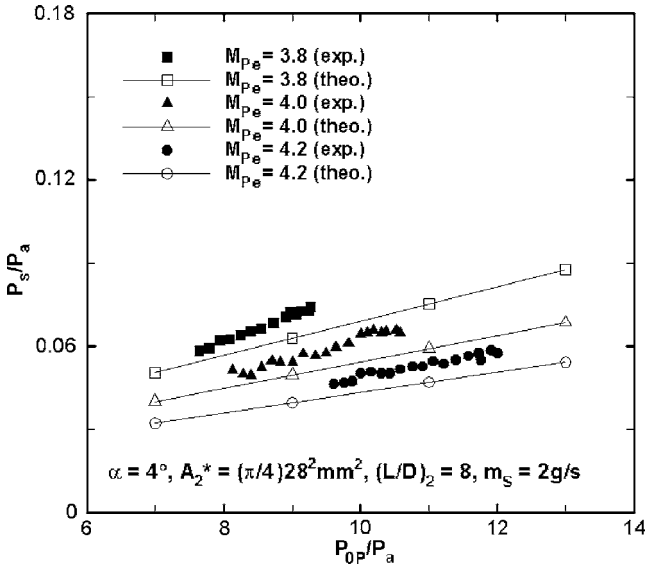

Fig. 11 Performance curves with various primary inlet Mach number

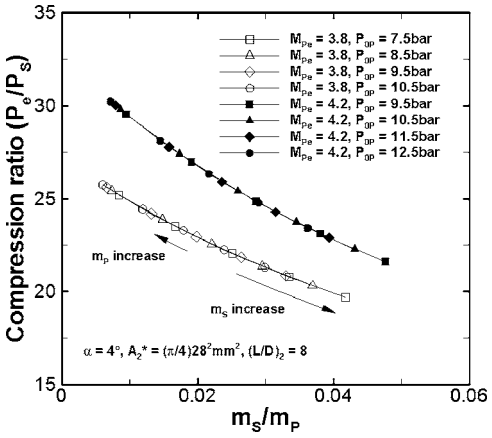

Fig. 13 Compression ratio with entrainment ratio

static pressure downstream the shock, location n, can be obtained by substituting flow properties at the exit of the mixing region into the normal shock relations. It is further assumed that the pressure is recovered in the diffuser of efficiency 100%.

3.4 Results and Discussion. Predicted secondary flow pressure is plotted against measurement as a function of primary stagnation pressure for different primary inlet Mach number in Fig. 11. The geometric configuration of the test case is given on the figure. As the pressure loss due to the shock is underestimated in the present analytical model, the predicted secondary flow pressure is always slightly lower than the measurement. The discrepancy between the prediction and measurement is not so large considering the drastic assumptions made on the flow.

Figure 12 shows secondary flow pressure with respect to the mass flow rate ratio. Mach number at the exit of the primary nozzle is 4.0. In the figure, the solid line is for constant primary mass flow rate and the dashed line is a constant secondary mass flow rate. With the increase of the secondary mass flow rate, the secondary flow pressure increases. Along the dashed line, the secondary flow pressure increases with the increase of the primary mass flow rate, as the primary mass flow rate is proportional to the primary stagnation pressure. The discrepancy between the measurement and prediction becomes larger as the primary stagnation pressure increases. This is because the underestimation of the stagnation pressure loss by assuming oblique shock at the primary nozzle exit becomes more significant at the case of the higher primary stagnation pressure.

Using the analysis, the compression ratio, Mach number of secondary flow, and the location of aerodynamic choking were all calculated with respect to entrainment ratio. It is difficult or often impossible to measure these quantities accurately in the experiments. The calculated compression ratio is plotted in Fig. 13. The compression ratio is defined as the ratio of the ambient pressure to the secondary flow pressure. The compression ratio is inversely proportional to the mass flow rate ratio. A higher compression ratio can be obtained by increasing the primary nozzle area ratio, as in Fig. 13. Figure 14 shows the Mach number of secondary flow with respect to the ratio of the mass flow rates. Since Mach number and static pressure of the secondary flow are inversely proportional to each other, the Mach number of the secondary flow increases with larger area ratio of primary nozzle and lower primary exit pressure. If the primary Mach number increases, the secondary Mach number increases also as the secondary flow pressure decreases. The location of the aerodynamic choking for the secondary flow was calculated and presented in Fig. 15. Choking distance, L_f, is defined as the distance from the inlet of the mixing chamber to the choking point, as in Fig. 10. If the secondary mass flow rate increases, choking distance decreases, because a larger effective area is needed for the choking of the secondary

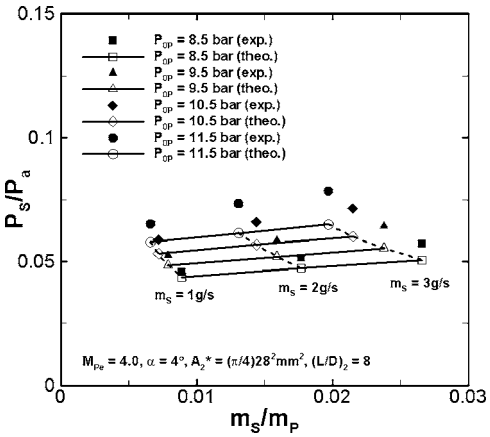

Fig. 12 Secondary flow pressure with entrainment ratio for primary inlet Mach number=4.0

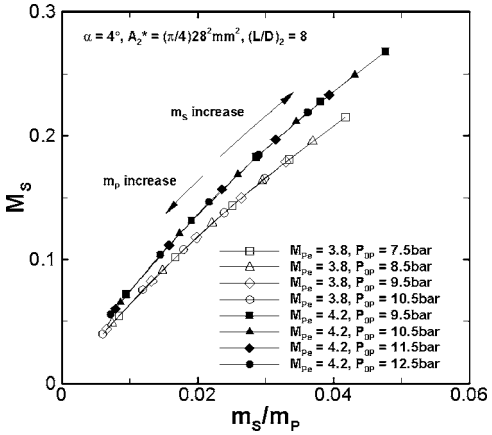

Fig. 14 Secondary flow Mach number with entrainment ratio

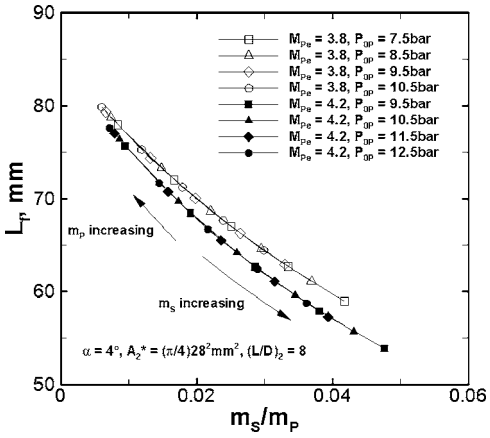

Fig. 15 Distance to choking location with entrainment ratio

flow. On the other hand, if the primary mass flow rate increases, the secondary flow pressure increases and choking distance increases.

4 Conclusion

Through careful experiments involving variation of the geometric parameters of an annular injection supersonic ejector equipped with a second-throat, it is found that the starting pressure of the ejector depends on the length of the mixing chamber. The effect of the mixing chamber length appears in two distinct ways. First, for length less than the critical value, the starting primary pressure is determined by the throat area ratio of the second-throat to the primary nozzle. In this case, the starting pressure can be estimated with reasonable accuracy by the normal shock theory. In contrast, for mixing chamber length greater than the critical value, the starting pressure depends on the length of the mixing chamber on the top of the throat area ratio. The unstarting pressure of the ejector is also measured and found to be simply proportional to the throat area ratio. The starting and unstarting pressures are affected by the second-throat L/D ratio, but the effects are very small.

The static pressure of the secondary flow is also strongly influenced by the primary nozzle shape and the strength of the oblique shock wave that originates from the primary nozzle. This indicates that the static pressure at the primary nozzle exit determines the static pressure of the secondary flow. In order to achieve lower operating pressure for the secondary flow, a primary nozzle with a large area ratio should be used. This geometry, however, requires higher starting and unstarting primary pressures. Finally, the geometric conditions of the second-throat do not affect the secondary flow pressure, as the secondary flow is aerodynamically choked inside the mixing chamber and the pressure.

A theoretical model of an annular injection supersonic ejector equipped with a second-throat was developed assuming that the secondary flow is choked aerodynamically by the expansion of the primary flow in the mixing chamber and the secondary flow pressure is determined by this choking phenomena. This assumption automatically satisfies that the secondary flow pressure is not affected by the geometric condition of the second-throat as shown in the experiments. We focus on predicting the pressure of the secondary flow and the results show reasonably good agreements with the measurement considering the complex nature of the process and the simplicity of the model. However, the analysis predicts the secondary flow pressure slightly lower than measured. This is partly anticipated as we approximated the funnel shaped shock as a two-dimensional oblique shock. Additionally, using the analysis, we can obtain design parameters such as the compression ratio, the Mach number of the secondary flow, and the location of the aerodynamic choking of the secondary flow.

Nomenclature

List of symbols

A = cross sectional area, mm^2
D = diameter, mm
h = specific enthalpy, J/Kg
M = Mach number
m = mass flow rate, g/s
L = length, mm
P = pressure, bar
T = temperature, K
v = velocity, m/s

Greek symbols

α = contraction angle of mixing chamber, degree
γ = specific heat ratio
θ = Mach wave angle
ρ = density, Kg/m^3

Subscripts

a = ambient condition
cr = critical length of mixing chamber
e = ejector exit
f = aerodynamic choking point of secondary flow
i = inlet of mixing chamber (exit of primary nozzle)
m = mixing chamber
max = outer diameter at primary nozzle exit
n = downstream of normal shock
P = primary flow
S = secondary flow, duct diameter of secondary flow
st = starting condition
unst = unstarting condition (stopping operating)
0 = stagnation state
2 = second-throat (diffuser throat)

Superscripts

$*$ = throat

References

[1] Sun, D. W., and Eames, I. W., 1995, "Recent Developments in the Design Theories and Applications of Ejectors—A Review," J. Inst. Energy, **68**, pp. 65–79.

[2] Boreisho, A. S., Khailov, V. M., Malkov, V. M., and Savin, A. V., 2000, "Pressure Recovery System for High Power Gas Flow Chemical Laser," *Proc. of XIII International Symposium on Gas Flow & Chemical Lasers—High Power Laser Conference*, Florence, Italy, pp. 401–405.

[3] Malkov, V. M., Boreisho, A. S., Savin, A. V., Kiselev, I. A., and Orlov, A. E., 2000, "Choice of Working Parameters of Pressure Recovery Systems for High-Power Gas Flow Chemical Lasers," *Proc. of XIII International Symposium on Gas Flow & Chemical Lasers—High Power Laser Conference*, Florence, Italy, pp. 419–422.

[4] Kim, S., Jin, J., Kwon, H., and Kwon, S., 2004, "Development of a Rational Design Procedure for a Pressure Recovery System for HPCL," XV International Symposium on Gas Flow & Chemical Lasers—High Power Laser Conference, Prague, Czech Republic, Proc. of SPIE Vol. 5777-26.

[5] Foster, R. W., Escher, W. J. D., and Robinson, J. W., 1989, "Studies of an Extensively Axisymmetric Rocket Based Combined Cycle (RBCC) Engine Powered SSTO Vehicle," AIAA Paper No. 89-2294.

[6] Escher, W. J. D., 1993, "A Retrospective on Early Cryogenic Primary Rocket Subsystem Designs as Integrated Into Rocket-Based Combined-Cycle (RBCC) Engines," AIAA Paper No. 93-1944.

[7] Kim, S., and Kwon, S., 2003, "Development of Ejector System for Chemical Lasers Operating (I)—Design Parameter Study of Supersonic Ejector for Chemical Lasers Operating," KSME Int. J., **27**(12), pp. 1673–1680.

[8] Kim, S., Jin, J., and Kwon, S., 2004, "Development of Ejector System for Chemical Lasers Operating (II)—Optimal Design of the Second-Throat Type Annular Supersonic Ejector," KSME Int. J., **28**(10), pp. 1231–1237.

[9] Annamalai, K., Visvanathan, K., Sriramulu, V., and Bhaskaran, K. A., 1998, "Evaluation of the Performance of Supersonic Exhaust Diffuser Using Scaled Down Models," Exp. Therm. Fluid Sci., **17**, pp. 217–229.

[10] German, R. C., Bauer, R. C., and Panesci, J. H., 1966, "Methods for Determining the Performance of Ejector-Diffuser Systems," J. Spacecr. Rockets, **3**, pp. 193–200.

[11] Fabri, J., and Siestrunk, R., 1958, "Supersonic Air Ejectors," in *Advances in Applied Mechanics*, Vol. 5, H. L. Dryden and Th. von Karman, eds., Academic

Press, New York, pp. 1–33.
[12] Fabri, J., and Paulon, J., 1958, "Theory and Experiments on Supersonic Air-to-Air Ejectors," NACA-TM-1410.
[13] Lear, W. E., Parker, G. M., and Sherif, S. A., 2002, "Analysis of Two-Phase Ejectors With Fabri Choking," J. Mech. Eng. Sci., **216**(C5), pp. 607–621.
[14] Lear, W. E., Sherif, S. A., and Steadham, J. M., 2000, "Design Considerations of Jet Pumps With Supersonic Two-Phase Flow and Shocks for Refrigeration and Thermal Management Applications," Int. J. Energy Res., **24**, pp. 1373–1389.
[15] Mikkelsen, C. D., Sandberg, M. R., and Addy, A. L., 1976, "Theoretical and Experimental Analysis of the Constant-area, Supersonic-Supersonic Ejector," U.S. Army Research Office, Grant No. DAHC 04-75-G-0046, and Dep. of Mechanical and Industrial Eng., Univ. of Illinois at Urbana-Champaign, Urbana, IL.
[16] Huang, B. J., Jiang, C. B., and Hu, F. L., 1985, "Ejector Performance Characteristics and Design Analysis of Jet Refrigeration System," ASME J. Eng. Gas Turbines Power, **107**, pp. 792–802.
[17] Huang, B. J., Chang, J. M., Wang, C. P., and Petrenko, V. A., 1999, "A 1D Analysis of Ejector Performance," Int. J. Refrig., **22**, pp. 354–364.
[18] Chunnanond, K., and Aphornratana, 2004, "An Experimental Investigation of a Steam Ejector Refrigerator: The Analysis of the Pressure Profile Along the Ejector," Appl. Therm. Eng., **24**, pp. 311–322.
[19] German, R. C., Bauer, R. C., and Panesci, J. H., 1966, "Methods for Determining the Performance of Ejector-Diffuser Systems," J. Spacecr. Rockets **3**(2), pp. 193–200.
[20] Emanuel, G., 1976, "Optimum Performance for a Single-Stage Gaseous Ejector," AIAA J., **14**(9), pp. 1292–1296.

Computational Analysis of a Inverted Double-Element Airfoil in Ground Effect

Stephen Mahon
Ph.D. Research Student

Xin Zhang
Professor

Aerospace Engineering,
School of Engineering Sciences,
University of Southampton,
Southampton SO17 1BJ, UK

The flow around an inverted double-element airfoil in ground effect was studied numerically, by solving the Reynolds averaged Navier-Stokes equations. The predictive capabilities of six turbulence models with regards to the surface pressures, wake flow field, and sectional forces were quantified. The realizable $k-\varepsilon$ model was found to offer improved predictions of the surface pressures and wake flow field. A number of ride heights were investigated, covering various force regions. The surface pressures, sectional forces, and wake flow field were all modeled accurately and offered improvements over previous numerical investigations. The sectional forces indicated that the main element generated the majority of the downforce, whereas the flap generated the majority of the drag. The near field and far field wake development was investigated and suggestions concerning reduction of the wake thickness were offered. The main element wake was found to greatly contribute to the overall wake thickness with the contribution increasing as the ride height decreased. [DOI: 10.1115/1.2353268]

1 Introduction

When located within close proximity to a ground plane, the flow field generated by an inverted wing increases in complexity when compared to the freestream case. Multielement wings in freestream produce a flow field dominated by viscous effects containing regions of highly curved streamlines, confluent boundary layers, and merging wakes [1]. The combination of a multielement wing flow field and a ground effect situation will, therefore, produce a highly complex, interactive, predominantly viscous flow field.

Inverted multielement wings in ground effect have applications within the motorsport industry. Modern racing cars utilize multielement front wings in order to maximize downforce within a physical geometry fixed by technical regulations. The front wing of a formula specification racing car operates in ground effect with ground clearance ranging between 70 and 100 mm [2]. Typically a racing car front wing generates 25–30% of the total downforce of the car [3], however it is commonly used as a trimming device balancing the car laterally. The location of a front wing is such that the generated wake and edge vortices influence downstream components of the car for example the undertray, diffuser and radiators. Therefore, both surface and far field aspects of the flow field generated by a front wing must be considered during the design of a racing car.

The field of multielement flows has challenged researchers, both experimentally and computationally for a long time. Smith [1] defined five beneficial effects of slots between wing elements. More recently Maddah and Bruun [4] offered a vortex based model which simulated the effects of varying wing and flap incidence. There has been a lack in research concerning multi-element wings in ground effect, especially computational based research. In 1997 Razenbach et al. [5] computationally investigated an inverted NACA 62_2-215 Mod B airfoil possessing a cove, with a 30% single slotted flap. Reynolds averaged Navier-Stokes (RANS) simulations were performed with a moving ground at a Reynolds number (Re) of 1.5×10^6 based on the chord. A fully structured chimera grid was used containing 30,734 cells with turbulence modeled by a variant of the standard $k-\varepsilon$ model. The grid used was extremely coarse compared to current computational investigations [6–8] in which grids typically contain of the order of 200,000 cells. The variation of the sectional forces with ride height was presented in conjunction with vorticity contour plots. The variation in sectional forces with ride height was captured accurately in addition to the force reduction phenomena. Based on previous research [9,10] the force reduction phenomena was attributed to the merging of the ground and airfoil boundary layers.

In 1998 Jasinski and Selig [8] experimentally investigated an inverted double-element wing in ground effect. The main element and flap were specifically designed for the investigation and were mounted in a single slotted configuration. The ground was stationary and impermeable during all investigations producing an unrealistic ground boundary layer. Both a two-dimensional wing and a three-dimensional wing with endplates were tested. No data was presented for the two-dimensional wing. Downforce results were presented for various flap incidences and freestream velocities ($\mathrm{Re}=0.7\times10^6$ to 1.3×10^6) for a fixed ride height of 0.3 of the chord.

Most recently Zhang and Zerihan [11,12] presented experimental force data, surface flow field data and off-surface flow field data for a generic inverted double-element wing in ground effect. Tests were performed at Reynolds numbers ranging between 7.35×10^5 and 7.65×10^5 based on the total chord. The surface pressures indicated that the majority of the downforce was generated by the main element. As with the previous investigations performed by Zerihan [13] and Zerihan and Zhang [14,15] the force reduction phenomena was attributed to the bursting of the lower edge vortices and separation on the suction surfaces of the wing. These findings are in contrast to the findings of Razenbach and Barlow [5,9,10].

So far investigations into multielement wings in ground effect have contributed to the general understanding of the flow physics. With the exception of Razenbach et al. [5] all previous investigations have been experimental and utilized finite span wings. The drive has been to investigate fully three-dimensional flows. However, the predictive capabilities of current computational techniques is such that two-dimensional investigations still pose a high degree of difficulty. There has been a lack of computational investigations into inverted multi-element airfoils in ground effect indicating a void in understanding.

This investigation will computationally investigate an isolated

Contributed by the Fluids Engineering Division of ASME for publication in the JOURNAL OF FLUIDS ENGINEERING. Manuscript received April 13, 2005; final manuscript received April 9, 2006. Assoc. Editor: Phillip M. Ligrani.

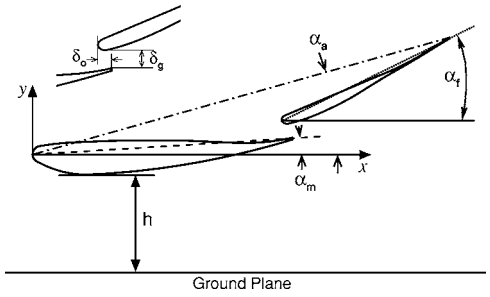

Fig. 1 Definition of the terms and coordinate system

inverted double-element airfoil in ground effect. Due to the practical applications of inverted double-element wings within motorsport the flow field is significantly influenced by surrounding bodywork, in particular the front wheels and chassis. However, the current understanding of the flow field generated by an isolated double-element airfoil in ground effect is incomplete. Therefore, this investigation aims to provide a foundation upon which further work may be conducted. In particular studies to quantify the performance of an inverted double-element wing within a practical application. This investigation with undertake quantitative comparisons with an isolated double-element airfoil in ground effect previously studied experimentally [13]. The influence of individual turbulence models and grid resolution will be initially assessed. Data will be quantitatively analyzed concerning the surface flow field, sectional forces, wake flow field, and their variation with ride height.

2 Numerical Method

2.1 Airfoil Geometry and Flow Condition. The airfoil used in this investigation comprised of two elements in a single slotted flap configuration. The main element was a derivative of the LS(1)-0413 MOD profile and possessed a finite trailing edge of 1.56 mm. The flap profile represented a typical profile used within motorsport and possessed a finite trailing edge of 0.95 mm. A detailed listing of the both profiles may be found in Zerihan [13]. Both elements of the airfoil were inverted such that the suction surfaces were closest to the ground plane. The chords of the main element (c_m) and flap (c_f) were 223.4 and 165.7 mm, respectively. For continuity within the results a total chord (c) of 380 mm was defined and used in all calculations of nondimensional values. The flap is located, with respect to the main element trailing edge, such that an overlap (δ_o) and gap (δ_g) of $0.024c$ and $0.032c$, respectively, were achieved. These values resulted from an experimental optimization investigation with regards to downforce [11].

The ride height (h) was defined as the vertical distance between the lowest point on the suction surface of the main element and the ground plane. The origin of the coordinate system was defined as the leading edge of the main element (Fig. 1). Incidence, defined as the angle between the chord and the horizontal, was positive for a nose down rotation. The reference incidence of the double-element airfoil (i.e., α_a=0 deg) was set such that the main element incidence (α_m) and flap incidence (α_f) were +3.6 deg and +15.5 deg, respectively.

All computations were performed at a Reynolds number of 7.86×10^5, based on the total chord of the airfoil, with a freestream velocity of 30 m/s. These conditions correspond to the experimental conditions [11,12]. Further information concerning the computational solver and configuration may be found in Mahon and Zhang [16].

2.2 Turbulence Models. Turbulence was modeled within the flow field through the use of one of six turbulence models; the one equation Spalart-Allmaras model [17], the standard $k-\varepsilon$ model [18], the $k-\omega$ SST model [19], the $k-\varepsilon$ RNG model [20], the realizable $k-\varepsilon$ model [21], and the standard $k-\omega$ model [22]. In all cases and with all turbulence models the boundary layers were resolved to the wall.

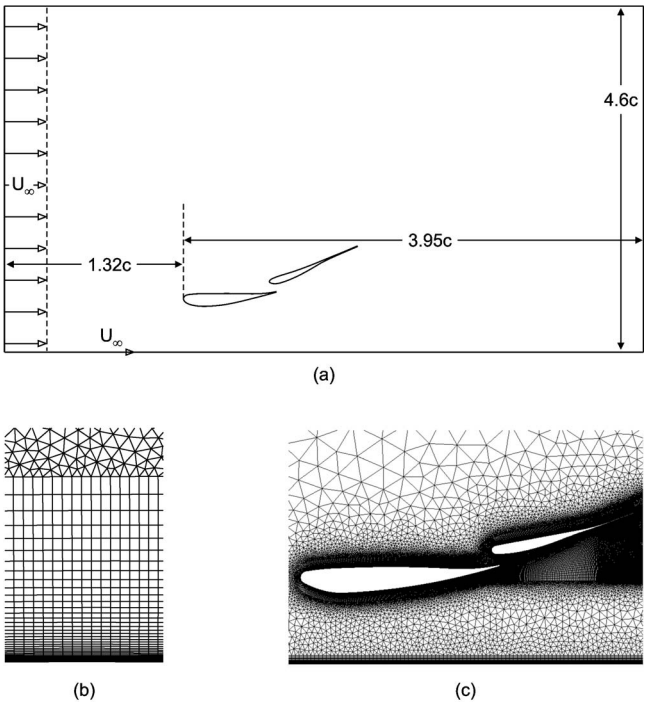

Fig. 2 Computational domain (*a*) schematic, (*b*) near wall grid, and (*c*) off-surface domains

2.3 Computational Grids. A multiblock hybrid grid design was used, containing both structured and unstructured blocks. At various ride heights, the relative grid topology and structure were maintained. A schematic of the computational domain and grid is shown in Fig. 2.

To capture the boundary layer of each element of the airfoil accurately, a hyperbolically extruded structured grid was used. A conventional structured block was used to capture the ground boundary layer. Within the ground and airfoil boundary layer blocks the initial cell spacing, normal to the wall, was set such that $y^+\approx1$ (Fig. 2(*b*)). Mapping the flap suction surface onto the lowest most connector, originating from the main element suction surface, created a structured block designed to capture the initial main element wake development. A separate structured block was positioned directly downstream of the airfoil with the purpose of capturing the development of the wakes from both the main element and flap. The remainder of the computational domain was unstructured and refined in areas of importance. The streamwise location of the airfoil is shown in Fig. 2 and was set as a result of a sensitivity study which was performed prior to conducting the final simulations.

The experimental results [13] used for validation of the computational results were obtained with the wing in a free transition configuration. In order for realistic simulations to be obtained the transition location was set within the computations through the use of a laminar zone located at the main element leading edge. The streamwise location was determined experimentally from oil flow visualization results [12] allowing it to be set a priori within the computational grids. For ride heights of $h/c\leqslant0.105$ transition was found to occur immediately at the main element leading edge hence a laminar zone was not required in these cases. This method of simulating transition assumed immediate transition to turbulence. Further information concerning the simulation of transition may be found in Czerwiec et al. [23].

The design of the supporting system utilized within the experimentation [13] was such that alterations in airfoil incidence were observed between the static and wind-on situations. These alterations in airfoil incidence, due to flexing of the wing, were dependent on the forces generated by the wing and ranged between −0.67 deg and −1.87 deg. For a specific ride height the variation in airfoil incidence and transition locations was taken into account when designing the computational grid.

The computational boundary conditions were configured to replicate the experimental conditions. The upstream boundary was modeled using a velocity inlet boundary condition. The corresponding inlet velocity was set at 30 m/s in a positive streamwise direction. Turbulence within the flow was prescribed using values of turbulence intensity and turbulent length scale. The turbulence intensity and length scale within the 2.1 m × 1.7 m wind tunnel facility were experimentally quantified at 0.3% and 0.039 m, respectively, at a freestream velocity of 30 m/s. The variance within the freestream velocity, turbulent length scale and turbulence intensity were experimentally quantified at 6.15×10^{-5}, 9.98×10^{-3}, and 4.82×10^{-4}, respectively, using a hot wire technique. A vertically uniform inlet condition was, therefore, prescribed.

The downstream boundary was modeled using a pressure outlet boundary condition. The gauge pressure was set at zero. The height of the upper edge of the domain above the simulated ground plane corresponded to the height of the wind tunnel test section. A slip wall boundary condition was imposed on the upper edge, therefore, imposing a zero cross-flow condition and removing the requirement of additional boundary layer resolution. This formulation was set in order to replicate the experimental conditions imposed by the roof of the wind tunnel test section. The surfaces of the airfoil and ground were modeled as solid walls with a no-slip condition enforced. The ground surface was provided with a translational velocity equal to freestream. Further details concerning the design of the moving ground facility within the 2.1 m × 1.7 m wind tunnel facility may be found in the work of Burgin et al. [24].

Prior to the final steady-state simulations the dependency of the solution on the resolution of the grid was investigated. A grid sensitivity study was performed at a ride height of $h/c=0.211$ with the airfoil at the reference incidence. Three grids were constructed: A coarse grid of 184,335 cells, a medium grid of 380,812 cells and a fine grid of 846,317 cells. Turbulence was modeled using the realizable $k-\varepsilon$ model with all three grids. The surface pressures and wake profiles at $x/c=1.066$ for all three grids are presented in Fig. 3. Very little variation in the results was observed. Although steady-state simulation were performed it was noted that with the fine grid unsteady features were detected, especially within the wake flow field. These effects were periodic and are illustrated in the wake profile for the fine grid between $y/c=-0.06$ and 0.06. Due to the presence of these temporal unsteady flow features the fine grid resolution was not applicable within the context of this investigation. Therefore, in all simulations the coarse grid resolution was used in order to reduce the computational cost while maintaining a valid steady state solution.

3 Results

3.1 Turbulence Models. A quantitative study of the six turbulence models previously stated, was conducted. Two cases were selected ($h/c=0.211$ and 0.079). $h/c=0.211$ represents a flow condition where the ride height of the airfoil is within the force enhancement region [12] and a thin dual wake flow field is observed. At $h/c=0.079$ the airfoil is close to maximum downforce and a thick main element wake is observed in addition to the thin flap wake. From this point on the main element and flap wakes will be referred to as the lower and upper wakes, respectively. The suitability of each turbulence model was quantitatively assessed using the surface flow features and wake characteristics.

At $h/c=0.211$ (Fig. 4(*a*)) all the turbulence models accurately

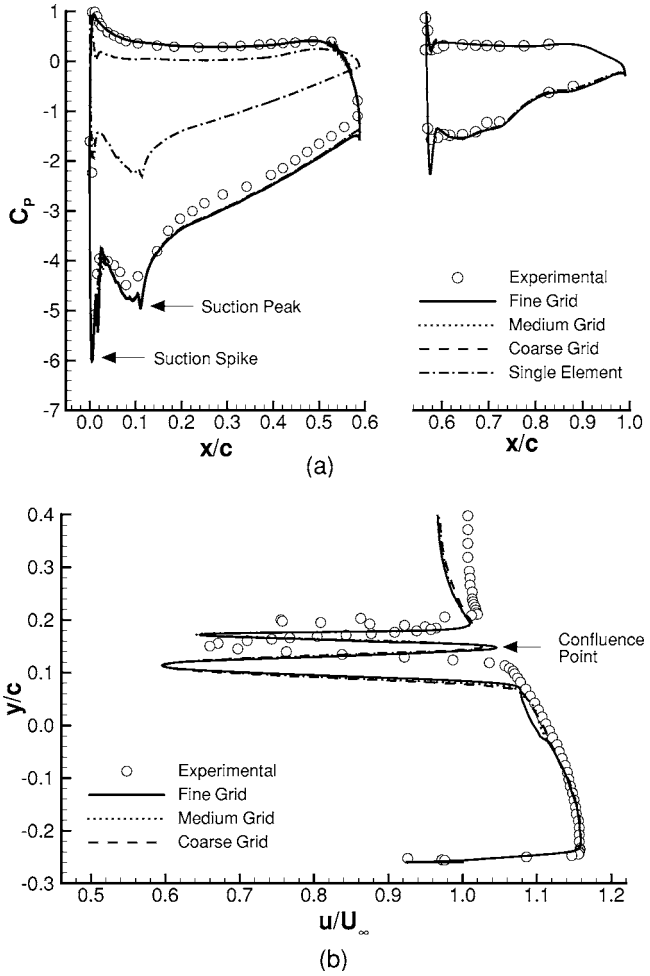

Fig. 3 Effect of grid resolution (*a*) surface pressure distributions and (*b*) wake profiles at $x/c=1.066$

captured the surface pressures over both the main element and flap. The leading edge stagnation pressures ($C_{P\text{stag}}$) on the main element and flap were correctly predicted by all turbulence models at streamwise location of $x/c=0.009$ and $x/c=0.567$, respectively. The streamwise location of the suction peak was found to be independent of turbulence model, occurring at $x/c=0.11$ in this configuration. The term suction peak refers to the value of maximum downforce downstream of the leading edge suction spike as illustrated in Fig. 3. The quantitative features of the surface pressures predicted by each turbulence model at $h/c=0.211$ are listed in Table 1.

Unlike the surface pressures variations were observed in the prediction of the velocity profile of the wake at $x/c=1.066$ (Fig. 4(*b*)). The experiential data presented was obtained by Zhang and Zerihan [12] using laser doppler anemometry (LDA) techniques. The agreement between the computational results and the experimental measurements within the core of the wake was poor for all six turbulence models. The agreement between the results obtained with each turbulence model however, was good. All the turbulence models accurately predicted the velocity profile between the ground plane and the lower boundary of the lower wake. It may be noted that towards the ground plane the nondimensional velocity (u/U_∞) decreases to approximately 0.89 then sharply increases to a value of unity. Since the ground plane is provided with a freestream velocity this trend seems incorrect. However, it must be remembered that the airfoil generates an adverse streamwise pressure gradient due to the recovery of the flow beneath the suction surface. This in turn generates a bound-

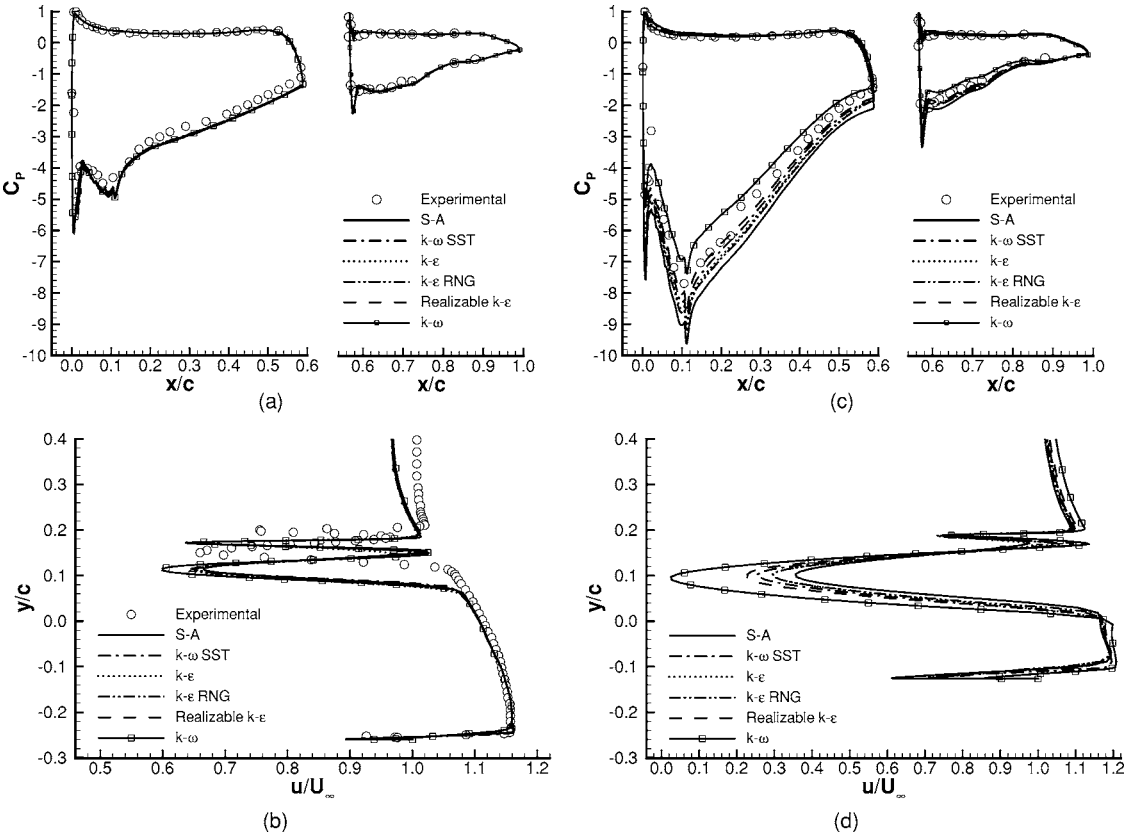

Fig. 4 Effects of turbulence models (*a*) surface pressures at $h/c=0.211$, (*b*) wake profiles at $x/c=1.066$ for $h/c=0.211$, (*c*) surface pressures at $h/c=0.079$, and (*d*) wake profiles at $x/c=1.066$ for $h/c=0.079$

ary layer along the ground plane originating from a streamwise location corresponding to the suction peak. The resulting ground boundary layer velocity profile is present at all ride heights and is accordingly present in all the computational wake profiles. The Spalart-Allmaras and realizable $k-\varepsilon$ models offered improved predictions concerning the ground boundary layer velocity profile.

The vertical location of the lower boundary of the lower wake was underpredicted by all six turbulence models. In addition the vertical location of the maximum velocity deficit within the lower wake (u_{low}/U_∞) and the actual maximum velocity deficit was underpredicted by all the turbulence models, with the exception of the realizable $k-\varepsilon$ model which overpredicted u_{low}/U_∞. The vertical location of the confluence point (Fig. 3) between the upper and lower wakes was underpredicted by all the turbulence models. The associated streamwise velocity (u_{conf}/U_∞) was captured well with the exception of the standard $k-\varepsilon$ model. The maximum velocity deficit within the upper wake (u_{top}/U_∞) was overpredicted by all the turbulence models. The vertical location of the upper boundary of the upper wake (δ_{top}) was best predicted by the $k-\varepsilon$ RNG model, all other turbulence models underpredicted the vertical location. Due to the varying predictions of the lower and upper wake boundaries a wide variation was observed within the

Table 1 Surface pressure information for various turbulence models; $h/c=0.221$

Turbulence Model	$C_{P\text{suc}}$	x/c at $C_{P\text{suc}}$
Experimental	–4.48	0.08
Spalart-Allmaras	–4.96	0.11
$k-\omega$ SST	–4.95	0.11
Standard $k-\varepsilon$	–4.93	0.11
$k-\varepsilon$ RNG	–4.94	0.11
Realizable $k-\varepsilon$	–4.91	0.11
Standard $k-\omega$	–4.93	0.11

Table 2 Wake profile information at $x/c=1.066$ for various turbulence models; $h/c=0.221$

	$u_{\min}/U_\infty$			y/c at $u_{\min}/U_\infty$			y/c at δ		δ_{99}/c	
Turbulence Model	Low	Top	Conf	Low	Top	Conf	Low	Top	Low	Top
Experimental	0.69	0.79	0.99	0.150	0.200	0.185	0.126	0.205	0.059	0.020
Spalart-Allmaras	0.67	0.64	1.02	0.113	0.172	0.153	0.082	0.182	0.071	0.029
$k-\omega$ SST	0.65	0.64	1.01	0.113	0.172	0.147	0.084	0.182	0.063	0.035
Standard $k-\varepsilon$	0.65	0.66	0.97	0.111	0.172	0.147	0.078	0.184	0.069	0.037
$k-\varepsilon$ RNG	0.65	0.66	1.02	0.111	0.172	0.151	0.078	0.184	0.073	0.033
Realizable $k-\varepsilon$	0.60	0.65	1.03	0.112	0.172	0.149	0.080	0.184	0.069	0.035
Standard $k-\omega$	0.60	0.65	1.03	0.112	0.172	0.149	0.080	0.184	0.069	0.035

predictions of the upper $((\delta_{99}/c)_{top})$ and lower $((\delta_{99}/c)_{low})$ wake thickness. The realizable $k-\varepsilon$ model and standard $k-\varepsilon$ model provided the best predictions of the lower wake and upper wake thickness, respectively. The quantitative features of the wake profiles predicted by each turbulence model at $x/c=1.066$, are listed in Table 2.

Figures 4(*c*) and 4(*d*) presents the surface pressures and wake profiles at $x/c=1.066$ respectively at a nondimensional ride height of 0.079. The variations within the surface pressures due to turbulence model remained consistent with those observed at $h/c=0.211$. However, the variations are easier to observe due to the increased magnitudes of the surface pressures. The surface pressures on both the main element and flap were most accurately predicted with the realizable $k-\varepsilon$ turbulence model. Experimental data concerning the wake flow field was not available at this lower ride height. However, the variations between the turbulence models remained consistent with those observed at $h/c=0.211$ and are easier to observe at this lower ride height.

The worst case uncertainty within the experimental surface pressure measurements was quantified at $C_p=0.0347$ at a streamwise location of $x/c=0.198$ [11]. The variations within the surface pressures due to turbulence model were worst at the lower of the two ride heights investigated. The maximum variation observed was $C_p=2.353$ at a streamwise location of $x/c=0.007$, corresponding to the suction peak.

3.2 Surface Pressures. With the influence of prescribed turbulence model quantified we may now proceed to investigate the effects of ride height variation. Calculations were performed at $h/c=0.395, 0.263, 0.211, 0.158, 0.132, 0.105$, and 0.079 and data concerning the surface pressures, wake flow field and sectional forces was extracted. Due to the poor agreement concerning the wake profiles the choice of turbulence model was based solely on the performance of each turbulence model with respect to the surface pressures. Accordingly the realizable $k-\varepsilon$ model was used in the simulations at various ride heights.

The calculated surface pressures are presented with experimental data in Fig. 5. Figures 5(*a*) and 5(*b*) present the surface pressures for high and low ride heights, respectively, using the realizable $k-\varepsilon$ turbulence model. At all ride heights the general features of the surface pressures over both elements were accurately predicted. The leading edge stagnation pressures on both the main element and flap were correctly predicted. The streamwise location of stagnation on the main element was found to move upstream with reducing ride height, decreasing from $x/c=0.011$ at $h/c=0.395$ to $x/c=0.006$ at $h/c=0.079$. Stagnation on the flap was found to be independent of ride height, occurring at $x/c=0.566$. The surface pressures on the pressure surfaces of both elements remain relatively independent of ride height, when compared to the suction surface pressures, and were accurately predicted for all ride heights.

The calculated surface pressures on the flap agreed well with the experimental data and captured the increase in suction surface pressures with decreasing ride height. The main element suction surface pressures were slightly overpredicted at all ride heights. The increase in main element suction surface pressures with decreasing ride height was accurately predicted. The streamwise location of the suction spike was consistently predicted at $x/c=0.004$ increasing in magnitude with decreasing ride height. Directly downstream of the leading edge suction spike a decrease in suction was observed at $x/c=0.024$. The curvature of the main element at this location was discontinuous resulting in a region of decelerated flow. Disturbances in the suction surface pressures between $x/c=0.024$ and $x/c=0.106$ were observed, corresponding to yet more discontinuities in the curvature. The streamwise location of the suction peak was consistently predicted at $x/c=0.11$ increasing in magnitude with decreasing ride height. The pressure recovery directly downstream of the suction peak was also accurately simulated at all ride heights.

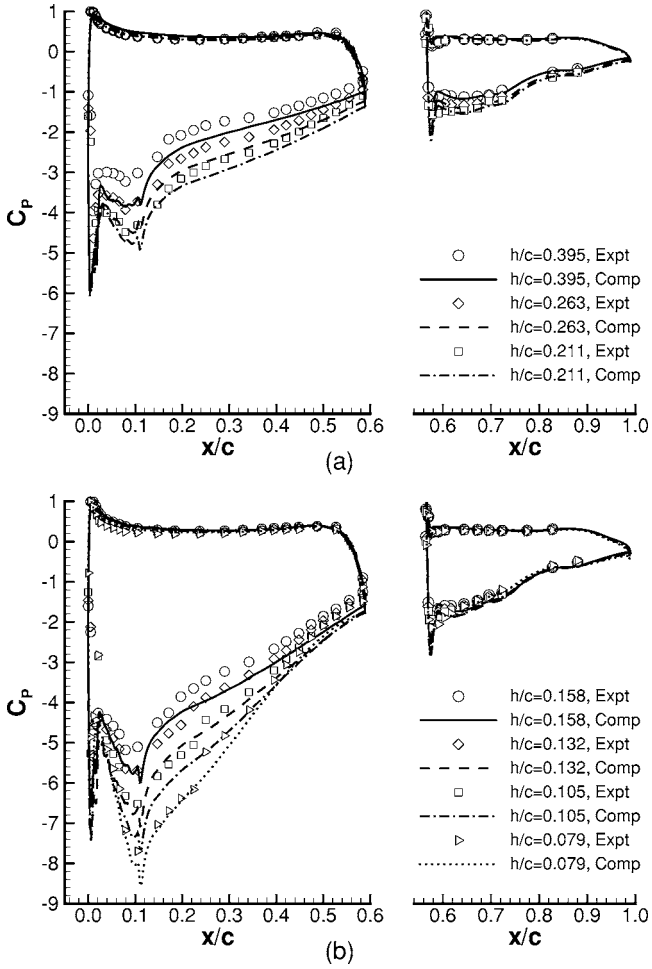

Fig. 5 Surface pressures at various ride heights (*a*) high ride heights (*b*) low ride heights; realizable $k-\varepsilon$

3.3 Sectional Forces. The calculated sectional forces generated by the airfoil at various ride heights are presented in Fig. 6(*a*). Experimental sectional forces, calculated from the measured surface pressures are also shown. The overall trend in sectional downforce (C_L) variation with ride height was captured. The overprediction of the surface pressures with the realizable $k-\varepsilon$ model resulted in overpredictions within the sectional downforce. Variations within the downforce trends were observed at $h/c=0.105$ caused by the removal of the laminar zone, since transition was found to occur immediately at the main element leading edge. The greatest discrepancies between the computational and experimental data was 15% at $h/c=0.132$.

The variation of the downforce, generated solely by the main element (C_{Lm}) and flap (C_{Lf}), with ride height is shown in Fig. 6(*b*). It is clear that the majority of the downforce is generated by the main element which varies similarly to the overall downforce with ride height. The percentage of total downforce due to the main element increased asymptotically as the ride height was reduced from $h/c=0.395$, until a maximum of approximately 84% was reached at $h/c=0.079$. Decreasing the ride height from $h/c=0.395$ to 0.132 caused the downforce generated by the flap to increase linearly. Further decreases in ride height resulted in the flap downforce decreasing until a minimum ride height was achieved. Similar downforce variations with ride height were observed experimentally [11].

3.4 Flow Between Airfoil and Ground. Figure 7 presents line contours of relative streamwise velocity (u/U_∞) for h/c

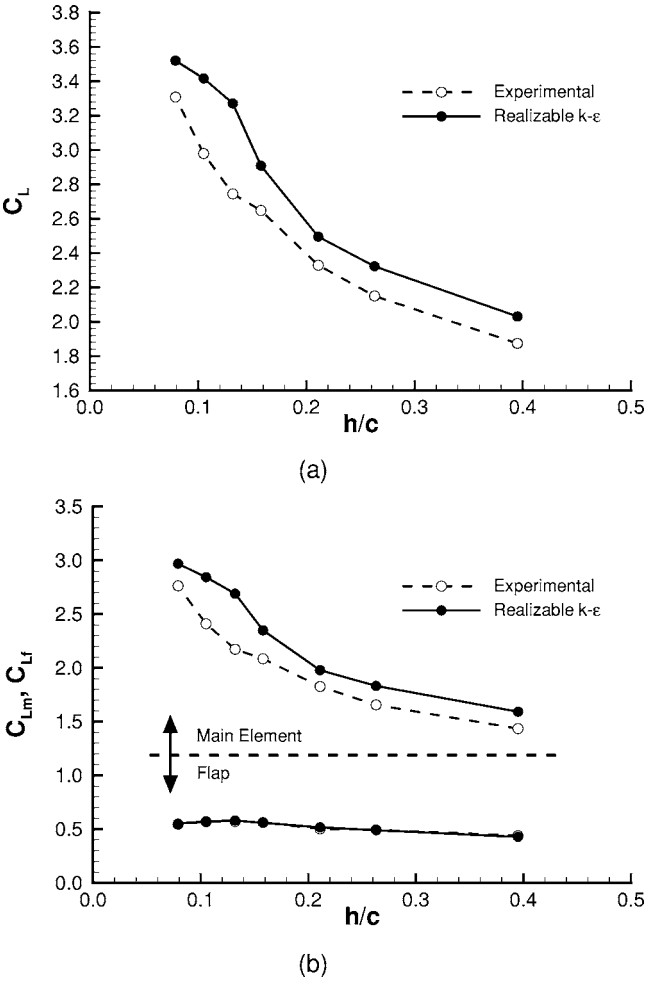

Fig. 6 Sectional forces at various ride heights (*a*) total downforce (*b*) downforce due to the main element and flap

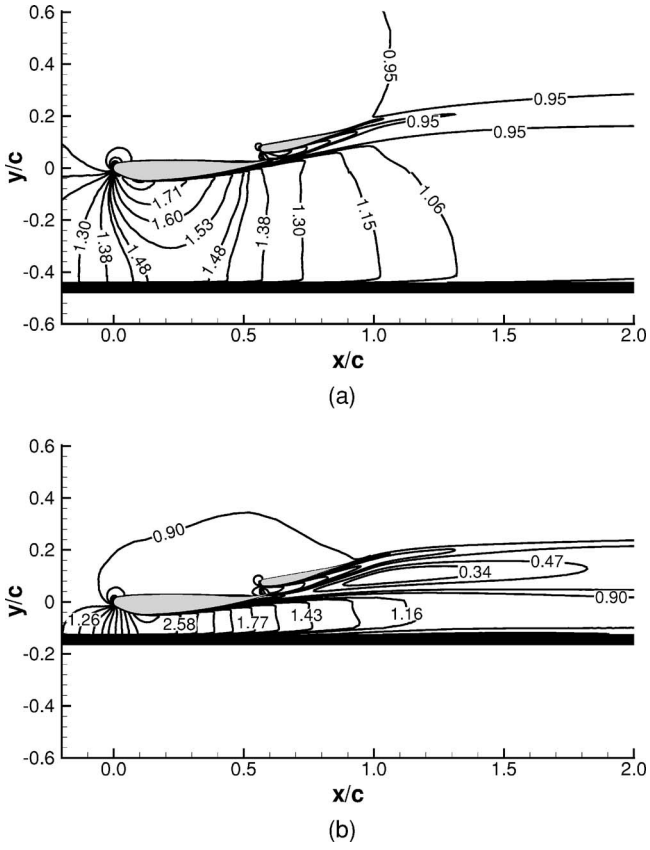

Fig. 7 Contours of u/U_∞ (*a*) $h/c=0.395$ (*b*) $h/c=0.079$; realizable $k-\varepsilon$

=0.395 and 0.079. The contours at $h/c=0.395$ (Fig. 7(*a*)) show a flow which is slightly accelerated when exiting the channel between the lower boundary of the lower wake and the ground plane, such that $\bar{u}/U_\infty \approx 1.0$. $\bar{u}$ is defined as the mean streamwise velocity at $x/c=0.990$ between the lower boundary of the lower wake and the ground plane. The main element wake is thin and follows the contour of the flap suction surface. A thin ground boundary layer is observed downstream of the airfoil originating from the point on the main element suction surface closest to the ground plane.

The contours at $h/c=0.079$ shows a highly accelerated flow with a maximum streamwise velocity of $u/U_\infty \approx 3.0$. A thick main element wake is observed which is amplified in thickness underneath the flap suction surface. The accelerated flow exiting beneath the main element trailing edge seems constrained by the ground plane and lower boundary of the lower wake forming a wall jet, such that $\bar{u}/U_\infty \approx 1.2$. The ground boundary layer is increased in thickness when compared to the higher ride height, originating from the streamwise location of the lowest point on the main element suction surface.

At nondimensional ride heights of $h/c>0.079$ no separation was observed on either the main element or flap suction surfaces. A small region of recirculation was observed directly downstream of the main element finite trailing edge at all ride heights. Separation was observed at $x/c=0.539$ on the main element suction surface for $h/c=0.079$. Experimental surface flow visualizations were not available at this ride height hence it could not be determined which prediction was correct.

3.5 Near Field Main Element Wake Development. The near field development of the main element wake, between the flap suction surface and the ground plane, can be observed in Fig. 7(*b*). For all ride heights the vertical distance between the top boundary of the main element wake and the flap suction surface remained of the order of the flap gap, linearly increasing downstream. It has already been noted that separation was not observed on the main element suction surface for $h/c \geq 0.105$. However, it must be remembered that the main element suction surface boundary layer is included within the calculation of the lower boundary of the lower wake therefore producing a value of wake thickness greater than would be expected.

The streamwise variation in main element wake thickness $((\delta_{99}/c)_{low})$ for various ride heights is presented in Fig. 8. The spreading rate of the main element wake $(\partial\delta_{99}/\partial x)$ was found to increase with a third order polynomial trend, for a set ride height. Reductions in ride height resulted in the spreading rate increasing with a maximum value of 0.891 occurring between $x/c=0.947$ and 0.984 for $h/c=0.079$. At this lowest ride height the main element wake increased in thickness between $x/c=0.624$ and 0.984 by over 430% and at the flap trailing edge was equivalent to 80% of the wake thickness observed at $x/c=1.066$.

3.6 Wake Flow Field. The variation in wake flow field with ride height and streamwise location is presented in Fig. 9. Figure 9(*a*) illustrates the variation in wake profiles with ride height at $x/c=1.066$. Three ride heights are shown for reasons of clarity, the quantitative data for which is listed in Table 3. The agreement between the experimental and computational data was good with the exception of the lower wake boundary and the velocity deficit within the lower wake. The increase in ground boundary layer thickness with decreases in ride height was captured, however the velocity deficit within the ground boundary layer was underpre-

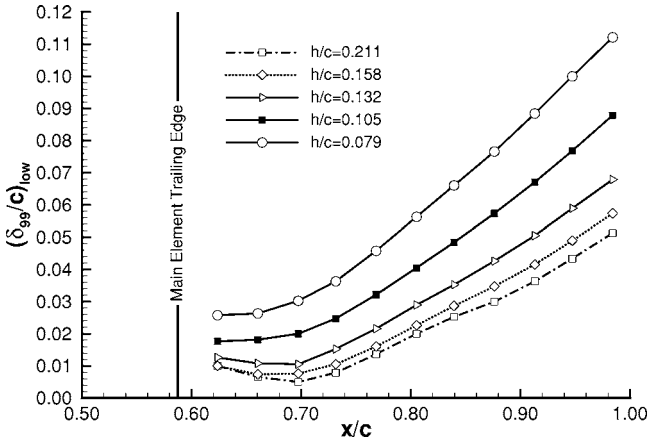

Fig. 8 Streamwise development of main element wake thickness at various ride heights; realizable $k-\varepsilon$

dicted for $h/c=0.395$ and overpredicted for $h/c=0.079$. The profile of the wall jet and associated velocities was captured well for all ride heights, however the lower wake boundary was underpredicted.

The velocity deficit within the lower wake was overpredicted for all ride heights however, the rate of velocity recovery was captured accurately. Decreases in ride height resulted in the velocity deficit increasing and the lower boundary of the lower wake

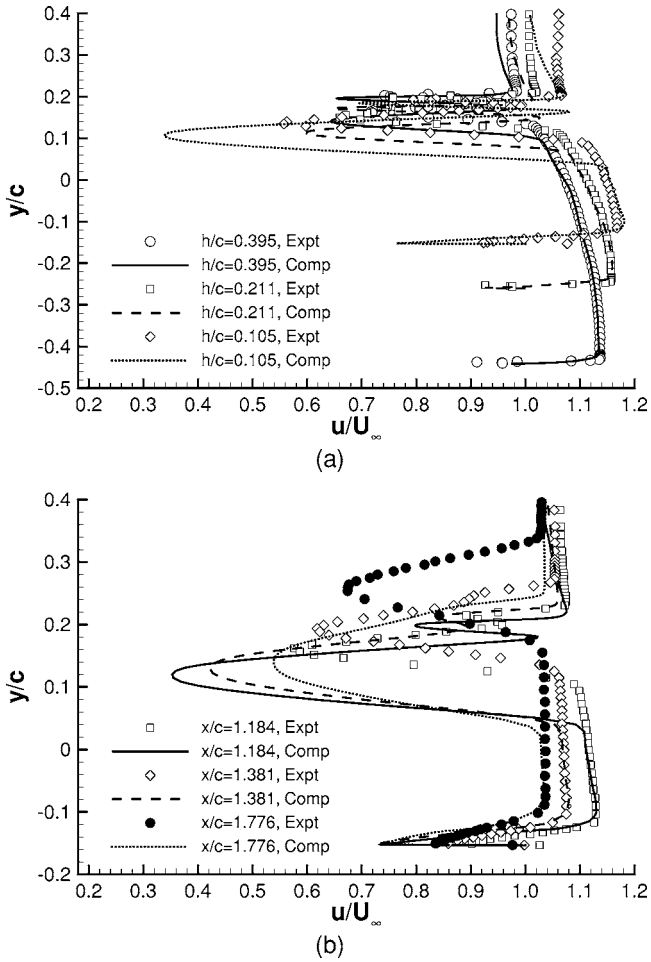

Fig. 9 Wake profiles (*a*) various ride heights at $x/c=1.066$ (*b*) various streamwise locations at $h/c=0.105$; realizable $k-\varepsilon$

getting closer to the ground plane. The velocity at the confluence point was generally overpredicted and increased, i.e., approached freestream, as the ride height decreased. The vertical location of the confluence point was generally underpredicted and decreased with decreasing ride height. The velocity deficit within the upper wake was underpredicted for all ride heights and increased with decreases in ride height. The vertical location of the upper wake deficit was underpredicted and decreased with decreasing ride height. The upper boundary of the upper wake was predicted accurately for all ride heights, however, the recovery to freestream and generally overpredicted resulting in a reduced streamwise velocity value.

The thickness of the lower wake was slightly overpredicted at all ride heights, a result of the underprediction with respect to the lower wake lower boundary. As the ride height was decreased the lower wake increased in thickness, primarily due to variations within the vertical location of the lower wake boundary. The upper wake thickness was overpredicted for all ride heights and decreased in thickness as the ride height decreased. All the trends within in the computational data, as described before, were also captured experimentally.

The streamwise variation in wake profile for a ride height of $h/c=0.105$ with the realizable $k-\varepsilon$ model is shown in Fig. 9(*b*) and listed in Table 4. Data concerning the upper wake at $x/c=1.318$ and 1.776 has been omitted from Table 4 since the two wakes had merged at these streamwise locations forming single wake. Although only data at $h/c=0.105$ is presented it must be noted that similar trends and features were observed at all the ride heights.

The thickness of the ground boundary layer was captured accurately for all streamwise locations, however, the velocity deficit within the boundary layer was overpredicted. With the exception of the lower wake lower boundary being underpredicted, the profile of the wall jet and the corresponding downstream velocity recovery was captured well. The velocity deficit within the lower wake was overpredicted for all streamwise locations. Experimentally, the vertical location of the wake was found to increase, a trend which was observed within the computational data albeit at a reduced rate. As a result the upper wake upper boundary was underpredicted computationally. The merging of the two wakes into a single wake was overpredicted between $x/c=1.381$ and 1.776 compared to between $x/c=1.184$ and 1.381 within the experimental data.

4 Discussion

The circulation around the main element was increased with the addition of the flap (Fig. 3). This was observed as increased suction on the lower surface and increased pressure on the upper surface. The pressure recovery over the suction surface of the main element remained constant. Smith [1] described the influence of a flap through five effects of which circulation effects and dumping effects were observable in the surface pressures.

A jet flow between the lower boundary of the lower wake and the ground plane was observed, especially at low ride heights ($h/c=0.079$). It is well documented that flows with large mean strain rates, such as jets, are difficult to model using turbulence models. The method adopted by the realizable $k-\varepsilon$ model is to calculate the eddy viscosity locally, therefore, allowing the model to remain realizable even in regions of large mean strain rates. Shih et al. [21] has shown that this modification results in a much improved simulations of jet flows in particular the spreading rates. It could, therefore, be hypothesized that improved simulations of the jet flow resulted in improved simulations of the lower boundary of the lower wake.

The channel created between the suction surfaces of the airfoil and the ground plane resembles a venturi nozzle. The flow entering between the main element leading edge and the ground plane is, therefore, initially accelerated until the throat of the nozzle (the lowest point on the main element suction surface) then deceler-

Table 3 Wake profile information at $x/c=1.066$ for various ride heights

		u_{min}/U_∞			y/c at u_{min}/U_∞			y/c at δ		δ_{99}/c	
h/c	Expt/CFD	Low	Top	Conf	Low	Top	Conf	Low	Top	Low	Top
0.395	Expt	0.72	0.74	0.93	0.164	0.203	0.190	0.136	0.217	0.054	0.027
	Real $k-\varepsilon$	0.64	0.65	0.98	0.140	0.195	0.174	0.105	0.215	0.069	0.041
0.211	Expt	0.66	0.76	0.96	0.150	0.200	0.184	0.124	0.207	0.060	0.023
	Real $k-\varepsilon$	0.60	0.65	1.03	0.112	0.172	0.149	0.080	0.184	0.069	0.035
0.105	Expt	0.58	0.80	0.99	0.134	0.192	0.180	0.102	0.198	0.078	0.013
	Real $k-\varepsilon$	0.34	0.70	1.08	0.105	0.184	0.165	0.050	0.192	0.115	0.027

ated underneath the downstream section of the main element and the flap. The rate of acceleration and deceleration is dependent on the shape of the nozzle and hence the ride height, with low ride heights generating greater velocities. The surface pressures illustrate this process with decreases in ride height generating suction surface pressures of greater magnitude, while the pressure surface pressures remain relatively constant. The streamwise location of the suction peak was independent of ride height at $x/c=0.11$, corresponding to the throat of the channel and, therefore, the location of highest velocity. At high ride heights the accelerated flow underneath the airfoil could recover to a freestream value prior to the airfoil trailing edge. Reducing the ride height created a velocity recovery rate which could not be physically achieved. Therefore a flow which possessed a greater than freestream value of velocity, such that $\bar{u}/U_\infty > 1.0$, was generated, i.e., a wall jet. This feature has been previously observed for a single element aerofoil in ground effect [16].

Studying Fig. 7 it may be noted that presence of the main element wake seemed to divide the flow field beneath the airfoil into two regions; a region extending downstream from beneath the main element and a region extending downstream from the slot between the two elements. At a ride height of $h/c=0.079$ the flow exiting the slot possessed a greater than freestream velocity with a profile similar to that of a jet. It could be hypothesized that since the slot flow is feeding into a region of enclosed suction, unlike a freestream case, which increases in magnitude with decreasing ride height the velocity must increase through the slot in accordance with continuity. Smith [1] stated that the presence of a second element would not produce a slot flow with high velocity which would seem to be in contradiction with this finding. However, in theory this is still correct since the increases in slot flow velocity seemed to be caused by the enclosed suction region beneath the flap and any subsequent variations with ride height. The variations within the velocities corresponding to the slot flow were less than those observed within the wall jet, therefore, producing smaller variations within the flap suction surface pressures.

It was noted that the main element generated the majority of the downforce. Since the magnitude of the suction forces associated with the main element were greater than those for the flap it is logical that the main element would generate the majority of the downforce, a finding which has been previously observed [12]. The contribution by each element to the total drag has, however, not been observed experimentally due to the design of the test rigs and a lack of viscous force data on the surfaces. The computational data indicated that the majority of the drag generated by the airfoil was caused by flap, of which the pressure drag provided the main contribution. It must be noted that the flap and the surrounding flow field is at a high incidence, therefore, any downforce produced by the flap will contain a large horizontal component observed as drag.

The wake generated by the wing consisted predominantly of the main element wake which increased in thickness as the ride height decreased. The thickness of the flap wake and the corresponding velocity deficit was relatively independent of ride height and remained thin for all cases. The majority of the main element wake thickness was generated underneath the flap suction surface where the wake was seemingly amplified by the region of enclosed suction beneath the airfoil. It may also be noted that within this region of the airfoil at low ride heights the wall jet, exiting from beneath the main element, started to recover towards a freestream value of velocity. Reducing the ride height resulted in a greater spreading rate of the main element wake (Fig. 8) and therefore a thicker overall wake. The region of recirculation directly downstream of the main element finite trailing edge contributed greatly to the main element wake. It could, therefore, be hypothesized that a sharp main element trailing edge would reduce the main element wake significantly. Within a motorsport application the reduced wake could increase the performance of components located downstream of the airfoil/wing.

The spreading of the main element wake was overpredicted for all cases, in particular the vertical location of the lower boundary was underpredicted. The computations conducted were two-dimensional whereas in reality the flow field generated by a wing in ground effect is intrinsically three-dimensional. Therefore, the effects of the wing tip vortices were excluded from the computation. It could be hypothesized that the upwash generated by wing tip vortices may influence the wake flow field, deflecting the main element and flap wakes upwards. Improvements may therefore be obtained through the use of three-dimensional simulations of a finite span wing in ground effect.

Table 4 Wake profile information at various streamwise locations for $h/c=0.105$

		u_{min}/U_∞			y/c at u_{min}/U_∞			y/c at δ		δ_{99}/c	
x/c	Expt/CFD	Low	Top	Conf	Low	Top	Conf	Low	Top	Low	Top
1.066	Expt	0.58	0.80	1.00	0.134	0.192	0.180	0.102	0.198	0.078	0.013
	Real $k-\varepsilon$	0.34	0.70	1.08	0.105	0.184	0.165	0.050	0.192	0.115	0.027
1.184	Expt	0.58	0.89	0.96	0.162	0.215	0.200	0.120	0.222	0.080	0.022
	Real $k-\varepsilon$	0.35	0.80	1.02	0.120	0.198	0.180	0.055	0.210	0.125	0.030
1.381	Expt	0.62	-	-	0.194	-	-	0.141	0.260	0.119	-
	Real $k-\varepsilon$	0.42	0.85	0.89	0.130	0.210	0.195	0.055	0.225	0.140	0.030
1.776	Expt	0.67	-	-	0.254	-	-	0.180	0.329	0.149	-
	Real $k-\varepsilon$	0.54	-	-	0.140	-	-	0.040	0.240	0.200	-

5 Conclusion

A computational investigation into a double-element airfoil in ground effect was undertaken. The effects of turbulence model, grid resolution and ride height were all investigated, and the following conclusions may be drawn:

- All the turbulence models accurately captured the surface pressures over the range of ride heights. Discrepancies were observed within the wake flow field. Improvements within the predictive capabilities of the solver were observed with the realizable $k-\varepsilon$ turbulence model. These improved predictions were more readily observed at low ride heights.
- The majority of the downforce was generated by the main element, whereas the majority of the drag was generated by the flap.
- The spreading rate of the main element wake beneath the flap suction surface greatly increased with decreases in ride height. As a result the overall wake thickness increased as the ride height was reduced.
- The main element finite trailing edge, and the corresponding downstream recirculation region, greatly contributed to the main element wake. It was hypothesized that reductions in wake thickness may be achieved with a sharp main element trailing edge.
- The underprediction of the vertical location of the lower boundary of the main element wake could have been due to the lack of three-dimensionality. Improvements over the current simulation may, therefore, be achieved by simulating a double-element wing of finite span.

Acknowledgment

The authors would like to thank Honda Racing F1 for their input and discussion, in particular Jonathan Zerihan and David Jeffery. Stephen Mahon would like to dedicate this technical paper to his late father Tony Mahon.

Nomenclature

c = total chord, 380 mm
C_L = sectional lift coefficient, $L/\frac{1}{2}\rho U_\infty{}^2 c$
C_p = coefficient of pressure, $(p-p_\infty)/\frac{1}{2}\rho U_\infty{}^2$
$C_{P\text{stag}}$ = coefficient of pressure at the leading edge stagnation point
$C_{P\text{suc}}$ = coefficient of pressure at maximum suction
h = ride height
L = lift, positive indicates downforce, i.e., force in a negative y-direction
p = static pressure
Re = Reynolds number, $\rho_\infty U_\infty c/\mu$
t = time
u,v,w = streamwise, traverse and spanwise velocity components
$\bar{u}$ = mean streamwise velocity at $x/c=0.99$ between the lower boundary of the lower wake and the ground plane
u_{conf} = u velocity component at wake confluence point
u_{low} = minimum u velocity component in lower wake
u_{top} = minimum u velocity component in upper wake
U_∞ = freestream velocity
x,y = Cartesian coordinates, x positive downstream, y positive upwards
y^+ = nondimensional length, yU_τ/υ

Greek Symbols

α = incidence, positive for nose down rotation
δ_g = flap gap
δ_{low} = lower boundary of lower wake thickness
δ_o = flap overlap
δ_{top} = upper boundary of upper wake thickness
δ_{99} = wake thickness as measured by 99% displacement thickness
μ = viscosity
ρ = density

Subscripts

a = airfoil
f = flap
m = main element
conf = wake confluence point
low = lower wake
top = upper wake
∞ = freestream value

References

[1] Smith, A. M. O., 1975, "High-Lift Aerodynamics," J. Aircr., **12**(6), pp. 501–530.
[2] Agathangelou, B., and Gascoyne, M., 1998, "Aerodynamic Design Considerations of a Formula 1 Racing Car," SAE Publication 980399.
[3] Jeffrey, D., and Alperin, M., 2000, "Aspects of the Aerodynamics of Year 2000 Formula One Racing Cars. 3rd Mira International Vehicle Aerodynamics Conference, 18–19 October 2000, Rugby.
[4] Maddah, S. R., and Bruun, H. H., 2002, "An Investigation of Flow Fields over Multi-element Aerofoils," J. Fluids Eng., **124**, pp. 154–165.
[5] Ranzenbach, R., Barlow, J. B., and Diaz, R. H., 1997, "Multi-Element Airfoil in Ground Effect—An Experimental and Computational Study," AIAA Pap. 97–2238.
[6] Rogers, S. E., 1994, "Progress in High-lit Aerodynamic Calculations," J. Aircr., **31**(6), pp. 1244–1251.
[7] Moitra, A., 2002, "Automated CFD Analysis of Two-Dimensional High-Lift Flows," J. Aircr., **39**(4), pp. 662–667.
[8] Jasinski, W. J., and Selig, M. S., 1998, "Experimental Study of Open-Wheel Race Car Front Wings," SAE Publication 983042.
[9] Ranzenbach, R., and Barlow, J. B., 1994, "Two-Dimensional Airfoil in Ground Effect, an Experimental and Computational Study," SAE Publication 942509.
[10] Ranzenbach, R., and Barlow, J., 1996, "Cambered Airfoil in Ground Effect—An Experimental and Computational Study," SAE Publication 960909.
[11] Zhang, X., and Zerihan, J., 2002, "Aerodynamics of a Double Element Wing in Ground Effect," AIAA Pap. 2002–0834.
[12] Zhang, X., and Zerihan, J., 2003, "Aerodynamics of a Double-Element Wing in Ground Effect," AIAA J., **41**, pp. 1007–1016.
[13] Zerihan, J. D.C., 2001, "An Investigation Into the Aerodynamics of Wings in Ground Effect," PhD thesis, University of Southampton, Southampton, UK.
[14] Zerihan, J. D.C., and Zhang, X., 2000, "Aerodynamics of a Single Element Wing in Ground Effect," J. Aircr., **37**(6), pp. 1058–1064.
[15] Zerihan, J., and Zhang, X., 2001. "A Single Element Wing in Ground Effect; Comparisons of Experiments and Computation," AIAA Pap. 2001–0423.
[16] Mahon, S., and Zhang, X., 2005. "Computational Analysis of Pressure and Wake Characteristics of an Aerofoil in Ground Effect," J. Fluids Eng., **127**(2), pp. 290–298.
[17] Spalart, P. R., and Allmaras, S. R., 1992. "A One-Equation Turbulence Model For Aerodynamic Flows," AIAA Pap. 92–0439.
[18] Launder, B. E., and Spalding, D. B., 1974, "The Numerical Computation of Turbulent Flows," Comput. Methods Appl. Mech. Eng., **3**, pp. 269–289.
[19] Menter, F. R., 1994. "Two-Equation Eddy-Viscosity Turbulence Models for Engineering Applications," AIAA J., **32**(8), pp. 1598-1605.
[20] Yakhot, A., and Orszag, S., 1986, "Renormalization Group Analysis of Turbulence: I Basic Theory," J. Sci. Comput., **1**(1), pp. 1–51.
[21] Shih, T.-H., Liou, W. W., Shabbir, A., Yang, Z., and Zhu, J., 1995, "A New k-ϵ Eddy Viscosity Model for High Reynolds Number Turbulent Flows," Comput. Fluids, **24**, pp. 227–238.
[22] Wilcox, D. C., 1988, "Multiscale Models for Turbulent Flows," AIAA J., **26**(11), pp. 1311–1320.
[23] Czerwiec, R., Edwards, J. R., Rumsey, C. L., Bertelrud, A., and Hassan, H. A., 2000, "Study of High-Lift Configurations Using k–ζ Transition/Turbulence Model," J. Aircr., **37**(6), pp. 1008–1016.
[24] Burgin, K., Adey, P. C., and Beatham, J. P., 1986, "Wind Tunnel Tests on Road Vehicle Models Using a Moving Belt Simulation of Ground Effect," J. Wind. Eng. Ind. Aerodyn., **22**, pp. 227–236.

V. Huijnen[1]
e-mail: V.Huijnen@tue.nl

L. M. T. Somers

R. S. G. Baert[2]

L. P. H. de Goey

Section Combustion Technology,
Faculty of Mechanical Engineering,
Eindhoven University of Technology,
Eindhoven, 5600 MB, Netherlands

C. Olbricht

A. Sadiki

J. Janicka

Chair of Energy and Powerplant Technology,
Faculty of Mechanical Engineering,
Darmstadt University of Technology,
Peterstr. 30,
Darmstadt, D-64287,
Germany

Study of Turbulent Flow Structures of a Practical Steady Engine Head Flow Using Large-Eddy Simulations

The prediction performance of two computational fluid dynamics codes is compared to each other and to experimental data of a complex swirling and tumbling flow in a practical complex configuration. This configuration consists of a flow in a production-type heavy-duty diesel engine head with 130-mm *cylinder bore. One unsteady Reynolds-averaged Navier-Stokes (URANS)-based simulation and two large-eddy simulations (LES) with different inflow conditions have been performed with the KIVA-3V code. Two LES with different resolutions have been performed with the FASTEST-3D code. The parallelization of the this code allows for a more resolved mesh compared to the KIVA-3V code. This kind of simulations gives a complete image of the phenomena that occur in such configurations, and therefore represents a valuable contribution to experimental data. The complex flow structures gives rise to an inhomogeneous turbulence distribution. Such inhomogeneous behavior of the turbulence is well captured by the LES, but naturally damped by the URANS simulation. In the LES, it is confirmed that the inflow conditions play a decisive role for all main flow features. When no particular treatment of the flow through the runners can be made, the best results are achieved by computing a large part of the upstream region, once performed with the FASTEST-3D code. If the inflow conditions are tuned, all main complex flow structures are also recovered by KIVA-3V. The application of upwinding schemes in both codes is in this respect not crucial.*
[DOI: 10.1115/1.2353259]

Introduction

In internal combustion engines, the level of turbulence plays an important role in the optimization of the efficiency. Turbulence will be highly anisotropic, due to swirling and tumbling motions. This requires a dedicated turbulence modeling approach. In this study several approaches are compared on a complex engine geometry.

In recent history, several approaches and many different turbulence models have been developed to account for the turbulence effects in practical situations. The starting point in the numerical turbulence modeling originates from the classical Reynolds-averaged Navier-Stokes RANS k-ϵ model. Most industrial computational codes still rely on this type of model. Advantages are the robustness, the relative simplicity, and the relatively low computational cost. However, this model has been denounced in the academic world for its failure in the modeling of anisotropic turbulence, which occurs in practically all industrial applications where complex geometries are present.

The RANS approach has been extended to unsteady-RANS (URANS) and models have been developed with second moment Reynolds stress closures and near-wall treatment (see, e.g., Pope [1] and references therein). Notwithstanding many reported successes on generic anisotropic turbulence cases these models have never become standard in industrial code (see, e.g., Hanjalić [2] and Laurence [3]). One reason is that the coupling of these turbulence models is less robust than in the case of an eddy-viscosity closure. This implies a firm knowledge on turbulence theory and a large experience to handle simulations where these models are incorporated. Simplifications, by replacing the second-moment closure, wherein six transport equations for the Reynolds stress terms are solved, with algebraic stress models (ASM) on the one hand improve the stability and numerical efficiency of the model, but on the other hand inherently decrease the modeling accuracy, as all ASM models are based on simplifications of the full Reynolds stress equations, as pointed out by Hanjalić [2].

More recently, stimulated by the large increase of computational resources and the development of new computational fluid dynamics (CFD) codes, a new approach to turbulence modeling has become within reach. In the so-called classical large-eddy simulation (LES) approach all important turbulent scales are resolved. These scales contain most of the turbulent kinetic energy and thus are responsible for the transport of most of the species concentrations. Thus, only turbulence on the smallest scales requires additional modeling. The LES approach has been shown to be successful on a broad range of generic cases. An early overview of a LES approach for engine applications has been given by Celik [4], whereas Haworth [5] presented computations on a simplified piston-cylinder assembly. However, theoretical limitations make the use of the LES approach in practical applications questionable.

The first problem is that the isotropic turbulence in the near-wall region is restricted to very small scales. This requires a very fine mesh with, on the one hand, adapted mesh types and, on the other hand, large computational resources (see, e.g., Sagaut [6] or Pope [1]).

The second problem concerns the limited accuracy of the numerical scheme. All turbulent scales up to the inertial subrange are to be evaluated explicitly on the available mesh. However, any numerical scheme influences the effective filter size (Geurts [7]). Moreover, in the inertial subrange the turbulent kinetic energy cascades within scales of the same order of magnitude. Thus, the subgrid model is based on the lowest resolved turbulent scales.

[1]URL: http://www.combustion.tue.nl
[2]Also at TNO Automotive, Powertrains, Delft, The Netherlands.

Contributed by the Fluids Engineering Division of ASME for publication in the JOURNAL OF FLUIDS ENGINEERING. Manuscript received December 5, 2005; final manuscript received April 21, 2006. Assoc. Editor: Ye Zhou.

For any correct turbulence model this implies that these scales need to be evaluated correctly, i.e., the numerical dissipation should be much smaller than the modeled subgrid-scale dissipation, such that the modeling part is dominant (see, e.g., Piomelli [8]).

The third problem concerns the inflow boundary condition. Lund et al. [9] showed that in case of using nonphysical inflow boundary conditions, such as a constant velocity inflow or random fluctuations, a long development period may be required to reproduce the correct mean and turbulence statistics. One way to decrease this dependence is to create physically reasonable inflow boundary conditions (Klein et al. [10]).

The questions raised by the considerations mentioned above can now be formulated: What turbulence approach is appropriate when modeling a complex geometry? Secondly, how accurate do the turbulence models need to be to achieve reasonable results? Precisely which effects are modeled correctly in the URANS approach and which in the LES approach? With respect to the LES approach, what will be the influence of the above mentioned details of the turbulence modeling on the results? In order to investigate these questions the flow in a steady state engine geometry is studied both numerically and experimentally.

For the numerical part, two CFD codes have been used: KIVA-3V (Amsden et al. [11]) and FASTEST-3D (see, e.g., Mengler [12]). With KIVA-3V, a URANS k-ϵ simulation and two coarse LES have been performed. With FASTEST, two LES with different grid resolutions have been conducted, one on a relatively coarse mesh, comparable to the mesh in KIVA-3V, and one that is doubly resolved. Particle image velocimetry (PIV) experiments have been performed at different heights in the cylinder (de Leeuw [13]) to observe the mean structures in the flow.

In Sec. 2, details of the modeling and the numerical procedures used in both codes are briefly described. Sections 3 and 4 outline the experimental setup and the corresponding numerical configuration, respectively. Results of the different models compared to the experiments are presented and discussed in Sec. 5. Some concluding remarks are drawn in Sec. 6.

2 Modeling and Numerical Procedure

To numerically describe the complex flow configuration under investigation, the modeling approach used and the numerical procedure applied to solve the modeled governing equations are outlined in this section. Because two codes are concerned, the description is divided in two parts, each focused on the particular code.

2.1 KIVA-3V. The KIVA-3V code is an advanced computer program for the numerical calculation of transient, three-dimensional chemically reactive fluid flows with sprays. It is written primarily for simulating flows in reciprocating internal combustion engines. The governing equations consist of the continuity equation and the momentum equation. They are statistically averaged following an ensemble averaging procedure for RANS or filtered for LES where a Favre decomposition has been applied

$$\frac{\partial \bar{\rho}\tilde{u}_i}{\partial t} + \frac{\partial}{\partial x_j}(\bar{\rho}\tilde{u}_j\tilde{u}_i) = \frac{\partial}{\partial x_j}\bar{\rho}(\tilde{\sigma}_{ij} - \tau_{ij}) + \bar{\rho}g_i - \frac{\partial \bar{p}}{\partial x_i} \tag{1}$$

In this equation

$$\tilde{\sigma}_{ij} = \tilde{\nu}\left(\frac{\partial \tilde{u}_i}{\partial x_j} + \frac{\partial \tilde{u}_j}{\partial x_i}\right) \tag{2}$$

To close the Reynolds stress tensor τ_{ij} in the averaged momentum equation, the Boussinesq approximation along with the standard k-ϵ model is adopted

$$\tau_{ij} = C_\mu \frac{k^2}{\epsilon}\left(\frac{\partial \tilde{u}_i}{\partial x_j} + \frac{\partial \tilde{u}_j}{\partial x_i}\right) \quad C_\mu = 0.09 \tag{3}$$

In the filtered momentum equations, the subgrid scale stress tensor is closed following the classical Smagorinky ansatz

$$\tau_{ij} = \tau_{ij}^{\mathrm{SGS}} = \tilde{\nu}_t\left(\frac{\partial \tilde{u}_i}{\partial x_j} + \frac{\partial \tilde{u}_j}{\partial x_i}\right) \tag{4}$$

In particular, the so-called wall adapting local eddy-viscosity (WALE) model as proposed by Nicoud [14] is adopted to take into account the anisotropy of the turbulence. This model is based on the traceless symmetric part of the square of the velocity gradient tensor γ_{ij}. By introducing a short notation for the gradients

$$\alpha_{ij} = \frac{\partial \tilde{u}_i}{\partial x_j} \tag{5}$$

this tensor can be written as

$$\gamma_{ij} = \frac{1}{2}\alpha_{im}\alpha_{mj} - \frac{1}{3}\delta_{ij}\alpha_{kl}\alpha_{kl} \tag{6}$$

We can construct from this tensor the operator G_γ

$$G_\gamma = \gamma_{ij}\gamma_{ij} \tag{7}$$

By using this operator, we can construct an eddy-viscosity that scales at the walls to its theoretical value of y^3 with y the distance to the walls

$$\nu_t = (C_w\Delta)^2 \frac{G_\gamma^{3/2}}{\tilde{S}_{ij}\tilde{S}_{ij} + G_\gamma^{5/4}} \quad C_w = 0.5 \tag{8}$$

with $\tilde{S}_{ij} = \frac{1}{2}(\alpha_{ij} + \alpha_{ji})$. To be solved numerically, these closed governing equations are discretized using the finite-volume method. Consequently the LES equations are filtered implicitly.

The computational grids are built with hexahedrons. The velocity components are defined at the vertex centers while all thermodynamic variables are cell centered quantities. In KIVA-3V, the arbitrary Lagrangian Eulerian concept is used to model the displacement of the grid nodes, as is required for engine simulations. In this method two phases can be distinguished. Firstly, the Lagrangian evaluation of equations of motion. In this phase the source terms and diffusive terms are evaluated. This can be done implicitly, explicitly, or semi-implicitly, based on considerations of both stability and efficiency.

In the second phase, all cells are mapped back onto the Eulerian grid. This phase is evaluated explicitly and can be divided in subcycles. The time step of the subcycle is based on on the Courant stability criterion. Details on the properties of the numerical schemes can be found in Amsden et al. [11].

The accuracy of the convective scheme is improved by the implementation of a nonlinear total variation diminishing (TVD) scheme (Hirsch [15]). The motivation for using the TVD description lies in its stability preservation. The numerical model described above has been validated in different configurations, such as a square duct geometry (Huijnen [16]), and, using different subgrid-scale models, a spatially developing free jet (Celik [17]) and a mixing layer (Sone [18]).

2.2 FASTEST-3D. The filtered Navier-Stokes equations along with the filtered continuity equation describe the behavior of any Newtonian fluid

$$\frac{\partial \bar{\rho}}{\partial t} + \frac{\partial \bar{\rho}\tilde{u}_i}{\partial x_i} = 0 \tag{9}$$

$$\frac{\partial \bar{\rho}\tilde{u}_i}{\partial t} + \frac{\partial}{\partial x_j}(\bar{\rho}\tilde{u}_i\tilde{u}_j) = \frac{\partial}{\partial x_j}\bar{\rho}(\tilde{\sigma}_{ij} - \tau_{ij}^{\mathrm{SGS}}) - \frac{\partial \bar{p}}{\partial x_i} \tag{10}$$

where

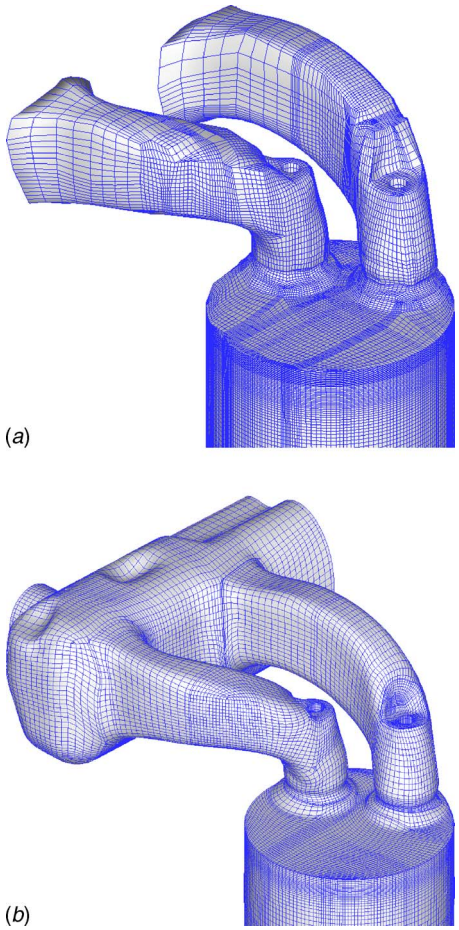

Fig. 1 Geometry of a cylinder with inflow manifold. (*a*) KIVA simulations and (*b*) FASTEST simulations.

$$\tilde{\sigma} = \tilde{\nu}\left(\frac{\partial \tilde{u}_i}{\partial x_j} + \frac{\partial \tilde{u}_j}{\partial x_i}\right) \tag{11}$$

A simple Smagorinsky model is employed for the subgrid scale (SGS) stress-tensor τ_{ij}^{SGS}, with Lilly's formulation of Germano's dynamic procedure for the determination of the model coefficient [19]. No special wall treatment is used. Instead, the boundary layer is resolved and it is expected that the dynamic procedure is able to capture the correct asymptotic behavior of the SGS model when approaching the wall [20].

All the governing equations are integrated into the three-dimensional finite-volume CFD code FASTEST-3D. The code features geometry-flexible block-structured, boundary-fitted grids with a collocated, cell-centered variable storage. Second-order central schemes taking into account the grid nonorthogonality by means of multi-linear interpolation ([21]) are used for spatial discretization.

Pressure-velocity coupling is achieved via a SIMPLE procedure. As time integration scheme the second-order implicit Crank-Nicolson method is used. The resulting set of linear equations is solved iteratively using a seven-diagonal strongly implicit procedure (SIP)-solver. The code is parallelized based on domain decomposition using the MPI message passing library. For details on the method refer to, e.g., Mengler [12] or Durst and Schäfer [22].

3 Experimental Setup

For this study the geometry of a heavy duty diesel engine is investigated (Fig. 1). The so-called low-swirl cylinder head incorporates four valves: two inlet and two exhaust valves. The bore diameter D is 130 mm. In the experiments and simulations a constant valve lift of the inlet valves of 9 mm is applied. The exhaust valves are closed. Such a steady flow setup is often used to characterize a production type cylinder head experimentally. Classically, only the angular momentum of the swirling flow is determined. For the current simulation studies, a constant mass flow of 204 g/s is applied through the cylinder, where the piston is removed. This corresponds approximately the maximum flow rate as occurs during the inflow phase at the intake stroke in a running engine at full load. The corresponding Reynolds number Re_{inlet} based on the port diameter and the flow rate is around 2.2×10^5. The simulations are compared to experiments performed by de Leeuw [13]. The experimental setup to perform PIV experiments consists of a double-cavity ND-YAG laser with a pulse energy of 200 mJ, a repetition frequency of 10 Hz, and a pulse duration of 9 ns. The sheet thickness was approximately 1.5 mm. Oil droplets with a diameter of 4 μm are used for the seeding. The interrogation area size of the PIV algorithm was set to 64×64 pixels to have a sufficient seeding density.

A set of 100 raw velocity fields was used for validation and analysis. A normal distribution for the ensemble of the magnitude of all velocity vectors in the field is assumed and vectors with a length more than three times the standard deviation are rejected. For each velocity vector, deviation from the local median was determined. Vectors are rejected based on this local deviation in magnitude and direction. Finally, all rejected vectors are replaced by an interpolation from neighboring vectors. Details of the experimental setup can be found in Doosje [23].

Accurate laser-Doppler anemometry experiments have been performed that revealed that the accuracy of the vector fields away from the walls is approximately 10%. The PIV experiments are therefore useful to observe a trend in the flow fields. The second-moment statistics (the turbulence intensities) will only give qualitative information, as the range of uncertainty can be estimated on the order of 30%, when independent measurement series are compared. The experimental errors are acceptable for the comparison to the performed simulations as only trends in the simulation data will be considered. For accurate, detailed engine flow validation more extensive experimental as well as numerical studies have to be performed.

Table 1 List of performed simulations

Simulation	Resolution	Turbulence model	Inflow BC.
Kiva A	400,000	URANS k-ϵ	equal
Kiva B	400,000	LES WALE	equal
Kiva C	400,000	LES WALE	matching to *FASTEST B*
FASTEST A	500,000	LES/dynamic	turbulent
FASTEST B	2,500,000	LES/dynamic	turbulent

4 Numerical Setup

To gain insight on the performance of the numerical models in the codes in predicting the flow characteristics under study, different numerical configurations have been designed in terms of grid sizes, model combinations, and inflow conditions. They are summarized in Table 1.

4.1 KIVA-3V. Three simulations have been performed with KIVA-3V. All simulations used the same mesh (Fig. 1(*a*)). This mesh consist of approximately 400,000 cells, refined at the top of the cylinder. In the first simulation *Kiva A*, the classical RANS k-ϵ model is adopted. The other simulations are performed in the LES mode. In the second simulation referred to as *Kiva B*, the inflow boundary condition is set from simple considerations of equal mass flow through the two runners. In the third simulation, simulation *Kiva C*, the actual space-dependent flow profiles through the two runners is controlled such that it equals the mean

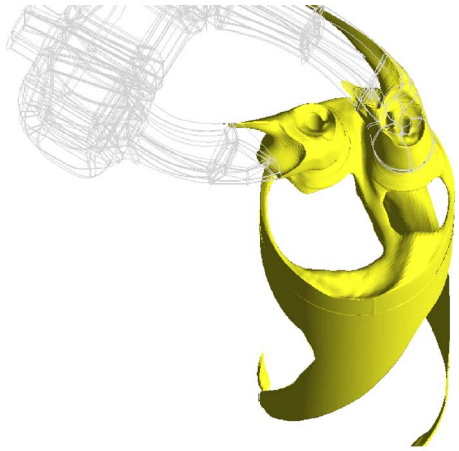

(*a*)

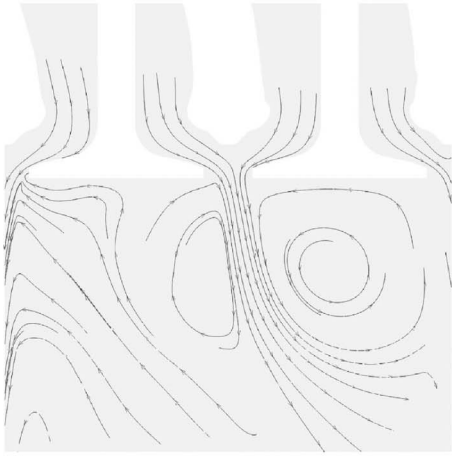

(*b*)

Fig. 2 (*a*) The isosurface of the $\langle \tilde{w} \rangle$ component illustrating the mean swirl. (*b*) Streamlines illustrating the tumble process. Simulation *FASTEST B*.

Fig. 3 Location of the plane where the data are evaluated

velocity profiles at these planes as found in the FASTEST results.

In all simulations, a continuative outflow boundary is defined at the bottom; i.e., all gradients are set to zero. The influence of this downstream boundary is assumed to be sufficiently reduced by setting the height of the cylinder three times the diameter D, while performing the main analysis up to $z=1.75D$.

4.2 FASTEST-3D. Two calculations have been carried out using the FASTEST code. The first computation had a relatively coarse resolution, this simulation is referred to as *FASTEST A*. The number of cells reaches 500.000 cells. In second simulation, the grid-cell size is reduced in every direction, which results in a total of 2.6×10^6 cells, simulation *FASTEST B*. As the FASTEST code applies a multi-block strategy, this implies that so-called O-grids can be used, which will improve the quality of the mesh, especially at all curved areas near the walls. In the FASTEST simulations, a larger part of the inflow manifold is simulated, compared to the KIVA simulations. Therefore, the fluid is naturally distributed over

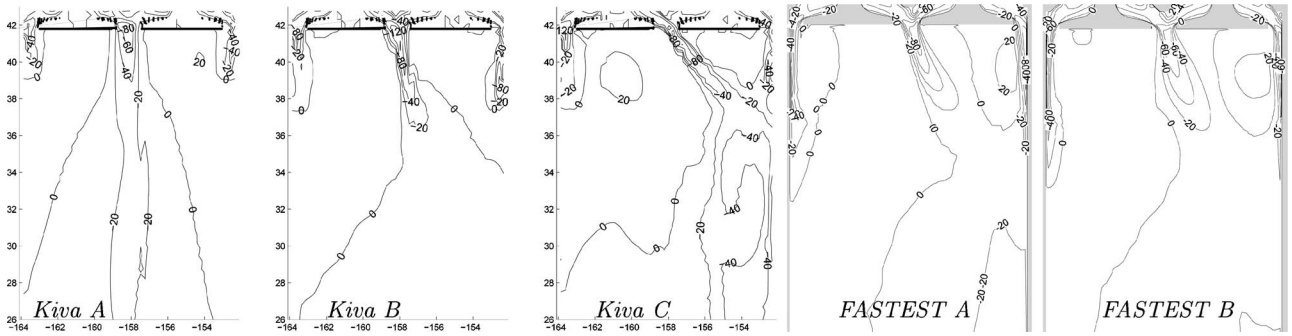

Fig. 4 $\langle \tilde{w} \rangle$-component velocity fields in the plane indicated in Fig. 3. Contour levels are shown in steps of 20 m/s.

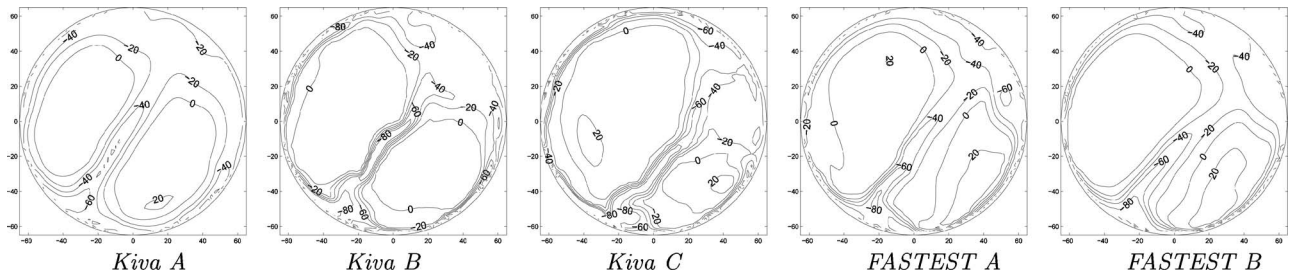

Fig. 5 $\langle \tilde{w} \rangle$ velocity fields at $Z=0.25D$ below the cylinder head

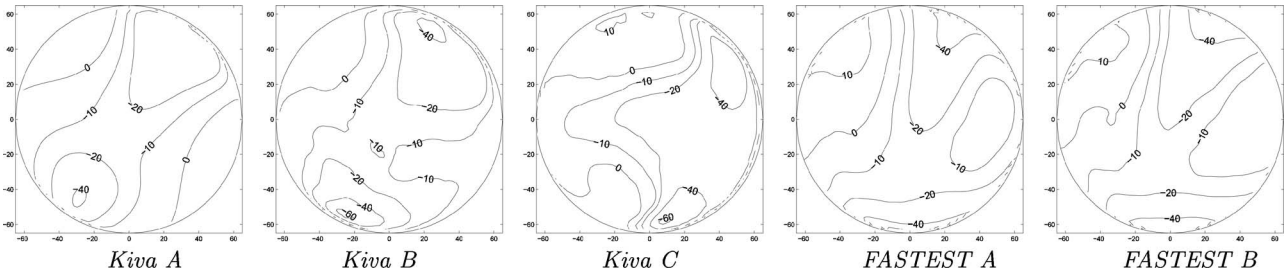

Fig. 6 $\langle \tilde{w} \rangle$ velocity fields at $Z=1.25D$ below the cylinder head

the two inflow runners.

Moreover, at the inflow plane turbulent inflow conditions are provided consisting of a correlated inflow field with turbulent statistics based on pipe flow measurements, Eggels [25]. This procedure is based on the inflow generator developed by Klein et al. [10], and is adapted for arbitrary surfaces. At the bottom a continuative outflow boundary condition is defined.

4.3 Computation Requirements. The computational time for both the KIVA-3V and FASTEST simulations was approximately two months on different high-performance computing facilities. The *FASTEST A* is parallelized on two CPUs, where *FASTEST B* has used eight CPUs. All KIVA-3V simulations ran on a single CPU. The simulated physical time equals 0.15 s, which is estimated to

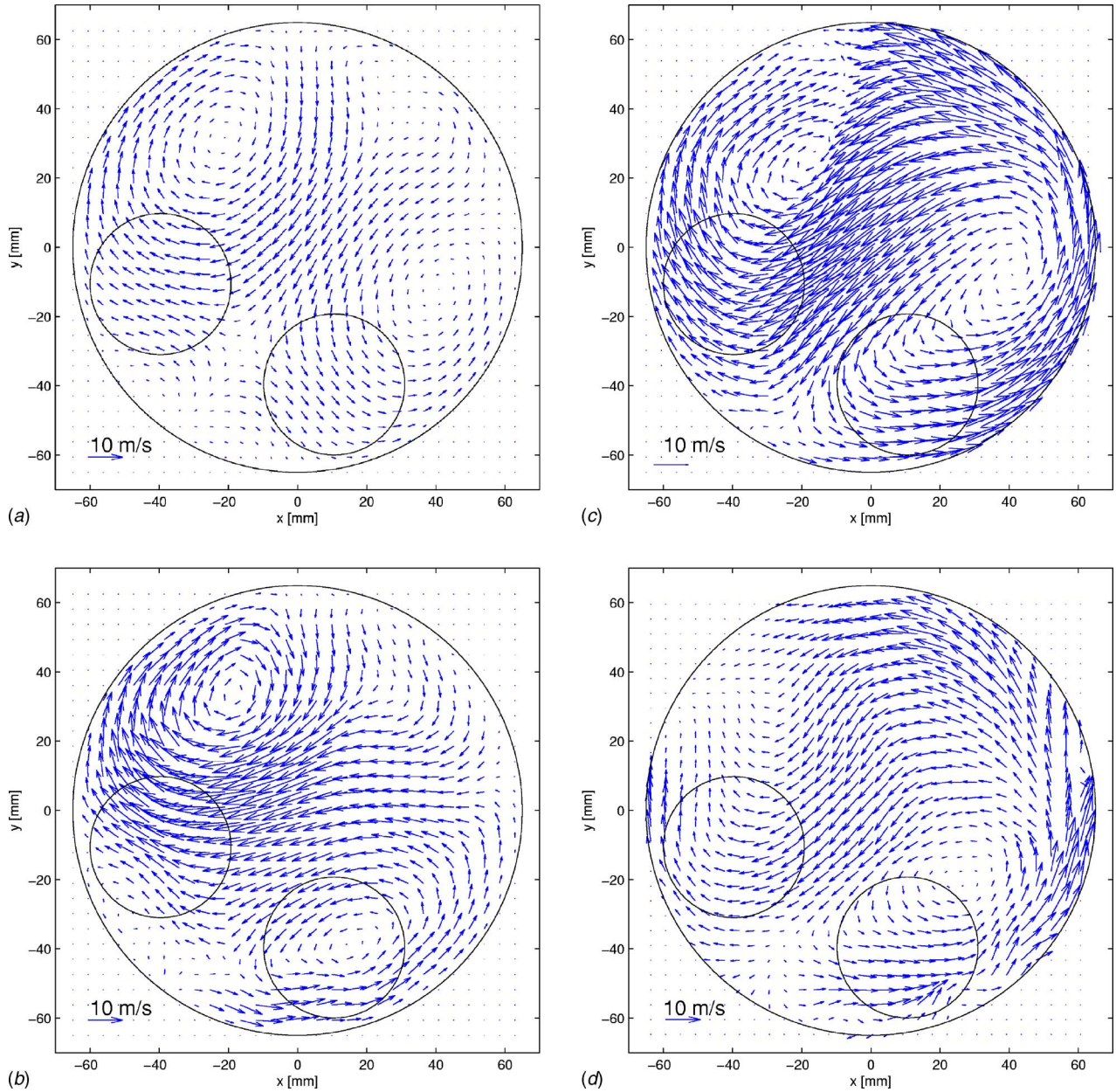

Fig. 7 Mean spanwise velocity fields at $Z=1.25D$ below the cylinder head. (*a*) *Kiva A*, (*b*) *Kiva B*, (*c*) *FASTEST B*, and (*d*) PIV.

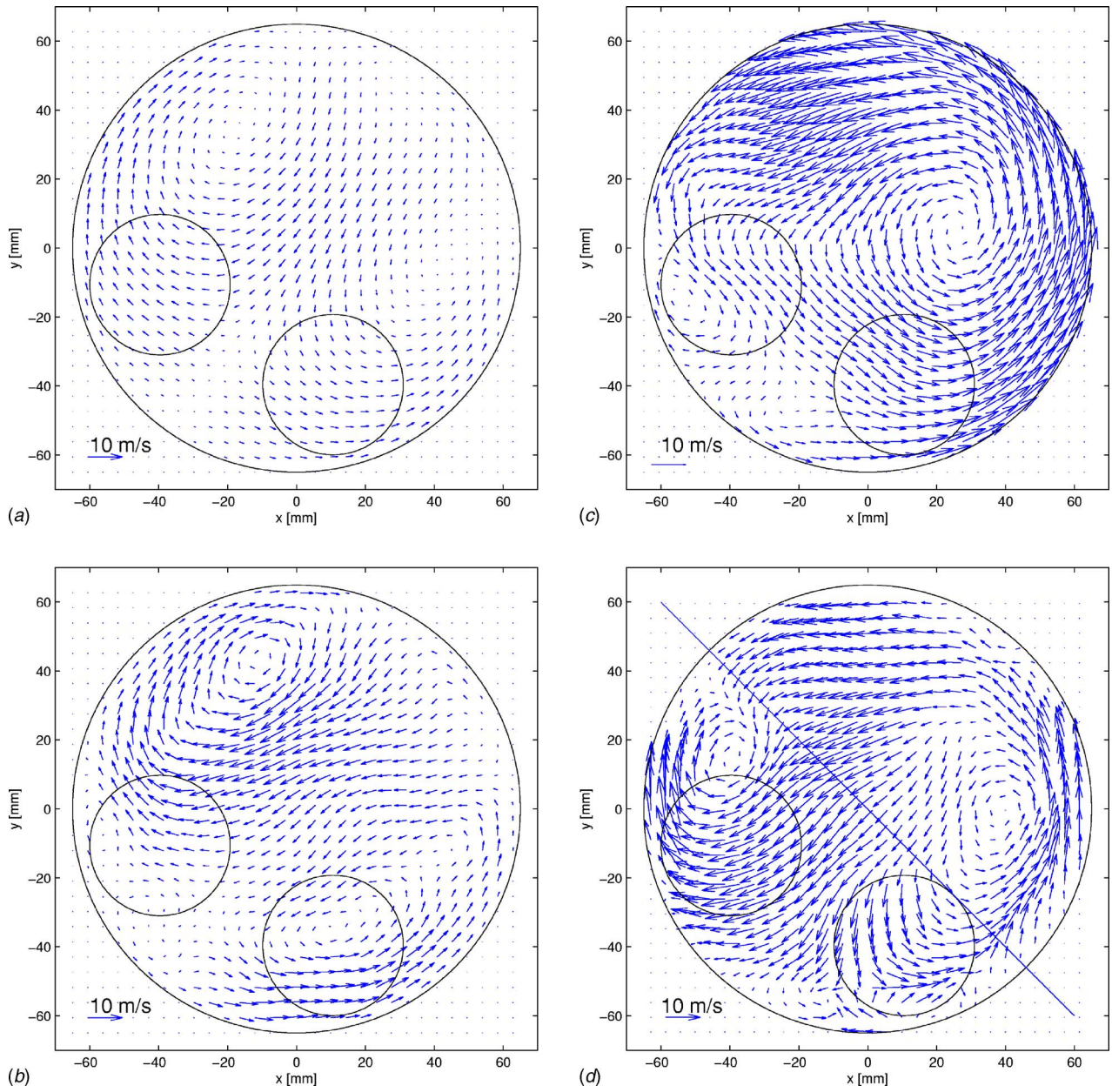

Fig. 8 Mean spanwise velocity fields at $Z=1.75D$ below the cylinder head. (*a*) *Kiva A*, (*b*) *Kiva B*, (*c*) *FASTEST B*, and (*d*) PIV.

be sufficient to capture approximately 100 large-scale turbulent time scales.

5 Results and Discussion

In this section, the results from the simulations are presented and discussed. To understand the origin of a specific detail of the flow structure it is important to consider the complete flow in the system. The main features of the flow may be illustrated by Fig. 2. In the left figure, a typical isosurface of the mean vertical velocity component $\langle \vec{w} \rangle$ is displayed, which is extracted from the data from simulation *FASTEST B*. This isosurface shows the presence of two jet-like structures in the cylinder, opposite to each other.

When following these structures downwards along the cylinder walls, a clear mean rotational flow is observed, like a swirling motion. The right picture (Fig. 2(*b*)) shows the streamlines of the mean velocity field on a cross section in the domain. Two recirculation areas can be identified that illustrate the second effect special to engine geometries: the tumble. The size of the tumbling motion scales to the size of the valves.

In the next subsections, the mean flow properties are first considered, focusing on the tumble and the swirling motion. The turbulent flow properties will then be considered. All data are compared on several planes in the domain. A vertical plane is extracted such that it crosses the two valves (Fig. 3).

Moreover, at three locations, $Z=0.25D$, $Z=1.25D$, and $Z=1.75D$ below the cylinder head, horizontal cross sections are extracted, with D being the cylinder diameter. At the lower two levels, PIV data of the flow field in the spanwise direction are available.

5.1 Tumble. Figure 4 shows the contour levels of the mean vertical velocity fields for the five different cases. It is observed that in all simulations, except for the URANS simulation *Kiva A*, the flow is directed towards the right valve. This can be explained

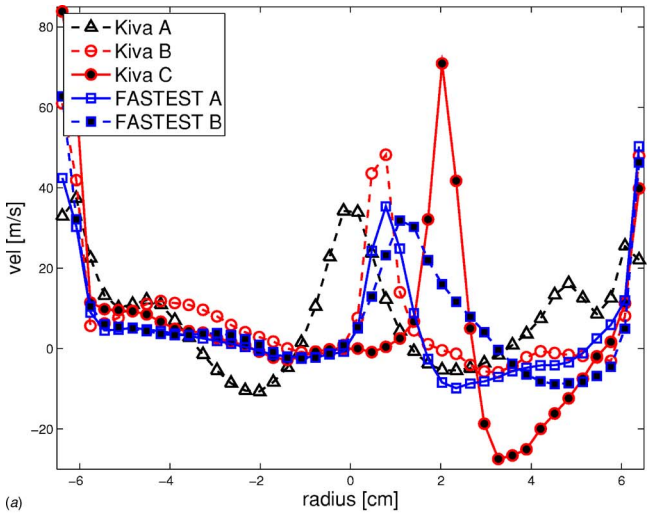

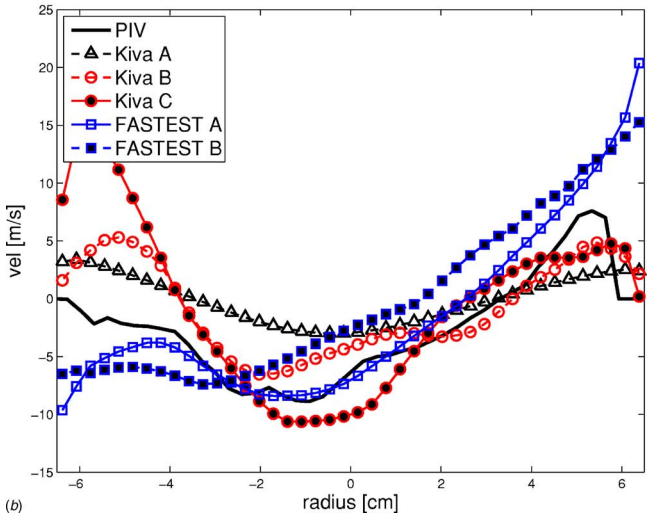

Fig. 9 Mean spanwise velocity magnitude at different heights below the cylinder head. (*a*) Height=0.25*D* and (*b*) height =1.75*D*.

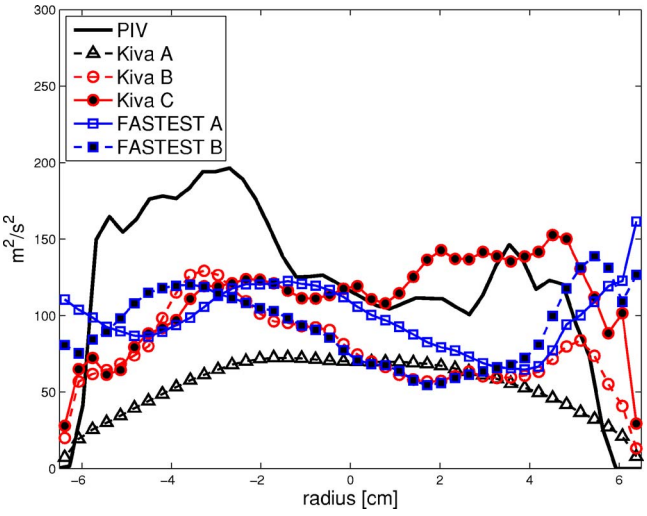

Fig. 10 Resolved turbulence intensities at *Z*=1.75*D* below the cylinder head, along the line indicated in Fig. 8(*d*).

by the inflow geometry (Fig. 3). The runners induce a strong jet directed to the wall of the cylinder. The angle and strength of this jet will determine the strength of the swirling motion in the cylinder. The jet in *Kiva C* is more inclined towards the wall than in *Kiva B* and *FASTEST A,B*.

The resemblance of the two FASTEST simulations indicates that these simulations can be considered grid independent, even though for an implicit filtering this is very hard to guarantee. The two jets emerging between the valve and the cylinder walls do not penetrate deeply into the cylinder as the shear at the walls is too large. These jets will be mainly responsible for the tumbling effects.

This tumble is best observed from Fig. 5. In case *Kiva A*, the two tumbling regions are equally large, consistent with the $\langle\tilde{w}\rangle$-contour plot from Fig. 4. In the other simulations the tumbling region at the right side of the cylinder is slightly smaller than the left side, which is in correspondence with the centered jet in the previous figure.

The *Kiva C* simulation predicts a relatively large deviation between the two tumbling regions. The jets at the right side are that close to each other such that they merge and become a single, large, downward-moving flow. This can already be observed in Fig. 6, which shows the $\langle\tilde{w}\rangle$ contour plot at 1.25 *D* below the cylinder head.

This figure also shows that in the *Kiva A,B* and *FASTEST A,B*, these jets remain more distant from one another in correspondence to Fig. 2(*a*). Both jets remain present up to the bottom, although the location and shape from simulation *Kiva B* is different from the results of FASTEST. Whereas the velocity magnitudes close to the cylinder walls tend to zero, they remain large in the FASTEST simulations. Moreover, by comparing the streamwise velocity fields at $Z=0.25D$ and $Z=1.25D$ it can be observed that in all *Kiva* simulations the jet remains at the same location, whereas in both FASTEST simulations the mean swirl has rotated the flow field in the counterclockwise direction. Again, the main features of the flow field in both FASTEST simulations are equal, indicating that this simulation is relatively grid independent. Therefore in the next sections the results from simulation *FASTEST A* will not be shown anymore.

5.2 Turbulent Unsteady Structures. When looking at the mean spanwise velocity fields in Figs. 7 and 8, it is found with URANS simulation in *Kiva A* that the large-scale vortices are relatively weak.

The LES show a stronger contribution to the vortical motions. In all cases, two large-scale vortical structures are found, in correspondence with the PIV experimental data. In case *Kiva B*, without the velocity correction at the inflow planes, the vortical structures are not equal in strength, just like the FASTEST results and experiments. When matching the inflow in *Kiva C*, results deteriorate compared to the experiments. The balancing of the flow in the two runners is perturbed.

The mean spanwise velocity vector field from simulation *FASTEST B* changes from a complex flow structure near the valves to two counter-rotating vortices (Fig. 7). However, lower in the cylinder the stronger counterclockwise vortex still survives (Fig. 8). This is in contrast to the experiments and the simulations from KIVA-3V. Here, the two counter-rotating vortical structures remain present from top to bottom. The numerical dissipation in the FASTEST simulations due to the upwind blending and the influence of the outflow boundary condition will be the reason for this.

In Fig. 9, the spanwise velocity magnitudes are plotted over the diagonal line, as is illustrated in Fig. 8(*d*) (PIV). This line is chosen such that the strength of the two vortices can be visualized as clearly as possible, in order to compare the simulations quantitatively with one another and with experiments. Figure 9(*a*) shows the spanwise flow field close to the valves. Here the strong jet in the centerline and the two jets at the sides are clearly visible.

This figure illustrates that already close to the valves the cen-

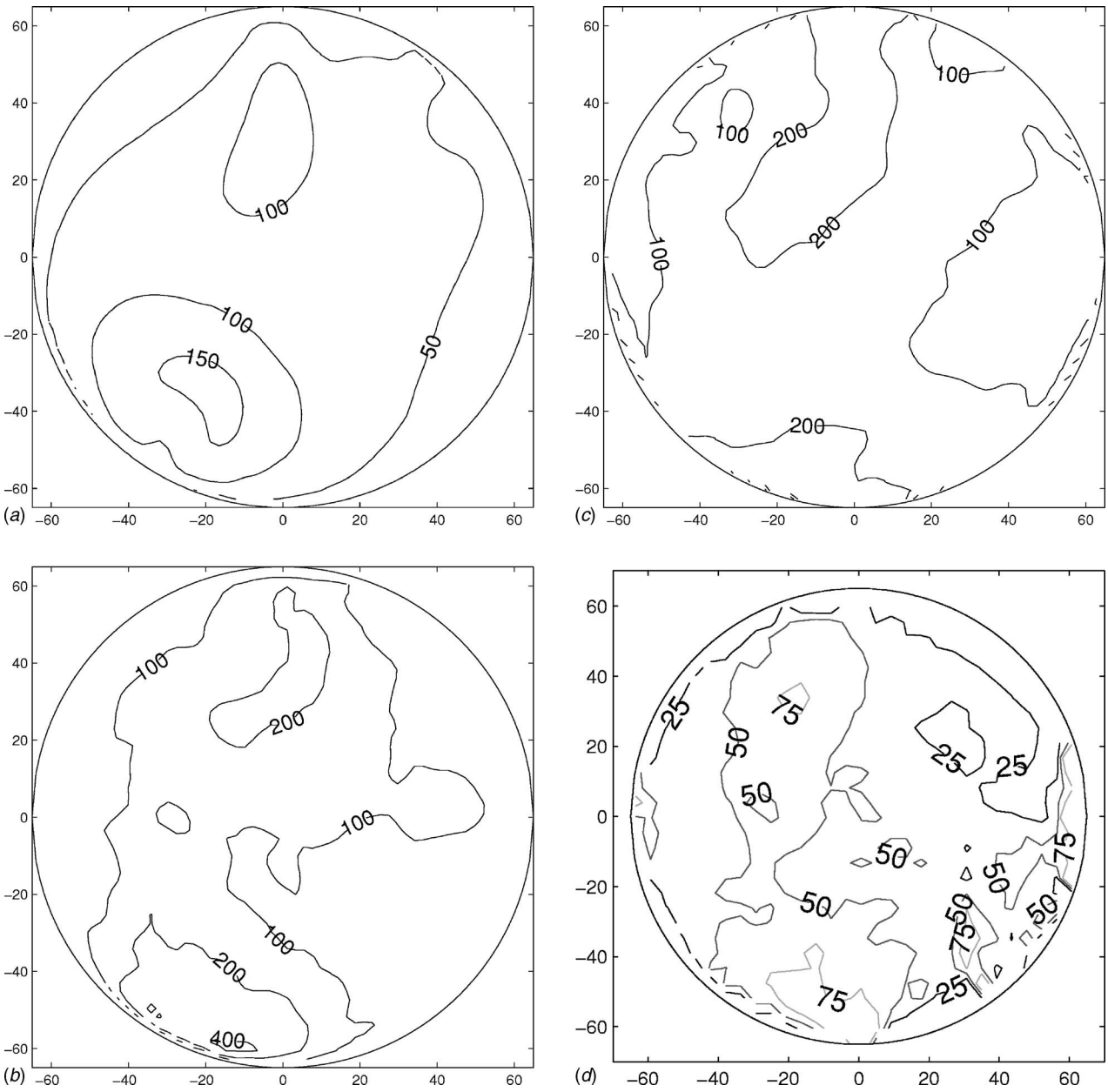

Fig. 11 Turbulence intensities *k* at *Z*=1.25*D* below the cylinder head. (*a*) *Kiva A*, (*b*) *Kiva B*, (*c*) *FASTEST B*, and (*d*) PIV.

terline jet is not identical for all simulations, while the main profile characteristics are almost reproduced by all except for the case *Kiva C*. In fact, simulation *Kiva A* shows the maximum relatively far to the left side, whereas simulation *Kiva C* has an extreme peak shifted to the right. There is also a deviation between the two FASTEST simulations. Based on these results, it can be concluded that the inflow profiles are decisive for an accurate prediction of the down-cylinder velocity and turbulence profiles.

Figure 9(*b*) shows the same quantity at 1.75*D*. At this location two clear counterrotating vortices are present in the experimental data (Fig. 8(*d*)). When looking at the lines, it can be concluded that the URANS simulation *Kiva A* could not capture the behavior shown by PIV, while the two other simulations (*Kiva B, C*) accomplish a clear correspondence at the right-hand side of the domain. Close to the left side of the domain the flow remains largely overpredicted, corresponding with the wrong prediction of the location of the smaller vortex.

Simulation *FASTEST B* is relatively far off at this height in the cylinder. This line illustrates that there is only a single rotational structure left: the mean spanwise velocity magnitude from simulation *FASTEST B* increases steadily from −5 m/s in the left side to +15 m/s on the right side. Simulation *FASTEST A* displays the same features: the velocity is underpredicted on the left side and overpredicted on the right hand side.

5.3 Resolved Turbulence Fields. As the turbulence intensity has a real impact on the mixing, which in turn affects the combustion in internal combustion engines, it is important to analyze how two different solvers predict the turbulent kinetic energy evolution (Figs. 10–13). Figure 11 shows an estimation of the turbulence intensities at *Z*=1.25*D* compared to the experimental data. The two main hotspots can be found opposite to each other, similar to observations from Fig. 6.

This indicates that a large correspondence between the jet flow and the turbulence levels can be expected. Figure 10 shows the resolved turbulence intensity profiles at *Z*=1.75*D* for the five simulations and the experiments. The experiments show a larger level on the left side, which is in correspondence with the trend in

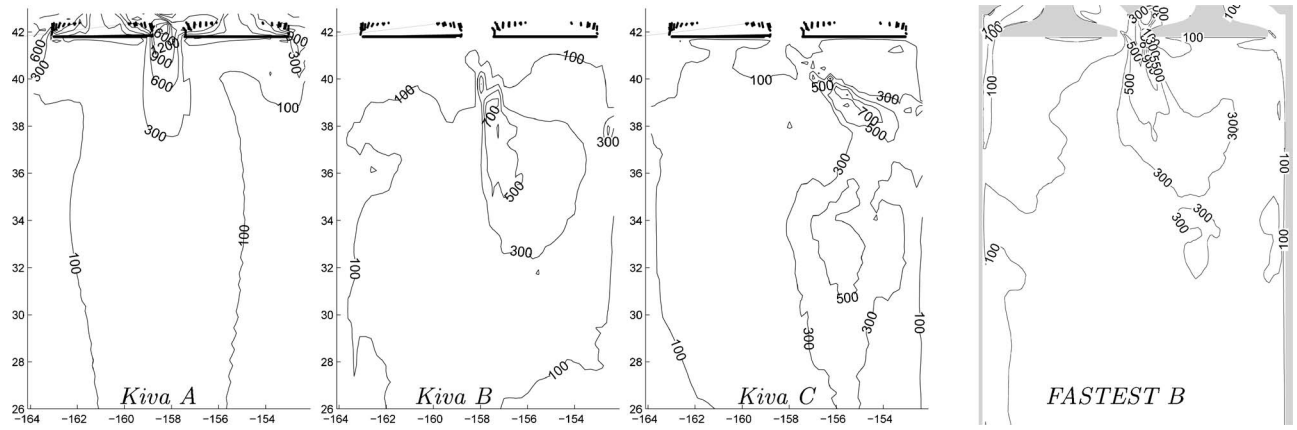

Fig. 12 Turbulence intensities at the plane indicated in Fig. 3. (*a*) *Kiva A*, (*b*) *Kiva B*, (*c*) *Kiva C*, and (*d*) *Fastest B*.

Fig. 11. This trend is recovered by simulations *Kiva B* and *FASTEST A, B*. However, at the right side of the domain these simulations behave quite differently from each other and from the experimental data. This can be explained by the jet whose location has a large influence on the location of the total resolved turbulent kinetic energy. Whenever the jet is not predicted correctly, the turbulence levels are far off, as well. It must kept in mind that the uncertainty of the PIV data increases rapidly close to the cylinder walls.

In simulation *Kiva A*, the turbulence level remains fairly low and constant over the complete range. The URANS model is apparently far more diffusive and reduces the extrema. Figure 12 shows the resolved turbulence intensity in the same vertical plane as for Fig. 4. Similar observations can be made from these figures, whereas the URANS simulation *Kiva A* shows a symmetric solution, simulation *Kiva B* and *FASTEST B* show an increase of turbulence to the right-hand side. *Kiva C* has a larger inclination angle in this direction.

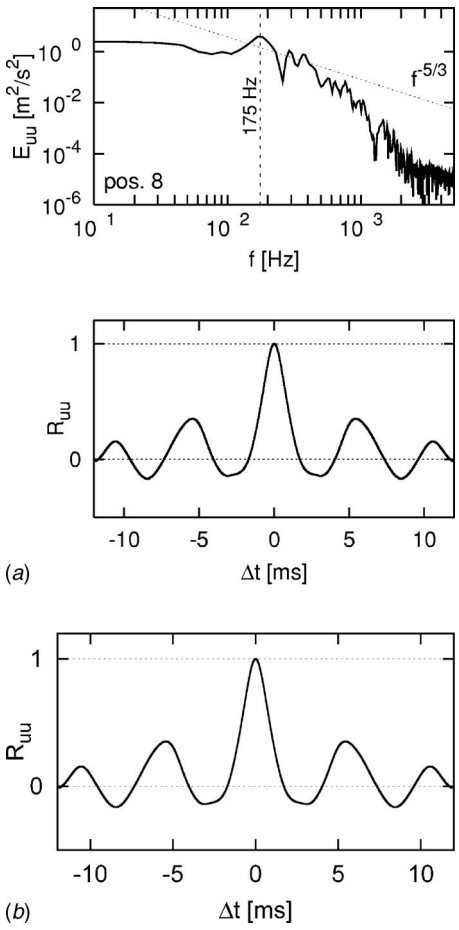

Fig. 13 Energy spectrum and auto-correlation function of the *u* velocity component at *Z*=1.75*D*, *x*=30 mm, *y*=0 mm.

Figure 13 shows an example of an energy spectrum and auto-correlation function as it is found from simulation *FASTEST B*. The location where the data are analyzed is at $z=1.75D$ below the cylinder head, $x=30$ mm, $y=0$ mm. The $\tilde{u}$-velocity component is considered. From the auto-correlation function, the oscillatory behavior of the flow is clearly observed. This frequency is identified to be the peak in the energy spectrum at $f=175$ Hz. The-5/3 slope is not recovered, illustrating the inhomogeneity and anisotropy of the flow.

From the available simulation data, a movie has been generated [24]. This movie revealed the additional presence of high-frequency oscillations near the valves (a process of detachment and reattachment) and low-frequency oscillations towards the bottom of the simulation: the swirling motion. The high-frequency oscillations could not be observed in the KIVA-3V simulations due to an excessive numerical diffusion.

5.4 Turbulence Mechanisms. Let us now concentrate on the turbulence mechanisms present in the cylinder or on the contribution of different velocity components and their fluctuations on the total fields. It is illustrative to have a close look at simulation *FASTEST B* because most detailed information is available in this case. Figure 14(*a*) shows the mean velocity fields close to the valves. Large velocity magnitudes at the cylinder walls are present in spanwise (u) and streamwise (w) direction. The second component (v) is zero at the walls as this is the wall normal direction.

Large velocities are also observed in the middle of the domain. The maximal (negative) contribution is in the streamwise direction. The largest contribution to the total velocity magnitude at the center jet arises from the w-component. This indicates that the magnitude of the swirl is somewhat smaller than the magnitude of the jet.

When looking at profiles of correlations of velocity fluctuations at this location in Fig. 14(*b*), the $\langle\tilde{u}\tilde{u}\rangle$, $\langle\tilde{v}\tilde{v}\rangle$, and $\langle\tilde{w}\tilde{w}\rangle$ components contribute to the total resolved turbulent kinetic energy level k. However, the magnitude and location of the peaks of the different components is not the same and therefore turbulence is not homogeneous in these regions. Away from the jets, where turbulence levels are relatively small and equal in size, a more homogeneous turbulence solution is found.

Figure 14(*c*) shows the velocity magnitudes for the different

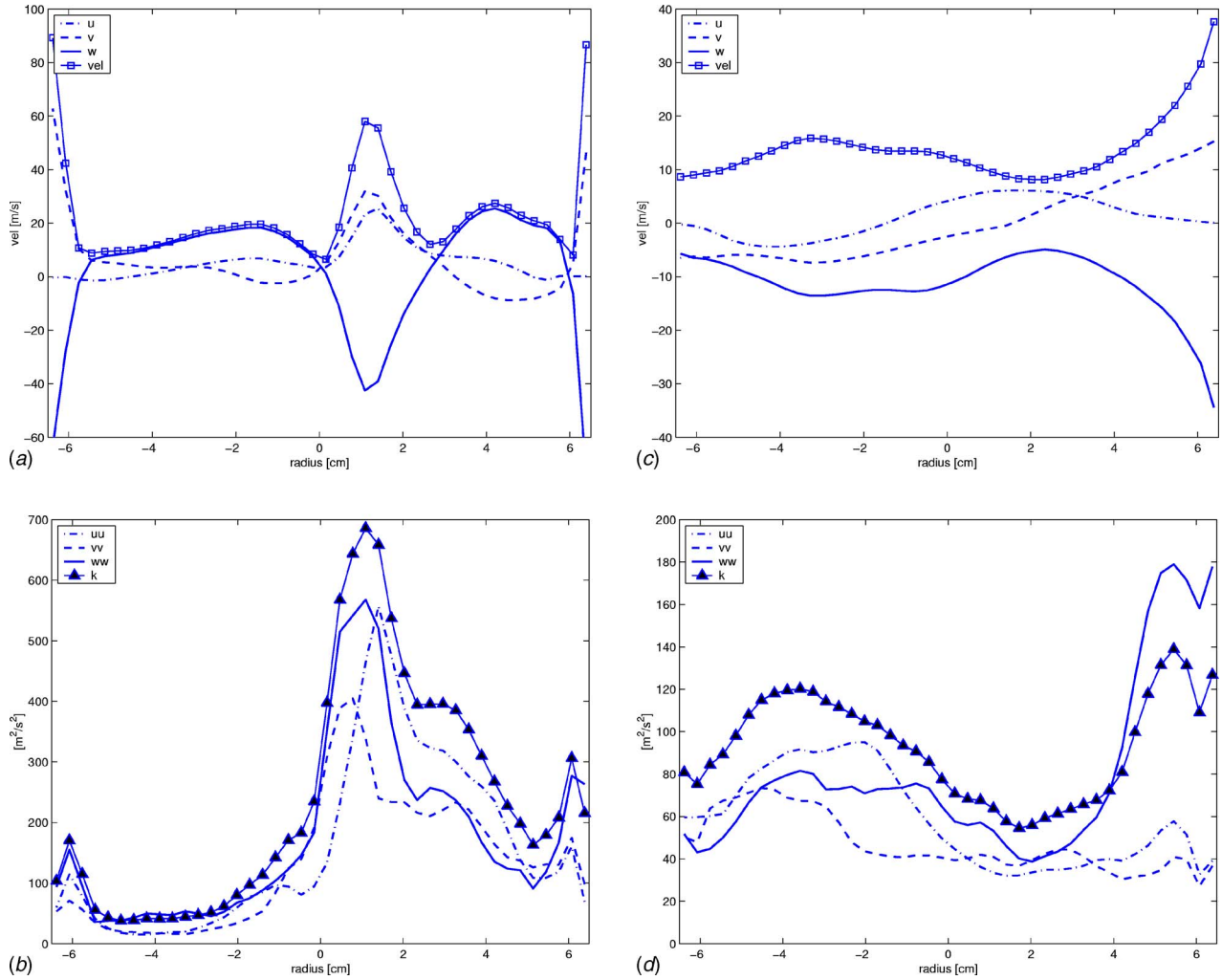

Fig. 14 Simulation *FASTEST B*. (*a, b*) Velocities and turbulence intensities at $Z=0.25D$ below the cylinder head. (*c, d*) The same at $Z=1.75D$.

components at $Z=1.75D$. Here, the absolute magnitude is more equally distributed over all three components at the middle and left side of the domain. Only at the right-hand side the differences become larger. The w-component has the largest contribution to the total velocity magnitude due to one of the jets.

In Fig. 14(d) a similar observation can be made: the contribution to k is relatively equal at the left side of the domain for all three turbulent components, whereas at the jet the $\langle \tilde{w}''\tilde{w}'' \rangle$ contribution is much larger. Here an assumption of homogeneous turbulence will fail.

5.5 General Remarks. From the performed simulations, it turns out that the URANS k-ϵ simulation with KIVA-3V is able to recover some of the complex flow effects as occurring in the cylinder. However, all mean flow structures are very weak as the k-ϵ model is very dissipative. The turbulence levels themselves are therefore predicted relatively low in the complete domain. The computational expenses are only a fraction of the LES as a steady situation is reached in a short period of time.

Near the valves where the geometry is very curved, the computational cells are severely skewed. This compels the introduction of some numerical diffusion by some upwinding in the convection scheme. Yet results from the two FASTEST calculations indicate that this solution seems to be grid independent with respect to the main features and the implicit filtering used. Moreover, the FASTEST simulations show good correspondence to experimental data in the upper region of the cylinder. Therefore, it is concluded that the influence of the numerical dissipation is sufficiently small to have confidence in the results, especially in the region near the cylinder head.

Down the cylinder some flow features, such as the two counter-rotating vortical structures disappear. This is probably due the influence of the outflow boundary, as this effect occurs in both FASTEST simulations. The KIVA-3V simulation with the same inflow velocity at the two runners shows results comparable to the FASTEST simulations for the mean flow and turbulent quantities in the cylinder. However, high-frequency oscillations near the valves are not recovered by these KIVA-3V simulations. The flow field from the KIVA code with realistic inflow boundary conditions does not improve the results and still gives a discernible difference in flow structure.

This illustrates that the distribution of mass through the two runners will have a crucial influence on the flow field downstream in the cylinder. Circumventing the problem by applying the steady boundary conditions from a more detailed simulation does not guarantee success. This illustrates the problem of the inflow conditions for LES in complex configurations. Therefore, it is suitable to include a larger part of the upstream domain into the computational domain, as done in the FASTEST simulations. The so-called immersed boundary conditions can be of great help in this concern.

To gain more confidence in the unsteady flow behavior, a LES is preferable to a URANS-based calculations, although in the near-wall regions a hybrid approach may be more suitable (see, e.g., Temmerman et al. [26]). It appears that reasonable in-cylinder flow results can be achieved when only modeling a relatively small part of the upstream region, basically because the flow around the valves will create the main turbulent structures. As pointed out above, the best approach is to include a larger part of the upstream region into the computational domain. With this approach tumbling frequencies can be well recovered from the simulation data.

6 Conclusions

In this study, a number of simulations are presented of a complex turbulent, swirling, and tumbling flow in an engine cylinder that arise due to the inlet manifold. Two LES with FASTEST have been performed: one with a relatively coarse mesh and one on a more refined mesh. Three different simulations with KIVA-3V have been carried out: a URANS simulation, a LES with equal inflow velocity at the two runners, and finally a LES where the inflow data are extracted from the best resolved FASTEST simulation.

Comparing the performance of these two different codes, it appears that the multi-block meshing strategy in the FASTEST code relieves the task to mesh very curved regions near the valves, compared to KIVA-3V. Additionally the parallelization of the FASTEST code allows for a more resolved mesh compared to the KIVA-3V code. As the velocities near the valves are very large while the resolution at this location is high, the time step is limited. Moreover, large domains in the upstream and downstream directions have to be taken into account and in the LES statistics over sufficient independent turbulent time scales is required. These features make the simulation and evaluation of a "realistic" geometry a challenging task.

The data analysis and comparison of the different simulations with each other and with experiments is sometimes difficult as small differences in the complex flow result in large differences of specific flow quantities at specific locations. The complex flow structure gives rise to an inhomogeneous turbulence distribution. This originates largely from the strong jets. This inhomogeneous effect on the turbulence is well observed by the LES, but naturally damped by the URANS k-ϵ simulation.

By showing the sensitivity of the flow pattern on inflow conditions in a steady geometry it can be concluded that this will be very sensitive on any changes in inflow conditions as encountered in moving piston geometries: any erroneous valve-motion modeling and grid handling will lead to relatively large deviations in the flow patterns. Overall, it can be concluded that by comparing the different simulations with each other, one gains a better understanding of the ongoing flow process in complex flow configurations within specific complex geometries under study. This kind of simulations may give a complete image of the phenomena that occur in such cases, and represents a valuable contribution to experimental data, where inherently only a little information on the flow details can be visualized. Thereby, the amount of performed simulations may indicate the range of the uncertainty that can be expected while this is normally invisible in a single simulation.

Acknowledgment

The research reported in this paper is sponsored in Germany by the BMBF through the project "Turbulente Strömungen in der Energietechnik."

References

[1] Pope, S. B., 2000, *Turbulent Flows*, Cambridge University Press, Cambridge, UK.
[2] Hanjalić, K., 1994, "Advanced Turbulence Closure Models: A View of Current Status and Future Prospects," Int. J. Heat Fluid Flow, **15**(3), pp. 178–203.
[3] Laurence, D., 2004, "Applications of Reynolds Averaged Navier Stokes Equations to Industrial Flows," *von Karman Institute Lecture Notes*, Rhode Saint Genése, Belgium.
[4] Celik, I., Yavuz, I., and Smirnov, A., 2001, "Large Eddy Simulations of In-Cylinder Turbulence for Internal Combustion Engines: A Review," Int. J. Engine Research, **2**(2), pp. 119–148.
[5] Haworth, D. C., and Jansen, K., 2000, "Large-Eddy Simulation on Unstructured Deforming Meshes: Towards Reciprocating IC Engines," Comput. Fluids, **29**, pp. 493–524.
[6] Sagaut, P., 2002, *Large Eddy Simulation for Incompressible Flows: An Introduction*, Springer-Verlag Berlin, Germany.
[7] Geurts, B. J., 2005, "Database-Analysis of Interacting Errors in Large-Eddy Simulation," *Proceedings of the Quality Assessment of Unsteady Methods*.
[8] Piomelli, U., 1999, "Large Eddy Simulation: Achievements and Challenges," Prog. Aerosp. Sci., **35**, pp. 335–362.
[9] Lund, T. S., Wu, X., and Squires, K. D., 1998, "Generation of Turbulent Inflow Data for Spatially-Developing Boundary Layer Simulations," J. Comput. Phys., **140**, pp. 233–258.
[10] Klein, M., Sadiki, A., and Janicka, J., 2003, "A Digital Filter Based Generation of Inflow Data for Spatially Developing Direct Numerical or Large Eddy Simulations," J. Comput. Phys., **186**(2), pp. 652–665.
[11] Amsden, A. A., O'Rourke, P. J., and Butler, T. D., 1989, "Kiva-II: A Computer Program for Chemically Reactive Flows With Sprays," Technical Report la-11560-ms, Los Alamos National Laboratory.
[12] Mengler, C., 2001, "Grobstruktursimulation der Strömungs- und Mischungsfelder Komplexer Anwendungsnaher Konfigurationen," Ph.D. thesis, TU Darmstadt.
[13] de Leeuw, R., 2005, "Comparison of PIV and LDA on a Stationary Flow-Bench of a Heavy-Duty Cylinder-Head," Master's thesis, TU/e, Eindhoven, The Netherlands.
[14] Nicoud, F., and Ducros, F., 1999, "Subgrid-Scale Stress Modelling Based on the Square of the Velocity Gradient Tensor," Flow, Turbul. Combust., **62**, pp. 183–200.
[15] Hirsch, C., 1990, *Numerical Computation of Internal and External Flows*, Wiley, Chichester, UK.
[16] Huijnen, V., Somers, L. M. T., Baert, R. S. G., and de Goey, L. P. H., 2005, "Validation of the LES Approach in Kiva-3V on a Square Duct Geometry," Int. J. Numer. Eng., **64**, pp. 907–919.
[17] Celik, I., Yavuz, I., Smirnov, A., Smith, J., Amin, E., and Gel, A., 2000, "Prediction of In-Cylinder Turbulence for IC Engines," Combust. Sci. Technol., **153**, pp. 339–368.
[18] Sone, K., and Menon, S., 2003, "Effect of Subgrid Modeling on the In-Cylinder Unsteady Mixing Process in a Direct Injection Engine," ASME J. Eng. Gas Turbines Power, **125**, pp. 435–443.
[19] Lilly, D., 1992, "A Proposed Modification of the Germano Subgrid-Closure Method," Phys. Plasmas, **4**(3), pp. 633–635.
[20] Lesieur, M., and Metais, O., 1996, "New Trends in Large Eddy Simulations of Turbulence," Annu. Rev. Fluid Mech., **28**, pp. 45–82.
[21] Lehnhäuser, T., and Schäfer, M., 2002, "Improved Linear Interpolation Practice for Finite-Volume Schemes on Complex Grids," Int. J. Numer. Methods Fluids, **38**, pp. 625–645.
[22] Durst, F., and Schäfer, M., 1996, "A Parallel Blockstructured Multigrid Method for the Prediction of Incompressible Flow," Int. J. Numer. Methods Fluids, **22**, pp. 549–565.
[23] Doosje, E., Bastiaans, R. J. M., and Baert, R. S. G., 2004, "Application of PIV to Characterize the Flow-Phenomena of a Heavy-Duty Cylinder Head on a Stationary Flow-Bench," *Proceedings of the EUROPIV 2 Workshop*.
[24] http://w3.wtb.tue.nl/nl/organisatie/combustion_technology/research/projects/turbulence_modeling_with_kiva_3v_code/
[25] Eggels, J. G. M., Unger, F., Weiss, M. H., Westerweel, J., Adrian, R. J., Nieuwstadt, F. T. M., and Friedrich, R., 1994, "Fully Developed Pipe Flow: A Comparison Between Direct Numerical Simulation and Experiment," J. Fluid Mech., **268**, pp. 175–209.
[26] Temmerman, L., Hadžiabdić, M., Leschziner, M. A., and Hanjalić, K., 2005, "A Hybrid Two-Layer URANS-LES Approach for Large Eddy Simulation at High Reynolds Numbers," Int. J. Heat Fluid Flow, **26**, pp. 173–190.

Active Flow Control in Circular and Transitioning S-duct Diffusers

A. M. Pradeep
Assistant Professor
Department of Aerospace Engineering,
Indian Institute of Technology,
Bombay, 400 076,
India
e-mail: ampradeep@aero.iitb.ac.in

R. K. Sullerey
Professor
Department of Aerospace Engineering,
Indian Institute of Technology,
Kanpur, 208 016,
India
e-mail: suller@iitk.ac.in

Performance enhancement of three-dimensional S-duct diffusers by secondary flow and separation control using vortex generator jets is the objective of the current experimental investigation. Two different diffuser geometries namely, a circular diffuser and a rectangular—to—circular transitioning diffuser were studied. The experiments were performed in uniform inflow conditions at a Reynolds number of 7.8×10^5 *and the performance evaluation of the diffusers was carried out in terms of static pressure recovery and quality (flow uniformity) of the exit flow. Detailed measurements that included total pressure, velocity distribution, surface static pressure, skin friction, and boundary layer measurements were taken and these results are presented here in terms of static pressure rise, distortion coefficient, total pressure loss coefficient, and the transverse velocity vectors at the duct exit. The use of vortex generator jets resulted in around 26% in total pressure loss and about 22% decrease in flow distortion coefficients in the circular and transitioning diffusers. The mass flow rate of the air injected through the VGJ was about 0.1% of the mass flow rate of the main flow for secondary flow control and about 0.06% of the main flow for separation control. The physical mechanism of the flow control devices used has been explored. The structure of the vortices generated by the control methods are presented in the form of smoke visualization images. The method of flow control used here is perceived to have applications in turbomachinery like turbines and compressors.* [DOI: 10.1115/1.2353263]

Introduction

S-duct diffusers are specially designed inlets through which air is taken from the external flow and supplied to the engines of a combat aircraft. Hence these diffusers form a vital component of any air breathing engine. The use of geometrically complex ducts becomes inevitable and hence has been a subject of interest to several researchers. As is expected of an aircraft intake, the flow must be decelerated while achieving as uniform flow as possible at the compressor face with minimum stagnation pressure loss. S-duct diffusers used in air intakes generally have high degrees of centerline curvature due to their short length that in turn results from severe space constraints. Due to centerline curvature, there are cross-stream pressure gradients resulting in migration of boundary layer fluid in the direction of the pressure gradient giving rise to secondary flows. Within the boundary layer this imparts cross-flow velocities creating non-uniform total pressure profiles. In addition, there is a stream-wise pressure gradient resulting from increasing cross-sectional area. The combined effect may result in increased total pressure nonuniformity (i.e., distortion) and total pressure loss at the duct exit. The intake must not only deliver air to the engine with minimum total pressure loss but also flow at the compressor face with minimum distortion.

Performance improvement in terms of total pressure distribution and recovery in diffusing S-ducts using low-profile vortex generators was studied by Reichert and Wendt [1]. Later, Reichert and Wendt [2] presented a compilation of the previous study with additional data on the effectiveness of various vortex generator configurations in reducing exit flow distortion of circular S-ducts.

Subsequently, Reichert and Wendt [3] used tapered-fin type vortex generators to control secondary flows. The application of vortex generators here differed from conventional point of view of vortex generators as devices that re-energize the boundary layer by mixing free stream and boundary layer fluids, rather the objective was to control the development of secondary flows.

Contributed by the Fluids Engineering Division of ASME for publication in the JOURNAL OF FLUIDS ENGINEERING. Manuscript received February 24, 2006; final manuscript received May 5, 2006. Assoc. Editor: Phillip M. Ligrani.

Reichert and Wendt [1–3] in their papers presented a detailed description on the flow physics involved in an S-duct diffuser and how secondary flows affect the diffuser performance in terms of outflow quality and pressure recovery. The studies also show how vortex generators improve diffuser performance by effectively controlling secondary flows. The development of secondary flows in curved passages and their theoretical explanations was described in detail by Lakshminarayana [4].

Foster et al. [5] conducted measurements in flow through a rectangular-to-semi annular transition duct to demonstrate the effectiveness of vortex generators to reduce the circumferential total pressure distortion.

Sullerey et al. [6] studied the effectiveness of boundary layer fences and tapered fin vortex generators in controlling secondary flows. The study revealed that significant improvement in performance could be achieved by judicious use of the passive control devices. Further, Sullerey and Pradeep [7] also studied the effect of inflow distortion on S-duct diffuser performance and the performance enhancement by the use of tapered-fin vortex generators.

The effect of diffuser centerline offset and active boundary layer control by wall suction and blowing on diffuser performance was studied by Ball [8]. The effectiveness of wall suction and blowing in separation control was investigated. The centerline offset, hole area, and blowing slot height were varied to attain optimum performance. It was observed that good performance enhancement could be achieved by small amounts of wall suction or blowing upstream of the separation point.

Kwong and Dowling [9] investigated active control in wide-angled diffusers using steady blowing. The new jet geometries used were compared with conventional blowing methods. Active feedback control was employed to control separation that occurred in the rectangular diffuser used. It was concluded that a combination of steady and unsteady blowing could give better diffuser performance in terms of pressure recovery and reduced pressure oscillations.

Innes et al. [10] reported a set of experiments designed to show the effectiveness of air jet vortex generators for the control of separation on a complex airfoil. A three-element airfoil in a con-

figuration typical of landing and take-off was studied. The study revealed a substantial improvement in the normal force coefficient and the stall angle of attack.

Johnston and Nishi [11] developed an active separation control method termed as the vortex generator jet (VGJ). Their study at low speeds demonstrated that the cross-stream mixing associated with the vortices generated by the VGJ is effective in separation control and has potential applications in both internal and external flow situations. Compton and Johnston [12] studied the stream wise vortex production by pitched and skewed jets in a two-dimensional flow with a turbulent boundary layer. Skew angles in the range of 45–90 deg resulted in maximum vorticity levels. The vortices produced by the jets were similar to those produced by a small solid vortex generator. Fric and Roshko [13] and later on Kelso et al. [14] described and visualized the vortical structures in the wake of a transverse jet. The vortices formed in the wake of the jet were shown to be fundamentally different from the vortex shedding from solid bluff bodies.

Barberopoulos and Garry [15] and Zhang [16] studied the vortex structures in the vicinity of VGJs by surface flow visualizations. High turbulence levels were observed to accompany the vortices. It was observed that as the vortex moves downstream, its strength reduces whereas it grows in size.

Khan and Johnston [17] have described in detail the vortex development from VGJ. Johnston [18] in his review article describes the application of VGJ for separation control and also the use of pulsed vortex generator jets. The addition of pulsing was observed to provide a more efficient use of the jet fluid. It was also observed that it might be possible to gain better control by using pulsed vortex generator jets than that with steady VGJ. Hamstra et al. [19] reported significant reduction in diffuser exit flow distortion with micro-vortex generators and jets. However, the paper does not give details of the flow control method.

Bons et al. [20] studied the application of pulsed vortex generator jets to control separation on the suction surface of a low-pressure turbine blade. In a similar study, Volino [21] used synthetic vortex generator jets to control boundary layer separation from the suction side of a low-pressure turbine airfoil. Significant reductions in the wake loss profiles were observed in both cases.

Rixon and Johari [22] investigated the development of a steady vortex generator jet in a turbulent boundary layer. The physics of jet-boundary layer interaction were explored using the jet pitched at 45 deg and skewed at 90 deg. Active secondary flow control using VGJ in two-dimensional S-duct diffusers was recently reported by Sullerey and Pradeep [23,24]. A significant improvement in diffuser performance was obtained.

Pradeep and Sullerey [25] have presented the results of secondary flow control in circular S-duct diffusers using vortex generator jets. The present experimental investigation was carried out to study the effectiveness of vortex generator jets in secondary flow and separation control in three-dimensional S-duct diffusers namely circular and transitioning S-duct diffusers. In addition, detailed smoke visualization experiments were carried out in order to study the physical mechanism of flow control (of secondary flow as well as separation) by VGJs.

The S-duct diffusers have curvatures and divergence angles of typical combat aircraft inlet geometry. The VGJs for secondary flow control were positioned in such a manner that the vortices generated by their interaction with the main flow have an orientation opposing the secondary flows. The VGJs for separation control were placed such as to cause efficient mixing between the freestream and the boundary layer fluid. The flow visualization studies substantiated the VGJ orientations both for secondary flow and separation control. The VGJ skew angles and jet-to-freestream velocity ratios were varied to optimize diffuser performance.

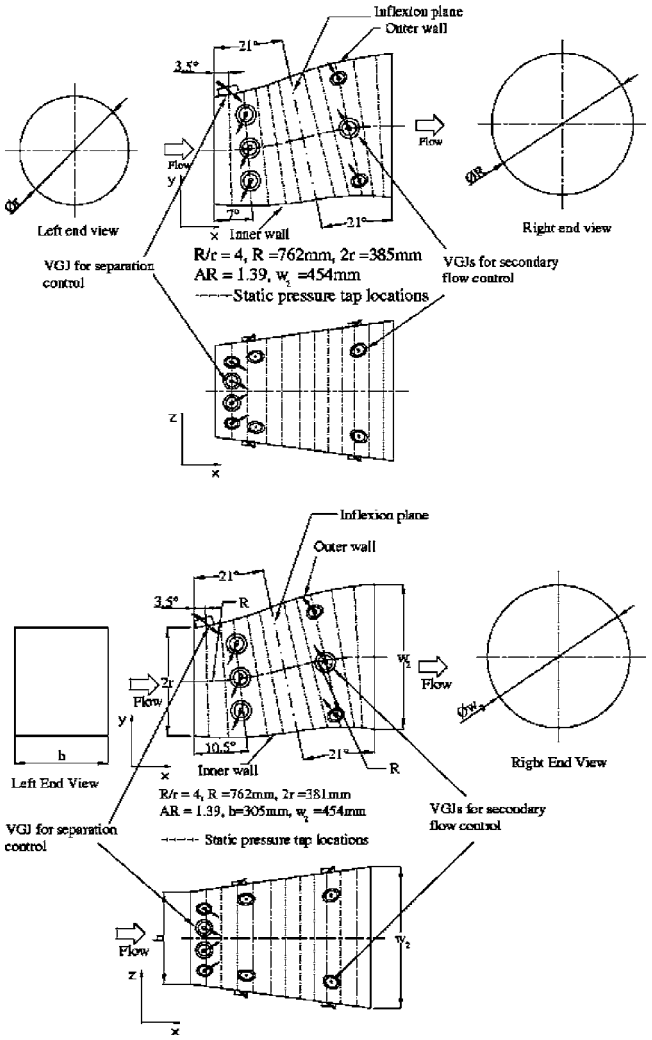

Fig. 1 (*a*) Circular diffuser geometry. (*b*) Rectangular-to-circular transitioning diffuser geometry.

Experimental Set Up and Procedure

The measurements were carried out in an open-circuit wind tunnel. A blower discharged air through a diffuser into a large settling chamber with a honeycomb and three sets of wire mesh screens. A contraction section of an area ratio of 17 accelerated the flow into the test section entrance of cross-section area of 380 mm (width) $\times$305 mm (height). A large contraction ratio ensured a uniform flow at the inlet. The measured free stream turbulence level of the inlet flow was less than 0.5%. Between the contraction and the S-duct diffuser, a straight duct of 300 mm length was provided to obtain fully developed, zero pressure gradient turbulent boundary layer at the diffuser inlet. Detailed velocity measurements were carried out across the diffuser inlet (free-stream) and in the inlet boundary layers. The diffuser inlet flow was kept uniform with an average wall boundary layer momentum thickness equal to 0.2% of the inlet width. The tests were carried out at a Reynolds number of 7.8×10^5 based on the diffuser inlet width (free stream velocity=31 m/s and Mach number=0.1). A constant area duct extension of 300 mm length was also placed at the diffuser exit to provide smooth, continuous flow exiting the duct.

S-duct Diffusers. Two different geometries of diffusers were studied: One was a diffuser with circular cross-section (Fig. 1(*a*)) and the other was a rectangular-to-circular transitioning S-duct diffuser (Fig. 1(*b*)), The area ratio and semi-divergence angle of

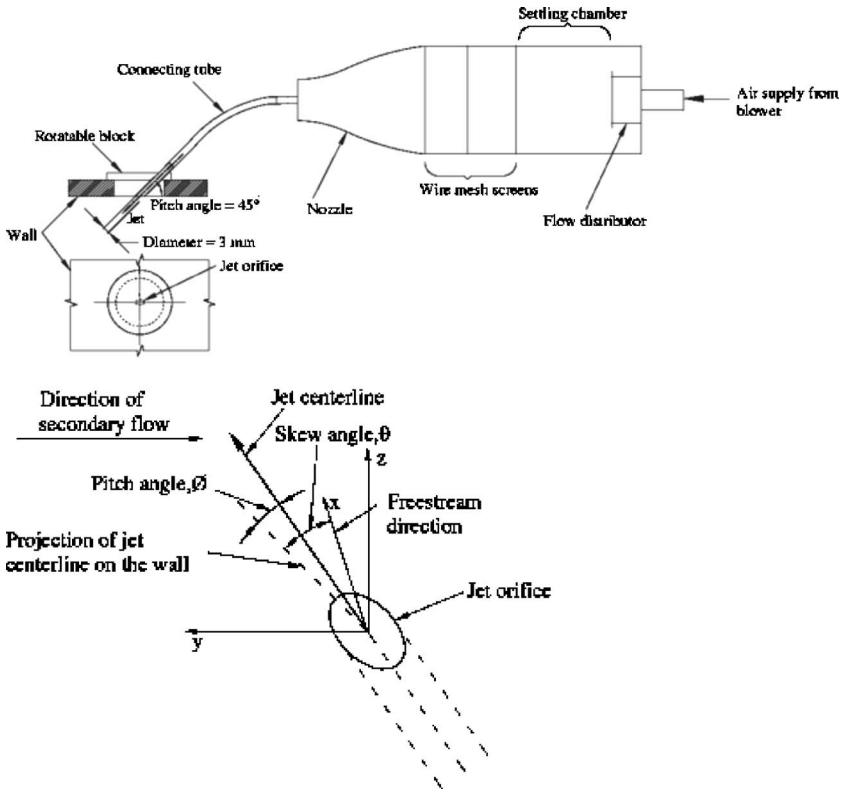

Fig. 2 (*a*) Vortex generator jet geometry and flow arrangement. (*b*) Definition of coordinate system and vortex generator jet angles.

the diffusers were 1.39 and 8 deg, respectively. The semi-divergence angle corresponds to an equivalent straight diffuser of same area ratio. The centerline radius ratios of the diffusers were kept at four. Two planar circular arcs with identical radii defined the duct centerline. The plane at which the centerline curvature changes from concave to convex is known as the inflection plane. The circular diffuser geometry was designed based on the design details provided by Reichert and Wendt [3]. The transitioning diffuser was designed using the standard transition rule for rectangle to circle transition (Miau et al. [26]). The area of the diffuser was varied along centerline of the diffuser in accordance with the transition rule. A nondiffusing straight transition section of 300 mm length was used to connect the circular diffuser to the rectangular tunnel exit section. The diffusers were fabricated using fiber-reinforced plastic that ensured smooth interior walls.

Vortex Generator Jet. The VGJ arrangement used in the present study (Fig. 2(*a*)) was designed in line with Johnston and Nishi [11] and has been described in Sullerey and Pradeep [24]. In previous studies [6,7,23,24] carried out using tapered fin vortex generators, a set of three vortex generators at locations of maximum secondary flow strength was observed to give the best performance. Hence, it was decided to use the same number of VGJs in the present study too.

Figure 2(*a*) gives the vortex generator jet flow arrangement and the VGJ defining angles with reference to the secondary flow are shown in Fig. 2(*b*). In the present investigation, the pitch angle was kept fixed at 45 deg (based on Johnston and Nishi [11] and the skew angle was varied (in the range 0–140 deg) to obtain best performance. The set of three VGJs at the two locations were oriented in such a manner that the vortices generated from interaction of the VGJs with the freestream would tend to nullify the secondary flows, i.e., the VGJs were directed towards the high pressure side (as secondary flows occur from the high pressure side to the low pressure side). The best performance condition was obtained by varying the skew angle of the VGJ. The air supply to the VGJs was provided from a separate centrifugal blower. At each station, the three VGJs were supplied air through a compartment consisting of a settling chamber, three wire mesh screens and a nozzle (refer Fig. 2(*a*)). This was done to ensure uniform air supply to all the VGJs. The velocity of each VGJ was measured using a fine Pitot tube of 0.8 mm diameter simultaneously to ensure that all the jets had equal velocity. For separation control, four VGJs in an orientation as shown in Figs. 1(*a*) and 1(*b*) were used. This orientation was used based on Sullerey and Pradeep [23] were tapered fin vortex generators were used for separation control. The present orientation would result in a generation of vortices similar to those produced by tapered-fin vortex generators.

Active Control Circuit. Figure 3 gives a schematic of the active control circuit with a feedback loop. A sublayer fence connected to a differential pressure transducer (ASX01DN from M/s Honeywell, Inc.) was used as the feedback control sensor. The pressure transducer had a response time of 100 μs. The design details of the sublayer fence will be discussed in later sections. The voltage output of the pressure transducer was input to the active control circuit. A comparator would sense the voltage from

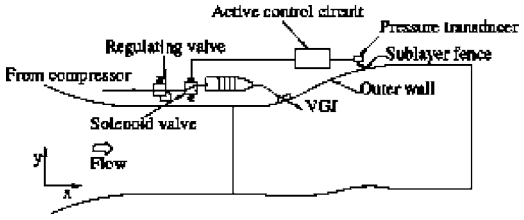

Fig. 3 Active control circuit

the pressure transducer and if the voltage was less than the preset voltage (kept close to zero as this would indicate that the flow is close to separation), the solenoid valve would be switched on thus in turn switching on the VGJs. If the voltage from the pressure transducer were greater than the preset voltage, the solenoid would be switched off. A surface-mountable hot film sensor (Senflex SF9902 from M/s Taosystem, Inc.) was also used instead of the pressure transducer to study the effect of changing the feedback sensor. The hot film sensor was used in combination with a Dantec mini-CTA. The output from the CTA was supplied to the feedback control circuit.

Experimental Procedure

The initial experiments were carried out on the bare diffusers, i.e., without any flow control devices. After the initial measurements, tapered-fin vortex generators were used to optimize the circumferential location of the VGJs. The axial locations were fixed based on the wall static pressure distribution as was done in earlier studies [6,7,23,24]. The VGJs were placed axially in regions of highest pressure differentials to neutralize the secondary flow (from high pressure to low pressure wall). A set of three tapered fin vortex generators was observed to give best diffusers performance. Hence the same number of VGJs was used too. Span wise (y-direction) array of three VGJs were employed, one before the inflection plane and one after it with the objective of control of secondary flow in the diffusers.

Instrumentation and Measurement Techniques

The measurements included diffuser wall static pressure distributions, mean velocities, boundary layer and skin friction measurements and flow angularity. A Furness (FCO510 model) digital multi-channel micro-manometer was used for all pressure measurements. The static pressure measurements were taken with wall pressure taps at nine axial stations on each diffuser. Each station had nine circumferential pressure taps of 0.8 mm diameter. There were fifteen pressure taps at the inflection plane, diffuser inlet and exit. The C_P values were expected to be within one percent uncertainty (on the basis of 30 measurements at a given station).

The skin friction measurements were made using wall mounted Preston tubes of 0.8 mm diameter and sublayer fences of fence height 0.1 mm. The design and calibration details of Preston tubes and sublayer fences can be obtained from Patel [27] and Vagt and Fernholtz [28], respectively. These were fitted along the centerline of inner and outer walls at nine stations. Sublayer fences were used in regions of adverse pressure gradients, as its accuracy is higher in such situations compared to Preston tubes. The Preston tubes and sublayer fences were calibrated using linear voltage displacement transformer (LVDT) displacement sensor based floating element shear stress sensor. This device comprised of a floating element that would remain flush with the wall where the skin friction is to be measured. The floating head was cylindrical in shape with a diameter of 8 mm. The central part of the sensor was an LVDT (MHR005 from M/s Measurement Specialties, Inc., USA) that could detect displacements up to 0.127 mm. The sensor was calibrated for shear force using fractional weights attached to the floating element. The skin friction measurements were expected to be within 2% uncertainty. More than the skin friction measurements, the basic purpose of using Preston tubes and sublayer fences in the present experiments was to detect regions of flow separation. Details on the LVDT displacement based wall shear sensor can be obtained from Pradeep and Sullerey [29]. The sublayer fences were also successfully used to detect secondary flows. With the fence aligned to the free stream, the sign of the pressure difference indicates the direction of secondary flows. Frei and Thomann [30] have discussed floating element sensors for shear stress measurement. The paper also discusses their calibration and use in adverse pressure gradients.

The boundary layer measurements were made on all four walls at inlet, inflection, exit planes of the S-duct diffuser, and at several stations downstream of the VGJ. Boundary layer measurements were also made at stations where the boundary layer was expected to thicken due to secondary flows and to observe the effect of VGJ on the boundary layer thickness. A 0.8 mm diameter pitot probe was used for this purpose. The boundary layer measurements were taken by traversing the probe in intervals of 0.5 mm. The turbulence intensities were measured using a hot-wire probe of 5 μm diameter connected to a Dantec mini-CTA. The total pressure and velocity measurements (including flow angularity) were made using a five-hole conical probe of diameter 6.4 mm based on the design details provided by Ohman and Nguyen [31]. The probe was calibrated using a calibration rig similar to Nowak [32]. For probe traverse, an accurate three-dimensional traverse system (least count 0.5 mm) was used. The five-hole probe was calibrated with one-degree interval and hence the accuracy in flow angularity was expected to be within one degree. Detailed flow measurements using five-hole probe were made at the inflection and the diffuser exit plane for various configurations tested. The total pressure measurements were expected to be within one percent uncertainty.

The uncertainties in the above measurements were estimated based on Abernathy et al. [33], Moffat [34], and Kline [35].

Smoke visualization was carried out to study the physical mechanism of vortex generator jets. A 25 mW Helium-Neon laser was used with a cylindrical lens to get a sheet of light. Smoke was generated using a silicon oil smoke generator. The images were captured using a color CCD camera (PixelFly from M/s CookeCorp, Inc.) that had a pixel resolution of 1248×1260. The maximum number of frames that could be captured per second was 25. Some of the images were analyzed after image processing using tools like edge detection from MATLAB for a better understanding of the flow phenomena.

Table 1 Effect of skew angle on diffuser static pressure recovery (VR=1.0)

Skew angle in degrees	90	110	130	135	140
Mass averaged C_P	0.263	0.278	0.286	0.295	0.289

Results and Discussion

Vortex generator jets (VGJs) were used for separation as well as secondary flow control. The results of VGJs for secondary flow control in a rectangular diffuser have been reported by Sullerey and Pradeep [23,24]. In the present investigation, the results of active secondary flow and separation control in three-dimensional S-duct diffuser geometries are presented. The separation control is over and above the secondary flow control. The results of the secondary flow control, separation control, and smoke visualization are presented separately in the subsequent subsections in that order.

Active Secondary Flow Control. The best performance combination of skew angle and velocity ratio for secondary flow control was arrived at by detailed investigations for a range of skew angle (where the vortex created by jet flow interacting with free stream would be opposing the secondary flow present in the flow field) and velocity ratio. Some of the results of the effect of variation of skew angle are given below. In all cases the pitch angle was kept at 45 deg in line with Johnston and Nishi [11].

Since external energy is added to the diffuser, the definition of C_p (as given in the Nomenclature) was used to account for the VGJ energy addition.

Table 1 gives the variation of static pressure recovery at the transitioning diffuser exit for different skew angles at a velocity ratio of 1.0. A VGJ skew angle of 135 deg (refer Fig. 2(b) for VGJ orientation) in both the planes resulted in the best performance. Also in their previous study, Sullerey and Pradeep [23,24] had

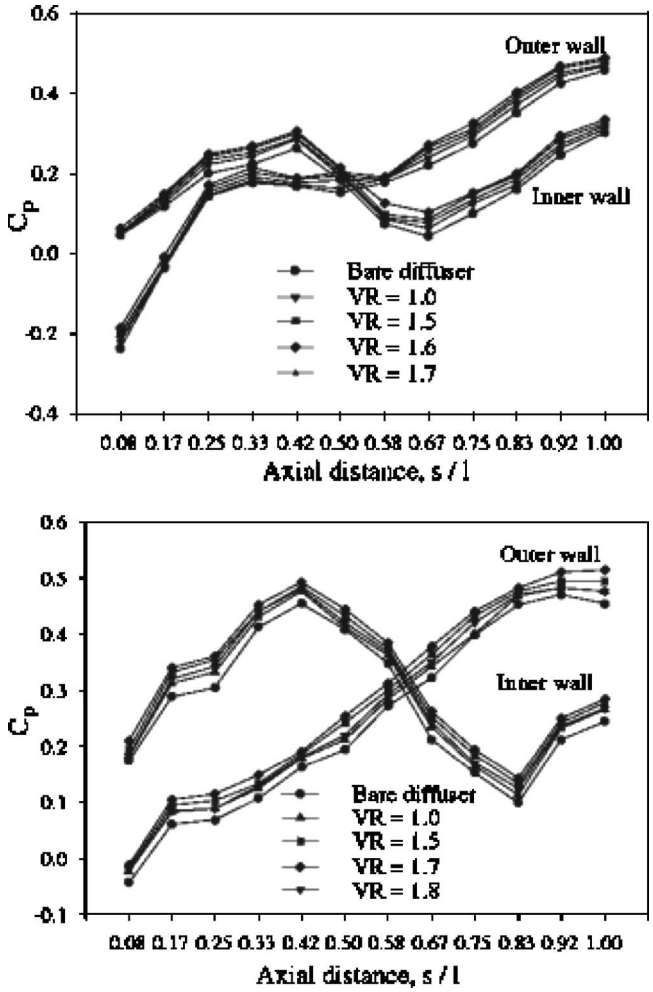

Fig. 4 (*a*) Wall static distribution along the inner and outer walls of the circular diffuser. (*b*) Wall static distribution along the inner and outer walls of the transitioning diffuser.

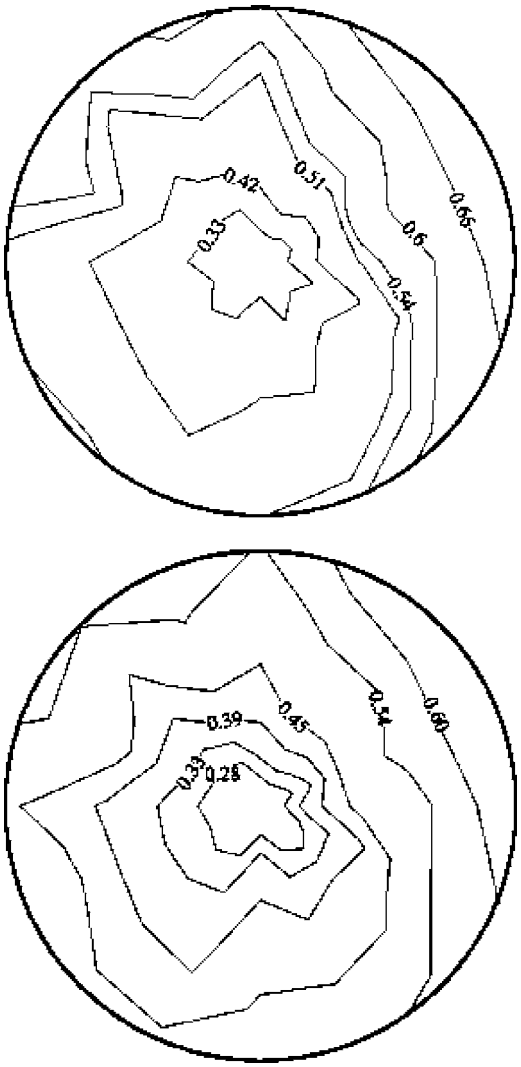

Fig. 5 Total pressure loss coefficient contours at the exit of (*a*) bare circular diffuser (*b*) diffuser with VGJ

observed that a VGJ skew angle of 135 deg resulted in the best performance improvement in a two-dimensional S-duct diffuser. The velocity ratio was varied with the skew angle fixed at 135 deg.

The circumferential locations of the VGJs were decided from preliminary experiments carried out using passive control devices namely tapered-fin vortex generators. The axial locations, however, were fixed based on the wall static pressure distribution of the bare diffusers.

Figure 4(*a*) and 4(*b*) give the static pressure distributions along the inner and outer walls (refer Fig. 1 for definition of inner and outer walls) of the circular and rectangular-to-circular transitioning diffusers, respectively. The C_P distributions are shown in terms of nondimensional axial distance from the diffuser inlet that refers to the locations where the static pressure taps were fixed.

The inner and outer wall pressures at a particular station can be seen to differ considerably. The wall pressure differentials between the inner and outer wall creates secondary flows by causing a slow moving boundary layer fluid to move from high pressure to low pressure regions. The secondary flow in the plane upstream of the inflection plane has a direction from the inner wall to the outer wall. Since the wall curvature changes after the inflection plane, the direction of the secondary flow at the plane downstream of the inflection plane of the diffuser is opposite (i.e., from the outer wall to the inner wall) to that at the former plane. The VGJ skew angle was, therefore, measured and varied in a clockwise sense (i.e., pointing towards the inner wall) in the plane upstream of the inflection plane while that at the second plane in the counterclockwise direction (pointing towards the outer wall).

As is evident from Figs. 4(*a*) and 4(*b*), jet to free stream velocity ratios of 1.6 and 1.7 in the circular and transitioning diffusers, respectively, give the best static pressure recovery. Therefore, the results discussed below will be for these cases. The kinetic power ratio, KPR involved in using the VGJs was calculated as approximately 0.28% of the main flow for the circular diffuser and 0.32% of the main flow for the transitioning diffuser. The mass flow rates of the air injected through the VGJs were 0.1 and 0.11% of the main flow for the circular and transitioning diffusers, respectively.

The effectiveness of VGJs in improving the flow quality can be assessed by looking into the total pressure loss coefficient contours of the circular diffuser given in Figs. 5(*a*) and 5(*b*) without and with VGJs, respectively. Figure 5(*a*) shows that the losses are higher towards the outer wall as was also observed in the case of the transitioning diffuser. This is due to the increased curvature along that wall. A noticeable reduction in the total pressure losses can be observed from the figures. The extent of the high loss region has been significantly reduced from 0.33–0.66 to 0.27–0.60 on employing VGJs. Similar improvement in the performance of the transitioning diffuser can be seen from the total pressure loss coefficient distribution given in Figs. 6(*a*) and 6(*b*) with and with-

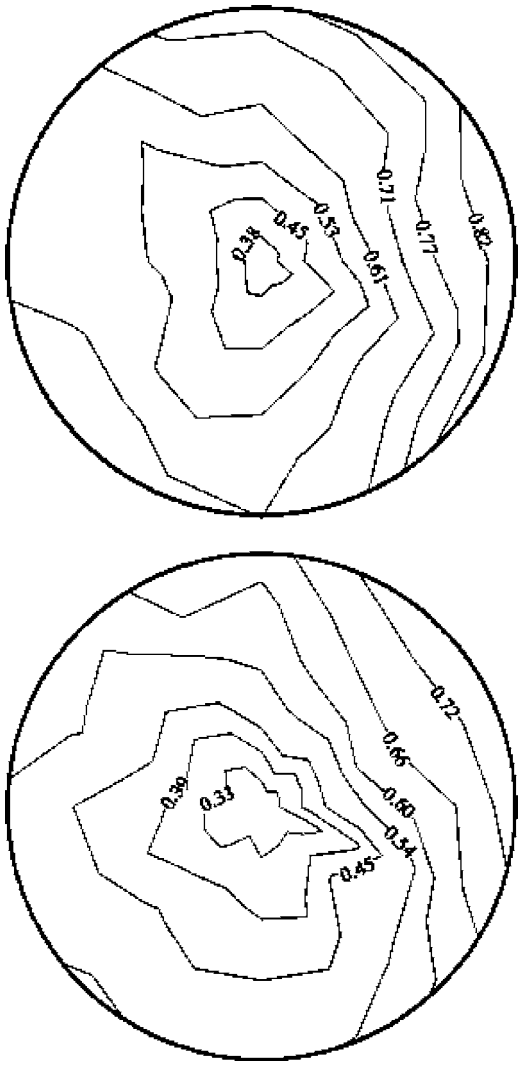

Fig. 6 Total pressure loss coefficient contours at the exit of (*a*) bare transitioning diffuser (*b*) diffuser with VGJ

out VGJs, respectively. The range of the loss coefficient reduced from 0.37–0.82 to 0.36–0.73. Thus, the extent of the high loss region has been significantly reduced on employing VGJs.

The transverse velocity vectors at the circular diffuser exit are plotted in Figs. 7(*a*) and 7(*b*) and those at the transitioning diffuser exit in Figs. 8(*a*) and 8(*b*) without and with VGJs, respectively. The flow nonuniformity in the bare circular diffuser is lesser that the transitioning diffuser. This is due to the fact that a transitioning diffuser has a more complex geometry compared to the circular diffuser. The magnitudes of the secondary flow vectors at the diffuser exit have been reduced considerably with the application of VGJ. Around 25% reduction in the secondary flow vector magnitude (expressed as a fraction of the inlet freestream velocity) was observed in the case of the circular diffuser. The reduction in secondary flow vector magnitude with VGJ was 18% in the transitioning diffuser.

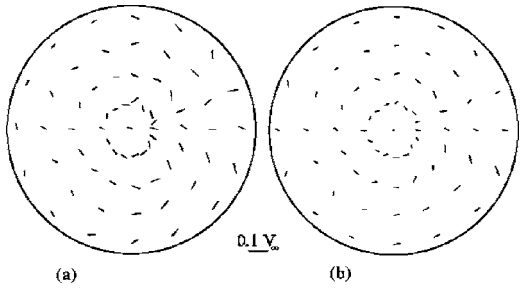

Fig. 8 Transverse velocity vectors at the exit of (*a*) bare transitioning diffuser (*b*) diffuser with VGJ

The boundary layer momentum thicknesses (as a percentage of the inlet width) at the bare diffuser exit were 1.50 and 3.01% at the inner and outer walls, respectively. The corresponding values with the VGJs were 0.96 and 2.76%, respectively. The boundary layer momentum thicknesses at the bare transitioning diffuser exit were 1.55 and 3.11% at the inner and outer walls, respectively. The corresponding values with the VGJs were 1.01 and 2.82%, respectively. The reductions in momentum thickness are yet another indication of the effective reduction in the exit flow distortion.

The turbulence intensity at the bare circular diffuser exit (average of five points along the centerline) was 0.96%, whereas with VGJs the turbulence intensity reduced to 0.73%. The reduction in the turbulence intensity also indicates reduction in flow distortion. The turbulence intensities at the bare transitioning diffuser exit and with VGJs were 1.74 and 1.23%, respectively.

Table 2 gives the summary of results for the circular and transitioning diffusers with and without the VGJs. The effectiveness of the VGJs can be seen from the improvement in all the performance parameters. The VGJs have, therefore, been found to be

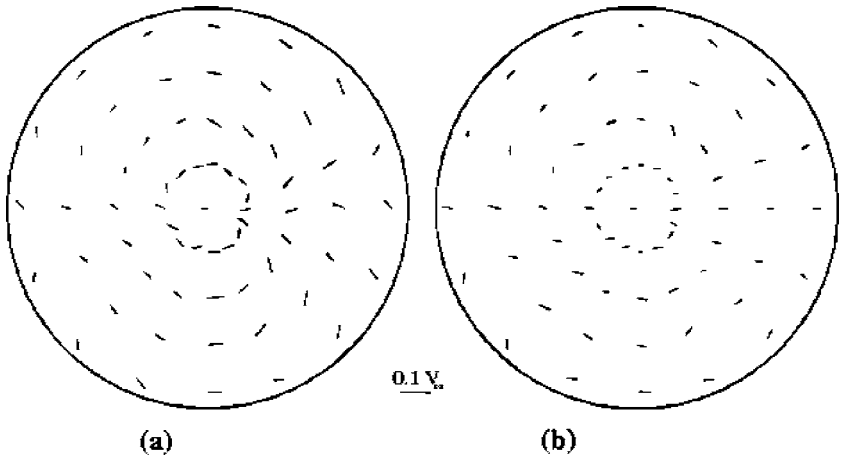

Fig. 7 Transverse velocity vectors at the exit of (*a*) bare circular diffuser (*b*) diffuser with VGJ

Table 2 Summary of active secondary flow control in the diffusers

Diffuser geometry	Exit flow property	Bare diffuser	Diffuser with tapered-fin vortex generators	Diffuser with VGJ
Circular diffuser	Mass averaged C_P	0.283	0.298	0.327
	D_C	0.851	0.810	0.751
	ϖ	0.393	0.361	0.328
Transitioning diffuser	Mass averaged C_p	0.261	0.281	0.312
	D_C	0.867	0.827	0.762
	ϖ	0.413	0.384	0.357

much more effective than tapered-fin vortex generators that were used to optimize the location of VGJs. Tapered-fin vortex generators owing to their physical presence in the flow field results in drag losses and there is little control over these devices other than changing their geometry. VGJs on the other hand can be controlled in terms of skew angle and velocity ratio and moreover VGJs do not result in any drag losses when not in operation.

Active Separation Control. The VGJ flow control methodology was also applied for separation control in the diffusers. Both the diffusers had separated flow on the outer wall. The VGJs for separation control were applied in a manner as shown in Fig. 1. This configuration resulted in vortices that would cause effective mixing of the freestream with the low momentum boundary layer fluid. The VGJs were placed at a 45 deg orientation as shown in the figure as this configuration resulted in the best performance of the diffusers. VGJs were used as steady jets as well as with active feedback control. The feedback control arrangement was discusses earlier (Fig. 3).

Figures 9(*a*) and 9(*b*) give the wall static pressure distributions along the side walls of the circular and transitioning diffusers at

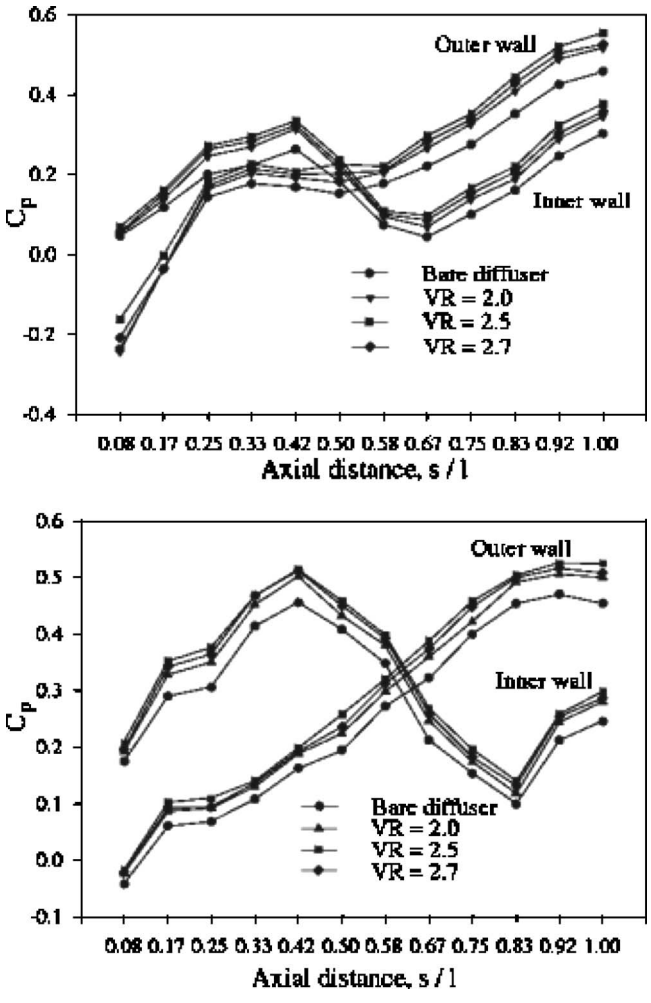

Fig. 9 (*a*) Wall static pressure distribution along the inner and outer walls of the circular diffuser. (*b*) Wall static pressure distribution along the inner and outer walls of the transitioning diffuser.

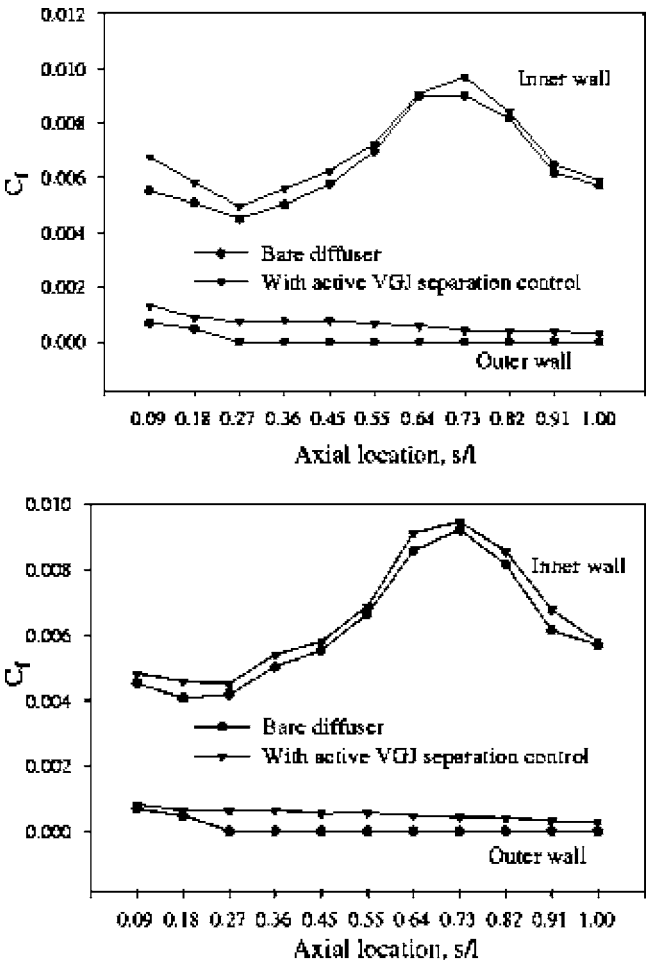

Fig. 10 (*a*) Skin friction distribution along the inner and outer walls of the circular diffuser. (*b*) Skin friction distribution along the inner and outer walls of the transitioning diffuser.

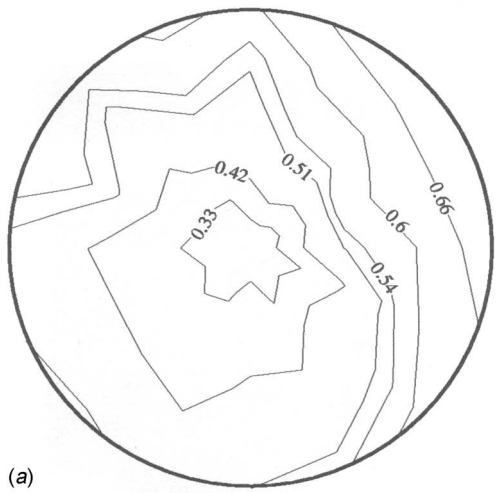

(*a*)

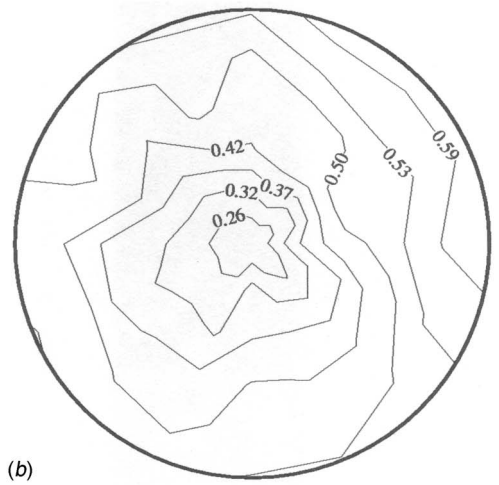

(*b*)

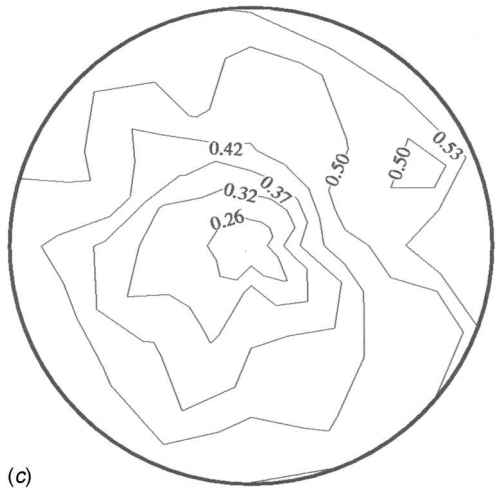

(*c*)

Fig. 11 Total pressure loss coefficient contours at circular diffuser exit (*a*) bare diffuser (*b*) with continuous jets (*c*) with active feedback control

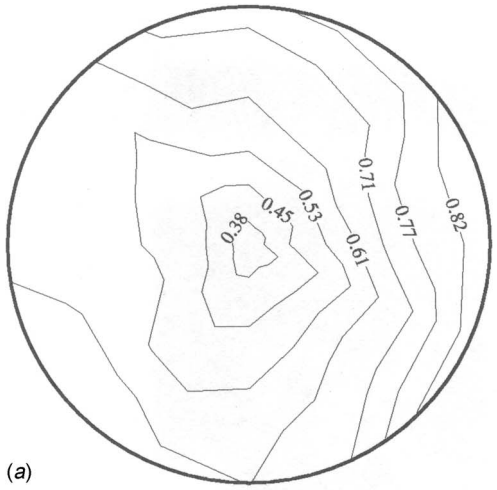

(*a*)

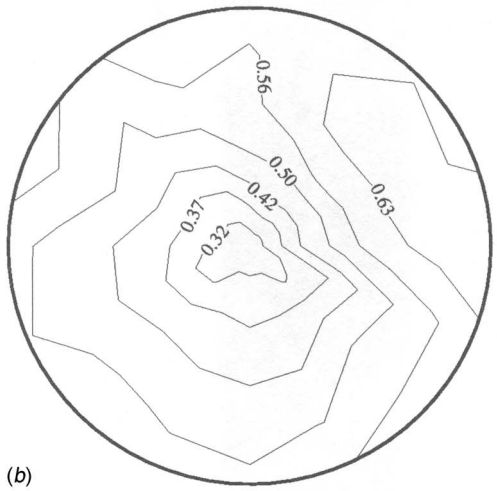

(*b*)

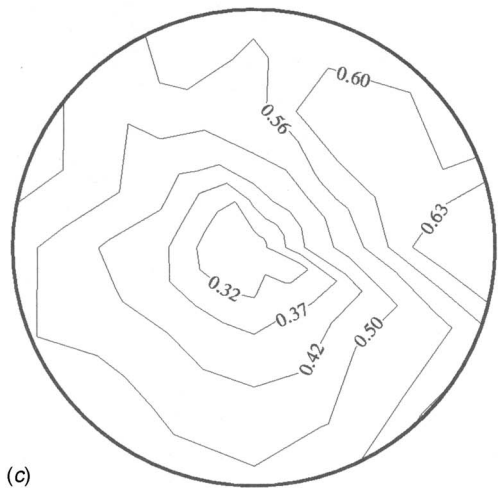

(*c*)

Fig. 12 Total pressure loss coefficient contours at transitioning diffuser exit (*a*) bare diffuser (*b*) with continuous jets (*c*) with active feedback control

different jet-to-free stream velocity ratios, respectively. The best performance of the diffusers was achieved at a velocity ratio of 2.5. Significant improvement in wall static pressure can be observed from the figures.

Figures 10(*a*) and 10(*b*) show the variation of skin friction coefficient along the inner and outer walls of the circular and transitioning diffusers, respectively. Zero C_f at several locations on the outer wall indicates flow separation. With VGJs, the separated region no longer exists in both the diffusers.

The total pressure loss coefficient contours at the circular diffuser exit are given in Figs. 11(*a*)–11(*c*) for the bare diffuser, with continuous jets and with feedback control. The loss coefficient ranged from 0.33 to 0.66 in the bare diffuser. This was reduced to

Table 3 Summary of active separation control in the diffusers

Diffuser geometry	Exit flow property	Bare diffuser	Diffuser with VGJ	Diffuser with tapered fin vortex generators on outer wall	Diffuser with steady VGJ on outer wall	Diffuser with Active feedback control loop
Circular diffuser	Mass averaged C_P	0.283	0.327	0.331	0.341	0.347
	D_C	0.851	0.751	0.736	0.692	0.687
	ϖ	0.393	0.328	0.312	0.292	0.289
Transitioning diffuser	Mass averaged C_p	0.261	0.292	0.304	0.309	0.314
	D_C	0.867	0.742	0.725	0.713	0.708
	ϖ	0.413	0.357	0.334	0.321	0.318

0.25–0.58 with VGJs. The extent of high loss regions were significantly reduced with steady VGJs and further reduced with feedback controlled VGJs.

The total pressure loss coefficient contours of the transitioning diffuser are given in Figs. 12(*a*)–12(*c*) for bare diffuser, with continuous jet and with feedback control, respectively. In the bare diffuser, the total pressure loss coefficient ranged from 0.37 to 0.82. This reduced to 0.34–0.64 with VGJs. The region of high loss region (of the order of 0.64) is less extensive with active feedback control loop. Moreover, the extent of low loss region is greater with the feedback control as compared to continuous jets.

Table 3 summarizes the results of the active separation control of the diffusers in terms of mass averaged C_P, distortion coefficient, D_C and total pressure loss coefficient, ϖ at the diffuser exit. The mass averaged C_P of the circular diffuser increased from 0.283 to 0.341 with continuous VGJs and further to 0.347 with feedback control. The distortion coefficient reduced from 0.851 to 0.687 with feedback controlled VGJs. Similar improvement is also observed in total pressure loss coefficient. The performance parameters of the transitioning diffuser also showed significant improvement as is evident from the table.

Thus VGJs are found to be most effective when used with a feedback control. The jet mass flow was around 0.06% and the KPR was 0.1% of the main flow for both the diffusers. The mass flow rate was substantially lower than the blowing ratios used by Ball [8] (2–5% of the main flow) and by Kwong and Dowling [9] (around 10% of the main flow).

The tapered fin vortex generators also resulted in the performance enhancement, however, to a lesser extent as compared to VGJs. This is due to the greater drag losses created by these devices due to their physical presence in the flow even when their operation is not required.

The experiments with the hotfilm sensor as the feedback sensor did not yield any better of a performance than the sublayer fence-pressure transducer combination. This was primarily because the hotfilm sensor is flow direction independent, where as the sublayer fence could detect the flow direction. Moreover in the present experiments, the transients in the separated region are expected to be well within the response time of the pressure transducer.

Physical Mechanism of Vortex Generator Jets. In order to study the physical mechanism of the VGJ effectiveness in the secondary flow and separation control, smoke visualization was employed. The skew angle of the VGJ was varied in the range of 90–150 deg (for secondary flow control arrangement) and the

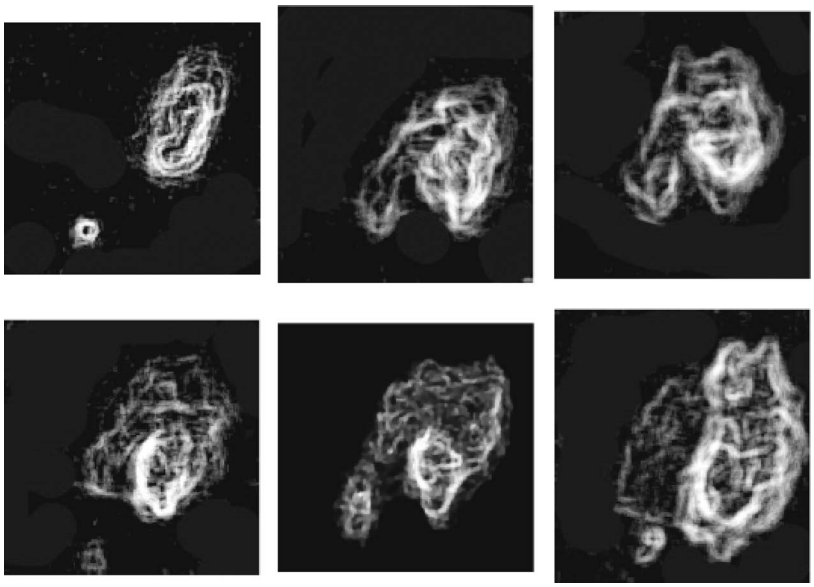

Fig. 13 Structure of vortices at downstream locations (*a*) 10 jet diameters (*b*) 20 jet diameters, and (*c*) 30 jet diameters

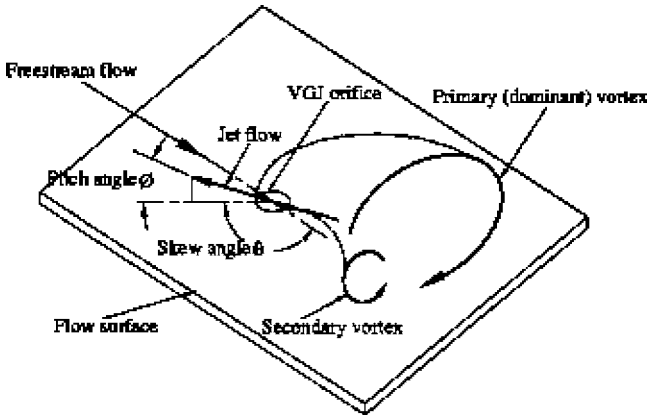

Fig. 14 Schematic of the structure of the vortices generated by a VGJ

vortex structures at these angles were captured. The jet-to-freestream velocity ratio was kept at 1.5 (as the best diffuser performance was achieved for this velocity ratio as reported by Sullerey and Pradeep [23,24]). For separation control arrangement the VGJ skew angle was kept at 45 deg in an orientation as shown in Fig. 1 and the velocity ratio was kept at 2.0. As mentioned earlier, the smoke images were processed using the edge detection tool of MATLAB as the processed images gave more details about the vortices. Figure 13(*a*) gives the smoke visualization image of a single jet at 90 and 135 deg skew angles, respectively, at a location 10 jet diameters downstream of the jet injection. The vortex structures at downstream locations of 20 and 30 jet diameters are given in Figs. 13(*b*) and 13(*c*). The size of the vortex at 135 deg skew angle is clearly much more than that at 90 deg. The VGJs were found to be most effective for secondary flow control when used with a skew angle of 135 deg as reported in Sullerey and Pradeep [23,24] as well as observed in the present study. The VGJs in the study were placed in such a manner that the vortices emanating due to the interaction of the VGJs with the freestream had an orientation opposing the secondary flows. The increased size of the vortex at a skew angle of 135 deg causes effective reduction of secondary flows. Zhang [16] too observed that the size of the vortex increases as it moves downstream, whereas its strength decreases. The vortices emanating from the VGJ consist of a large dominant primary vortex and a small weak secondary vortex as illustrated in Fig. 14. The sense of rotation of the vortices as observed during the experiments is also shown in the figure. This observation is consistent with that of Rixon and Johari [22].

Table 4 gives the boundary layer momentum thicknesses (as percentage of the diffuser inlet diameter and diffuser inlet width for the circular and transitioning diffuser, respectively) at three downstream locations for the bare diffuser and diffuser with VGJ on. The table also gives the turbulence intensities at these locations. The turbulence intensity was measured at a height of 0.5 times the jet diameter which was well within the boundary layer. The momentum thickness can be seen to reduce with VGJs on. The turbulence intensity on the other hand increases substantially with the VGJs. This is in line with the observations of Khan and Johnston [17] and Compton and Johnston [12]. The basic mechanism that comes into play while using the VGJs for secondary flow control (in the orientation used in the present experiments) is the introduction of vortices in such a manner that it opposes the naturally occurring secondary flows thus nullifying their effect. In earlier work done by Reichert and Wendt [2], tapered-fin vortex generators were used as boundary layer diverting devices to control secondary flows. The visualization study carried out by them demonstrates the mechanism of control. In previous studies carried out by Sullerey and Pradeep [23,24] tapered-fin vortex generators and VGJs were used with an idea of controlling secondary flows by introducing vortices opposing the naturally occurring secondary flows.

There have been other extensive visualization studies on VGJs like Compton and Johnston [12], Barberopoulos and Garry [15], Zhang [16], and Khan and Johnston [17] that demonstrated that VGJs too result in stream wise vortices that are similar to the vortices generated by conventional solid vortex generators. However, the vortices from a VGJ grow much more in size as it moves downstream as compared to the vortices from a solid vortex generator. This is the main reason for VGJ being more effective than solid vortex generators. Moreover, the drag losses associated with VGJs would be much less compared to solid vortex generators.

Since the strength of the vortices could not be estimated, it is not possible to comment about the role of strength of the vortices in secondary flow control. It was observed during the experiments that secondary flows themselves are weak in the diffusers studied. The maximum secondary flow vector magnitude observed was of the order of 18% of the freestream velocity. Hence it is expected that it is the size of the vortex that would play a dominant role in secondary flow control.

Figures 15(*a*)–15(*c*) gives the smoke visualization images of the VGJs in a configuration used for separation control at three different downstream locations namely, 30, 90, and 120 jet diameters, respectively. In Fig. 15(*a*) the four vortices are seen to be separate and smaller in size. Further away, i.e., 90 jet diameters downstream, the vortices are larger and the two center vortices have coalesced. At 120 jet diameters downstream (Fig. 15(*c*)), the vortices are indistinguishable and are much larger in size than that closer to the VGJs injection location. Therefore, VGJs are more effective in separation control as it causes efficient mixing of the low energy boundary layer fluid with the free stream.

Table 4 Boundary layer momentum thickness and turbulence intensities

Measurement location		Boundary layer Momentum thickness		Turbulence intensity	
		Bare diffuser	Diffuser with VGJ	Bare diffuser	Diffuser with VGJ
Location 1 (10 jet diameters downstream)	Circular diffuser	2.53	2.10	0.97	2.51
	Transitioning diffuser	2.58	2.18	1.71	2.78
Location 2 (20 jet diameters downstream)	Circular diffuser	2.56	2.16	0.96	2.47
	Transitioning diffuser	2.62	2.21	1.68	2.47
Location 3 (30 jet diameters downstream)	Circular diffuser	2.62	2.21	0.94	2.41
	Transitioning diffuser	2.68	2.31	1.66	2.42

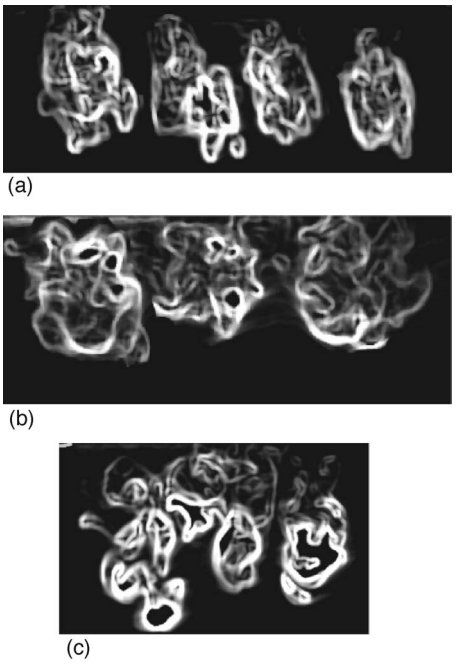

Fig. 15 Structure of vortices at downstream locations (*a*) 30 jet diameters (*b*) 90 jet diameters, and (*c*) 120 jet diameters from the VGJ

In secondary flow control, the larger the size of the vortex, the better would be the control. This is because secondary flow is not confined merely to the boundary layer; it extends over the entire cross section of the diffuser. Therefore, VGJ at 135 deg skew angle resulted in best performance improvement of the diffuser. In the case of separation control, it is effective mixing of the low momentum boundary layer fluid with the high momentum free stream that results in reduction / elimination of the separated zone. VGJs when used in the present configuration would cause efficient mixing of the boundary layer and the freestream compared to tapered-fin vortex generators. The smoke visualization of the VGJs for secondary flow control were captured at locations 10, 20, and 30 jet diameters as the VGJs are placed close to the planes where secondary flows are to be controlled. On the other hand, for separation control, VGJs are required to be effective over a larger distance and hence the images were taken at distances of 30, 90, and 120 jet diameters.

Conclusions

Secondary flow and separation control in circular and transitioning S-duct diffusers using vortex generator jets was successfully studied in the experimental investigation. Substantial improvement in performance of the diffusers was achieved by the use of VGJs. The use of vortex generator jets for secondary flow control resulted in around 14 and 20% decrease in total pressure loss and flow distortion coefficients in the transitioning and circular diffusers, respectively. Similar improvement in mass averaged static pressure recovery was also observed. The turbulence intensities at the exit of the diffusers reduced by around 30% when the jets were operational. This also indicates reduction in flow distortion due to secondary flow control. The performance improvement was achieved using only a fraction of the energy of the order of 0.3%) from the main flow.

In active separation control using VGJs, both steady VGJs and VGJs with feedback control were tried. Feedback control further improves the effectiveness of VGJs. The active control method proved to be significantly more effective than passive control method (tapered fin vortex generators). The distortion coefficient reduced by over 25% in all the diffusers. The total pressure loss coefficient reduced by about 48% in the rectangular diffuser and by around 30% in the transitioning and circular diffusers.

An attempt was made to explain the physical mechanism of VGJs in secondary flow and separation control. It was observed that the vortices generated when the VGJs were oriented at 135 deg skew angle (for secondary flow control) have sizes greater than those at other orientations.

The performance improvement achieved using the active flow control method namely, vortex generator jets were higher than that with the passive flow control device namely, tapered fin vortex generators. The application of VGJs has potential of secondary flow control in several other flow situations including turbo machinery.

Nomenclature

AR = area ratio of the diffuser
C_p = pressure coefficient $=((p-p_{\text{ref}})(\dot{m}_d+\dot{m}_j)/(1/2\rho V_d^2\dot{m}_d+1/2\rho V_j^2\dot{m}_j)$
C_f = skin fiction coefficient
D_c = distortion coefficient $=(p_{\text{oav}}-p_{\text{omin}})/q_{\text{av2}}$
KPR = kinetic power ratio $=\dot{m}_j V_j^2/\dot{m}_d V_d^2$
R = duct centerline radius of curvature
Re = Reynolds number based on inlet diffuser width
V = fluid velocity
VR = jet to freestream velocity (at inlet plane) ratio $=V_j/V_{\infty 1}$
$\dot{m}$ = mass flow rate
ϕ = pitch angle of the vortex generator jet
θ = skew angle of the vortex generator jet
ϖ = average total pressure loss coefficient $=(p_{o1}-p_{o2\text{av}})/\left(1/2\rho V_\infty^2\right)$
ρ = fluid density
h = diffuser height
l = duct centerline length
p = static pressure
p_o = total pressure
q = dynamic head
r = diffuser inlet radius (for circular diffuser) or diffuser inlet half width (for transitioning diffuser)
s = distance along the duct centerline from diffuser inlet
w = diffuser exit diameter
y = distance along duct centerline radius from inner wall of the diffuser
z = distance along diffuser height from the bottom of the diffuser
R/r = diffuser radius ratio

Subscripts

av = average value
d = diffuser
j = jet
max = maximum value
min = minimum value
ref = inlet plane (reference)
1,2 = notations for inlet and exit planes
∞ = free stream value at inlet plane
o = total pressure

Mass averaged quantities are defined in the following manner: $\bar{p}=1/\dot{m}\int_0^A p d\dot{m}$

Where, $\bar{p}$ is any mass averaged quantity, p is a measured quantity to be mass averaged, and $\dot{m}$ is the mass flow rate through the area A.

References

[1] Reichert, B. A., and Wendt, B. J., "Experimental Investigation of S-duct Flow

Control using Arrays of Low Profile Vortex Generator," AIAA Paper 93-0018, 1993.
[2] Reichert, B. A., and Wendt, B. J., "Improving Diffusing S-duct Performance by Secondary Flow Control," NASA Technical Memorandum 106492, 1994.
[3] Reichert, B. A., and Wendt, B. J., 1996, "Improving Curved Subsonic Diffuser Performance with Vortex Generators," AIAA J., **34**, pp. 65–72.
[4] Lakshminarayana, B., 1996, "*Fluid Dynamics and Heat Transfer of Turbomachinery*," 1st ed. Wiley, New York, pp. 322–328.
[5] Foster, J., Wendt, B. J., Reichert, B. A., and Okiishi, T. H., 1997, "Flow through a Rectangular – to – Semi-annular Diffusing Transition Duct," J. Propul. Power, **13**, pp. 312–317.
[6] Sullerey, R. K., Mishra, S., and Pradeep, A. M., 2002, "Application of Boundary Layer Fences and Vortex Generators in Improving the Performance of S-duct Diffusers," J. Fluids Eng., **124**, pp. 136–142.
[7] Sullerey, R. K., and Pradeep, A. M., 2002, "Effectiveness of Flow Control Devices on S-duct Diffuser Performance in the Presence of Inflow Distortion," Int. J. Turbo Jet Engines, **19**, pp. 259–270.
[8] Ball, W. H., 1985, "Tests of Wall Suction and Blowing in Highly Offset Diffusers," J. Aircr., **22**, pp. 161–167.
[9] Kwong, A. H. M., and Dowling, A. P., 1994, "Active Boundary-Layer Control in Diffusers," AIAA J., **32**, pp. 2409–2414.
[10] Innes, F., Pearcey, H. H., and Sykes, D. M., 1995, "Improvements in the Performance of a Three Element High Lift System by the Application of Airjet Vortex Generators," Aeronaut. J., **99**, pp. 265–274.
[11] Johnston, J. P., and Nishi, M., 1990, "Vortex Generator Jets – Means for Flow Separation Control," AIAA J., **28**, pp. 989–994.
[12] Compton, D. A., and Johnston, J. P., 1992, "Streamwise Vortex Production by Pitched and Skewed Jets in a Turbulent Boundary Layer," AIAA J., **30**, pp. 640–647.
[13] Fric, T. F., and Roshko, A., 1994, "Vortical Structures in the Wake of a Transverse Jet," J. Fluid Mech., **279**, pp. 1–47.
[14] Kelso, R. M., Lim, T. T., and Perry, A. E., 1996, "An Experimental Study of Round Jets in Cross-flow," J. Fluid Mech., **306**, pp. 111–144.
[15] Barberopoulos, A. A., and Garry, K. P., 1998, "The Effect of Skewing on the Vorticity Produced by an Airjet Vortex Generator," Aeronaut. J., **102**, pp. 171–177.
[16] Zhang, X., 2003, "The Evolution of Co-rotating Vortices in a Canonical Boundary Layer with Inclined Jets," Phys. Fluids, **15**, pp. 3693–3702.
[17] Khan, Z. U., and Johnston, J. P., 2002, "On Vortex Generating Jets," Int. J. Heat Fluid Flow, **21**, pp. 506–511.
[18] Johnston, J. P., "Pitched and Skewed Vortex Generator Jets for Control of Turbulent Boundary Layer Separation: A Review," FEDSM99-6917, Proceedings of 3rd ASME/JSME Joint Fluids Engineering Conference, San Francisco, California, USA, 1999.
[19] Hamstra, J. W., Miller, D. N., Truax, P. P., Anderson, B. A., and Wendt, B. J., 2000, "Active Inlet Flow Control Technology Demonstration," Aeronaut. J., **104**, pp. 473–479.
[20] Bons, J. P., Sondergaard, R., and Rivir, R. B., 2001, "Turbine Separation Control using Pulsed Vortex Generator Jets," ASME J. Turbomach., **123**, pp. 198–206.
[21] Volino, R. J., 2003, "Separation Control on Low-Pressure Turbine Airfoils using Synthetic Vortex Generator Jets," ASME J. Turbomach., **125**, pp. 765–777.
[22] Rixon, G. S., and Johari, H., 2003, "Development of a Steady Vortex Generator Jet in a Turbulent Boundary Layer," J. Fluids Eng., **125**, pp. 1006–1015.
[23] Sullerey, R. K., and Pradeep, A. M., "Secondary Flows and Separation in S-duct Diffusers – Their Detection and Control," FEDSM2003-45109, *Proceedings of the 4th ASME/JSME Joint Fluids Engineering Conference*, Honolulu, Hawaii, USA, 2003.
[24] Sullerey, R. K., and Pradeep, A. M., 2004, "Secondary Flow Control using Vortex Generator Jets," J. Fluids Eng., **126**, pp. 650–664.
[25] Pradeep, A. M., and Sullerey, R. K., "Secondary Flow Control in Circular S-duct Diffusers using Vortex Generator Jets," AIAA2004-2615, AIAA 2nd Flow Control Conference, Portland, Oregon, USA, 2004.
[26] Miau, J. J., Leu, T. S., Chou, J. H., Lin, S. A., and Lin, C. K., 1990, "Flow Distortion in a Circular-to-Rectangular Transition," AIAA J., **28**, pp. 1447–1456.
[27] Patel, V. C., 1965, "Calibration of the Preston Tube and Limitations on its Use in Pressure Gradients," J. Fluid Mech., **23**, pp. 185–208.
[28] Vagt, J. D., and Fernholz, H., 1973, "Use of Surface Fences to Measure Wall Shear Stress in Three-Dimensional Boundary Layers," Aeronaut. Q., **24**, pp. 87–91.
[29] Pradeep, A. M., and Sullerey, R. K., 2003, "A Displacement Based Wall Shear Stress Sensor," J. Inst. Eng. (India), Part AG, **84**, pp. 27–31.
[30] Frei, D., and Thomann, H., 1980, "Direct Measurements of Skin Friction in a Turbulent Boundary Layer with a Strong Adverse Pressure Gradient," J. Fluid Mech., **101**, pp. 79–95.
[31] Ohman, L. H., and Nguyen, V. D., "Applications of the Five Hole Probe Technique for Flow Field Surveys at the Institute for Aerospace Research," *Proceedings of the AGARD Meeting on Wall Interference, Support Interference and Flow Field Measurements*, 1993.
[32] Nowak, C. F. R., 1973, "Improved Calibration Method for a Five-hole Spherical Pitot Probe," J. Phys. E, **3**(1-2), p. 21.
[33] Abernethy, R. B., Benedict, R. P., and Dowell, R. B., 1985, "ASME Measurement Uncertainty," J. Fluids Eng., **107**, pp. 161–164.
[34] Moffat, R. J., 1985, "Using Uncertainty Analysis in the Planning of an Experiment," J. Fluids Eng., **107**, pp. 173–180.
[35] Kline, S. J., 1985, "The Purposes of Uncertainty Analysis," J. Fluids Eng., **107**, pp. 153–160.

N. P. Costa
e-mail: ncosta@fe.up.pt

R. Maia
e-mail: rmaia@fe.up.pt

M. F. Proença
e-mail: fproenca@fe.up.pt

Departamento de Engenharia Civil,
Faculdade de Engenharia da Universidade do Porto,
Rua Dr. Roberto Frias,
4200-465 Porto,
Portugal

F. T. Pinho[1]
Centro de Estudos de Fenómenos de Transporte,
Faculdade de Engenharia da Universidade do Porto,
Rua Dr. Roberto Frias,
4200- 465 Porto,
Portugal
and
Universidade do Minho, Largo do Paço, 4704-553 Braga, Portugal
e-mail: fpinho@fe.up.pt

Edge Effects on the Flow Characteristics in a 90 deg Tee Junction

Measurements of pressure drop were carried out for the flow of a Newtonian fluid in 90 deg *tee junctions with sharp and round corners. Rounding the corners reduced the energy losses by between 10 and 20%, depending on the flow rate ratio, due to the reduction in the branching flow loss coefficient, whereas the straight flow basically remained unaffected. The corresponding detailed measurements of mean and turbulent velocities for a Reynolds number of 31,000 and flowrate ratio of 50% showed that rounding the corner lead to an increase in turbulence in the branch pipe. The increased turbulence diffused momentum more efficiently thus reducing the length of the recirculation by 25% with its width and strength also decreasing in magnitude. The overall effect of the increased dissipation due to turbulence and reduced dissipation due to mean flow irreversibilities in the recirculation was a decrease in the corresponding loss coefficient.*
[DOI: 10.1115/1.2354524]

1 Introduction

Tee junctions are frequently present in industrial systems and water distribution networks where there is the need to separate or merge flows. Disturbances from a condition of straight fully developed flow, such as those created by fittings and accessories, dissipate extra energy [1], which is directly proportional to the intensity of the disturbance. Since 90 deg tee junctions are very disturbing accessories that lead to separated and reverse flows they account for large energy losses if present in large quantities, hence improvements are welcome to reduce the energy bill.

Rounding the corner can help reduce pressure losses, but the separating point becomes dependent on the outlet flowrate ratio, outlet to inlet pipe diameter ratio, pipe roughness, and flow regime. The extent and magnitude of these changes are still poorly understood and documented and constitute the motivation for the present study. Here, the diverging turbulent Newtonian flow in a 90 deg tee junction with sharp corners is experimentally investigated in detail and its flow characteristics are compared with those pertaining to a similar junction with rounded corners.

The amount of available information on 90 deg T-junction flows is rather limited or old and consequently less accurate. The flow is highly complex and three-dimensional and is not accessible to any simplified theoretical analysis. The first series of systematic experimental work in this geometry was carried out in Munich by Vogel [2], who investigated the division and merging of flows in nonsymmetric bifurcations, analyzing the effects of branch pipe diameter and edge radius. Gardel [3,4] included the effects of area ratio, branch angle, and curvature of the junction and derived semi-empirical expressions for the local loss coefficients.

In the 1960s various researchers attempted to justify theoretically the semi-empirical formulas [5]. A theoretical definition of the streamlines and wall pressure distribution in the 90 deg tee was carried out by Iwanami et al. [6] based on the potential flow theory to help understand the mechanisms of pressure loss. They considered the straight pressure loss similar to that in a sudden enlargement whereas the branch pressure loss was modeled as the sum of the loss in a contraction followed by a sudden enlargement. Other investigations in the nineteen sixties and seventies were aimed at confirming and extending results of previous research [7].

More recently, Maia [7] concluded that the traditional pressure field characterization was no longer enough to improve the design of pipe accessories, but required a deeper knowledge of the relationship between flow geometry, pressure field, and flow kinematics. Sierra Espinosa et al. [8,9] investigated round-edge tees and compared a limited set of measurements with simulations by the standard $k-\epsilon$ model, the renormalization group theory (RNG) $k-\epsilon$ model and the standard Reynolds stress (RSM) turbulence models. These models were able to predict the mean flow qualitatively, but the comparisons involving the standard $k-\epsilon$ and RNG models were poor except on the approach flow. Downstream of the T-junction, the RSM could not predict the mean flow as well it overpredicted significantly the extent of the recirculation region in the branch pipe, but it reproduced well the anisotropy of the Reynolds stress tensor. However, careful inspection shows that none of these models did a good job. Recently, Páal et al. [10] used an RSM and the shear stress transport (SST) $k-\omega$ model of Menter [11] to calculate the flow in a 90 deg tee junction with sharp edges; they were able to predict the mean flow reasonably well, but k was significantly under-predicted. The good performance of the SST model was due to its improved ability to deal with separated and rapidly strained flows.

Systematic investigations on the effects of rounding the corner were initially carried out by Boldy [12] and Ito and Imai [13],

[1]Corresponding author.

Contributed by the Fluids Engineering Division of ASME for publication in the JOURNAL OF FLUIDS ENGINEERING. Manuscript received September 9, 2005; final manuscript received May 7, 2006. Assoc. Editor: Timothy J. O'Hern.

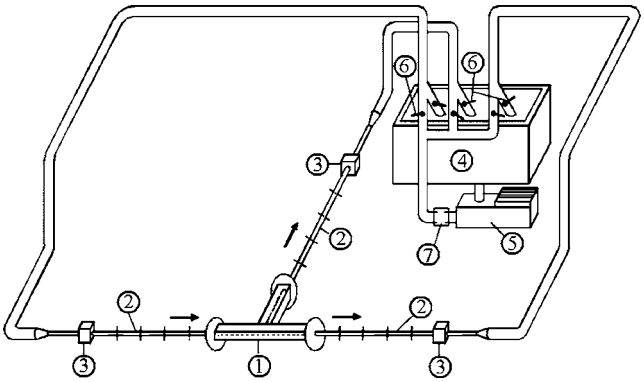

Fig. 1 Schematic representation of the experimental set-up: (1) Tee test section (flow field characterization), (2) pipe test section (pressure field characterization), (3) flowmeter, (4) tank, (5) pump, (6) valve, (7) pulsation dampener

which became the basis of the standard data on energy loss coefficients for tee junctions of the British Hydromechanics Research Association (BHRA) [14].

Today, there is renewed interest on tee junction flows because of the usefulness of diverging flows as separating devices for multi-phase systems found in chemical and power plants [15–17] and the presence of a large number of bifurcations in living organisms even though here the bifurcation angle is less severe [21–25]. In general, in two-phase flow bifurcations there is phase separation with dramatic effects on the pressure differences, and this strongly depends on the geometry, its orientation and type of fluid. Expressions for pressure drop were developed, commonly based on single-phase loss coefficients, taking into account the effects of branch orientation, flow direction (horizontal or vertical, upward, or downward) and its interaction with phase separation [15–17]. More recent research developed split models for annular gas/ liquid separation and measured in detail such flows and in particular the position of the interface [18,19]. Numerical methods have also been developed to deal with gas-liquid and liquid-liquid phase separation in *T*-junctions; Issa and Oliveira [20] used a pressure-volume fraction velocity correction scheme in a conventional seggregated two fluid approach finite volume method.

In living organisms, bifurcations are present in the respiratory and the circulatory system. Here, the approach flow is never fully developed, the pipe is tapered, the flow is time-dependent and the angle of bifurcation is usually well below 90 deg. These investigations are usually in the laminar flow regime [21], very often transient [22], fluids are non-Newtonian [23] and geometries have similarities to true arteries [24], i.e., consecutive junctions in tapered ducts and transient flow. Less often, but equally important, are investigations in the convergent flow as carried out by Ravensbergen et al. [25], amongst others.

The present contribution is aimed at experimentally characterizing and comparing the flows in two similar tees having different edges at the junction: One has a sharp-edged connection between the branch pipe and the main straight pipes whereas the second tee has round edges.

2 Test Rig and Instrumentation

The experiments were carried out in the closed loop rig schematically shown in Fig. 1. The test section was made of two parts: The three 2 m long pipes (pipe test section) and the corresponding extension forming the tee junction test section. The pipe test sections were manufactured from drawn tube with internal diameters of 30.8 mm±45 μm. To reduce optical refraction of laser beams, during the laser-Doppler anemometry measurements, the tee test section was carefully machined from rectangular blocks of acrylic. It is comprised of the bifurcation piece and the three adjoining straight pipes, each of these with 19–26 diameters of overall length for the straight and branch pipes, respectively.

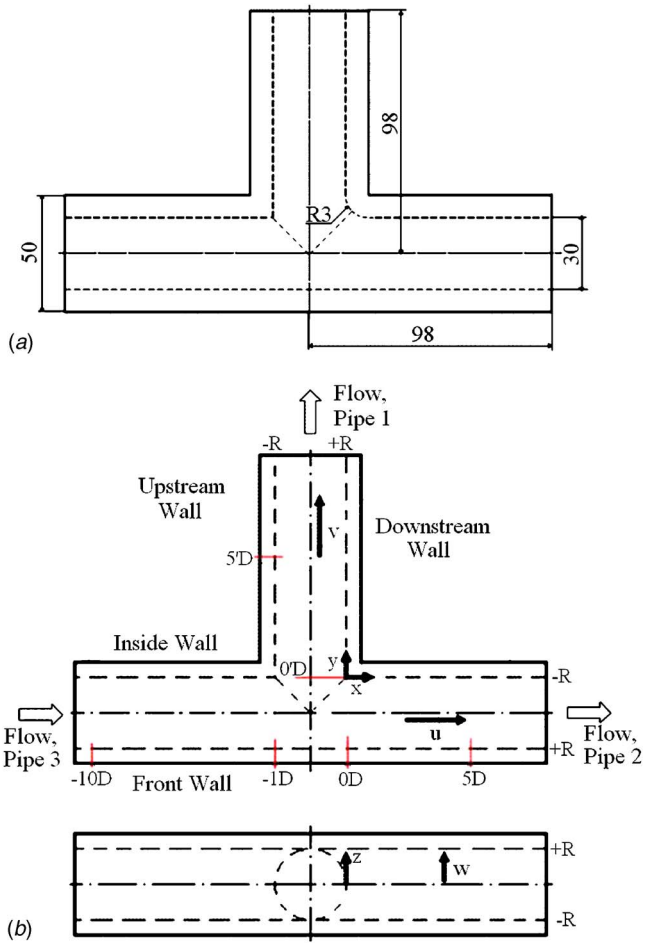

Fig. 2 Test section drawings and co-ordinate system: (*a*) Bifurcation piece: Comparison between sharp-edge tee (left) and rounded-edge tee (right). Dimensions in [mm]; (*b*) coordinate system, position of some diametric measuring planes and terminology.

For the sharp-edge tee bifurcation the pipes were drilled from a single block of acrylic to diameters of 30.1 mm±20 μm. The round-edge tee, which had a ratio of edge radius of curvature to pipe diameter equal to 0.1, was manufactured from two blocks of acrylic using a high precision CAD-CAM system. Then, the two halves were closed and the internal pipe was carefully polished to remove any internal steps/ seams. The internal diameters were checked by means of precision gauges and found to be equal to 30.06 mm±10 μm. Figure 2(*a*) compares the geometries of the sharp (left side) and round-edge (right side) tees, whereas Fig. 2(*b*) shows the coordinate system, the location of some measuring planes and the terminology used throughout this work. The square outer cross-sections of both tees and of the leading pipes minimized refraction of laser beams.

The water flow was continuous and was driven by a volumetric Mohno pump supplied by a constant head tank. A variable speed controller operated the pump and three valves controlled the flow distribution to the two outflow pipes. Pulsation dampeners were also located after the pump to ensure that the flow was continuous. For the detailed velocity measurements the inlet pipe Reynolds number was equal to 32,000 and the flowrate partition to the straight and branch outlet pipes was 50%/50%. For the pressure

measurements the inlet Reynolds number varied from 5000 to 32,000 while the volumetric flowrate ratio Q_1/Q_3 was varied from 0 to 1 (branch flow rate over inlet flow rate).

The flow rates were monitored by three magnetic flowmeters, one in each pipe, and the temperature of the water was monitored by means of a PTC100 sensor located in the open tank. The water temperature variation during each test run was within the sensor uncertainty of ±0.5°C, because of the large volume of water in the rig, but varied along the year. Its influence on the viscosity was taken into account to maintain the inlet flow conditions. The 95% confidence level uncertainties of the flowrate measurements varied between 2.5% and 0.6% at low and high flowrates, respectively.

Pressure measurements were carried out along the pipes to obtain the loss coefficients for the straight and branched flows. On each pipe there were seven measuring planes in the 2 m nearer to the bifurcation and in each of these measuring planes there were four pressure taps uniformly distributed around the perimeter of the pipe and connected to each other. The pressure from each pressure section was connected to a differential pressure transducer via a valve switchboard. The differential pressure transducer was a Rosemount, model 3051C, and was interfaced with a computer via an AD converter. The uncertainties of the pressure differences were of 6.7% at Re=15,000, decreasing to 1.2% at Re =40,000. These uncertainties were estimated following the square root of the sum of squares procedure explained in detail in Coleman and Steele [26]. Here, the total relative uncertainty ($E_{\Delta p}/\Delta p$) was calculated from the total systematic ($B_{\Delta p}$) and precision ($P_{\Delta p}$) uncertainties following Eq. (1):

$$\frac{E_{\Delta p}}{\Delta p} = \sqrt{\left(\frac{B_{\Delta p}}{\Delta p}\right)^2 + \left(\frac{P_{\Delta p}}{\Delta p}\right)^2} \tag{1}$$

The total systematic uncertainties included contributions from the fossilized uncertainty of the transducer, its resolution and the fossilized total uncertainty from the calibration procedure. During calibration, the pressure transducer ports could be switched to measure the pressure difference between two independently filled water columns, their heights measured by electrodes positioned using two verniers. The precision uncertainty was given by

$$P_{\Delta p} = t\frac{S_{\Delta p}}{\sqrt{N}} \tag{2}$$

where $S_{\Delta p}$ is the standard deviation of the sample of N readings (N=1000 pressure readings) and t=2 since the sample was larger than 10 (as recommended by Coleman and Steele [26]). More details of the uncertainty analysis are given in Costa [27].

Mean and turbulent velocity measurements in the pipes and tees were carried out by means of laser-Doppler anemometry. The LDA used was a miniaturized fiber optics system from INVENT, model DFLDA, similar to that described in detail by Stieglmeier and Tropea [28], with a 120 mm front lens mounted onto the 30 mm diameter probe (probe S30). Scattered light was collected by a photodiode in the forward- and backscatter modes, depending on optical access. In particular, in the T-junction test section the measurements could only be done in backscatter mode, because of the size of the supports of the ducts and the bulky receiving optical unit. The main characteristics of the anemometer are listed in Table 1.

The signal from the photodiode was processed by a TSI 1990 C counter, which contained the filters required to remove the pedestal. It operated in the single measurement per burst mode, frequency validation was set at 1% and 16 signal cycles were used for each valid measurement. The counter was interfaced with a computer via a DOSTEK 1400A card, which provided the statistical quantities. To measure the three components of the velocity vector with a 1D LDA we followed standard procedures. For all velocity components Snell's law [29] was taken into account to quantify the effects of curvature of the pipe walls in positioning the LDA measuring volume, in the value of the LDA conversion factors and in determining the orientation of the velocity component being measured at the control volume. For the streamwise velocity the plane of laser beams was diametric and the control volume was traversed radially along the laser light direction from wall to wall. To measure the tangential and radial velocity components the plane containing the laser beams was perpendicular to the pipe axis. The control volume was traversed radially along the laser light direction to measure the tangential velocity. Radial traversing the control volume along the direction perpendicular to the direction of the LDA measured a combination of the radial and tangential velocity components that required post-processing.

Table 1 Main characteristics of the laser-Doppler system (more characteristics in Table 1 of Stieglmeier and Tropea [28])

Laser wavelength	820 nm
Laser power	100 mW
Laser diameter	3.5 mm
Measured half-angle of beams in air	3.81 deg
Size of measuring volume in water (e^{-2})	
minor axis	37 μm
major axis	550 μm
Fringe spacing in air	6.31 μm
Frequency shift	1.0 MHz

The maximum uncertainties in the streamwise mean and rms velocities at a 95% confidence level are of 0.9% and 2.5% in low turbulence regions and of 1.5% and 5.5% in high turbulence regions close to walls, respectively. The uncertainty in the measurements of the cross-stream mean and rms velocity components is 1.4% and 6.0% in low and high turbulence regions, respectively. To estimate the uncertainties in the LDA measurements we followed Durst et al. [30] and Albrecht et al. [29], and took into account the specificities of the system used, which are described in detail by Stieglmeier and Tropea [28]. The total uncertainties of the mean and rms velocities were estimated on the basis of following contributions: Statistics (5000 data samples), clock accuracy and number of fringe effects, averaging process, beam alignment relative to geometry, effect of small scale fluctuations, and velocity gradient broadening. No corrections to gradient broadening were applied to the measured data and the broadening due to the number of fringes was always well below 0.4%, because the number of static fringes was six, the number of periods in signal processing was 16, the fringe spacing was 6.31 μm, the counter used had a clock frequency of 500 MHz, the shift frequency was 1 MHz, and the velocities measured corresponded to Doppler frequencies less than 0.3 MHz. Measurements could be performed to within 200 μm of the wall.

The anemometer was mounted on a milling machine with movement in the three coordinate directions and the positional uncertainty was ±100 μm in all three directions.

3 Experimental Results and Discussion

3.1 Sharp-Edge Tee

3.1.1 Pressure-Field Characterization. According to the flow configuration of Fig. 2, the energy equations for the two flow paths are given by

$$p_3 + \frac{1}{2}\alpha_3\rho U_3^2 = p_1 + \frac{1}{2}\alpha_1\rho U_1^2 + f_3\frac{L_3}{D_3}\rho\frac{U_3^2}{2} + f_1\frac{L_1}{D_1}\rho\frac{U_1^2}{2} + \Delta p_{3-1} \tag{3}$$

$$p_3 + \frac{1}{2}\alpha_3 \rho U_3^2 = p_2 + \frac{1}{2}\alpha_2 \rho U_2^2 + f_3 \frac{L_3}{D_3}\rho \frac{U_3^2}{2} + f_2 \frac{L_2}{D_2}\rho \frac{U_2^2}{2} + \Delta p_{3-2} \tag{4}$$

for the branched and the straight flows, respectively. The subscripts 1–3 refer to the branch pipe, the straight outlet pipe, and the inlet pipe, respectively. The static pressure is p, U is the bulk velocity (in the absence of subscript U represents U_3), ρ is the density of the fluid, f is Darcy's friction coefficient for fully developed flow in a pipe of diameter D, and the length is L. The length of a pipe is measured from the position of the pressure tap to the intersection of the three pipes. The pressure losses associated with the tee are given by Δp_{3-j} in the trajectory from pipe 3 to pipe j. The energy shape factors (α) are taken to be 1, the usual engineering practice in calculations when the flow is turbulent. From the pressure measurements taken along the straight pipes, in regions of fully developed flow, the values of the Darcy friction factors were determined for each pipe. The pressure losses in the tee were subsequently evaluated from the measured pressure differences and application of Eqs. (3) and (4). The corresponding local loss coefficients are defined as

$$K_{31} \equiv \frac{\Delta p_{3-1}}{\frac{1}{2}\rho U_3^2} \tag{5}$$

$$K_{32} \equiv \frac{\Delta p_{3-2}}{\frac{1}{2}\rho U_3^2} \tag{6}$$

It is important to note at this stage that the inlet Reynolds numbers (Re_3) of the measured flows are low for a turbulent flow. In contrast, some data from the literature shown in Figs. 3–5, pertain to high Reynolds number flows where the loss coefficients are already independent of the Reynolds number.

For these experimental conditions, Figs. 3 and 4 present the variations of coefficients K_{31} and K_{32} with inlet pipe Reynolds number and flow rate partition and compare the measurements with data from the literature. Looking first at our measurements in Figs. 3(a) and 4(a), it is clear that at high Reynolds numbers both coefficients are independent of Re, whereas at low Reynolds numbers K_{31} decreases and K_{32} increases with Re. The variation of both coefficients with flow rate ratio, shown in Figs. 3(b) and 4(b), is nonmonotonic, with minimum values of K_{31} at $Q_1/Q_3 \cong 0.4$ and of K_{32} at $Q_1/Q_3 \cong 0.2$. The variations in the magnitude of K_{32} in relation to Re and Q_1/Q_3 are stronger than the variations in K_{31}, but only in relative terms.

Comparisons with the literature are shown in Figs. 3(b) and 4(b); they are reasonably good considering the experimental uncertainties, differences in Reynolds number, variations in the geometry, and in the inlet flow conditions. In particular, for our measurements at a Reynolds number of 32,000 and a flow rate ratio of 50%, the values of K_{31} and K_{32} are equal to 0.86 and 0.036, respectively. This is the flow condition at which the mean and turbulent velocity fields, presented in the next two subsections, were investigated in detail.

3.1.2 Inlet Flow Field. We start by presenting radial profiles of the mean and rms velocities in the inlet pipe. In Fig. 5(a) wall coordinates are used whereas Figs. 5(b)–5(d) and 6 show plots in physical coordinates. In particular, data for two upstream sections are presented (−10 and −5 D) and in Fig. 5 they are also compared with classical data from the literature [31–33]. More recent literature data [34,35] concentrate on the near wall region and pertain to very low flow Reynolds numbers, and they also agree with the classical data away from the near wall region. Given our set-up and LDA system, the classical data are adequate for these comparisons. The axial mean velocity in wall coordinates in Fig. 5(a) compares well with the log-law and the experimental data.

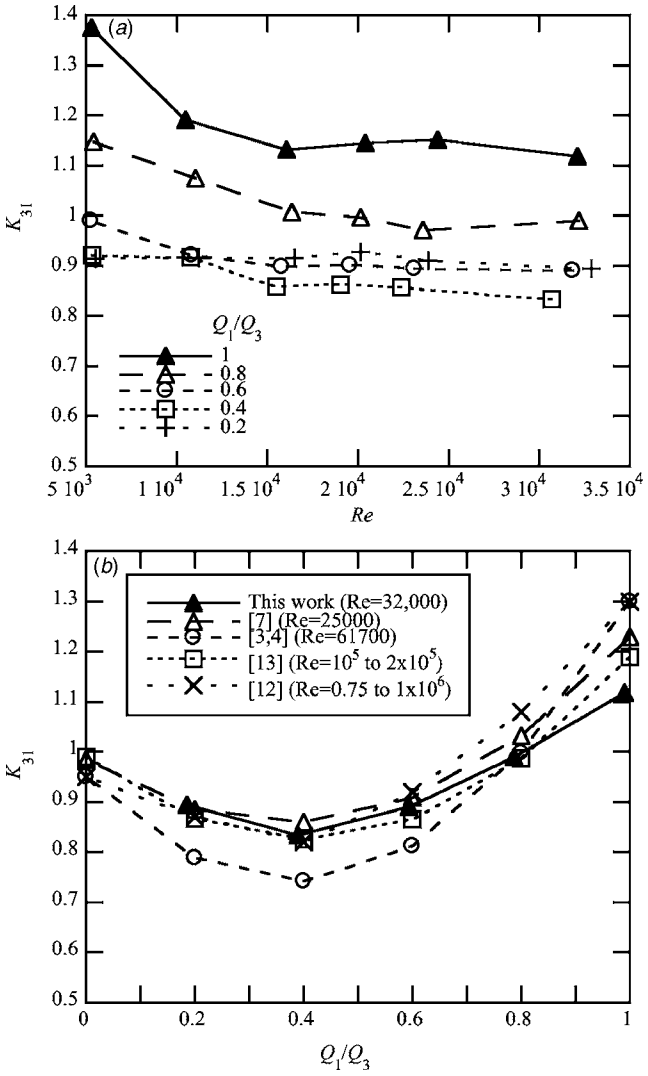

Fig. 3 Variation of the local loss coefficient K_{31} in a sharp edge 90 deg tee: (a) Effect of Reynolds number and flow rate ratio; (b) comparison with literature

The corresponding data in physical coordinates shown in Fig. 6, at a Reynolds number of 35,000, are also consistent with the literature and the ratio between the centerline and bulk velocities, slightly exceeding 1.2, was also expected.

In terms of turbulence data, the profiles of the rms velocities are also in good agreement with the literature. Near the wall the measured data exceed the literature values, because they were not corrected for mean gradient broadening effects. In conclusion, the inlet flow is well developed upstream the bifurcation both in terms of mean and turbulent flow.

3.1.3 Mean Flow Field. Figure 7 presents radial profiles of the axial mean and rms velocities inside the bifurcation region to illustrate the distortion of the flow at the inlet (−1 D) and inside (−0.5 D) the bifurcation. Here and elsewhere, the data were normalized by the inlet pipe bulk velocity ($U=U_3$). The distortion in the axial velocity is maintained between −1 and −0.5 D, while part of the fluid goes into the branch pipe. The slightly increased turbulence at −0.5 D could be associated with the small flow deceleration in the region. The flow remains symmetric in the z-direction as we can see from the profile of the axial mean velocity taken vertically at −1 D.

The mean flow is best understood with the vector plot of the mean velocity in the x-y horizontal diametric plane of Fig. 8. In

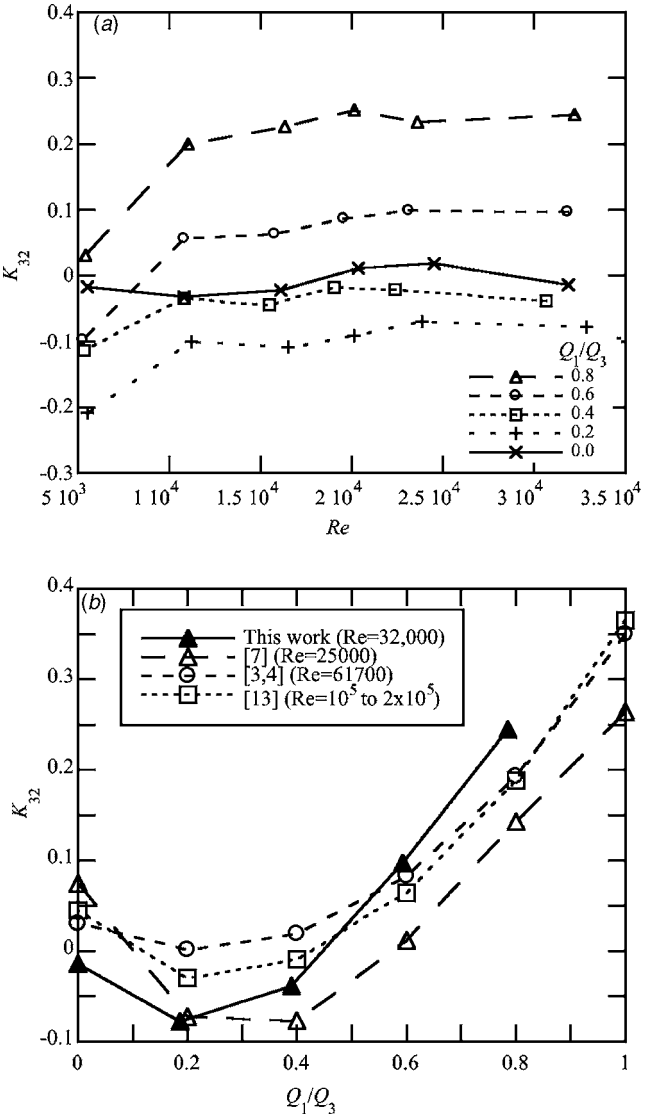

Fig. 4 Variation of the local loss coefficient K_{32} in a sharp edge 90 deg tee: (*a*) Effect of Reynolds number and flow rate ratio; (*b*) comparison with literature

the inlet and main outlet pipes u is the streamwise velocity and v is the cross-stream velocity; in the branch pipe the role of these two velocity components change. In referring to measuring stations, a prime designates the branch pipe, and negative values identify stations inside the bifurcating regions (cf. Fig. 2: 0 D and 0′ D represent the entrance to the outlet and branch pipes, respectively).

On approaching the beginning of the bifurcation (−1.0 D) the flow in the inlet pipe deviates towards the inside wall. At the middle of the bifurcation (−0.5 D) the maximum normalized streamwise velocity has dropped only to about 0.9, indicating that in the first half of the junction the main flow does not deviate significantly towards the side branch (see also Fig. 7), because the recirculation zone at the edge of the upstream wall of the branch pipe blocks the passage of fluid, which goes into the branch pipe only at the downstream half of the junction. This can also be seen in the radial profiles of the streamwise velocity in the branch pipe of Fig. 9. Here, it is clear that the recirculation bubble becomes wider than the radius of the branch pipe, starting from the upstream wall (cf. profiles from 0.25′ to 1.5′ D).

The recirculation bubble in the branch pipe is about 2.0′ D long, its width remains fairly constant and the maximum streamwise velocities occur between 1.1′ and 1.5′ D. The shape of the recirculating region at its end is rather strange; at 2.0′ D the flow near the upstream wall is already positive but there is still a small negative velocity near the pipe axis showing that the recirculation has detached from the wall to form a bubble in the center of the pipe. This pattern is similar to that measured by Maia [7] under laminar flow conditions, even though here the flow is turbulent. Close inspection of the vectors inside the recirculating region show also that the fluid is moving away from the wall, and continuity requires that an inflow into the wall region must take place. This leads to a strong 3D flow with the w velocity component feeding fluid into this region from above and below the horizontal diametric plane. Some measurements of w were carried out in this region and confirm this finding as shown in Fig. 10. Here, "radial" profiles of the vertical velocity (w) measured 10 mm above and 10 mm below the diametric horizontal plane are plotted. Negative values of r correspond to the vicinity of the upstream wall where strong jets are seen feeding fluid into the recirculation. Velocities w are positive below the diametric plane and vice versa.

Because the flow deviation into the branch mostly takes place near the end of the bifurcation, the shape of the streamwise velocity profile at the beginning of the straight outlet pipe (plane 0.0 D), shown in Fig. 11 (circles), is almost symmetric. However, downstream of the entrance to the outlet straight pipe the streamwise velocity profiles become quickly distorted due to the large values of v/U in combination with the sudden appearance of the wall, leading to profiles of u/U strongly skewed towards the inside wall. Flow redevelopment in the straight outlet pipe takes a while to be noticed: At 2.0 D the fluid is already accelerating at the outside wall but at 5.0 D the profile is still distorted.

Cross-stream velocities in the horizontal direction in the main and branch pipes (v and u, respectively) are very low everywhere (not exceeding 5% of inlet bulk velocity) except at the entrance to the pipes where the flow tends to be aligned at 45 deg relative to both the x and y axis and attains values of 15% of the inlet bulk velocity.

In the vertical plane the flow remains symmetric as can be assessed by some radial profiles of the streamwise velocity taken in a vertical cross-stream direction and plotted as crosses in Fig. 11. Compared with the horizontal profiles of Fig. 11 the evolution of u/U is quite different. While the velocity at the center of the pipe quickly decreases on going downstream, near the upper and bottom walls it increases and the profile remains symmetric, an indication of the strong three-dimensional character of the flow. In contrast, in the horizontal plane the streamwise velocity profiles are asymmetric and the peak velocity is observed to remain near the inside wall for a long time (cf. circles in Fig. 11). It is also worth mentioning that for this flowrate ratio (50%) no flow separation was observed in the main outlet pipe.

3.1.4 Turbulent Flow Field. Figures 12–14 present profiles of the normalized u' and v' in the bifurcation, the straight outlet pipe and branch pipe of the sharp-edge tee, respectively.

Starting in the bifurcation, Fig. 12 shows that the turbulence increases as the fluid moves from the inlet pipe towards the exit, but the larger increase in u'/U is seen near the front wall, probably a consequence of production of $\overline{u'^2}$ by normal rate of strain-normal Reynolds stress interaction (first term on the right-hand-side (RHS) of Eq. (7)), as suggested by Hinze [36]. In fact, on entering the bifurcation the mean flow is already deviating towards the inside wall, because of the imminent change in direction of 50% of the fluid that goes into the branch pipe. The consequence is a fluid deceleration in the front wall region of the bifurcation due to depletion of fluid ($\partial u/\partial x < 0$) leading to a positive first term on the RHS of Eq. (7)

$$\text{Production of } \overline{u'^2} = -\overline{u'^2}\frac{\partial u}{\partial x} - \overline{u'v'}\frac{\partial u}{\partial y} - \overline{u'w'}\frac{\partial u}{\partial z} \qquad (7)$$

From 0.0 to 1.0 D, in the straight outlet pipe, the horizontal

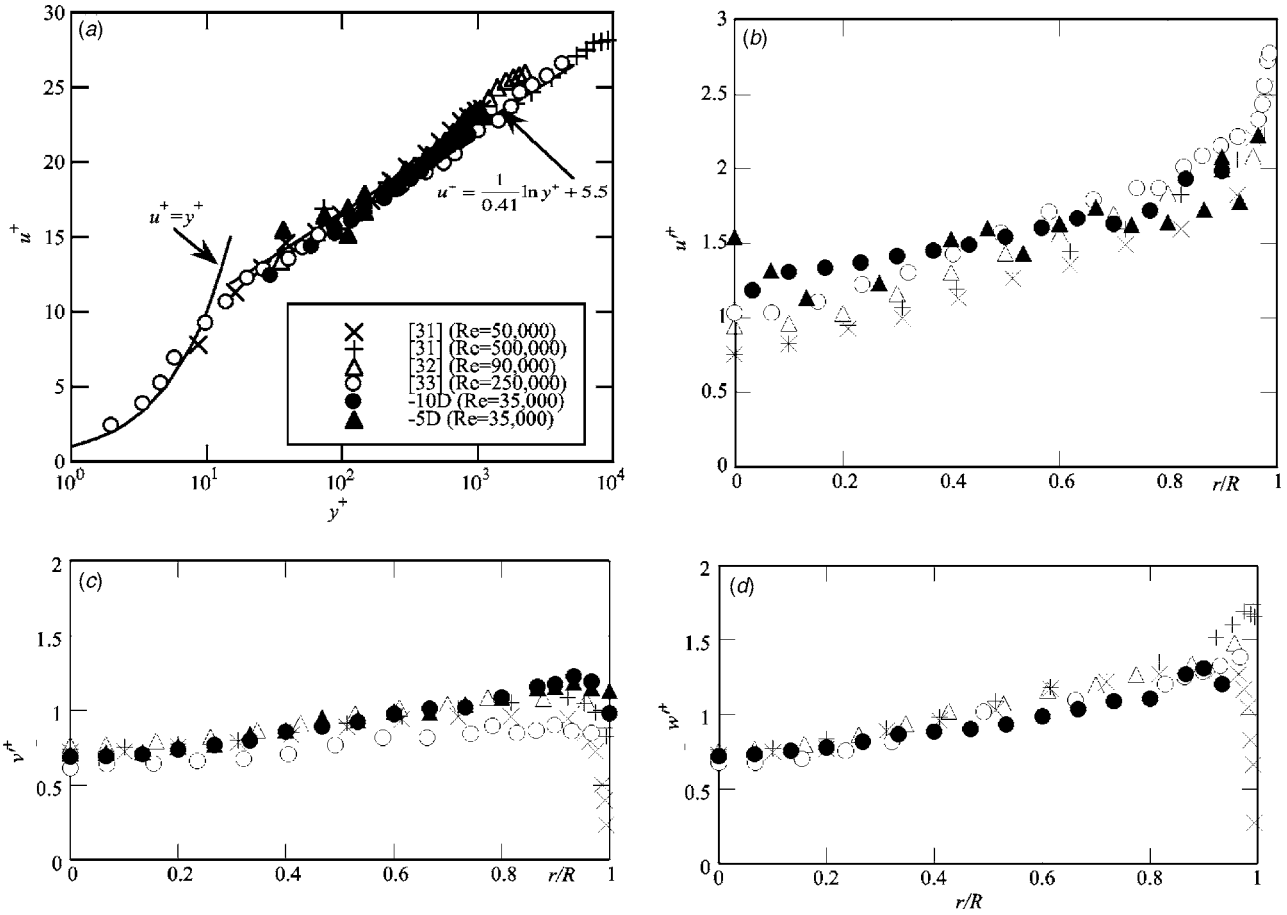

Fig. 5 Comparison between the literature and measured velocity profiles upstream of the tee junction (–10 and –5 D): (*a*) Axial velocity (in wall coordinates); (*b*) axial rms velocity; (*c*) radial rms velocity; (*d*) tangential rms velocity

profiles in Fig. 13(*a*) show that u'/U decreases in the front wall region ($r>0$) and increases in the inside wall region ($r<0$). In the former region the boundary layer is weak (circles in Fig. 11 show a low shear rate), because this region has been previously depleted of fluid and so the turbulence production by shear velocity gradient and shear Reynolds stress interaction (the second term on the RHS of Eq. (7)) will be smaller than at the equivalent region in the inlet pipe. Also, fluid with lower turbulence is being advected from the inside wall region of the outlet pipe into the front wall region, thus decreasing turbulence by fluid mixing as

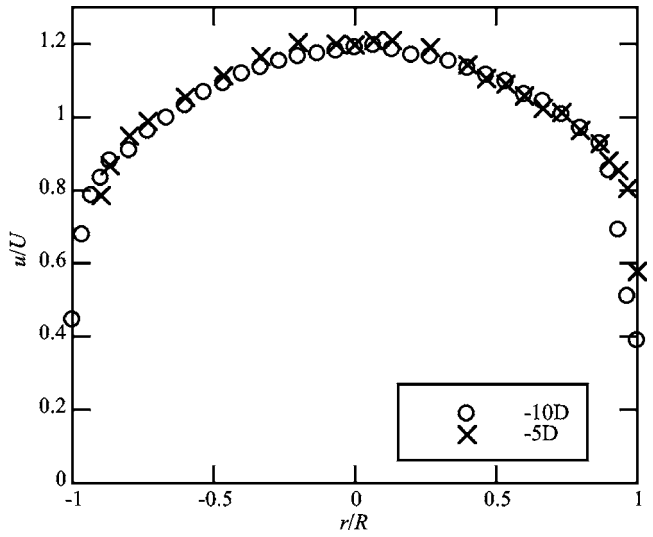

Fig. 6 Radial profiles of the normalized axial mean flow upstream of the tee junction (–10 and –5 D) at Re=35,000

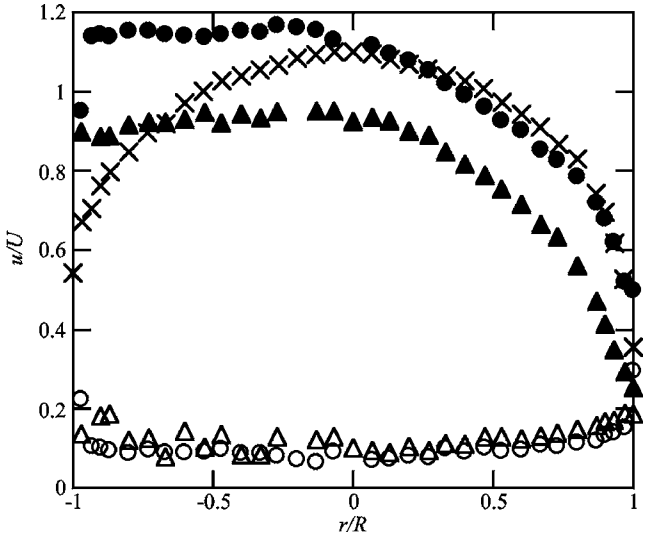

Fig. 7 Radial profiles of mean (closed symbols) and rms axial velocity (open symbols) in the bifurcation region of the sharp-edge tee: –1 D (○), –0.5 D (△); vertical cross-stream profile at –1 D (×)

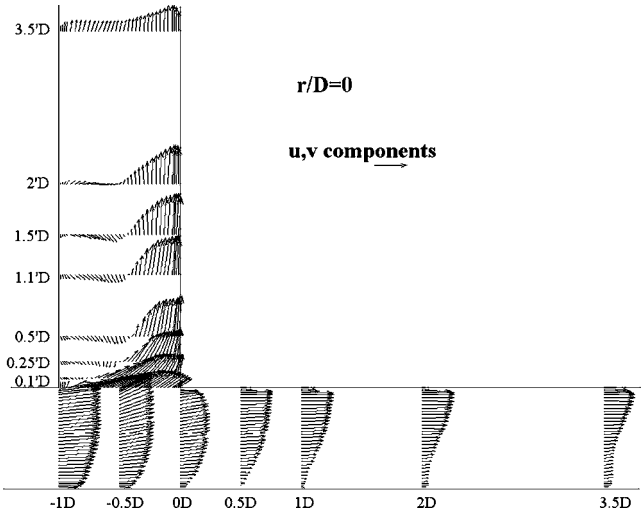

Fig. 8 Vector plot of the mean velocity in the horizontal diametric plane *x-y* of the bifurcation of the sharp-edge tee for Re=32,000 and $Q_1/Q_3=50\%$. The scale vector corresponds to $u/U=1$.

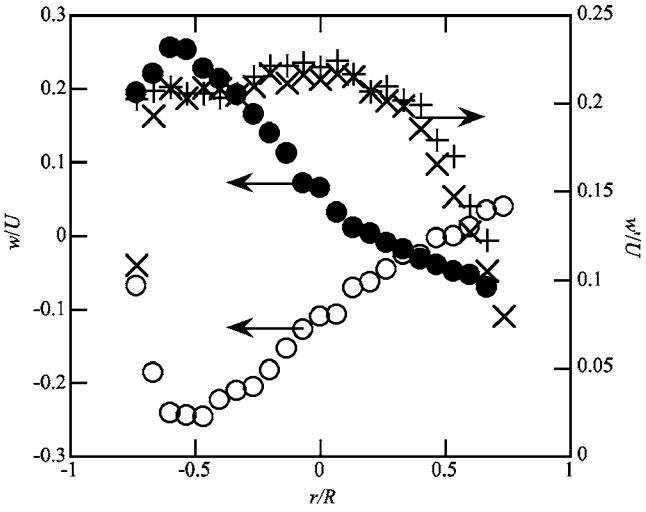

Fig. 10 "Radial" profiles of w/U (○, ●) and w'/U (×, +) measured 10 mm above (○, ×) and 10 mm below (●, +) the diametric horizontal plane at 2.0′ D for the sharp edge tee flow at Re=32,000 and $Q_1/Q_3=50\%$

well as by fluid acceleration in the front wall region ($\partial u/\partial x>0$ implies $-\overline{u'^2}\partial u/\partial x<0$ in Eq. (7)). Conversely, in the inside wall region turbulence increases for the opposite reasons. Since we cannot measure the Reynolds shear stresses in a pipe with a 1D LDA system (unless a refractive index matching technique is used), the two shear contributions to Eq. (7) could not be quantified and the above interpretation is merely qualitative, but nevertheless it is in agreement with the specialized literature [36,37].

In the outlet pipe, the profiles of rms velocities are symmetric along the vertical cross-stream direction and also show decreasing turbulence near the walls on moving downstream.

To analyze the turbulence in the branch pipe it is convenient to write down the expression for the production of the corresponding streamwise normal Reynolds stress, in Eq. (8)

$$\text{Production of } -\overline{v'^2} = -\overline{u'v'}\frac{\partial v}{\partial x} - \overline{v'^2}\frac{\partial v}{\partial y} - \overline{v'w'}\frac{\partial v}{\partial z} \qquad (8)$$

As seen in Fig. 9, there is a very strong shear layer in the center of the branch pipe, between the attached recirculating region and the jet along the downstream wall of the tee. Here, there will be production of $\overline{v'^2}$ by shear interactions (first term on the right-

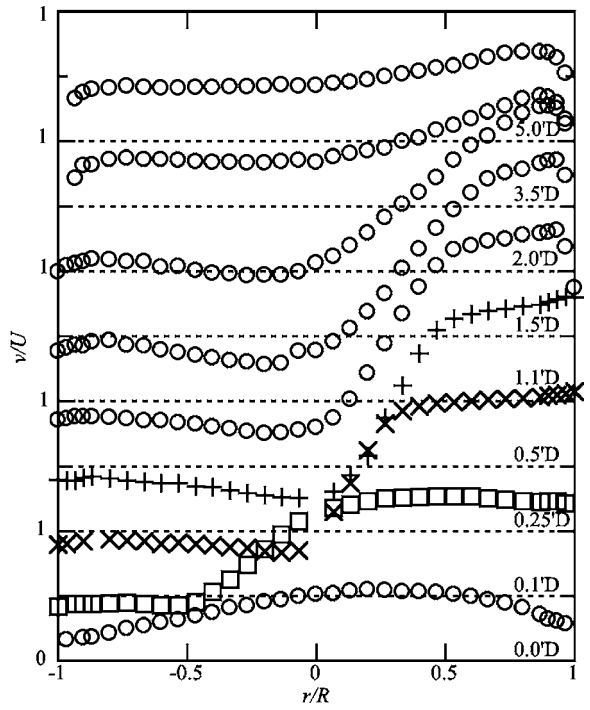

Fig. 9 Radial profiles of streamwise velocity in the branch pipe of the sharp-edge tee for Re=32,000 and $Q_1/Q_3=50\%$

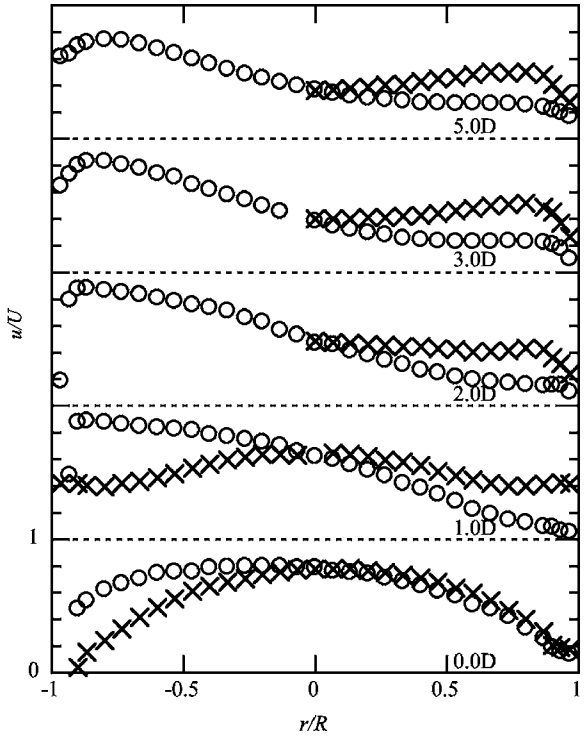

Fig. 11 Radial profiles of streamwise velocity in the outlet pipe of sharp edge tee for Re=32,000 and $Q_1/Q_3=50\%$: ○—measurements in horizontal plane; ×—measurements in vertical plane (full and half profiles)

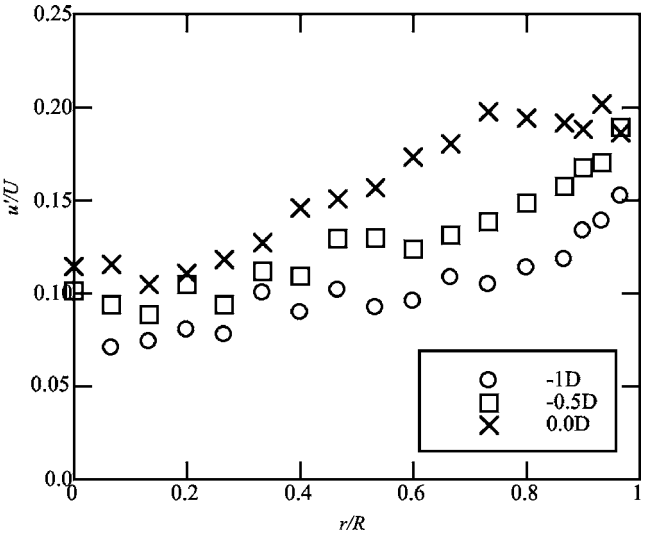

Fig. 12 Radial profiles of u'/U in the junction region of the sharp-edge tee for Re=32,000 and $Q_1/Q_3=50\%$, measured between the axis and the front wall

hand-side (RHS) of Eq. (8)) and consequently there is a maximum in the profiles of v'/U near the pipe center (at $r/R \approx -0.25$, +0.1, and +0.2 in stations $x=0.1'$ D, $0.25'$ D, $0.5'$ D, and until $1.5'$ D) shown in the horizontal radial plots in Fig. 14(*a*).

Large streamwise mean velocity gradients $\partial v/\partial y$ are found along the downstream wall of the branch pipe due to the strong wall jet (initially positive (fluid acceleration), later negative (fluid deceleration)). This will contribute to initially decrease (at $r/R \approx 1$, from stations $x=0.0'-0.5'$ D), and later increase (at $r/R \approx 1$, for stations $x \geq 1.1'$ D) the values of v' in this region via the second term on the RHS of Eq. (8). There is also an increase in turbulence within the recirculation (near the wall for $r/R<0$), but here there will also certainly be important contributions from turbulent diffusion and advection. The advective transport of turbulence into this recirculating region includes contributions of fluid from above and below the horizontal diametric plane, which has turbulence of the order of $0.2U$ (cf. w' data above/below diametric plane in Fig. 10). This level of turbulence is in excess of what is found at the early stages of the recirculation (see profiles of v' at $0.0'$ to $0.25'$ D in Fig. 14(*a*)). Further downstream, all turbulence components decrease as the flow starts to redevelop.

Horizontal radial traverses of u', not shown here for conciseness, also show the turbulence increase in the center of the branch pipe when moving from $0.0'$ to $1.1'$ D, followed by a decrease, but near the walls u' always remains low, even inside the recirculation. Vertical cross-stream profiles of v' and u' are plotted in Figs. 14(*a*) and 14(*b*), respectively, and also show well the increase in turbulence in the center of the branch pipe up to $1.1'$ D, associated with the presence of the shear layer bordering the recirculation, and its decrease on going further downstream. Note that in the branch pipe the variations of v' are more intense because this is the velocity component that is being directly produced (for fully developed flow in the branch pipe, production of $\overline{u'^2}$ is zero and this normal Reynolds stress acquires its energy via pressure strain redistribution).

3.2 Round-Edge Tee: Comparison With the Sharp Edge

3.2.1 Pressure Field Characterization. The variations of the local loss coefficients for the straigth (K_{32}) and branched pipes (K_{31}) are presented in Figs. 15 and 16 as a function of the inlet Reynolds number and flowrate ratio. The figures include data from the literature and show variations which are similar to those

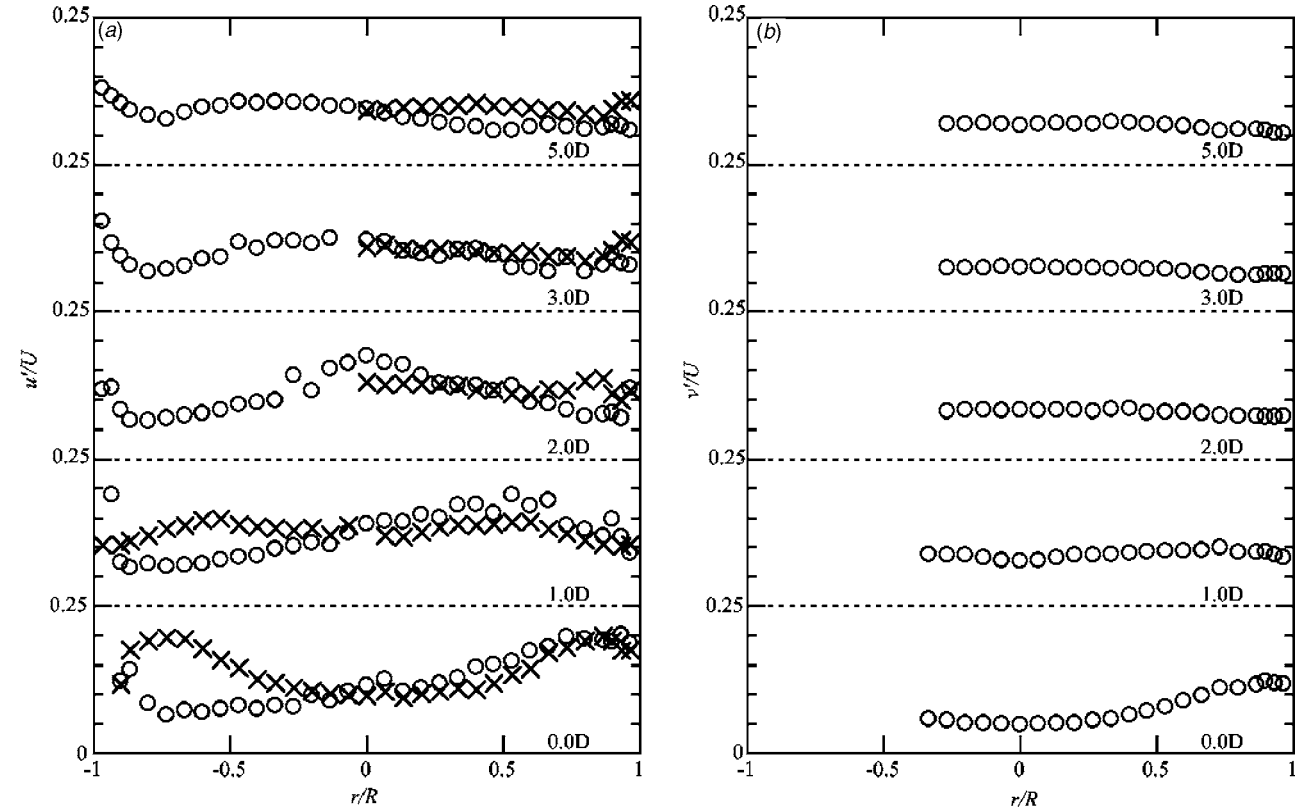

Fig. 13 Radial profiles of u'/U and v'/U in the outlet straight pipe of the sharp-edge tee for Re=32,000 and $Q_1/Q_3=50\%$. (*a*) u'/U (◯: Horizontal cross-stream profile; ×: Vertical cross-stream profile); (*b*) v'/U (vertical cross-stream profile).

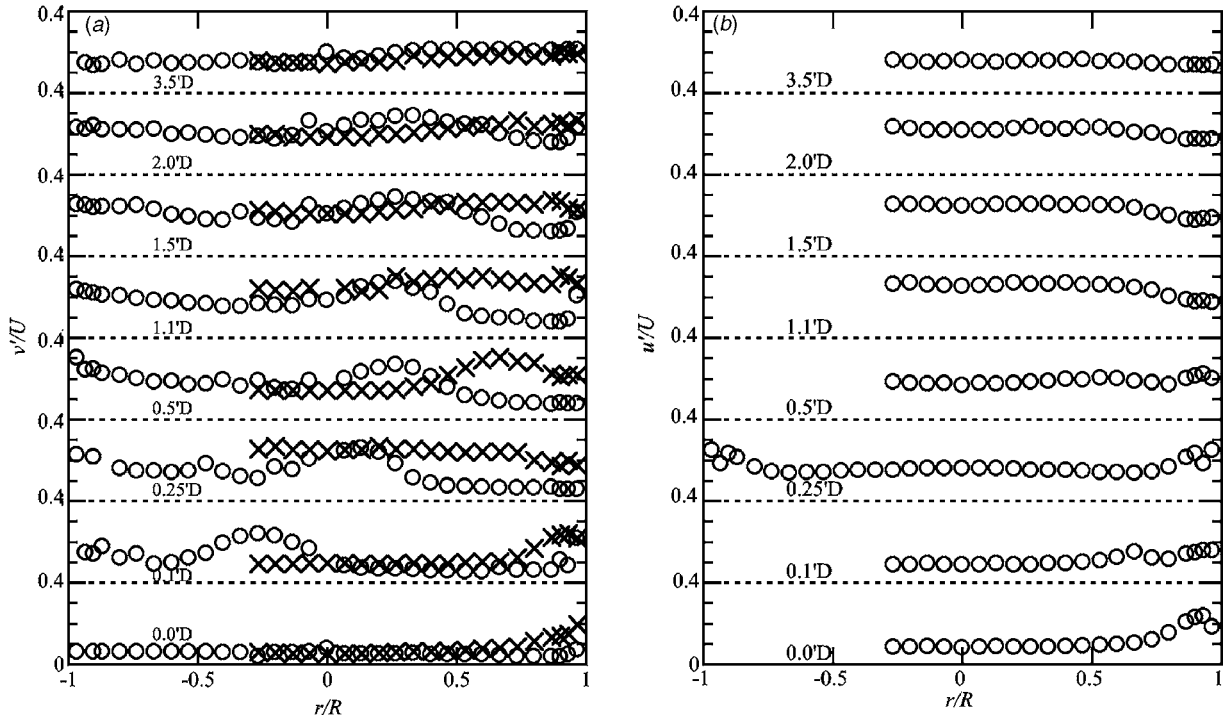

Fig. 14 Radial profiles of v'/U and u'/U in the branch pipe of the sharp-edge tee for Re=32,000 and Q_1/Q_3=50%. (*a*) v'/U (○—horizontal measurement; ×—vertical measurement); (b) u'/U (vertical cross-stream profile).

seen in Figs. 3 and 4 for the sharp edge tee, but now taking lower numerical values especially for coefficient K_{31} on account of the less severe conditions due to a round edge.

Careful inspection of these figures and direct comparison between Figs. 3 and 15 show that rounding the corner reduces the pressure loss for the branched flow especially at high flow rate ratios, i.e., when a higher proportion of fluid is forced to go through the branch pipe: For $Q_1/Q_3=1$ and Re$>$15,000 there is a reduction in K_{31} from about 1.1 to 0.9, whereas at $Q_1/Q_3=0.4$, when K_{31} goes through a minimum, the decrease is from 0.85 to about 0.75 and at $Q_1/Q_3=0.2$ the difference is even smaller. This agrees with the literature, although more pronounced effects may be found there for more rounded corners. As a matter of fact our measurements pertain to a less rounded corner than those of Maia [7], but correspond to Reynolds numbers of the same magnitude (27,000 against our 30,000) leading to higher values for the loss coefficients: At $Q_1/Q_3=0.8$ we measured $K_{31}\approx 0.8$ against a value of around 0.52 measured by Maia [7].

At low Reynolds number, the variation of K_{32} with the Reynolds number is opposite to that seen for the sharp tee: Whereas K_{32} increases with Re for the sharp tee, it decreases for the round tee. At high Reynolds numbers the straight flow is basically unperturbed by the shape of the corner and the differences in K_{32} are within experimental uncertainty, as shown by a direct comparison between Figs. 4(*b*) and 16(*b*) for Re$\approx$31,000. However, as the Reynolds number is reduced the pressure loss becomes lower for the sharp edge tee, i.e., there is no advantage in rounding the corner as far as K_{32} is concerned. This has also been seen by Maia [7] at a Reynolds number of 26,000 (with a smoother edge curvature), who also stated that the curves for K_{32} in the literature are considered universal, i.e., independent of R/D, when the Reynolds number is high.

The comparison between the round and sharp-edge tees should not be made simply by looking at individual flow paths and loss coefficients. Rounding the corner affects differently the two local loss coefficients, therefore, it is advantageous to compare the performance of both tees by looking at the total energy loss. This is achieved defining a total loss coefficient (K_D) accounting for all the energy dissipated in the tee as

$$K_D = \frac{Q_1}{Q_3}K_{31} + \frac{Q_2}{Q_3}K_{32} \tag{9}$$

For both tees, the variation of K_D with the flow rate ratio at a constant Reynolds number of around 31,000 is shown in Fig. 17 from where it becomes clear the advantage of the round-edge tee. At low flow rate ratios there is basically no difference, but for Q_1/Q_3 of around 0.4 the difference is already of 10% and rising to 20% at higher flow partitions.

3.2.2 Mean Flow Field. The general features of the mean flow are similar to those seen with the sharp edge tee, the few differences requiring a detailed inspection of the mean flow field. Starting at the bifurcation region, profiles of the stream-wise mean velocity at −1 and −0.5 D are plotted in Fig. 18; at the inside wall region the velocities are consistently higher by 5–10% than for the sharp edge tee (compare with Fig. 7), because the flow enters more easily into the branch pipe when the corner is round. Detailed inspection of the vector plot in Fig. 19 show also important differences relative to the flow in the sharp edge tee inside the branch pipe of Fig. 8: For the round tee at 1.5′ D the velocity vectors inside the recirculation are less negative whereas at 2.0′ D they are already positive, suggesting a shorter recirculation than for the sharp tee.

The radial profiles of the streamwise velocity inside the branch pipe plotted in Fig. 20 are directly comparable to those for the sharp tee in Fig. 9. They confirm that for the round tee the attached recirculation ends at around 1.5′ D (for the sharp tee that happens at around 2.0′ D), even though there is still a recirculation separated from the wall in the center of the pipe, the velocity in the downstream wall jet peaks at 1.1′ D, rather than at 1.5′ D as in the sharp tee, and the velocities within the recirculation are less negative than for the sharp tee. Flow redevelopment is also

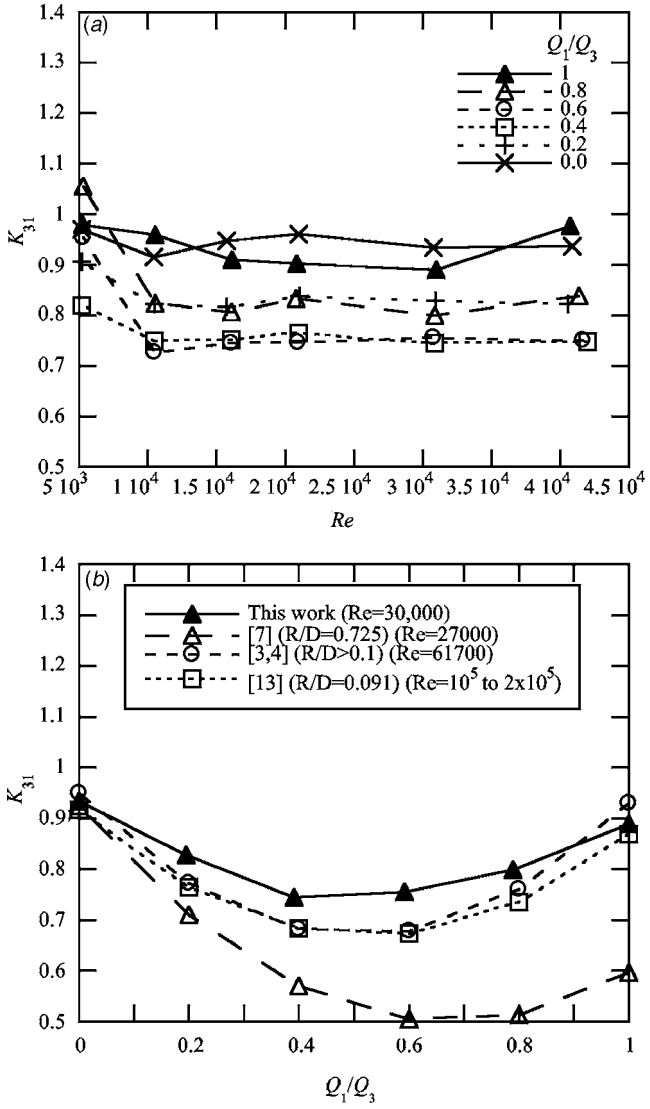

Fig. 15 Variation of the local loss coefficient K_{31} in a rounded edge (R/D=0.1) 90 deg tee: (*a*) Effect of Reynolds number and flow rate ratio; (*b*) comparison with literature

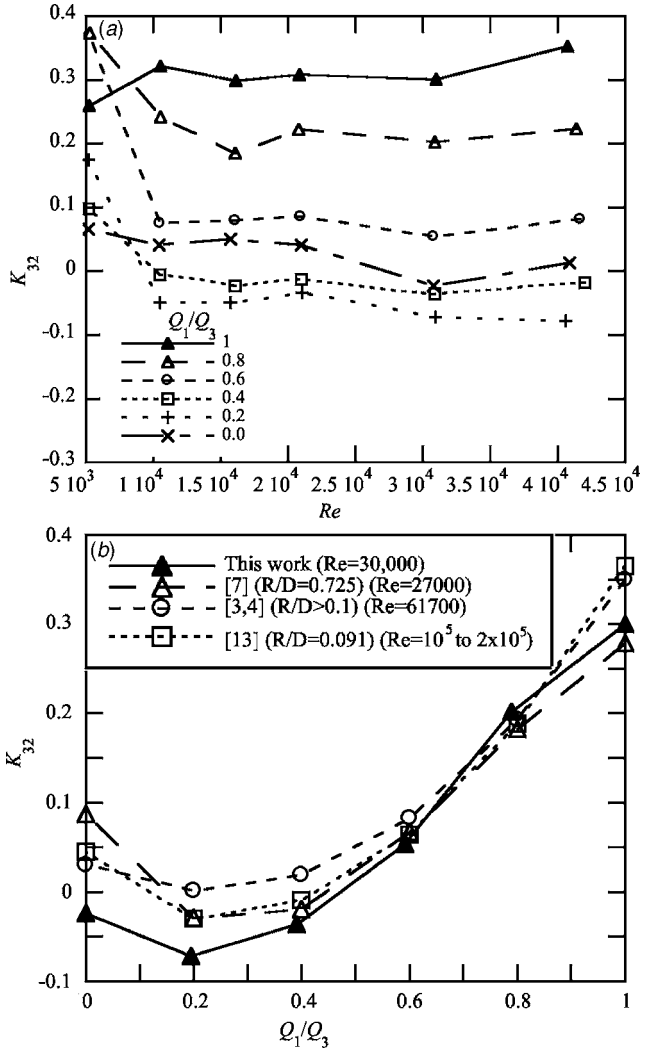

Fig. 16 Variation of the local loss coefficient K_{32} in a rounded edge (R/D=0.1) 90 deg tee: (*a*) Effect of Reynolds number and flow rate ratio; (*b*) comparison with literature

quicker with the round tee (cf. the profile at $5.0'$ D which is almost flat), i.e., the main effect of rounding the edge is to reduce the length, width, and strength of the separated flow region. A decrease in the recirculation length has also been observed in the limited experiments of Sierra-Espinosa et al. [9] in a similar flow situation, but with a different edge curvature, and these findings are consistent with the lower energy loss measured for the flow going into the branch (lower K_{31}) when the corner is rounded.

Regarding the flow in the straight outlet pipe, the radial profiles of streamline mean velocity in Fig. 21 pertain to the round-edge tee and are to be compared with the corresponding profiles for the sharp tee of Fig. 11. The velocity profiles are almost identical and differences seen in profiles of the cross-stream velocity (not shown) are within experimental uncertainty. As already mentioned, the flow is symmetric relative to the mid-plane of the tee and this is well shown in the radial profiles of streamwise velocity taken vertically and plotted as crosses in Fig. 21.

3.2.3 Turbulent Flow Field. For the round tee the profiles of u'/U and v'/U are always higher than for the sharp tee, but in varying degrees. Inside the bifurcation region the differences are insignificant since they are within experimental uncertainty. For the straight outlet pipe the turbulence data are plotted in Fig. 22

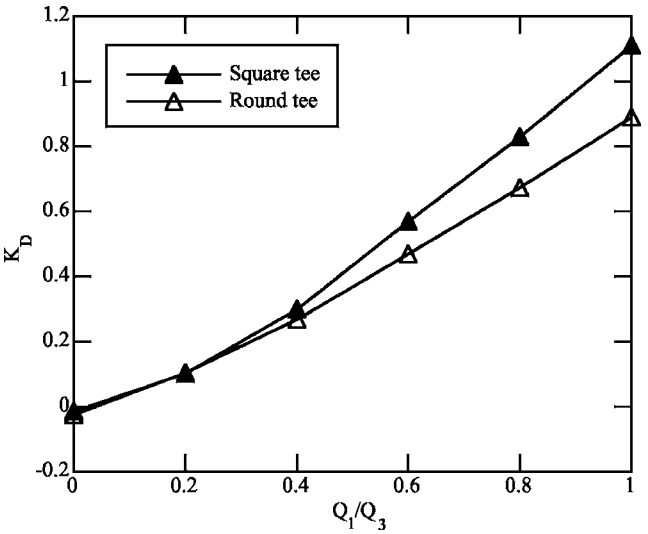

Fig. 17 Comparison between the sharp and round corner tees in terms of total energy loss for Re≈31,000

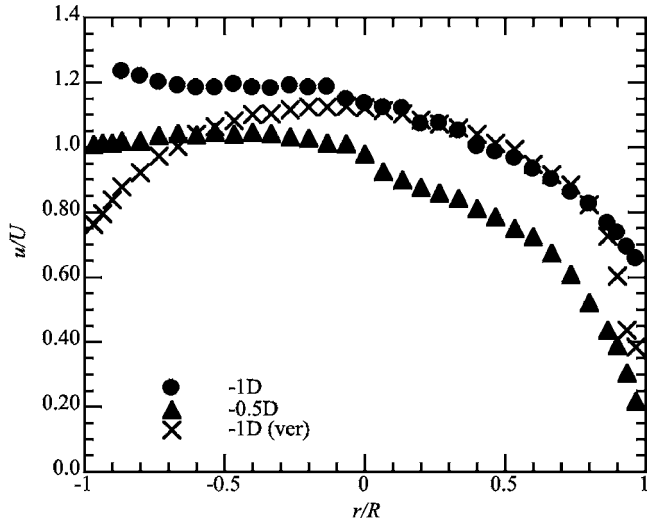

Fig. 18 Radial profiles of mean axial velocity in the bifurcation region of the round tee for Re=32,000 and Q_1/Q_3=50%: –1 D (○), –0.5 D(△); Vertical cross-stream profile at –1 D (×)

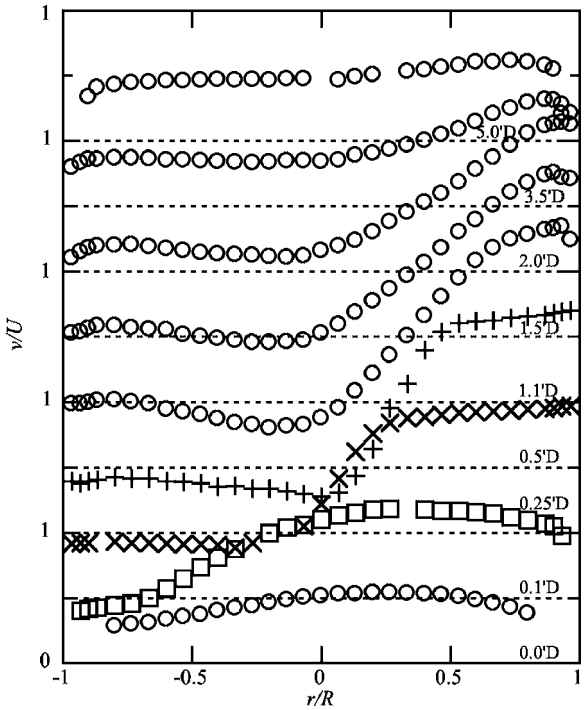

Fig. 20 Radial profiles of the longitudinal velocity in the branch pipe of the round edge tee flow for Re=32,000 and Q_1/Q_3=50%

and although the differences relative to the sharp tee data in Fig. 13 are larger than in the bifurcation region, these differences in rms velocities are too close to the measurement uncertainty and clearly insufficient to have a measurable impact on the mean flow, and by consequence on the loss coefficient K_{32} at this medium/high Reynolds number.

In the branch pipe the mean flow showed a shorter recirculation for the round edge tee and the rms velocities in Fig. 23, and their comparison with the corresponding results for the sharp tee of Fig. 14, are consistent with these findings. Looking at the turbulence profiles, and especially at the streamwise component (v'/U), the following sequence of events is observed: At the beginning of the branch pipe ($0.0'-0.5'$ D) the levels of turbulence in both the

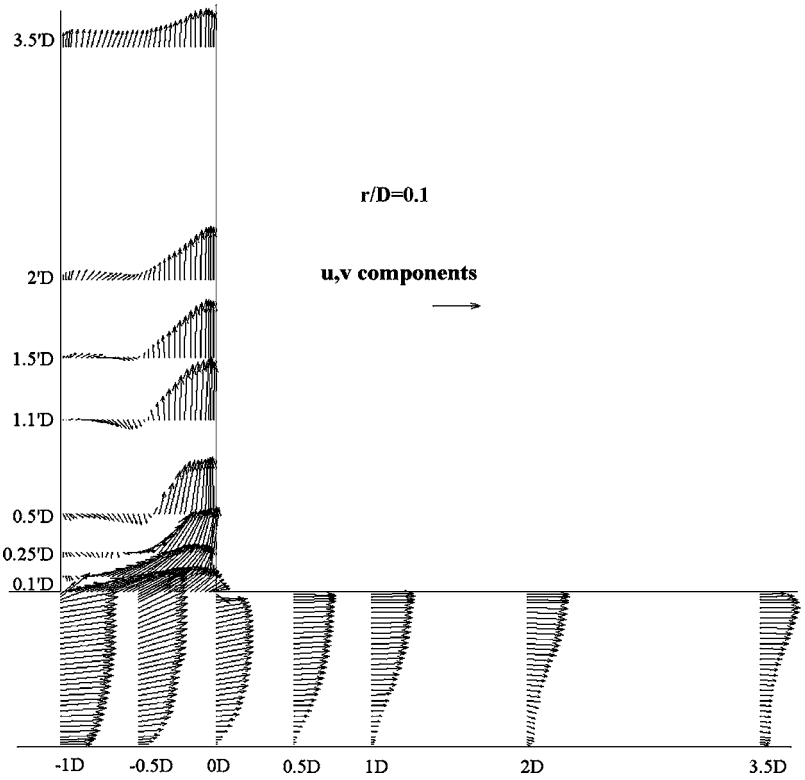

Fig. 19 Vector plot of the mean velocity in the horizontal diametric plane *x-y* of the rounded corner tee junction for Re=32,000 and Q_1/Q_3=50%. Vector scale corresponds to u/U=1.

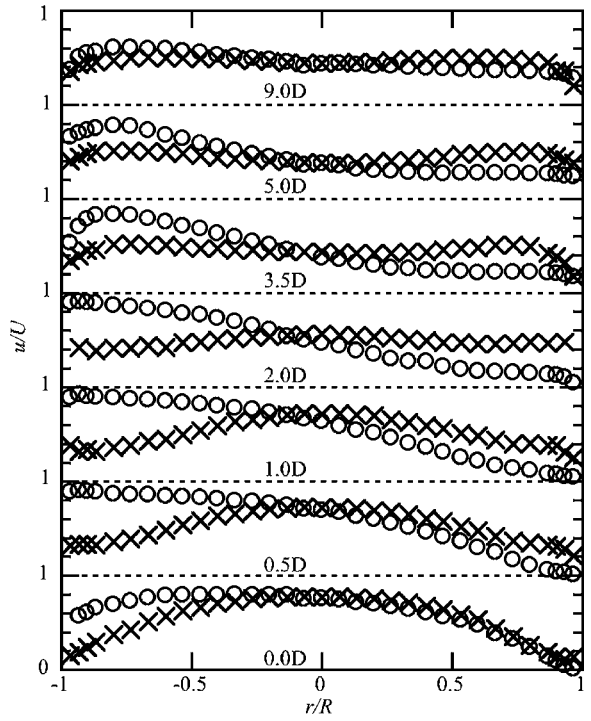

Fig. 21 Radial profiles of streamwise velocity in the outlet pipe of the round-edge tee for Re=32,000 and Q_1/Q_3=50%: ○—measurements in horizontal plane; ×—measurements in vertical plane

square and round tees are similar. At 1.1′ D the turbulence in the region $-0.5 \leqslant r/R < 1$ for the round tee is clearly higher than for the sharp tee. At this plane (1.1′ D) the peak velocities in the downstream wall jet were also seen for the round tee geometry (in Sec. 3.2.2). The higher turbulence enhances flow mixing and reduces the size of the recirculating flow, as is typical in other situations with separated flow such as in sudden expansion flows [38]. At 1.5′ D the levels of turbulence in the region $-1 < r/R \leqslant +0.5$ are similar for both geometries, but higher elsewhere for the round tee. Note that the length of the attached recirculation for the round tee is around 1.5′ D and that for the sharp tee is 2.0′ D. Henceforth, the flow along the upstream wall becomes attached for the round tee and the turbulence decreases on going downstream during flow redevelopment, whereas for the sharp tee turbulence continues to increase until 2.0′ D, when the recirculation region separates from the upstream wall. This is obvious when comparing the profiles measured at 2.0′ D, where the round tee has everywhere a lower turbulence than the sharp tee, and also further downstream at 3.5′ D.

The recirculation in the branch pipe is the main flow characteristic responsible for the dissipation of energy in the tee, hence its decrease in size and strength, due to the higher levels of turbulence in the branch pipe, has a positive effect in the reported reduction of K_{31}.

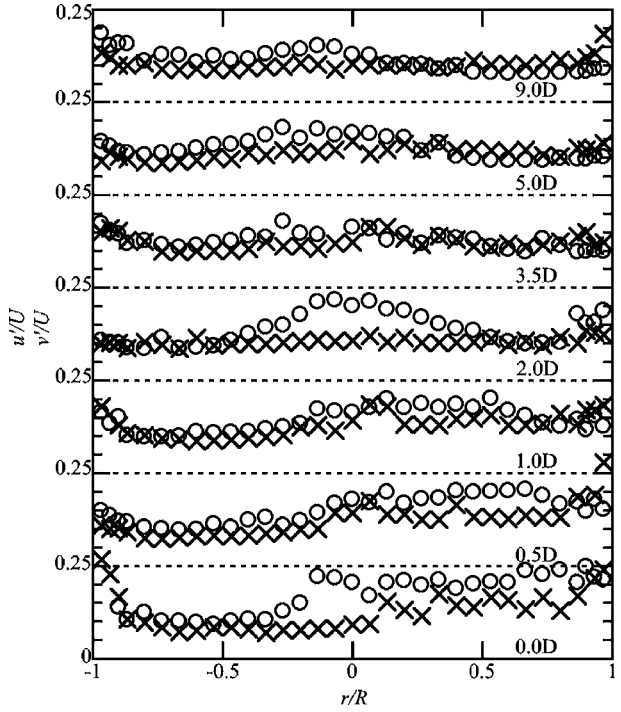

Fig. 22 Horizontal cross-stream profiles of u'/U (○) and v'/U (×) velocities in the outlet pipe of the round-edge tee for Re=32,000 and Q_1/Q_3=50%

4 Conclusions

Detailed measurements of pressure variation, mean, and turbulent velocities were carried out for the flow of water in two 90 deg tee junctions with sharp and rounded edges. The detailed mean and turbulent velocity fields were measured for a flow rate ratio of 50% and inlet Reynolds numbers of 32,000 and 30,000, respectively. In both geometries, the loss coefficient of the branched flow was higher than for the straight flow, as expected, because of flow separation in the branch pipe and the absence of separation in the main outlet duct. Rounding the edge of the junction (r/R =0.1) lead to higher turbulence in the branch pipe which resulted in a shorter, thinner, and weaker recirculation bubble region, thus reducing the loss coefficient of the branched flow.

Rounding the corner also did not affect the characteristics of the flow going into the outlet straight pipe at Re≈31,000, expressing the current behavior of common turbulent flows. Moreover, the increase in dissipation in the branched flow coefficient and in terms of the total energy loss (K_D) is enough to justify that the rounded tee is obviously more efficient for all the investigated Reynolds numbers.

Acknowledgment

The authors are grateful to JNICT who funded this work through project PBIC/C/CEG/2440/95 and are also thankful to A. Schulte who carried out some of the initial measurements and helped to set-up the rig.

Nomenclature

B_T = systematic uncertainty of variable T
D_1, D_2, D_3 = diameters of pipes 1, 2, and 3
E_T = total uncertainty of variable T
f_1, f_2, f_3 = Darcy friction factor for fully developed pipe flow in pipes 1, 2, and 3
k = turbulent kinetic energy
K_{31} = loss coefficient in tee flow from the inlet to the branch pipe, Eq. (5)
K_{32} = loss coefficient in tee flow from the inlet to the straight outlet pipe, Eq. (6)
K_D = total loss coefficient of bifurcation, Eq. (9)
L_1, L_2, L_3 = lengths of pipes 1, 2, and 3
p = pressure
P_T = precision uncertainty of variable T
Q_1, Q_2, Q_3 = flowrate in pipes 1, 2, and 3
Re = Reynolds number based on inlet pipe diameter and bulk velocity

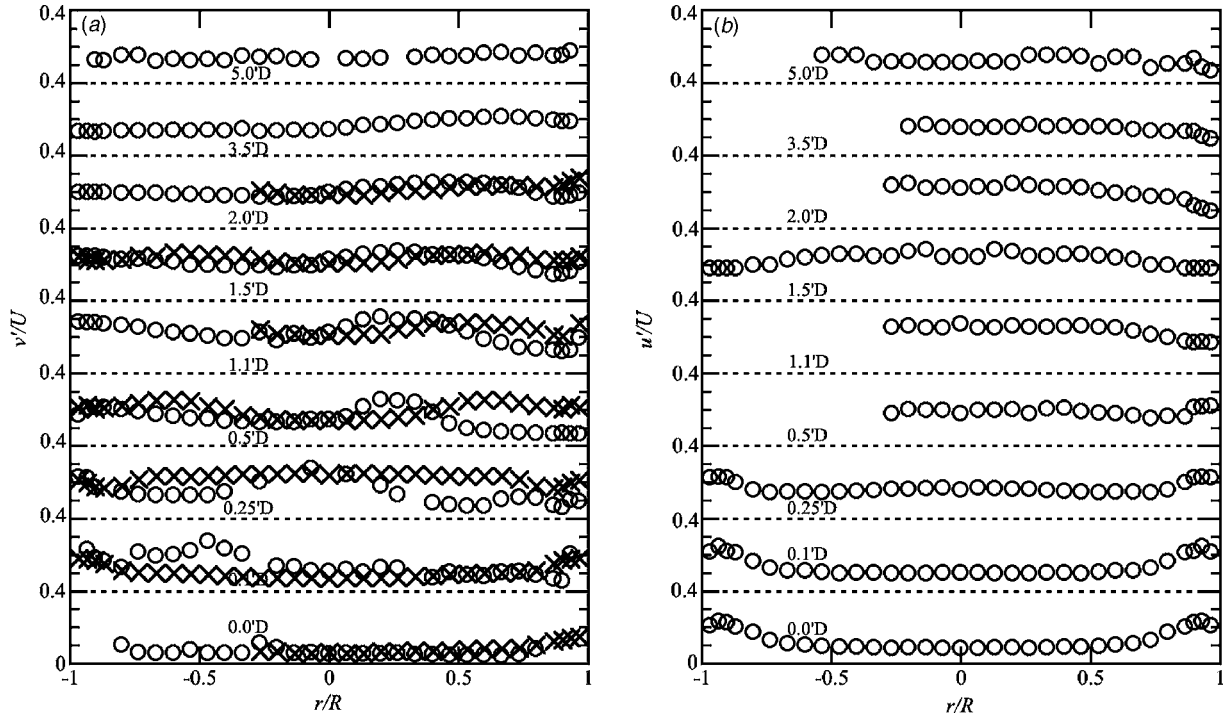

Fig. 23 Radial profiles of v'/U and u'/U in the branch pipe of the round-edge tee for Re=32,000 and Q_1/Q_3=50%. (*a*) v'/U (○—horizontal profile; ×—vertical profile); (*b*) u'/U (vertical cross-stream profile).

u = local mean (time-average) velocity in x direction (streamwise direction for inlet and straight outlet pipes and radial direction, at horizontal diametric plane, for branch pipe)

u' = local rms velocity in x direction (streamwise direction for inlet and straight outlet pipes and radial direction, at horizontal diametric plane, for branch pipe)

$\overline{u'^2}$ = normal Reynolds stress in x direction

U = bulk velocity

v = local mean (time-average) velocity in y direction (radial direction at horizontal diametric plane for the inlet and straight outlet pipes and streamwise direction for branch pipe)

v' = local rms velocity in y direction (radial direction at horizontal diametric plane for the inlet and straight outlet pipes and streamwise direction for branch pipe)

$\overline{v'^2}$ = normal Reynolds stress in y direction

w = local mean velocity in z direction

w' = local rms velocity in z direction

$\overline{w'^2}$ = normal Reynolds stress in z direction

Greek

α = energy shape factor

ϵ = rate of dissipation of k

Δp = pressure difference

ρ = fluid density

Subscripts

1 = refers to outlet branch pipe

2 = refers to outlet straight pipe

3 = refers to inlet pipe

References

[1] White, F. M., 1999, *Fluid Mechanics*, 4th ed., McGraw-Hill, New York.

[2] Vogel, G., 1926, 1928, "Investigation of the Loss in Right-Angled Pipe Branches," *Mitt. Hydraulischen Instituts der Tech. Hoschul. Munchen*, n. 1, 75-90 (1926), n. 2, 61-64 (1928) (translation by Voetsch, C. Technical Memorandum n. 299, US Bureau of Reclamation, 1932).

[3] Gardel, A., 1957, "Les Pertes de Charge Daus les Écoulements au Travers de Branchements en Té," Bull. Tech. Suisse Romande, **9**(4), pp. 123–130.

[4] Gardel, A., 1957, "Les Pertes de Charge Dansles Écoulements au Travers de Branchements en Té," Bull. Tech. Suisse Romande, **10**(5), pp. 143–148.

[5] Katz, S., 1967, "Mechanical Potencial Drops at a Fluid Branch," Trans ASME, paper 67, pp. 732–736.

[6] Iwanami, S., Suu, T., and Kato, H., 1969, "Study on Flow Characteristics in Right-Angled Pipe Fittings," Bull. Jpn. Soc. Mech. Eng., **12**(53), pp. 1041–1050.

[7] Maia, R. J., 1992, "Numerical and Experimental Investigations of the Effect of Local Losses in Piping Systems. Methods and Techniques for its Systematic Investigation. The Specific Case of the Flow in a 90 deg Tee Junction (*in Portuguese*)," PhD thesis, University of Porto, Portugal.

[8] Sierra- Espinosa, F. Z., Bates, C. J., and O'Doherty, T., 2000a, "Turbulent Flow in a 90 deg Pipe Junction. Part 1: Decay of Fluctuations Upstream the Flow Bifurcation," Comput. Fluids, **29**, pp. 197–213.

[9] Sierra- Espinosa, F. Z., Bates, C. J., and O'Doherty, T., 2000b, "Turbulent Flow in a 90 deg Pipe Junction. Part 2: Reverse Flow at the Branch Exit," Comput. Fluids, **29**, pp. 215–233.

[10] Páal, G., Maia, R., and Pinho, F. T., 2003, "Numerical Predictions of Turbulent Flow in a 90 deg Tee Junction," *Proc. 12th Int. Conf. on Modeling Fluid Flow.* Budapest, Hungary, 3–6 September, paper IFO-31, pp. 573–580.

[11] Menter, F., 1994, "Two-Equation Eddy Viscosity Turbulence Models for Engineering," AIAA J., **32**, pp. 1598–1605.

[12] Boldy, A. P., 1970, "Performance of Dividing and Combining Tees," *BHRA Technical Report 1061*.

[13] Ito, H., and Imai, K., 1973, "Energy Losses at 90 deg Pipe Junctions," *Journal of The Hydraulics Division, Proceedings of ASCE*, 99, HY9.

[14] Miller, D. S., 1986, Internal Flow Systems. *BHRA Fluid Engineering*, Cranfield, UK, 3rd ed.

[15] Katsaounis, A., Aust, E., Fürst, H. D., and Schultheiss, G. F., 1983, "Pressure Drop in Tee-Junctions with Liquids and Gas-Liquids," *Proc. 21st National Heat Transfer Conference*, Seattle, pp. 139–146.

[16] Reimann, J., and Seeger, W., 1986, "Two-Phase Flow in a Tee-Junction With a Horizontal Inlet, Part II: Pressure Differences," Int. J. Multiphase Flow, **12**, pp. 587–608.

[17] Seeger, W., Reimann, J., and Müller, U., 1985, "Phase-Separation in a T-Junction With a Horizontal Inlet," *2nd Int. Conference on multi-phase flow*, paper A2, London.

[18] Azzopardi, B. J., and Rea, S., 1999, "Modeling the Split of Horizontal Annular Flow at a T-Junction," Chem. Eng. Res. Des., **77**(A8), pp. 713–720.

[19] Azzopardi, B. J., and Rea, S., 2001, "The Split of Horizontal Stratified Flow at a Large Diameter T-Junction," Chem. Eng. Res. Des., **79**(A4), pp. 470–476.

[20] Issa, R. I., and Oliveira, P. J., 1994, "Numerical Prediction of Phase Separation in Two-Phase Flow Through T-Junctions," Comput. Fluids, **23**, pp. 347–372.

[21] Carr, R. T., and Kotha, S. L., 1995, "Separation Surfaces for Laminar Flow in Branching Tubes — Effect of Reynolds Number and Geometry," J. Biomech. Eng., **117**, pp. 442–447.
[22] Khodadadi, J. M., 1990, "Wall Pressure and Shear Stress Variations in a 90 deg Bifurcation During Pulsatile Laminar Flow," J. Fluids Eng., **113**, pp. 111–115.
[23] Moravec, S., and Liepsch, D., 1983, "Flow Investigations in a Model of a Three-Dimensional Human Artery with Newtonian and non-Newtonian Fluids— Part I," Biorheology, **20**, pp. 745–759.
[24] Rindt, C. C. M., and van Steenhoven, A. A., 1996, "Unsteady Flow in a Rigid 3D Model of the Carotid Artery Bifurcation," ASME J. Biomech. Eng., **118**, pp. 90–96.
[25] Ravensbergen, J., Krijger, J. K. B., Hillen, B., and Hoogstraten, H. W., 1995, "Merging Flows in an Arterial Confluence: The Vertebro-Basilar Junction," J. Fluid Mech., **304**, pp. 119–141.
[26] Coleman, H. W., and Steele, W. G., 1999, *Experimentation and uncertainty analysis for engineers*, 2nd ed., Wiley, New York.
[27] Costa, N. F. P., 2003, "Pressure Losses in Tee-Junctions: The 60 deg Bifurcation," (in Portuguese), MSc thesis, FEUP, University of Porto.
[28] Stieglmeier, M., and Tropea, C., 1992, "A Miniaturized, Mobile Laser-Doppler Anemometer," Appl. Opt., **31**(21), pp. 4096–4105.
[29] Albrecht, H. E., Borys, M., Damaschke, N., and Tropea, C., 2003, *Laser-Doppler and Phase-Doppler Measurement Techniques*, Springer-Verlag, Berlin.
[30] Durst, F., Melling, A., and Whitelaw, J. H., 1981, *Principles and Practice of Laser-Doppler Anemometry*, 2nd ed., Academic, London.
[31] Laufer, J., 1954, "The Structure of Turbulence in Fully Developed Pipe Flow," *National Bureau of Standards*, Report 1154.
[32] Lawn, C. J., 1971, "The Determination of the Rate of Dissipation in Turbulent Pipe Flow," J. Fluid Mech., **48**, pp. 477–505.
[33] Townes, H. W., Gow, J. L., Powe, R. E., and Weber, N., 1972, "Turbulent Flow in Smooth and Rough Pipes," J. Basic Eng., **94**, pp. 353–362.
[34] Wei, T., and Willmarth, W. W., 1989, "Reynolds Number Effects on the Structure of a Turbulent Channel Flow," J. Fluid Mech., **204**, pp. 57–95.
[35] Durst, F., Jovanovic, J., and Sender, J., 1995, "LDA Measurements in the Near Wall Region of a Turbulent Flow," J. Fluid Mech., **295**, pp. 305–335.
[36] Hinze, J. O., 1975, *Turbulence*, 2nd ed., McGraw-Hill, New York.
[37] Heitor, M. V., Taylor, A. M. K. P., and Whitelaw, J. H., 1987, "The Interaction of Turbulence and Pressure-Gradients in a Baffle-Stabilized Premixed Flame," J. Fluid Mech., **181**, pp. 387–413.
[38] Castro, O. S., and Pinho, F. T., 1995, "Turbulent Expansion Flow of Low Molecular Weight Shear—Thinning Solutions," Exp. Fluids, **20**, pp. 42–55.

Thierry M. Faure
e-mail: thierry.faure@limsi.fr

François Lusseyran
e-mail: francois.lusseyran@limsi.fr

Pierre Gougat
e-mail: gougat@limsi.fr

Laboratoire d'Informatique pour la Mécanique et les Sciences de l'Ingénieur,
Unité Propre de Recherche 3251,
Centre National de la Recherche Scientifique,
Université Pierre et Marie Curie,
Paris 6,
B.P. 133,
91403 Orsay Cedex, France

François Launay
Institut de Physique Nucléaire d'Orsay,
Unité Mixte de Recherche 8608,
Centre National de la Recherche Scientifique,
15 rue Georges Clémenceau,
91406 Orsay Cedex, France
e-mail: launayf@ipno.in2p3.fr

Experimental Investigation of the Flow Distribution Inside a Tubular Heat Exchanger

The velocity field inside a new concept of heat exchanger, which is a component of a high protons linear accelerator, is investigated experimentally in order to validate the design. A full scale facility with optical accesses is used for the measurements by particle image velocimetry. The choice of the technique is set by the three-dimensional and strongly unsteady structure of the flow. A filtering procedure is applied to the recorded images before processing the velocity field with an optical flow algorithm using dynamical programming. The distribution of the velocity between the different tubes of the heat exchanger shows a large scatter of flow rate between these tubes. In addition, the turbulence characteristics are presented. [DOI: 10.1115/1.2353277]

1 Introduction

Although a flow developing inside a rectilinear duct is well known, the understanding of the behavior of fluid motion inside a system of branching tubes is difficult. One can argue that linear and singular head losses are tabulated [1], but they are not applicable to complex tube branching and cannot give a precise description of the velocity field. However, such geometries are of interest in many applications, but there is a lack of information about them. Investigations have been conducted for Y-shape bifurcations, such as the lung bifurcations flows. This geometry is characterized by a network of repeatedly bifurcating tubes with a diameter decreasing progressively, each bifurcation is forming an angle of around 70 deg between the two downstream tubes. The Reynolds number is less than and of the order of 10,000. The first experiments were conducted with intrusive techniques, such as pressure probes and hot-wire anemometry [2,3]. Fractal-like branching channel networks were analyzed numerically with temperature effect [4]. The lung bifurcations flows are oscillatory flows, and visualizations have been carried out [5]. The issue of drops dynamics inside the lung geometry has been studied numerically using a boundary integral formulation [6]. Recent numerical simulations have also been done for a better understanding of the flow structure and particle deposits [7,8]. Extensive investigations have been conducted with laser Doppler velocimetry (LDV) and particle image velocimetry (PIV) oscillatory flows [9–12]. Another type of Y-shape bifurcation flow is the blood flow in arteries, with geometry close to that of the lung bifurcation [13]. Doppler ultrasonic velocimetry measurements and visualizations have been conducted inside the Y-shape bifurcation of a rectangular section channel with different bifurcation angles [14]. A variation of the Y-shape bifurcation is the 45 deg junction investigated for laminar inlet conditions [15]. An industrial domain of application of branching tube flows is flat plate solar energy collectors [16]. In that geometry, there is a straight-angle bifurcation, and the change in diameter between the upstream and downstream tubes generates strong singularities and recirculation regions. PIV measurements have been conducted in a 90 deg bifurcation under pulsating conditions, within a rectangular section channel [17].

The present work reports the measured flow inside a new heat exchanger design, which is a component of a high-current protons linear accelerator, for inlet flow rates in the operating range 3–15 l/min. The objective is to provide a complete set of data for understanding the fluid dynamics inside the exchanger and for future comparison to numerical simulations for a validation of the design. Its geometry is three-dimensional and combines bifurcations with an angle of 70 deg and orthogonal branching of six tubes with a change of diameter. This geometry is original, and the turbulence characteristics are helpful for understanding heat transfer. Particular attention is devoted to the comparison of the measured velocity distribution between each of the six tubes because the flow rate distribution inside the tubes is the main technological issue.

2 Experimental Setup

2.1 Hydraulic Loop. The hydraulic loop is made of a water circuit to feed the heat exchanger model (Fig. 1). A single stage radial pump rotating at a nominal speed of 2850 rpm permits the water circulation inside the closed-loop circuit. It is fed by a 30 l water tank with a bypass on the pump outlet. Downstream of the pump, there is a regulation valve and two flowmeters for the measurement of the inlet flow rate. The water goes through the heat exchanger model and comes back toward the feeding tank. Flow seeding is provided by 10 μm dia glass spheres coated with a silver film; their density is 1400 kg/m^3.

2.2 Heat Exchanger Model. The new concept of the heat exchanger for cooling the high-current protons accelerator is given in Fig. 2. It depicts a complex three-dimensional geometry

Contributed by the Fluids Engineering Division of ASME for publication in the JOURNAL OF FLUIDS ENGINEERING. Manuscript received July 7, 2005; final manuscript received May 15, 2006. Assoc. Editor: Malcolm J. Andrews.

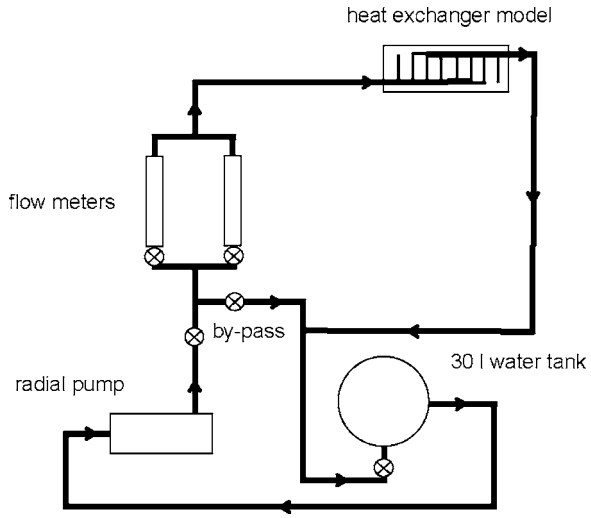

Fig. 1 Hydraulic loop

with changes in the duct diameter.

A full-scale heat exchanger model is made with aluminum and glass, this latter material permitting an easy optical access inside the central part of the tubes (Fig. 3). The heat exchanger consists of, following the flow direction: an inlet duct; an inlet collector feeding six parallel glass tubes, each one with a length of 44 mm; an outlet collector; and an outlet duct. The ducts and collectors are 8 mm dia, whereas the inside diameter of the tubes is 4 mm. The six parallel tubes and the inlet and outlet ducts are in the same plane, but the inlet collector is forming an angle of 25 deg with the parallel tubes plane, whereas the outlet collector is forming an angle of 155 deg with it. The exit of the inlet duct is located in front of tube number 2 and the entry of the outlet duct is in front of tube number 5. A stand-alone tube (on the right side of Fig. 3) with the same dimensions is placed on the model frame and can be fed by the water circuit, allowing the validation of the measurement technique on a well-known flow established inside a rectilinear channel. An additional tube (on the left of Fig. 3) contains a calibration target immersed in water for the measurement of the camera magnification.

2.3 Particle Image Velocimetry Apparatus

2.3.1 Laser Emission Device and Camera. Light emission is achieved with a laser YAG Quantel Twins Ultra, consisting of two sources emitting a 532 nm light flash with an energy of 30 mJ by pulse. Each pulse is 6 ns long. A cylindrical lens placed at the head emission end creates a light plane, which is directed toward the region of measurement by the means of a plane mirror. The image recording system consists of an 8-bit camera with 768 $\times$484 pixels, its focal depth is 25 mm. The image magnification

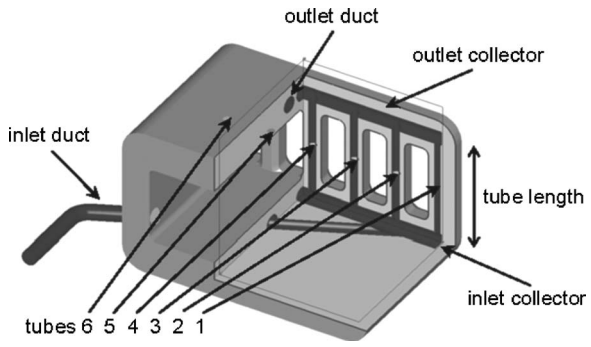

Fig. 2 View of the new heat exchanger model

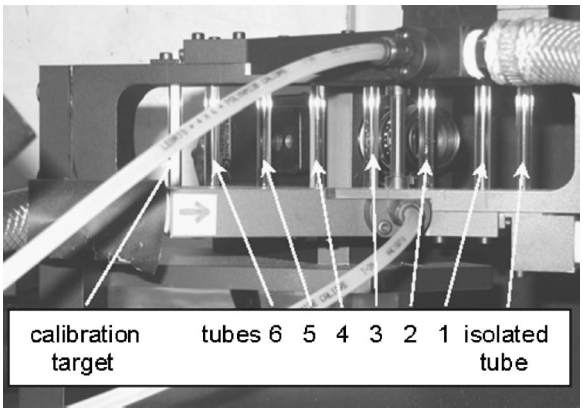

Fig. 3 Heat exchanger model

is 2.4. A Quantel DPS 01 box achieves the synchronization between laser emission and camera recording by the variation of the lag between two pulses. The laser emission head and the camera are placed on a one-axis traversing system to successively explore the flow inside each of the six tubes (Fig. 4). The axial translation accuracy is 1 μm. The laser sheet thickness is 0.25 mm and passes through the tube diameter without deviation along the tube height, forming an angle of 45 deg with the tube's alignment axis.

2.3.2 Optical Flow With Dynamical Programming. The method used for particle image displacement calculation is the optical flow using dynamical programming [18,19]. It is based on the minimization of the Minkowski L^p norm between two successive images. A division of the image in smaller and smaller slices allows the calculation of a displacement field by orthogonal iterations. The advantage of this method over other PIV methods is its ability to provide a high density field of one vector calculated by pixel, with high accuracy in the regions of strong gradient. Measurements are conducted with a mean ten pixel particle displacement between successive images. Thus, the time delay between two flashes is adjusted for the velocity inside the tube, and is varied from 84 μs to 422 μs. With this set of parameters, the measurement accuracy is 1/32 pixel, which corresponds to a relative velocity accuracy of 0.31%.

2.3.3 Image Filtering. A simple image-filtering method was developed in the course of this work and is compared to classical image-filtering techniques [20]. During the experiment setting, particular attention is devoted to laser light positioning and to the suppression of all the undesirable light reflections. However, some reflections remain in the recorded images and can alter the PIV processing (Fig. 5(*a*)). In order to eliminate these optical noise sources, it seems easy to subtract from an image with flow, an image recorded without flow where only undesirable reflections are present. But such a reference image is impossible to get straightforward because of the presence of the tracers in the flow, which modifies the background scattered light. An alternative to that issue is addressed in the average of all the recorded images with tracer images, statistically equally distributed in the measurement field. That reference image retains the undesired reflections and is well known for image subtraction in PIV measurements [21]. But this process implies a background noise estimate altered by the average of the particle traces. In addition, the average is affected by the light source variation with time. The image filtering obtained with this method is given in Fig. 5(*b*). Another classical way to obtain a reference image is to erode the initial image, which removes any isolated cluster, followed by a dilatation of the gray level. As a result, the only remaining traces are light reflections. This image can be used to filter the initial image, as it is presented in Fig. 5(*c*). To get rid of the light variation between the two sources and with time, an original and very simple method

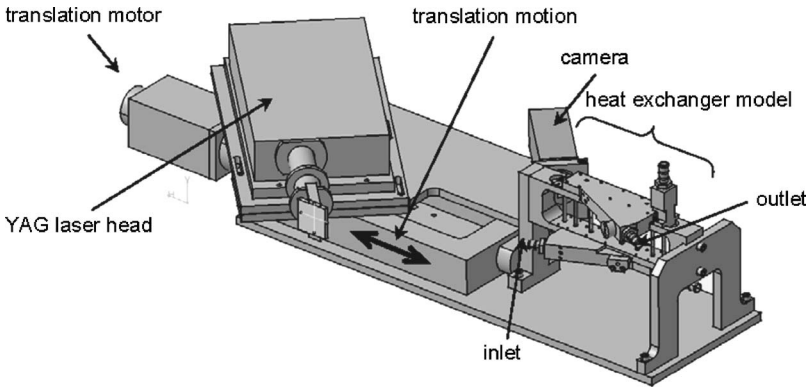

Fig. 4 Laser emission head and its translation system

has been implemented, which is compared to the previous ones. We have chosen to subtract to each image number n, the image recorded with the following flash coming from the same source, that is to say image number $n+2$ (Fig. 5(d)). It is worth noticing that almost no tracer identified on the rough image is rejected by this operation. The filtering residual can be estimated with the autocorrelation of the images. The zero correlation peak is identified on the images with any of the three filtering methods (Figs. 6(b)–6(d)), while the same peak is mixed with noise if no correction is applied (Fig. 6(a)). The cross-correlation of two successive images, without and with filtering, is given in Fig. 7. A correlation peak in zero is remaining with the method based on the erosion-dilatation (Fig. 7(c)). It is worth noting that, with the filtering by the subtraction of image n and $n+2$, as for the filtering with an averaged image, there is no residual zero displacement correlation peak, the only peak identified corresponds to the mean displacement of ten pixels. Figure 8 quantifies the improvement obtained by this processing with the histogram of the x average for the rough and filtered images (on the left) and with the cut of the cross-correlation at $\Delta y=0$ (on the right). One can observe the secondary peak at $\Delta x=0$ for the cross-correlation of the rough image, which vanishes completely on the filtered images. The only noticeable difference between the two filterings is the remaining wall tube reflections (Fig. 8, on the left, circle), which for filtering with an averaged image, is higher by a factor 2 in comparison to the filtering by subtraction of image n and $n+2$. Finally, the method based on the filtering by subtraction of image n and $n+2$ is used for this study.

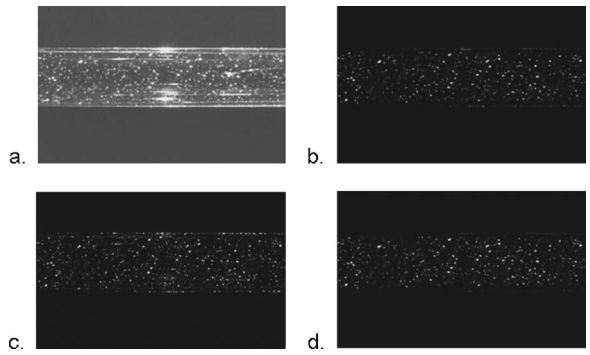

Fig. 5 Comparison between (*a*) a rough image, (*b*) an image with mean background noise subtraction, (*c*) with an eroded-dilated noise image subtraction, and (*d*) with subtraction of images *n* and *n*+2

2.3.4 Optical Deformations Correction. The optical path in the tube radial direction is modified by the presence of three media, air, glass, and water. The solution generally employed to reduce optical distortions with round tubes is to enclose the experimental setup within a rectangular water-filled box. In fact, an alternative solution was used for this study. The interfaces be-

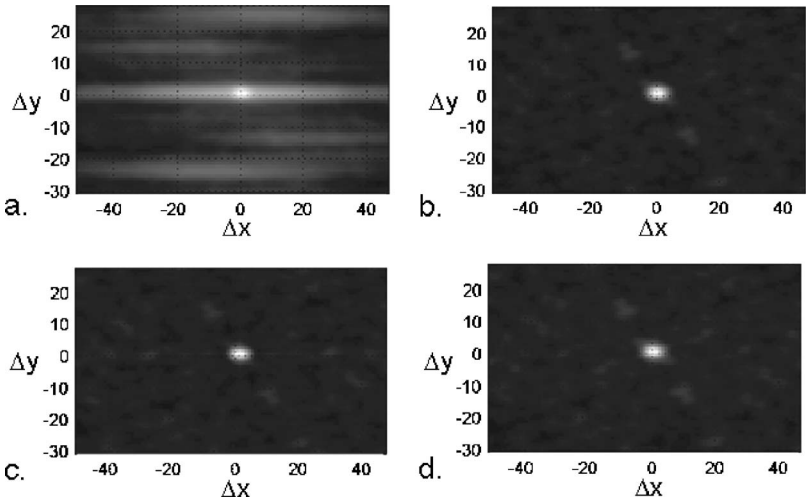

Fig. 6 Comparison between (*a*) the autocorrelation function of the rough image, (*b*) with mean background noise subtraction, (*c*) with an eroded-dilated noise image subtraction, and (*d*) with subtraction of images *n* and *n*+2

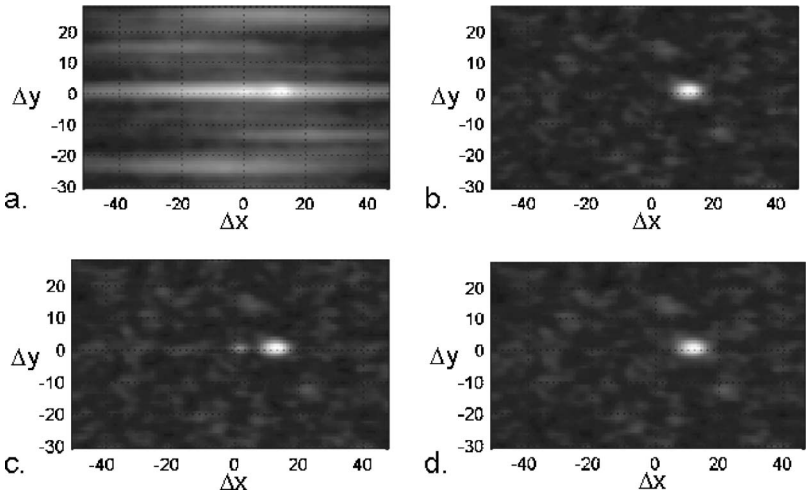

Fig. 7 Comparison between the cross-correlation function of (*a*) a couple of rough images, (*b*) with mean background noise subtraction, (*c*) with an eroded-dilated noise image subtraction, and (*d*) with subtraction of images *n* and *n*+2

tween air and glass, and between glass and water, generate light refractions and thus a deformation of the laser sheet image inside the tube and of the tracer image displacements (Fig. 9). A distance r inside the visualization plane will be observed as an apparent distance r_a inside the plane of the image of the camera, as a consequence of the angular deviations α_2, α_3, β_1, β_2.

The relationship between these two positions is obtained by solving

- Snell-Descartes equation for the interface between each medium

$$n_1 \sin \beta_1 = n_2 \sin \beta_2$$

$$n_2 \sin \alpha_2 = n_3 \sin \alpha_3$$

- The relationships of optical geometry provide the expressions for the angles α_2, α_3, β_1, β_2

$$\sin \alpha_2 = \frac{n_1}{n_2} \frac{r_a}{R_i}$$

$$\sin \alpha_3 = \frac{n_1}{n_3} \frac{r_a}{R_i}$$

$$\sin \beta_1 = \frac{r_a}{R_i + e}$$

$$\sin \beta_2 = \frac{n_1}{n_2} \frac{r_a}{R_i + e}$$

with the values of the refraction indices for air $n_1 = 1$, for glass $n_2 = 1.5$, for water $n_3 = 1.33$, and the internal tube radius $R_i = 2$ mm and its thickness $e = 1$ mm. The solution of this set of equations results in the apparent radial distance r_a as a function of the real radius r given by the expression plotted in Fig. 10

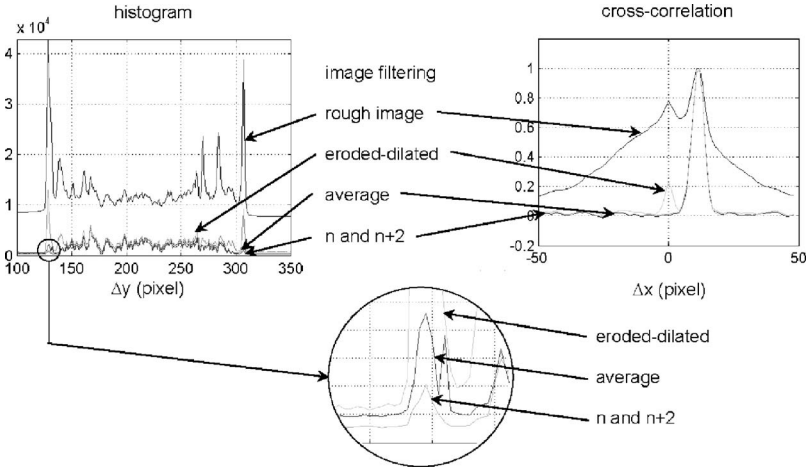

Fig. 8 Histogram of a rough image, with mean background noise subtraction and with subtraction of images *n* and *n*+2 (left) and cross-correlation at $\Delta y = 0$ for a couple of the same images (right)

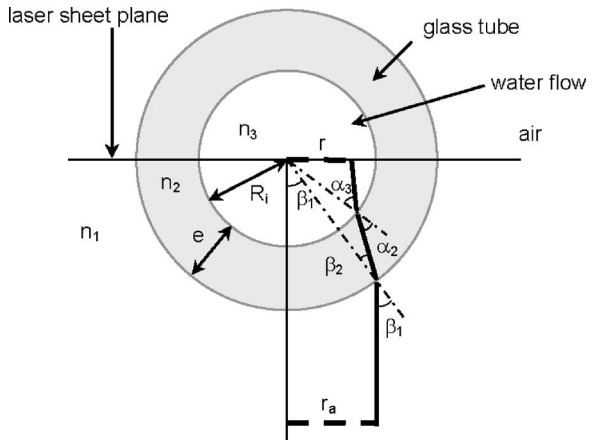

Fig. 9 Light path deformation caused by the different media

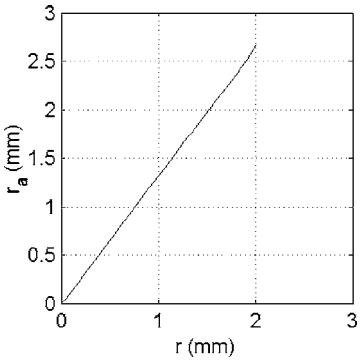

Fig. 10 Apparent radius function of the true radial position

$$r_a = r\frac{n_3}{n_1}\cos[\alpha_3 - (\beta_1 - \beta_2 + \alpha_2)]$$

This correction is taken into account for the radial positions for the measured displacements before velocity processing.

3 Results and Discussion

The flow inside the heat exchanger is investigated for flow rates between 3 l/min and 15 l/min, which correspond to inlet Reynolds numbers varying from 7960 up to 39,760. As the glass tubes are fixed in the aluminum frame and the camera positioning cannot be changed along the tube height, only the central half of the tubes length is explored in the plane of symmetry passing though the cylinder axes.

3.1 Error Analysis. We recall that PIV measurements are conducted with a mean ten pixel particle displacement between successive images. The time delay between two flashes is adjusted for the velocity inside the tube and is varied from 84 to 422 μs, according to the flow rate under consideration. With this set of parameters and the use of optical flow with dynamical programming for image displacement calculation, the measurement accuracy is 1/32 pixel, which corresponds to a relative velocity accuracy of 0.31%. The experimental results are obtained with the recording of 600 images providing 300 PIV fields for each tube. The average of these fields gives the mean velocity field inside each of the six heat exchanger tubes, with maximum statistical confidence accuracy on the mean velocity of 0.1m/s, corresponding to a maximum relative error of 2.5%. For the variances of the axial and radial velocity fluctuations and the shear stress of the axial-radial velocity fluctuations, the maximum statistical confidence accuracy is 0.015 m^2/s^2 corresponding to a maximum relative error of 5%.

3.2 Mean Flow. Mean velocity inside the measurement plane is obtained by PIV measurements. In order to analyze the flow behavior inside the six tubes, a grayscale map of the mean velocity field is provided for the central area of the tube, corresponding to the PIV camera field, with the same grayscale for each tube in Fig. 11, for the same inlet flow rate condition. The *x*-axis origin is located 11 mm downstream of the inlet collector-tube connection. We observe the axial evolution of the velocity profile. The distribution is strongly nonhomogeneous between the tubes, with a maximum velocity inside tube 2 and a minimum velocity inside tube 3. Figures 12 and 13 display the axial and radial velocity profiles inside the tubes for three axial positions of the investigated region. Inside tube 2, a strong axial velocity gradient is

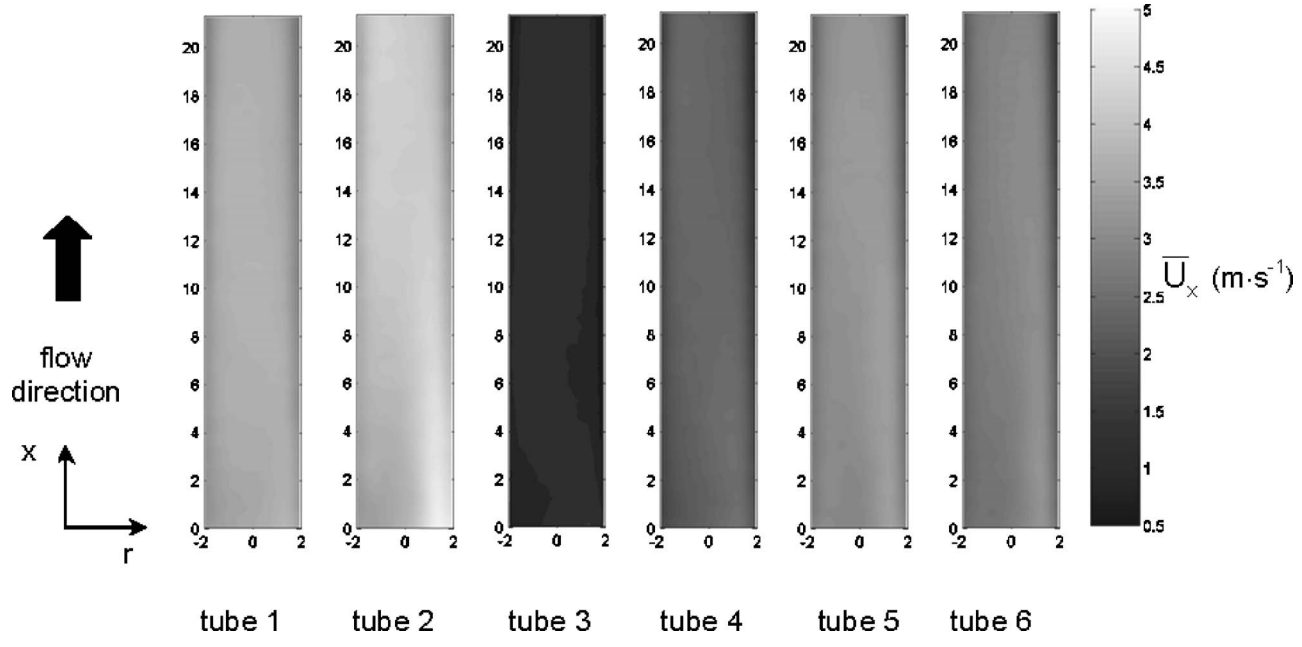

Fig. 11 Mean axial velocity distribution in the tubes for the inlet flow rate 12 l/min

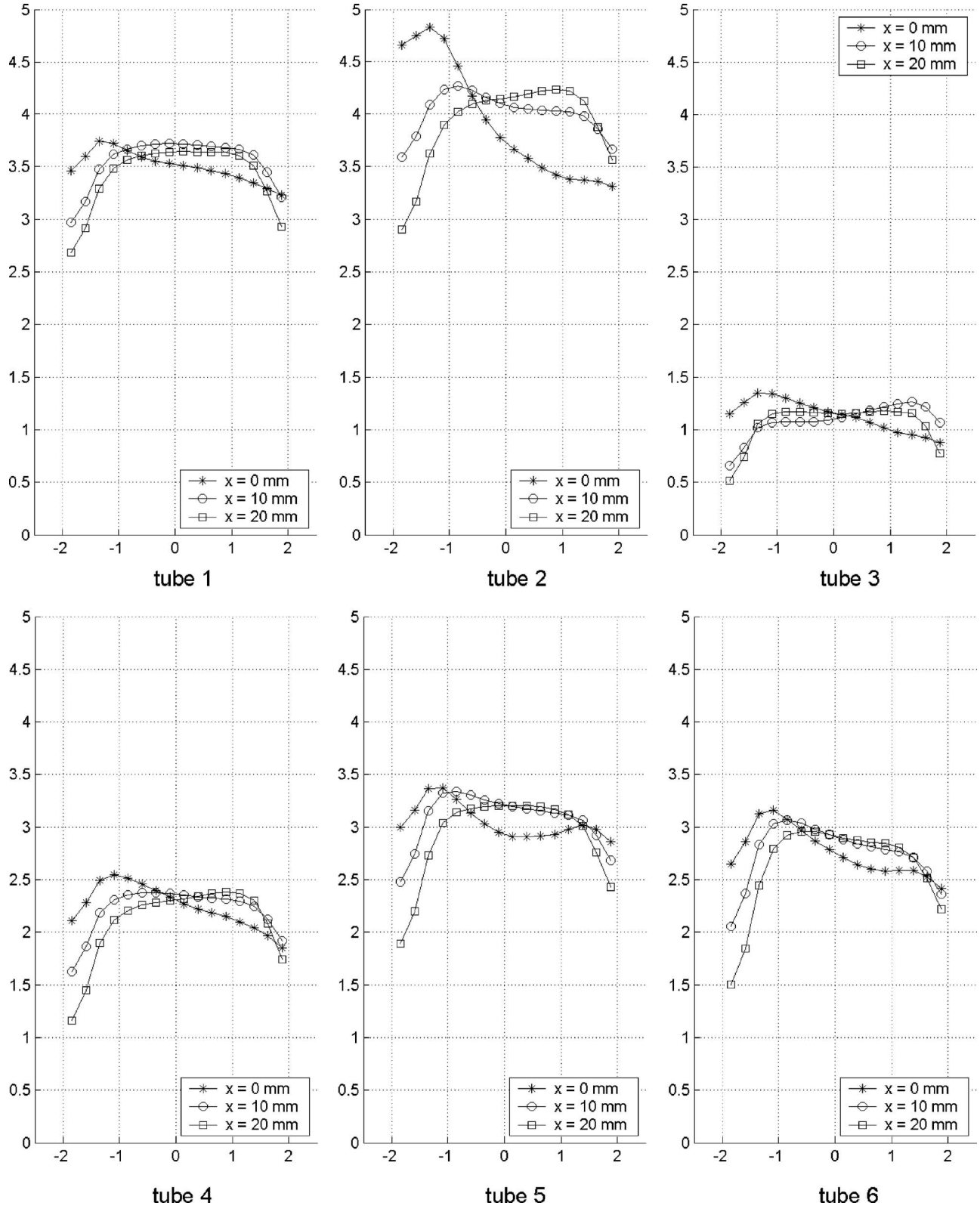

Fig. 12 Radial evolution of the axial velocity for three axial positions inside the tubes and for the inlet flow rate 12 l/min

present along a diameter for the first explored axial distance (x =0 mm). The velocity is smooth in the middle of the explored window (x=10 mm) and tends toward the inversion of the gradient for x=20 mm. This is evidence of the presence of a strongly nonestablished three-dimensional flow. The same behavior is found inside the other tubes. As the radial velocity and its gradient are small, the continuity equation yields to a strong gradient of the tangential velocity in the direction of the azimuth, which is not measured in the study. Tube 3 displays an axial velocity smaller a factor of 4 from tube 2. The radial gradient has the same shape at

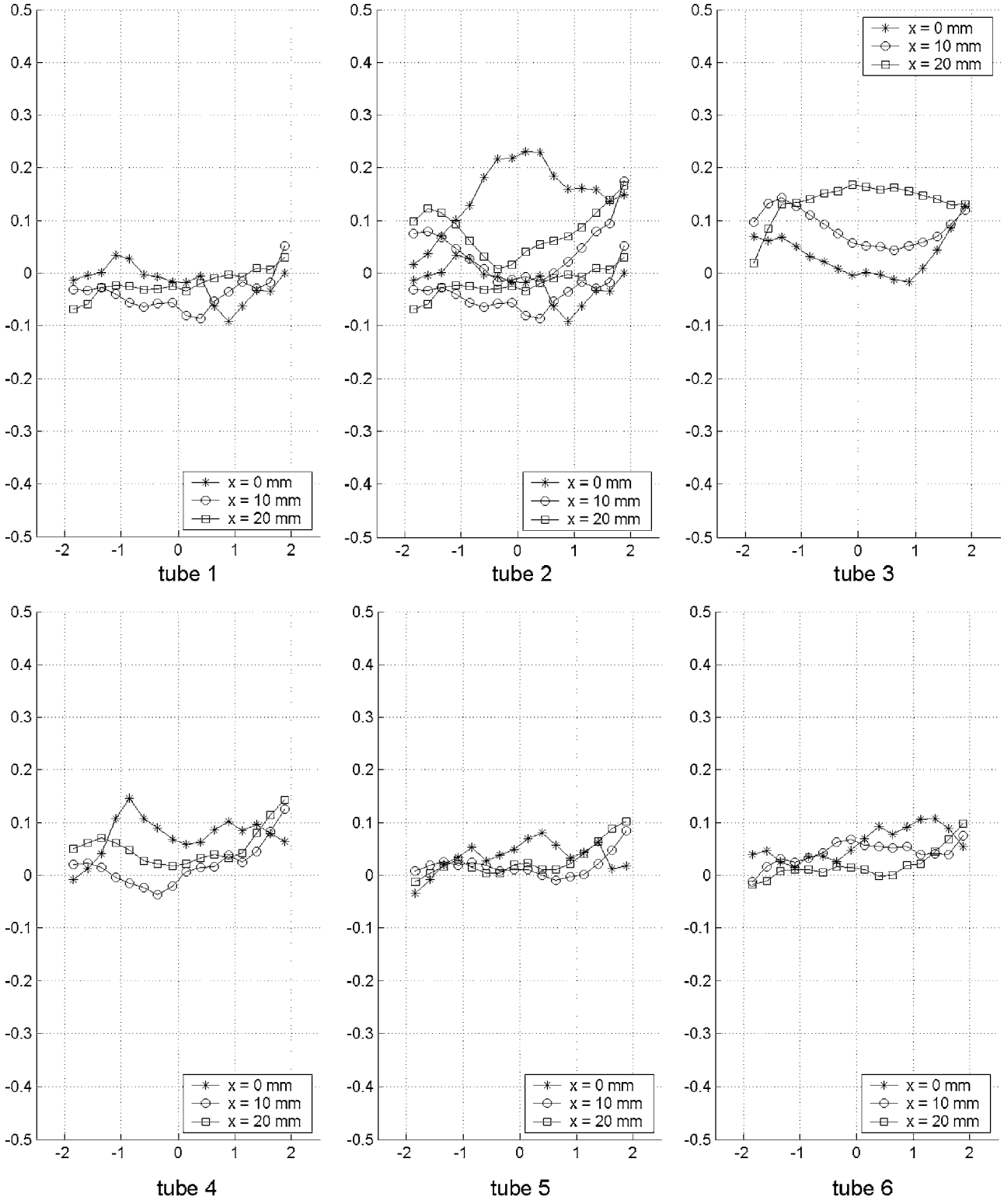

Fig. 13 Radial evolution of the radial velocity for three axial positions inside the tubes and for the inlet flow rate 12 l/min

$x=0$ mm, but is inversed for $x=10$ mm and shows an established profile for $x=20$ mm, which is consistent with the lower Reynolds number inside this tube. The radial velocity component and gradient remain low and are represented with a smaller scale in Fig. 13. The larger amplitude is found in tube 2 where the axial velocity is a maximum value. The heat transfer coefficient is proportional to the axial velocity gradient near the wall. As the axial velocity is zero on the wall, although it is not measured for this particular position, the greater the velocity inside a tube is, the larger the velocity gradient. The larger heat transfer between the fluid and the exchanger is obtained for tube 2. We observe on the axial velocity (Fig. 12) that the heat transfer is asymmetric inside each tube in the first half of the length and tends to a uniform distribution when the flow reaches an established velocity profile.

3.3 Velocity Distribution Between Tubes. The velocity is

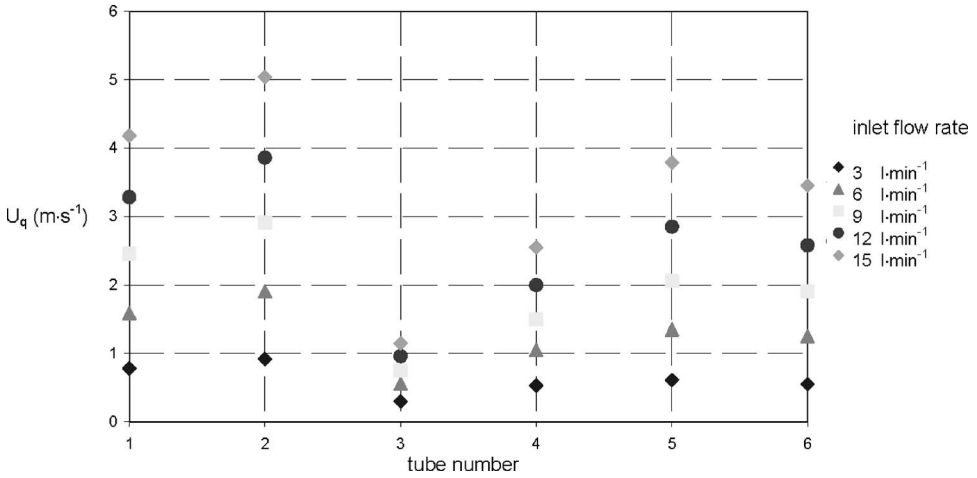

Fig. 14 Averaged reference velocity U_q distribution inside the tubes for five inlet flow rates

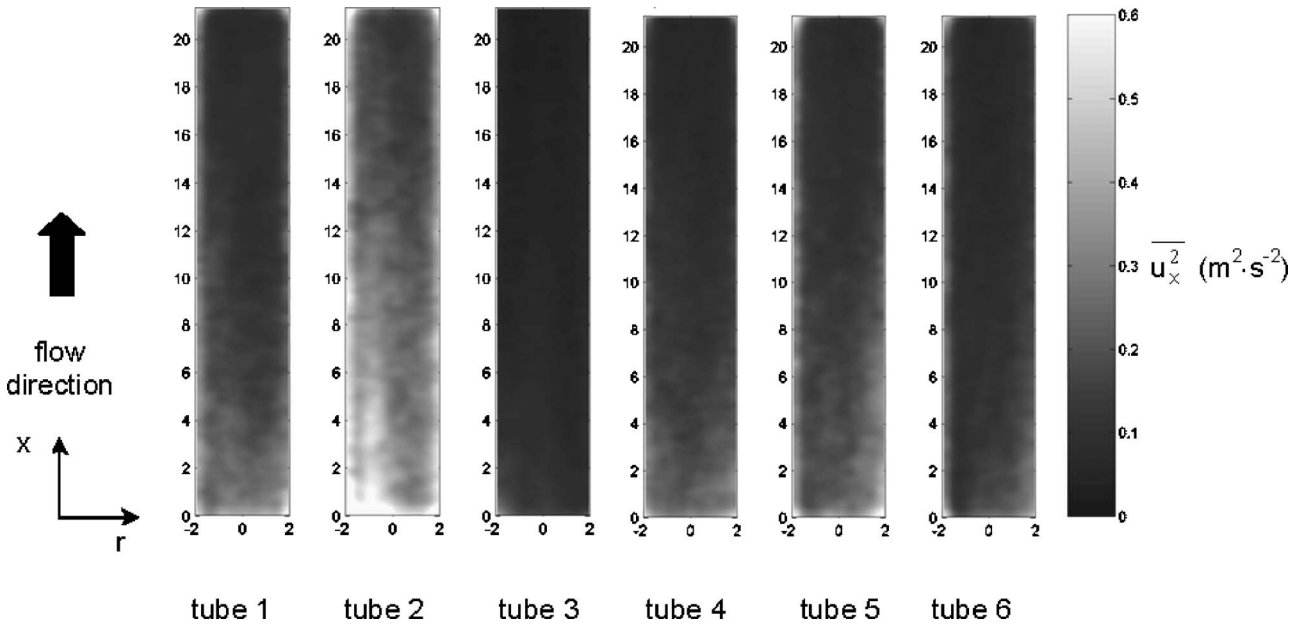

Fig. 15 Variance of the axial velocity fluctuations for the inlet flow rate 12 l/min

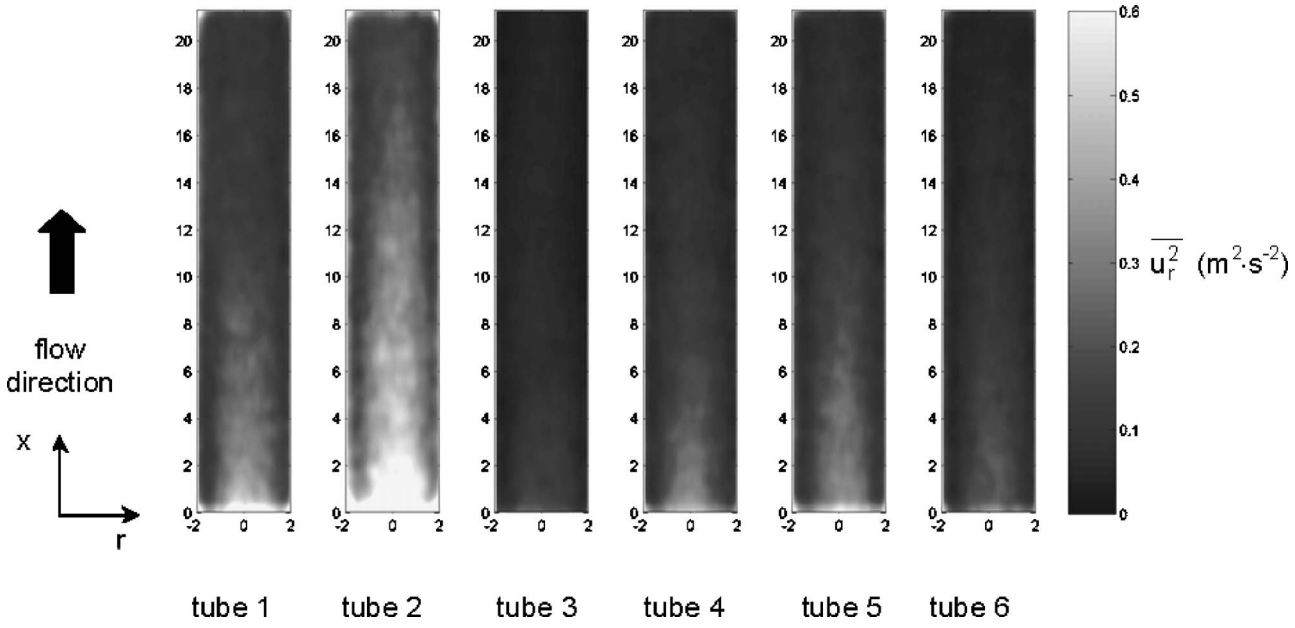

Fig. 16 Variance of the radial velocity fluctuations for the inlet flow rate 12 l/min

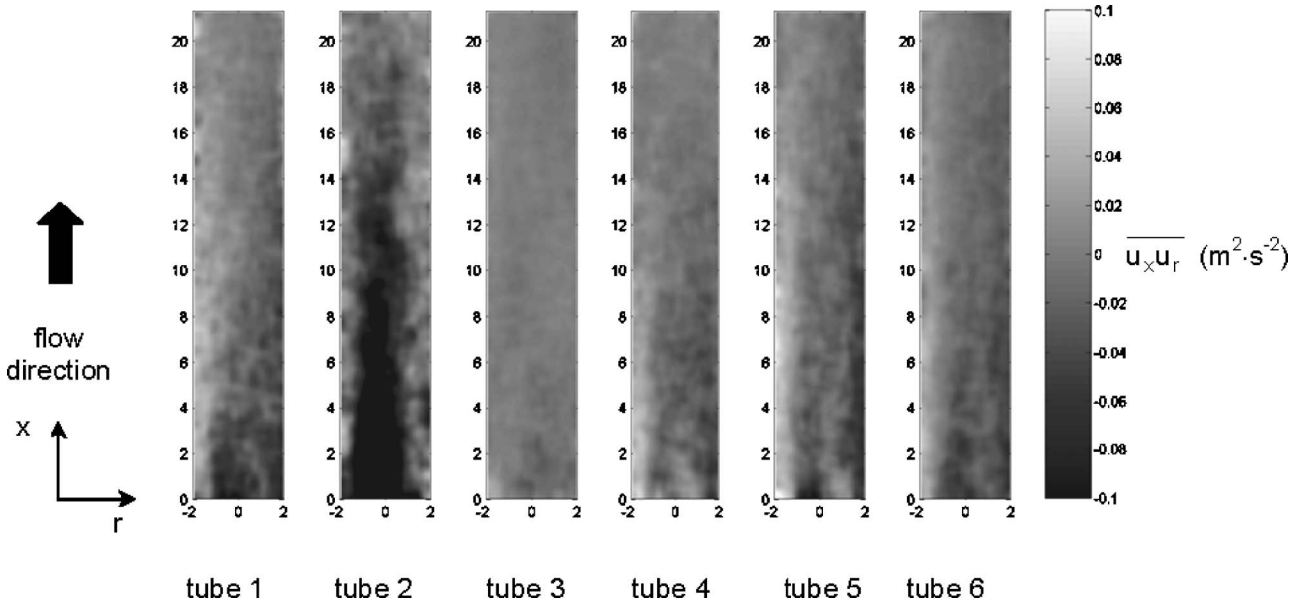

Fig. 17 Shear stress of the axial-radial velocity fluctuations for the inlet flow rate 12 l/min

averaged in the radial and axial directions and the distribution of the reference velocity U_q between the six tubes of the heat exchanger is displayed in Fig. 14, for five inlet flow rates varying from 3 l/min to 15 l/min. It has been checked that this reference velocity U_q is not far from the flow velocity through each one of the tubes by comparing the inlet flow rate measured with the flow meters to the integration of the measured velocities along the six tubes. For every inlet flow rate, the velocity distribution along the tubes shows a minimum value for tube 3 and a maximum value for tube 2, with a second local maximum value for tube 5. In fact, a careful examination of the heat exchanger geometry proves that tube 2 is in front of the junction between the inlet collector and the inlet duct and tube 5 is in front of the junction between the outlet collector and the outlet duct, which makes a traversing flow easier. This must be the reason why higher axial velocities are found inside these tubes for any flow rate.

3.4 Turbulent Flow. The statistical convergence of the second-order moments of velocity fluctuations is obtained with an estimated accuracy of 0.05 m^2/s^2 or a relative error of 0.3%. The variance of the axial velocity fluctuations (Fig. 15) shows a maximum intensity in the beginning of the investigation region and in the wall neighborhood of tube 2, which is the channel with the maximum flow rate. Note the dissymmetry of the variance of axial fluctuations with higher levels in the left part of the tube. That is the evidence of a recirculating region, which is present after the collector-tube connection and which spreads in the first third of tube 2. The turbulence is lower in the other tubes, especially inside tube 3, where the mean velocity is the lowest. Similar comments can be made for the variance of the radial velocity fluctuations (Fig. 16). The turbulence feature for the radial component is more symmetrical inside tube 2 than it is for the axial component. Figure 17 presents the axial-radial shear with higher amplitude and dissymmetry for tube 2. The large central negative region is typical of the recirculation coming from the connection between the inlet collector and tube 2. This is the evidence that the flow is highly anisotropic inside this tube.

4 Conclusion

The flow inside a heat exchanger, which is a component developed for cooling a high-current protons linear accelerator, has been investigated experimentally. A full-scale water model has been built for the study, and a PIV system has been implemented on the setup. The noise light refraction and displacement distortions inside the tubes have been corrected. Regarding the fluid dynamics inside the heat exchanger, the study focused on velocity distribution between each one of the small tubes. It is found, for the range of investigated inlet Reynolds numbers, that velocity distribution among the tubes does not depend on the flow rate. The global velocity field shows three-dimensional features. The velocity reaches a maximum value in tube 2 and a minimum value in tube 3, with a second relative maximum value in tube 5. For every inlet flow rate, the velocity ratio between tubes 2 and 3 is 4. The heat transfer coefficient is proportional to the velocity gradient near the wall, and it is asymmetric inside each tube in the first half of the length and tends to a uniform distribution when the flow is established. The larger velocity gradient inside tube 2 provides a larger heat transfer coefficient and a better heat transfer efficiency than the other tubes. The turbulent components measured show higher levels inside tube 2, which will be more efficient in terms of heat transfer.

Acknowledgment

The authors are indebted to A. Chaboche, A. Stephen, and L. Vatrinet, for building the facility, and to V. Bourdin and S. Rieublanc for the improvements brought to the hydraulic loop. They would like to thank D. Rougier, J. Bissiriex, and J. P. Baronick for the conception of the heat exchanger model.

References

[1] Idel'cik, I. E., 1986, "Memento des Pertes de Charges" (French translation from Russian) Eyrolles, Paris.
[2] Pedley, T. J., Schroter, R. C., and Sudlow, M. F., 1971, "Flow and Pressure Drop in Systems of Repeatedly Branching Tubes," J. Fluid Mech., **46**(2), pp. 365–383.
[3] Pedley, T. J., 1977, "Pulmonary Fluid Dynamics," Annu. Rev. Fluid Mech., **9**, pp. 229–274.
[4] Alharbi, A. Y., Pence, D. V., and Cullion, R. N., 2003, "Fluid Flow Through Microscale Fractal-Like Branching Channel Networks," ASME J. Fluids Eng., **125**, pp. 1051–1057.
[5] Haselton, F. R., and Scherer, P. W., 1982, "Flow Visualization of Steady Streaming in Oscillatory Flow Through a Bifurcating Tube," J. Fluid Mech., **123**, pp. 315–333.
[6] Manga, M., 1996, "Dynamics of Drops in Branched Tubes," J. Fluid Mech., **315**, pp. 105–117.
[7] Comer, J. K., Kleinstreuer, C., and Zhang, Z., 2001, "Flow Structures and Particle Deposition Patterns in Double-Bifurcation Airway Models. Part 1: Air Flow Fields," J. Fluid Mech., **435**, pp. 25–54.
[8] Zhang, Z., Kleinstreuer, C., and Kim, C. S., 2002, "Gas-Solid Two-Phase Flow

in a Triple Bifurcation Lung Airway Model," Int. J. Multiphase Flow, **28**, pp. 1021–1046.
[9] Corieri, P., 1994, "Experimental and Numerical Investigation of Flows in Bifurcations Within the Lung Airways," Ph.D. thesis, Université Libre de Bruxelles.
[10] Ramuzat, A., and Riethmuller, M. L., 2002, "Étude Expérimentale des Écoulements Oscillatoires dans un Modèle de Bifurcations Multiples Tridimensionnel," 8ème Congrès Francophone de Vélocimétrie Laser, Orsay (France), Sept. 17–20, pp. 125–130.
[11] Ramuzat, A., 2002, "Techniques de Mesures Non-invasives Appliquées aux Écoulements Biologiques: Étude des Bifurcations Pulmonaires Successives," Ph.D. thesis, von Karman Institute for Fluid Dynamics and Université Paris XII Val de Marne.
[12] Theunissen, R., Corieri, P., and Riethmuller, M. L., 2004, "Application de la PTV à la Modélisation d'Écoulements d'Aérosols dans les Voies Aériennes Pulmonaires," 9ème Congrès Francophone de Vélocimétrie Laser, Brussels (Belgium), Sept. 14–17, pp. K.5.1–K.5.9.
[13] Ku, D. N., 1997, "Blood Flow in Arteries," Annu. Rev. Fluid Mech., **29**, pp. 399–434.
[14] Rieu, R., Pelissier, R., and Farahifar, D., 1989, "An Experimental Investigation of Flow Characteristics in Bifurcation Models," Eur. J. Mech. B/Fluids, **8**(1), pp. 73–101.
[15] Ethier, C. R., Prakash, S., Steinman, D. A., Leask, R. L., Couch, G. G., and Ojha, M., 2000, "Steady Flow Separation Patterns in a 45 Degree Junction," J. Fluid Mech., **411**, pp. 1–38.
[16] Kubilay, E., 1982, "Répartition du Débit et Pertes de Charge Singulières d'un Absorbeur Solaire Tubulaire," Ph.D. thesis, Université Pierre et Marie Curie, Paris VI.
[17] Nikolaidis, N. M., and Mathioulakis, D. S., 2002, "Axial and Secondary Flow Study in a 90 deg Bifurcation Under Pulsating Conditions Using PIV," ASME J. Fluids Eng., **124**, pp. 505–511.
[18] Quénot, G. M., 1992, "The Orthogonal Algorithm for Optical Flow Detection Using Dynamic Programming," Proc. IEEE, **III**, pp. 249–252.
[19] Quénot, G. M., Pakleza, J., and Kowalewski, T. A., 1998, "Particle Image Velocimetry With Optical Flow," Exp. Fluids, **25**(3), pp. 177–189.
[20] Faure, T. M., Lusseyran, F., Gougat, P., and Launay, F., 2004, "Exploration de l'Écoulement dans un Échangeur de Chaleur Tubulaire par Vélocimétrie par Images de Particules," 9ème Congrès Francophone de Vélocimétrie Laser, Brussels (Belgium), Sept. 14–17, pp. K.4.1–K.4.8.
[21] Rémy, D., and Buisine, D., 2005, "Caractérisation à l'Aide de la Tomographie et de la PIV d'une Structure Spirale Apparaissant dans une Cavité Rotor-Stator Aspirée," Actes du Colloque FLUVISU 11, June 7–9, Ecully (France).

Thermocapillary Instabilities of Low Prandtl Number Fluid in a Laterally Heated Vertical Cylinder

B. Xu[1]
e-mail: bxu@wsu.edu

X. Ai

B. Q. Li

School of Mechanical and Materials Engineering,
Washington State University,
Pullman, WA 99164

Stabilities of surface-tension-driven convection in an open cylinder are investigated numerically. The cylinder is heated laterally through its sidewall and is cooled at free surface by radiation. A seeding crystal at constant temperature is in contact with the free surface. Axisymmetric base flow is solved using the high-order finite difference method. Three-dimensional perturbation is applied to the obtained base flow to determine the critical Marangoni numbers at which the axisymmetry is broken. The eigenvalue matrix equation is solved using linear fractional transformation with banded matrix structure taken into account. Critical Marangoni-Reynolds numbers are obtained at various boundary conditions. [DOI: 10.1115/1.2353278]

Keywords: Marangoni flow, linear stability analysis, crystal growth

1 Introduction

It is well known that convection in material processing systems causes nonuniform distribution of dopant concentration. The inhomogeneous dopant distribution can be frozen into solid state and therefore defects the crystal produced [1]. Deep understanding of instabilities of the convective flow is crucial in the production of high-quality crystal.

In most of the materials processing systems, convective flow may be induced by either buoyancy (Rayleigh-Bénard effect) or surface tension (Marangoni effect). In a terrestrial environment, both Rayleigh-Bénard effect and the Marangoni effect present and often the Marangoni convection is overshadowed by the Rayleigh-Bénard convection. However, for thin layers of fluid or in a microgravity environment, the thermocapillary effect dominates the flow. The first stability analysis of the Marangoni flow was conducted by Pearson [2]. Since then, numerous efforts have been made to understand the Marangoni convection. Reviews on the topic can be found by Levich and Krylov [3], Davis [4], and Schatz and Neitzel [5]. Most of the previous investigations were focused on thermocapillary convection in liquid layers with infinite horizontal extent. Previous investigations on thermocapillary convection in laterally bounder fluid layer are limited. For flow layers with free surface in rectangular cavities, stability analyses are given in [6–8]. In cylindrical configurations, Vrentas et al. [9] investigated the stabilities of the convective flow driven only by buoyant or thermocapillary effects. Critical Rayleigh numbers and Marangoni numbers are reported for various aspect ratios using a fluid with infinite Prandtl number. Wagner et al. [10] conducted three-dimensional (3D) numerical simulations of natural convection in an open vertical cylinder with various boundary conditions imposed at the top surface. Both two-dimensional (2D) and 3D perturbations were applied to the flow. They have shown that axisymmetric perturbation may lead to nonaxisymmetric 3D flow. Dauby et al. [11] presented a linear stability analysis of coupled Bénard-Marangoni convection in a vertical cylinder. Both insulated and conducting sidewalls are considered in their work. However, a conductive basic state was used with the conducting sidewall in their study. It is well known that when the temperature gradient is imposed parallel to the free surface, the convective flow occurs at any value of the temperature gradient and no static basic state is possible. However, when the temperature gradient is small enough, the induced convection is either one- or two-dimensional and, at certain threshold, the convection becomes three-dimensional [5]. For thermocapillary convection driven by horizontal temperature gradient, extensive experimental observations have been reported [12–15]. Hoyas et al. [16] studied the stability of a large Prandtl number fluid contained in a laterally heated cylindrical annulus. Two base flow patterns, corotating rolls and return flow pattern, were observed in their results. More recently, Sim et al. [17] conducted 3D numerical simulations of the thermocapillary convection in open cylindrical annuli. Calculations were conducted at various aspect ratios for a fluid with a Prandlt number of 6.84. It was found that the critical azimuthal wave number depends on the aspect ratio.

Instabilities of the low Prandtl number flow (liquid metals and semiconductor melts) in Czochralski crystal growth system are investigated in the present study. The crucible is heated through its sidewall at constant heat flux. A seeding crystal of constant temperature is in contact with the center part of the top surface. Between the edge of the seeding crystal and the vertical wall is the free surface. Melts in the crucible are cooled by both radiation at the free surface and conduction at the seeding crystal interface. The main objective of the present study is to determine the critical Marangoni numbers at which the thermocapillary convection loses its axisymmetry and the flow becomes 3D. Obtained information is helpful in the design of high-quality crystal growth systems in both a terrestrial environment and microgravity. A high-order finite difference method is used to solve the governing equations of axisymmetic base flow. Infinitesimal disturbance is applied to the obtained axisymmetric base flow, and linear stability analysis is carried out. The results from the present numerical model are compared to previous theoretical and numerical studies, and good agreements have been obtained. The stability analysis is carried out at various boundary conditions to reveal how the boundary conditions may affect the stability of the flow.

2 Problem Fomulation

The crucible is a vertical cylinder with height H and radius R, as shown schematically in Fig. 1. A constant heat flux q is sup-

[1]Author to whom correspondence should be addressed.

Contributed by the Fluids Engineering Division of ASME for publication in the JOURNAL OF FLUIDS ENGINEERING. Manuscript received August 7, 2005; final manuscript received March 10, 2006. Assoc. Editor: Malcolm J. Andrews.

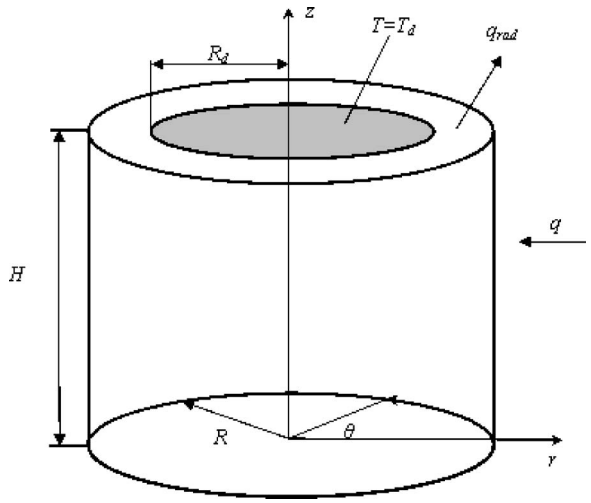

Fig. 1 Schematics of the cylinder being studied

plied to the vertical wall, and the bottom is adiabatic. The top surface is nondeformable flat free surface. A seeding crystal of radius R_d at constant temperature T_d is in contact with the top surface. At the free surface, the fluid is cooled by radiation. The cylindrical coordinate system used is also shown in Fig. 1. The melt is an incompressible Boussinesq fluid of which surface tension is only a function of temperature

$$\sigma = \sigma_0 - \gamma(T - T_0) \tag{1}$$

where σ is the surface tension, T the fluid temperature, subscript 0 denotes a reference state, and $\gamma = -d\sigma/dT$ the negative rate of change of surface tension with temperature. The melt flow inside the crucible is governed by the conservation laws of mass, momentum, and energy, of which the dimensionless governing equations are written as

$$\nabla \cdot \mathbf{u} = 0 \tag{2}$$

$$\frac{\partial \mathbf{u}}{\partial t} + (\mathbf{u} \cdot \nabla)\mathbf{u} = -\nabla p + \nabla^2 \mathbf{u} \tag{3}$$

$$\frac{\partial T}{\partial t} + (\mathbf{u} \cdot \nabla)T = \frac{1}{\mathrm{Pr}}\nabla^2 T \tag{4}$$

where $\mathbf{u}$ is the velocity vector, t the time, p the pressure, T the temperature, and $\mathrm{Pr} = \nu/\alpha$ the Prandtl number, where α is the thermal diffusivity and ν the kinematic viscosity. To obtain the dimensionless governing equations given above, the scaling factors R, ν/R, T_m, R^2/ν, and $\rho\nu^2/R^2$ are used for length, velocity, temperature, time, and pressure, respectively, where T_m is the reference temperature, α the thermal diffusivity, and ρ the density.

The governing equations (Eqs. (2)–(4)) are subject to the following boundary conditions. At the free surface ($z=H$ and $R_d < r < R$),

$$\frac{\partial u_r}{\partial z} = \mathrm{Re}_\gamma \frac{\partial T}{\partial r} \tag{5}$$

$$\frac{\partial u_\theta}{\partial z} = \mathrm{Re}_\gamma \frac{\partial T}{r\,\partial\,\theta} \tag{6}$$

$$u_z = 0 \tag{7}$$

$$\frac{\partial T}{\partial z} = -\mathrm{Rad}(T^4 - T_{\mathrm{amb}}^4) \tag{8}$$

where $\mathrm{Re}_\gamma = \gamma T_m R/\mu\nu$ is the Marangoni-Reynolds number, $\mathrm{Rad} = \delta\varepsilon T_m^3 R/\kappa$ the radiation number, and T_{amb} the temperature of ambient air, where μ is the dynamic viscosity, δ the Stefan-Boltzmann constant, ε the emissivity, and κ the thermal conductivity. At the crystal interface ($z=H$ and $0 \le r \le R_d$),

$$u_r = u_z = u_\theta = 0 \tag{9}$$

$$T = T_d \tag{10}$$

At the vertical wall ($0 \le z \le H, r=R$),

$$u_r = u_z = u_\theta = 0 \tag{11}$$

$$\frac{\partial T}{\partial r} = q \tag{12}$$

where q is the heat flux at the vertical wall. At the bottom ($z=0$, $0 \le r \le R$),

$$u_r = u_z = u_\theta = \frac{\partial T}{\partial z} = 0 \tag{13}$$

At the centerline ($0 \le z \le H, r=0$),

$$u_r = u_\theta = 0 \tag{14}$$

$$\frac{\partial u_z}{\partial r} = \frac{\partial T}{\partial r} = 0 \tag{15}$$

Note that in Eqs. (5) and (6), the surface-tension gradient induced by temperature gradient along the free surface is balanced by shear stress. Equation (7) indicates that the free surface is flat and nondeformable. The Marangoni-Reynolds number characterizes the Marangoni effect.

3 Linear Stability Analysis

The axisymmetric base flow is solved from the governing equations and the boundary conditions given in Eqs. (2)–(15) by setting the azimuthal velocity component to zero. To investigate the stability of the obtained velocity vector $(\bar{U}_r, \bar{U}_z, 0)$, pressure $\bar{P}$, and temperature $\bar{T}$, infinitesimal disturbance is applied to the base flow as

$$\begin{pmatrix} U_r \\ U_z \\ U_\theta \\ P \\ T \end{pmatrix} = \begin{pmatrix} \bar{U}_r \\ \bar{U}_z \\ 0 \\ \bar{P} \\ \bar{T} \end{pmatrix} + \begin{pmatrix} U_r' \\ U_z' \\ U_\theta' \\ P' \\ T' \end{pmatrix} \tag{16}$$

For the perturbation applied to the base flow (the last term on the right-hand side of Eq. (16)), we seek a solution of the form

$$\begin{pmatrix} U_r' \\ U_z' \\ U_\theta' \\ P' \\ T' \end{pmatrix} = \begin{pmatrix} \hat{U}_r(r,z) \\ \hat{U}_z(r,z) \\ \hat{U}_\theta(r,z) \\ \hat{P}(r,z) \\ \hat{T}(r,z) \end{pmatrix} \exp(im\theta + \varpi t) \tag{17}$$

where m is the azimuthal wave number, i the square root of -1, and ω the complex wave speed, which is given by

$$\varpi = \varpi_r + i\varpi_i \tag{18}$$

Here, ω_i is the azimuthal frequency of oscillation and ω_r the damping growth rate. According to linear stability theory, when $\omega_i=0$, the disturbance grows or decays monotonically. When $\omega_i \neq 0$, the perturbation is oscillatory with frequency of ω_i. The perturbation decays and the base flow is stable if $\omega_r<0$. When $\omega_r>0$, the perturbation grows with time and the base flow loses its axisymmetry. The neutral state is determined by $\omega_r=0$.

To carry out the stability analysis, the governing equations are rewritten with an assumption of slight compressibility as [18,19]

$$\frac{\partial p}{\partial t} + (\mathbf{u}\cdot\nabla)p + \frac{1}{\mathrm{M}}\nabla\cdot\mathbf{u} = 0 \tag{19}$$

$$\frac{\partial \mathbf{u}}{\partial t} + (\mathbf{u}\cdot\nabla)\mathbf{u} = -\frac{1}{\mathrm{M}}\nabla p + \left[\nabla^2\mathbf{u} + \frac{1}{3}\nabla(\nabla\cdot\mathbf{u})\right] \tag{20}$$

$$\frac{\partial T}{\partial t} + \mathbf{u}\cdot\nabla T = \frac{1}{\mathrm{Pr}}\nabla^2 T \tag{21}$$

Here, M is the Mach number in the fluid given by $\mathrm{M}=U/C$, where U is the flow speed and C the acoustic speed in the fluid. Substituting Eqs. (16) and (17) into Eqs. (19)–(21) and subtracting the base flow from it, we obtain the final perturbation equations as

$$\varpi\hat{P} + \hat{U}_r\frac{\partial P}{\partial r} + \hat{U}_z\frac{\partial P}{\partial z} + U_r\frac{\partial \hat{P}}{\partial r} + \frac{imU_\theta\hat{P}}{r} + U_z\frac{\partial \hat{P}}{\partial z} + \frac{1}{\mathrm{M}}\left[\frac{\hat{U}_r}{r} + \frac{\partial \hat{U}_r}{\partial r} + \frac{im\hat{U}_\theta}{r} + \frac{\partial \hat{U}_z}{\partial z}\right] = 0 \tag{22}$$

$$\varpi\hat{U}_r + U_r\frac{\partial \hat{U}_r}{\partial r} + \hat{U}_r\frac{\partial U_r}{\partial r} + U_z\frac{\partial \hat{U}_r}{\partial z} + \hat{U}_z\frac{\partial U_r}{\partial z} + \frac{imU_\theta\hat{U}_r}{r} - \frac{2\hat{U}_\theta U_\theta}{r} = -\frac{1}{\mathrm{M}}\frac{\partial \hat{P}}{\partial r} + \frac{4}{3}\frac{\partial^2\hat{U}_r}{\partial r^2} + \frac{\partial^2\hat{U}_r}{\partial z^2} - \left(\frac{\delta^2}{r^2} + \frac{4}{3r^2}\right)\hat{U}_r + \frac{im}{3r}\frac{\partial \hat{U}_\theta}{\partial r} + \frac{1}{3}\frac{\partial^2\hat{U}_z}{\partial r\,\partial z} - \frac{7im}{3r^2}\hat{U}_\theta + \frac{4}{3r}\frac{\partial \hat{U}_r}{\partial r} \tag{23}$$

$$\varpi\hat{U}_z + U_r\frac{\partial \hat{U}_z}{\partial r} + \hat{U}_r\frac{\partial U_z}{\partial r} + U_z\frac{\partial \hat{U}_z}{\partial z} + \hat{U}_z\frac{\partial U_z}{\partial z} + \frac{imU_\theta}{r}\hat{U}_z = -\frac{1}{\mathrm{M}}\frac{\partial \hat{P}}{\partial z} + \frac{\partial^2\hat{U}_z}{\partial r^2} + \frac{4}{3}\frac{\partial^2\hat{U}_z}{\partial z^2} + \frac{1}{3}\frac{\partial^2\hat{U}_r}{\partial r\,\partial z} + \frac{im}{3r}\frac{\partial \hat{U}_\theta}{\partial z} + \frac{1}{r}\frac{\partial \hat{U}_z}{\partial r} + \frac{1}{3r}\frac{\partial \hat{U}_r}{\partial z} - \frac{m^2}{r^2}\hat{U}_z \tag{24}$$

$$\varpi\hat{U}_\theta + U_r\frac{\partial \hat{U}_\theta}{\partial r} + \hat{U}_r\frac{\partial U_\theta}{\partial r} + U_z\frac{\partial \hat{U}_\theta}{\partial z} + \hat{U}_z\frac{\partial U_\theta}{\partial r} + im\frac{U_\theta}{r}\hat{U}_\theta + \frac{U_r\hat{U}_\theta + \hat{U}_rU_\theta}{r} = -\frac{im}{r\mathrm{M}}\hat{P} + \frac{\partial^2\hat{U}_\theta}{\partial r^2} + \frac{\partial^2\hat{U}_\theta}{\partial z^2} + \frac{im}{3r}\frac{\partial \hat{U}_r}{\partial r} + \frac{im}{3r}\frac{\partial \hat{U}_z}{\partial z} + \frac{1}{r}\frac{\partial \hat{U}_\theta}{\partial r} + \frac{7im}{3r^2}\hat{U}_r - \frac{1}{r^2}\left(\frac{4m^2}{3}+1\right)\hat{U}_\theta \tag{25}$$

$$\varpi\hat{T} + U_r\frac{\partial \hat{T}}{\partial r} + \hat{U}_r\frac{\partial T}{\partial r} + U_z\frac{\partial \hat{T}}{\partial z} + \hat{U}_z\frac{\partial T}{\partial r} + \frac{imU_\theta\hat{T}}{r} = \frac{1}{\mathrm{Pr}}\left[\frac{\partial^2\hat{T}}{\partial r^2} + \frac{\partial^2\hat{T}}{\partial z^2} + \frac{1}{r}\frac{\partial \hat{T}}{\partial r} - \frac{m^2}{r^2}\hat{T}\right] \tag{26}$$

It is noted that in order to obtain the final perturbation equations, the base flow was solved using the governing equations with slight compressibility assumption (Eqs. (19)–(21)).

The following boundary conditions are applied to the perturbation equations (Eqs. (22)–(26)) to close the problem. At free surface ($z=H$ and $R_d<r<R$),

$$\frac{\partial \hat{U}_r}{\partial z} = \mathrm{Re}_\gamma\frac{\partial \hat{T}}{\partial r} \tag{27}$$

$$\frac{\partial \hat{U}_\theta}{\partial z} = \mathrm{Re}_\gamma\frac{im\hat{T}}{r} \tag{28}$$

$$\hat{U}_z = 0 \tag{29}$$

$$\frac{\partial \hat{T}}{\partial z} = -4\,\mathrm{Rad}\,T^3\hat{T} \tag{30}$$

At the crystal interface ($z=H$ and $0\le r\le R_d$),

$$\hat{U}_r = \hat{U}_z = \hat{U}_\theta = \hat{T} = 0 \tag{31}$$

At the vertical wall ($0\le z\le H, r=R$) and the bottom ($z=0$, $0\le r\le R_d$),

$$\hat{U}_r = \hat{U}_z = \hat{U}_\theta = \frac{\partial \hat{T}}{\partial z} = 0 \tag{32}$$

At the centerline ($0\le z\le H, r=0$),

$$\hat{U}_r = \hat{U}_\theta = 0 \tag{33}$$

$$\frac{\partial \hat{U}_z}{\partial r} = \frac{\partial \hat{T}}{\partial r} = 0 \tag{34}$$

4 Numerical Scheme

Details on the numerical schemes used in the present study are given by Ai [20]; hence, only a brief description is presented here. The base flow is solved using a high-order finite difference method because of its spectral-like accuracy, computational efficiency, and outstanding flexibility in dealing with irregular geometry and various boundary conditions. The spatial derivatives are discretized by the compact method. In the present model, the high-order finite difference model is developed using compact central difference scheme, which has a fourth-order accuracy in the approximations of both the first- and second-order spatial derivatives. The fourth-order compact approximation derived by means of five-point Legendre interpolation is adopted here.

In the present numerical model, time integration for the axisymmetric base flow is carried out by using the method of the combined Runge-Kutta and fractional step, as presented by Le and Moin [21]. The method is based on the predictor-corrector algorithm, which is one of the Runge-Kutta methods. In this method, each time step is divided into three substeps. At each substep, the KM time-splitting scheme developed by Kim and Moin [22] is used along with the staggered mesh to handle the pressure term.

Using the compact high-order finite difference method, Eqs. (22)–(26), along with the boundary conditions given by Eqs. (27)–(34), are discretized, and the final equation is written in the form of an eigenvalue matrix equation,

$$\mathbf{AX} = \omega\mathbf{BX} \tag{35}$$

where $\mathbf{A}$ and $\mathbf{B}$ are coefficient matrices, $\mathbf{X}=\{\hat{u}_r,\hat{u}_z,\hat{u}_\theta,\hat{T},\hat{p}\}^T$ is an assembling vector of the eigenfunction. This matrix equation is solved by linear fractional transformation with a banded matrix structure taken into account using the LAPACK library. The obtained leading eigenvalue determines the stability of the axisymmetric base flow.

It is noted that the flux boundary condition at the vertical wall may introduce a vorticity singularity occuring at the free surface-

Table 1 Comparison of critical Marangoni numbers at various azimuthal wave numbers between our results and those from Dauby et al. [11]

m	Our model	Dauby et al. [11]
0	169	163.57
1	122	109.08
2	162	160.15
3	261	257.86

solid boundaries interface [23]. However, Chénier et al. have found that for the finite difference method used in the present model automatically regularize the singularity [24]. In other words, the numerical solution converges as the mesh is refined.

5 Results and Discussions

The presented numerical model is validated against previous theoretic and numerical studies. Consider a horizontal layer of fluid confined by a vertical cylindrical wall. The bottom surfaces of the liquid layer are in contact with rigid surface that is kept at constant temperature of 1. The sidewall is adiabatic. All rigid walls are no-slip. The top surface is a free surface cooled by ambient air according to Newton's cooling law. The effect of the buoyancy is ignored ($\mathrm{Ra}=\rho g\beta\Delta T/\mu\kappa=0$) and it is assumed that the small perturbation applied to the temperature field does not change the heat loss at the top surface ($\mathrm{Bi}=0$). Bi is the Biot number at the free surface given by $\mathrm{Bi}=hR/\kappa$, where h is the heat transfer coefficient. For this case, since the imposed temperature gradient is perpendicular to the free surface, a quiescent base state is possible if Marangoni number ($\mathrm{Ma}=\gamma\Delta TH/\mu\kappa$) is small enough. When Ma is greater than certain threshold, convective flow induced by the Marangoni effect sets in [5]. The critical Marangoni numbers obtained using the present model are compared to those from Dauby et al. [11] for a cylinder of aspect ratio of 1 ($R=H=1$) in Table 1. As shown in Table 1, the present model is in good agreement with the results of Dauby et al. [11] for insulated sidewalls. The critical Marangoni numbers for $m=1$ and $m=2$ at various aspect ratios are shown in Fig. 2. As the aspect ratio is increased, the sidewall effects decrease and, therefore, the critical Marangoni number decreases and approaches the theoretic prediction of that for an unbounded layer of fluid. For an infinite horizontal layer of fluid, Pearson [2] obtained the critical Marangoni number of 79.6 when the bottom wall is conducting. When the aspect ratio is 15, our numerical model gives the critical

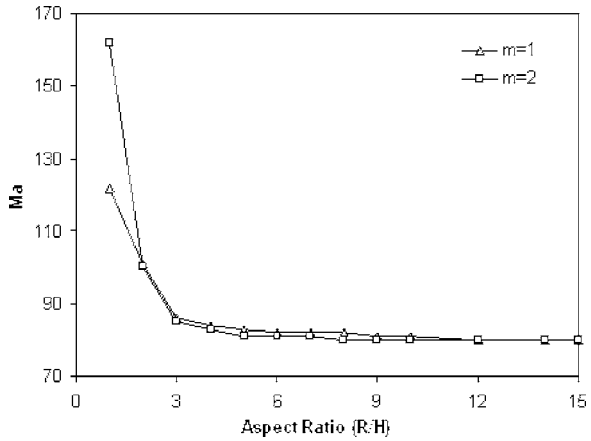

Fig. 2 Critical Marangoni number of Marangoni convection in a vertical cylinder for $m=1$ and 2 at various aspect ratios

Table 2 Maximum growth rate obtained for $R=H=1$, $\mathrm{Re}_\gamma=10^4$, $q=1$, and $m=1$, using different meshes

$N_r\times N_z$	Maximum growth rate, ω_r
16×16	−44.93263264
21×21	−44.05996232
26×26	−43.91683525
31×31	−43.92716348
36×36	−43.95662202
41×41	−43.98049958

Ma of 81 for both $m=1$ and $m=2$. As it is demonstrated above, good agreements have been achieved between the present numerical model and the previous studies.

Before any simulation results are presented, a mesh-dependent test is carried out to determine the mesh to be used in the present study. Real parts of the leading eigenvalues obtained using different meshes are listed in Table 2. For a trade-off between computational accuracy and optimal computing time, a mesh with 26 uniformly spaced nodes in both r and z directions is used for the results presented in this paper. Further refinement of the mesh produces results with an uncertainty of $<1\%$. The other parameters used in simulations are listed in Table 3.

Typical flow patterns and isothermals for axisymmetric base flow in a cylinder of $R=H=1$ are given in Figs. 3–5. The dimensionless time step used for the simulations is 10^{-6}, unless convergence requires a smaller time step. The convergence is claimed when the following criteria is met:

$$\max|x_{t+1}(r,z)-x_t(r,z)|<10^8$$

where i and $i+1$ are the time step and $x(r,z)$ denotes local parameters, such as velocity vectors, temperature, and pressure. Figure 3 shows the base flow when $\mathrm{Re}_\gamma=2\times10^4$, $q=1$, and $R_d=0$. The fluid is heated through the sidewall and cooled at the free surface by radiation. A convective loop is formed with the fluid, ascends near the vertical wall, and descends at the center due to the heating at the lateral wall. A small recirculation can be observed near the upper right corner of Fig. 3(*a*). The flow pattern is similar to the first type of base flow observed by Hoyas et al. [16]. Along the free surface, the fluid temperature is higher near the sidewall and lower at the center. Marangoni flow from the sidewall toward the center is driven by the temperature gradient. The fluid at the top surface is cooled only by radiation, and therefore, the temperature gradient imposed along it is small. As a result, the Marangoni flow induced along the free surface is weak. Figure 4 shows the base flow for $\mathrm{Re}_\gamma=2\times10^4$, $q=2$, and $R_d=0.5$. In this case, a seeding crystal with a radius of 0.5 is in contact with the top surface; the top surface is cooled by both the radiation and conduction. The lateral heat flux for this case ($q=2$) is larger than $q=1$ for that shown in Fig. 3. As a result, a larger temperature gradient is imposed along the free surface, especially near the edge of the crystal, as shown in Fig. 4(*b*). This larger temperature gradient induces stronger Marangoni flow [Fig. 4(*a*)]. The strong surface tension driven flows have a strong effect on the flow pattern near the top surface. However, it does not change the bulk flow structure

Table 3 Parameters used in the calculations

Parameter	Value
R	1.0
H	1.0
Pr	0.02
Rad	1.0
T_{amb}	0.0
T_d	0.0
M	10^{-6}

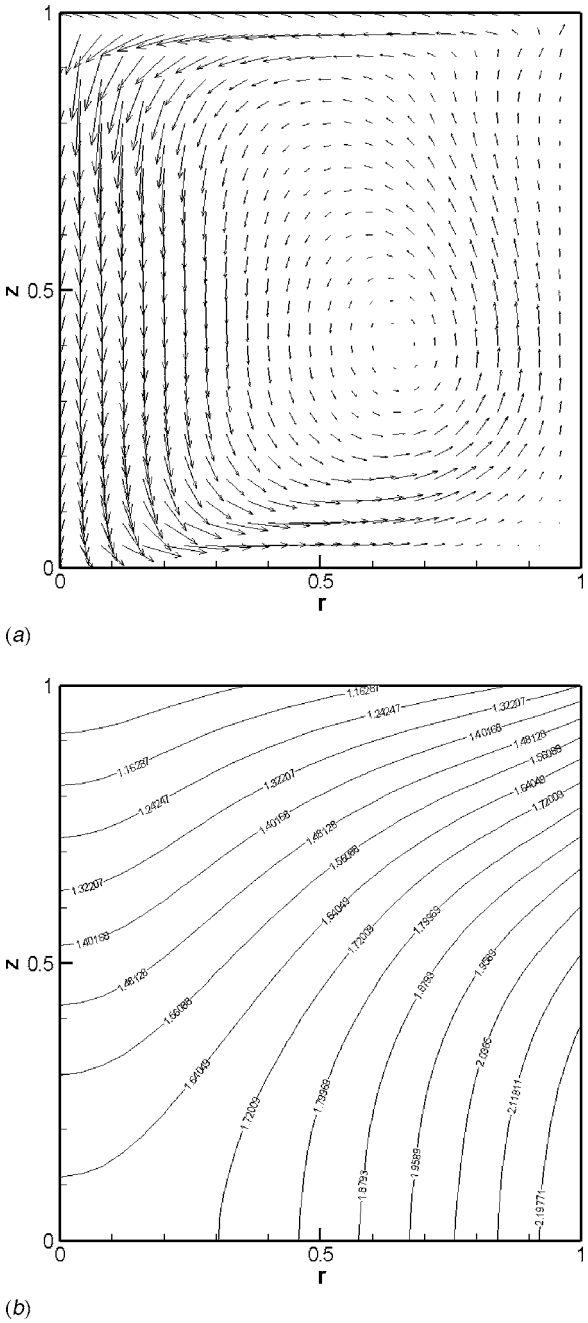

Fig. 3 Velocity field (*a*) and isotherms (*b*) of the base flow corresponding to $R=H=1$, $\mathrm{Re}_\gamma=2\times10^4$, $q=1.0$, and $R_d=0$

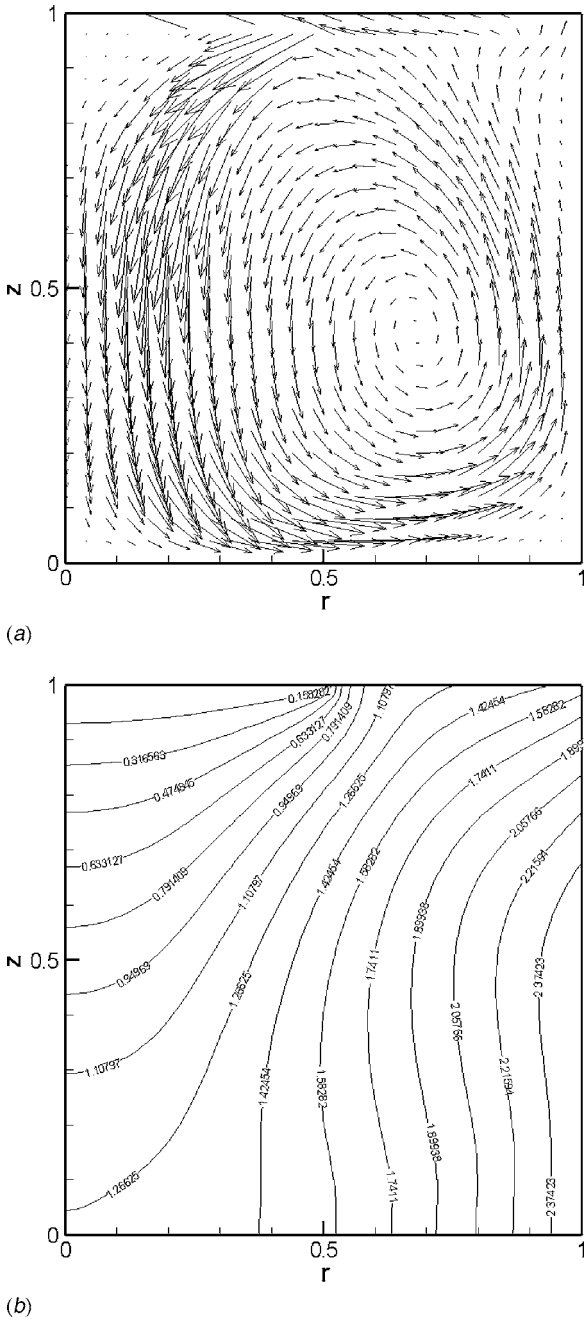

Fig. 4 Velocity field (*a*) and isotherms (*b*) of the base flow corresponding to $R=H=1$, $\mathrm{Re}_\gamma=2\times10^4$, $q=2.0$, and $R_d=0.5$

much. Base flow pattern at higher Marangoni-Reynolds number is shown in Fig. 5 for $\mathrm{Re}_\gamma=4\times10^4$, $q=2$, and $R_d=0.5$. For this case, the temperature gradient along the free surface is similar to that shown in Fig. 4(*b*). However, much stronger Marangoni flow is induced due to the higher Re_γ. The stronger free surface flow induces stronger bulk flow. A recirculation loop is formed beneath the seeding crystal. The bulk flow structure does not change much due to the increase in Marangoni-Reynolds number.

A stability analysis of the base flow is carried out to determine the critical Re_γ values at which the flow loses its axisymmetry. The stability analysis is carried out at various boundary conditions to investigate how the boundary conditions change the stability of the flow. For each given set of the boundary conditions, the flow becomes unstable when the Marangoni-Reynolds number is increased. Re_γ is updated using the bisection method to locate the critical Marangoni-Reynolds number at which the real part of the leading eigenvalue vanishes. For laterally bounded liquid layers in cylindrical configurations, the continuous wave number is replaced by discrete azimuthal modes [25,26]. The present study is focused on the axisymmetry-breaking instabilities, and the critical Marangoni-Reynolds numbers are presented for azimuthal wave number from 0 to 9. Figure 6 shows the stability curves obtained for a cylinder of $R=H=1$ with R_d of 0 and 0.5, respectively. For both of the cases, the most dangerous azimuthal mode is found to be 1. When there is no seeding crystal present, the critical Marangoni-Reynolds number is found to be 27,791. The critical Marangoni-Reynolds number is increased to 35,307 when a seeding crystal with R_d of 0.5 present. This increase is critical Grashof in not surprising considering the fact that the seeding crystal imposes a solid boundary at the free surface. The solid boundaries

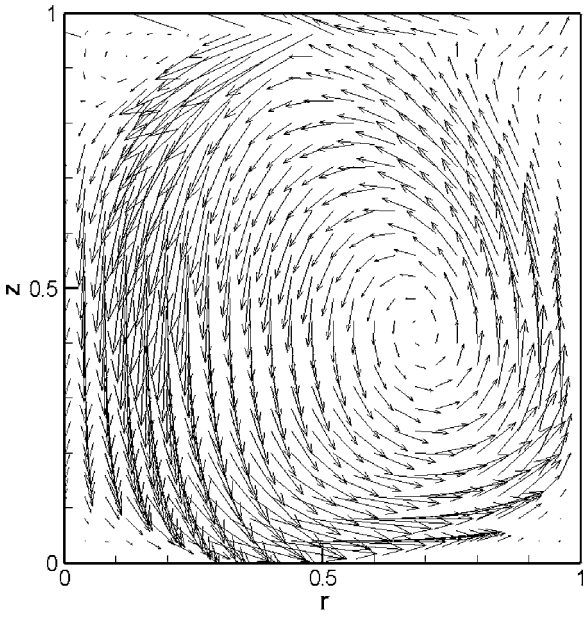

(*a*)

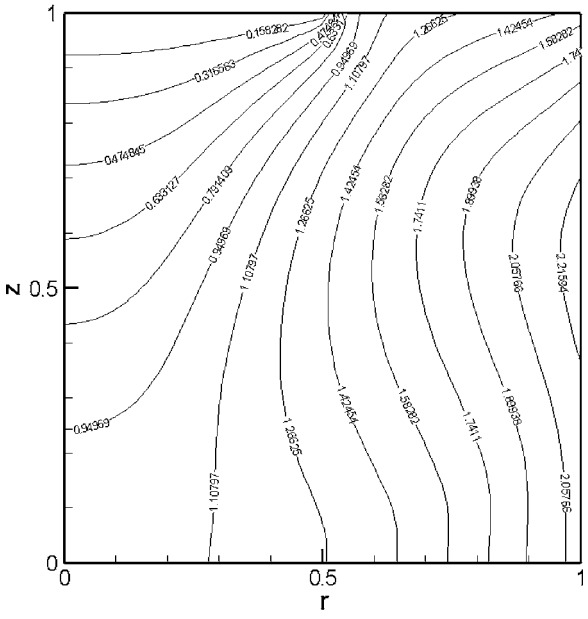

(*b*)

Fig. 5 Velocity field (*a*) and isotherms (*b*) of the base flow corresponding to $R=H=1$, $\mathrm{Re}_\gamma=4\times10^4$, $q=2.0$, and $R_d=0.5$

always stabilize the convective flow. The neutral curves for different laterally heating values are depicted in Fig. 7. The neutral curves are presented for $q=1$ and 2. With the lateral heat flux of 2, the critical Re_γ is found to be 19,243, which is lower than that of 27,791 for the $q=1$ case. This indicates that the lateral heating accelerates the onset of 3D convection in the crucible. The typical eigenvalue spectrum of the flow under investigation is shown in Fig. 8. This figure shows that both real and complex growth rates are possible. The complex growth rate always occurs in conjugate pairs. The leading eigenvalue is a real number. Contours of the temperature perturbations at critical state within $z=0.5$ cross-sectional surface are shown in Fig. 9. The perturbation patterns corresponding to azimuthal mode of 1 consist of a pair of maxima and minima along the azimuthal direction [26]. This indicates that the 3D convection occurs when the axisymmetric base flow becomes unstable and those conditions are found by means of a 3D perturbation applied to the axisymmetric base flow.

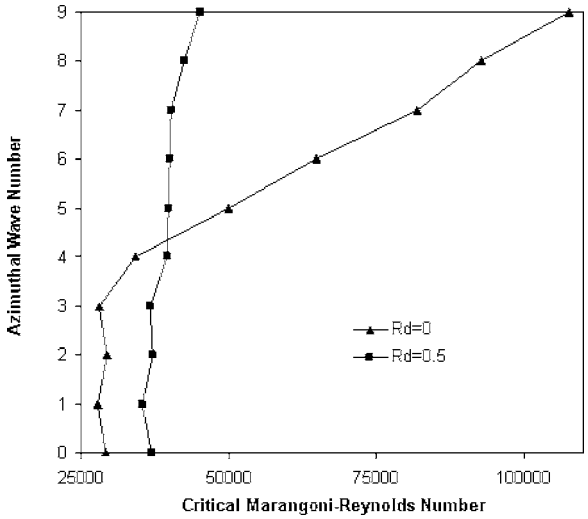

Fig. 6 Critical Marangoni-Reynolds numbers with different seeding crystal sizes for $R=H=1$ and $q=1.0$

6 Summary

This paper presents a numerical study on Marangoni stability of low Prandtl number fluid contained in a vertical cylinder. The fluid is heated through the sidewall at constant heat flux and cooled at the free surface via radiation. The axisymmetric base flow is solved using high-order finite difference method. Small perturbations are applied to the base flow with assumption of slight compressibility. The final perturbation equations are projected into an eigenvalue matrix equation and solved by linear fractional transformation. The numerical model is compared to previous numerical and theoretical studies, and good agreements have been found between the present model and previous studies. Critical Marangoni-Reynolds numbers are calculated at various boundary conditions. It was found that the seeding crystal delays the breakup from the axisymmetric base flow and the lateral heating unstabilizes the flow. The most dangerous azimuthal mode for all the cases is found to be 1.

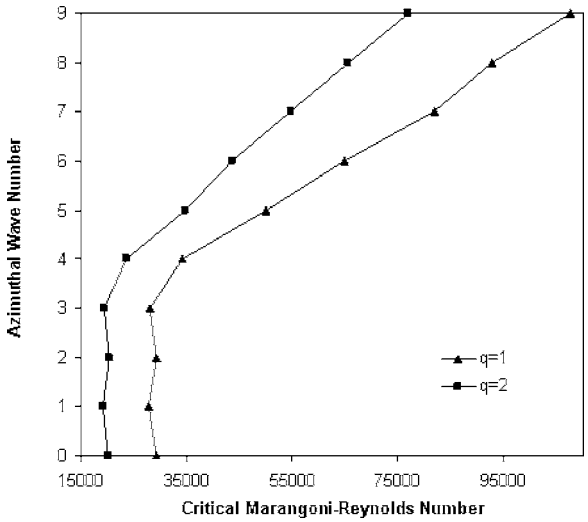

Fig. 7 Critical Marangoni-Reynolds numbers with different lateral heat fluxes for $R=H=1$ and $R_d=0$

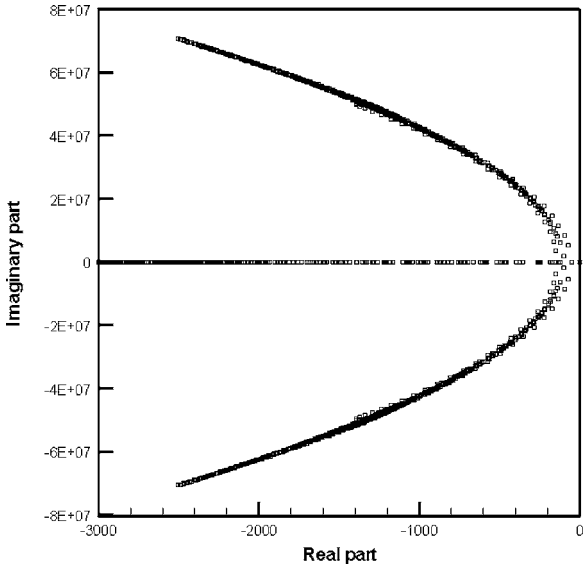

Fig. 8 Eigenvalue spectrum of base flow with $R=H=1$, $\mathrm{Re}_\gamma=27791$, $m=1$, $q=1.0$, and $R_d=0$

Acknowledgment

Partial support of this work by NASA (Grant No. NAG8-1693) and DOE (Grant No. DE-FC07-01ID14189) is gratefully acknowledged. This work was partially supported by the National Center for Supercomputing Applications under Grant No. CTS050035N and utilized the IBM P690.

Nomenclature

Bi = Biot number
g = gravity acceleration
H = height of cylinder
h = heat transfer coefficient
M = Mach number
Ma = Marangoni number
m = azimuthal wave number
Pr = Prandtl number
p = pressure
q = heat flux at vertical wall
R = cylinder radius
R_d = seeding crystal radius
Rad = radiation number
Re_γ = Marangoni Reynolds number
T = temperature
T_{amb} = ambient temperature
T_d = temperature of seeding crystal
T_m = reference temperature
t = time
$\boldsymbol{u}$ = velocity vector

Greek Letters

α = thermal diffusivity
β = thermal expansion coefficient
γ = negative rate of change of surface tension with temperature
δ = Stefan-Boltzmann constant
ε = emissivity
σ = surface tension
κ = thermal conductivity
μ = viscosity
ν = kinematic viscosity
ρ = density
ω = complex wave speed

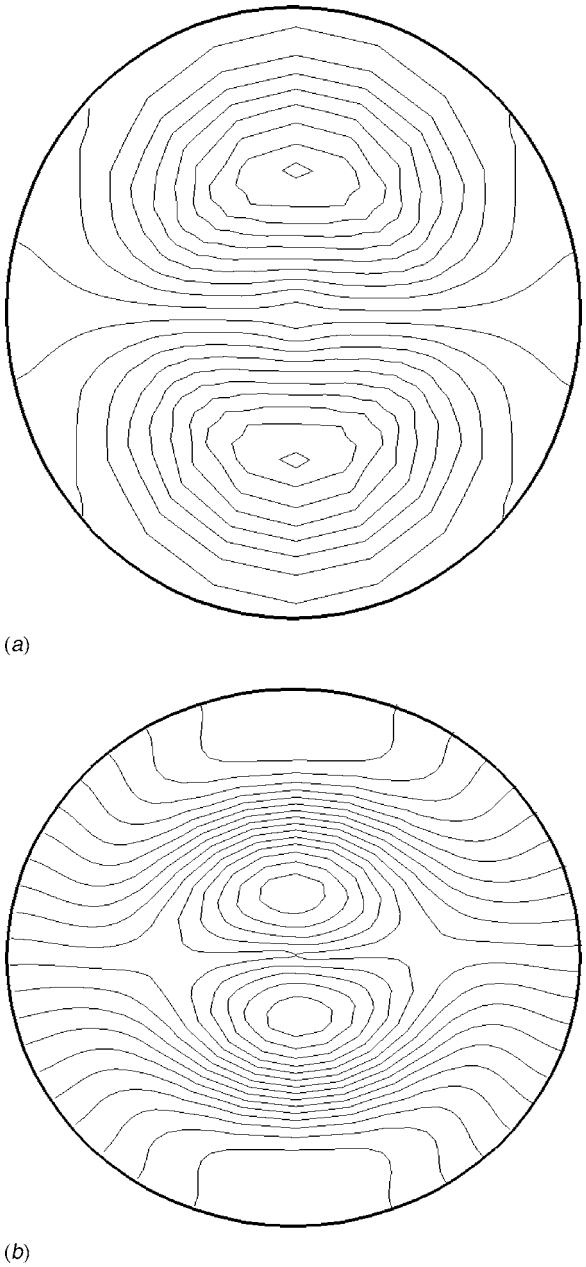

Fig. 9 Patterns of temperature perturbation at the $z=05$ cross-sectional surface corresponding to $R=H=1$, $m=1$: (*a*) $\mathrm{Re}_\gamma=27791$ and $R_d=0$; (*b*) $\mathrm{Re}_\gamma=35307$ and $R_d=0.5$

Subscripts

amb = ambient
d = seeding crystal

References

[1] Hurle, D. T. J., 1966, "Temperature Oscillations in Molten Metals and Their Relationship to Growth Striae in Melt-Grown Crystal," Philos. Mag., **13**, pp. 305–310.
[2] Pearson, J. R. A., 1958, "On Convection Cells Induced by Surface Tension," J. Fluid Mech., **4**, pp. 489–500.
[3] Levich, H. G., and Krylov, V. S., 1969, "Surface Tension-Driven Phenomena," Annu. Rev. Fluid Mech., **1**, pp. 293–316.
[4] Davis, S. H., 1987, "Thermocapillary Instabilities," Annu. Rev. Fluid Mech., **19**, pp. 403–435.
[5] Schatz, M. F., and Neitzel, G. P., 2001, "Experiments on Thermocapillary Instabilities," Annu. Rev. Fluid Mech., **33**, pp. 93–127.
[6] Peltier, L. J., and Biringen, S., 1993, "Time-Dependent Thermocapillary Convection in a Rectangular Cavity: Numerical Results for a Moderate Prandtl

Number Fluid," J. Fluid Mech., **257**, pp. 339–357.
[7] Sab, V., Kuhlmann, H. C., and Rath, H. J., 1996, "Investigation of Three-Dimensional Thermocapillary Convection in a Cubic Container by Multi-grid Method," Int. J. Heat Mass Transfer, **39**, pp. 603–613.
[8] Xu, J., and Zebib, A., 1998, "Oscillatory Two- and Three-Dimensional Thermocapillary Convection," J. Fluid Mech., **364**, pp. 187–209.
[9] Vrentas, J. S., Narayanan, R., and Agrawal, S. S., 1981, "Free Surface Convection in Bounded Cylindrical Geometry," Int. J. Heat Mass Transfer, **24**(9), pp. 1513–1529.
[10] Wagner, C., Friedrich, R., and Narayanan, R., 1994, "Comments on the Numerical Investigation of Rayleigh and Marangoni Convection in a Vertical Circular Cylinder," Phys. Fluids, **6**(4), pp. 1425–1433.
[11] Dauby, P. C., Lebon, G., and Bouhy, E., 1997, "Linear Bénard-Marangoni Instability in Rigid Circular Containers," Phys. Rev. E, **56**(1), pp. 520–530.
[12] Schwabe, D., Möller, U., Schneider, J., and Scharmann, A., 1992, "Instabilities of Shallow Dynamic Thermocapillary Liquid Layer," Phys. Fluids A, **4**, pp. 2368–2381.
[13] Ezersky, A. B., Garcimartín, A., Burguete, J., Mancini, H. L., and Pérez-García, C., 1993, "Hydrothermal Waves in Marangoni Convection in a Cylindrical Container," Phys. Rev. E, **47**(2), pp. 1126–1131.
[14] Favre, E., Blumendeld, L., and Daviaud, F., 1997, "Instabilities of a Liquid Layer Locally Heated on its Free Surface," Phys. Fluids, **9**(5), pp. 1473–1475.
[15] Garnier, N., and Chiffaudel, A., 2001, "Two Dimensional Hydrothermal Waves in an Extended Cylindrical Vessel," Eur. Phys. J. B, **19**, pp. 87–95.
[16] Hoyas, S., Herrero, H., and Mancho, A. M., 2002, "Thermal Convection in a Cylindrical Annulus Heated Laterally," J. Phys. A, **35**, pp. 4067–4083.
[17] Sim, B.-C., Zebib, A., and Schwabe, D., 2003, "Oscillatory Thermocapillary Convection in Open Cylindrical Annuli. Part 2. Simulations," J. Fluid Mech., **491**, pp. 259–274.
[18] Jing, C. J., Imaishi, N., Yasuhiro, S., and Miyazawa, Y., 1999, "Three-Dimensional Numerical Simulation of Spoke Pattern in Oxide Melt," J. Cryst. Growth, **200**, pp. 204–212.
[19] Ding, Y., and Kawahara, M., 1998, "Linear Stability of Incompressible Fluid Flow Using a Mixed Finite Element Method," J. Comput. Phys., **139**(2), pp. 243–273.
[20] Ai, X., 2004, "The Instability Analysis and Direct Numerical Simulation of Turbulent Flows in Electromagnetically Levitated Droplets," Ph.D. thesis, Washington State University, Pullman, WA.
[21] Le, H., and Moin, P., 1991, "An Improvement of Fractional Step Methods for the Incompressible Navier-Stokes Equations," Int. J. Numer. Methods Fluids, **92**, pp. 369–379.
[22] Kim, J., and Moin, P., 1985, "Application of a Fractional-Step Method to Incompressible Navier-Stokes Equations," J. Comput. Phys., **59**, pp. 308–323.
[23] Chénier, E., Delcarte, C., Kasperski, G., and Labrosse, G., 2002, "Sensitive of the Liquid Bridge Hydrodynamics to Local Capillary Contributions," Phys. Fluids, **14**(9), pp. 3109–3117.
[24] Chénier, E., Delcarte, C., and Labrosse, G., 1999, "Stability of the Axisymmetric Buoyant-Capillary Flows in a Laterally Heated Liquid Bridge," Phys. Fluids, **11**(3), pp. 527–541.
[25] Johnson, D., and Narayanan, R., 1999, "A Tutorial on the Rayleigh-Marangoni-Bénard Problem with Multiple Layers and Side Wall Effects," Chaos, **9**(1), pp. 124–140.
[26] Rubinov, A., Erenburg, V., Gelfgat, A. Yu., Kit, E., Bar-Yoseph, P. Z., and Solan, A., 2004, "Three-Dimensional Instabilities of Natural Convection Flow in a Vertical Cylinder With Partially Heated Sidewall," ASME J. Heat Transfer, **126**, pp. 586–599.

On the Effectiveness of Ion Slip on Steady MHD Flow and Heat Transfer Above a Rotating Disk With Ohmic Heating

Hazem Ali Attia[1]
Department of Math.,
College of Science,
Al-Qasseem University,
P.O. Box 237,
Buraidah 81999, Saudi Arabia

The steady flow and heat transfer of a conducting fluid due to the rotation of an infinite, nonconducting disk in the presence of an axial uniform steady magnetic field are studied considering the ion slip and the Ohmic heating. The relevant equations are solved numerically using finite differences and the solution shows that the inclusion of the ion slip gives some interesting results. [DOI: 10.1115/1.2234785]

Keywords: rotating disk flow, hydromagnetic flow, heat transfer, numerical solution, finite differences

Introduction

The hydrodynamic flow due to an infinite rotating disk was first introduced by von Karman [1]. He formulated the problem in the steady state and used similarity transformations to reduce the governing partial differential equations to ordinary differential equations. Asymptotic solutions were obtained for the reduced system of ordinary differential equations [2]. The extension of the steady hydrodynamic problem to the transient state was done by Benton [3]. The influence of an external uniform magnetic field on the flow due to a rotating disk was studied [4,5] without considering the Hall effect. Aboul-Hassan and Attia [6] studied the steady hydromagnetic problem taking the Hall effect into consideration. The problem of heat transfer from a rotating disk at a constant temperature was first considered by Millsaps and Pohlhausen [7] for a variety of Prandtl numbers in the steady state. Sparrow and Gregg [8] studied the steady state heat transfer from a rotating disk maintained at a constant temperature to fluids at any Prandtl number. Later Attia [9] extended the problem discussed in Refs. [7,8] to the unsteady state in the presence of an applied uniform magnetic field.

The effect of uniform suction or injection through a rotating porous disk on the steady hydrodynamic flow induced by the disk was investigated [10–12]. Later Attia extended the problem to the case of an unsteady hydromagnetic flow in the presence of an external uniform magnetic field without considering the Hall effect [13]. The effect of uniform suction or injection on the flow of a conducting fluid due to a rotating disk was studied [14] considering the Hall current with the neglect of the ion slip.

In the present work the steady hydromagnetic flow of a viscous, incompressible, and electrically conducting fluid due to the uniform rotation of an infinite, nonconducting, disk in an axial uniform steady magnetic field is studied considering the ion slip and the Ohmic heating. The governing nonlinear differential equations are solved numerically using the finite difference approximations. Some interesting effects for the Hall current, and the ion slip are reported.

Basic Equations

The disk is assumed to be insulating and rotating in the $z=0$ plane about the z-axis with a uniform angular velocity ω. The fluid is assumed to be incompressible and has density ρ, kinematical viscosity ν, and electrical conductivity σ. An external uniform magnetic field is applied in the z-direction and has a constant flux density B_0. The magnetic Reynolds number is assumed to be very small, so that the induced magnetic field is negligible. The electron-atom collision frequency is assumed to be relatively high, so that the Hall effect and the ion slip cannot be neglected [15]. Due to the axial symmetry of the problem about the z-axis, the cylindrical coordinates (r,φ,z) are used. For the sake of definiteness, the disk is taken to be rotating in the positive φ direction. Due to the symmetry about the $z=0$ plane, it is sufficient to consider the problem in the upper half space only.

The fluid motion is governed by the continuity equation, the Navier-Stokes equation, and the generalized Ohm's law [15] which are, respectively, given by

$$\vec{\nabla}\cdot\vec{V}=0 \tag{1}$$

$$\rho(\vec{V}\cdot\vec{\nabla})\vec{V}=-\vec{\nabla}p+\mu\nabla^2\vec{V}+\vec{J}\times\vec{B}_0 \tag{2}$$

$$\vec{J}=\sigma\left[\vec{E}+\vec{V}\times\vec{B}_0-\beta(\vec{J}\times\vec{B}_0)+\frac{\beta\mathrm{Bi}}{B_0}(\vec{J}\times\vec{B}_0)\times\vec{B}_0\right] \tag{3}$$

where $\vec{E}$ is the electric field which results from charge separation and is in the z-direction which implies that it has no effect on Lorentz force term $\vec{J}\wedge\vec{B}_0$ and consequently on the equations of motion. The last term in the last equation expresses the ion slip effect, where $\beta=1/nq$ is the Hall factor, n is the electron concentration per unit volume, $-q$ is the charge of the electron, and Bi is the ion slip parameter [15]. In cylindrical coordinates, the velocity vector is written as

$$\vec{V}=u\vec{e}_r+v\vec{e}_\varphi+w\vec{e}_z$$

Expressing the rest of vectors in Eq. (3) in cylindrical coordinates and solving for the unknown vector $\vec{J}$ and, in turn, substituting in Eqs. (1) and (2), the set of equations of steady motion takes the form

$$u_{,r}+\frac{u}{r}+w_{,z}=0 \tag{4}$$

[1]On leave from: Dept. of Eng. Math. and Physics, Fac. of Eng., El-Fayoum University, El-Fayoum, Egypt.

Contributed by the Fluids Engineering Division of ASME for publication in the JOURNAL OF FLUIDS ENGINEERING. Manuscript received December 21, 2004; final manuscript received January 26, 2006. Assoc. Editor: Dennis Siginer.

$$\rho\left(uu_{,r}+wu_{,z}-\frac{v^2}{r}\right)+\frac{\sigma B_0^2}{(\alpha^2+B_e^2)}(\alpha u-\mathrm{Be}v)+p_{,r}$$
$$=\mu\left(u_{,rr}+\frac{u_{,r}}{r}-\frac{u}{r^2}+u_{,zz}\right) \quad (5)$$

$$\rho\left(uv_{,r}+wv_{,z}+\frac{uv}{r}\right)+\frac{\sigma B_0^2}{(\alpha^2+\mathrm{Be}^2)}(\alpha v+\mathrm{Be}u)$$
$$=\mu\left(v_{,rr}+\frac{v_{,r}}{r}-\frac{v}{r^2}+v_{,zz}\right) \quad (6)$$

$$\rho(uw_{,r}+ww_{,z})+p_{,z}=\mu\left(w_{,rr}+\frac{w_{,r}}{r}+w_{,zz}\right) \quad (7)$$

where Be ($=\sigma\beta B_0$) is the Hall parameter which can take positive or negative values and $\alpha=1+\mathrm{BeBi}$. The boundary conditions are given as

$$z=0,\ u=0,\ v=r\omega,\ w=0 \quad (8a)$$

$$z\to\infty,\ u\to 0,\ v\to 0,\ p\to p_\infty \quad (8b)$$

Equation (8*a*) indicates the no-slip conditions of viscous flow applied at the surface of the disk. Far from the surface of the disk, all fluid velocities must vanish aside the induced axial component as indicated in Eq. (8*b*). We introduce von Karman transformations [1]

$$u=r\omega F,\ v=r\omega G,\ w=\sqrt{\omega\upsilon}H,\ z=\sqrt{\upsilon/\omega}\zeta,\ p-p_\infty=-\rho\upsilon\omega P$$

where ζ is a nondimensional distance measured along the axis of rotation, F, G, H, and P are nondimensional functions of the modified vertical coordinate ζ. We define the magnetic interaction number γ by $\gamma=\sigma B_0^2/\rho\omega$ which represents the ratio between the magnetic force to the fluid inertia force. With these definitions, Eqs. (4)–(8) take the form

$$\frac{dH}{d\zeta}+2F=0 \quad (9)$$

$$\frac{d^2F}{d\zeta^2}-H\frac{dF}{d\zeta}-F^2+G^2-\frac{\gamma}{(\alpha^2+\mathrm{Be}^2)}(\alpha F-\mathrm{Be}G)=0 \quad (10)$$

$$\frac{d^2G}{d\zeta^2}-H\frac{dG}{d\zeta}-2FG-\frac{\gamma}{(\alpha^2+\mathrm{Be}^2)}(\alpha G+\mathrm{Be}F)=0 \quad (11)$$

$$\frac{d^2H}{d\zeta^2}-H\frac{dH}{d\zeta}-\frac{dP}{d\zeta}=0 \quad (12)$$

$$\zeta=0,\ F=0,\ G=1,\ H=0 \quad (13a)$$

$$\zeta\to\infty,\ F\to 0,\ G\to 0,\ P\to 0 \quad (13b)$$

The above system of Eqs. (9)–(11) with the prescribed boundary conditions given by Eq. (13) are sufficient to solve for the three components of the flow velocity. Equation (12) can be used to solve for the pressure distribution if required.

Due to the difference in temperature between the wall and the ambient fluid heat transfer takes place. The energy equation, by neglecting the viscous dissipation, takes the form [7,8]

$$\rho c_p\left(u\frac{\partial T}{\partial r}+w\frac{\partial T}{\partial z}\right)=k\left(\frac{\partial^2 T}{\partial z^2}+\frac{\partial^2 T}{\partial r^2}+\frac{1}{r}\frac{\partial T}{\partial r}\right)+\frac{\sigma B_0^2}{\alpha^2+Be^2}(u^2+v^2) \quad (14)$$

where T is the temperature of the fluid, c_p is the specific heat at constant pressure of the fluid, and k is the thermal conductivity of the fluid. The last term in Eq. (14) represents the Ohmic heating. The boundary conditions for the energy problem are that the temperature by continuity considerations, equals T_w at the surface of the disk. At large distances from the disk, $T\to T_\infty$ where T_∞ is the temperature of the ambient fluid. In terms of the nondimensional variable $\theta=(T-T_\infty)/(T_w-T_\infty)$ and using Von Karman transformations, Eq. (14) takes the form

$$\frac{1}{\mathrm{Pr}}\frac{d^2\theta}{d\zeta^2}-H\frac{d\theta}{d\zeta}+\frac{\gamma\mathrm{Ec}}{\alpha^2+\mathrm{Be}^2}(F^2+G^2)=0 \quad (15)$$

where Pr is the Prandtl number given by, $\mathrm{Pr}=c_p\mu/k$ and Ec $=\omega^2r^2/c_p(T_w-T_\infty)$ is the Eckert number. The boundary conditions for the energy problem, in terms of θ and Von Karman transformations, are expressed as

$$\theta(0)=1,\ \zeta\to\infty:\theta\to 0 \quad (16)$$

It should be pointed out that the similarity aspects of the transformation are linked to the supposition that the velocity and temperature do not change shape at different values of r. Also, the idea of angular symmetry has been invoked; i.e., $\partial/\partial\varphi=0$.

The heat transfer from the disk surface to the fluid is computed by application of Fourier's law

$$Q=-k\left(\frac{dT}{dz}\right)_w \quad (17)$$

Introducing the transformed variables, the expression for q becomes

$$Q=-k(T_w-T_\infty)\sqrt{\frac{\omega}{\nu}}\frac{d\theta(0)}{d\zeta} \quad (18)$$

By rephrasing the heat transfer results in terms of a Nusselt number defined as, $\mathrm{N_u}=Q\sqrt{\omega/\nu}/k(T_w-T_\infty)$ the last equation becomes

$$\mathrm{N_u}=-\frac{d\theta(0)}{d\zeta} \quad (19)$$

The system of nonlinear ordinary differential equations (9)–(11) and (15) is solved under the conditions given by Eqs. (13) and (16) for the three components of the flow velocity and temperature distribution, using the Crank-Nicolson method [16]. The resulting system of difference equations has to be solved in the infinite domain $0<\zeta<\infty$. A finite domain in the ζ-direction can be used instead with ζ chosen large enough to ensure that the solutions are not affected by imposing the asymptotic conditions at a finite distance. The independence of the results from the length of the finite domain and the grid density was ensured and successfully checked by various trial and error numerical experimentations. Computations are carried out for $\zeta_\infty=12$ and it is found that a value of $\zeta_\infty=10$ is adequate for the ranges of the parameters studied here. It should be pointed that the steady state solutions reported by Attia and Aboul-Hassan [14] are reproduced by setting $\mathrm{Bi}=0$ in the present results. These comparisons lend confidence in the correctness of the solutions presented in this paper.

Results and Discussion

Figures 1(*a*) and 1(*b*) present the profile of the radial velocity component F for various values of the ion slip parameter Bi and for $\mathrm{Be}\leqslant 0$ and $\mathrm{Be}\geqslant 0$, respectively. In these figures $\gamma=1$. Figure 1 shows that for $\mathrm{Be}=-0.5$ and $\mathrm{Bi}=0$, the radial flow reverses its direction at a certain distance from the disk. Increasing Bi, for $\mathrm{Be}<0$, leads to a negative F for all ζ as a result of increasing the effective conductivity ($=\gamma/(\alpha^2+\mathrm{Be}^2)$) which increases the damping force on F. Figure 1(*a*) indicates also that for $\mathrm{BeBi}>0$, increasing the magnitude of Bi increases F due to the decrease in the effective conductivity which decreases the damping force on F. Large values of Bi reduce the effective conductivity more which corresponds to the hydrodynamic case. Figure 1(*b*) indicates that when $\mathrm{Be}>0$ and $\mathrm{Be}>0$, increasing Bi decreases F for some ζ. This may be attributed to the fact that in the magnetic force term in Eq. (7), the effect of Bi on the numerator is stronger than its effect on the denominator which increases the damping

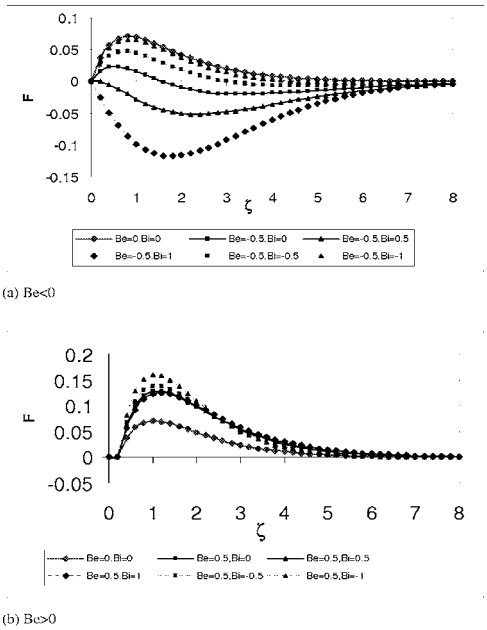

Fig. 1 Steady state profile of the radial velocity component *F* for various values of the Hall parameter Be and the ion slip parameter Bi

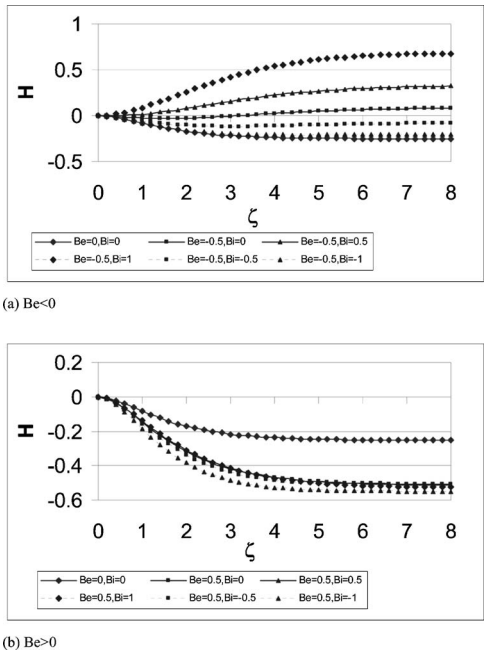

Fig. 3 Steady state profile of the vertical velocity component *H* for various values of the Hall parameter Be and the ion slip parameter Bi

force on F and consequently decreases F for some ζ. Also, for $Bi<0$, increasing the magnitude of Bi increases F for small ζ and then decreases it for larger ζ. This accounts for a crossover in the F-ζ chart with Bi. It is of interest to detect that the variation of F with Bi depends on ζ.

Figures 2(a) and 2(b) present the profile of the azimuthal velocity component G for various values of the ion slip parameter Bi and for $Be\leqslant 0$ and $Be\geqslant 0$, respectively. In both figures, $\gamma=1$. As shown in Fig. 2(a), small negative values of Be increases G as a result of decreasing the magnetic damping. Increasing Bi, with Be<0, decreases G, due to the increase in the effective conductivity. Figure 2(a) shows also that for negative values of Bi, increasing the magnitude of Bi increases G due to the decrease in the damping force on G. Figure 2(b) describes the same findings. For BeBi>0, increasing Bi increases G, while for BeBi<0, increasing the magnitude of Bi decreases G.

Figures 3(a) and 3(b) present the profile of the axial velocity component H for various values of the ion slip parameter Bi and $Be\leqslant 0$ and $Be\geqslant 0$, respectively. In these figures $\gamma=1$. As shown in Fig. 3(a), for Be$=-0.5$ and Bi$=0$, the axial velocity H reverses its direction at a certain ζ. Increasing Bi increases H, as a result of decreasing F, and reverses its direction for all ζ. Figure 3(b) shows that for Be>0, increasing the magnitude of Bi, in general, decreases H as a result of increasing F. It is also shown in Fig. 3(b) that the axial flow is always towards the disk for all values of Bi.

Table 1 present the variation of the Nusselt number N_u with the Hall parameter Be, and the ion slip parameter Bi for Pr$=0.7$ and 10. In these tables $\gamma=1$ and Ec$=0.2$. It is clear that For Pr$=10$ and Be<0, increasing Bi increase Nu. For Pr$=0.7$ and Be<0, increasing Bi decreases Nu, but increasing Bi more increases Nu.

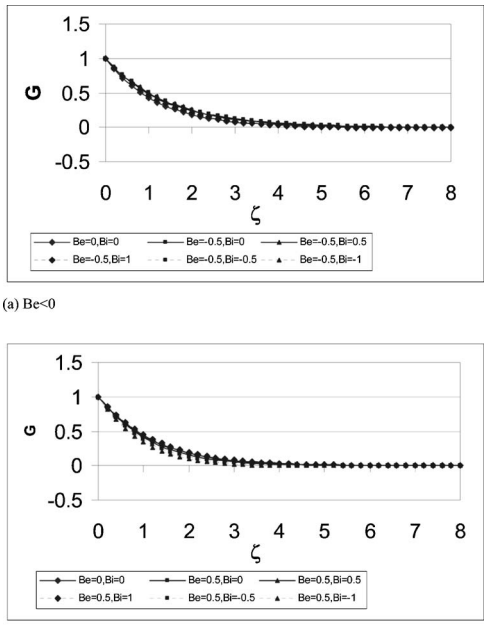

Fig. 2 Steady state profile of the azimuthal velocity component *G* for various values of the Hall parameter Be and the ion slip parameter Bi

Table 1 Variation of the steady state value of N_u with Be, Bi, and Pr

N_u	Pr=0.7	Pr=10
Be=0, Bi=0	0.1646	0.2346
Be=−0.5, Bi=0	0.1136	0.1155
Be=−0.5, Bi=0.5	0.0474	0.3415
Be=−0.5, Bi=1	−0.0556	−1.1095
Be=−0.5, Bi=−0.5	0.1573	0.3841
Be=−0.5, Bi=−1	0.1875	0.5574
Be=0.5, Bi=0	0.2321	0.5659
Be=0.5, Bi=0.5	0.2425	0.6872
Be=0.5, Bi=1	0.2509	0.7702
Be=0.5, Bi=−0.5	0.2184	0.3791
Be=0.5, Bi=−1	0.1996	0.0827

For $Be > 0$, increasing the magnitude of Bi increases Nu for all Pr. It is seen in Table 1 that increasing Pr increases N_u. The influence of Be and Bi on Nu is more pronounced for higher Pr than smaller values of Pr. It is seen also that the effect of the ion slip on N_u becomes more apparent for $Be < 0$ than for $Be > 0$ for all values of Pr.

Conclusion

The steady magnetohydrodynamic (MHD) flow due to an infinite rotating disk was studied with heat transfer considering the Hall effect and the ion slip and the Ohmic heating. The inclusion of the Hall effect and the ion slip reveals some interesting phenomena and it is found that the signs of the Hall and ion slip parameters are important. It was found that both the radial and vertical velocity components reverse direction for certain values of the magnetic field, the Hall and the ion slip parameters. The variation of the velocity components with the ion slip depends on ζ especially for positive values of the ion slip parameter. Also, the effect of the ion slip parameter is more apparent for positive values of the Hall parameter than negative values. The heat transfer at the surface of the disk is found to depend on the magnitude and the sign of the Hall and ion slip parameters. The dependence of the heat transfer on the Hall and ion slip parameters was found to depend on the Prandtl number and becomes more clear for higher values of the Prandtl number. Also, the variation of the heat transfer with the ion slip was shown to depend upon the sign of the Hall parameter.

References

[1] von Karman, T., 1921, "Uber Laminare und Turbulente Reibung," Z. Angew. Math. Mech., **1**(4), pp. 233–235.

[2] Cochran, W. G., 1934, "The Flow Due to a Rotating Disk," Proc. Cambridge Philos. Soc., **30**(3), pp. 365–375.

[3] Benton, E. R., 1966, "On the Flow Due to a Rotating Disk," J. Fluid Mech., **24**(4), pp. 781–800.

[4] El-Mistikawy, T. M. A., and Attia, H. A., 1990, "The Rotating Disk Flow in the Presence of Strong Magnetic Field," *Proc. 3rd Int. Congress of Fluid Mechanics*, Cairo, Egypt, Jan. 2–4, Vol. 3, pp. 1211–1222.

[5] El-Mistikawy, T. M. A., Attia, H. A., and Megahed, A. A., 1991, "The Rotating Disk Flow in the Presence of Weak Magnetic Field," *Proc. 4th Conference on Theoretical and Applied Mechanics*, Cairo, Egypt, Nov. 5–7, pp. 69–82.

[6] Aboul-Hassan, A. L., and Attia, H. A., 1997, "The Flow Due to a Rotating Disk With Hall Effect," Phys. Lett. A, **228**, pp. 286–290.

[7] Millsaps, K., and Pohlhausen, K., 1952, "Heat Transfer by Laminar Flow From a Rotating Disk," J. Aeronaut. Sci., **19**, pp. 120–126.

[8] Sparrow, E. M., and Gregg, J. L., 1960, "Mass Transfer, Flow, and Heat Transfer About a Rotating Disk," ASME J. Heat Transfer, **82**, pp. 294–302.

[9] Attia, H. A., 2002, "On the Effectiveness of Uniform Suction-Injection on the Unsteady Flow Due to a Rotating Disk With Heat Transfer," Int. Commun. Heat Mass Transfer, **29**(5), pp. 653–661.

[10] Stuart, J. T., 1954, "On the Effects of Uniform Suction on the Steady Flow Due to a Rotating Disk," Q. J. Mech. Appl. Math., **7**, pp. 446–457.

[11] Kuiken, H. K., 1971, "The Effect of Normal Blowing on the Flow Near a Rotating Disk of Infinite Extent," J. Fluid Mech., **47**(4), pp. 789–798.

[12] Ockendon, H., 1972, "An Asymptotic Solution for Steady Flow Above an Infinite Rotating Disk With Suction," Q. J. Mech. Appl. Math., **25**, pp. 291–301.

[13] Attia, H. A., 1998, "Unsteady MHD Flow Near a Rotating Porous Disk With Uniform Suction or Injection," Fluid Dyn. Res., **23**, pp. 283–290.

[14] Attia, H. A., and Aboul-Hassan, A. L., 2001, "Effect of Hall Current on the Unsteady MHD Flow Due to a Rotating Disk With Uniform Suction or Injection," Appl. Math. Model., **25**(12), pp. 1089–1098.

[15] Sutton, G. W., and Sherman, A., 1965, *Engineering Magnetohydrodynamics*, McGraw-Hill, New York.

[16] Ames, W. F., 1977, *Numerical Methods in Partial Differential Equations*, 2nd ed., Academic Press, New York.

Numerical and Experimental Studies of the Flow Field in a Cyclone Dryer

P. Bunyawanichakul
School of Engineering,
University of Tasmania,
Hobart, TAS, Australia
e-mail: prachab@postoffice.sandybay.utas.edu.au

M. P. Kirkpatrick
School of Aerospace, Mechanical and
Machatronics Engineering,
University of Sydney,
Sydney, NSW,
Australia

J. E. Sargison

G. J. Walker

School of Engineering,
University of Tasmania,
Hobart, TAS, Australia

The performance of a newly developed cyclone dryer is investigated using RANS-based single-phase computational fluid dynamics (CFD) and experimental model studies. The cyclone dryer is a cylindrical tower, divided by conical orifices into several chambers; recirculation of the flow within individual chambers ensures adequate retention time for drying of the transported solid material. Numerical calculations are performed using the commercial CFD code CFX5.7 for different mesh types, turbulence models, advection schemes, and mesh resolution. Results of the simulation are compared with data from experimental model studies. The RNG k-ε turbulence model with hexahedral mesh gives satisfactory results. A significant improvement in CFD prediction is obtained when using a second order accurate advection scheme. Useful descriptions of the axial and tangential velocity distributions are obtained, and the pressure drop across the cyclone dryer chamber is predicted with an error of approximately 10%. The optimized numerical model is used to predict the influence of orifice diameter and chamber height on total pressure drop coefficient. [DOI: 10.1115/1.2354523]

Keywords: cyclone dryer, numerical simulation, computational fluid dynamics, experimental measurement, axial velocity distribution, tangential velocity distribution, pressure drop coefficient

1 Introduction

At harvest, rice grain usually has a high moisture content (24–33% wet basis) which, if not reduced, allows microbial growth causing biochemical deterioration of the grain. Drying of the paddy grain (rice) from its fresh harvest moisture content to a more manageable level (18% wb.) is currently the only practical method to lower the rate of deterioration of grain [1]. Satisfactory drying of newly harvested grains typically requires a residence time of several minutes.

The cyclone dryer is a medium-residence time dryer with the solids retained for 5–30 min. This type of dryer has been used for drying S-PVC and other polymers. Nebra et al. [2], Korn [3], Heinze [4], and Ulrich [5] give a brief description of the design and working principles of cyclone dryers. However, in their work the design and scaling relationships were obtained by pilot plant scale testing rather than theoretical considerations.

To make further improvements to cyclone dryer designs, a good understanding of the fluid dynamics is required. Analytical techniques do not allow changes in geometry to be readily assessed. Reynolds-average Navier-Stokes (RANS) based computational fluid dynamics (CFD) models provide an economical means of understanding the complex fluid dynamics and how it can be influenced by changes in design and operating conditions. Validation of results is required to establish confidence in the predictions.

A review of archival literature revealed no research involving simulation of cyclone dryers, but significant advances have been made in simulating cyclone separators. Boysan et al. [6] who were early users of the CFD technology, applied the algebraic stress model (ASM) to simulations of a cyclone separator. Later Zhou et al. [7], Modigell et al. [8], and Hoekstra et al. [9] applied CFD to this problem with varying success. But their works dealt only with two-dimensional prediction of the single-phase flow in the cyclones and treated the flow field as axisymmetric and steady.

To get more details of the complicated flow field in cyclone devices it is necessary to perform numerical simulations in three-dimensions. Several researchers have conducted numerical simulations of cyclone separators in three-dimensions (Griffiths et al. [10]; Zhao et al. [11]; Yoshida et al. [12,13]; Montavon et al. [14]; Schimdit et al. [15]; Wang et al. [16]; Derksen et al. [17]; Derksen [18]; Witt et al. [19]). These authors tested a number of turbulence models, ranging from the algebraic stress model [11], standard k-ε [12,13,19,14], RNG k-ε [10], and a Reynolds stress model [16,19]. Their studies have demonstrated that CFD still cannot produce a very accurate description of the flow field because of difficulties in modeling the phenomena occurring in swirling flow. Calculated results for pressure drop agree only moderately well with the experimental data. The experimental pressure drop was larger than the calculated pressure drop by 60%, 15%, and 16% for standard k-ε [13], RNG k-ε [10], and Reynolds stress model [16], respectively.

Recently, large eddy simulation (LES) was used to predict the unsteady, spiral shape, and vortex core characteristics of a cyclone separator [15,17,18]. Good agreement with experimental data was obtained, both in terms of the average velocity and velocity fluctuations, when high spatial and temporal resolution was used. The superiority of the LES approach as compared with the Reynolds-average approach was clearly illustrated but at greatly increased computational cost.

The objective of this paper is to present predictions of the gas-phase flow field and pressure drop through a laboratory scale cyclone dryer using RANS based CFD. A model developed using the commercial code CFX5.7 is run for three-dimensional single-phase gas flow in the cyclone dryer. Simulation parameters such as mesh type, turbulence model, advection scheme, and level of mesh resolution are tested to find the best combination for flows of this type. The computed flow behavior is compared with experimental results to establish a level of confidence in the numerical predictions. Mean flow field and pressure drop prediction are then presented using the optimized simulation parameters. Finally,

Contributed by the Fluids Engineering Division of ASME for publication in the JOURNAL OF FLUIDS ENGINEERING. Manuscript received August 30, 2005; final manuscript received March 10, 2006. Assoc. Editor: Surya P Vanka.

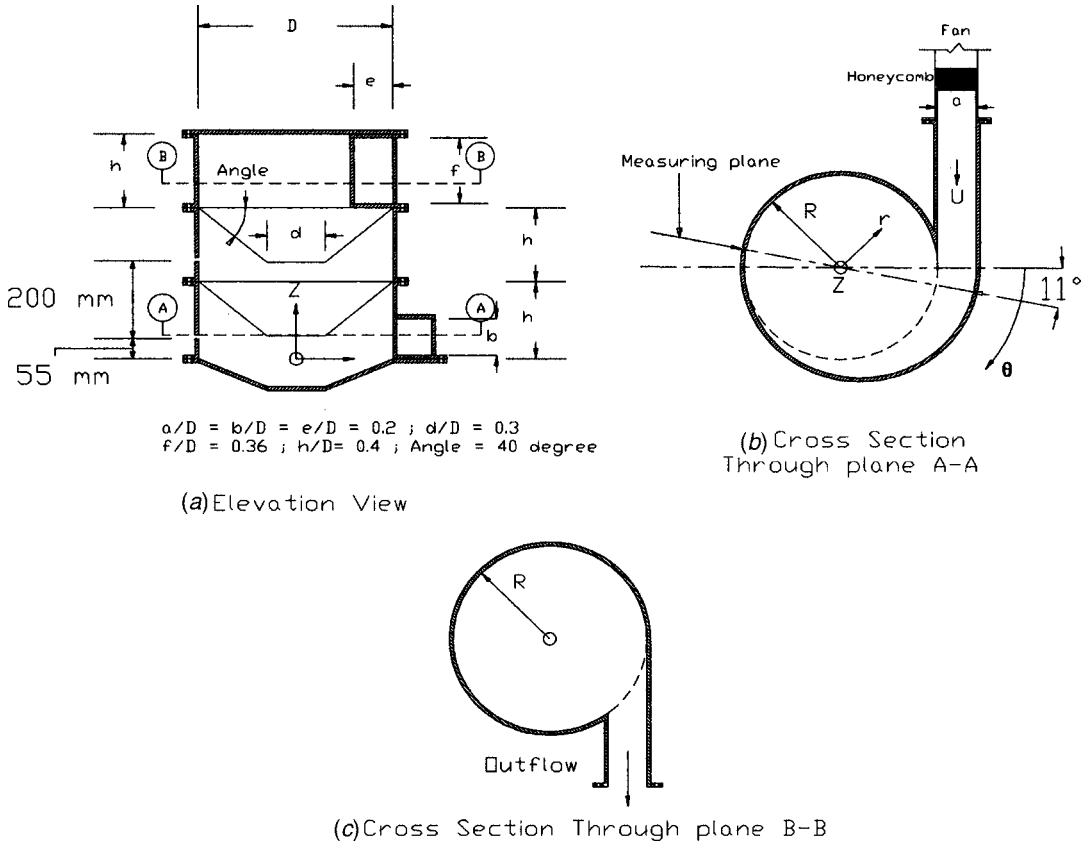

Fig. 1 Sketch of the cyclone dryer geometry in *x-z* and *x-y* plane. The configuration geometric ratio and measuring positions are also shown.

the effects of orifice diameter and chamber height on the pressure drop are investigated. This is the first stage in the development of a computational method for cyclone dryer design.

2 Flow Geometry

The geometry of the cyclone dryer used for the initial numerical investigation is shown in Fig. 1. It is characterized by the principal diameter D, and the geometric ratios detailed in Fig. 1. The diameter of the model cyclone dryer tested is 500 mm, similar to the design of Korn [3]. The orifice angle of 40 deg is greater than the angle of repose of the granular material to ensure that the grains can slide along the surface to the air jet at the orifice to achieve the necessary recirculation of grain within the dryer chamber for the ultimate drying application. The cylindrical coordinate directions are defined in Fig. 1. The origin of the coordinate system is located at the level of the interface between the conical-bottom and the cylindrical body.

3 Experimental Studies

3.1 Experimental Set-up. In order to judge the quality of the numerical simulations, experimental data were required. The cyclone dryer model used to validate the numerical results was constructed from transparent 10 mm thick acrylic. It is characterized by eight dimensions that are each expressed as a ratio to the cyclone dryer diameter as shown in Fig. 1. Air is drawn from the atmosphere through a horizontal duct to a centrifugal blower with a flow straightening honeycomb at exit. It is then fed tangentially to the lower cyclone chamber and finally discharged freely to the atmosphere from the upper chamber. The air flow-rate is adjusted by a variable frequency speed control ac motor unit. A bell mouth nozzle is fitted at the fan inlet in order to measure the air flow-rate through the system. The nozzle pressure differential is measured via a wall pressure tapping.

A three-hole modified wedge probe detailed in Fig. 2 was used

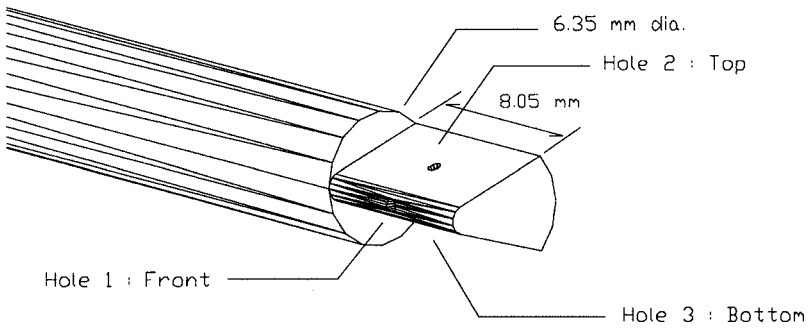

Fig. 2 Details of the modified wedge three-hole probe head

to measure radial profiles of time-average axial and tangential velocity in the cyclone dryer chambers. This device indicates the flow direction on one plane only. The axial and tangential velocity components are calculated from the direction and magnitude of velocity. The three-hole probe was calibrated in a wind tunnel against a pitot-static probe. The calibration results showed that the uncertainties of local angle and velocity measurement in two-dimensional flow were both less than 1% over the range of calibration. The sensors were connected to a pressure scanner (Furness FCS421) linked to a micromanometer (Furness FC012) which displayed pressure differential in mmH_2O. A personal computer with LABVIEW program was used to control the data acquisition, change channels, and write data files in terms of voltages at the desired sampling rate. The estimated uncertainties in this experiment were ±6% for total pressure and ±2% for velocity. The radial velocity component was not measured.

While nonzero pitch angle related by radial velocity components within the model dryer could have caused deviations from the 2D probe calibration, these effects are thought to have been acceptably small in the outer vortex region $|r/R| > 0.4$. Here the CFD prediction indicated the pitch angles to be generally less than 2 deg and the likely measurement errors from this source are less than 1 deg in angle and 2% in flow speed. Larger errors would have occurred for velocity measurements in the inner core region $|r/R| < 0.4$ at $z=0.055$ m, where pitch angles of up to 10 deg were predicted. The inner core measurements at $z=0.255$ m must be considered unreliable due to predicted pitch angles averaging 20 deg, with higer peaks. Additional measurement error is likely in regions of high shear at the edge of the vortex core due to flow nonuniformity over the probe head.

As shown in Fig. 1(*a*), axial and tangential velocity profiles were measured at two axial positions (planes at $z=0.055$ and 0.255 m) by means of the three-hole probe. At each axial location, the measurement probe was traversed in the radial direction, in a diametral plane 11 deg circumferentially from the tangential inlet connection point. The position of the probe traverse is shown in Fig. 1(*b*).

3.2 Experimental Results. Figure 3 presents typical measured radial profiles of mean tangential and axial velocity. The tangential velocity profile in Fig. 3(*b*) shows the expected Rankine (or combined) type vortex, consisting of an outer potential flow vortex with a region of near solid body rotation at the core. This flow pattern has been reported in flow field measurements of cyclone separators by several researchers [20,21]. The maximum tangential velocity rises to 2.5 and 1.5 times the inlet air velocity at the first and second measurement stations, respectively.

For measurements taken at $z=0.055$ m, the position of maximum tangential velocity is very close to the cyclone orifice diameter ($r/R=\pm 0.3$), indicating an almost symmetrical swirl flow in the lowest chamber of the cyclone dryer. At $z=0.255$ m, the vortex core is offset from the orifice center, indicating an eccentric swirl flow pattern in the higher chamber.

The axial velocity profile in Fig. 3(*a*) has a maximum at the orifice diameter ($r/R=\pm 0.3$) at both $z=0.055$ m and $z=0.255$ m. In the outer core, the magnitude of the axial velocity is nearly constant except in the near wall region, which shows a variation depending on the direction of the local air-flow. The magnitude of the peak tangential and axial velocity decreases from chamber to chamber due to turbulent diffusion and shear losses inside the cyclone dryer.

The velocity distribution was found to retain a high degree of similarity for a range of inlet velocities. Another measurement at 11 m/s inlet velocity showed a slight reduction in the relative value of the peak tangential velocity, but no change in its position. Thus, the results for a 9 m/s inlet velocity are used here to validate the numerical simulation results in the following section.

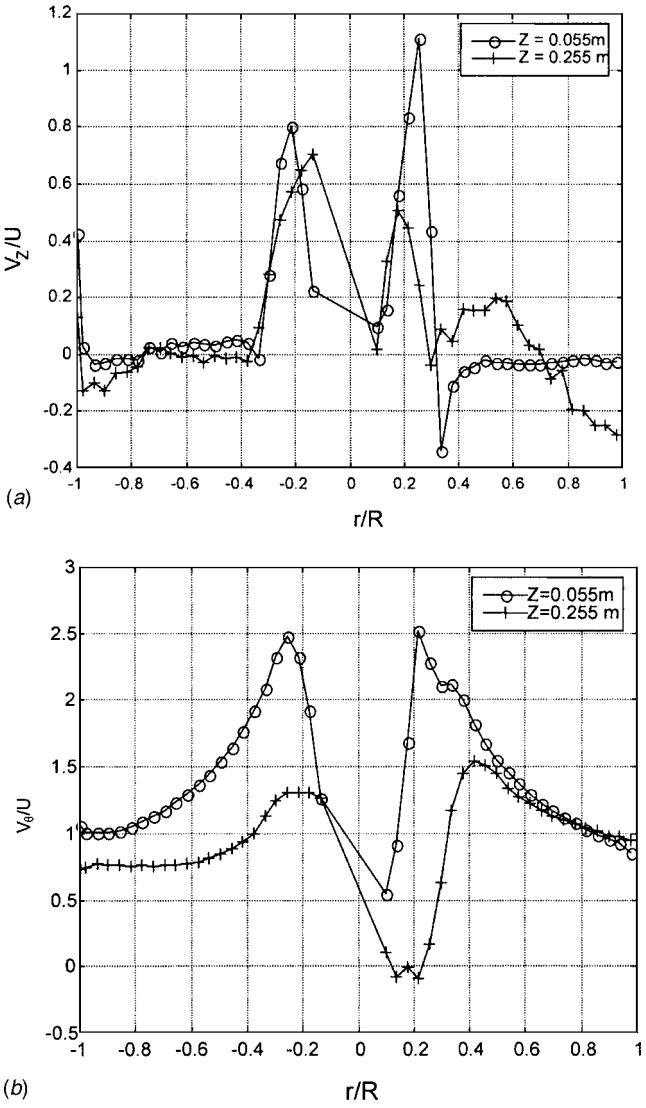

Fig. 3 Measured radial variation of velocity components at different elevations: (*a*) Axial velocity, (*b*) tangential velocity

4 Numerical Studies

4.1 Numerical Set-up and Solution Technique. The fluid dynamics of isothermal laminar and turbulent flows can be described by the Navier-Stokes equations

$$\frac{\partial \rho}{\partial \tau} + \nabla \cdot (\rho U) = 0 \tag{1}$$

$$\frac{\partial \rho U}{\partial \tau} + \nabla \cdot (\rho U \otimes U) = -\nabla P + \nabla \cdot (\mu(\nabla U + (\nabla U)^T)) \tag{2}$$

Solution of the above equations by analytical techniques is only possible for very simple cases. Numerical methods have been developed but are complicated by the addition of Reynolds stress terms ($-\rho \overline{U' \otimes U'}$) to the right-hand side of Eq. (2). To obtain values for the Reynolds stress terms, standard turbulence models are used. The models used in this study were the standard k-ε, RNG k-ε, and SSG Reynolds stress turbulence models. See, for example, CFX 5.7 user, CFX-5. Solver theory [22] for details.

A finite volume method was used to find a steady-state solution of the above set of partial differential equations. For each iteration, the full set of equations is solved using an algebraic multigrid method (AMG). The hydrodynamic equations are solved si-

multaneously as a single system. This solution approach uses a fully implicit discretization of the equations at any given iteration. Transport equations for turbulence properties are then solved. The solution procedure is repeated until the convergence criteria are met.

A series of definition files was created to obtain simulation results from CFX5.7. The simulation assumes isothermal (25°C) flow of a generic ideal gas with a reference pressure of 1 atm. Fluid enters the domain with uniform velocity of 10 m/s normal to inlet surface. The outlet boundary was specified with an average static pressure of 0 Pa. This is compatible with the experimental set-up, in which air was discharged freely to the atmosphere. A no-slip adiabatic wall boundary condition was applied for the remaining surfaces in the domain.

Boundary conditions for k and ε at the inlet were determined by assuming a turbulence intensity of 5%. A high turbulence intensity was expected due to the combined effect of the fan discharge and honeycomb mesh. A simulation using a turbulence intensity of 1% at the inlet was also run. This change was found to have only a small effect on the results. The values of k and ε at inlet were calculated using $k=\frac{3}{2}I^2U^2$ and $\varepsilon=k^{3/2}/0.3D_h$, respectively.

4.2 Numerical Validation. To investigate the effect of different modeling parameters and approaches, the following tests were performed:

(1) Mesh and turbulence modeling test:

— Tetrahedral mesh with SSG Reynolds stress turbulence model;
— hexahedral mesh with standard and RNG k-ε turbulence model.

(2) Advection scheme test:

— Upwind differencing scheme;
— "high resolution" differencing scheme;
— second order accuracy advection scheme.

(3) Grid resolution sensitivity test.

Distributions of the normalized axial and tangential velocity components V_z and V_θ as well as the total pressure drop coefficient $C_{\Delta P}=\Delta P/\frac{1}{2}\rho U^2$, were compared with the experimental results.

4.2.1 Effect of Mesh Type and Turbulence Model. Two strategies have been used for the mesh generation. They are an unstructured mixed element mesh and a structured hexahedral mesh. Meshes were produced using the ANSYS commercial grid generator ICEM 5.0. Figure 4 shows the structured hexahedral and unstructured mixed element mesh geometry.

Simulations were run for a tetrahedral mesh with the SSG Reynolds stress turbulence model and a hexahedral mesh with the k-ε turbulence model, using an upwind differencing scheme and maximum RMS residual level of 10^{-6}.

For the tetrahedral mesh, tight convergence could not be obtained for the k-ε turbulence model. However, the SSG Reynolds Stress turbulence model converged well for this kind of mesh. For the hexahedral mesh, on the other hand, excellent convergence of the k-ε turbulence model was obtained while the SSG Reynolds stress turbulence model did not converge.

To examine the combined effect of turbulence model and mesh type, results for the tangential and axial velocity components at the two heights, $z=0.055$ and 0.255 m, are presented in Figs. 5 and 6. Radial position was nondimensionalized with respect to the cyclone dryer radius and velocity is nondimensionalized by the mean inlet velocity. Results are presented at a circumferential location 11 deg from the point where the inlet duct is attached (see Fig. 1).

As shown in Figs. 5 and 6, a significant under-prediction of the tangential velocity was obtained with both the SSG Reynolds stress turbulence model and k-ε turbulence models. The results obtained with the k-ε turbulence model show reasonable success in predicting the axial velocity. Both standard and RNG k-ε turbulence models are able to predict the radial location of the axial velocity peak, but a discrepancy occurs in the SSG Reynolds Stress turbulence model prediction.

The predicted velocity distributions were nearest to the experimental results for the standard and RNG k-ε turbulence models. For this reason, the standard k-ε and RNG k-ε turbulence models with hexahedral mesh are used for the remaining investigations.

4.2.2 Effect of Differencing Scheme. In order to raise the level of confidence in the simulations, further improvement is required. The standard k-ε and RNG k-ε turbulence model with hexahedral mesh were run using upwind differencing, "high resolution" differencing and a second order accurate advection scheme. With the upwind differencing scheme a first order accurate numerical discretization is used to calculate the advection terms in the discrete equations, while a second order accurate numerical discretization is used to calculate the advection term for the second order accu-

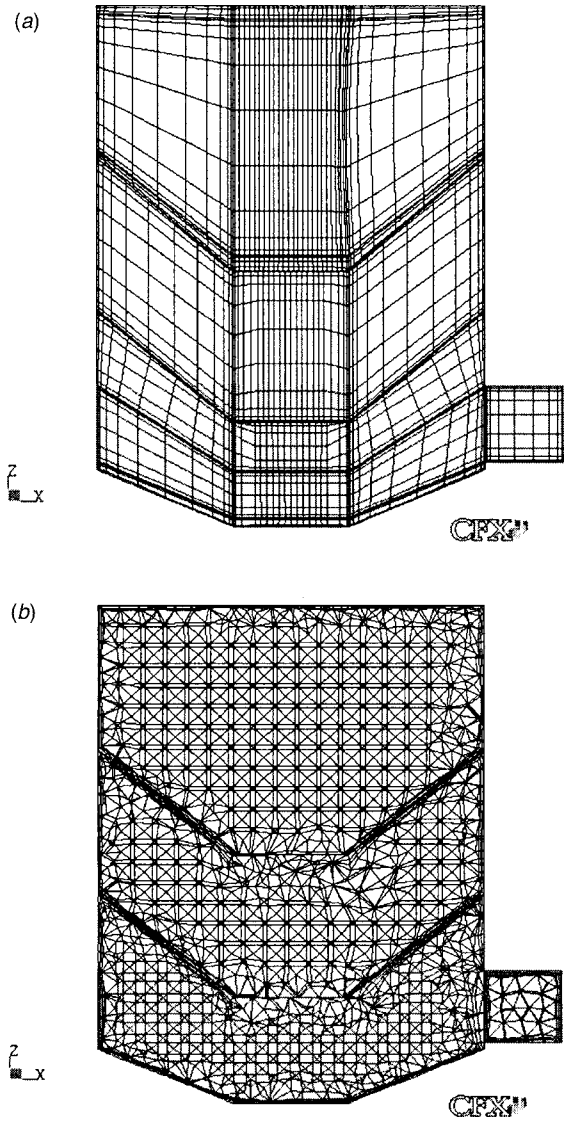

Fig. 4 Structured hexahedral and unstructured mixed element mesh of simulation geometry at center cutting plane 90 deg from inlet (*a*) 58,780 element hexahedral mesh, (*b*) 103,579 element unstructured mixed element mesh

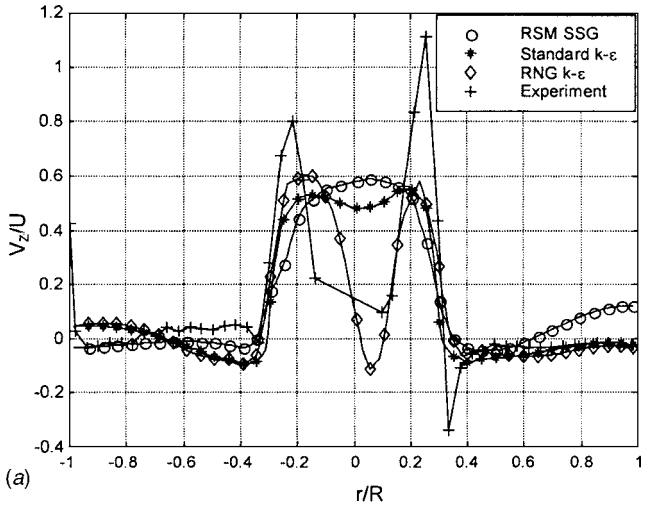

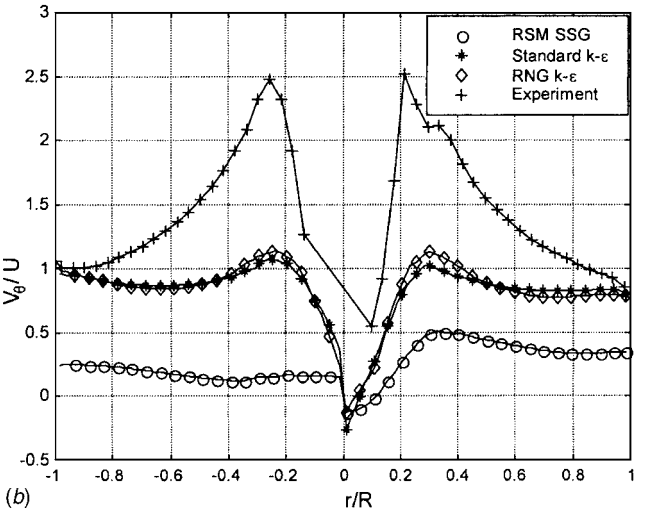

Fig. 5 Influence of turbulence model on predicted velocity profiles at 0.055 m elevation: (*a*) axial velocity, (*b*) tangential velocity

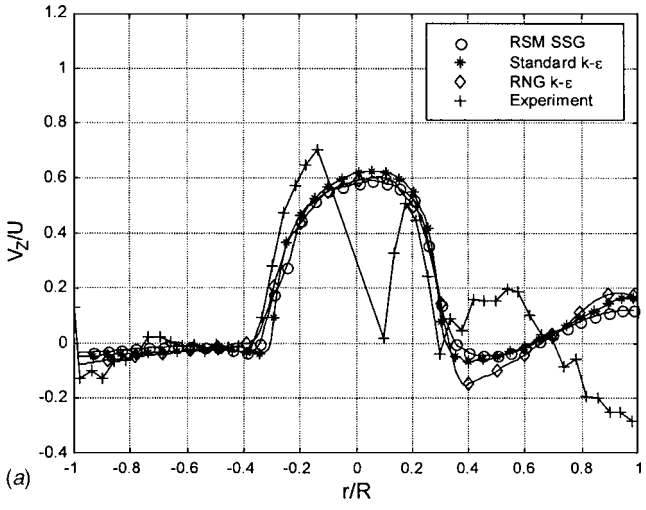

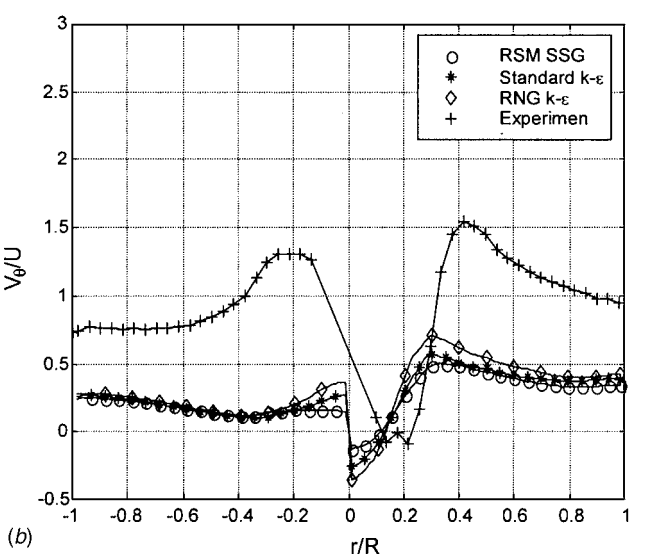

Fig. 6 Influence of turbulence model on predicted velocity profiles at 0.255 m elevation: (*a*) axial velocity, (*b*) tangential velocity

rate advection scheme. In the "high resolution" differencing scheme, the advection term is calculated using either a first or second order accurate numerical discretization depending on the local flow field in order to enforce a boundedness criterion. In flow regions with low gradients of flow variables, a second order accurate numerical discretization is used for accuracy. In areas where the flow field changes sharply, a first order accurate numerical discretization is used to prevent overshoots and undershoots and maintain robustness.

CFX definition files were set up with the automatic initial condition and a required minimum RMS residual level of 10^{-6}. Figures 7–10 show the axial and tangential velocity profiles for various differencing schemes with the standard and RNG k-ε turbulence models. These figures also show the results obtained using the upwind differencing scheme discussed in the previous section.

For both standard k-ε and RNG k-ε turbulence models, the tangential velocity was under-predicted at both measurement planes when using the upwind differencing scheme. The sharp gradient of axial velocity near the cyclone orifice cannot be captured due to the diffusive nature of this differencing scheme. The results obtained with the "high resolution" and second order accurate advection schemes significantly improve the predicted tangential and axial velocity profiles.

The second order accurate advection scheme clearly gives much better agreement than the other differencing schemes for both the magnitude and position of the maximum axial and tangential velocity. As in the previous discussion, the RNG k-ε turbulence model gives a slightly higher value than the standard k-ε turbulence model.

An overall measure of the accuracy of various differencing schemes and turbulence models is provided by the total pressure drop coefficient, which is an important parameter in dryer design. The numerical results obtained with various differencing schemes and turbulence models are compared with the experimental pressure drop values in Table 1. These results clearly show that the RNG k-ε turbulence model with the second order accurate advection scheme gives a closer prediction of the total pressure drop coefficient than the standard k-ε turbulence model and other differencing schemes. We conclude that the RNG k-ε turbulence model is the most appropriate scheme available in CFX for modeling flow in a cyclone dryer.

4.2.3 Effect of Mesh Resolution Level. To investigate the effect of truncation errors in the spatial discretization, simulations were run at three levels of mesh resolution. The three hexahedral meshes used for this test have 58,780, 278,976, and 475,232 elements. The coarsest mesh, with 58,780 elements, was used in the previous simulations. Figure 11 shows details of the meshes with

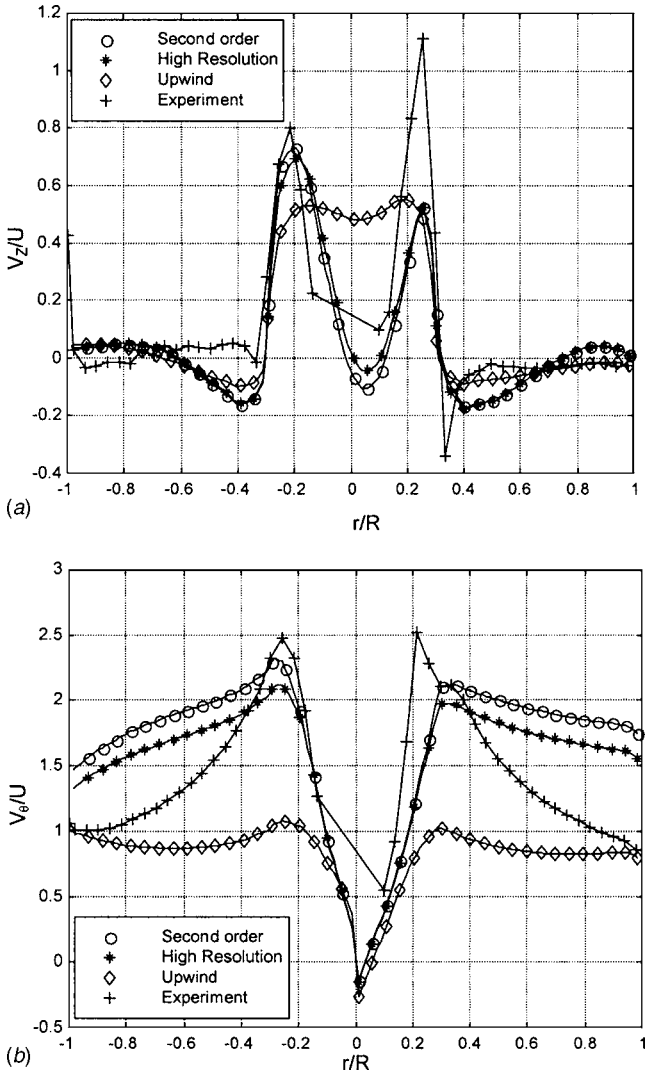

Fig. 7 Influence of advection scheme on predicted profiles at 0.055 m elevation for standard *k*-ε turbulence model: (*a*) axial velocity, (*b*) tangential velocity

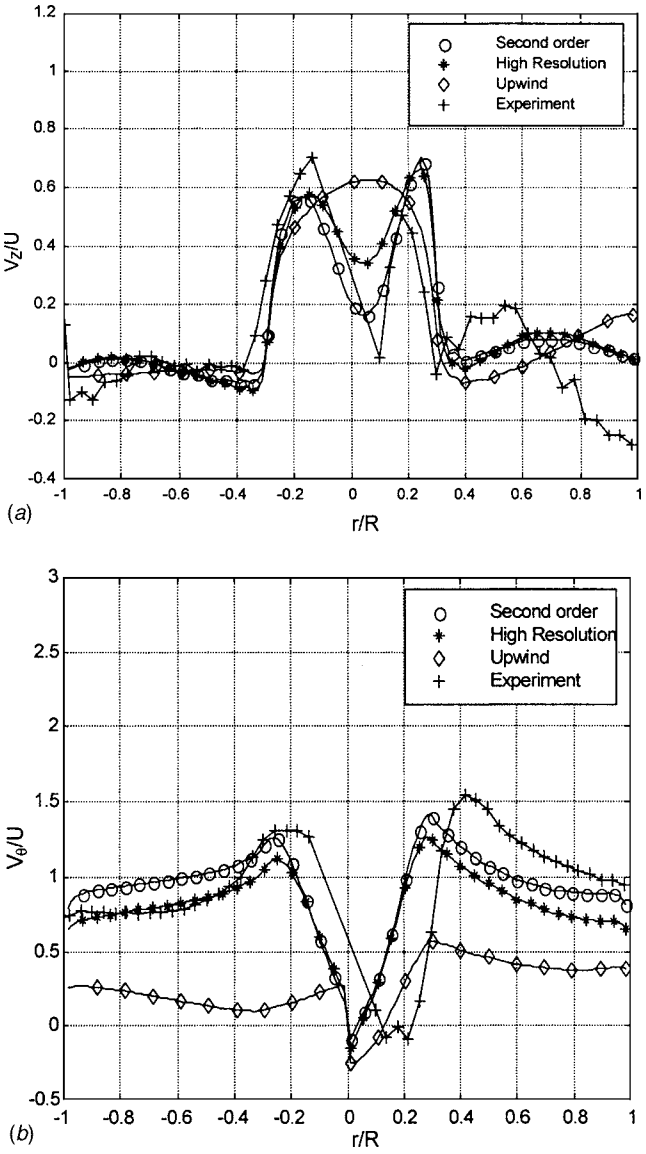

Fig. 8 Influence of advection scheme on predicted profiles at 0.255 m elevation for standard *k*-ε turbulence model: (*a*) axial velocity, (*b*) tangential velocity

278,976 and 475,232 elements. The 58,780 element mesh is shown in Fig. 4(*a*). The following comparison was made at a height of $z=0.055$ m from the reference level.

The tangential and axial velocity profiles for three levels of mesh resolution are plotted and compared with experimental data in Fig. 12. As the mesh resolution increases, the solution changes only slightly while the computational time increases considerably compared with the initial mesh resolution (57,780 elements). A similar trend in results (not shown here) was obtained for the radial velocity profiles comparison at a height of $z=0.255$ m. Based on this investigation, the solution at the initial resolution (58,780 elements) was selected as being adequately mesh independent.

4.2.4 Performance of Optimized Model. As shown in the previous sections, the optimized model with RNG *k*-ε turbulence model and hexahedral mesh gives good agreement with the experimental velocity data in the central part of the cyclone dryer. Close to the outer walls of the dryer, however, the tangential velocity calculated by the model is significantly higher than the experimental data. Poor prediction of the free vortex distribution in the outer core has also been reported by Hoekstra et al. [9] and Griffiths et al. [10] for cyclone separator simulations. They have ascribed this discrepancy to the assumption of isotropic turbulence inherent in the *k*-ε turbulence model, which leads to excessive turbulent viscosity [9,10,16]. In spite of this deficiency the optimized model still gives good agreement for the pressure drop prediction.

To further assess the performance of the optimized model for prediction of the pressure drop across the dryer, the simulation was run with the uniform inlet velocity values of 8, 10, and 13 m/s. Figure 13 compares the variation of the total pressure drop coefficient with Reynolds number (based on cyclone dryer diameter and inlet air velocity) for the experiment and simulation. The optimized model gives good agreement with the experimental data, predicting the pressure drop to within 10% in each case and giving a reasonable indication of the variation of total pressure drop coefficient with Reynolds number. This is an improvement over results of Griffiths et al. (1996) [10]. Their model of a cyclone separator used a similar turbulence model and mesh, and gave a 15% error for the pressure drop.

5 Numerical Predictions

Figure 14 shows fluid velocity vectors in diametral planes at circumferential angles of 0 and 90 deg from the inlet plane. These

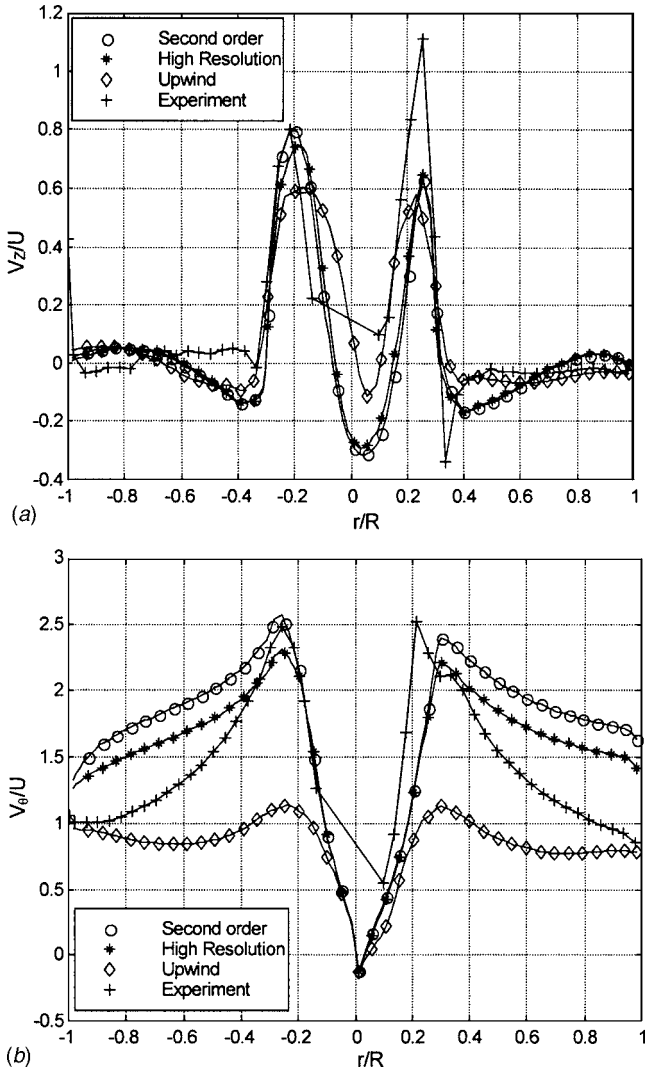

Fig. 9 Influence of advection scheme on predicted profiles at 0.055 m elevation for RNG k-ε turbulence model: (*a*) axial velocity, (*b*) tangential velocity

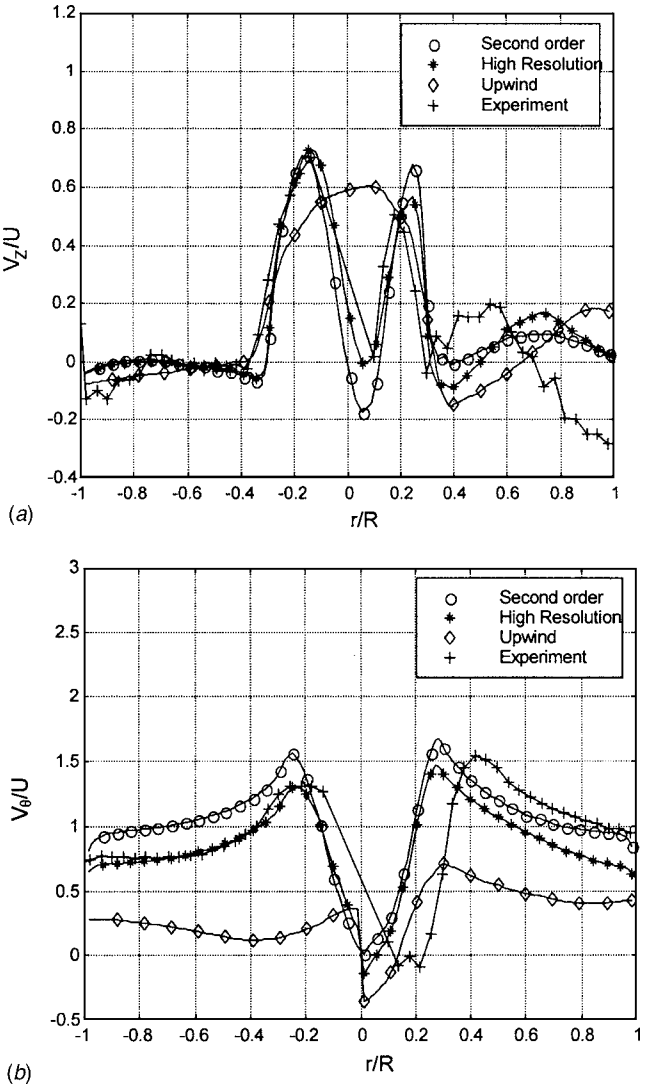

Fig. 10 Influence of advection scheme on predicted profiles at 0.255 m elevation for RNG k-ε turbulence model: (*a*) axial velocity, (*b*) tangential velocity

figures show the flow field to vary significantly with circumferential position. They also indicate the complicated structure of the velocity field in the cyclone dryer chambers.

In the lowest chamber, air-flow separates at the wall into upward and downward streams at a point close to the middle of the inlet pipe. Upward flow is present along the wall surface above the middle of the inlet pipe. This flow continues downward along the surface of the orifice plate and short circuits through the orifice to the next chamber. The downward stream continues along the conical bottom and then turns upward at the middle of the cyclone dryer.

The air core has an asymmetric pattern in the second chamber. The swirl velocity becomes weaker when passing from chamber to chamber as can be seen in the velocity plot of tangential velocity at various levels of the cyclone dryer in Fig. 15.

In the highest chamber, the flow pattern is different from the other chambers in the sense that the upward flowing air core has vanished. The vortex core is deflected from the cyclone axis and bends toward the exit pipe. This causes a re-circulation inside the highest chamber, which is clearly seen in Fig. 14(*a*).

To illustrate how the optimized computer model can be used for engineering design, simulations were performed for a cyclone dryer with modified geometry. Simulations were performed for orifice diameters of 12.5 and 17.5 cm and chamber heights of 18 and 22.5 cm. The numerical prediction results for the different designs are compared in the following discussion.

Comparison of the total pressure drop coefficient at different orifice diameters and chamber heights is shown in Fig. 16. The figure show that the total pressure drop coefficient decreases when

Table 1 Influence of numerical model on predicted total pressure drop coefficient and comparison with experiment. Model geometry as shown in Fig. 1.

Source condition	Total pressure drop coefficient
Experimental measurements (U=9–11 m/s)	16–17
Numerical Simulations (U=10 m/s)	
Standard k-ε Turbulence Model	
—Upwind differencing scheme	5.3
—High resolution differencing scheme	12.5
—Second order accuracy advection scheme	14.0
RNG k-ε turbulence model	
—Upwind differencing scheme	6.5
—High resolution differencing scheme	13.5
—Second order accuracy advection scheme	15.3

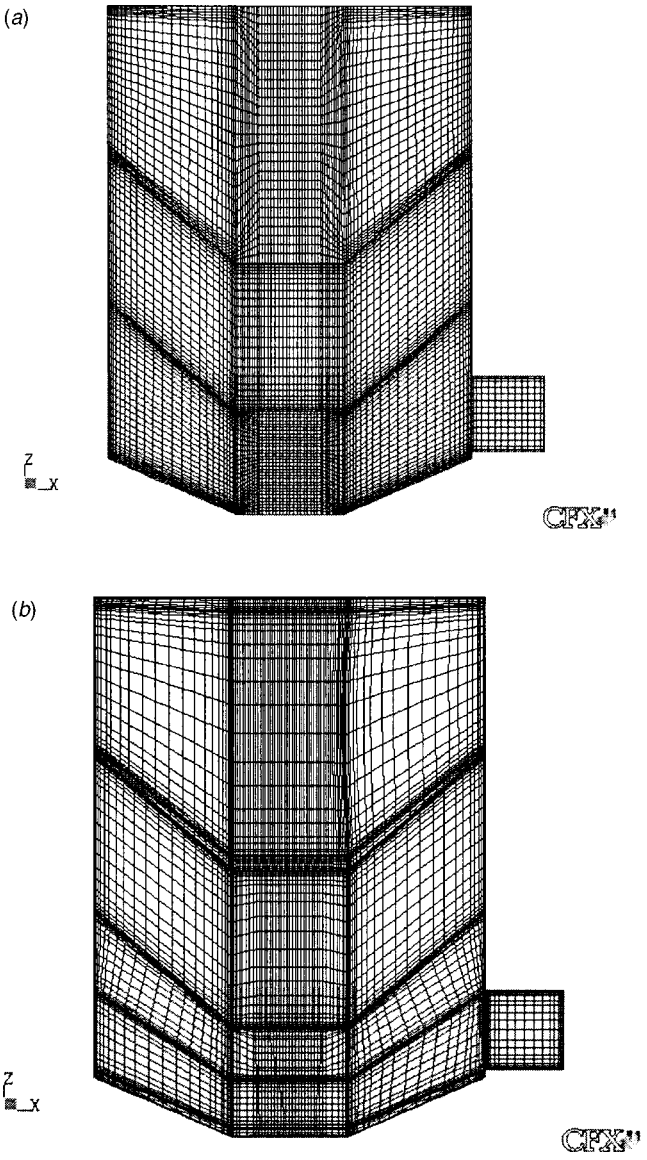

Fig. 11 Structured hexahedral meshes of different resolution (*a*) 278,976 elements, (*b*) 475,232 elements

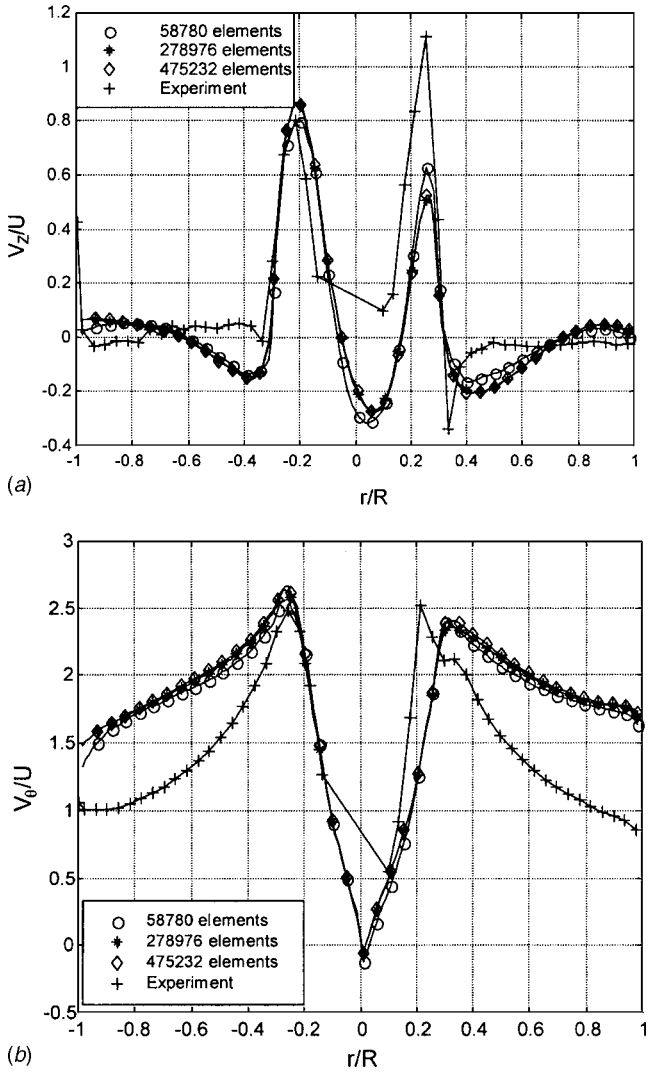

Fig. 12 Influence of mesh resolution on velocity distribution predicted at 0.055 m elevation by RNG k-ε turbulence model: (*a*) axial velocity, (*b*) tangential velocity

the orifice diameter increases. There are probably two main factors contributing to this trend. Assuming that the discharge coefficient of the orifice remains approximately constant, maintaining the same flow rate through a smaller orifice diameter will lead to a higher pressure drop; conservation of angular momentum will require a higher tangential velocity of the vortex core and increase shear losses.

The variation in the total pressure drop coefficient for different chamber heights is somewhat counter-intuitive. Figure 17 shows that the pressure drop across the cyclone dryer decreases with increasing chamber height, while experience from pipe flow suggested that the total pressure drop coefficient should increase with increasing chamber height. The observed decrease with increasing chamber height is probably due to increasing diffusion of the vortex core, which reduces the intensity of the secondary circulation such that the reduction in wall shear stress more than offsets the increase in surface area.

6 Conclusions

Simulation of the flow field inside a three-chamber cyclone dryer has been carried out using the CFX5.7 solver. A level of

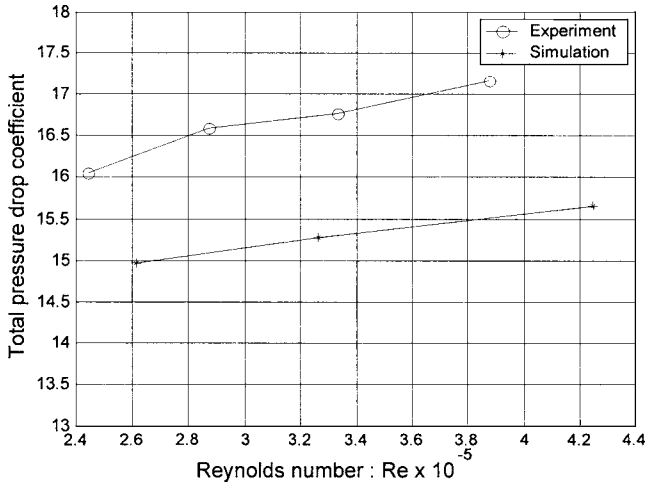

Fig. 13 Pressure drop characteristics from simulation and experiment

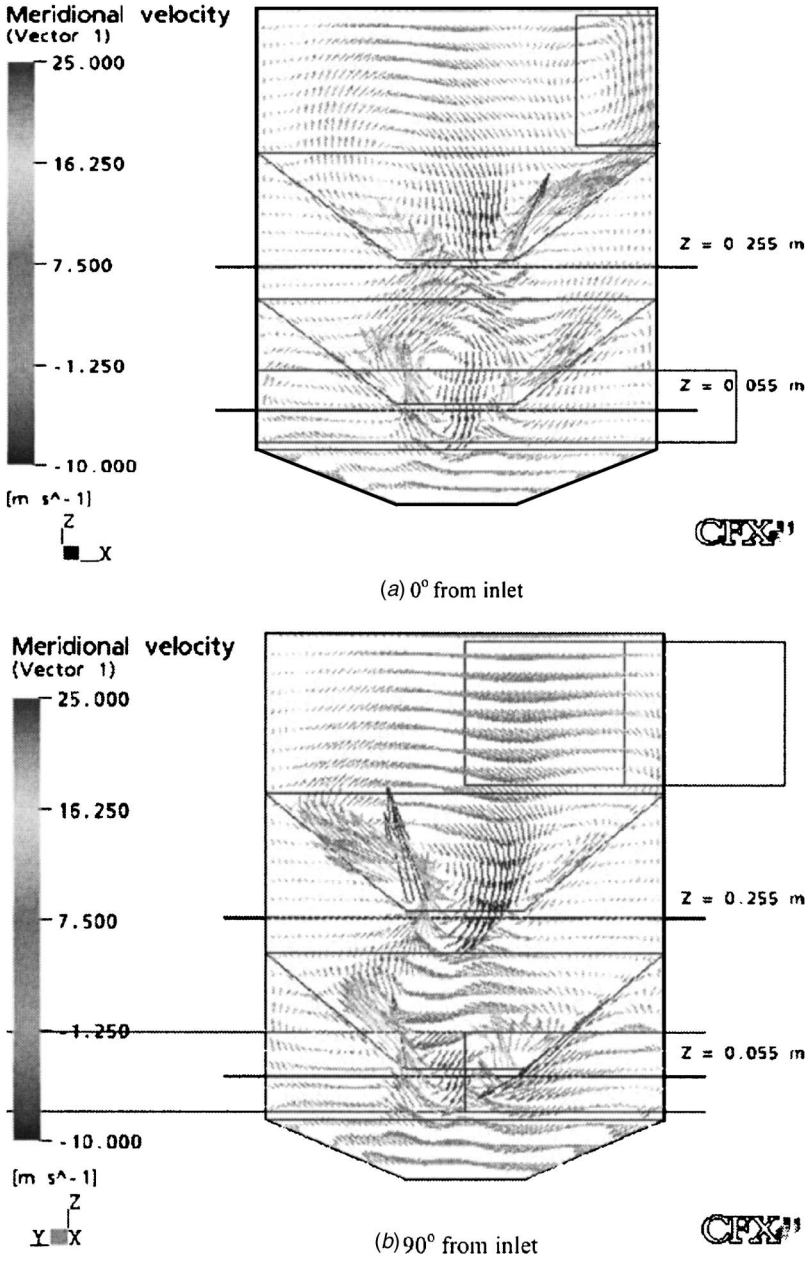

Fig. 14 Meridional velocity vector plot in different diametral planes (*a*) 0 deg from inlet, (*b*) 90 deg from inlet

confidence in the simulation results was established through a comparison with experimental results. Axial and tangential velocity profiles along the cyclone dryer radius at two heights above the reference level were used to evaluate the effect of simulation parameters. The SSG-Reynolds stress turbulence model with a tetrahedral mesh showed the poorest agreement with the experimental results. The results obtained using the standard and RNG k-ε turbulence model with hexahedral mesh showed fair to good agreement with the experimental data, both in terms of the axial and tangential velocity distributions, and the total pressure drop coefficient.

A major improvement in simulation results was obtained when the second order accurate advection scheme was used. The results were not significantly changed when the mesh resolution increased. The advection scheme was found to be the most important parameter for improving simulation results.

A comparison of numerical and experimental results showed that the RNG k-ε turbulence model with hexahedral mesh and second order accurate advection scheme gives the best agreement with experimental data. Although it produces more linear radial variation of tangential velocity outside the vortex core region than the free vortex distribution seen in the experimental data, the axial velocity and total pressure drop coefficient were reasonably well predicted. The discrepancy in tangential velocity distribution is believed to be due to the assumption of isotropic turbulence hypothesis inherent in the k-ε turbulence model, which leads to excessive turbulent viscosity [9,10,16].

The accuracy of the computer model has been demonstrated through good agreement between the calculated and measured axial velocity distribution and pressure drop prediction. The model gives an excellent prediction of the magnitude and position of the peaks of the tangential and axial velocity, with 10% error in

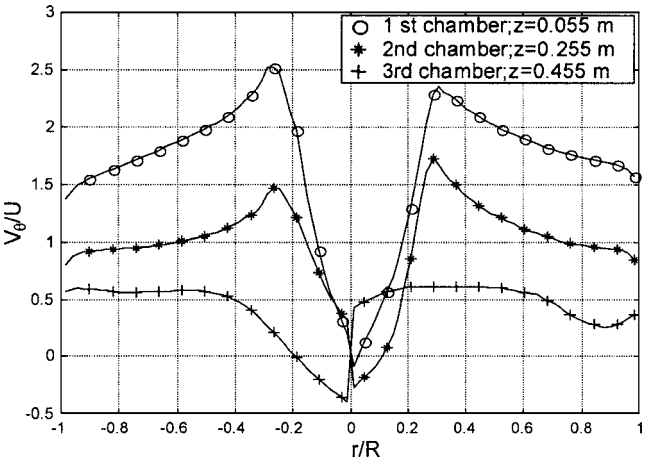

Fig. 15 Radial variation of tangential velocity component at different elevations on 0 deg cut plane from cyclone inlet

the prediction of pressure drop. This level of error is somewhat lower than in previous work (15% error) on cyclone separator loss prediction [9].

The current simulations highlight the complex flow phenomena occurring inside the cyclone dryer chambers. Effects of orifice diameter and chamber height on pressure drop was studied. As expected, a smaller orifice diameter gives an increased pressure drop. A counter-intuitive behavior of pressure drop was observed when chamber height was varied. The pressure drop was found to decrease as chamber height increases. This is probably due to increasing diffusion of the vortex core, which reduces the intensity of the secondary circulation such that the reduction in wall shear stress more than offsets the increase in surface area.

Acknowledgment

The support of School of Engineering, University of Tasmania for the cyclone dryer prototype fabrication and ANSYS, Inc. for the CFX academic software licence is gratefully acknowledged. The first author would like to express his gratitude to Srinakarinwirot University, Thailand for financial support during his PhD study at the University of Tasmania.

Nomenclature

D = cyclone body diameter (m)
I = turbulence intensity (%)
P = total pressure (Pa)
U = mean inlet velocity (m/s)
V = velocity (m/s)

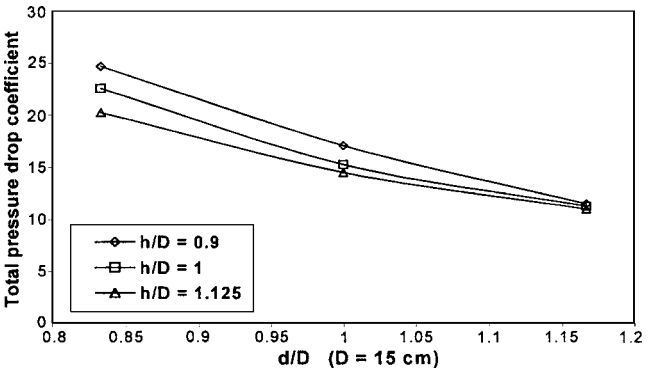

Fig. 16 Predicted influence of orifice diameter on total pressure drop coefficient for various chamber heights

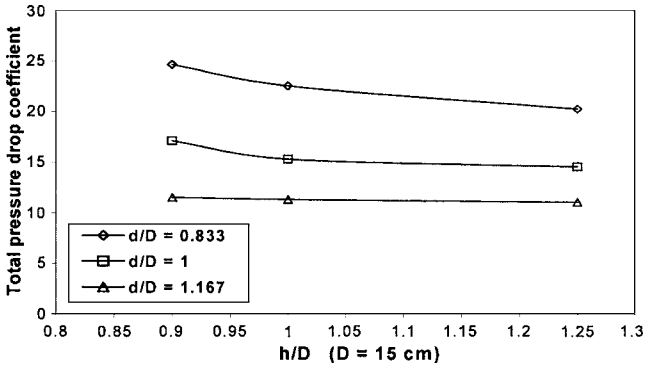

Fig. 17 Predicted influence of chamber height on total pressure drop coefficient or various orifice diameters

k = turbulent kinetic energy per unit mass ($(m/s)^2$)
ε = turbulent dissipation rate (m^2/s^3)
μ = viscosity (kg/ms)
ρ = density (kg/m^3)
τ = time (s)
r = radial position (m)
θ = circumferential position (deg)
z = axial position (m)

Dimensionless parameters

$C_{\Delta P}$ = total pressure drop coefficient $=\Delta P/\frac{1}{2}\rho U^2$
Re = Reynolds number $=\rho UD/\mu$

Subscripts

m = meridional
r = radial
z = axial
θ = tangential

References

[1] Discroll, R. H., and Adanezak, T., 1985, "Drying Systems for the Humid Tropics. Preserving Grain Quality by Aeration and In-Store Drying," *Proceedings of International Seminar*, Kuala Lumpur, Malaysia, Oct. 9–11 1985; B. R. Champ and E. Highley, eds.; AICAR: Canberra, Australia, pp. 58–68.
[2] Nebra, S. A., Silva, M. A., and Mujumdar, A. S., 2000, "Drying in Cyclones—A Review," Drying Technol., **18**, pp. 791–832.
[3] Korn, O., 2001, "Cyclone Dryer: A Pneumatic Dryer With Increased Solid Residence Time," Drying Technol., **19**, pp. 1925–1937.
[4] Heinze, C., 1984, "New Cyclone Dryer for Solid Particles," Ger. Chem. Eng, **7**, pp. 274–279.
[5] Ulrich, W., 2002, "Cyclone Dryer," 13th International Drying Symposium (IDS 2002), Beijing, China, Aug. 27–30, Vol. B., pp. 867–873.
[6] Boysan, F., Ayers, W. H., and Swithenbank, J., 1982, "A Fundamental Mathematical Modeling Approach to Cyclone Design," Trans. Inst. Chem. Eng., **16**, pp. 222–230.
[7] Zhou, L. X., and Soo, S. L., 1990, "Gas-Solid Flow and Collection of Solids in a Cyclone Separator," Powder Technol., **63**, pp. 45–53.
[8] Modigell, M., and Weng, M., 2000, "Pressure Loss and Separation Characteristics Calculation of a Uniflow Cyclone With a CFD Method," Chem. Eng. Technol., **23**, pp. 753–758.
[9] Hoekstra, A. J., Derksen, J. J., and Van Der Akker, H. E. A., 1999, "An Experimental and Numerical Study of Turbulent Swirling Flow in Gas Cyclones," Chem. Eng. Sci., **54**, pp. 2055–2065.
[10] Griffiths, W. D., and Boysan, F., 1996, "Computational Fluid Dynamics (CFD) and Empirical Modeling of the Performance of a Number of Cyclone Samples," J. Aerosol Sci., **27**, pp. 281–304.
[11] Zhao, J. Q., and Abrahamson, J., 1999, "The Flow in Conical Cyclones," Second International Conference on CFD in the Minerals and Process Industries, Melbourne, Australia, Dec. 6–8, 1999; CSIRO, pp. 497–502.
[12] Yoshida, H., Saeki, T., Hashimoto, K., and Fujioka, T., 1991, "Size Classification of Sub-Micron Powder by Air Cyclone and Three-Dimensional Analysis," J. Chem. Eng. Jpn., **24**, pp. 640–647.
[13] Yoshida, H., Fukui, K., Yoshida, K., and Shinoda, E., 2001, "Particle Separation by Iinoya's Type Gas Cyclone," Powder Technol., **118**, pp. 16–23.
[14] Montavon, C. A., Grotjans, H., Hamill, I. S., Phillips, H. W., and Jones, I. P., 2000, "Mathematical Modelling and Experimental Validation of Flow in a Cyclone," 5th International Conference on Cyclone Technologies, Warwick, UK, 31 May–2 June, 2000; BHR Group, pp. 175–186.

[15] Schmidt, S., and Blackburn, H. M., 2003, "Simulation of Turbulent Flow in a Cyclonic Separator," Third International Conference on CFD in the Minerals and Process Industries, Melbourne, Australia, Dec. 10–12 2003; CSIRO, pp. 365–369.
[16] Wang, B., Xu, L. X., Xiao, G. X., Chu, K. W., and Yu, A. B., 2003, "Numerical Study of Gas-Solid Flow in a Cyclone Separator," Third International Conference on CFD in the Minerals and Process Industries, Melbourne, Australia, Dec. 10–12 2003; CSIRO, pp. 371–376.
[17] Derksen, J. J., 2003, "Separation Performance Predictions of a Stairmand High-Efficiency Cyclone," AIChE J., **49**, pp. 1359–1371.
[18] Derksen, J. J., and Van den Akker, H. E. A., 2000, "Simulation of Vortex Core Precession in a Reverse-Flow Cyclone," AIChE J., **46**, pp. 1317–1331.
[19] Witt, P. J., and Mittoni, L. J., 1999, "Validation of a CFD Model for Predicting Gas Flow in a Cyclone," CHEMECA99, Newcastle, Australia, Dec. 26–29.
[20] Shepherd, C. B., and Lapple, C. E., 1940, "Flow Pattern and Pressure Drop in a Cyclone Dust Collector," Ind. Eng. Chem., **31**, pp. 1246–1248.
[21] Stairmand, C. J., 1949, "Pressure Drop in a Cyclone Separator," Engineering (London), **168**, pp. 408–413.
[22] ANSYS, 2004, "Turbulence and Wall Function Theory" and "Initial Condition Modeling," In CFX-5. Solver theory, ANSYS, Canada Ltd., Waterloo.

A Computational and Experimental Investigation of the Human Thermal Plume

Brent A. Craven
e-mail: bac207@psu.edu

Gary S. Settles

Gas Dynamics Laboratory,
Department of Mechanical and Nuclear Engineering,
The Pennsylvania State University,
University Park, PA 16802

The behavior of the buoyant plume of air shed by a human being in an indoor environment is important to room ventilation requirements, airborne disease spread, air pollution control, indoor air quality, and the thermal comfort of building occupants. It also becomes a critical factor in special environments like surgery rooms and clean-rooms. Of the previous human thermal plume studies, few have used actual human volunteers, made quantitative plume velocity measurements, or considered thermal stratification of the environment. Here, a study of the human thermal plume in a standard room environment, including moderate thermal stratification, is presented. We characterize the velocity field around a human volunteer in a temperature-stratified room using particle image velocimetry (PIV). These results are then compared to those obtained from a steady three-dimensional computational fluid dynamics (CFD) solution of the Reynolds-averaged Navier-Stokes equations (RANS) using the RNG k-ε two-equation turbulence model. Although the CFD simulation employs a highly simplified model of the human form, it nonetheless compares quite well with the PIV data in terms of the plume centerline velocity distribution, velocity profiles, and flow rates. The effect of thermal room stratification on the human plume is examined by comparing the stratified results with those of an additional CFD plume simulation in a uniform-temperature room. The resulting centerline velocity distribution and plume flow rates are presented. The reduction in plume buoyancy produced by room temperature stratification has a significant effect on plume behavior. [DOI: 10.1115/1.2353274]

Introduction

The human body is continually exchanging energy with its environment. As a result of the thermoregulatory process, the body core temperature remains relatively constant at 37°C (98.6°) [1]. From conservation of energy, in order to maintain this body core temperature the rate of metabolic heat production must be balanced by the net rate of heat loss to the surroundings [2]. In general, the human body rejects heat to the environment by a combination of radiation, convection, evaporation, and respiration. More specifically, Murakami et al. [3] suggest that these mechanisms account for 38.1%, 29.0%, 24.2%, and 8.7%, of the total heat loss, respectively.

Radiation and convection both depend on the temperature difference between the body's surface and its surroundings. For convection the temperature of the surrounding air is important, while for radiation it is the temperature and placement of surrounding solid surfaces that matters. Evaporative heat loss depends on the temperature of the body surface, the relative humidity of the ambient air, and salt in the perspiration. In a quiescent ambient environment the combined effect of these heat transfer mechanisms is to bring the body surface to a steady-state temperature somewhat below that of the body core. At moderate room temperatures and with ordinary levels of activity, the average person can generate up to 100 Watts of thermal energy [4,5].

Given this elevated body surface temperature, a temperature gradient forms in the surrounding air that drives buoyant convection, and a thermal free-convection boundary layer develops about the human body. Initially this boundary layer, which begins at the feet, is laminar. However, as the flow proceeds up the legs, transition occurs and the upper body becomes enveloped in turbulent flow. At the shoulders and atop the head, the boundary layer separates and regions of recirculation form. This phenomenon has been observed in experiments using schlieren photography, Refs. [5,6] and Figs. 1 and 2, which detects temperature gradients in air by way of the associated gradients of refractive index. Finally, the separated flow above the shoulders mixes with the buoyancy-driven flow from the head and rises above the body to form what is known as the *human thermal plume*.

Knowledge of the behavior and underlying physics of the human thermal plume is essential to indoor air quality control for thermal comfort, the study of contaminant transport from the human body, and the understanding of the entrainment of respirable particles into the human breathing zone. The design of effective heating, ventilation, and air conditioning (HVAC) systems for climate control and fresh air delivery also hinges on the flow rate of the human thermal plume. One experimental study [7] showed that typical HVAC systems only evacuate approximately 1/8th of the estimated 40 liters/s flow rate produced by the human plume, thus resulting in a stale indoor environment. Indeed, ASHRAE Standard 62.1-2004 mandates a ventilation rate of only 7.5 liters/s per person for acceptable indoor air quality. Not only bioeffluents from the skin, but also expired air is entrained into the plume. These bioeffluents are usually mixed with the surrounding room air rather than being removed, which can result in the spread of disease.

Exfoliated human skin is the most prevalent particulate in the human thermal boundary layer and plume. On average, a complete layer of skin is shed every 1 to 2 days [9], releasing a million skin scales/min with a 14 μm average diameter and a size range from sub-μm to 50 μm. Most inhaled air comes from the human boundary layer that contains these particles, from which 6000 to 50,000 particles/liter of air enter the human nose. Most clothing is permeable to this particle stream. As a consequence of this prolific human particle generation and subsequent plume transport, ordinary house dust consists of 70–90% human skin flakes, often

Contributed by the Fluids Engineering Division of ASME for publication in the JOURNAL OF FLUIDS ENGINEERING. Manuscript received June 1, 2005; final manuscript received March 19, 2006. Assoc. Editor: Malcolm J. Andrews.

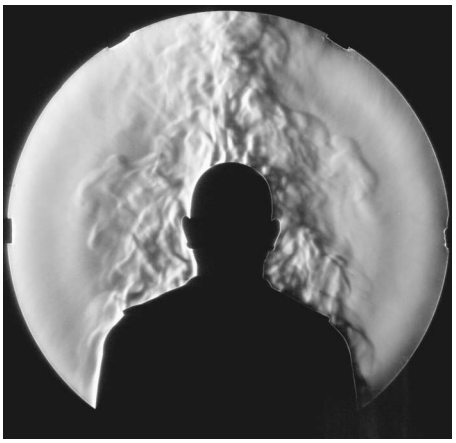

Fig. 1 Schlieren image of the human thermal plume, front view, captured using a 1.0 m aperture double-pass coincident schlieren system with inherently high sensitivity to weak thermal gradients [8]

covered with microorganisms. Such particulate contamination from people has been a problem in microelectronics manufacturing for many years.

Recently the human thermal plume has been recognized as a potential whole-body chemical trace sampling system [4,10]. If the plume is collected and sampled, its contaminant burden may be analyzed for various purposes including medical diagnosis and substance detection. Utilizing this concept, an explosive trace detection "portal" has been implemented for aviation security screening [11].

Thus for many reasons a complete understanding of the detailed fluid dynamics of the human thermal plume is useful. In principle, experiments involving live human subjects provide the most accurate results, though heated mannequins have been used in some previous studies (e.g., [3,7,12]). However, in practice, experimental measurements of the human thermal plume are difficult to obtain and are limited in detail. Here, computational fluid dynamics (CFD) is used as a supplement to optical flow measurements in order to provide a more complete description of the plume.

Objectives

The main objective of the present work is to characterize the human thermal plume in a typical quiescent thermally stratified room environment using a CFD simulation and experimental velocity measurements obtained by particle image velocimetry (PIV). The effects of room thermal stratification on the plume are also explored via comparison with a second CFD simulation of the plume in a uniform environment.

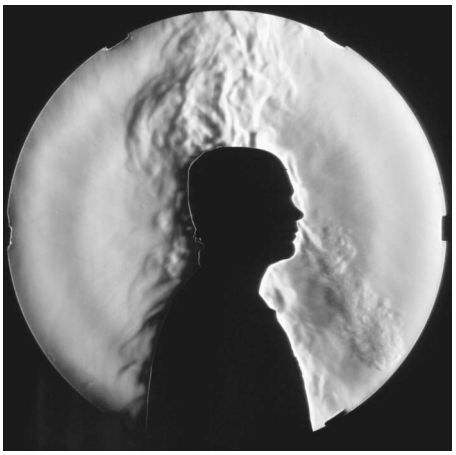

Fig. 2 Schlieren image of the human thermal plume, side view. Notice also the warm turbulent exhaled air from the nose of the subject.

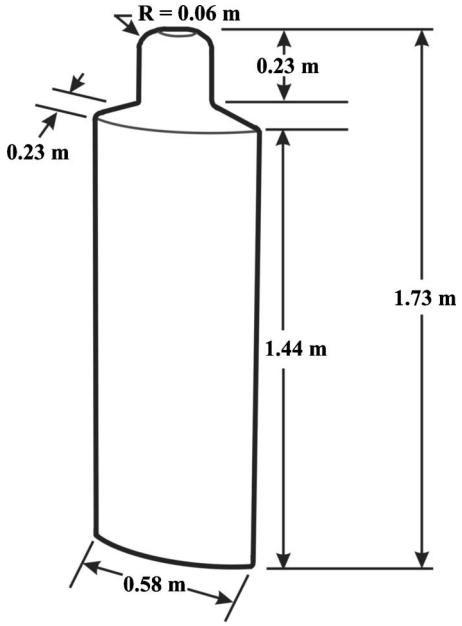

Fig. 3 Computational model of the human form

Computational Methodology

Assumptions. The present CFD simulation assumes a human being of average height [13] standing in a large quiescent room. The specific dimensions of the CFD model, shown in Fig. 3, were chosen so as to coincide with those of our human volunteer. For simplification, though, arms and legs are omitted from the model. Thus, we assume the secondary features of the human form are irrelevant to the formation of the human thermal plume. Consequently, the CFD model represents a standing human with arms held close to the torso.

Since the primary objective is the analysis of convective heat transfer from the human body, radiation, evaporation, and respiration are not directly modeled. However, the combined effect of these mechanisms of heat transfer is implicit in the specification of a constant model surface temperature boundary condition, based on experimental data.

Clothing was likewise not directly modeled. However, the net effect of clothing in reducing the outermost surface temperature of a clothed human is also implicit in the specified model surface temperature. In general clothing has an insulating effect, so that the outer surface of the garments forms the true boundary condition of the human body for convective heat transfer [1,2]. Physically, the small air gap between the skin and the clothing resists heat transfer. Thus, in modeling the human thermal plume, our constant CFD-model surface temperature is set equal to the experimentally obtained average external clothing temperature of our human subject, who wore overalls having a clothing insulation value of approximately 0.30 clo [2].

The human boundary layer and thermal plume are here considered fully turbulent for simplicity. In general, the stability of a free-convection boundary layer depends on the ratio of the buoyancy to viscous forces (i.e., Rayleigh number, Ra [14]). Experiments show that transition on heated vertical surfaces occurs at $Ra \approx 10^9$. Considering the free-convection boundary layer over a human body at a surface temperature of 26.6°C with ambient air at 21.3°C, this corresponds to a height of about 1.2 m above the floor. Since our CFD model height is 1.73 m, the boundary layer

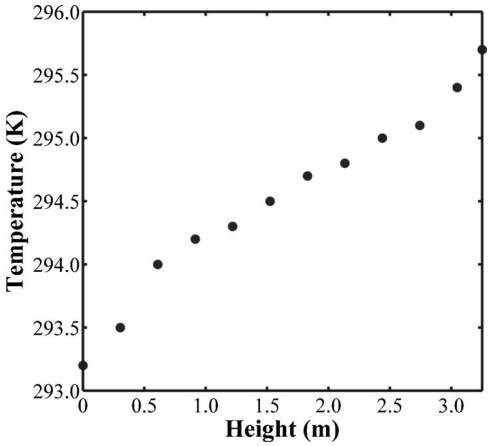

Fig. 4 Experimental room stratification temperature profile

above about chest level and the entire thermal plume are considered turbulent. Since the current work is primarily focused on the plume rather than the boundary layer, the additional difficulty of computationally simulating transition on the body is not presently warranted.

Turbulence Model. A two-equation k-ε turbulence model was chosen for closure of the Reynolds-averaged Navier-Stokes equations because of its proven reliability in modeling free shear flows [15]. In particular, the renormalization group (RNG) k-ε model has been shown superior to the standard k-ε model in predicting room airflows [16], making it the presently preferred choice. This was confirmed in preliminary calculations using the standard and RNG k-ε models and a k-ω turbulence model.

Thermal Stratification. In modeling the human thermal plume in a standard room environment, the effect of any thermal stratification must be included. Temperature measurements were made in the stably stratified room where our human-subject PIV measurements were taken, under identical experimental conditions. The vertical temperature distribution is approximately linear, as shown in Fig. 4.

Quantitatively, the stratification amplitude may be characterized by S, the nondimensional stratification parameter, which appears in the nondimensional form of the energy equation. Following a standard definition (e.g., [17–19]): $S=H/(T_S-T_{\infty,H/2})dT_\infty/dh$, where H is the height of our subject/model, T_S corresponds to the average external surface temperature of our subject/model, $T_{\infty,H/2}$ is the air temperature at $H/2$, and dT_∞/dh is the ambient temperature gradient, which is constant if the room is linearly stratified.

In the present study $S=0.24$. Comparing this to the maximum acceptable stratification level suggested by ASHRAE [2], the present stratification is at a moderately low level. Assuming linear stratification, an ambient temperature gradient of no more than 4.4°C/m is recommended for 80% acceptability [2]. For the appropriate H and T_s of our subject, a room having a 4.4°C/m temperature gradient corresponds to a stratification parameter of $S=1.35$. A parametric study of the influence of $0 \leqslant S \leqslant 1.35$ on the human plume would be interesting, but is outside the present scope.

Boundary Conditions. The various boundary conditions specified in the computational domain are shown in Fig. 5. Due to the complexity of this problem, matching the temperature stratification profile of Fig. 4 requires a closed-domain approach: The computational domain is a "sealed" room with a heat sink in the sidewall to exactly compensate for the plume convection at steady-state. Alternatively, the simpler case of a uniform room temperature distribution—simulated for comparison purposes—worked best with an open domain approach. The corresponding

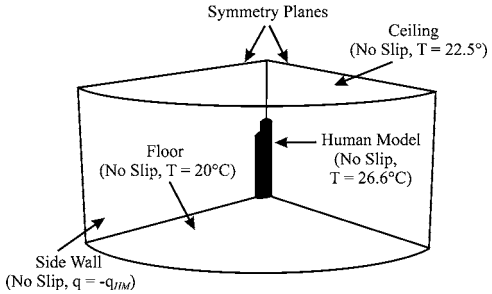

Fig. 5 Boundary conditions for thermally stratified CFD domain

boundary conditions for this case are illustrated in Fig. 6.

The large thermally stratified "room" in which the CFD-model human was placed consisted of an impermeable floor, ceiling, and side walls. The ceiling height was set to 3.25 m, corresponding to that in the experiment. Thus, the influence of the ceiling height on the human thermal plume (as opposed to the case of a free-air plume) was captured in the present simulation. Also the lateral radius of the CFD domain was specified to be 5 m; large enough to avoid significant sidewall effects on the human thermal plume. This is confirmed in our CFD results by a nearly-quiescent ambient room environment, where velocities are on the order of 0.01 m/s (more than an order of magnitude less than velocities in the plume).

To reduce the required CPU time, symmetry boundary conditions were used in both the coronal (shoulder-to-shoulder) and sagittal (front-to-back) planes. Symmetry in the sagittal plane is justified by the simplified CFD model of the human form shown in Fig. 3 (no facial features).

The constant surface temperature boundary condition of the CFD human model, 26.6°C, is the average of 40 measurements made at various locations on the external clothing surface of our human volunteer under experimental conditions. (The actual average skin temperature, also based on an average of 40 measurements at the same locations, is 31.8°C.)

In the case of the stratified room environment, the temperature of the floor and ceiling were specified to correspond to those measured experimentally (20° and 22.5°, respectively). However, the thermal boundary condition at the sidewall is more involved. To obtain a steady-state solution, the side wall was used as a heat sink, where the corresponding heat flux was varied iteratively until it matched that generated by the human model (35.32 W). This resulted in a stably-stratified CFD room environment with a temperature profile closely matching that of Fig. 4.

To compute the plume in a uniform-temperature environment, though, the floor, ceiling, and side walls are all assumed adiabatic (Fig. 6). A pressure-inlet boundary condition is applied near the

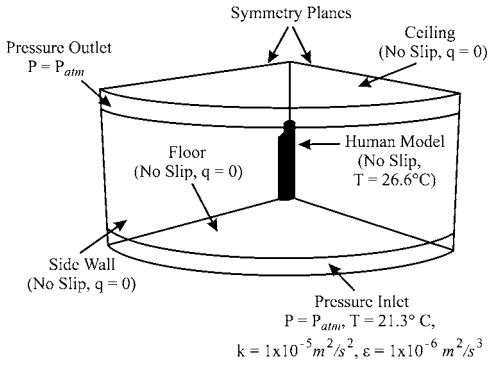

Fig. 6 Boundary conditions for uniform-temperature CFD domain

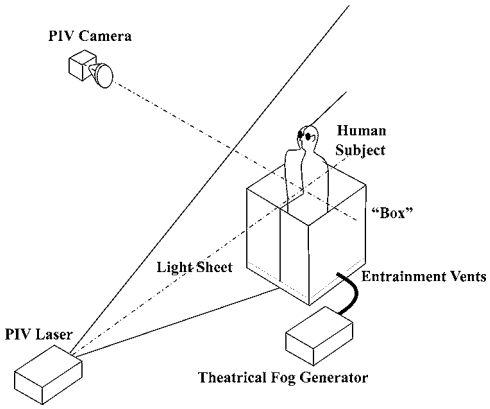

Fig. 7 Schematic of experimental setup

floor, with $p=1$ atm and $T=21.3\,^{\circ}\mathrm{C}$ (the average temperature in the stably-stratified experimental room). A corresponding pressure outlet near the ceiling is subject to the outflow boundary condition: $p=1$ atm.

The turbulence model requires turbulent inlet boundary conditions to be specified at a pressure inlet, even though in reality the air is laminar and nearly stagnant there. Thus, values for turbulent kinetic energy, k, and turbulent dissipation rate, ε, were set so as to obtain very low levels of incoming turbulence.

In both stratified and uniform-environment simulations the Boussinesq approximation was used, where all fluid properties are assumed constant and are evaluated at an appropriate reference temperature, except for density in the buoyancy term of the governing equations [14]. A reference temperature of $21.3\,^{\circ}\mathrm{C}$ is used in both cases.

Grid Generation. Even with the discussed simplification, the geometry of the shoulders and head of the CFD human model required an unstructured tetrahedral meshing scheme. The grid was adapted such that its density was greatest near the model, where proper resolution of the boundary layer is desired, while a comparatively course grid was used in the far field. The near-wall mesh on the human model was adapted so as to resolve the entire free-convection boundary layer. No wall functions were used.

Simulation Summary. The present simulations were performed on a single Pentium IV, 3.5 GHz processor. A second-order-accurate finite-volume method was used to solve the governing equations [20]. A grid-dependency study was performed, and upon substantial refinement of the grid the solution was shown to be grid-independent. After refining the grid from nearly 700,000 tetrahedra to almost 1 million tetrahedra, negligible changes in the centerline velocity distribution, velocity profiles, and plume flow rates were observed. In the refined case the average y^+ value at cells neighboring the surface of the human model was 2.5. Thus, adequate boundary-layer resolution is presumed in this study.

Experimental Methodology

A human male volunteer, standing 1.73 m ($5'8''$) tall and weighing 79.4 kgf (175 lb), was our experimental subject. He wore cotton-polyester-blend overalls, with a clothing insulation value of approximately 0.30 clo [2], during all experiments.

Properly seeding the thermal plume of this human subject with particles for PIV measurement was a challenge. As shown in Fig. 7, the subject stood in a rectangular box of dimensions $1.00\times0.81\times0.51$ m. Vents at the bottom allowed the entry of make-up air. The subject was centered in an elliptical hole in the top surface of the box. To ensure the uninhibited motion of the free-convection boundary layer over the subject, a gap of approximately 150 mm separated the subject from the edges of this elliptical hole.

Fig. 8 Experimental PIV images of the particle-laden flowfield

Theatrical fog, consisting of particles of approximately 5 μm in diameter, was injected into the box. Since the experimental field-of-view includes only the head and shoulders of the subject, this box served as a plenum or "stilling chamber" from which the human boundary layer entrained particle-laden air.

A 1 mm thick vertical laser light sheet from a 200 mJ double-pulse Nd:Yag laser illuminated the seeded boundary layer and thermal plume of the human subject in first the coronal and later the sagittal plane. A CCD digital camera [21] was used to capture some 300 image pairs per ensemble of the seeded flowfield.

In preliminary experiments without a human subject, the theatrical fog particles were seen to be essentially neutrally buoyant in the surrounding air. Measured drift velocities in these experiments were random and more than an order of magnitude slower than the measured velocities within the human thermal plume. We thus assume thermal equilibrium and negligible particle settling speed under present experimental conditions.

Due to the large required PIV field-of-view, the magnification was such that individual fog particles could not be resolved. However, small particle-laden turbulent eddies in the plume serve the role of PIV "particles" and are correlated by the PIV software to yield a measurement of the eddy convective-velocity field in the flow. From an uncertainty analysis, the overall error in these measurements was approximately ±0.01 m/s. Figure 8 shows sample images of the experimental flowfield in both the coronal and sagittal planes, taken directly from the PIV data. As a consequence of this PIV technique, turbulent quantities could not be measured experimentally. Thus, no comparison with the modeled turbulence of the CFD simulation can be made.

Results and Discussion

Velocity Contours. The qualitative features of the free-convection boundary layer and thermal plume of both the experimental subject and the CFD model are the same as those revealed in Figs. 1 and 2. Figures 9 and 10 show PIV and CFD contours, respectively, of velocity magnitude in the coronal plane. Just above the shoulders and head, regions of low velocity due to flow separation are apparent. Upon separation from the shoulders, the former boundary layer mixes with the buoyancy-driven flow from the head to form the human thermal plume. In these figures the outer edge of the plume is arbitrarily defined by a value of 10% of the maximum plume centerline velocity.

Higher velocities are seen near the shoulder and head in the CFD results, Fig. 10, compared to the experimental data, Fig. 9. This is explainable by the differences in the shape of the head and shoulders of the actual human subject and those of the simulation. In particular, the sharp corners of the shoulders and head of the CFD model cause regions of local acceleration that are not seen in the experimental results. However, these lesser features have a negligible impact on the development of the overall human thermal plume well above head height, thus confirming our initial assumption that the appendages and other lesser features of the

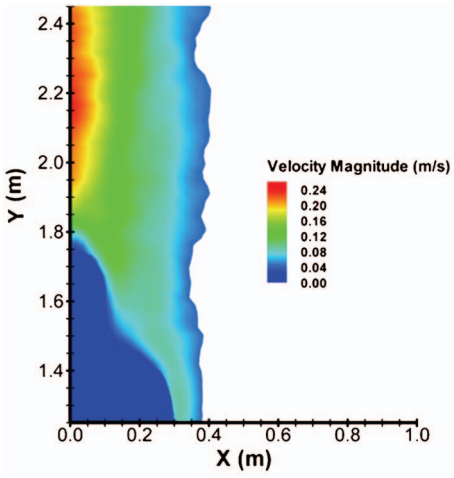

Fig. 9 Contours of velocity magnitude in the coronal plane (PIV)

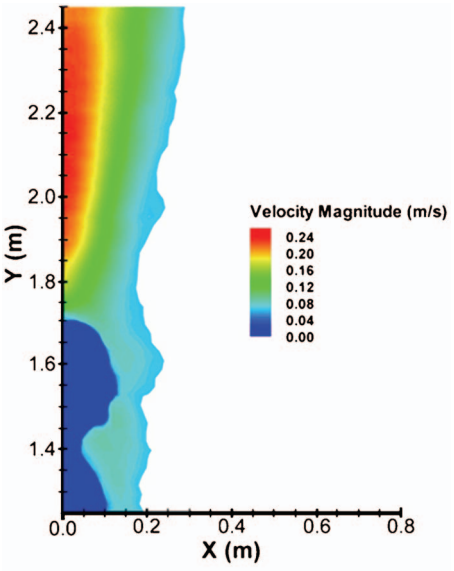

Fig. 11 Contours of velocity magnitude in the sagittal plane (PIV)

human form are of secondary importance.

Some discrepancy in the apparent spreading rate of the human thermal plume is also seen in Figs. 9 and 10. An exact comparison is complicated by the irregularity or raggedness of the plume's outer boundary in the PIV results. This, in turn, arises from the inherent unsteadiness of the plume edge due to passing turbulent eddies. Considering the characteristic length and time scales of this flow, eddy motion is quite slow. Thus, ideally, more than 300 image pairs at five pairs per second would be required to yield a smooth plume edge. This was not possible here, but a reasonable comparison with CFD occurs nonetheless.

Lastly, comparing Figs. 8 and 9 with Figs. 3 and 10, CFD appears to predict a smaller region of separated flow above the shoulder of the model, compared to PIV data. This may be attributed to the k-ε turbulence model used in this simulation, which has been shown to underpredict the extent of separation [15]. However, this discrepancy is tolerated given the model's superior performance in free shear flows, such as the plume. Although separated flow also exists above the head, a similar discrepancy is not observed here; the amount of separation is slight in both CFD and PIV results.

The sagittal plane is shown in Figs. 11 and 12, showing contours of velocity magnitude from PIV and CFD, respectively. The comparison is quite good despite obvious differences in body geometry. As in the coronal-plane case, higher velocities occur near the head and chest in the CFD model, compared to the experimental results. A similar explanation applies here as well. Further, the boundary layer over the CFD model in Fig. 12 is significantly thicker than that shown in the experimental results. This is explained by the initial assumption of turbulence and no attempt to model transition in our computation. Thus, an initially turbulent boundary layer forms at the base of the CFD model, while in the experiment transition is delayed until farther downstream. Lastly, notice how the respiration of our human volunteer caused disruption of the boundary layer about the face. This was shown in the schlieren photograph of Fig. 2 and is evident from the velocity contours in Fig. 11.

Centerline Velocity. In further investigating the plume dynamics, the behavior of the centerline velocity is now considered. Figure 13 compares experimental and CFD results of velocity magnitude along the plume centerline as a function of height from the floor. Centerline velocities obtained from PIV measurements

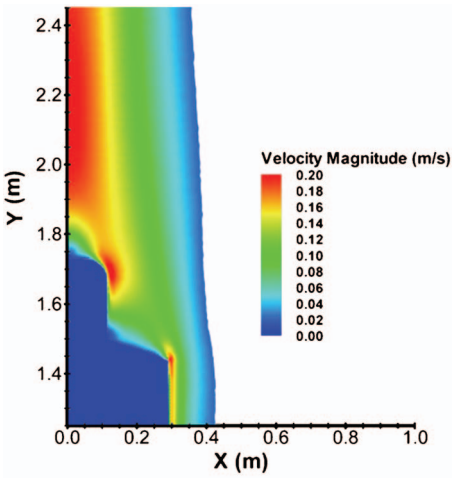

Fig. 10 Contours of velocity magnitude in the coronal plane (CFD, stratified flow)

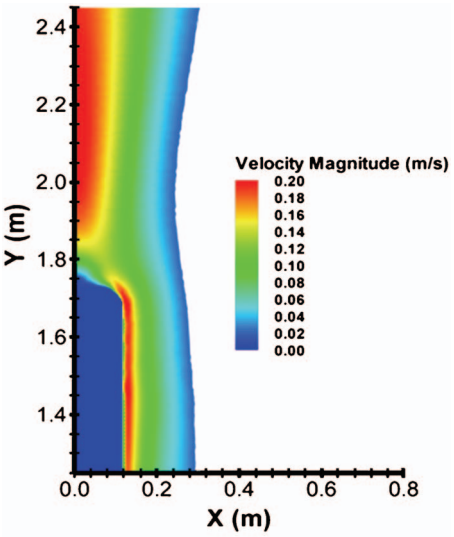

Fig. 12 Contours of velocity magnitude in the sagittal plane (CFD, stratified flow)

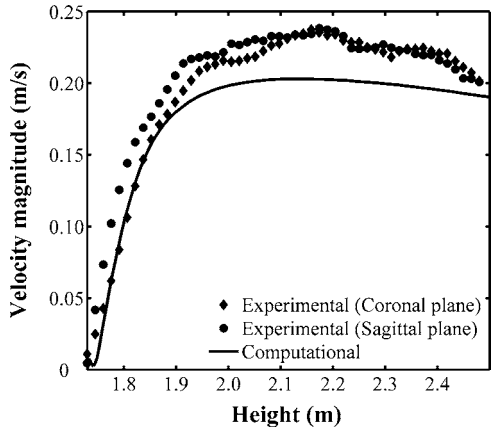

Fig. 13 Plume centerline velocity distribution with height

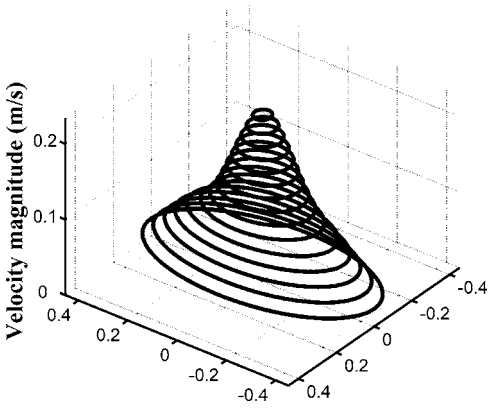

Fig. 15 Contours of velocity magnitude above the human subject at a height of 2.13 m

in the coronal and sagittal planes are both shown. Note that the plume centerline begins at 1.73 m, the height of our experimental subject and of the CFD model.

Initial velocities in the rising plume are small. However, due to buoyancy, the flow accelerates upward. Upon reaching a maximum velocity, the plume then decelerates due to a reduction in buoyancy as it mixes with the surrounding air and approaches the ceiling. From PIV, the comparison of coronal and sagittal plane measurements of centerline velocity is quite good. In both cases a maximum centerline velocity of 0.24 m/s occurs at a height of 2.16 m from the floor (0.43 m above the head of the subject). From CFD, a maximum velocity of 0.20 m/s occurs at a height of 2.12 m. Thus, the CFD somewhat underpredicts the measurement in this case. However, these values are nonetheless consistent with those of Murakami et al. [3] in a CFD simulation of the human thermal plume in a nonlinearly stratified room, who report a maximum velocity of 0.23 m/s.

Velocity Profiles. Velocity profiles were extracted from the PIV and CFD results at a height of 2.13 m, the approximate location of the maximum plume centerline velocity, in both the coronal and sagittal planes. The comparison is shown in Fig. 14. Here velocity and distance have been normalized by the centerline velocity and the half-shoulder-width of our human volunteer (0.29 m), respectively.

Profiles in the sagittal plane for CFD and PIV compare quite well. Both velocity profiles exhibit the Gaussian profile shape typical of turbulent jets and plumes. In the coronal plane, however, the comparison is not as strong. This is explainable by the deficiency of the k-ε turbulence model in predicting separation. The impact of a larger separated flow region above the shoulder on the downstream velocity profile is apparent in the PIV results, whereas the separation was less extensive in the CFD results and this effect is not observed. Further, the general shape of both profiles is quite broad in extent. Neither profile appears Gaussian. But, as noted by Turner [22], immediately above an extended heat source the velocity profiles are not expected to exhibit a self-similar Gaussian profile shape. A downstream distance of multiple source diameters is required before the effect of the extended source is "forgotten" and the plume profiles approach a self-similar shape.

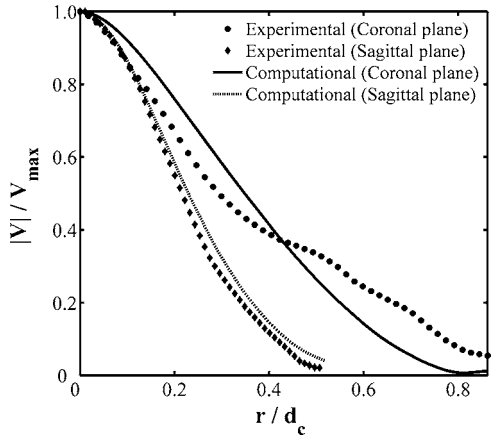

Fig. 14 Normalized plume velocity profiles at a height of 2.13 m above the floor

Plume Flow Rate. To fully characterize the human thermal plume in a linearly stratified room environment, the volumetric flow rates above the computational model and the experimental subject were extracted. Flow rate was calculated at discrete heights ranging from 1.93 to 2.43 m, in increments of 0.1 m, by integrating the velocity data over the plume cross-sectional area. This was done internally within the CFD code. However, the PIV data were only taken in two mutually orthogonal planes, so obtaining the experimental flow rate was not so simple.

PIV velocity contours were plotted in horizontal planes at each of the prescribed heights, assuming an elliptical contour shape. A subsequent numerical integration of the data yielded the approximate volumetric flow rate in the experiment. Figure 15 shows an example of the contours at a height of 2.13 m, the approximate location of the maximum centerline velocity.

The resulting volumetric flow rate of the experimental and computed human thermal plume versus height is shown in Fig. 16. The plume growth is seen to be approximately linear with respect to height. A maximum discrepancy of 22% occurs at the maximum height where the comparison was made, 2.45 m. A majority of this discrepancy may be attributed to the difficulty of determining the experimental flow rate from velocity data in only two planes. Additionally, in the foregoing comparisons of velocity magnitude, CFD was shown to slightly underpredict experimental plume velocities. Thus flow rate, which is an integration of the velocity profiles, will naturally amplify this discrepancy. Nonetheless, in a linearly stratified room environment with $S=0.24$, plume flow rates above a human are found to be in the 20–35 L/s range, depending on the height from the floor.

Effect of Thermal Stratification. The effect of thermal stratification on the human thermal plume is examined by comparing the stratified CFD results having $S=0.24$, discussed above, with those obtained from a CFD simulation of the plume in a room with a uniform air temperature of 21.25° (the average air temperature within the stratified room). The prescribed boundary conditions were shown in Fig. 6.

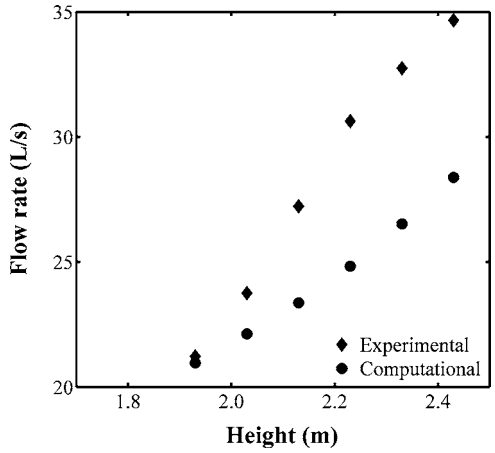

Fig. 16 Volumetric flow rate of the human thermal plume at various heights above the floor

At approximately neck height on the model human in the stratified room, the local temperature difference between body and air is equivalent to that imposed on the entire body in the uniform-temperature case. Above the neck, the temperature difference, and thus the buoyancy force, decreases in the upward direction. Thus, in the stratified room, even prior to the formation of the plume there is some reduction in buoyancy compared to the uniform case. Consequently we expect velocities and flow rates in the plume in a stratified environment to be smaller than those in the uniform environment. Figure 17, a comparison of the plume centerline velocity for the two cases, shows that this is indeed the case.

As shown, the maximum centerline velocity of the plume in a uniform environment is 0.3 m/s, while that in the stratified room is only 0.2 m/s. The location of maximum velocity also differs notably between the two cases: 2.70 m in uniform versus 2.12 m in stratified environment. Thus the reduction in plume buoyancy due to stratification, even for moderately low levels of stratification, is substantial. Note also that the centerline velocity must vanish at the ceiling height of 3.25 m.

There is a similar effect of stratification on volumetric flow rate. The flow rate of the human thermal plume in the present uniform environment is in the 70–80 L/s range, compared to only 20–30 L/s with stratification. This effect accounts for some of the considerable scatter in plume flow rates reported in previous studies, none of which address stratification.

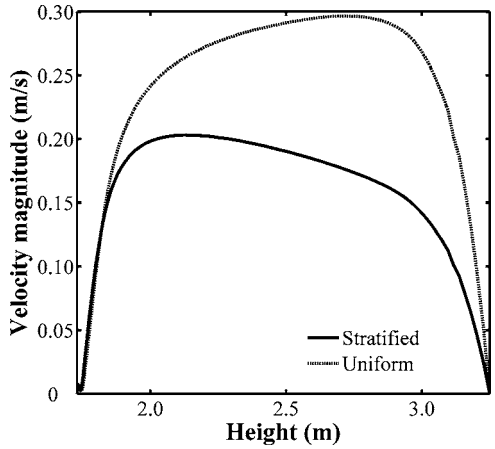

Fig. 17 Comparison of centerline velocity distribution in the human thermal plume for stratified and uniform room environments

Conclusions

Experimental velocity measurements were made using particle image velocimetry (PIV) and a computational fluid dynamics (CFD) simulation was performed of the human thermal plume in a standard room environment with moderate thermal stratification. The effects of thermal stratification on the plume were explored via comparison with the results of a CFD simulation in a uniform environment.

Both qualitatively and quantitatively, the PIV data and schlieren images of the free-convection boundary layer and thermal plume of a human subject agreed generally well with the computational simulation of flow about a simplified model of a person. Buoyancy accelerates the plume upward, but mixing and the presence of a ceiling eventually slow it down. PIV and CFD yielded maximum plume centerline velocities of 0.24 and 0.20 m/s, respectively, both of which occurred at a height of approximately 2.15 m above the floor, or 0.42 m above head height.

Velocity profiles were extracted from the PIV and CFD plume results at a height of 2.13 m, near the location of maximum centerline velocity, in both the coronal and sagittal planes of the human body. These results also compare well except in the coronal plane due to a slight discrepancy in the extent of upstream separation predicted above the shoulder of our CFD model, compared to the experimental measurements.

The volume flux of air in the human thermal plume in a stratified room environment is important in various disciplines. Here it was determined at several heights above the human volunteer and from the computational simulation. An approximately linear growth of plume flow rate with height was observed.

Finally, the effect of thermal stratification was considered by comparing the stratified plume results with those of a CFD simulation in a uniform-temperature environment. This reveals a significant reduction in plume buoyancy due to stratification, which dramatically affects both the magnitude and distribution of plume centerline velocity. Likewise a 3:1 reduction in plume volume flux resulted from room stratification under present conditions.

In summary, we have shown that the human thermal plume can be adequately modeled using current CFD methods, given sufficient experimental data for comparison. This study has highlighted the strong effect of low-to-moderate levels of thermal room stratification, which might have otherwise been overlooked. Higher levels of stratification are expected to have an even greater impact on plume behavior. It is clear that a person standing in a room is not thermally isolated, but rather the characteristics of the entire room must be considered.

Acknowledgment

The authors thank J.D. Miller and L.J. Dodson of the Penn State Gas Dynamics Lab for their assistance, and especially Wayne J. Smith, Jr., who volunteered to be the subject of the experimental measurements.

References

[1] Vander, A. J., Sherman, J. H., and Luciano, D. S., 1994, *Human Physiology: The Mechanisms of Body Function*, McGraw-Hill, Inc., New York.
[2] Anonymous, 2005, "Thermal Comfort," in *ASHRAE Fundamentals Handbook*, Chap. 8, pp. 8.1–8.11.
[3] Murakami, S., Kato, S., and Zeng, J., 2000, "Combined Simulation of Airflow, Radiation and Moisture Transport for Heat Release From a Human Body," Build. Environ., **35**(6), pp. 489–500.
[4] Gowadia, H. A., and Settles, G. S., 2001, "The Natural Sampling of Airborne Trace Signals From Explosives Concealed Upon the Human Body," J. Forensic Sci., **46**(6), pp. 1324–1331.
[5] Clark, R. P., and Edholm, O. G., 1985, *Man and his thermal environment*, E. Arnold, London.
[6] Lewis, H. E., Foster, A. R., Mullan, B. J., Cox, R. N., and Clark, R. P., 1969, "Aerodynamics of the Human Microenvironment," Lancet, **322**(7609), pp. 1273–1277.
[7] Homma, H., and Yakiyama, M., 1991, "Examination of Free Convection Around Occupant's Body Caused by Its Metabolic Heat," ASHRAE Trans., **94 part 1**(3118), pp. 104–124.

[8] Settles, G. S., 2001, *Schlieren and shadowgraph techniques: Visualizing phenomena in transparent media*, Springer-Verlag, Berlin.
[9] Clark, R. P., and Cox, R. N., 1973, "The generation of aerosols from the human body," in *Airborne Transmission and Airborne Infection: Concepts and Methods*, Wiley, New York, Chap. 95, pp. 413–426.
[10] Settles, G. S., 2005, "Sniffers: Fluid-Dynamic Sampling for Olfactory Trace Detection in Nature and Homeland Security - the 2004 Freeman Scholar Lecture," J. Fluids Eng., **127**(2), pp. 189–218.
[11] Settles, G. S., June 13, 2000, "Chemical Trace Detection Portal Based on the Natural Airflow and Heat Transfer of the Human Body," U. S. Patent US Patent 6,073,499.
[12] Murakami, S., Zeng, J., and Hayashi, T., 1999, "CFD Analysis of Wind Environment Around a Human Body," J. Wind. Eng. Ind. Aerodyn., **83**, pp. 393–408.
[13] Snyder, M., 2004, "Human Factors Recommendations," Transportation Security Administration Human Factors Personnel, personal communication.
[14] Incropera, F. P., and DeWitt, D. P., 2002, *Fundamentals of Heat and Mass Transfer*, Wiley, New York.
[15] Menter, F. R., 1994, "Two-Equation Eddy-Viscosity Turbulence Models for Engineering Applications," AIAA J., **32**(8), pp. 1598–1605.
[16] Chen, Q. Y., and Chao, N. T., 1997, "Comparing Turbulence Models for Buoyant Plume and Displacement Ventilation Simulation," Indoor and Built Environment, **6**(3), pp. 140–149.
[17] Angirasa, D., and Peterson, G. P., 1997, "Natural Convection Heat Transfer From an Isothermal Vertical Surface to a Fluid Saturated Thermally Stratified Porous Medium," Int. J. Heat Mass Transfer, **40**(18), pp. 4329–4335.
[18] Lin, W., Armfield, S. W., and Morgan, P. L., 2002, "Unsteady Natural Convection Boundary-Layer Flow Along a Vertical Isothermal Plate in a Linearly Stratified Fluid With $Pr > 1$," Int. J. Heat Mass Transfer, **45**(2), pp. 451–459.
[19] Angirasa, D., and Srinivasan, J., 1992, "Natural Convection Heat Transfer From an Isothermal Vertical Surface to a Stable Thermally Stratified Fluid," ASME J. Heat Transfer, **114**(4), pp. 917–923.
[20] Anonymous, 2003, "FLUENT 6.1 User's Guide."
[21] Anonymous, 2003, "IDT ProVISION User Manual: Particle Image Velocimetry."
[22] Turner, J. S., 1973, *Buoyancy effects in fluids*, Cambridge University Press, Cambridge, Massachusetts.

Numerical Prediction Method for Growth and Deformation of Filter Cakes

A. J. Parry
Schlumberger Riboud Product Center,
1 rue Henri Becquerel,
92140 Clamart, France
e-mail: aparry@clamart.oilfield.slb.com

During filtration of a fluid-solid mixture, a filter cake composed of solids is formed on the upstream side of the permeable interface—the filtrate or clean fluid passes through but not the solids. This paper describes a multi-dimensional calculation framework to carry out numerical simulations of growth and deformation of a filter cake. Two examples of cake growth and deformation phenomena of interest to the oil industry are the sticking of drill string within a wellbore and the sealing of wellbore sections by expandable packers. The calculation algorithm is based on the algebraic slip mixture model, involving the solution of a non-linear transport equation for solids concentration and the mass- and momentum-conservation equations of the mixture for the velocity and pressure field. The matrix stress and flow permeability are expressed as functions of solids concentration. The viscosity in the momentum equations is modeled using the Bingham approach and proportionality between yield stress and solids matrix pressure. Velocity and pressure fields are split into filtration and deformation components, thus permitting a stable calculation scheme. The simulated results match reasonably experimental observations.
[DOI: 10.1115/1.2354526]

Keywords: mud cake, filter cake, differential-pressure sticking, filtration model

1 Introduction

The growth and deformation of filter cakes are of interest in a wide range of fields in engineering. For example, in oil or gas drilling with a drilling fluid, mud cake is formed on the borehole wall when pressure within the wellbore is higher than the pore pressure in the rock. The filtrate enters the formation and leaves behind the deposit of solids that form the filter cake, (see simplified schematic in Fig. 1), across which is the pressure gradient from well to pore pressure. The drill string can get stuck if it becomes embedded in the cake as rather high net forces acting on the drill string will push it against the wall. A further problem for mud-cake analysis in the wellbore is the sealing of different sections of the well by packers, the interaction of these packers with the cake, and the resulting sealing efficiency.

Recent modeling approaches for filter cakes include lumped-parameter method for the prediction of filter cake growth and erosion Dewan and Chenevert [1] and Parn-anurak and Engler [2]. In this paper, we will develop a method for computation of multi-dimensional filter cake growth and deformation, including erosion. There are choices of calculation techniques available for the study of fluid-solid multi-phase flow problems. Two popular techniques are those designated as Lagrangian-Eulerian and Eulerian-Eulerian multiphase flow models [3]. In the former, the particle phase is treated as an ensemble of particle trajectories or parcels entities and is studied by following each particle entity's motion in a Lagrangian frame of reference. The latter approach is where the solids phase is treated as a fluid. In each method, the two phases interact by exchanging momentum. Under certain conditions, the second method can be simplified to a drift-flux model or algebraic slip mixture model (for example, [4]) where the slip between phases is expressed algebraically. In this case, the momentum equation for the mixture is solved along with the solids-concentration equation. This method is justified when the slip velocity can be explicitly expressed as a function of flow parameters and is the method pursued in this paper for the calculation of filter cake flow phenomena.

The calculation procedure is based on the solution of a nonlinear transport equation for solids concentration and the mass and momentum conservation equations of the mixture. A feature of the procedure is the splitting of the velocity and pressure fields into filtration and deformation components. The viscosity in the momentum equations is modeled using the Bingham approach and proportionality between yield stress and solids matrix pressure.

This paper describes a multidimensional calculation framework to analyze flow-related phenomena during the growth and deformation of a filter cake. The general principles are developed in Sec. 2 and detailed for the filtration of a water-based mud into a rock, as could occur for the drilling fluid in an oil well where a filter cake is grown on the well/rock interface. The procedure enables the calculation of filter cake growth as well as the dynamics when the cake interacts with macroscopic solid bodies or is eroded by flow adjacent to the cake. In Sec. 3 the method is applied to the case of the filtration-cell sphere-torque test and squeeze displacement of filter cake.

2 Description of Model for Growing and Deforming Filter Cakes

2.1 Governing Equations for Growth and Deformation. In this section, we develop the transport equation for the solids volume fraction within the solids-fluid mixture ϕ. Algorithmic details for the resolution of the growth and deformation problem will be explained. We first establish some basic relationships for matrix stress and permeability to derive the transport equation.

Within the filter cake, we suppose the solids-matrix shearing stresses are small compared to the dilatational stress. Neglecting inertia, the total stress acting on an element of filter cake is the sum of fluid pressure p, and matrix stress (solids pressure) φ, so that, following Sherwood [5]

Contributed by the Fluids Engineering Division of ASME for publication in the JOURNAL OF FLUIDS ENGINEERING. Manuscript received September 19, 2005; final manuscript received May 9, 2006. Assoc. Editor: Dennis Siginer.

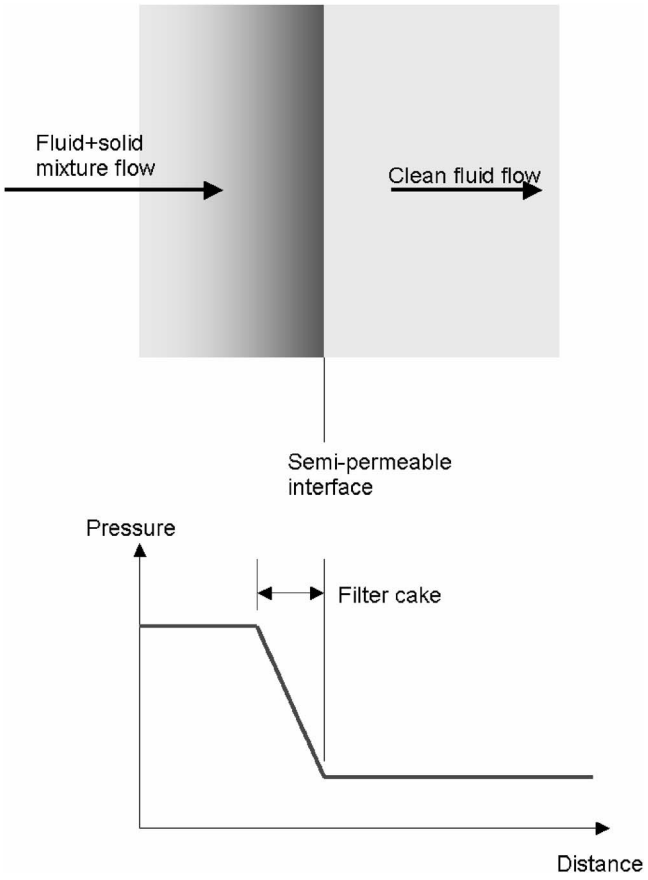

Fig. 1 Schematic of filter cake growth

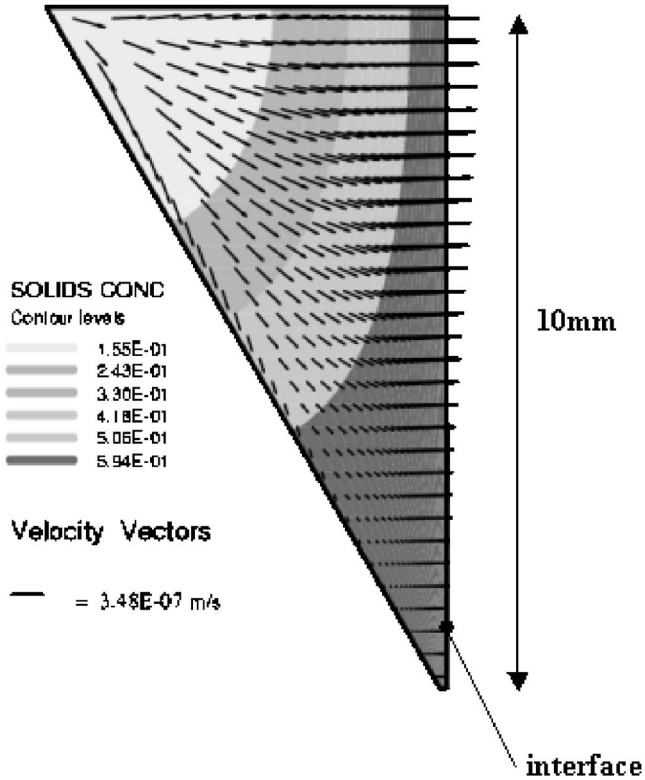

Fig. 2 Cake growth in a 30 deg wedge space shown at 24,000 s, 800 psi (5,515,840 N/m^2), and 10% upstream solids concentration

$$\nabla(p+\varphi)=0 \tag{1}$$

Darcy's law relates the slip velocity between the solids and fluid and the pressure gradient. In the absence of additional body forces, Darcy's law is expressed as, following Sherwood [5]

$$-\frac{\kappa}{\mu}\nabla p=\vec{u}_{\text{mixture}}-\vec{u}_{\text{solid}}=(1-\phi)(\vec{u}_{\text{liquid}}-\vec{u}_{\text{solid}}) \tag{2}$$

where $\vec{u}_{\text{mixture}}$ is the total velocity defined by

$$\vec{u}_{\text{mixture}}=\vec{u}_{\text{solid}}\phi+\vec{u}_{\text{liquid}}(1-\phi) \tag{3}$$

and κ is the permeability according to this choice of velocity definition.

With Eqs. (1)–(3), the volume-conservation equation for the solids is transformed

$$\frac{\partial\phi}{\partial t}=-\nabla(\phi\vec{u}_{\text{solid}})=-\nabla(\phi\vec{u}_{\text{mixture}})+\nabla\left(\frac{\phi\kappa}{\mu}\frac{d\varphi}{d\phi}\nabla\phi\right) \tag{4}$$

resulting in a transport equation for ϕ with diffusivity

$$D=\frac{\phi\kappa}{\mu}\frac{d\varphi}{d\phi} \tag{5}$$

Equations (1)–(5) follow the derivations in the paper by Sherwood [5].

The deformation/filtration problem can, in principle, be simulated by solving this solids concentration transport equation along with the mixture mass- and momentum- conservation equations, following the usual drift flux model approach (for example, [4]). The momentum equation contains Darcy resistance terms. The author is not aware of solution methods for this set of equations which provide robust solutions in very low permeability zones. For this reason, as well as the fact that in filter cake growth, the filtration velocity field is quasi-one-dimensional and known exactly at the interface (see later), we treat the delicate balance between filtrate velocity and cake growth in a more robust, approximate manner. Particularly, we split the mixture velocity field into two components, the filtration velocity and the cake deformation velocity. The filtration velocity is directed towards the semi-permeable interface. Stream tubes formed from the filtration velocity field define the filtrate flow rate distribution. The deformation velocity field is the component of the mixture velocity which deforms and erodes the cake. The splitting and Eqs. (4) and (5) lead to

$$\frac{\partial\phi}{\partial t}=-\nabla(\phi\vec{u}_{\text{def}})-\nabla(\phi\vec{u}_{\text{filtration}})+\nabla(D\nabla\phi) \tag{6}$$

where $\vec{u}_{\text{filtration}}$ at a general position is determined from the concentration and concentration gradient field. A convenient approximation relates $\vec{u}_{\text{filtration}}$ to the value at the interface point closest to the position of interest. The value of $\vec{u}_{\text{filtration}}|_{\text{int}}$ can be calculated directly from Darcy's law applied at the interface where the solids velocity is set to zero

$$\vec{u}_{\text{filtration}}\Big|_{\text{int}}=\left(\frac{D}{\phi}\nabla\phi\right)_{\text{int}} \tag{7}$$

With this treatment for $\vec{u}_{\text{filtration}}$, the solids-volume fraction ϕ is solved by the equation

$$\frac{\partial\phi}{\partial t}=-\nabla(\phi\vec{u}_{\text{def}})+\nabla(D\nabla\phi)-[\vec{C}_{\text{dir}}C_{\text{bal}}(\vec{u}_{\text{filtration}}|_{\text{int}})\nabla(\phi)] \tag{8}$$

The unit vector $\vec{C}_{\text{dir}}$ locally orients the filtration velocity in direction of $\nabla\phi$, and is applied only if the local concentration is above a predefined threshold. This ensures that the vector direction orientation is not adjusted far upstream of the cake. The balance

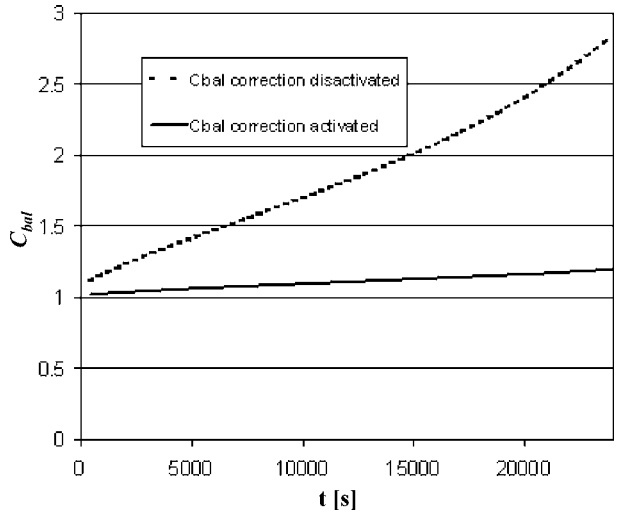

Fig. 3 Variation of solids deposition rate factor with and without correction for the 30 deg wedge space as a function of time

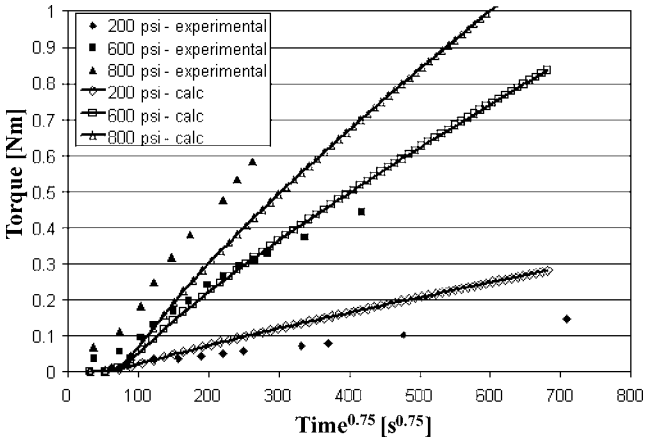

Fig. 5 Torque required to turn the sphere about an axis normal to the permeable interface as a function of time, at 200, 600, and 800 psi (1.379 MN/m^2, 4.137 MN/m^2, and 5.516 MN/m^2, respectively), experimental data from Sherwood [5]

factor C_{bal} accounts for approximations in the determination of $\vec{u}_{\text{filtration}}$ from $\vec{u}_{\text{filtration}}|_{\text{int}}$. An approximate specification for this factor is to evoke overall conservation of solids mass, involving accumulation within the domain volume and net flux into the volume across the boundaries, leading to

$$C_{\text{bal}} = \frac{\dfrac{d\left(\int_V \phi dV\right)}{dt} - \int_{\text{inlet/outlet}} \phi \vec{n} \cdot \vec{u}_{\text{def}} dS_{\text{inlet/outlet}}}{\phi_\infty \int_{\text{int}} \vec{n} \cdot \vec{u}_{\text{filtration}} dS_{\text{int}}} \tag{9}$$

where ϕ_∞ is the upstream concentration value just outside of the cake, S is the area of the interface or inlet/outlet flow boundary, $\vec{n}$ is the normal vector of the area, and V is the domain volume. In this sense, C_{bal} is a global correction factor for the solids-deposition rate in the filter cake.

In the absence of deformation, the ϕ field is calculated with Eq. (8), which reduces to a non-linear diffusion equation since the convection term (first term on right-hand side) disappears. Therefore, in this situation, the growth of filter cake can be treated with a general purpose diffusion equation solver. In the general case, the deformation velocity is calculated by solving, in addition to the above transport equation, the mass- and momentum- conservation equations for the mixture, with viscosity expressed by the modified Bingham model

$$\mu_e = \mu_0 + \frac{\tau_y}{\gamma}[1 - e^{-\gamma/\gamma_0}] \tag{10}$$

where $\tau_y = C_{\text{friction}} \varphi(\phi)$ and $\mu_0 = C_{\text{visc}} \tau_y$.

γ is the second invariant of strain rate and γ_0 is an arbitrarily small regularization parameter which avoids convergence problems related to very high viscosity as the strain rate tends to zero. Tests must be carried out for each flow to check if the regularization parameter is sufficiently small. C_{visc} is a constant relating plastic viscosity to yield stress. For the case of a homogeneous mixture the values of τ_y and μ_0 become constant. C_{friction} is the coefficient of friction. For the work in this paper, the factor C_{friction} is taken to be constant and needs to be determined from experimental data. For the filter cake calculations shown in this report we have taken $C_{\text{visc}} = 0.001$ s, and as a consequence the relative values of μ_0/μ_e are small and C_{visc} is insignificant.

Solution of the mixture mass- and momentum- conservation equations along with the non-linear particle concentration equation permits the calculation of simultaneous cake growth and deformation phenomena.

From Sherwood [5], empirical matrix-stress and permeability relations for a water based mud are

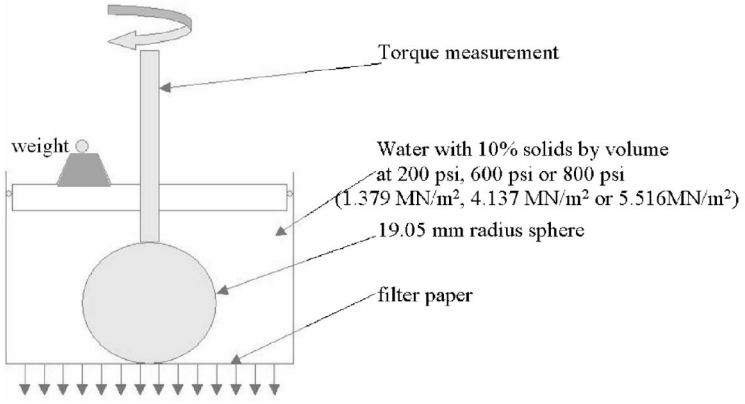

Fig. 4 Schematic of sphere torque test cell

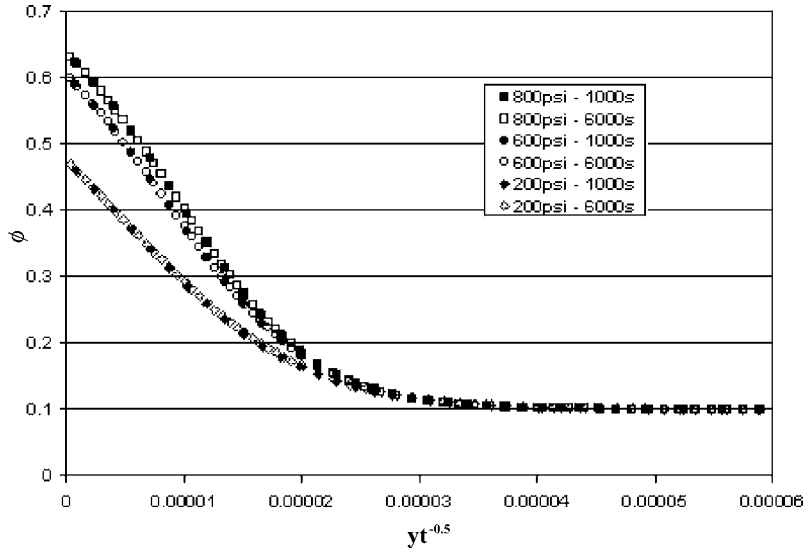

Fig. 6 Profiles of solids concentration within the cake (far from the sphere contact region) as a function of the Lagrangian similarity variable $yt^{-1/2}$ at 200, 600, and 800 psi (1.379 MN/m², 4.137 MN/m², and 5.516 MN/m², respectively)

$$\varphi = A\left(\frac{\phi}{1-\phi}\right)^{1/\alpha} \tag{11}$$

$$\kappa = \frac{D_0 \mu \alpha}{\phi A}\left(\frac{1-\phi}{\phi}\right)^{1-\beta+1/\alpha} \tag{12}$$

where $A=1.7$ MPa, $\alpha=0.48$, $D_0=1.8\times10^{-10}$ m²/s and $\beta=1.9$, resulting in the diffusivity

$$D = D_0 \frac{\phi^{\beta-2}}{(1-\phi)^{\beta}} \tag{13}$$

2.2 Boundary Conditions. For the case of a high-permeability medium downstream of the semi-permeable interface, the fluid pressure at the interface, p_{int}, is assumed uniform and equal to the pressure of the downstream medium. Thus, the value of solids concentration at the interface, ϕ_{int}, can be imposed using Eq. (1)

$$(p+\varphi)_{\text{int}} = p_{\text{sum}}|_{\text{int}} \tag{14}$$

and with the matrix stress empirical relation (11) for a water based mud

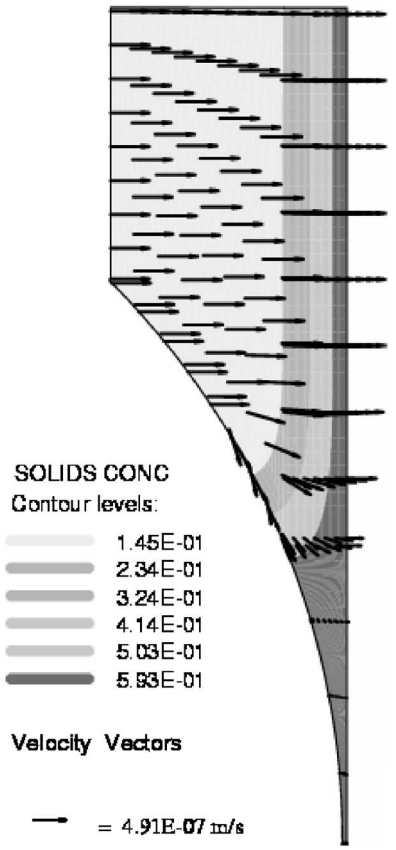

Fig. 7 Solids concentration and filtration velocity vector plots at t=6000 s with 800 psi (5,515,840 N/m²)

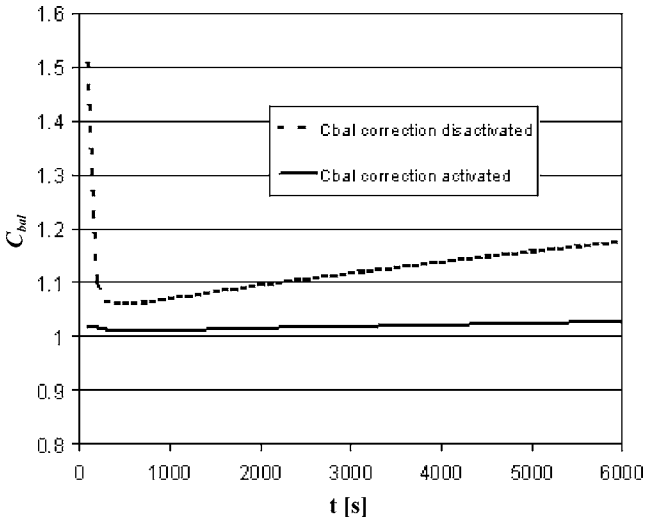

Fig. 8 Variation of solids deposition rate factor with and without correction, 800 psi (5,515,840 N/m²)

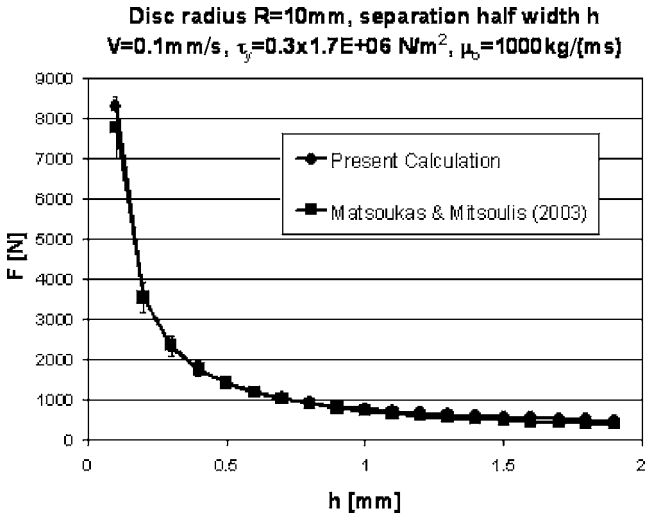

Fig. 9 Disk force versus separation *h*, homogeneous Bingham fluid

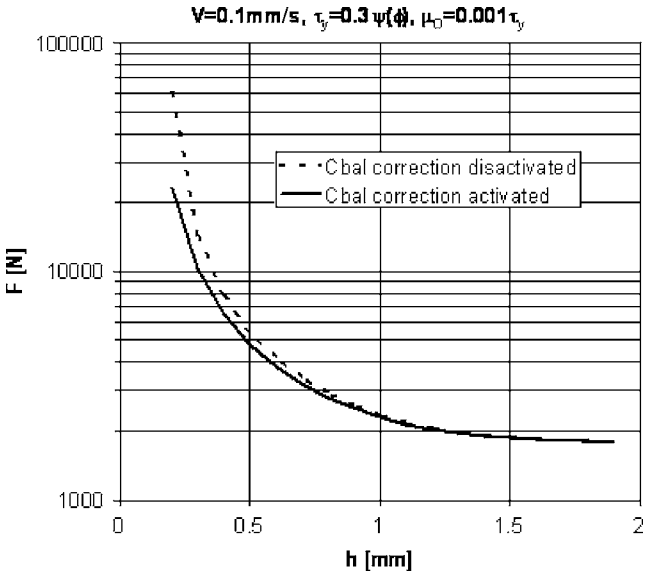

Fig. 10 Disk force versus separation *h*, filter cake

$$\phi_{\text{int}} = \frac{1}{\left[\dfrac{p_{\text{sum-int}} - p_{\text{int}}}{A}\right]^{-\alpha} + 1} \tag{15}$$

$p_{\text{sum}}|_{\text{int}}$ is the pressure at the interface, resulting from the solution of the mixture mass and momentum equations of the split scheme presented earlier. In the case where there is no deformation and just filtration occurring then this pressure represents the pressure upstream of the mud-cake, which is uniform. On impermeable walls ϕ shall obey a Neumann boundary condition of zero normal gradient.

As an alternative to the Dirichlet boundary condition (15) at the interface the net solids flux condition may be evoked

$$0 = \vec{n} \,.\, (\vec{u}_{\text{filtration}}\phi - D \nabla \phi)_{\text{int}} \tag{16}$$

If the downstream medium has relatively low permeability and the uniform-pressure condition is no longer valid, the flow phenomena in the upstream and downstream media are coupled.

2.3 Solution Method. The above model and procedure were implemented in the finite volume based fluid flow solver, called CAFFA (computer-aided fluid flow analysis) [6], where a multiblock nonorthogonal grid scheme was adopted with collocated variable arrangement and arbitrary Lagrangian-Eulerian formulation allowing domain deformation. The dependent variables were the Cartesian or cylindrical velocity components, pressure and solids concentration.

3 Simulation Examples

This section demonstrates and validates the calculation method for the filter cake created from a water based mud (Sec. 2.1). The flow within a 30 deg wedge is studied, followed by the study of filter cake growth around a sphere. Finally, the behaviour of a filter cake under squeeze flow is also studied.

3.1 30 deg Wedge Flow. The approximation for $\vec{u}_{\text{filtration}}$ (Sec. 2.1) in a general multidimensional case is validated by studying the filter cake growth into a 30 deg wedge space. Figure 2 shows the solids-concentration and filtration velocity vectors after 24,000 s (6.667 h) under a constant pressure of 800 psi (5,515,840.0 Pa) relative to a uniform interface pressure and far-field solids-volume concentration of 10%. Figure 3 shows that with the correction procedure a maximal solids-volume-conservation imbalance of 20% is achieved at the end of the time interval even though the concentration distribution is highly skewed while without correction an imbalance of 280% occurs. This comparison confirms that the method of imposition for the filtration velocity field using $\vec{C}_{\text{dir}}$ and C_{bal} is quite effective.

In the particular case of fully one-dimensional growth, the numerical procedure predicts the correct ratio of accumulation of solids volume to outflow and it is not necessary to activate the correction factor C_{bal}.

3.2 Sphere Torque Test. Reid et al. [7] described experiments in which a filter cake was allowed to grow around a sphere in contact with a permeable interface. Figure 4 shows the schematic for the test cell. Filter cake was grown on the filter paper and around the sphere and measurements of the torque required to free the sphere were carried out at several instants during the growth.

For the calculations presented here, it is assumed that the filter cake repairs itself after each freeing torque measurement. The freeing torque is determined by integrating over the surface of the sphere the yield stress times radius from axis of rotation. Since we do not calculate the deformation velocity field, the solids-concentration equation is solved as a diffusion equation. Figure 5 shows comparisons with experiment of freeing torque against scaled time. The yield stress is determined from the matrix stress (Eq. (11)) using a proportionality constant of $C_{\text{friction}}=0.3$, to best fit the data. All pressures are measured relative to the uniform filter paper pressure. The simulated and experimental torque values agree best for the 600 psi (4.137 MN/m^2), case. For the 800 psi (5.516 MN/m^2), case the torque is under-predicted, whereas for the 200 psi (1.379 MN/m^2), case the torque is over-predicted. In view of the assumptions in the model this level of agreement is reasonably good. The two-dimensional cake in the contact region significantly affects the torque. A torque calculation based on a one-dimensional approximation for the cake growth would lead to values an order of magnitude less than the multidimensional approach for the time range studied [0,6000 s]. The sphere surface proves to be the surface of minimum torque thus justifying the choice of this surface for the torque calculation. Figure 6 shows the solids-concentration profiles against the time scaled interface distance (as used by Sherwood [5]) far away from the sphere contact region, in the one-dimensional region, where y is the normal distance from filter paper. For each pressure the concentration profiles with the above similarity variable collapse onto the same curves, which is in-line with the analysis of Sherwood.

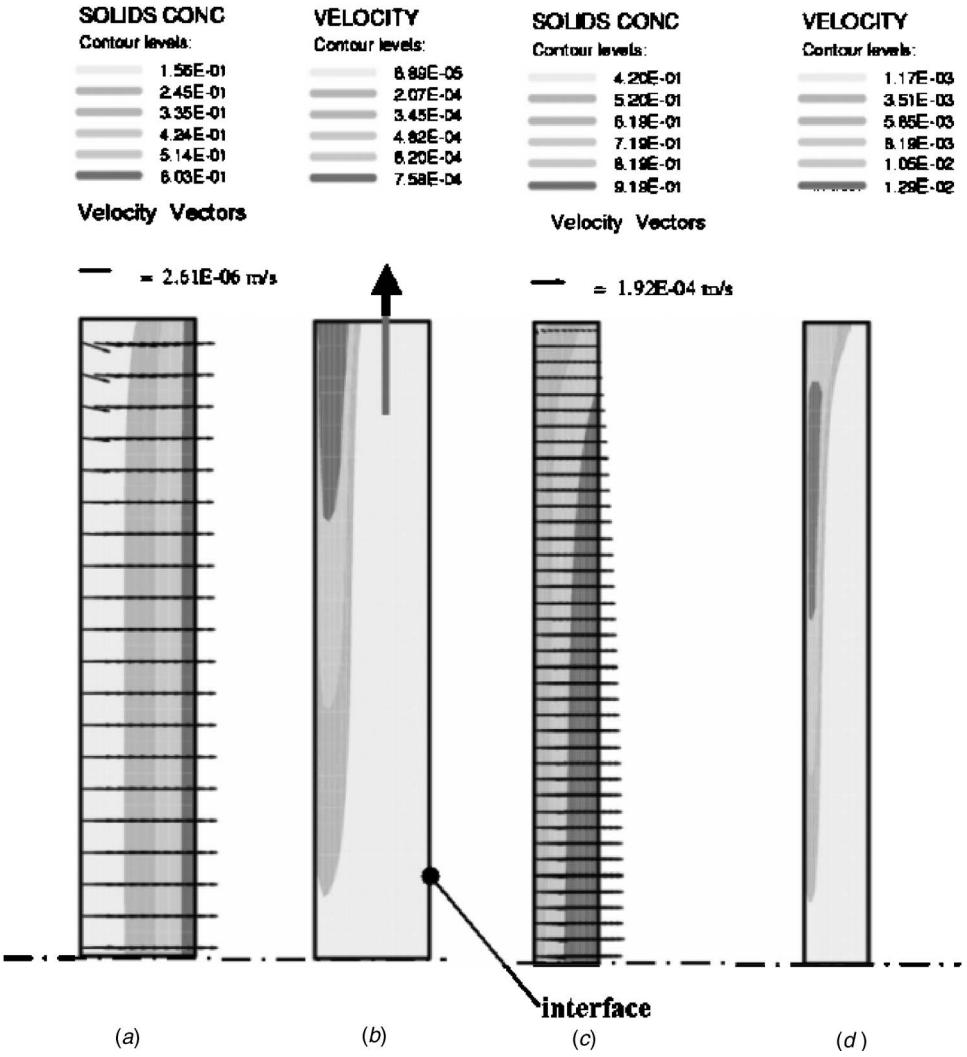

Fig. 11 (*a*) solids concentration and filtration velocity at $h/R=0.19$, (*b*) deformation velocity [m/s] at $h/R=0.19$, (*c*) solids concentration and filtration velocity at $h/R=0.02$, (*d*) deformation velocity [m/s] at $h/R=0.02$. Axial coordinate stretched by 10 for (*c*) and (*d*).

Figure 7 shows the concentration and filtration velocity field for the 800 psi (5,515,840 N/m^2) case at $t=6000$ s. Figure 8 shows the solids-deposition rate imbalance as a function of time for the 800 psi (5,515,840 N/m^2) case. The method of imposition of the filtration velocity field is seen to be effective in producing maximum accumulation errors of about 3% at the end of the time range considered.

3.3 Squeeze Flow Under a Rigid Disk. We compare the squeeze flow results of Matsoukas and Mitsoulis [8] for a homogeneous Bingham fluid between two approaching disks, of radius R, separation half width h, and approach velocity for each plate V. This comparison is done in order to validate the code for squeeze flow in a homogeneous Bingham fluid.

Figure 9 shows comparisons of disk force against separation for the present method and the force equation proposed by Matsoukas and Mitsoulis. This force equation has ±10% uncertainty due to curve fitting results from a creep-flow finite-element method applied over a large parameter range. The present method uses the general transient-moving-grid technique with all inertia terms retained. For the calculations in this section we take the regularization parameter $\gamma_0=0.01\ s^{-1}$ after verifying that smaller values do not change significantly the flow field and force values. This value is close to the value used by Matsoukas and Mitsoulis in their

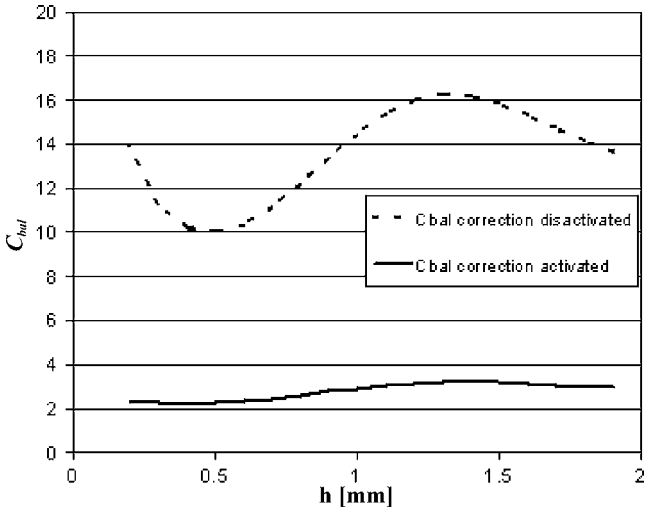

Fig. 12 Variation of solids deposition rate factor with and without correction for squeeze flow test of filter cake

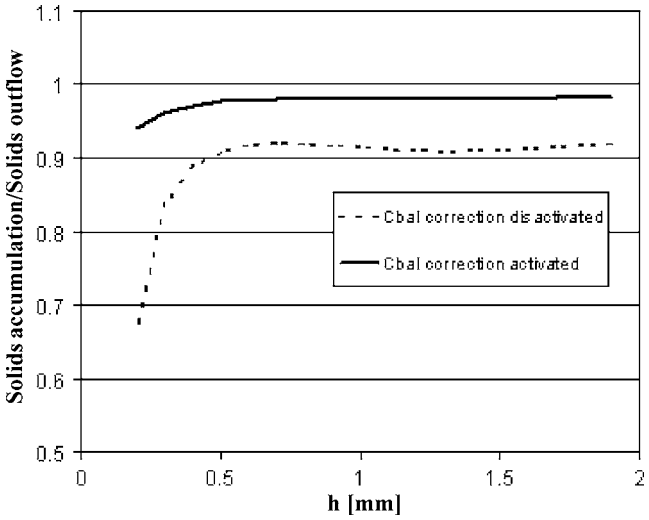

Fig. 13 Ratio of solids accumulation rate to outflow rate for squeeze flow test of filter cake

paper. The results from the two methods compare as expected.

Next is a simulation of a single disk of the same dimensions coming into contact with an interface on which there is a filter cake. The filter cake is from water-based mud, grown for 3000 s at 800 psi (5,515,840 N/m^2) with upstream solids concentration of 10%. Here, h represents the distance from the disk to the permeable interface. This case combines deformation and filtration. For calculation of C_{bal} we choose ϕ_∞ as the initial solids concentration of 10%.

Figure 10 shows the disk force for filter cake squeeze displacement. The results with and without C_{bal} correction differ for very small separation distance. As the disk approaches the interface the pressures increase to such an extent that the filtration velocity is no longer small compared with the deformation velocity or disk velocity. Here filtration-velocity corrections are important, since the filtration flux becomes comparable to the deformation flux.

Figure 11 shows solids-concentration contours and filtration and deformation velocities at $h/R=0.19$ and $h/R=0.02$. At $h/R=0.02$, the filtration velocity is comparable to $V(=0.0001\ m/s)$.

Figure 12 shows C_{bal} as a function of squeeze distance. The correction method provides much better C_{bal} characteristics, but even so C_{bal} rests about 3, which is far from the desired value close to unity. However, Fig. 13 shows that the ratio of solids-accumulation rate to solids-outflow rate, which should of course be unity, rests close to unity when correction is employed and the worst-case ratio is 0.95.

4 Conclusions

Equations have been derived to describe multidimensional growth and deformation of filter cakes taking into account the spatial and temporal variation of solids concentration in the cake. We document calculations of the simultaneous growth and deformation of filter cakes using an implementation of the multidimensional model in a finite volume arbitrary Lagrangian-Eulerian code. The technique uses splitting of the filtration and deformation processes, which is possible for low filtration velocities. The results compare reasonably with some existing experimental data, and the method has proven robust. Example calculations have been shown for the dynamics of mud cakes. The procedures explained are applicable to other filter cakes by appropriate adjustment of the model expressions and constants.

Acknowledgment

I thank J. D. Sherwood, at Schlumberger Cambridge Research, Cambridge CB3 OEL, England, for his advice on the method and the development of the mathematical physics for the problem. Also, I am grateful to my colleagues, G. Daccord and M. G. Luling, of Schlumberger Riboud Product Center, 1 rue Henri Becquerel, 92140 Clamart, France, for fruitful discussions and assistance.

Nomenclature

A = empirical constant, $\varphi=A(\phi/1-\phi)^{1/\alpha}$
$\vec{C}_{dir}$ = local orientation unit vector for filtration velocity
C_{bal} = correction factor for global solids mass conservation
$C_{friction}$ = friction coefficient for yield stress
C_{visc} = ratio of plastic viscosity to yield stress
D = solids concentration diffusivity
D_0 = empirical constant, $D=D_0[\phi^{\beta-2}/(1-\phi)^{\beta}]$
p = fluid pressure
p_{sum} = sum of fluid and matrix pressure, $p_{sum}=p+\varphi$
$\vec{u}_{def}$ = deformation component of mixture velocity
$\vec{u}_{filt}$ = filtration component of mixture velocity
$\vec{u}_{liquid}$ = liquid velocity
$\vec{u}_{mixture}$ = mixture velocity, $\vec{u}_{mixture}=\vec{u}_{def}+\vec{u}_{filt}$
$\vec{u}_{solid}$ = solids velocity

Greek Symbols

ϕ = solids concentration by volume
φ = matrix stress
α = empirical constant, $\varphi=A(\phi/1-\phi)^{1/\alpha}$
β = empirical constant, $\kappa=(D_0\mu\alpha/\phi A)(1-\phi/\phi)^{1-\beta+1/\alpha}$
γ = second invariant of strain rate
γ_0 = regularization parameter, $\mu_e=\mu_0+(\tau_y/\gamma)[1-e^{-\gamma/\gamma_0}]$
κ = permeability
μ = liquid viscosity
μ_e = effective viscosity of mixture
μ_0 = plastic viscosity of mixture
τ_y = yield stress

References

[1] Dewan, J. T., and Chenevert, M. E., 2001, "A Model for Filtration of Water-base Mud During Drilling: Determination of Mudcake Parameters," Petrophysics, **47**(3), pp. 237–250.
[2] Parn-anurak, S., and Engler, T. W., 2005, "Modeling of Fluid Filtration and Near Wellbore Damage Along a Horizontal Well," J. Pet. Sci. Eng., **46**(3), pp. 149–160.
[3] Crowe, C., Sommerfeld, M., and Tsuji, Y., 1998, *Multiphase Flows With Droplets and Particles*, CRC Press, Boca Raton.
[4] Manninen, M., Taivassalo, V., and Kallio, S., 1996, "On the Mixture Model for Multiphase Flow," Valtion Teknillinen Tutkimuskeskus Publications 288, Technical Research Centre of Finland.
[5] Sherwood, J. D., 1998, "Differential Pressure Sticking of Drill String," AIChE J., **44**(3), pp. 711–721.
[6] Ferziger, J. H., and Peric, M., 2002, *Computational Methods for Fluid Dynamics*, 3rd ed., Springer, New York.
[7] Reid, P. I., Meeten, G. H., Way, P. W., Clark, P., Chambers, B. D., and Gilmour, A., 1996, "Mechanisms of Differential Sticking and a Simple Well Site Test for Monitoring and Optimizing Drilling Mud Properties," *Proc. SPE/IADC Drilling Conf.*, SPE 35100, Society of Petroleum Engineers, Richardson, TX.
[8] Matsoukas, A., and Mitsoulis, E., 2003, "Geometry Effects in Squeeze Flow of Bingham Plastics," J. Non-Newtonian Fluid Mech., **109**, pp. 231–240.

Characterization of the Nonaerated Flow Region in a Stepped Spillway by PIV

António Amador
Hydraulic and Environmental Department.,
Technologic School of Barreiro,
IPS,
R. Stinville No. 14 Quimiparque,
Barreiro 2830-144, Portugal
e-mail: antonio.amador@estbarreiro.ips.pt

Martí Sánchez-Juny
e-mail: marti.sanchez@upc.edu

Josep Dolz
e-mail: j.dolz@upc.edu

Hydraulic, Maritime and Environmental Department,
Polythecnic University of Catalonia (UPC),
C. Jordi Girona Campus Nord 1/3 Ed. D1,
Barcelona 08034, Spain

The development of the roller-compacted concrete (RCC) as a technique of constructing dams and the stepped surface that results from the construction procedure opened a renewed interest in stepped spillways. Previous research has focused on studying the air-water flow down the stepped chute with the objective of obtaining better design guidelines. The nonaerated flow region enlarges as the flow rate increases, and there is a lack of knowledge on the hydraulic performance of stepped spillways at high velocities that undermines its use in fear of cavitation damage. In the present, study the developing flow region in a stepped channel with a slope 1v:0.8h is characterized using a particle image velocimetry technique. An expression for the growth of the boundary layer thickness is proposed based on the streamwise distance from the channel crest and the roughness height. The local flow resistance coefficient is calculated by application of the von Kármán integral momentum equation. The shear strain, vorticity, and swirling strength maps obtained from the mean velocity gradient tensor are presented. Also, the fluctuating velocity field is assessed. The turbulent kinetic energy map indicates the region near the pseudobottom (imaginary line joining two adjacent step edges) as the most active in terms of Reynolds stresses. The turbulence was found to be very intense with maximum levels of turbulence intensity from 0.40 to 0.65 measured near the pseudobottom. Finally, the quadrant analysis of the velocity fluctuations suggests the presence of strong outflows of fluid from the cavities as well as inflows into the cavities. It is conjectured that the mass transfer/exchange between cavities and main stream, play an important role in the high levels of turbulent energy observed. [DOI: 10.1115/1.2354529]

Keywords: stepped spillway, skimming flow, flow characteristics, boundary layer, turbulence

Introduction

The development of new construction techniques (e.g., roller-compacted concrete) is directly responsible for a renewed in interest for stepped spillways, and a number of research projects have been conducted over the past three decades [1–3]. For a given stepped geometry, the flow regime can be nappe, transition, or skimming flow. Nappe flow occurs at low flows and can be characterized by a succession of free-falling nappes [3]. In skimmimg flow, the water flows as a coherent stream over the pseudobottom formed by the outer step edges; beneath it three-dimensional cavity vortices develop and recirculation is maintained through transmission of shear from the main stream [4]. Between the upper limit of nappe flow and the onset of skimming flow a transition flow exists separating these characteristic limits [5].

Skimming flow is usually found for typical design discharges of stepped spillways. The flow along the chute can be divided into distinct regions. In the initial flow stage, there is no air entrainment, the free surface is smooth and glassy, next to the stepped invert turbulence is generated, and the boundary layer develops. The start of natural air entrainment is defined by the point where the boundary layer reaches the water surface and the turbulent energy of the vortices is large enough to exceed the surface tension and gravity effects. Downstream rapid and strong free-surface aeration is observed.

Previous research has focused on studying the air-water flow down a stepped chute with the objective of obtaining better design guidelines [5–7]. Most studies did not investigate the turbulence characteristics with the exception of [8,9].

The nonaerated flow region enlarges as the flow rate increases, and there is a lack of knowledge on the hydraulic performance of stepped spillways at high velocities that undermines its use in fear of cavitation damage [10]. In the present work an experimental study was conducted to study the nonaerated flow region on a large model flume using particle image velocimetry (PIV) instrumentation. The use of this nonintrusive technique aimed at improving the understanding of the physical processes responsible for enhancement of turbulence production. The effects of the steps on the mean and fluctuating velocity field are investigated and discussed. The behavior of the separated free shear layer formed behind the roughness elements is studied, and the wall shear stress is determined. An effort is made to identify coherent structures that may contribute to turbulence production.

Experimental Setup

The experiments were conducted in a rectangular stepped channel assembled at *A Coruna* University and is 0.50 m wide, 2.0 m high (from crest to toe), and has a step height (h) of 0.05 m. The bottom inclination is 51.3 deg corresponding to a slope of 1:0.8 ($v:h$) typical of RCC dams (Fig. 1). The tested unit water discharge (q) was 0.11 m^2/s, which corresponds to a Reynolds number ($Re=q/\nu$) of 1.1×10^5. The electromagnetic flowmeter installed in the supply conduit of the model had an accuracy of $\pm2\%$.

The PIV system is composed of a double-pulsed Nd-Yag laser, with 400 mJ of energy per pulse, a 1024×1280 pixel resolution, high sensitive peltier-cooled, charge-coupled device (CCD) cam-

Contributed by the Fluids Engineering Division of ASME for publication in the JOURNAL OF FLUIDS ENGINEERING. Manuscript received February 9, 2005; final manuscript received April 7, 2006. Review conducted by Joseph Katz.

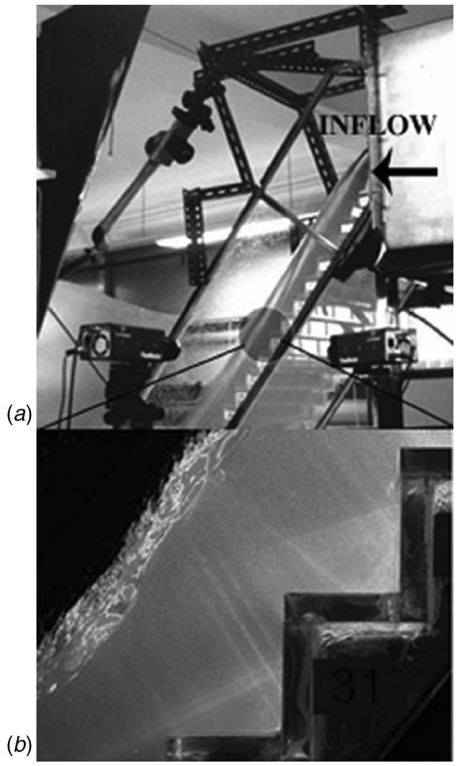

Fig. 1 (*a*) **Developing flow region in stepped spillway with** $q = 0.11\ m^2/s$, $h = 0.05$ **m,** $\alpha = 51.3$ **deg.** (*b*) **Image captured by CCD camera for steps E34** ($X/ks = 13.04$) **and E33 at** ($X/ks = 15.09$).

era. A Nikkor 50 mm 2.8, together with a narrow bandwidth filter that passes the 532 nm light from the Nd-Yag laser, is mounted on the CCD camera. An electronic sequencer synchronizes the camera and laser pulses.

The water was seeded with 70 μm ceramic microspheres. The images cover two steps. Bigger measurement areas imply unacceptable perspective errors (Fig. 1). The camera captured double-frame, double-exposure particle images. The separation time was adjusted at 200–250 μs between two laser pulses in order to give a maximum particle image displacement of eight pixels.

Both image frames are subdivided into small interrogation areas that are partially overlapping. Interrogation areas at identical positions in the image frames are correlated by means of fast Fourier transformation. From the two-dimensional (2D) cross-correlation function, the position of the highest peak representing the mean displacement of the particle images is estimated. In order to obtain high-accuracy estimators of the particle displacements, the correlation peak position is calculated at the subpixel level by the three-point Gaussian interpolation scheme. The accuracy of the resulting PIV estimators is ~0.1 pixel, which in the present study corresponds to an accuracy regarding the measured velocities of 50–62.5 mm/s.

Zero offsetting is applied in order to optimize the signal and to minimize biasing effects in the PIV estimators [11]. The interrogation of the images initiates with large dimensions of the interrogation areas that are reduced in size after each interrogation. In this way, high dynamic velocity ranges can be combined with a high spatial resolution. In this study adaptive interrogation area sizes have been used from 128×128 pixels to 32×32 pixels, with an overlapping of 50% (i.e., 16 pixels).

Some data sets are checked on peak-locking effects by examining the statistics of the PIV estimators at subpixel level. All data are validated on outliers by the median test [12,13]. Detected outliers are substituted by the local mean value of its neighboring estimators.

A total number of 500 velocity fields have been recorded with separation time of 1 s. Statistical independency of each velocity field has been investigated by calculating the temporal correlation of the velocities at a specific location in the flow. Therefore, a location in the upper region of the overlying flow, the shear layer, and within the step cavity has been observed. For all three locations, no velocity correlation is found already after a time delay of 1 s. The statistical sampling theory is used to assess the errors in the computed mean and RMS as a function of a given number of samples. The error interval for the mean velocity (ε_{mean}) is defined as follows [14]:

$$\varepsilon_{mean} = \pm \frac{Z\sigma}{\sqrt{N}} \tag{1}$$

where Z is a factor related with the confidence level, σ is the standard deviation of the velocity for an infinite number of samples, and N is the number of samples.

Similarly, the relative error interval for the rms velocity (ε_{rms}) can be computed from [14]

$$\varepsilon_{rms} = \pm \frac{Z}{\sqrt{2N}} \tag{2}$$

In Eqs. (2) and (3), $Z = 1.96$ is used, which corresponds to a confidence level of 95%. Therefore, for the RMS velocity, the computed interval is $\varepsilon_{rms} = \pm 62.0$ mm/s (roughly 6% of the standard deviation velocity). The error interval for the mean velocity depends on the local turbulence level. The estimated error intervals for the mean velocity are $\varepsilon_{mean} = \pm 10.0$ mm/s (0.3% of the computed mean velocity) in the upper region of the overlying flow, $\varepsilon_{mean} = \pm 43.6$ mm/s (2.7 % of the computed mean velocity) in the shear layer and finally $\varepsilon_{mean} = \pm 30.1$ mm/s (5.9% of the computed mean velocity) within the step cavity.

The study region comprises seven steps. The distance from the spillway crest to their outer edges (X) is respectively of 0.343 m (step E35), 0.407 m (step E34), 0.471 m (step E33), 0.535 m (step E32), 0.599 m (step E31), 0.663 m (step E30), and 0.727 m (step E29).

Mean Velocity Field

The mean velocity field over the seven steps were obtained from 500 instantaneous velocity fields. The velocity vector spacing is 2.0 mm (i.e., 16 pixels), and kriging interpolation was chosen as gridding method.

From the mean velocity contour map, shown in Fig. 2, it can be observed that the flow is accelerating and developing in the downstream direction. The flow over the steps consists of a turbulent boundary layer next to the pseudobottom (imaginary line joining two adjacent step edges) and a frictionless fluid flow region above. Near the free surface, the velocity varies from 2.8 to 3.7 m/s, corresponding to the potential flow velocity.

A well-defined recirculation zone occupies part of the step cavities. The quasisteady rollers are maintained through the transmission of shear stress from the overlying flow [15]. Considering the recirculatory motion a solid body rotation, for an equivalent circumference trajectory of 2 cm, the angular velocity and frequency of rotation were estimated to be approximately 40–50 $rads^{-1}$ and 6–8 Hz in the steps studied.

Turbulent Boundary Layer. The boundary layer growth in the study region was evaluated. The boundary layer thickness (δ) is defined as the perpendicular distance from the pseudobottom to where the velocity is 99% of its maximum value (U_0). The boundary thickness was obtained from the 40 velocity profiles obtained over steps E34, E33, E31, and E29 (Fig. 3). This is a difficult quantity to estimate, since it depends on measurements of small velocity differences and of the irregular behavior of the outer edge of the boundary layer. The development of the boundary layer may be expressed by [16]

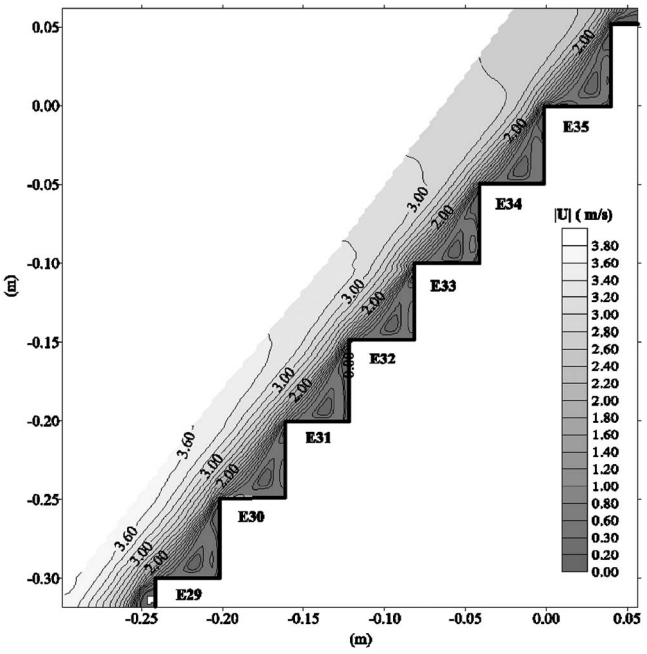

Fig. 2 Contour map of mean absolute velocity ($|U|$)

$$\frac{\delta}{X} = a\left(\frac{X}{k_s}\right)^{-b} \tag{3}$$

where X is the streamwise distance from the start of the growth of the boundary layer assumed to be the spillway crest; k_s is the roughness height $k_s = h\cos\alpha$, and a and b are constants, which according to the experimental results are equal to 0.112 and 0.309, respectively.

In Fig. 3, other integral measures of the boundary layer obtained from the velocity profiles are also shown, as the displacement thickness (δ^*)

$$\delta^* = \int_0^\delta \left(1 - \frac{U(y)}{U_0}\right) dy \tag{4}$$

the momentum thickness (θ)

$$\theta = \int_0^\delta \frac{U(y)}{U_0}\left(1 - \frac{U(y)}{U_0}\right) dy \tag{5}$$

The use of the von Kármán integral momentum equation [17] allows the estimation of the flow resistance coefficient (c_f) in the developing flow region

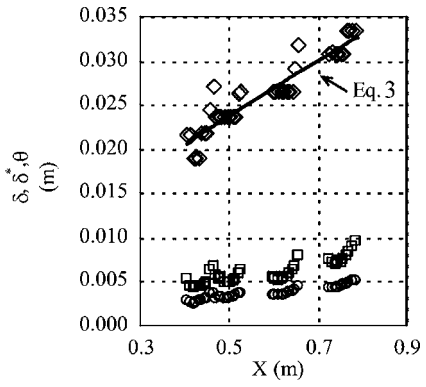

Fig. 3 Evolution of the δ(◇), δ^*(□), θ(○)

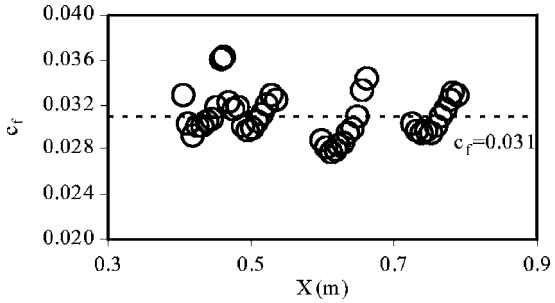

Fig. 4 Flow resistance coefficient (c_f) along the stepped spillway

$$c_f \equiv \frac{\tau_w}{\frac{1}{2}\rho U_0^2} = 2\frac{d\theta}{dx} + \frac{4\theta + 2\delta^*}{U_0}\frac{dU_0}{dx} \tag{6}$$

where τ_w=pseudobottom shear stress.

It was considered that the momentum thickness (θ) increased linearly in the flow direction (x) in accordance with [18], which studied a similar surface. The data analysis gave a $d\theta/dx = 0.0052$. The term dU_0/dx is deduced from the Bernoulli equation. In Fig. 4, is plotted the flow resistance calculations for four step cavities. The c_f seem to present a linear growth at each half end of the step cavity and a global constant mean value of 0.031 for all step cavities.

Velocity Distribution. The mean velocity distribution can be divided in two zones: above the boundary layer, where the mean velocity can be considered constant and equal to the ideal-fluid flow velocity (U_0), and the boundary layer, where the mean velocity gradient is relevant. In Fig. 5, mean velocity profiles normal to the pseudobottom and taken at different positions along the step cavities of the steps E34, E33, E31, and E29 are shown. It can be appreciated that the velocity profiles in the boundary layer are self-similar, using as characteristic scales $U_0(X)$ and $\delta(X)$. At the step edges, the velocity distribution in the boundary layer can be approximated by a power law [3]

$$\frac{U}{U_0} = \left(\frac{y}{\delta}\right)^{1/N} \tag{7}$$

The exponent N determined for the four step edges is around 3.0 in close agreement with the value of 3.3 obtained by [6] using a flushed Pitot tube in a similar model of a stepped spillway. In conventional smooth spillways, the value of $N=6.0$ from the analysis of [19,20], is usually suggested for the developing boundary layer upstream of the inception point. The comparison shows that the mean velocity profile rises much more steeply from the reference level (y=0) in smooth spillways than in stepped spillways and then is flatter away from the "bottom."

Between the step edges ($0 < x < L_{cav}$), the velocity profiles suggest a local developing mixing layer that forms at the step edge. Defining the characteristic width (b) of the mixing layer as [17]:

$$b(x) = y_{0.9}(x) - y_{0.1}(x) \tag{8}$$

where y_α is the coordinate y where $U = \alpha U_0$.

In Fig. 6, the spreading of the mixing layer is shown by plotting the evolution of $y_{0.9}/k_s$ and $y_{0.1}/k_s$ along the cavities of steps E34, E33, E31, and E29. It seems that the mixing layer spreads linearly with a maximum of b at $x/L_{cav}=0.7$. The displacement of $y_{0.1}$ to the interior of the cavity is much more noticeable than the variation of $y_{0.9}$ to the free surface. This is a typical characteristic of a mixing layer that spreads preferentially into the low speed stream [17]. The maximum reverse flow velocities found in the recirculation zone are $0.15U_0$ and are located near the step surfaces.

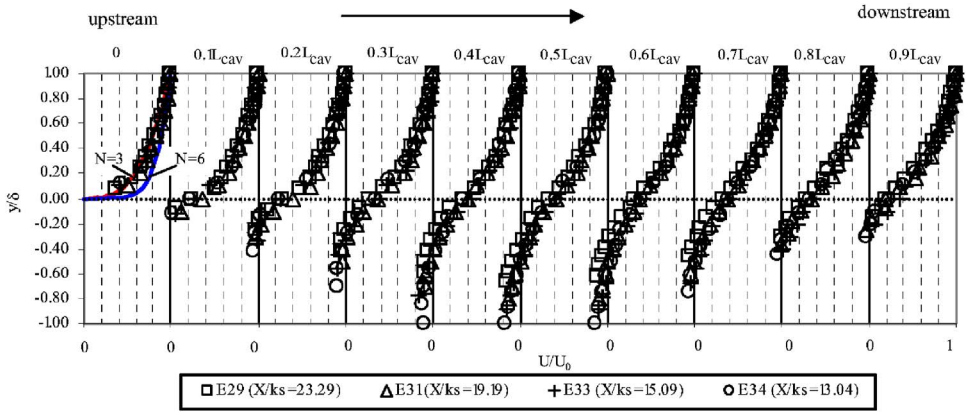

Fig. 5 Mean velocity profiles (U/U_0) normal to the pseudo-bottom, along the step cavities (L_{cav}) analyzed

Mean Velocity Gradient Tensor. The 2D PIV data provides two velocity components. This data can be differentiated in two directions, and thus, some terms of the mean velocity gradient tensor or deformation tensor can be estimated with PIV. Therefore the spanwise vorticity (ω_z) and in-plane shear strain (ε_{xy}) can be determined as follows:

$$\omega_z = \frac{dV}{dx} - \frac{dU}{dy} \tag{9}$$

$$\varepsilon_{xy} = \frac{dU}{dy} + \frac{dV}{dx} \tag{10}$$

The second-order central-difference scheme was employed for estimation of the spatial derivatives; this scheme is implemented for data spaced at uniform ΔX, according:

$$\left(\frac{d\phi}{dx}\right)_i = \frac{\phi_{i+1} - \phi_{i-1}}{2\Delta X} \quad O(\Delta X^2) \tag{11}$$

The shear strain contour map (Fig. 7) shows maximum levels just behind the step edge, where the separation of the shear layer begins. The peaks of shear strain develop in the flow direction, highlighting the pseudobottom as the most active zone in terms of shear stress. A gradual decrease of the shear strain is observed towards the free surface, where the flow can be considered irrotational.

Assuming the turbulent-viscosity hypothesis valid, as the production/generation of turbulent kinetic energy (P) is defined by [17]

$$P = -\overline{u' \cdot v'} \cdot \varepsilon_{xy} = \nu_t \cdot \varepsilon_{xy} \cdot \varepsilon_{xy} \tag{12}$$

where $\overline{u' \cdot v'}$ is the mean Reynolds shear stress and ν_t is the turbulent viscosity.

The production (P) is proportional to the mean shear strain rate. It is possible then to identify the zone just behind the outer step edge as a region of formation and growth of large-scale turbulent structures, associated with local pressure reduction in the vicinity of the vortex cores.

The vorticity contour map (Fig. 8) presents a similar pattern with the shear strain map; the negative vorticity is due to counterclockwise rotation. Very high levels of vorticity are generated immediately downstream of the corner and occur over a relatively small characteristic thickness. This is most likely linked to the rapid onset of small-scale vortical structures, which appear immediately downstream the leading corner of the cavity. The dominant vorticity levels extend along the separated shear layer between the leading (upstream) and trailing (downstream) corners of the steps. Within the cavity, the flow pattern exhibit a large-scale recirculation flow, the vorticity results from agglomeration of the small-scale concentrations. The vorticity level inside the cavity varies

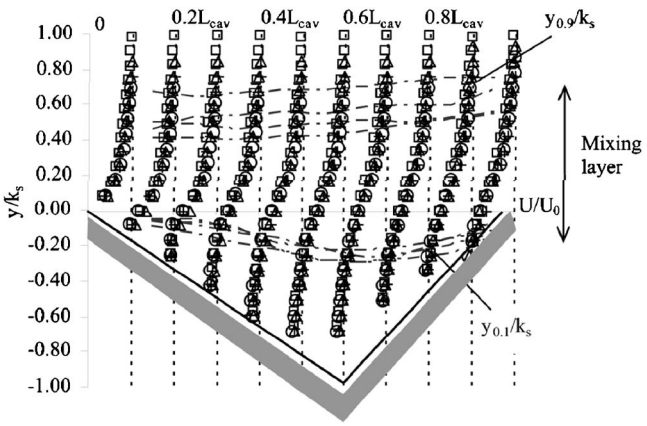

Fig. 6 Mean velocity profiles (U/U_0) and variation of y_α along the step cavities analyzed. Symbols as in Fig. 5.

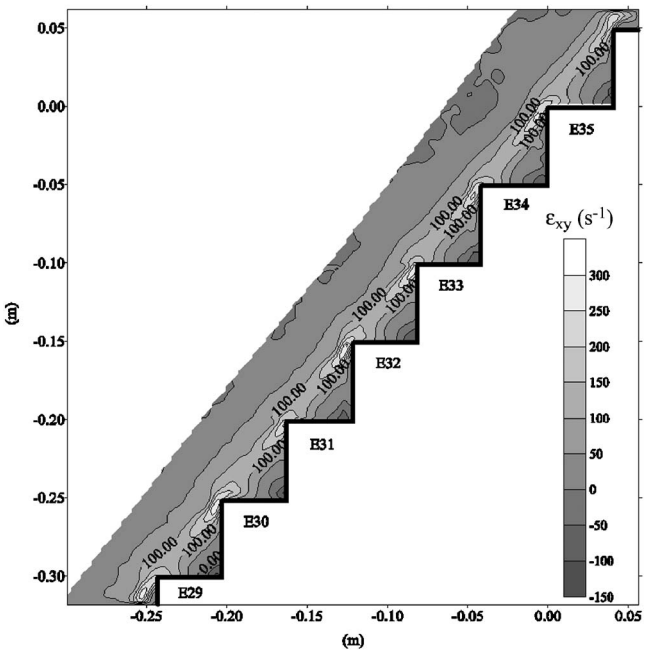

Fig. 7 Contour map of mean shear strain (ε_{xy})

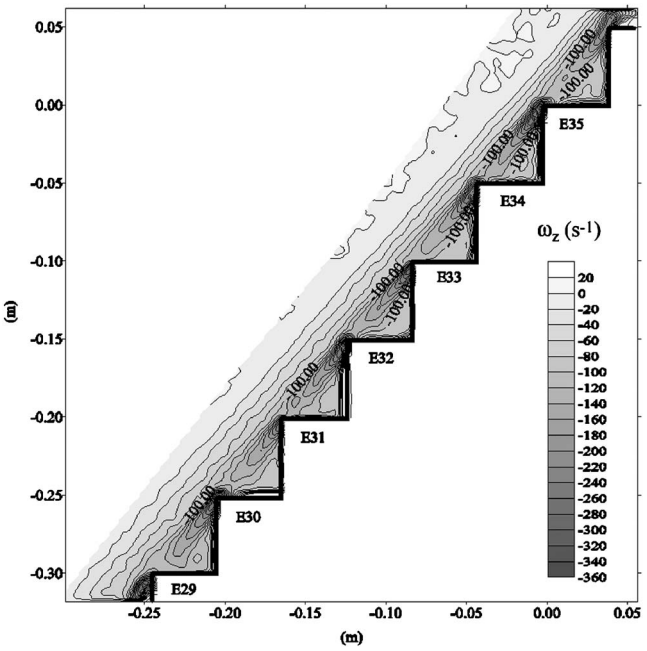

Fig. 8 Contour map of mean spanwise vorticity (ω_z)

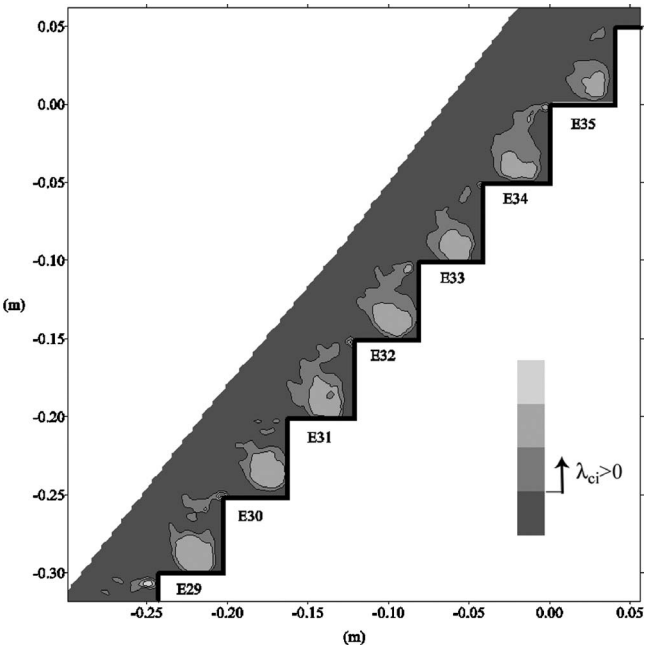

Fig. 9 Contour map of swirling strength

between 80 s^{-1} and 100 s^{-1}, which is in close agreement with the angular velocities estimated from the mean velocity field for the large recirculation zone, following the Stokes theorem equation.

The vorticity not only identifies vortex cores but also any shearing motion present in the flow. Reference [21] proposed vortex identification based on the swirling strength. This method does not reveal regions that contain significant vorticity but do not have any local swirling motion (i.e., shear layers). It is based on the analysis of the mean, local velocity gradient tensor and its corresponding eigenvalues. The local 2D velocity gradient tensor will either have two real eigenvalues (λ_r) or a pair of complex conjugate eigenvalues ($\lambda_{cr} \pm \lambda_{ci}$). The vortices are identified by plotting isoregions of $\lambda_{ci} > 0$ [21]. Isoregions of swirling strength are shown in Fig. 9. Swirling strength is noted just behind the step edge and inside the cavity due to the presence of the recirculation vortex. This quantity proved to be more useful than vorticity as a means of identifying eddies.

Turbulence Characteristics

The 500 velocity fields measured allow studying the mean velocity field and the fluctuating velocity field.

The turbulent kinetic energy was chosen to represent the turbulent flow field. As the spanwise velocity component is not available; it is estimated from the other two components. The turbulent kinetic energy (k) is then expressed by [22]

$$k = \frac{3}{4}\left(\overline{u'^2} + \overline{v'^2}\right) \tag{13}$$

where $u' = u - U$ is the velocity fluctuation in the streamwise direction, $v' = v - V$, the velocity fluctuation in the transverse direction.

Figure 10 confirms that the maximum turbulent kinetic energy is located in the region near the pseudobottom. In the shear strain field (Fig. 7), the region of production of turbulent kinetic energy was identified: the mean velocity gradient removes kinetic energy from the mean flow and transfers it to the fluctuating velocity field. It can also be observed that the turbulent kinetic energy levels are increasing in the downstream direction with more and more important values appearing in the overlying flow closer to the free surface.

Turbulence Intensity Distribution. As for the mean velocity, ten equally spaced turbulence intensity profiles were obtained over the cavities of steps E34, E33, E31, and E29. The turbulence intensity in the flow direction (T_u) is defined as

$$T_u(y) = \frac{\sigma_u(y)}{U(y)} \tag{14}$$

where $\sigma_u(y)$ is the root mean square of the streamwise component of turbulent velocity and $U(y)$ is the mean streamwise velocity at the y coordinate.

A gradual reduction of the turbulence intensity towards the edge of the boundary layer (δ) can be observed in Fig. 11. In the transition between the boundary layer and the irrotational flow

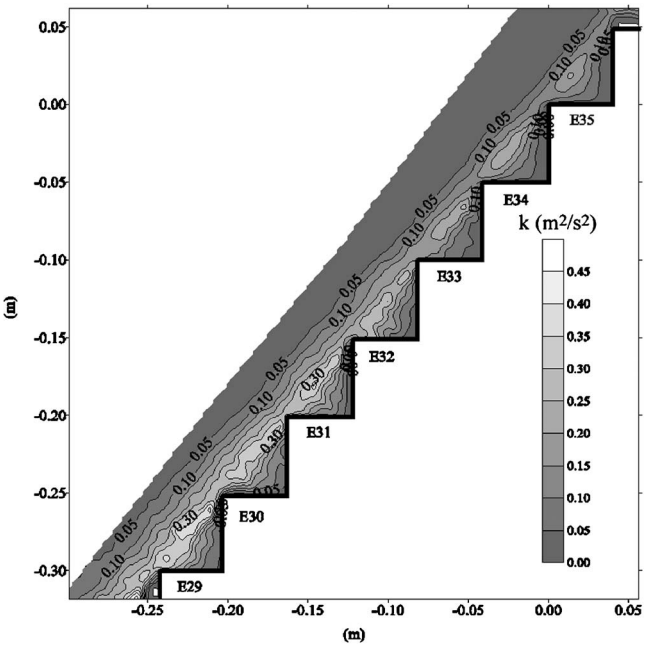

Fig. 10 Contour map of turbulent kinetic energy (k)

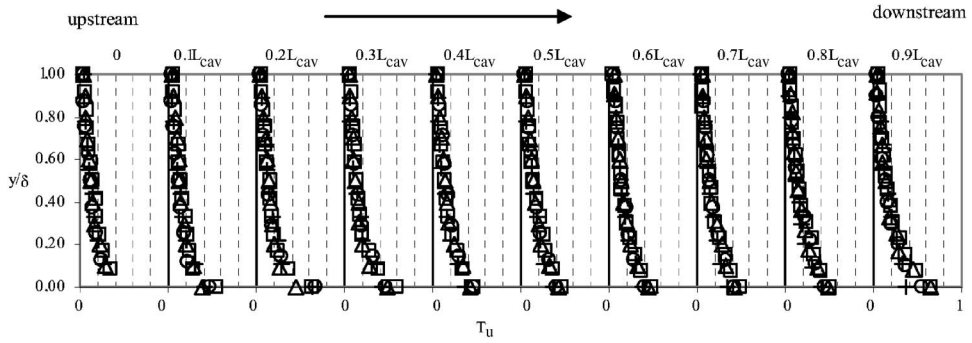

Fig. 11 Turbulence intensity (T_u) profiles normal to the pseudobottom, along the step cavities analyzed. Symbols as in Fig. 5.

region were measured turbulence intensity (T_u) levels of 0.04. Near the pseudobottom ($y/\delta \approx 0$) the turbulence intensity ranges from 0.40 to 0.65. The degree of turbulence intensity is much higher than the maximum levels reported for a turbulent boundary layer over a smooth open channel, $T_u=0.2$ [23]. The increase in the magnitudes of the flow turbulence will cause larger pressure fluctuations over the boundary surfaces of the steps than the usually found over a conventional smooth spillway.

Quadrant Analysis. The $u'v'$ quadrant-splitting scheme is one of the existent education techniques to study turbulent structures [24]. This technique is based on the joint distribution of the velocity fluctuations on both longitudinal ($u'=u-U$) and vertical ($v'=v-V$) components. Four quadrants are defined in the $u'v'$ plane (Fig. 12): quadrant I ($u'>0$ and $v'>0$); quadrant II ($u'<0$ and $v'>0$); quadrant III ($u'<0$ and $v'<0$), and quadrant IV ($u'>0$ and $v'<0$).

Each quadrant represents an event. Quadrant II is associated with "ejection," which can be schematically characterized by an upward movement ($v'>0$) of a low-speed fluid ($u'<0$); in quadrant IV are the sweeps that are downward movements ($v'<0$) of high-speed ($u'>0$) fluid. Events in these regions correspond to the production of turbulent energy (see Eq. (10)). Quadrants I and III are outward and inward interactions, respectively.

In Fig. 12, the cross-hatched zone is bounded by the curves

$$|u' \cdot v'| = H \cdot \sigma_u \cdot \sigma_v \tag{15}$$

where σ_u and σ_v are the root-mean-square values of the u and v velocity components. Only the region out of the cross-hatched zone is considered contributing to the events. The threshold values defined by H, allow distinguishing high-magnitude events (H high) and most frequent events ($H=0$).

The quadrant contributions in each velocity field can be evaluated by the following discriminating function [25]:

$$I_H^i(x,y,n) = \begin{cases} 1, & [u'(x,y,n), v'(x,y,n)] \in Q^i \wedge |u' \cdot v'| > H \cdot \sigma_u \cdot \sigma_v \\ 0, & \text{otherwise} \end{cases} \tag{16}$$

The occurrence probability ($f_{H=x}^i$) of each quadrant (Q^i), over the 500 (N) instantaneous velocity fields can be determined by

$$f_{H=x}^i = \frac{\sum_{n=1}^{N} I_{H=x}^i(x,y,n)}{N} \tag{17}$$

In this study two threshold values were adopted: $H=0$, where all events within a quadrant are considered; and $H=2$ where only the strongest events are considered. The value 2 has been used in other quadrant analysis studies [26].

Figure 13 and 14, show that the events associated to quadrant II and IV are the most frequent or have the highest probability in the flow field. For $H=0$ (Fig. 13), ejections (Q^2) have the highest

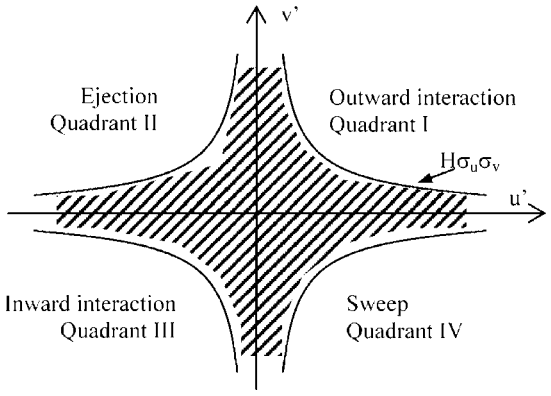

Fig. 12 Definition sketch of the $u'v'$ plane (after [23])

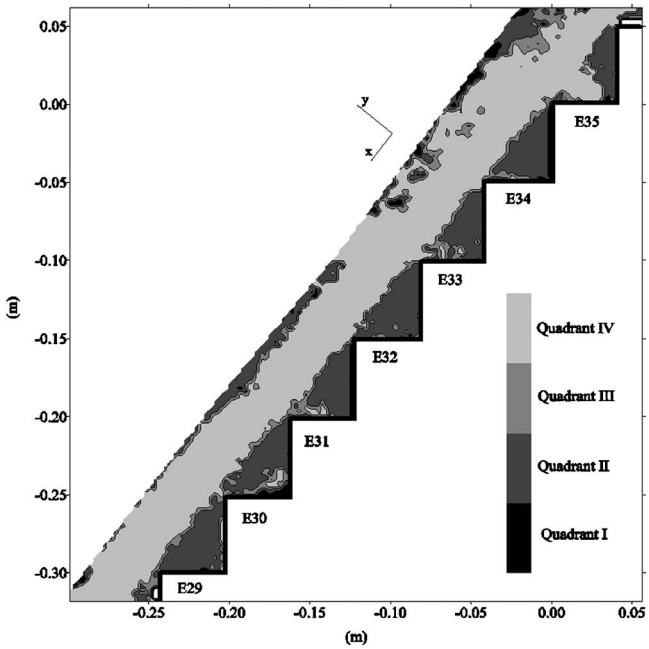

Fig. 13 Contour map of the dominant quadrant in terms of occurrence probability for $H=0$

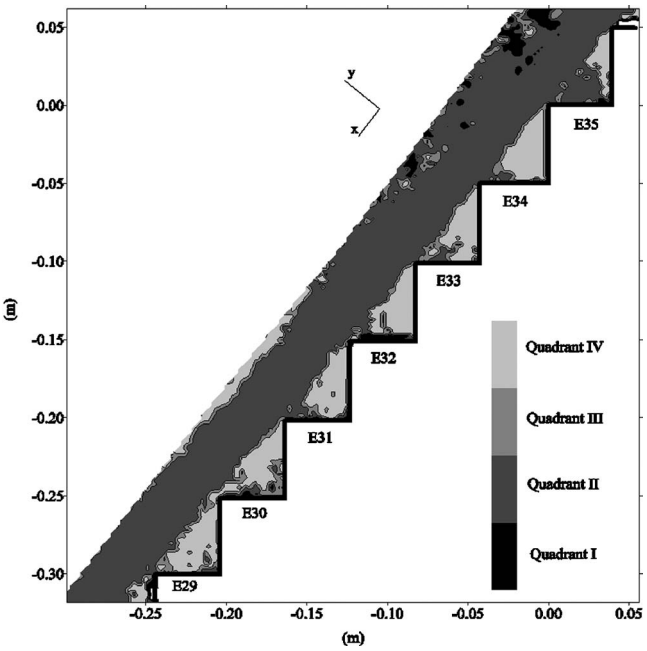

Fig. 14 Contour map of the dominant quadrant in terms of occurrence probability for $H=2$

probability of occurrence over the region near the pseudobottom and inside the step cavity, whereas the sweeps (Q^4) are the most frequent in the upper region of the overlying flow.

For the high-magnitude events, $H=2$ occurs precisely the inverse. In the zone near the pseudobottom and inside the cavity, the highest probabilities of occurrence are for the sweeps, and in the upper region of the coherent stream that skims over the steps the dominant event is the ejection (Fig. 14). The previous considerations seem to corroborate the flow visualizations over transverse square cavities made by Djenidi et al. [18]. The visualizations indicated random occurrence of three types of events: outflows from the cavities into the overlying flow, inflows into the cavities, and periods where the overlying flow skims over the cavities with no significant exchange of fluid. The highest occurrence probability of high-magnitude ejections in the overlying flow (Fig. 14) corroborates the existence of important outflows from the cavities.

Continuity demands that an outflow that occurs at a spanwise location must be balanced, at the same time, by one or more inflows at other spanwise positions into the cavity, and that would explain why sweeps are dominant inside the cavity. In [18], it is also observed that outflows occur sequentially in the downstream direction: an outflow from one cavity is followed by another in the adjacent downstream cavity. These sequences of outflows indicate that the initiating mechanism for the outflows may be triggered by the overlying flow rather than have its origin within the cavity [27,18]. The passage of quasistreamwise vortices near the pseudobottom could pump fluid out of the cavities as these turbulent structures have associated pressure minimum at its core. The outflows of strong magnitudes from the cavities into the overlying flow could play an important role in the increased turbulent intensities measured over stepped spillways in comparison with smooth spillways.

Conclusions

The experimental study presented herein investigated the developing flow region in stepped spillways with typical slopes of RCC dams. The main conclusions are summarized below:

1. In the region upstream, the inception point the flow is accelerating and the turbulent boundary layer is developing and growing in the downstream direction. The recirculation inside the step cavity can be approximated to a solid body rotation. The velocities measured confirm the hypothesis of irrotational flow in the region closer to the free surface.
2. The boundary layer thickness, δ, depends on the distance from the spillway crest and roughness height and can be predicted for stepped spillways by Eq. (3).
3. The von Kármán integral momentum equation was applied to estimate the flow resistance coefficient (c_f). The mean value obtained was 0.031.
4. The shear strain (Fig. 7) and vorticity (Fig. 8) contour maps agree in showing maximum levels just behind the step edges, where the separation of the shear layer begins. These regions can be associated with the formation and growth of large-scale turbulent structures that are convected in the downstream direction. The swirling strength proved to be an appropriate quantity to identify existent eddies in the mean velocity field (Fig. 9).
5. The measured turbulence intensities (T_u) between 0.40 and 0.65 near the pseudobottom are much higher than the maximum levels reported for smooth open channels.
6. A quadrant analysis was performed to study turbulent structures. It shows that "ejections" are the most frequent events in the region near the pseudobottom and "sweeps" dominate the upper region of the skimming flow, Fig. 13. When considering only high magnitude events ($H=2$), the opposite situation occurs. The sweeps are dominant near the pseudobottom and inside the cavity and the ejections are more frequent in the upper region of the overlying flow, Fig. 14. This analysis seems to corroborate the flow visualizations of [18]. Along the span of the cavities, the outflows alternate with inflows of appreciable magnitude and contribute in producing and maintaining turbulence intensities and Reynolds shear stresses by exchanging momentum between the cavities and overlying layers. The fluid trapped within the cavities functions as a natural reservoir of low momentum that facilitates the exchange of momentum between cavities and the overlying stream. It is conjectured that these would help maintaining a higher turbulent energy of the flow over a stepped spillway in comparison with a smooth spillway.

Acknowledgment

The authors would like to acknowledge *CITEEC* (Centro de Innovación Tecnoloxica en Edificación e Enxeneria Civil) and Prof. Jerónimo Puertas from *A Coruña* University for giving the conditions for the realization of the experimental work. The first author acknowledges the financial support of the Fundação para a Ciência e Tecnologia (Portugal, Praxis XXI, BD/3056/2000) and the helpful discussions of Dr. Gerber Van der Graaf.

Nomenclature

E = energy head
E_0 = maximum energy head
H = hole size value
I_H^i = discriminating function
L_{cav} = distance between step edges, roughness spacing
N = exponent of velocity power law and number of PIV realizations
P = rate of production of turbulent kinetic energy
Q^i = quadrant i of the plane $u'v'$
T_u = turbulence intensity in the flow direction
$U(y)$ = mean velocity in x direction at coordinate y
U_0 = ideal-fluid flow velocity
$\bar{U}$ = mean flow velocity
$V(y)$ = mean velocity in y direction at coordinate y

X = streamwise distance from spillway crest to the outer step edge
Z = factor related with confidence level
$b(x)$ = characteristic width of the mixing layer
c_f = flow resistance coefficient
d = flow depth
d_0 = ideal-fluid depth
f_H^i = occurrence probability event I with hole-size value of H
g = gravitational acceleration
h = step height
k = turbulent kinetic energy
$k_s = h \cos \alpha$ = roughness height perpendicular to pseudobottom
q = discharge per unit width
u = instantaneous velocity in x direction
$u' = u - U$ = velocity fluctuation in x direction
v = instantaneous velocity in y direction
$v' = v - V$ = velocity fluctuation in y direction
x = streamwise coordinate axis
y = transverse coordinate axis
y_α = coordinate y where $U = \alpha U_0$
z = spanwise coordinate axis
ΔE = head of energy loss
ΔX = vector spacing
α = chute angle from horizontal
δ = boundary layer thickness
δ^* = displacement thickness
δ^e = energy thickness
$\varepsilon_{\text{mean}}$ = uncertainty in the mean value
ε_{rms} = uncertainty in the RMS value
ε_{xy} = mean shear strain
ν = kinematic viscosity of water
ν_t = turbulent kinematic viscosity
λ = eigenvalue of the velocity gradient tensor
θ = momentum thickness
ρ = density of water
σ_u = root mean square of streamwise component of velocity
σ_v = root mean square of transverse component of velocity
τ_w = pseudobottom shear stress
ω_z = mean spanwise vorticity

References

[1] Essery, I., and Horner, M., 1978, "The Hydraulic Design of Stepped Spillways," CIRIA Report No. 33, London, 2nd ed.

[2] Chanson, H., 1995, *Hydraulic Design of Stepped Cascades, Channels, Weirs and Spillways*, Pergamon, Oxford.

[3] Chanson, H., 2001, *The Hydraulics of Stepped Chutes and Spillways*, Swets & Zeitlinger, Lisse, The Netherlands.

[4] Gonzalez, C., and Chanson, H., 2004, "Interactions Between Cavity Flow and Main Stream Skimming Flow: an Experimental Study," Can. J. Civ. Eng., **31**, pp. 33–44.

[5] Boes, R. M., and Hager, W., 2003, "Two-Phase Flow Characteristics of Stepped Spillways," J. Hydraul. Eng., **129**(9), pp. 661–670.

[6] Matos, J., 1999, "Air Entrainment and Energy Dissipation on Flow Over Stepped Spillways," Ph.D. thesis, Technical University of Lisbon, IST, Lisboa (in Portuguese).

[7] Ohtsu, I., Yasuda, Y., and Takahashi, M., 2004, "Flow Characteristic of Skimming Flow in Stepped Channels," J. Hydraul. Eng., **130**(9), pp. 860–869.

[8] Ohtsu, I., and Yasuda, Y., 1997, "Characteristics of Flow Conditions on Stepped Channels," *Proc. 27th IAHR Biennal Congress*, San Francisco, Theme D, ASCE, New York, pp. 583–588.

[9] Chanson, H., and Toombes, L., 2002, "Air Water Flows Down Stepped Chutes: Turbulence and Flow Structure Observations," Int. J. Multiphase Flow, **28**, pp. 1737–1761.

[10] Amador, A., Sánchez-Tembleque, F., Sánchez-Juny, M., Puertas, J., and Dolz, J., 2004, "Velocity and Pressure Field in Skimming Flow in Stepped Spillways," *Hydraulics of Dams and River Structures*, F. Yanzdandoost and J. Attari, eds., Taylor & Francis, London, pp. 279–286.

[11] Westerweel, J., Dabiri, D., and Gharib, M., 1997, "The Effect of a Discrete Window Offset on the Accuracy of the Cross-Correlation Analysis of Digital PIV Recordings," Exp. Fluids, **23**, pp. 20–28.

[12] Keane, R., and Adrian, R., 1990, "Optimization of Particle Image Velocimeters Part I: Double Pulsed Systems," Meas. Sci. Technol., **1**, pp. 1202–1215.

[13] Westerweel, J., 1994, "Efficient Detection of Spurious Vectors in Particle Image Velocimetry," Exp. Fluids, **16**, pp. 236–247.

[14] Freek, C., Sousa, J., Hentschel, W., and Merzkirch, W., 1999, "On the Accuracy of a MJPEG-Based Digital Compression PIV-System," Exp. Fluids, **27**, pp. 310–320.

[15] Rajaratnam, N., 1990, "Skimming Flow in Stepped Spillways," J. Hydraul. Eng., **116**, pp. 587–591.

[16] U.S. Bureau of Reclamation, 1977, Hydraulic Design Criteria-Sheet 111-18 to 111-18/5, Corps of Engineers, USA.

[17] Pope, S., 2000, *Turbulent Flows*, Cambridge University Press, Cambridge, England.

[18] Djenidi, L., Elavarasan, R., and Antonia, R., 1999, "The Turbulent Boundary Layer Over Transverse Square Cavities," J. Fluid Mech., **395**, pp. 271–294.

[19] Cain, P., 1978, "Measurements Within Self-Aerated Flow on a Large Spillway," Ph.D. thesis, University of Canterbury, New Zealand.

[20] Chanson, H., 1989, "Flow Downstream of an Aerator: Aerator Spacing," J. Hydraul. Res., **27**(4), pp. 519–536.

[21] Adrian, R., Christensen, K., and Liu, Z., 2000, "Analysis and Interpretation of Instantaneous Turbulent Velocity Fields," Exp. Fluids, **29**, pp. 275–290.

[22] Sousa, J., and Pereira, J., 2002, "DPIV Study of the Effect of a Gabble Roof on the Flow Structure Around a Surface-Mounted Cubic Obstacle," Exp. Fluids, **37**, pp. 409–418.

[23] Nezu, I., and Nakagawa, 1993, *Turbulence in Open-Channel Flows*, Balkema, Leiden, The Netherlands, IAHR Monograph Series.

[24] Willmarth, W., and Lu, S., 1972, "Structure of the Reynolds Stress Near the Wall," J. Fluid Mech., **55**, pp. 65–92.

[25] Cellino, M., and Lemmin, U., 2004, "Influence of Coherent Flow Structures on the Dynamics of Suspended Sediment Transport in Open-Channel Flow," J. Hydraul. Eng., **130**(11), pp. 1077–1088.

[26] Belanger, T., and Roy, A., 1998, "Effects of a Pebble Cluster on the Turbulent Structure of a Depth-Limited Flow in a Gravel-Bed River," Geomorphology, **25**, pp. 249–267.

[27] Townes, H., and Sabersky, R., 1966, "Experiments on the Flow Over a Rough Surface," Int. J. Heat Mass Transfer, **9**, pp. 729–738.

Influence of Flow Coefficient, Stagger Angle, and Tip Clearance on Tip Vortex in Axial Compressors

Yong Sang Yoon
e-mail: perfect1@snu.ac.kr

Seung Jin Song

School of Mechanical and Aerospace Engineering,
Seoul National University,
San 56-1,
Shillim dong, Kwanak gu,
Seoul, 151-744, Korea

Hyoun-Woo Shin
GE Transportation,
Aircraft Engines,
1 Neumann Way,
Cincinnati, Ohio, 45215

Experiments have been performed on the low speed research compressor (LSRC) at General Electric Aircraft Engines to investigate the effects of flow coefficient, stagger angle, and tip clearance on tip vortex. Time resolved casing pressure distributions over the third stage rotor have been acquired with high-frequency-response pressure transducers. Also, tip vortex strength and trajectory have been estimated from the casing pressure fluctuations which have been obtained simultaneously from various axial locations. As flow coefficient decreases, tip vortex gets strengthened and migrates upstream. The stagger angle increase weakens the tip vortex and moves it downstream slightly because the blade loading is decreased. However, tip leakage vortex is influenced mainly by tip clearance, and there exists a "critical" tip clearance which determines the type of tip vortex trajectory ("straight" or "kinked"). As predicted by others, tip vortex gets strengthened with increasing tip clearance. However, unlike the predictions, the tip vortex trajectory moves upstream with increasing tip clearance. Furthermore, with tip clearance above a "critical" value, the tip vortex trajectory is no longer straight but shows a kink in the passage. [DOI: 10.1115/1.2354522]

Keywords: axial compressor, tip clearance, stagger angle, flow coefficient, tip leakage flow, tip vortex trajectory, vortex strength

Introduction

In turbomachines, the gap between the casing and rotor blade tip results in leakage flows as shown in Fig. 1. This unsteady, three-dimensional leakage flow rolls up into a tip vortex that increases the endwall blockage; decreases compressor performance; and deteriorates stability. Therefore, the tip leakage flow has long been an important research topic for turbomachinery designers. Since the pioneering study of Rains [1], many studies have been conducted. Khalid et al. [2] have presented a methodology for quantifying compressor endwall blockage due to tip leakage flow. Storer [3] predicts that the principal mechanism of loss (entropy) creation due to tip leakage flow is the mixing of passage and leakage flows. Focusing on the structure of tip vortex itself, Lakshminarayana [4] suggests a "retained lift" approach to analyze the vorticity shed at blade tips, and Martinez-Sanchez [5] has developed an analytical model which predicts the tip vortex trajectory as a function of blade loading. Chen et al. [6] have developed a similarity analysis to examine tip vortex kinematics, and predict a kink in the vortex trajectory at the blade trailing edge. From their numerical analysis, Hoying et al. [7] predict that tip vortex moves upstream with decreasing flow coefficient and pops out upstream of rotor blade leading edge at the stall point. Furthermore, Furukawa et al. [8] predict tip vortex breakdown at flow rates less than that corresponding to the peak of the compressor characteristic.

Many experimental studies have been conducted as well. The roll-up of tip leakage flows into vortices has been measured by various investigators (e.g., Hunter and Cumpsty [9], Inoue and Kuroumaru [10], Wagner et al. [11], and Inoue et al. [12]). Inoue et al. [13,14] and Marz et al. [15] have measured unsteady casing static pressure and its deviation to detect tip vortex, and Mailach [16] has located tip vortex by measuring the axial velocity and relative flow angle within the rotor blade passage near the tip region. Goto [17] has experimentally verified that, as the rotor tip clearance increases, the viscous region near the casing thickens due to the diffusion of the tip vortex. Storer and Cumpsty [18] predict that tip vortex begins at the minimum static pressure location on the blade and validate their prediction in a linear cascade test. According to Inoue et al. [13], the axial compressor rotor tip vortex gets strengthened with increasing tip clearance (up to 4.2% of blade chord length) and moves upstream as the flow coefficient decreases. In an axial flow fan, Jang et al. [19] also find that the vertical center of the leakage vortex is located radially over 94% of span; and that the tip leakage vortex migrates upstream when the flow coefficient degreases. Liu et al. [20] experimentally show that the tip vortex is stable at the design condition before breakdown occurs in the core of the tip leakage vortex at near stall condition. Despite such efforts, however, experimental data showing parametric variation of tip vortex are scarce. For example, to the authors' knowledge, the effects of stagger angle variation or "very large" tip clearances larger than 5% of the chord have not yet been reported in the literature. Therefore, the objective of this research is to help understand the tip vortex kinematics by measuring the influence of flow coefficient, stagger angle, and very large tip clearance. The vortex trajectory was estimated from time versus space (T-S) diagrams of unsteady static pressure obtained simultaneously at various axial locations on the casing

Experimental Facility

This research has been conducted on the low speed research compressor (LSRC) at GEAE, a low speed, four-stage, axial compressor shown in Fig. 2. The LSRC is a four-stage machine designed to represent the essential features of modern high-speed core compressors. The successful transfer of design philosophies verified in the LSRC to high-speed machines has been well estab-

Contributed by the Fluids Engineering Division of ASME for publication in the JOURNAL OF FLUIDS ENGINEERING. Manuscript received April 27, 2005; final manuscript received March 27, 2006. Assoc. Editor: Phillip M. Ligrani.

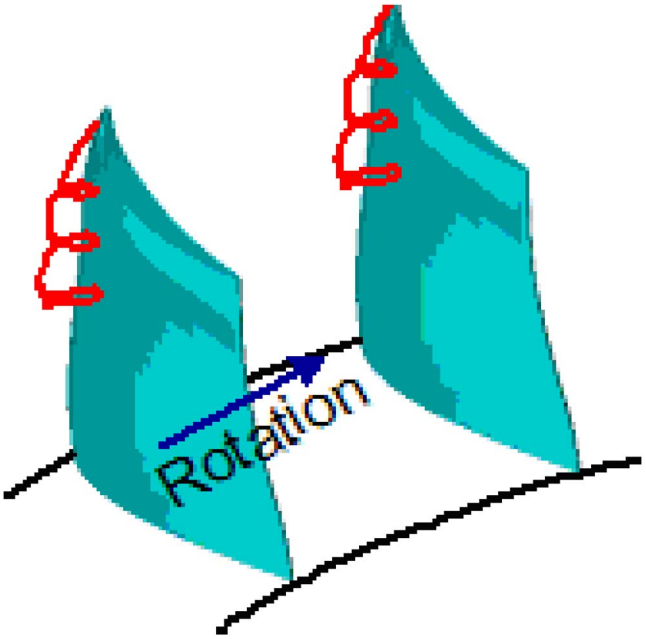

Fig. 1 Tip leakage vortex

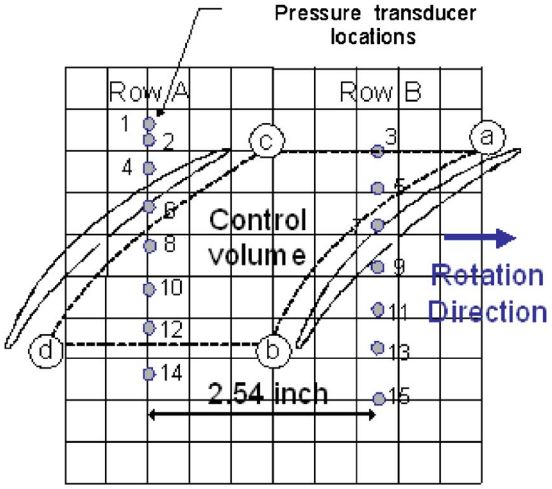

Fig. 3 Pressure transducer locations on the casing wall of Stage 3 rotor

lished. The facility has a constant casing diameter of 1.524 m, and the flow enters from the top through a bellmouth/inlet system, which filters the flow. After passing through the test section, the flow exits through a large, circular throttle plate that can be moved to change the compressor back pressure (or flow rate) by varying the exit area. The compressor is driven by a motor connected to a gear-box and has a design rotational speed of 900 RPM. More details about the facility can be found in Wisler [21].

Instrumentation

Compressor operating conditions (e.g., efficiency, pressure ratio, mass flow rate, etc.) are determined from the following steady state measurements. Inlet flow temperature has been measured by RTD sensors. The flow rate is determined at the compressor inlet from the pressure difference between upstream and downstream of the bullet nose (ogive) using pressure transducers with an accuracy of ±0.01% of the full scale values. Power input into the compressor is measured with a strain gauge-type torque meter in the drive shaft with an accuracy of ±0.07% of the measured torque. At each stage, eight circumferentially distributed static pressure taps are used to obtain casing pressure data, by using 6800 Pa (1 psi) and 13,600 Pa (2 psi) pressure transducers with an accuracy of ±0.01% of the full-scale values.

Inoue et al. [12] have found that the secondary flow due to tip vortex remains radially near the casing at about 95% of span as it goes downstream. Jang et al. [19] also reconfirmed the radial location of the core at 94% of span. Furthermore, tip vortex induces random pressure unsteadiness and, therefore, pressure fluctuations at the casing can be used to detect tip vortices. The time-resolved casing pressure has been measured by utilizing fifteen high frequency response pressure transducers with an accuracy of ±1.0% and a frequency response of 70 kHz. They are mounted on the casing of the third stage rotor (Fig. 3). These pressure transducers are installed in two rows 2.54 in apart to obtain a better resolution in the axial direction. The instantaneous analogue signals from the pressure transducers are digitized by an A/D converter with sixteen channels and a maximum sampling rate of 10 MS/s. For this study, fifteen channels have been used with a 100 kHz sampling rate (blade passing frequency is 810 Hz) for each channel. The data acquisition system is shown schematically in Fig. 4.

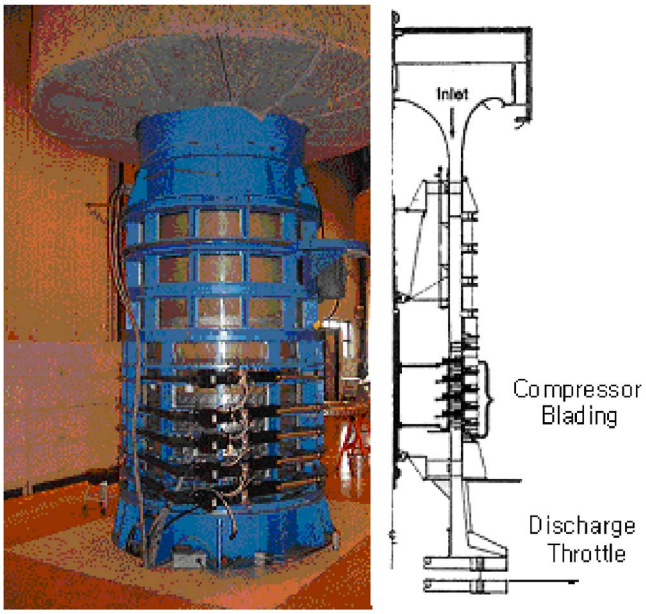

Fig. 2 Low speed research compressor (LSRC) at GE aircraft engines (GEAE)

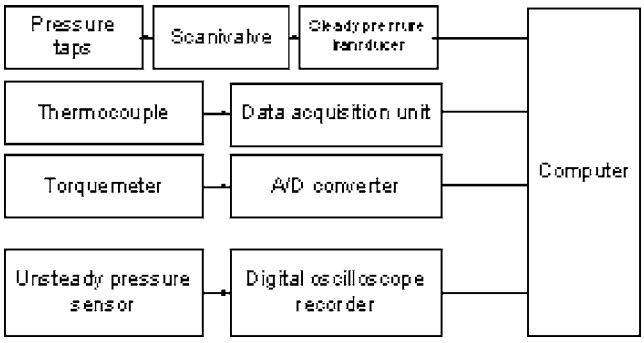

Fig. 4 Data acquisition system

Table 1 Test configurations

Configuration	Stagger angle	Tip clearance (t/C %)
Baseline	Nominal	Nominal (1.73)
Stagger	5 deg bigger	Nominal (1.73)
Tip	Nominal	Huge (5.48)

Test Configurations

Three configurations have been tested (Table 1)—(1) a nominal tip clearance and a nominal stagger angle (baseline); (2) a nominal tip clearance and the stagger angle 5 deg bigger than nominal one (stagger); and (3) a huge tip clearance and a nominal stagger angle (tip). The stagger angle is the angle between the axial line and the line connecting the leading and trailing edges of the blade (Fig. 5). In Fig. 5, the blade with the solid line has the nominal stagger angle and the blade with the dotted line has the increased stagger angle. The nominal tip clearance is 1.73% of the blade chord length and the "huge" clearance is 5.48%. This value is significantly larger than the maximum tip clearances ranging from 4% to 4.3% previously investigated by Inoue et al. [13], Storer et al. [18], and Chen [6]. For each configuration, three different flow coefficients have been tested—a high flow coefficient (low loading), the design flow coefficient, and a low flow coefficient (stall point).

Results and Discussion

Compressor characteristics, or graphs of the compressor pressure coefficient ψ plotted versus the flow coefficient ϕ, have been obtained for all configurations in Fig. 6. The two coefficients are defined as

$$\psi = \frac{c_p T_1}{\frac{1}{2}U_t^2}\left[\left(\frac{\Delta p}{p_1}+1\right)^{\gamma-1/\gamma}-1\right] \tag{1}$$

$$\phi = \frac{\dot{m}}{\bar{\rho} A U_t} \tag{2}$$

where Δp is the difference between the compressor outlet static pressure and inlet total pressure. The compressor operation range narrows (i.e., stall onset at a higher flow coefficient) and the pressure coefficient drops as tip clearance is increased (from baseline to tip configuration) because the increased tip clearance increases tip leakage flow which increases blockage and instability. The stagger configuration stalls at a lower flow coefficient, and its pressure coefficient also drops. Also, the operation range and the pressure coefficient are more sensitive to the change in the stagger angle than that in tip clearance.

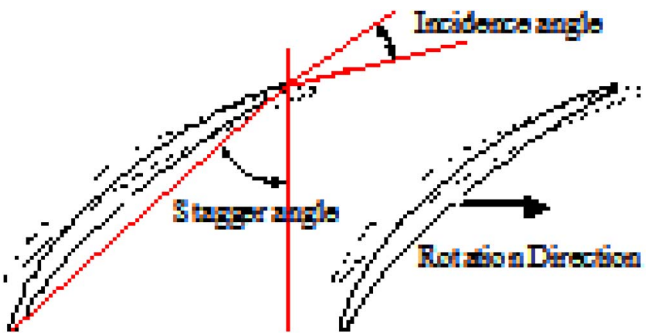

Fig. 5 Stagger angle setting

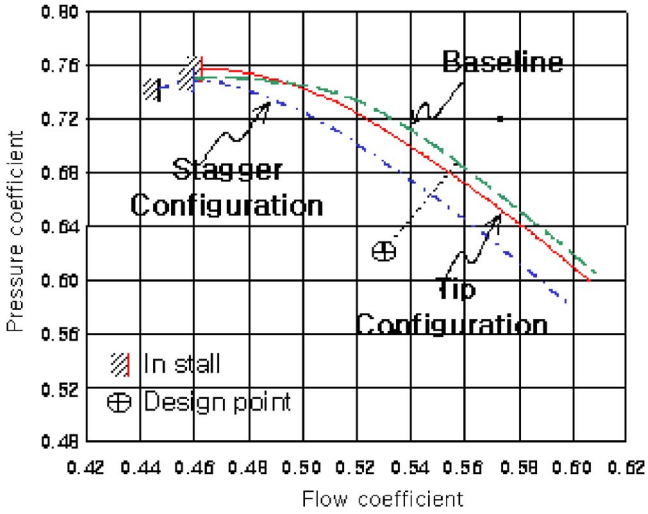

Fig. 6 Compressor characteristic curves

Static Pressure Distribution. For all test cases, phase-locked ensemble-averaged static pressure coefficient, $\bar{C}_p(t)$, distributions have been obtained as follows. Since the pressure transducers are located in two axial rows (Rows A and B in Fig. 3), the data from Row B are shifted by the time it takes for a rotor blade to move from Row A to Row B. Then, the shifted data from Row B are merged with the data from Row A. To get rid of the unsteady off-set, the averaged pressure values have been replaced with static pressure readings from static holes at the same axial location. Each pressure data set, $p_i(t)$, contains 10,000 data points, or about 1.47 rotor revolutions worth of data, and 256 such data sets have been acquired for each test condition. To remove the inlet condition effect of the third stage rotor, the phase-locked ensemble-averaged static pressure, $\bar{p}(t)$, is obtained from Eq. (1), where $\Delta p_i(t)$ is the pressure difference between $p_i(t)$ and the averaged unsteady static pressure at Location 1 in Fig. 3.

$$\bar{p}(t) = \frac{1}{256}\sum_{i=1}^{256}\Delta p_i(t) \tag{3}$$

Subsequently, $\bar{p}(t)$ values are normalized by $\frac{1}{2}\rho_1 U_t^2$, where ρ_1 is the compressor inlet density and U_t is the rotor tip velocity, to obtain the phase-locked ensemble-averaged pressure coefficient $\bar{C}_p(t)$.

$$\bar{C}_P(t) = \frac{\bar{p}(t)}{\frac{1}{2}\rho_1 U_t^2} \tag{4}$$

Figures 7–9 show contour plots of $\bar{C}_p(t)$ at three different flow coefficients for the baseline, stagger, and tip configurations, respectively. The minimum pressure near the suction side of each blade is indicated by the white region. The flow coefficient does not influence the minimum static pressure locations. Despite the decreasing flow coefficient, the minimum static pressure location still remains at the same spot. However, when the stagger angle is increased (from Figs. 7 and 8), the minimum static pressure locations near the suction surface shift downstream from the leading edge. In addition, the low pressure region covers a greater portion of the suction side chord. The increase in the stagger angle also lowers the pressure rise across the rotor. With increasing tip clearance (from Figs. 7–9), the static pressure rise across the rotor decreases as tip losses increase. Also, the minimum pressure locations near the suction surface shift downstream from the blade leading edge (baseline) to approximately 30% chord location (tip).

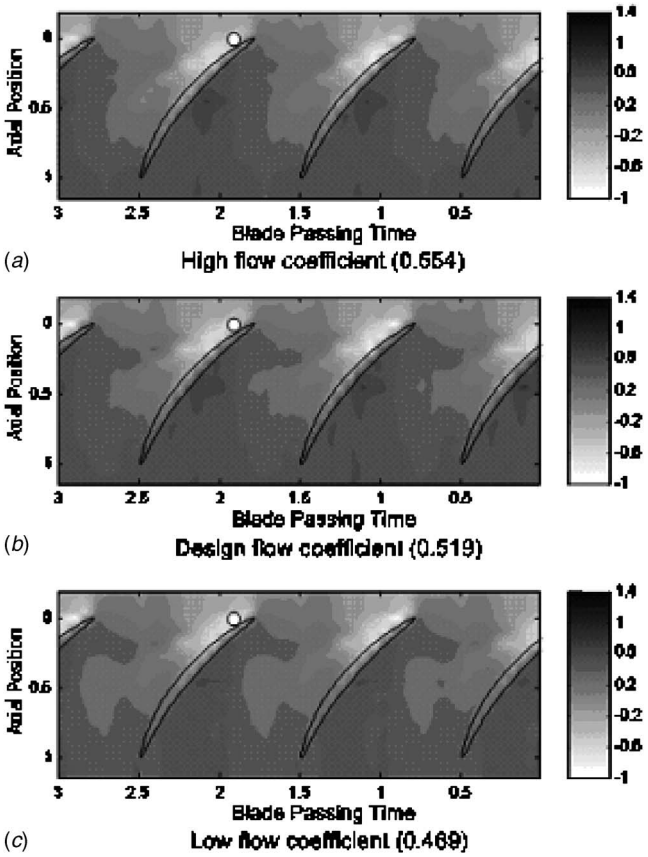

Fig. 7 $\bar{C}_p(t)$ distributions for the baseline configuration

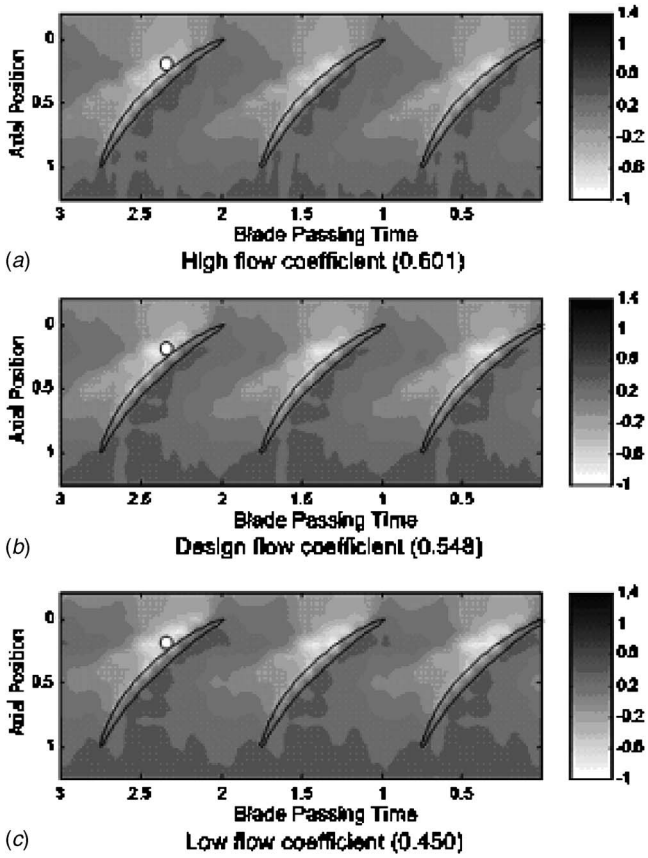

Fig. 8 $\bar{C}_p(t)$ distributions for the stagger configuration

Such trends have been analytically predicted by Chen [6] and Storer [18] and experimentally observed in compressor cascades and rotating compressor rigs by Storer [18] and Inoue et al. [13], respectively. Thus, the trends of the new data (Figs. 7–9) agree with previous findings and enhance confidence in the new data.

Random Pressure Unsteadiness. To detect the tip vortex, random pressure unsteadiness at each time is determined as

$$p_i'(t) = p_i(t) - \bar{p}(t) \tag{5}$$

Then, the absolute value of these deviations are obtained, ensemble-averaged, and nondimensionalized by the inlet dynamic pressure, $\frac{1}{2}\rho_1 U_t^2$

$$\bar{C}_{p_{\text{dev}}}(t) = \frac{\frac{1}{256}\sum_{i=1}^{256}\sqrt{p_i'(t)^2}}{\frac{1}{2}\rho_1 U_t^2} \tag{6}$$

Thus, the nondimensional mean in pressure deviation, $\bar{C}_{p_{\text{dev}}}(t)$, indicates random pressure unsteadiness, or fluctuations due to tip vortices.

Figures 10–12 show axial $\bar{C}_{p_{\text{dev}}}(t)$ distributions plotted versus time for the baseline, stagger, and tip configurations, respectively. The discrete random pressure unsteadiness regions over the blade tip (i.e., circles) are due to the discretely located pressure sensors. From Figs. 10–12 the influence of flow coefficient on tip vortex can be examined for all configurations. In the baseline configuration (Fig. 10), as flow coefficient decreases, the tip vortex is strengthened (i.e., bigger pressure fluctuations) and the vortex moves upstream slightly. The tip vortices for the stagger configuration (Fig. 11) are weaker than their counterparts in the baseline configuration (Fig. 10) but still show qualitatively similar dependence on flow coefficient. The strengthening and upstream migration of tip vortex with decreasing flow coefficient become clearer in the tip configuration (Fig. 12). Such trends are qualitatively consistent with Chen [6] and Hoying [7] predictions and the Inoue [14] experimental results. According to Chen [6], the tip vortex moves farther away from the suction surface as flow coefficient decreases because the convection time and the shed vortex sheet strength both increase. Hoying [7] also predicts that the tip vortex trajectory migrates upstream with decreasing flow coefficient due to the image vortex of the tip vortex in the casing. As flow coefficient decreases, the blade loading increases and consequently the tip leakage mass fraction increases. Thus, the tip vortex is strengthened and the induced-velocity also increases. Consequently, a new equilibrium point between the main flow velocity and the induced velocity is reached closer to the leading edge. Hoying [7] goes further and predicts that the tip vortex pops out upstream of the blade leading edge at stall inception. However, the experimental data shown in the Figs. 10(*c*) and 11(*c*) indicate that tip vortices remain downstream of the leading edge, even at stall, and, thus, disprove the last prediction. The experimental results by Jang et al. [19] also show the migration of tip vortex by decreasing flow coefficient but still in the passage.

In a linear cascade, Storer [18] has shown that the minimum pressure exists on the suction side where the compressor tip vortex begins due to the increased velocity. In the current investigation, with increasing tip clearance, the position of the minimum static pressure on the blade suction surface moves downstream. Thus, it can be inferred that the leakage jet flow forms farther downstream, and, similar trends have been observed by Inoue [13]. With nominal tip clearance (Fig. 10), the tip vortex begins at the leading edge where the minimum static pressure (white region), is located on the suction side of the blade (Fig. 7). When

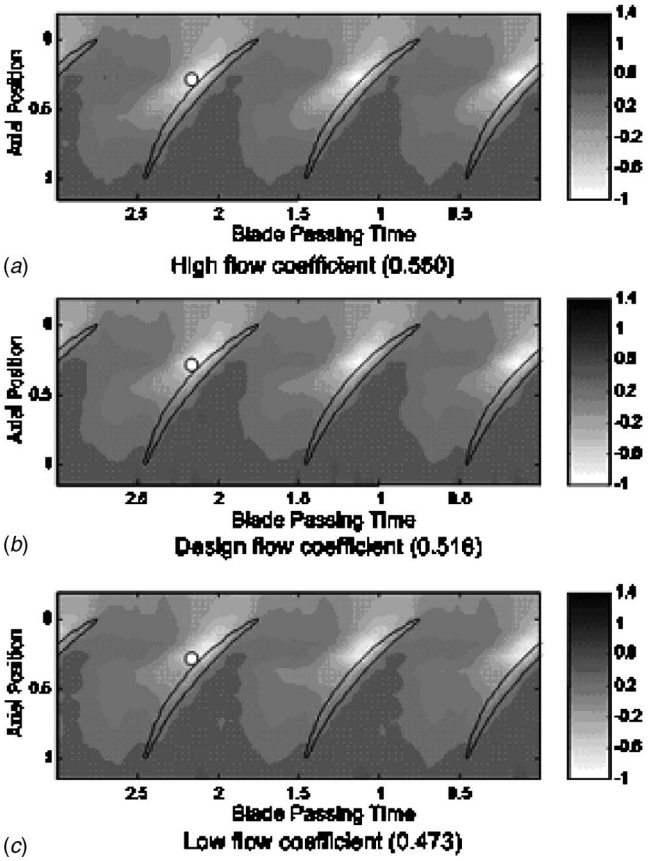

Fig. 9 $\bar{C}_p(t)$ distributions for the tip configuration

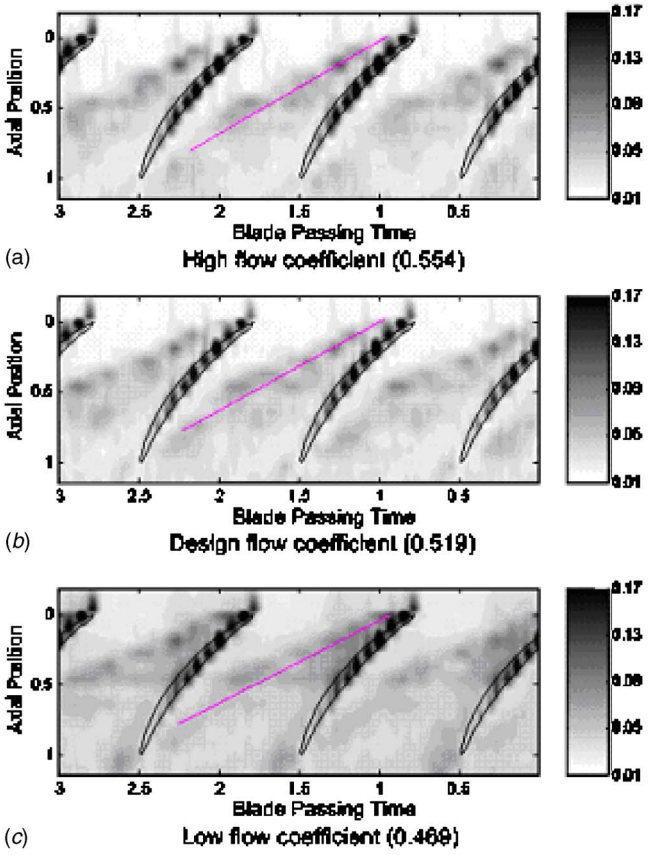

Fig. 10 $\bar{C}_{p_{\mathrm{dev}}}$ distributions for the baseline configuration

the tip gap is enlarged (Fig. 12), the starting location of the tip vortex moves downstream from the rotor leading edge, as does the minimum static pressure location (Fig. 9).

In the stagger configuration, the origins of the tip vortices still coincide with the loci of the minimum static pressure (Figs. 8 and 11). However, as the stagger angle is increased (from Figs. 10 and 11), the magnitudes of pressure random unsteadiness decrease visibly, signifying a reduction in tip vortex strength. The reduced blade loading due to the increased stagger angle likely decreases the tip leakage mass fraction, weakening the tip vortex. Also, the fraction of passage area affected by pressure fluctuations has been significantly reduced in Fig. 11 (relative to Figs. 10 and 12). Therefore, the blockage due to tip vortex can be assumed to have been reduced as well. Based on their numerical analysis, Khalid et al. [2] predict reductions in tip leakage mass flux, tip leakage flow angle relative to the blade, and blockage with increasing stagger angle. To the author's best knowledge, the new experimental results in Fig. 12 qualitatively validate their predictions for the first time. Furthermore, the vortex trajectory remains linear but the angle between the vortex trajectory line and the blade chordline is smaller in Fig. 11 than in Fig. 10. Thus, the tangential extent of the area affected by tip vortex has also been reduced.

At all flow coefficients, as tip gap is increased, the magnitudes of $\bar{p}_{\mathrm{dev}}(t)$ increase, indicating strengthened tip vortices (from Figs. 10 and 12). These results agree with Chen [6] and Storer [18] predictions and Inoue [13] measurement. Furthermore, as tip clearance increases, vortex trajectory moves upstream. For example, in Fig. 11(*b*), the tip vortex hits the adjacent blade near its trailing edge. In Fig. 13(*b*), the tip vortex moves upstream and hits the adjacent blade at near midchord location. These results are consistent with the experimental findings of Inoue [13] but inconsistent with the predictions of Martinez-Sanchez [5] and Chen [6]. Therefore, further modeling is needed in this regard.

The tip vortex trajectory is linear in the baseline (Fig. 10), but nonlinear (i.e., has a kink) in the tip configuration (Fig. 12). This finding is also new. Inoue [13] and Storer [18] do not find kinks in their in-passage vortex trajectory, probably because their clearances are below the "critical" value. Chen [6] predicts a kink in vortex trajectory, but at the blade trailing edge. However, in this study, the kink appears inside the passage and, therefore, is fundamentally different from that predicted by Chen [6]. Furukawa et al. [8] predict and Liu et al. [20] visualize tip vortex breakdown and kinked trajectory in axial compressors. However, they find vortex breakdown only on the positively sloped parts of the compressor characteristic, not on the negatively sloped part examined in this study. Therefore, a more likely explanation is the increased tip leakage flow rate. Unlike the baseline and stagger configurations (Figs. 10 and 11), the blade tip region pressure for the tip configuration (Fig. 12) shows high random unsteadiness (little black circle shape) only near the leading edge. For the baseline and stagger configurations, the tip leakage flow seems to pass through the tip clearance evenly between the leading and trailing edges. However, the tip leakage flow for the tip configuration in Fig. 13 appears to pass through mainly near the trailing edge. The increased tip leakage flow at chordwise locations toward the trailing edge could strengthen and deflect the tip vortex toward the adjacent blade, resulting in a kink (Fig. 13).

The tip vortex trajectory angle is plotted versus flow coefficient for all three configurations in Fig. 14. The tip vortex trajectory angle is calculated by the least-square fitting of a line through the loci of the maximum pressure random unsteadiness, $\bar{C}_{p_{\mathrm{dev}}}(t)$, at each chordwise location in the control volume shown in Figs. 3(*a*)–3(*d*). Axially, the data from pressure transducers from Positions 3 to 12 in Fig. 3 are considered. Tangentially, the data between the time lines (Figs. 3(*a*) and 3(*b*)) (0.12 blade passing period after the suction surface) and Figs. 3(*c*) and 3(*d*) (0.12

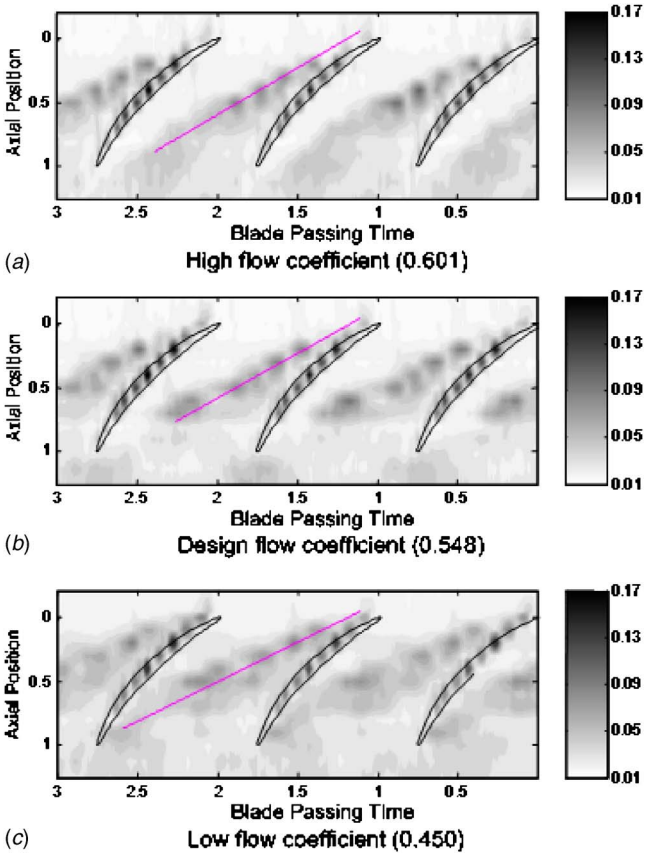

Fig. 11 $\bar{C}_{p_{\text{dev}}}$ distributions for the stagger configuration

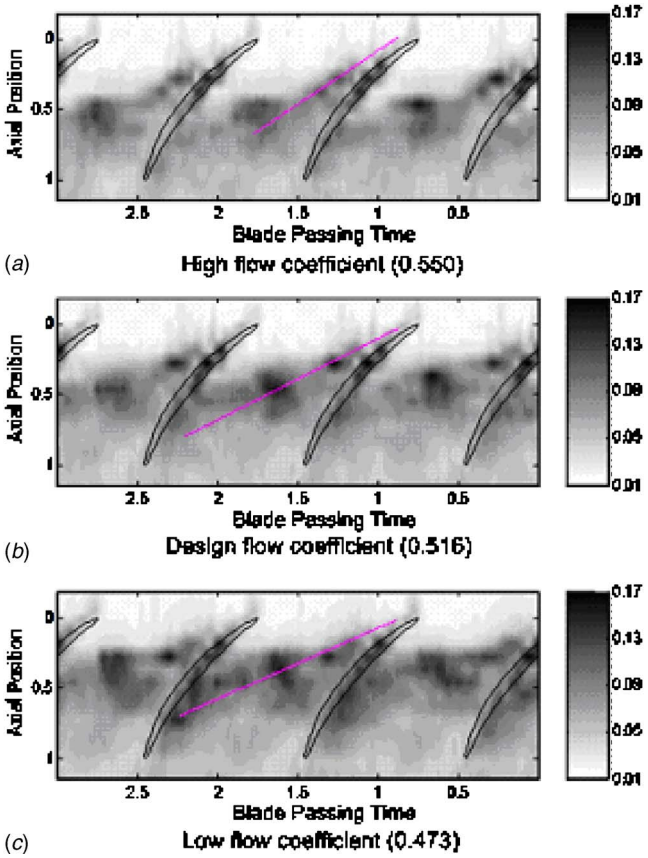

Fig. 12 $\bar{C}_{p_{\text{dev}}}$ distributions for the tip configuration

blade passing period before the pressure surface) are considered. The angle is defined to be positive clockwise from the axial direction pointing downstream; thus, a larger angle means that the tip vortex trajectory moves upstream. In all configurations, the vortex does migrate upstream as the flow coefficient decreases, but this sensitivity is more pronounced in the tip configuration. As stagger angle is increased, the vortex trajectory angle decreases but still exhibits a similar dependence on the flow coefficient.

Figure 15 shows the random pressure unsteadiness magnitude plotted versus flow coefficient for all configurations. The magnitude of the random pressure unsteadiness is defined as

$$\bar{\omega} = \frac{1}{10}\sum_{j=3}^{12}\left(\frac{1}{m}\sum_{i=1}^{m}\bar{C}_{p_{\text{dev}\,j}}(t_i)\right) \tag{7}$$

where $\bar{p}_{\text{dev}_j}(t_j)$ is the random pressure unsteadiness (Eq. (4)) from pressure transducers at locations 3–12 (Fig. 3). First, the pressure random unsteadiness, $\bar{C}_{p_{\text{dev}}}(t)$, values are time-averaged for the control volume at each position, and, these time-averaged values are averaged in the axial direction through 10 pressure transducers. The random pressure unsteadiness magnitude increases as tip clearance increases and decreases as stagger angle increases. In all configurations, the random pressure unsteadiness magnitude increases as flow coefficient decreases. Increased random pressure unsteadiness can indicate tip vortex strength increase.

Conclusions

The following conclusions can be drawn from this experimental study.

First, the study has reconfirmed the following:

(1) As predicted by Chen [6] and Hoying [7] and experimentally verified by Inoue et al. [13] and Jang et al. [19], the tip vortex is strengthened and moves upstream as flow coefficient decreases.
(2) Contrary to Hoying's [7] prediction, the tip vortex does not move upstream of the leading edge even at stall.
(3) Unlike the predictions of Martinez-Sanchez [5] and Chen [6], tip vortex trajectory moves upstream with increased tip clearance, confirming the experimental findings of Inoue et al. [13].
(4) As found by Storer [18] and Inoue [13], the tip vortex begins at the minimum static pressure site on the suction side near the tip region.

Second, the new findings of this experimental study are as follows:

(5) The flow coefficient does not influence the minimum static pressure locations on the blade.
(6) With increased stagger angle, the tip vortex is weakened and moves downstream, as predicted by Khalid et al. [2].
(7) The effects of "very large" tip clearance on tip vortex have been experimentally investigated, and there exists

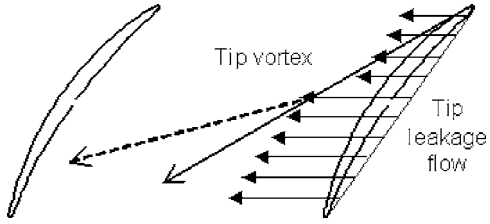

Fig. 13 Tip vortex trajectory kink

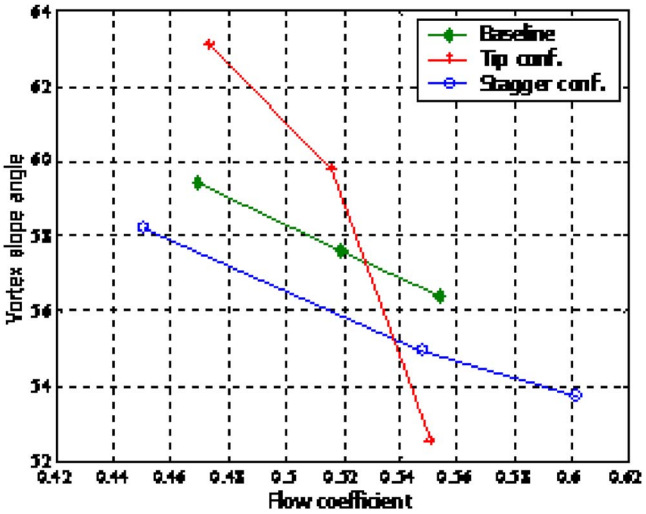

Fig. 14 Vortex trajectory angle versus flow coefficient for all configurations

a "critical" tip clearance which determines the type (linear versus nonlinear) and sensitivity (to flow coefficient) of the vortex trajectory.

(8) The tip vortex trajectory for the huge tip clearance configuration has a kink because of increased tip leakage mass flow rate between the mid chord and trailing edge of the blade. This increased tip leakage flow pushes the tip vortex toward the adjacent blade.

Acknowledgment

This research has been supported by the Micro Thermal Systems Center of KOSEF and by GE Transportation, Aircraft Engines. Special thanks are given to the technical staff at Aero Technology Laboratory (ATL) in GE for helping with the experiment.

Nomenclature

A = compressor annulus area
c_P = specific heat
C_p = pressure coefficient
$\dot{m}$ = flow rate
N = number of data sets or traces
P = pressure
ΔP = pressure difference
t = time
T_1 = compressor inlet temperature
U = rotor blade speed
U_t = rotor tip velocity
ϕ = flow coefficient
$\bar{\rho}$ = average density
$\bar{\omega}$ = tip vortex strength
ψ = compressor pressure coefficient

Superscripts

- = ensemble average
$'$ = perturbation component

Subscripts

dev = absolute deviation average
t = rotor tip
1 = compressor inlet

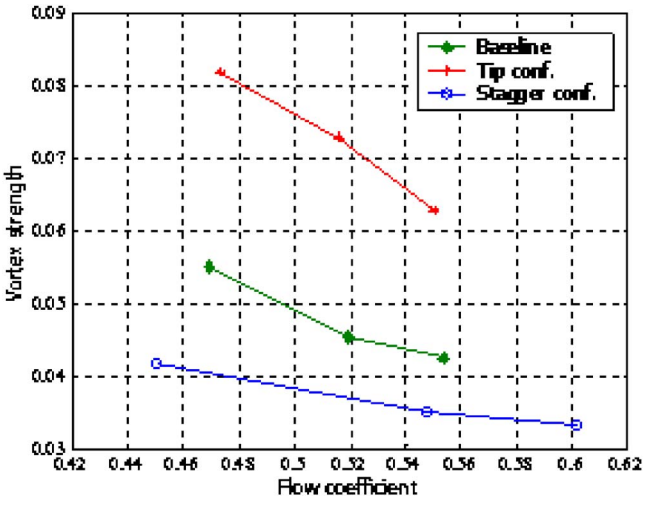

Fig. 15 Pressure random unsteadiness versus flow coefficient for all configurations

References

[1] Rains, D. A., 1954, "Tip Clearance Flow in Axial Flow Compressors and Pumps," Hydrodynamics and Mechanical Engineering Laboratories Report, No. 5.
[2] Khalid, S. A., Khalsa, A. S., Waitz, I. A., Tan, C. S., Greitzer, E. M., Cumpsty, N. A., Adamczyk, J. J., and Marble, F. E., 1999, "Endwall Blockage in Axial Compressors," ASME J. Turbomach., **121**(3), pp. 499–509.
[3] Storer, J. A., and Cumpsty, N. A., 1994, "An Approximate Analysis and Prediction Method for Tip Clearance Loss in Axial Compressors," ASME J. Turbomach., **116**(4), pp. 648–656.
[4] Lakshminarayana, B., and Pandya, A., 1984, "Tip Clearance Flow in a Compressor Rotor Passage at Design and Off-Design Conditions," ASME J. Eng. Gas Turbines Power, **106**(3), pp. 570–577.
[5] Martinez-Sanchez, M., and Gauthier, R. P., 1990, "Blade Scale Effects of Tip Leakage," Gas Turbine Laboratory Report #202, M.I.T.
[6] Chen, G. T., Greitzer, E. M., Tan, C. S., and Marble, F. E., 1991, "Similarity Analysis of Compressor Tip Clearance Flow Structure," ASME J. Turbomach., **113**(2), pp. 260–269.
[7] Hoying, D. A., Tan, C. S., Vo, Huu D., and Greitzer, E. M., 1999, "Role of Blade Passage Flow Structures in Axial Compressor Rotating Stall Inception," ASME J. Turbomach., **121**(4), pp. 735–742.
[8] Furukawa, M., Inoue, M., Saiki, K., and Yamada, K., 1999, "The Role of Tip Leakage Vortex Breakdown in Compressor Rotor Aerodynamics," ASME J. Turbomach., **121**(3), pp. 469–480.
[9] Hunter, I. H., and Cumpsty, N. A., 1982, "Casing Wall Boundary Layer Development Through an Isolated Compressor Rotor," ASME J. Eng. Power, **104**(4), pp. 805–818.
[10] Inoue, M., and Kuroumaru, M., 1984, "Three-Dimensional Structure and Decay of Vortices Behind an Axial Flow Compressor Rotor," ASME J. Eng. Gas Turbines Power, **106**(3), pp. 561–569.
[11] Wagner, J. H., Dring, R. P., and Joslyn, H. D., 1985, "Inlet Boundary Layer Effects in an Axial Compressor Rotor: Part 1-Blade to Blade Effects," ASME J. Eng. Gas Turbines Power, **107**(2), pp. 374–386.
[12] Inoue, M., Kuroumaru, M., and Fukuhara, M., 1986, "Behavior of Tip Leakage Flow Behind an Axial Compressor Rotor," ASME J. Eng. Gas Turbines Power, **108**(1), pp. 7–14.
[13] Inoue, M., and Kuroumaru, M., 1989, "Structure of Tip Clearance Flow in an Isolated Axial Compressor Rotor," ASME J. Turbomach., **111**(3), pp. 250–256.
[14] Inoue, M., Kuroumaru, M., Iwamoto, T., and Ando, Y., 1991, "Detection of a Rotating Stall Precursor in Isolated Axial Flow Compressor Rotors," ASME J. Turbomach., **113**(2), pp. 281–289.
[15] Marz, J., Gui, X., and Neise, W., 1999, "On the structure of Rotating Instabilities in Axial Flow Machines," Paper AIAA 99-IS-282 presented at the 14th ISABE, Florence, Italy.
[16] Mailach, R., Lehmann, I., and Vogeler, K., 2000, "Rotating Instabilities in an Axial Compressor Originating From the Fluctuating Blade Tip Vortex," 2000-GT-506.
[17] Goto, A., 1992, "Three-Dimensional Flow and Mixing in an Axial Flow Compressor With Different Rotor Tip Clearances," ASME J. Turbomach., **114**(3), pp. 675–685.
[18] Storer, J. A., and Cumpsty, N. A., 1991, "Tip Leakage Flow in Axial Compressors," ASME J. Turbomach., **113**(2), pp. 252–259.
[19] Jang, C.-M., Sato, D., and Fukano, T., 2005, "Experimental Analysis on Tip Leakage and Wake Flow in an Axial Flow Fan According to Flow Rates," ASME J. Fluids Eng., **127**(2), pp. 322–329.
[20] Liu, B., Yu, X., Wang, H., Liu, H., Jiang, H., and Chen, M., 2004, "Evolution of the Tip Leakage Vortex in an Axial Compressor Rotor," 2004-GT-53703.
[21] Wisler, D. C., 1985, "Loss Reduction in Axial-Flow Compressors Through Low-Speed Model Testing," ASME J. Eng. Gas Turbines Power, **107**(2), pp. 354–363.

Optimization of an Innovative Rotary Shaft Pump (RSP)

Jacob C. Allen
e-mail: allen.jake@gmail.com

Phillip M. Ligrani
e-mail: phil.ligrani@eng.ox.ac.uk

Donald Schultz Professor of Turbomachinery,
Department of Engineering Science,
Parks Road,
University of Oxford,
Oxford OX1 3PJ,
United Kingdom

This paper describes the optimization of rotary shaft pump performance, which is accomplished by comparing the performance of four different centrifugal rotary pump configurations: hooked blades pump, backward-curved blades ID=12.7 mm *pump, contoured base pump, and backward-curved blades* ID=19.1 mm *pump. Each of these devices utilizes a unique and simple impeller design where the blades are directly integrated into a shaft with an outer diameter of* 25.4 mm. *Presented for each pump are performance data including volumetric flow rate, pump head, and hydraulic efficiency. When pumping water, the most optimal arrangement with the hooked impeller blades produces a maximum flow rate of* 3.22 L/min *and a pump head as high as* 0.97 m.
[DOI: 10.1115/1.2353273]

Introduction

From the invention of the Noria waterwheel, used to raise irrigation water from rivers to farmlands at higher elevations, pumps have been continuously employed as means of transporting fluid. Furthermore, pumps have evolved to meet many specific requirements and into highly diverse classifications. Typically, they are considered in two main categories: dynamic and displacement. Displacement pumps *periodically* add energy to the fluid and are most commonly represented as reciprocating or rotary lobe types. On the other hand, dynamic pumps *continuously* add energy to the fluid. Centrifugal pumps are the most prevalent example of the dynamic type, operating with fluid entering axially and exiting radially.

Small reciprocating diaphragm or piston positive displacement pumps are used for relatively low-flow applications that require high pressure rises. They are useful for drug dosing purposes where continuous flow is not required. Some fluid control systems also use them as metering pumps to measure and control flow rates. Centrifugal pumps have been used for the last 150 years to transport fluid for many different industrial applications. As a result of this long history, their performance has been thoroughly characterized and many configurations have been developed. This has also lead to significant design improvements, giving them advantages over other kinds of pumps. Many industries, ranging from chemical processing plants to swimming pool filtration companies, use centrifugal pumps because of their low cost and high efficiency.

More recently, centrifugal pumps, such as the one developed by Yuhki et al. [1], have also found success as blood pumps for ventricular assist devices (VADs). Their small size, continuous flow rate, low power requirements, and minimal moving parts make them ideal for VADs and give them advantages over positive displacement pumps. Thus, in some cases, VADs use open impellers with curved blades attached to a hub that is connected to the end of a rotating shaft. For example, Klatte [2] developed and characterized several pumps with this configuration and obtained maximum non-dimensional head coefficient and flow coefficient of 0.61 and 0.12, respectively. Shen et al. [3], and Nishimura et al. [4] developed bearingless pumps where the impeller is not connected to a rotating shaft but rotates independently in a housing using a magnetic field. Thus, hydraulic efficiency is improved because the housing is completely sealed and fluid can only leave through the outlet. Nishimura et al.'s [4] pump produced a maximum flow rate of 5 L/min and a maximum pressure rise of 100 mmHg with a 50 mm dia impeller.

One disadvantage of these pumps lies in the design of the open impeller, where fluid can leak between the top edge of the blades and the stationary housing. As a result, the pump's hydraulic efficiency decreases. This form of leakage can be especially important to smaller pumps, such as those used as VADs, where the gap between the blades and the housing is relatively large compared to the overall height of the blades. The large gap employed with open impeller designs is also disadvantageous because the resulting locally augmented shear stresses can damage blood cells which pass through this part of the pump. To minimize this problem, eliminate leakage, and increase pump efficiency, the impeller design developed by Blanchard et al. [5] is used in the present investigation. Instead of having blades extending from the top of the impeller shaft, as with open impeller configurations, the design integrates the blades directly into the impeller shaft.

The current efforts are unique because an impeller design of this type has not been implemented into VADs, electronics cooling, or other fluid-flow applications. Besides having the advantage of increased efficiency, this design is simply and economically manufactured. In the present study, four different pump types are tested and compared in an effort to further optimize design and performance of rotating shaft pumps (RSPs) [5]. Measured are flow rate and pressure rise at different impeller rotational speeds. Hydraulic efficiency is also calculated from impeller geometry and other measured quantities. Each of the four pumps have different impeller configurations that are designated: backward-curved blades (ID=19.1 mm), backward-curved blades (ID =12.7 mm), hooked blades, and contoured base.

Pump Performance Theory

A centrifugal pump performs work on a fluid by means of a rotating shaft. As the fluid approaches the shaft, blades on the end of the shaft pick up the fluid, increase its velocity, and change its direction. This action forces the fluid to flow while a casing around the blades and fluid directs the flow. The increased fluid velocity and confining characteristic of the casing create resistance against the flow causing a rise in pressure. The increased fluid pressure and flow rate can then be used to transport the fluid or do work elsewhere.

Fluid flow inside a centrifugal pump impeller is complex, unsteady, and three-dimensional, but the fundamental theory can be simply described using velocity vectors of the fluid and the rotating impeller blades, as shown in Fig. 1. These quantities are used to determine the Euler work W_E and the actual pump head H_{actual} of a rotary pump, which, along with volumetric flow rate, are

Contributed by the Fluids Engineering Division of ASME for publication in the JOURNAL OF FLUIDS ENGINEERING. Manuscript received June 13, 2005; final manuscript received March 6, 2006. Review conducted by: Joseph Katz.

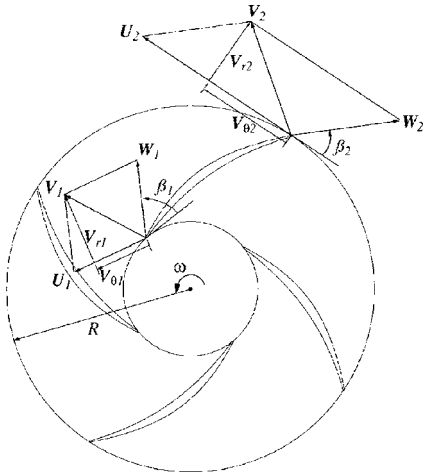

Fig. 1 Velocity diagrams at the inlet and discharge of a typical centrifugal pump impeller showing absolute fluid velocity *V*, relative fluid velocity *W*, impeller blade velocity *U*, and other velocity components

parameters determining pump performance. According to Ref. [6], the Euler work required by the pump is given in terms of flow volumetric flow rate Q, impeller and fluid velocity components, impeller rotational speed ω, and flow density ρ.

$$W_E = \frac{\rho Q}{\omega}(U_2 V_{\theta 2} - U_1 V_{\theta 1}) \tag{1}$$

This Euler work can also be given as dependent on Euler pump head using

$$W_E = \frac{\rho g Q}{\omega} H_E \tag{2}$$

where the Euler pump head H_E is given by

$$H_E = \frac{1}{g}(U_2 V_{\theta 2} - U_1 V_{\theta 1}) \tag{3}$$

or, alternatively,

$$H_E = \frac{1}{g}\left[U_2^2 - \frac{U_2 \cot(\beta_2) Q}{2\pi R b} - U_1 V_{\theta 1} \right] \tag{4}$$

In Eq. (4), the term $V_{\theta 1}$ represents the tangential component of the fluid velocity, or swirl, as the flow enters the impeller. In some situations, $V_{\theta 1}$ is approximated to be equal to the tangential velocity of the impeller U_1 and a correction factor σ_1 is applied to the swirl term. However, $V_{\theta 1}$ can be equal to zero in cases where the swirl is negligible. Therefore, the present study includes analysis of both swirl and nonswirl situations for the flow entering the impeller.

Equation (4) shows that the Euler pump head is linearly dependent on flow rate and decreases as volumetric flow rate increases, provided the impeller geometry is constant and a backward-curved blade design ($\beta_2 < 90$ deg) is used. To more accurately predict the pump head, additional factors related to impeller geometry are used to alter the magnitude of Euler pump head H_E given by Eq. (4). These include factors that quantify flow blockage from the finite thicknesses of the blades and flow deviation from the outlet blade angle. These effects are quantified using, respectively, blade blockage factor, and slip factor and are given by

$$B_f = \frac{A_{\text{impeller}} - A_{\text{blades}}}{A_{\text{impeller}}} \tag{5}$$

and

$$\sigma = 1 - \frac{V_{\theta s}}{U_2} \tag{6}$$

The blade blockage factor B_f is a ratio of the flow passage area to the total cross-sectional area of the impeller [7]. Slip factor σ is the ratio of the actual tangential velocity of the discharged fluid to the tangential velocity of the impeller [8]. This slip factor can be approximated using the empirical correlation developed by Wiesner [9], which is given by

$$\sigma \approx 1 - \frac{\sqrt{\sin \beta_2}}{n^{0.7}} \tag{7}$$

The actual pump head is subsequently obtained after slip factor and blade blockage factor are applied to Eq. (4) for Euler pump head. With zero inlet swirl, the actual pump head is then of the form

$$H_{\text{actual}} = \frac{1}{g}\left[\sigma U_2^2 - \frac{U_2 \cot(\beta_2) Q}{2\pi R b B_f} \right] \tag{8}$$

Another parameter used to characterize pump performance is hydraulic efficiency, which quantifies losses due to fluid friction, volute losses, and impeller losses. From Gorla and Khan [10], this parameter is given as the ratio of the measured pump head H_{pump} to actual pump head H_{actual} and is then defined using

$$\eta_h = \frac{H_{\text{pump}}}{H_{\text{actual}}} \tag{9}$$

Actual pump head, measured pump head, and hydraulic efficiency are then useful for comparison of a particular centrifugal pump's performance to the operation of other pumps.

Pump Configuration and Geometry

In a typical centrifugal rotary pump, the impeller blades rotate inside a stationary housing. Consequently, a gap must be left between the top of the blades and the housing so the impeller is able to rotate. When the pump is operating, fluid can leak between the top of the blades and the housing, which causes the hydraulic efficiency to decrease. The four pumps developed as part of the present study use a novel impeller design that eliminates the possibility of fluid leakage between the top of the blades and the housing. This design is based on a micromillimeter-scale pump initially developed by Blanchard et al. [5] with a 2.381 mm dia impeller and 0.38 mm tall blades. As shown in Fig. 2, this pump arrangement is produced by drilling a hole in one end of a shaft. Slots are then cut in the side of the shaft at the bottom of the drilled hole. The material left between the slots acts as the impeller blades, as shown in Fig. 2. Additional specific design details of each impeller configuration are shown in Fig. 3. With blades directly integrated into the impeller shaft, there is no gap between the housing above the blades and the blades where fluid can leak. This design also improves overall pump efficiency by inducing some prerotation of the fluid before it contacts the blades and, therefore, by reducing the sudden acceleration normally experienced by fluid as it enters the impeller blades in many other centrifugal pumps. The impellers are made from 25.4 mm dia polycarbonate rod stock. A lathe is used to drill the hole down the center of the shaft and to chamfer the transition from the inner diameter to the outer diameter. A milling machine and an indexing tool are used to cut the slots in the side of the impeller.

The impeller is mounted in the pump housing with bearings located on either side of a volute. The volute, shown in Fig. 4, is a 3.81 mm wide gap between the two surfaces of the pump housing that directs the flow from the impeller into the exit plenum. This pump uses an open volute design that is characterized by a large channel from the exit of the impeller to the plenum [5]. This arrangement reduces viscous losses and flow-turning losses that disturb fluid motion compared to pumps of similar size having spiral shaped volutes.

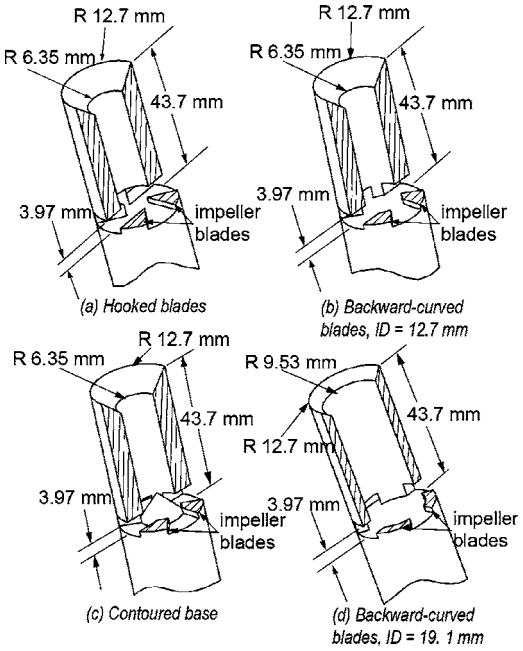

Fig. 2 Cutaway view of each impeller design tested, showing the inlet, impeller blades, and outlet holes. Cutaway pieces are cross-hatched.

The four different impeller designs used in this study are shown in Figs. 2 and 3. Each impeller has four equally spaced backward-curved blades, with $\beta_2=70$ deg and $h=3.97$ mm. β_2 is the angle the trailing edge of the blade makes with a line tangent to the outer diameter of the impeller shown in Figs. 1 and 3(*c*). The height of the blades h is the same as the height of the slots cut to define the blades, as mentioned earlier, and as shown in Fig. 2. The first design is a scaled replica of the Blanchard et al. [5] arrangement called the *backward-curved blades* ($ID=12.7$ mm) impeller. It is shown in Figs. 2(*b*) and 3(*b*). This is a basic impeller design. The second arrangement, called the *hooked blades* design, contains blades that extend into the inner diameter of the impeller, as shown in Figs. 2(*a*) and 3(*a*). This is done to induce fluid motion into the impeller and to accelerate the flow out into the volute. Another design, called the *contoured base* impeller, has a small cone at the base of the inlet passage, just upstream of the impeller blades, to direct the flow toward the impeller inlet, as shown in Figs. 2(*c*) and 3(*c*). The cone used for the contoured

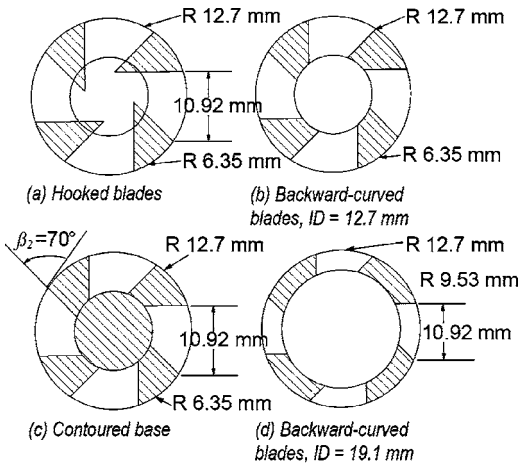

Fig. 3 Impeller design cross sections through the centers of the impeller blades

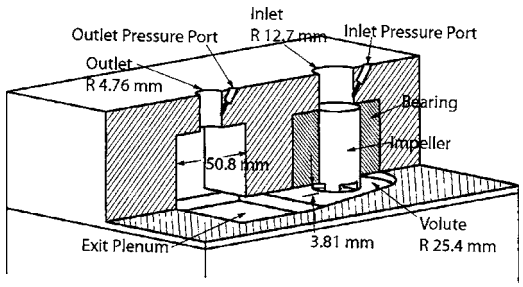

Fig. 4 Cutaway view of the pump assembly including the impeller, bearings, casing, volute, inlet, and outlet

base impeller is made on a lathe, inserted into the hole in the center of the shaft, and glued in place. This is intended to minimize flow-turning losses produced after the flows impinge directly onto the flat, bottom surface of the inlet passage. The fourth design, shown in Figs. 2(*d*) and 3(*d*), has a 19.1 mm i.d. and is called the *backward-curved blades* ($ID=19.1$ mm) design. The larger inner diameter of the impeller is intended to increase the incoming volumetric flow rate.

The pump housing is made from two pieces of polycarbonate. These are manufactured using a milling machine. When the top and bottom housing parts are connected, they define the volute and exit plenum, as shown in Fig. 4. Teflon® bushings made on a lathe are glued into 50.8 mm dia holes in the top and bottom casings. Teflon is used because of its low coefficient of friction with other plastics like polycarbonate. Leakage along the impeller shaft is eliminated by reducing the diameter of the shaft with an abrupt step, as it is adjacent to surrounding bearing material, as shown in Fig. 5. The bottom bearing material is thus bored into the same shape to match the two shaft outer diameters. This arrangement gives some larger frictional resistance to shaft rotation compared to some conventional designs. However, the present approach is advantageous because it gives minimal leakage and requires simple manufacturing. Analysis of bearing losses and the resulting reductions in efficiency are postponed to a future investigation because the present paper only considers issues directly related to hydrodynamic performance.

Experimental Apparatus

A schematic diagram of the experimental apparatus, shown in Fig. 6, consists of a reservoir of water, the pump/motor combina-

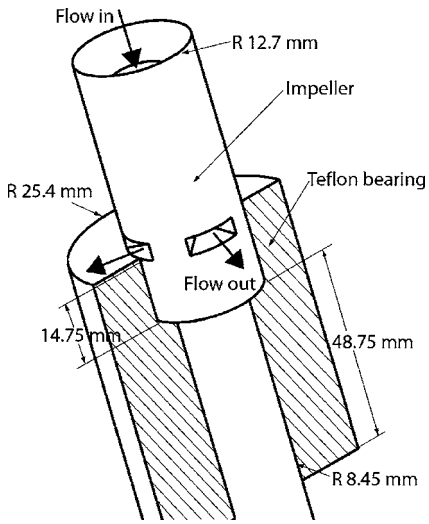

Fig. 5 Impeller and cross section of bottom bearing showing the arrangement employed to eliminate leakage

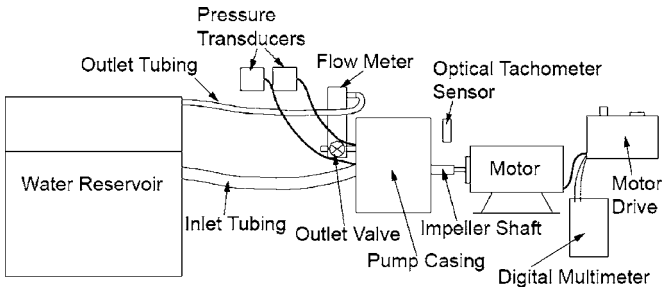

Fig. 6 Schematic diagram of the pump setup and data collection instrumentation

Table 1 Uncertainty values of experimental results showing nominal values at different impeller speeds.

	Nominal uncertainty values		
Variable	1500 rpm	2500 rpm	3300 rpm
H_{actual}, m	0.252±0.020	0.691±0.01	1.076±0.02
H_{pump}, m	0.15±0.035	0.439±0.02	0.78±0.02
η_h, %	59.3±16	63.5±3.8	72.5±2.3
Q, L/m	0.88±0.04	2.27±0.07	3.22±0.1
w, rad/s	157.1±0.01	261.8±0.01	345.6±0.02

tion, and all the instrumentation. The water level in the reservoir is set at the same level as the inlet of the pump so that the inlet gage pressure is approximately zero. The inlet tubing is connected to the reservoir to supply water and is 25.4 mm dia and 300 mm long. The 9.5 mm dia outlet tubing is the same length as the inlet tubing and feeds into the same reservoir to keep the overall water level constant. A rotameter, outlet tubing, and one pressure transducer are attached to the pump outlet. The other pressure transducer and inlet tubing are attached to the pump inlet. A 186.5 W Baldor AP7402 DC motor is used to rotate the impeller. It has a maximum speed of 3450 rpm, a maximum voltage of 90 V DC, and a maximum continuous current of 2.5 A.

The instrumentation includes two Validyne DP15-32-N-1-S-4-A pressure transducers, two Validyne CD15-A-1-A-1 carrier demodulators, a National Instruments PCI-6013 basic multifunction I/O board, and a Dell Workstation PWS 360 computer with a Pentium 4 3.20 GHz CPU, LabView 7.1 Virtual Instrument software, an Omega FL-4502-V rotameter, a Dwyer VFB-83 rotameter, a Monarch remote optical sensor (ROS-5W), a Monarch ACT-1B digital display panel, and a Keithley 128 digital multimeter. The uses of these different devices are described in the next section.

Experimental Procedures and Pump Assembly

To assemble the pump, the motor and the bottom half of the pump housing are fixed to an acrylic plate and the inner surfaces of the Teflon bearings are lubricated with silicon grease. Next, the desired impeller is inserted into the bottom half of the casing and the slots in the impeller are aligned with the volute surface. To connect the motor to the impeller, the motor shaft is inserted into a hole drilled axially in the bottom end of the impeller and a radial screw is tightened to fix them together. The top half of the housing is then attached to the bottom half with bolts positioned around the outside of the volute and the plenum. A plastic gasket made from transparency film is inserted between the two casing halves to stop fluid leakage where they join.

To assess the performance of the pump, the following quantities are measured: pressure rise, volumetric flow rate, shaft rotational speed, motor voltage, and motor current. The pump pressure rise is measured using two Validyne DP15-32-N-1-S-4-A pressure transducers with diaphragms rated at ±14 kPa. One side of each transducer is connected to 3.175 mm dia tubing, and the other side is left open to the atmosphere. This tubing is inserted into holes drilled next to the inlet and outlet, as shown in Fig. 4. The transducers produce outputs that are conditioned and amplified by two Validyne CD15-A-1-A-1 carrier demodulators to ±10 V DC. These signals are then proportional to the applied pressure and are acquired using a National Instruments PCI-6013 basic multifunction I/O board and a Dell Workstation PWS 360 computer with a Pentium 4 3.20 GHz CPU. The data voltage values are sampled at 500 Hz and continuously displayed with LabView 7.1 Virtual Instrument software. After properly conditioning the voltage signals, the transducers are calibrated to the maximum and minimum pressure limits of the diaphragms. For the maximum (14 kPa), the pressure resulting from a 139.7 cm tall column of water is applied to each transducer and the span is adjusted so that this pressure corresponds to a +10 V signal. The LabView software is programmed to take the difference of the two pressure signals to determine the total measured pressure head H_{pump} of the pump. The volumetric flow rate from the outlet of the pump is measured with an Omega FL-4502-V rotameter, with a maximum capacity of 6.31 L/min and a minimum flow rate of 0.631 L/min. For even lower flow rates, a Dwyer VFB-83 rotameter, which measures from 0.0631 to 0.631 L/min, is used. A valve on each meter allows the flow to be throttled to a specific flow rate.

The rotational speed of the impeller is measured with Monarch remote optical sensor (ROS–5W), which sends a signal to a Monarch ACT-1B digital display panel. A small square of reflective tape is adhered to part of the impeller that extends outside the casing, and a red LED light source is aimed at the tape. As the impeller turns, the sensor counts the revolutions per minute, which are read from the digital display unit. The motor voltage and current are measured with a Keithley 128 digital multimeter that is directly connected to a Baldor DC drive BC138 that controls the speed of the motor.

Before pumping, all air trapped in the volute and plenum is evacuated. The motor driving the shaft pump is then turned on and set to the desired speed. For each impeller design, pressure and flow rate data are collected at three different shaft speeds: 1500, 2500, and 3300 rpm. Data are also collected at constant shaft speed by partially closing the valve on the rotameter and throttling the water to the desired flow rate.

Uncertainty Magnitudes of Measured Quantities

The uncertainty analysis is performed using methods described by Moffat [11]. Table 1 presents uncertainty values for a 95% confidence level. Note that, at 1500 rpm, the pumps generate low pump head relative to the range of the pressure transducers. As a result, signal-to-noise ratios are decreased, standard deviations of samples are increased, and uncertainty magnitudes are increased. At 3300 rpm, uncertainty magnitudes are much lower because measured pressure rise magnitudes are well within the range of the pressure transducers, and signal-to-noise ratios are high.

Results and Discussion

Pressure rise and volumetric flow rate data are presented for each impeller design at three different impeller rotational speeds of 1500, 2500, and 3300 rpm. The variations of dimensional flow rate and dimensional pump head are shown in Figs. 7 and 8 as impeller speed is increased and while the outlet valve is fully open. Figure 7 illustrates that by increasing the impeller speed, the volumetric flow rate increases for all four pump configurations. Figure 8 also appears to exhibit the similar behavior except that the dependent variable is the measured pump head. According to Eqs. (4) and (8), pump head has some dependence on the square of U_2 and, hence, on the square of impeller speed. The near linear behavior of the data in Figs. 7 and 8 is probably due to the relatively small range of impeller speeds considered.

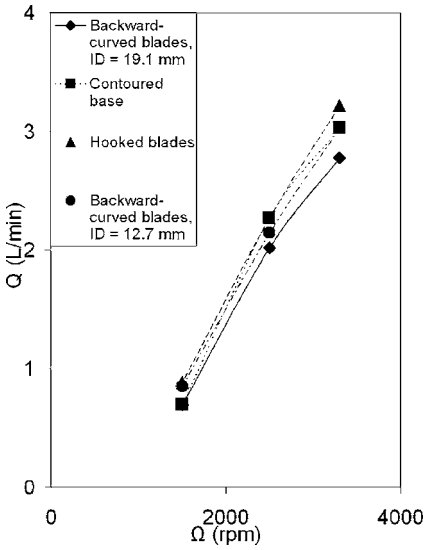

Fig. 7 Variation of flow rate with impeller speed for different impeller designs. Here, the outlet valve is completely open and, therefore, the throttling is constant.

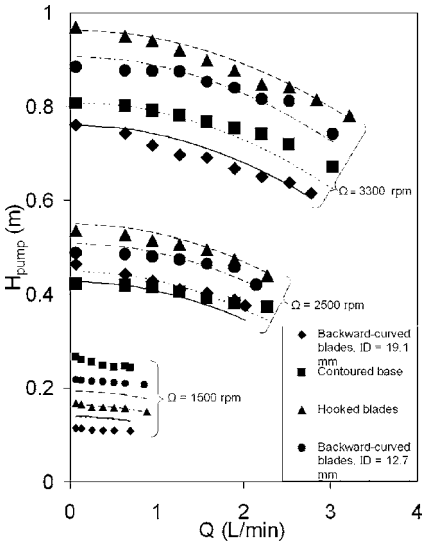

Fig. 9 Variation of pump head with flow rate for different impeller designs. The data are taken by closing a valve at the outlet of the pump for three constant impeller speeds. The curves show predicted pump head variations determined using the techniques described by Zaher [13].

Figures 7 and 8 show that the hooked blades configuration gives the highest flow rate and pump head of 3.22 L/min and 0.78 m, respectively, at the highest impeller speed of 3300 rpm. This is because the longer impeller blades within the hooked blade design are able to transfer more momentum to the fluid, increasing the flow velocity. Higher velocity gradients, from the leading to trailing edges of the impeller blades, do a greater amount of work on the fluid resulting in higher pressure rises across the impeller. This phenomenon is also illustrated by the backward-curved blades (ID=19.1 mm) impeller, which has the shortest blade lengths and produces the lowest pump head.

Figure 9 displays data for each impeller design for constant impeller speeds of 3300, 2500, and 1500 rpm. In order to acquire each data point, the flow is throttled by partially closing a valve located just downstream of the pump outlet to partially and restrict the flow through the outlet. Data points located on the left side of the plot are obtained when the valve is almost entirely closed, and data on the right side are obtained when the valve is completely open. For each impeller speed, the pumps display an increase in head as the flow is throttled, a characteristic generally associated with backward-curved blades. Equations (4) and (8) verify this, by showing that, for backward-curved blades, Euler work and actual pump head both increase as the volumetric flow rate decreases. A reduction in flow rate translates to a reduction of relative velocity at the trailing edge of the impeller blades and, therefore, an increase in Euler work or momentum transfer. Figure 9 shows that the hooked blades impeller performs better than the other designs with the highest pump head for 3300 rpm and 2500 rpm rotational speeds. As mentioned, such performance is attributed to the longer blades within the hooked blades impeller. The trend exhibited by the backward-curved blades (ID=19.1 mm) agrees with other experiments since increasing the shaft inner diameter, and decreasing the extents of the impeller blades gives decreased measured pump head [12]. At 1500 rpm, the hooked blades impeller apparently no longer outperforms all of the other impeller designs. However, note that the data at this rotational speed may be affected by high uncertainty magnitudes of pressure rise and volumetric flowrate data.

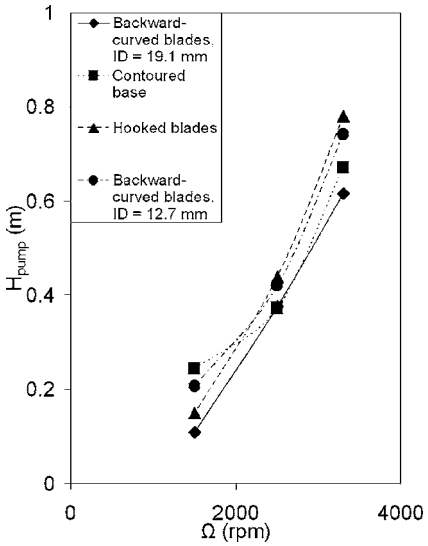

Fig. 8 Variation of pressure head with impeller speed for different impeller designs The outlet valve is completely open, and therefore, the throttling is constant.

The solid, dashed, and dotted lines in Fig. 9 show measured pump head distributions, which are predicted using the method described by Zaher [13]. With this approach, the measured pump head is determined after quantifying losses through the impeller and pump passage using velocity triangles and loss coefficients. The losses are computed with the help of three coefficients of loss, ξ_1, ξ_2, and m, as defined by Zaher [13]. For each impeller design, m is equal to 12, but ξ_1 and ξ_2 vary between the different impellers. For the backward-curved blades (ID=19.1 mm), $\xi_1=0.55$ and $\xi_2=0.03$, for the contoured base configuration, $\xi_1=0.3$ and $\xi_2=0.05$, for the hooked blades, $\xi_1=0.01$ and $\xi_2=0.01$, and for the backward-curved blades (ID=12.7 mm), $\xi_1=0.1$ and $\xi_2=0.04$. Figure 9 shows that the present measured pump head data are in fairly good agreement with Zaher's analytic procedures [13], especially for impeller rotational speeds of 2500 rpm and 3300 rpm.

Figure 10 also shows measured pump head distributions for an impeller rotational speed Ω of 3300 rpm. Included are values that are predicted analytically using Eqs. (5) and (7)–(9). Here, one value of hydraulic efficiency η_h is used for each pump configuration at an impeller speed of 3300 rpm. Values employed for the

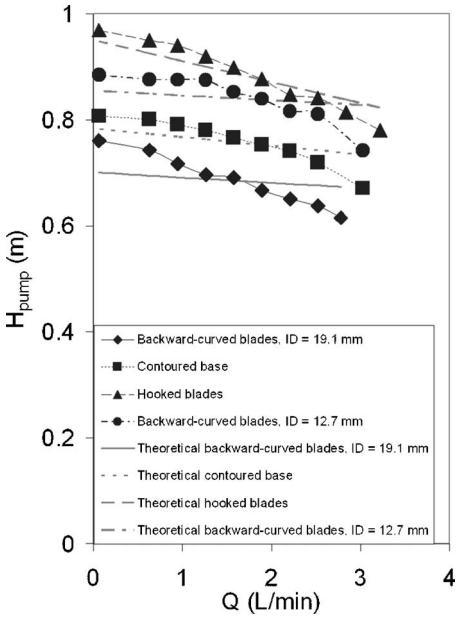

Fig. 10 Variation of pump head with flowrate for different impeller designs at impeller rotational speed of 3300 rpm. Lines give theoretical values determined using Eqs. (5) and (7)–(9).

backward-curved blades (ID=19.1 mm), contoured base, hooked blades, and backward-curved blades (ID=12.7 mm) are 0.56, 0.63, 0.77, and 0.69, respectively. Slip factor and blade blockage factor values of 0.63 and 0.66, respectively, are used for all four pump configurations, as determined using Eqs. (5) and (7). With these considerations in mind, Fig. 10 shows that the present data are in rough agreement with values predicted using Eqs. (5) and (7)–(9).

To more fully understand how pump head is affected by throttling, Fig. 11 is included. Here the x-axis gives the throttling percentage φ related to the degree that the outlet throttling valve is opened or closed. One-hundred-percent throttling means that the valve is completely closed, and 0% throttling means that the valve

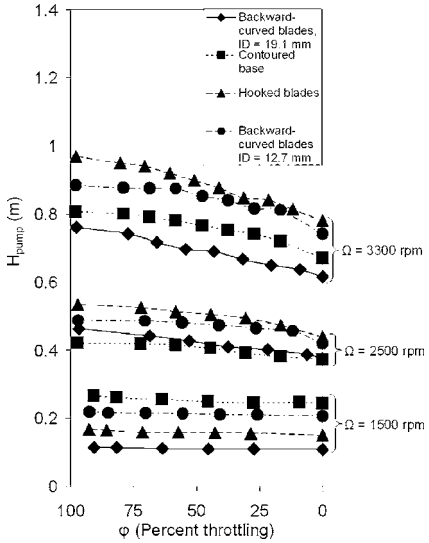

Fig. 11 Variation of pump head as the outlet valve is closed. φ=100% throttling means that the valve is completely closed and φ=0% throttling means that the valve is open.

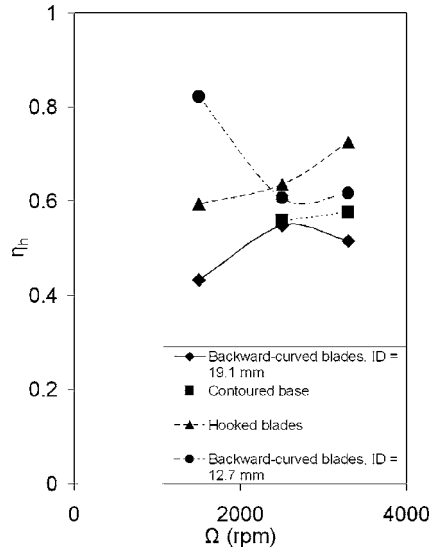

Fig. 12 Hydraulic efficiency as dependent upon the impeller speed. The outlet valve is completely open and therefore the throttling is constant.

is fully open. The trends suggest that pump head is only slightly affected by throttling the flow, particularly at low impeller speeds [6].

The variation of hydraulic efficiency as it depends on impeller speed for flow that is not throttled is shown in Fig. 12. These results are based on the data points given in Figs. 7 and 8, and thus, they are obtained with the outlet valve completely open. Recall that hydraulic efficiency is given by Eq. (9) and that it depends on H_{actual} from Eq. (8). H_{actual} then depends on the slip factor σ, which is calculated using Eq. (7) and is equal to 0.63 for all four impeller configurations. The hydraulic efficiencies for 2500 rpm and 3300 rpm in Fig. 12 are then consistent with data in Figs. 7 and 8, since the hooked blades impeller exhibits the highest values, and the backward-curved blades (ID=19.1 mm) arrangement exhibits the lowest efficiency magnitudes. Data values and variations for 1500 rpm in Fig. 12 are affected by the high uncertainty magnitudes of the data.

The data in Fig. 13 show hydraulic efficiency as it varies with flow rate when the flow is throttled for a constant impeller speed of 3300 rpm. From this plot, it is evident that the hydraulic efficiency increases in a manner that is similar to pump head when the flow is throttled. This similarity is present because pump head and hydraulic efficiency are directly related through Eq. (9). From these and other data, it is also evident that the most important physical characteristic that leads to increased hydraulic efficiency, for a particular volumetric flow rate or impeller speed, is the radial extent of the impeller blades. The contoured base, although intended to minimize flow-turning losses at the impeller inlet, does not lead to improved values of hydraulic efficiency, probably because of the added flow blockage produced by the contouring at the impeller inlet. At an impeller rotational speed of 3300 rpm, Fig. 13 shows that the hooked blades impeller has a maximum efficiency of 78% when no preswirl effects are included in the determination of the actual pump head H_{actual}. When preswirl is included in the determination of H_{actual}, this quantity decreases and hydraulic efficiency increases. Figure 13 then shows the change in hydraulic efficiency for the hooked blades impeller. The swirl term is $U_1V_{\theta 1}$, and accounts for angular momentum contained in the flow before it reaches the impeller blades. To determine this quantity, a correction factor is applied to the swirl term and $V_{\theta 1}$ is assumed to be equal to U_1. By introducing the swirl term, the actual pump work decreases to become close in value to the measured pump work.

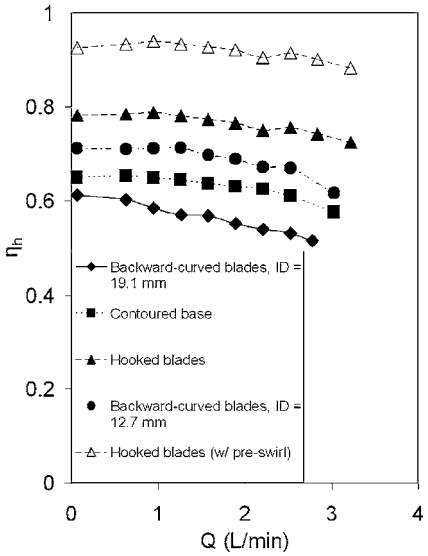

Fig. 13 Hydraulic efficiency data as dependent on flow rate. The flow is throttled at the outlet while each impeller is maintained for a constant impeller rotational speed of 3300 rpm. Also, one data set for the hooked blades impeller is shown in which swirl components are included.

Figure 14 compares a nondimensional pump head as it depends on nondimensional flow rate. These quantities are given as head coefficient and flow coefficient for each impeller design tested in this study, two millimeter-scale pumps [5], a larger centrifugal pump [8], and a blood pump [2]. This nondimensionalization is useful for evaluating the performance of pumps with different dimensions, flow rates, and pressure rises. Here, data are given at different flow rates obtained as the flow is throttled by restricting the flow at the outlet of the pumps. The impeller rotational speed is constant for each data set. The millimeter-scale pumps from Ref. [5] have dimensions that are ten times smaller than the pump used for this study, but they use the same open volute design. The miniature impellers also use an integrated blades/shaft impeller design, and are made in the same manner as the four impellers in this study. The miniature impeller with four backward-curved blades from Ref. [5], and the backward-curved blades (ID = 12.7 mm) impeller from the present study differ only in size and trailing-edge blade angles (β_2=85 deg as opposed to β_2=70 deg, respectively). The other miniature impeller from Ref. [5] has four radial blades with a trailing-edge blade angle, β_2, of 90 deg. The macroscale centrifugal pump [8] has an impeller diameter of 161.9 mm, five blades, and β_2=65 deg. The blood pump described by Klatte et al. [2] has an impeller diameter of 29.6 mm, five blades, and β_2=67 deg. As expected, the impellers from this study performed similarly to the miniature pumps but with a 100–150% increase in nondimensional head. Compared to the blood pump [2] and the large centrifugal pump [8], the pumps in this study act more like those with radial blades, since larger ranges of flow rates are produced without much change in the pump head. Both the blood pump [2] and the large centrifugal pump [8] have a greater range in pump head and a smaller range of flow rates compared to the impellers from the present study.

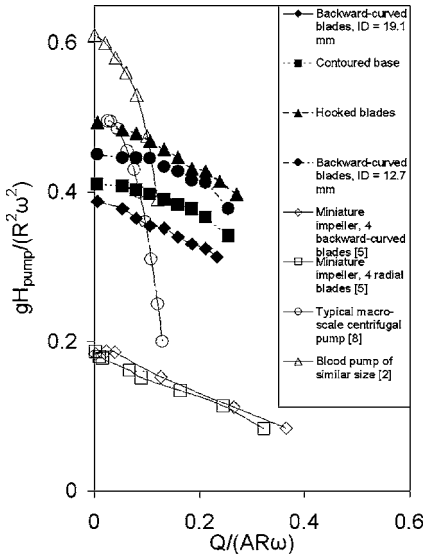

Fig. 14 Variation of normalized pump head with nondimensional flow rate comparing impeller designs tested in this study, two millimeter-scale pump designs [5], one typical macroscale pump [8], and a blood pump using an impeller with similar dimensions [2]. The speed of the pumps tested in this study is 3300 rpm, the miniature pump speed is 10,710 rpm, the macroscale pump speed is 800 rpm, and the blood pump speed is 3500 rpm.

Summary and Conclusions

Four different centrifugal pumps are designed, manufactured, tested, and characterized to determine the optimal pump configuration. These pumps use an impeller design that is simply and inexpensively manufactured, since the impeller and blades are directly integrated into the impeller shaft. This design also improves the hydraulic efficiency, compared to many other configurations, by eliminating leakage over the tops of the blades.

The impellers for each pump configuration have backward-curved blades with a 25.4 mm o.d. The four different pump impeller configurations are: (i) hooked blades, (ii) backward-curved blades (ID=19.1 mm), (iii) backward-curved blades (ID =12.7 mm), and (iv) contoured base. Pressure rise and flow rate data are collected for each configuration at different impeller speeds as the flow rate is throttled. The results obtained are comparable to those obtained from other centrifugal pumps, and show that pump head and volumetric flow rate increase with increasing shaft rotational speed (with invariant flow throttling) and that pump head increases when the flow is throttled with constant impeller shaft speed. Hydraulic efficiency also generally increases as the flow is throttled at constant rotational impeller speed, but can either increase or decrease (depending on the impeller configuration) as impeller speed is increased with a constant amount of flow throttling.

Of the different configurations considered, the hooked blades impeller gives the highest flow rate and pump head, 3.22 L/min and 0.78 m, respectively, at an impeller rotational speed of 3300 rpm and the outlet valve fully open (with no flow throttling). This configuration also gives the highest values of hydraulic efficiency (compared to the other three configurations tested), regardless of the volumetric flow rate or amount of flow throttling for pump impeller speeds of 2500 rpm and 3300 rpm. These values are higher or comparable to other pumps of similar size, which encourages further development and use of this pump configuration.

Acknowledgment

This project is supported by the Technology Commercialization Program of the University of Utah.

Nomenclature

A = impeller outlet area between two blades
A_{impeller} = total cross-sectional area of impeller
A_{blades} = total cross-sectional area of blades
B_f = blade blockage factor

b = impeller blade height
H_{pump} = measured pump head developed from inlet to outlet of the pump
H_{actual} = actual pump head
H_E = Euler pump head
m = loss coefficient [13]
Q = volumetric flow rate
R = radius of the impeller at the trailing edge of the impeller blade
U_1, U_2 = tangential velocity of the blades at the inner and outer diameters of the impeller, respectively
V_1, V_2 = absolute fluid velocity at the inner and outer diameters of the impeller, respectively
V_{r1}, V_{r2} = radial component of the absolute fluid velocity at the inner and outer diameters of the impeller, respectively
$V_{\theta 1}$ = tangential component of the absolute fluid velocity (preswirl) at the inner diameter of the impeller
$V_{\theta 2}$ = tangential component of the absolute fluid velocity at the outer diameter of the impeller
$V_{\theta s}$ = pump impeller slip velocity
W_1, W_2 = relative velocity of the fluid at the inner and outer diameters of the impeller, respectively
W_E = Euler work

Greek Symbols

β_1, β_2 = angle between the leading/trailing edges of an impeller blade and the tangent to the impeller inner/outer diameters, respectively
η_h = hydraulic efficiency
ξ_2, ξ_1 = loss coefficients [13]
ρ = local fluid density
σ = slip factor
σ_1 = swirl correction factor
φ = amount of throttling applied to the fluid at the outlet of the pump
ω = angular velocity of the impeller, $2\pi\Omega/60$
Ω = dimensional angular speed of the impeller

References

[1] Yuhki, A., Nogawa, M., and Takatani, S., 2000, "Development of a Compact, Sealless, Tripod Supported, Magnetically Driven, Centrifugal Blood Pump," Artif. Organs, **24**(6), pp. 501–505.
[2] Klatte, R., Smith, W. A., Dudzinski, D., and Lorez, M., 2002, "Centrifugal Blood Pump Impeller Test and Design," Technical Report, Cleveland Clinic Foundation, Cleveland.
[3] Shen, J. X., Tseng, K. J., and Vilathgamuwa, D. M., 2000, "A Novel Compact PMSM With Magnetic Bearing for Artificial Heart Application," IEEE Trans. Ind. Appl., **34**(4), pp. 1061–1068.
[4] Nishimura, K., Park, C-H., Akamatsu, T., Yamada, T., and Ban, T., 1996, "Development of a Magnetically Suspended Centrifugal Pump as a Cardiac Assist Device for Long-Term Application," ASAIO J., **42**(1), pp. 68–71.
[5] Blanchard, D., Ligrani, P., and Gale, B., 2005, "Performance and Development of a Miniature Rotary Shaft Pump (RSP)," ASME J. Fluids Eng. **127**(4), pp. 752–760
[6] Munson, B. R., Young, D. F., and Okiishi, T. H., 1998, *Fundamentals of Fluid Mechanics*, Wiley, New York, pp. 779–808.
[7] Ebaid, M. S. Y., Bhinder, F. S., and Khdairi, G. H., 2003, "A Unified Approach for Designing a Radial Flow Gas Turbine," ASME J. Turbomach., **125**(3), pp. 598–606.
[8] Brennen, C. E., 1994, *Hydrodynamics of Pumps*, Oxford University Press and Concepts NREC, ETI Inc., New York and Oxford, pp. 11, 24, 122.
[9] Wiesner, F. J., 1967, "A Review of Slip Factors for Centrifugal Impellers," ASME J. Eng. Power, **89**, pp. 558–572.
[10] Gorla, R. S. R., and Khan, A. A., 2003, *Turbomachinery: Design and Theory*, Marcel Dekker, New York, pp. 47–53.
[11] Moffat, R. J., 1988, "Describing the Uncertainties in Experimental Results," Exp. Therm. Fluid Sci., **1**, pp. 3–17.
[12] Schweiger, F., 1989, "Design Effects on Performance Characteristics of Centrifugal Pumps," ASME Paper No. 87-FE-6-B.
[13] Zaher, M. A., 2001, "Approximate Method for Calculating the Characteristics of a Radial Flow Pump," Proc. Inst. Mech. Eng., Part E: J. Process Mech. Eng., **215**(4), pp. 295–316.

Experimental Study of Drop Deformation and Breakup in a Model Multitoothed Rotor-Stator

David Megias-Alguacil[1]
e-mail: david.megias@ilw.agrl.ethz.ch

Erich J. Windhab

ETH-Zürich,
Laboratory of Food Process Engineering (LMVT),
Schmelzbergstrasse 9,
8092 Zürich, Switzerland

The objective of this work is to experimentally study the deformation behavior and breakup process suffered by a droplet submitted to the complex flow developed in a model multitoothed rotor-stator. The studied systems consist of an aqueous solution of polyvinylpyrrolidone in which droplets of diverse silicon oils are dispersed. Experiments are recorded with a digital camera, placed in vertical position, whose images are digitally analyzed. It is found that the drop deformation increases with increasing rotor rotational velocity, showing peaks of deformation corresponding to the proximity of the teeth. Drop breakup is achieved for all studied viscosity ratios. The breakup mechanism depends on the rotor-stator rotational dynamics, with breakup being more effective when the rotor teeth approach the stator teeth. [DOI: 10.1115/1.2354528]

Keywords: extrusion, rotor-stator, droplet, breakup

1 Introduction

Extrusion has become an important processing technique and is able to provide good mixing, structuring, and shaping qualities to the manufactured product. The versatility, high-productivity, low-cost and end-product quality [1] has led to the use of extrusion in many industrial fields like plastics [2,3], pharmaceuticals [4,5], chemicals, and ceramics [6,7], etc. Rossen and Miller [8] first described the use of extrusion in the food industry, and subsequently the technique has become widely used in multiple food production and applications [9,10].

There exist a large number of extruders, whose designs vary with respect to the number and arrangement of screws, number of flights per unit of length, etc. The most common devices used in industrial applications can be classified into two main categories: single and twin extruders (with co- and counterrotating screws) [11]. The design of the opposing surfaces of an extruder determines the behavior of the droplets of an emulsion, or particles in a dispersion, etc. However, visualization and analysis of the performance (especially the transient behavior) of such particles inside a real extruder is often complicated because of the mechanical design of the systems. Consequently, an extruder is considered a "black box" from the experimental point of view, in which the processes experienced by the particles cannot be fully tracked, although some numerical and experimental efforts have been carried out [12–14].

A new extruder design has been developed in our laboratory and, in order to better understand its future performance, it has been experimentally studied with a model rotor-stator setup. It should be noted that modeling with a rotor-stator has some obvious limitations with respect to a "real" industrial extruder: the rotor-stator is approximately a two-dimensional (2D) section of an extruder, with no transport in the z-axis. This allows us to observe the whole process that the drops experience. Also, the dimensions of the rotor-stator are much greater than those of the industrial extruder, sufficient to allow a good handling of the drops. The screw speeds used in industrial applications depends upon the viscosity of the treated materials and the particular manufacturing process. In our case, the limitation in rotational speeds arises from the breakup event of the drops under study, as well as the low viscosity of the continuous medium. However, the rates are of the same order of magnitude that those employed in extrusion of soft materials like polymers, where the speeds are in the range of few revolutions per minute [e.g., [15,16]].

In order to quantify the deformation of the sheared droplets, the widely used Taylor deformation parameter D [17] is used.

$$D = \frac{L - B}{L + B} \tag{1}$$

with L and B the semiaxis of the elliptical shape adopted by the droplet under the action of the flow.

2 Materials and Methods

The experimental setup used in this work is a model multitoothed rotor-stator device. Essentially, it consists of two rings ($R_{\text{inner}}=12.0\pm0.1$ cm, $R_{\text{outer}}=15.0\pm0.1$ cm) whose surfaces contain six teeth each. The teeth have an arc-of-circumference profile ending in abrupt corners of height $h=2.4\pm0.1$ cm with respect to the cylinder walls. Because of the presence of the teeth in both rotor (inner) and stator (outer) rings, the gap varies between 6.0 ± 0.1 cm and 1.2 ± 0.1 cm. Figure 1 schematically shows the device. This model rotor-stator is oriented horizontally, and the total width of the two rings is 4.3 ± 0.1 cm. A movable CCD digital camera (Sony DFW-V500, Japan) is attached vertically above the rotor-stator. Further digital analysis of the recorded movies allowed the determination of the time evolution of the drop deformation. In order to better track the sheared drops, both the rotor and stator were moved by corresponding electrical motors (Stealth, USA). Hence, a relative angular velocity ω between the rotor and stator is defined for each experiment. Since in industrial operating conditions only the rotor moves, we will therefore consider that the stator is at rest and the rotor moves at such angular velocity ω.

Both the droplet and continuous phase liquids were Newtonian. The continuous phase was made of a transparent solution of 15% by weight of polyvinylpyrrolidone (PVP) (Fluka, Germany) in water with a viscosity $\eta_c=400$ mPa·s. The dispersed droplets were made of several silicon oils (Wacker, Germany) whose transparency was eliminated by the addition of titanium oxide (0.2% by weight), thus providing sufficient optical contrast for analysis. The densities of both liquid phases ($\rho\approx1.03$ g/cm^3) were matched for inhibiting any flotation or sedimentation displace-

[1]Corresponding author.

Contributed by the Fluids Engineering Division of ASME for publication in the JOURNAL OF FLUIDS ENGINEERING. Manuscript received October 20, 2005; final manuscript received May 2, 2006. Assoc. Editor: Theodore Heindel.

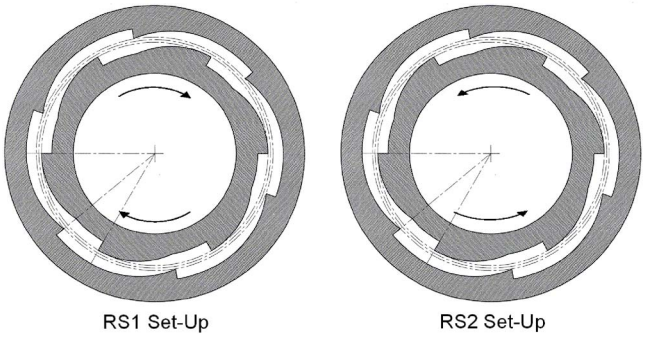

Fig. 1 Scheme of the multitoothed rotor-stator

ments of the immersed droplets, which could lead to a loss of the optical resolution. The silicon oils have the same density and interfacial tension with respect to the PVP solution, but different viscosities. The interfacial tension of such interface drop-fluid matrix was previously determined elsewhere [18], finding a value of $\sigma=31.2\pm0.5$ mN/m. The viscosity ratio, $\lambda=\eta_d/\eta_c$, for the dispersed (η_d) to the continuous (η_c) fluid phase varied from 0.1 up to 30. All experiments were carried out at room temperature, 25°C.

3 Discussion

Two dynamical conditions were used in our experiments, the first had the rotor moving clockwise (RS1), and the second, counterclockwise (RS2), as schematically shown in Fig. 1. In reality, these two conditions are not identical and the behavior of the sheared drops is different in each case.

In a complex device like this multitoothed rotor-stator, the applied flow is a mix of shear and elongational components, where magnitude depends on several parameters, such as the angular velocity of the rotor, ω, the direction of rotation (due to the asymmetry of the teeth) and, especially, the variable gap between the rotor and stator due to the particular geometry shown in Fig. 1. The particular rates experienced by the droplet also depend on its instantaneous position and the trajectory followed when sheared. The presence of the teeth makes the flow time dependant, where its magnitude fluctuates periodically (depending on ω). A complete numerical analysis of the flow is beyond the scope of this paper; however, tracking the displacement of drops enables an estimate of the flow rates as a function of the time (Fig. 2). These graphs allow us to better understand the flow fluctuations exerted by the movement of the rotor as well as to describe qualitatively the impact of the teeth on the flow [19,20].

In general, when the rotor moves clockwise (Fig. 1), the flow shows its maximum value in front of both rotor and stator teeth. On the contrary, regions of lower flow magnitude are located on the curved surfaces. This situation is repeated for each tooth along the whole circumference of rotor-stator. If the observation is fixed on a certain position, the periodical fluctuation of the flow magnitude should be noted. For the other dynamical situation, the rotor moving counterclockwise (Fig. 1), the fluid is compressed progressively by the approaching curved surfaces, with maximum intensity when the teeth align; after this point a sudden decrease of the flow magnitude is produced because the increase of the gap. Again, the profile is periodically repeated for each tooth.

The presence of stagnation areas close to the inner corners of both rotor and stator were also observed. When a drop was set in the vicinity of such corners, it was not affected by the flow and showed no deformation while keeping such position indefinitely without relative displacement.

3.1 Drop Deformation. When a liquid droplet is moderately sheared by the action of a flow, it adopts a three-dimensional ellipsoidal shape with, three different characteristic lengths corresponding to the main axis of such an ellipsoid. The projection of this geometry in the plane of shear is a two-dimensional ellipse that allows measurement of the deformation of the drop by the deformation parameter D, defined in Eq. (1).

3.1.1 Rotor Clockwise (RS1). As mentioned, when the rotor moved clockwise, its teeth approached those of the stator. Two

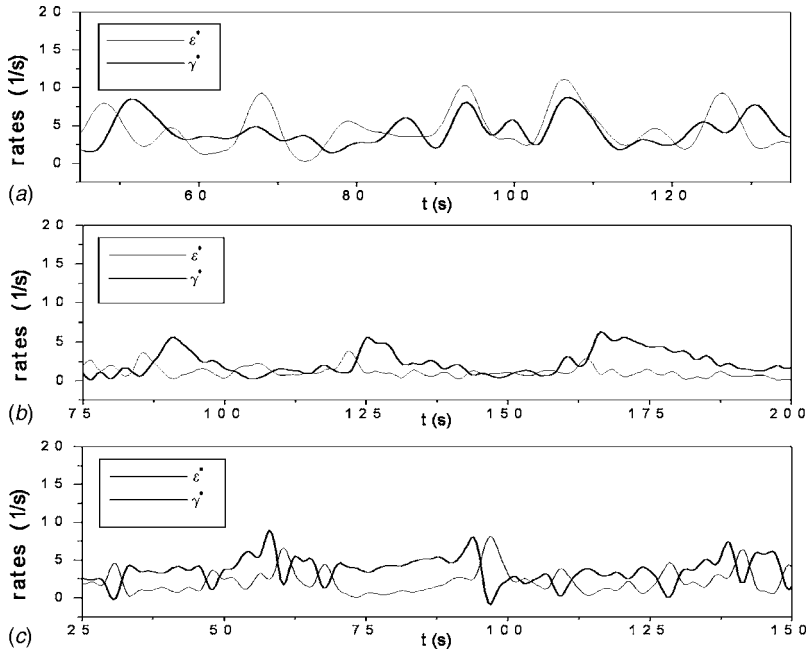

Fig. 2 Shear, $\dot{\gamma}$, and extensional, $\dot{\varepsilon}$, rates along: (a) flow-line close to the stator wall for $\omega=0.1$ 1/s and RS1 setup ($\lambda=0.3$); (b) flow-line in between the rotor and stator teeth for $\omega=0.1$ 1/s and RS1 setup ($\lambda=30$) and (c) flow-line in between the rotor and stator teeth for $\omega=0.08$ s^{-1} and RS2 setup ($\lambda=30$)

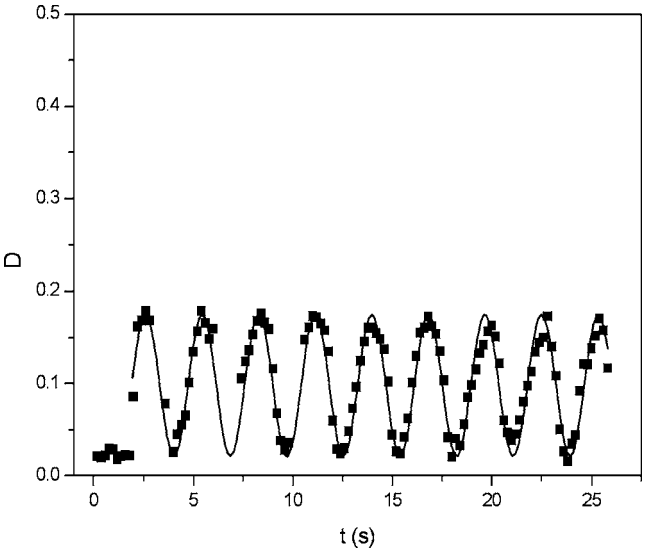

Fig. 3 Drop deformation parameter *D*, as a function of time when the rotor moves clockwise (RS1). λ=0.1 and ω=0.4 1/s. The drop insertion point was close to the stator wall. Solid line corresponds to a sinusoidal fitting.

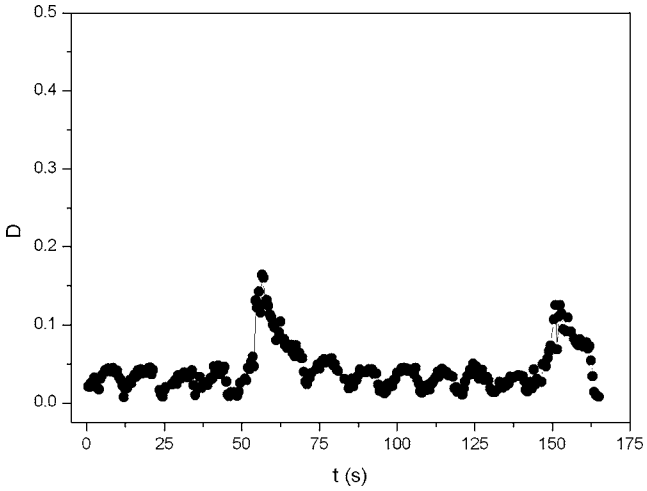

Fig. 4 Drop deformation parameter *D*, as a function of time when the rotor moves clockwise (RS1). λ=0.3 and ω=0.1 1/s. Drop insertion position close to the stator wall.

different insertion points were used for each λ in these RS1 experiments: (i) close to the stator wall and (ii) in-between both teeth of the rotor and stator.

When setting the drop close to the stator wall, it was observed that it moved parallel to the stator wall, between two consecutive stator teeth, without any radial displacement. The flow experienced by a drop along such a flow-line segment periodically changes as shown in Fig. 2(*a*) with local maxima corresponding to positions in which the rotor tooth approaches the drop. In particular, the extensional rate shows a continuous value altered by the approaching of the teeth; on the other hand, the shear rate is never constant since the gap between the rotor and stator varies continuously with time.

The drop was dragged by the flow caused by the rotor movement, being its displacement larger when the rotor teeth approached, because of the maxima in the extensional flow. The deformation parameter, *D*, expressed by Eq. (1) shows a reproducible periodic behavior respect to the experimental time, similar to that shown in Fig. 3, also observed for the whole range of λ and ω. These periodic oscillations can be fitted with a sinusoidal function similar to that displayed in Fig. 3. A Fourier Transform analysis of such a periodic behavior reveals that the main frequency of the deformation is six times that of the rotor angular frequency, ω. This is the frequency at which the teeth of the rotor and stator are aligned. This means that, as expected, the drop deformed up to a maximum value of D when the rotor teeth approached it, for later decrease such a high deformation once the teeth moved away and the gap between the rotor and stator increased, as shown in Fig. 3. Coupled with this oscillatory behavior, peaks in deformation were also observed when the drop was placed close to the wall (Fig. 4). These states correspond to the extra deformation experienced by the drop when overcoming one stator tooth in regions of high flow values. For low rotational speeds of the rotor ω, the drop could overcome the teeth of the stator, experiencing again the same process described above, but as soon as ω increased to a critical value, the drop was physically engaged in the stator tooth, not having time enough for avoiding this high rate region. In such a case, the breakup of the droplet was produced, as described later.

Figure 5 summarizes the drop deformation as a function of the rotor speed ω for the whole range of viscosity ratios. Note that ω is multiplied by the drop spherical radius *R* to better compare the results of different droplets. The symbols represent the mean value of the oscillating *D*, while the bars indicate the amplitude of such oscillations, as those displayed in Fig. 3. As expected, the deformation increases when increasing ω, also increasing the amplitude of the wave. This increment of *D* is linear with ω, and in agreement with Taylor [17], the slopes are almost coincident for all the viscosity ratios, λ, studied.

The drops initially inserted at the second position, that is, in-between the teeth of the rotor and the stator, showed a different performance. In these cases, the drop was not as confined as in the previous case, rather it moved along the center line of the gap between the rotor and stator, having more degree of freedom in its displacements. This is shown in Fig. 2(*b*). In this case, both shear and extensional rates display local maxima corresponding to the vicinity of both rotor and stator teeth, whereas the amplitude of their oscillations are smaller compared to the case of a flow-line close to the stator wall. A small delay of the appearance of the extensional rate maximum with regard to the shear rate maximum is observed.

In terms of deformation, the drop experiences a quasi-steady

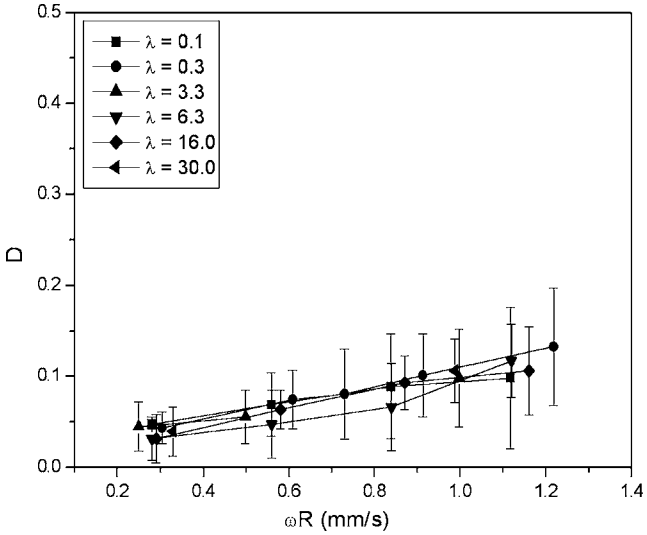

Fig. 5 Drop deformation parameter *D*, as a function of the product of the rotor angular velocity ω, and drop radius *R*, for the different viscosities ratios λ, when the rotor moves clockwise (RS1). Drop insertion position close to the stator wall.

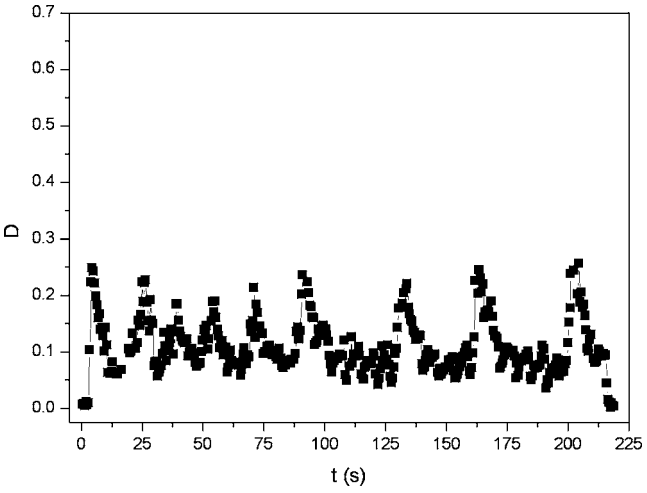

Fig. 6 Drop deformation parameter *D*, as a function of time when the rotor moves clockwise (RS1). λ=30 and ω=0.2 1/s. Drop insertion position in-between the rotor and stator teeth.

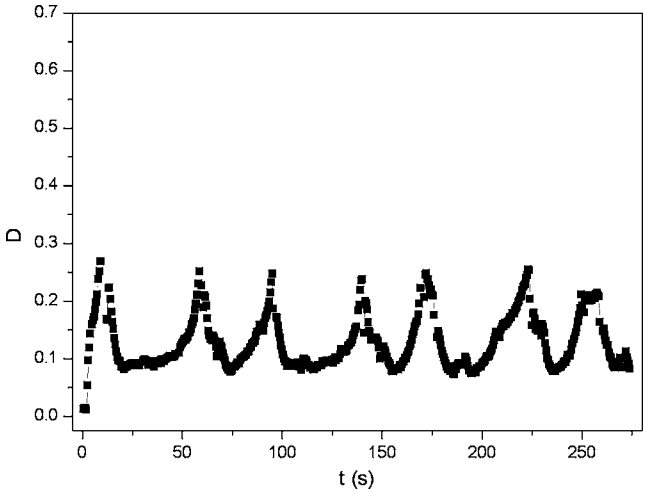

Fig. 8 Drop deformation parameter *D*, as a function of time when the rotor moves counterclockwise (RS2). λ=30 and ω =0.08 1/s.

state of deformation (base-line), altered by a sharp peak in D when the drop was close to the teeth, as displayed in Fig. 6. The expected periodic behavior of D is not so evident in this case, despite the deformation peaks. This is due to the small flow amplitudes shown in Fig. 2(*b*). The oscillatory character of the deformation is mainly expected for low rotor speeds, when the characteristic relaxation time of the corresponding droplet is below, or comparable to, the periodicity of the flow. Nevertheless, in such a case (small ω), since the deformation is very small and the drop migrates, this shape oscillation is masked, and then, not easily observed, especially when increasing the drop viscosity. On the other hand, at high ω the deformation peaks like those shown in Fig. 6, become closer and thus, the oscillation of the baseline cannot be observed in the graph.

Figure 7 shows the deformation of the drop as a function of the product ωR, for the case of clockwise rotor movement (RS1) where the drop was positioned in-between the rotor and stator teeth. The symbols here represent the averaged base-line value of D, and the bars indicate the maximum values obtained. Again, the deformation increases almost linearly with ω, as well as the maximal values of the peaks. Generally higher values of deformation (with respect to the base-line) were observed in this case when compared to those shown in Fig. 5, when the droplet was initially inserted close to the stator wall. In particular, the maximum values of the peaks are much higher than the amplitudes of the oscillations when the drops were placed close to the stator wall. Comparison of the deformation peaks corresponding to the two insertion positions (Figs. 4 and 6) indicate that both are of the same order of magnitude. These peaks of deformation are responsible for the drop breakup, as explained later.

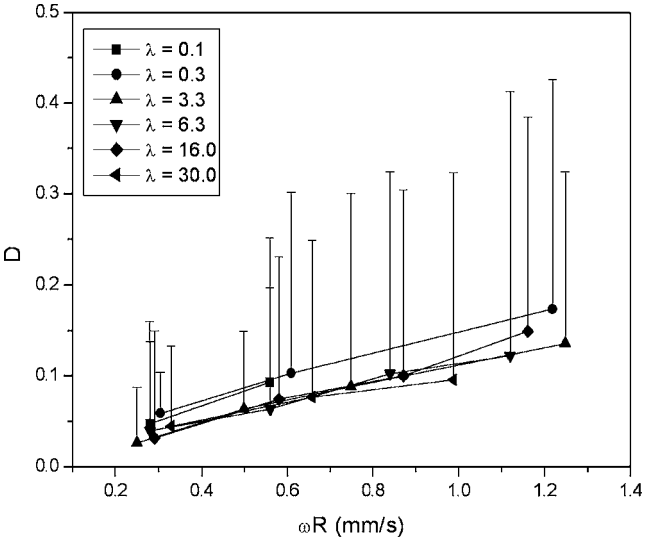

Fig. 7 Drop deformation parameter *D*, as a function of the product ωR, for the different viscosities ratios λ, when the rotor moves clockwise (RS1). Drop insertion position in-between the rotor and stator teeth.

3.1.2 Rotor Counterclockwise (RS2). When the rotor moved counterclockwise, its teeth moved away from those of the stator. Two insertion points for the drops were also considered when the rotor moved counterclockwise: (i) in-between the teeth of both rotor and stator, and (ii) in the center-line of the gap between them, with parallel walls. Both starting points gave the same results, indicating that these positions were equivalent in terms of deformation. Thus, only the results from insertion at the center-lines are discussed, although they can be applied to both cases.

Figure 2(*c*) shows the rates along a centered flow-line when the rotor moves counterclockwise. In this case, again both shear and extensional rates display local maxima corresponding to the vicinity of both rotor and stator teeth, in the same manner than those shown in Fig. 2(*b*) (rotor clockwise). Nevertheless, the asymmetry of the system manifolds in the reversed onset of the rates maxima: in this case, the extensional component is the delayed one.

Hence, similar trends to the previous case RS1 were found in the behavior of the droplets, with steady states of deformation plus corresponding peaks observed in the plots of D as a function of the experimental time, like that shown in Fig. 8. The explanation of this behavior is analogous to that given for the data in Fig. 6: the droplets moved in centered flow lines featuring a quasi steady state of deformation perturbed by abrupt jumps of D.

Figure 9 shows the deformation parameter measured with the counterclockwise rotor movement. Symbols mean the base-line values and the bars indicate the maximum deformation corresponding to the peaks. As expected, the drop deformation increases with increasing rotor speed, as well as the maximum for each viscosity ratio. Now, a small impact of λ can be detected in the plot, in which two groups, corresponding to the cases $\lambda < 6$, and $\lambda > 6$, can be distinguished. Almost linear dependencies of D with ω are observed. When comparing the data shown in Fig. 9 with those in Fig. 7, it is observed that the D values for the RS2 case are higher than the RS1 ones, for each viscosity ratio.

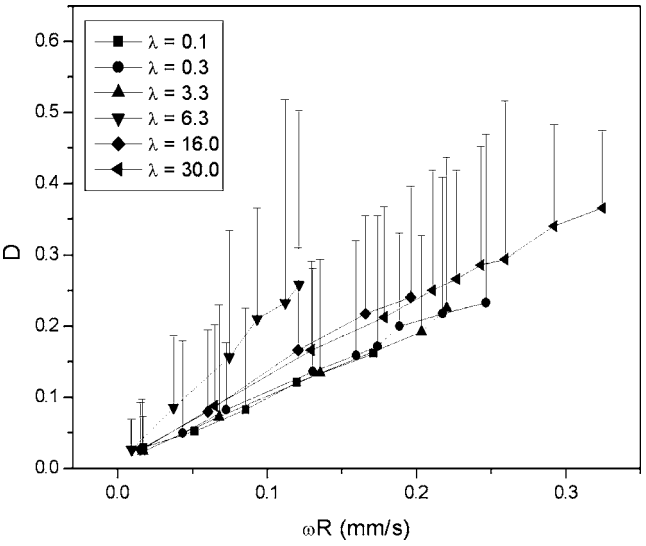

Fig. 9 Drop deformation parameter *D*, as a function of the rotor product ωR, for the different viscosities ratios λ, when the rotor moves counterclockwise (RS2)

3.2 Drop Breakup. The rupture of the drop was successfully attained for all the range of viscosity ratios, λ. The complex flow developed in the multitoothed rotor-stator is able to produce the drop breakup independently of the drop viscosity, and this fact also indicates the role played by the elongational flow components in such a task. Indeed, it is well known that the droplet break-up event does not occur for the case $\lambda > 1$ in simple shear flows [21]. The break-up of the droplets is also favored by the time-dependant flow type, already realized to be more likely to induce drop breakup [22]. Figure 10 shows as example some pictures corresponding to the break of drops in both set of experiments, RS1 and RS2.

3.2.1 Rotor Clockwise (RS1). For the case of clockwise rotor movement (RS1), it was observed that, independent of the insertion position of the droplet, its break-up occurred at one stator tooth. As discussed above, the droplet was dragged from its initial position until it touched with a stator tooth. In such a case, the initially ellipsoidal droplet was elongated into a "tear-drop" shape, and the stator tooth acted as a guillotine, cutting directly a rear section of the drop ($\lambda < 1$) or producing a very thin neck which followed in one or several secondary drops ($\lambda > 1$). The drop break-up occurred in the linear region of D versus ω, nevertheless higher and higher deformations were necessary for attaining the break-up when increasing the viscosity ratio λ, as shown in Fig. 11 (solid symbols). This indicates quantitatively the increasing of the elongation suffered by the drop prior to break. The critical deformation parameter, D_{crit}, is found to follow a power relationship respect to the viscosity ratio λ as

$$D_{crit} = 0.7\lambda^{0.09} \tag{2}$$

The corresponding "critical" rotor speeds, ω_{crit}, also increase when increasing the viscosity ratio toward a certain limiting value when $\lambda > 1$.

3.2.2 Rotor Counterclockwise (RS2). For the case of counterclockwise rotor movement (RS2), the "guillotine effect" described above was not observed. In this case, the effect of the stator tooth was also to increment the flow strength but the high sheared drop first developed a filament configuration prior to breakup due to Rayleigh instabilities. The mechanism is as follows: the drop is elongated when trapped in the narrowest channel between rotor and stator (in the other case it "snakes" avoiding the proximity of the tooth) and adopts the typical sigmoidal shape with pointed

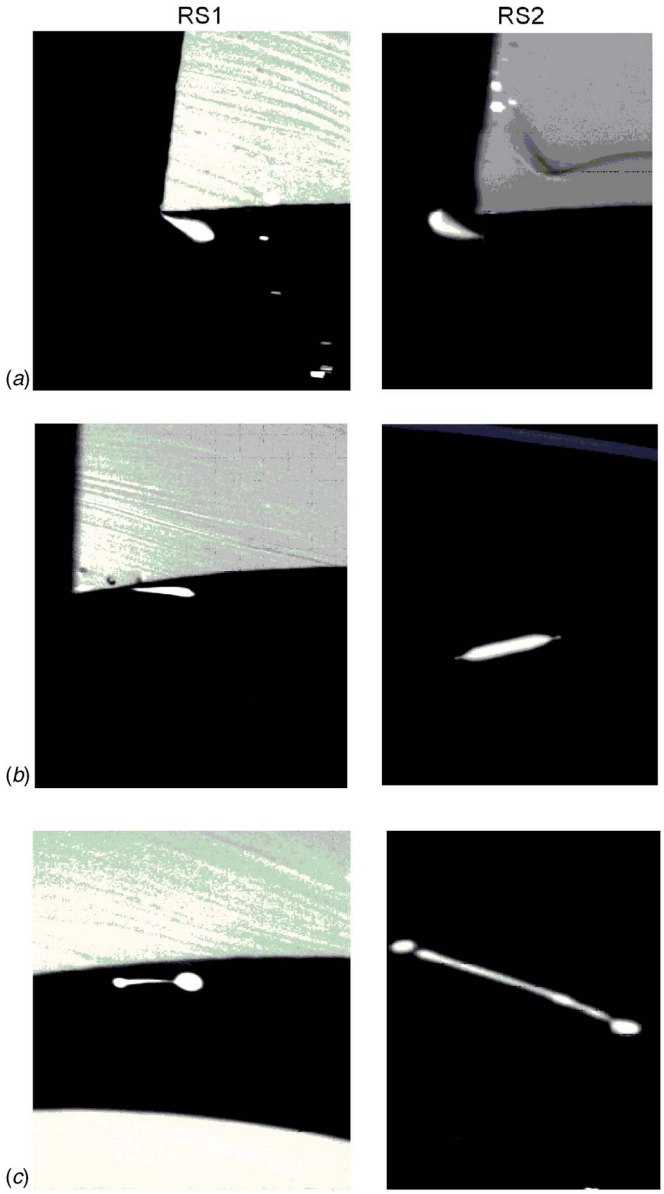

Fig. 10 Photographs of the drop breakup for the viscosity ratios: (*a*) λ=0.3, (*b*) λ=3.3, and (*c*) λ=30.0

ends [23]. The drop breakup takes place after leaving this narrow channel, in the region of widest gap (see Fig. 1) where the flow relaxes. Note in this case the impact that time-dependences on the flow exerted on the droplet break-up mechanism. That is, the alternation of the flow values from high to low rates favors the onset of Rayleigh waves on the filament surface which provoke its disintegration. With sufficient rates (e.g., λ=3.3 in Fig. 10), small satellite drops escaped out from the tips of the mother drop. When the viscosity ratio increased, the drop converted into a narrow filament and then broke up in the widest gap between the rotor and stator (region of flow relaxation). The filament gets longer and longer with λ, showing increasing values of D_{crit} (Fig. 11). As in the RS1 case, a power law was found

$$D_{crit} = 0.7\lambda^{0.07} \tag{3}$$

The critical rotation velocities for this rotor movement were found to be qualitatively similar to that found for the previous case, RS1. Apparently, out-of-the-trend values are those for λ =6.3 and λ=16.0 plotted in Fig. 11; however, an explanation for these cases is that the corresponding drops were "engaged" very

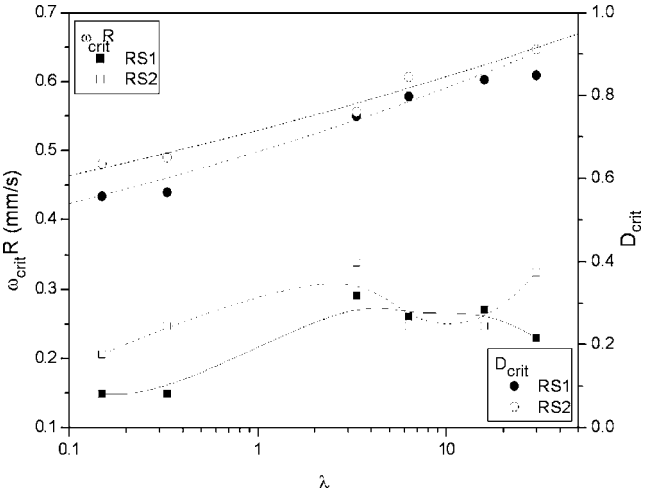

Fig. 11 Critical rotor speed (multiplied by the drop radius) and deformation for drop breakup as a function of λ. Lines for D_{crit} correspond to Eq. (3) (solid line) and Eq. (4) (dashed line).

close to the stator tooth. The later experienced the guillotine effect above described and further drop extension. This provoked an elongation that they could not resist, and consequently, broke up. As a result, their values are close to the corresponding RS1 ones. These cases must be considered as stochastic because the drop tends to stay at the center line of the gap due to compressive flow forces when this is narrowing. Beside this behavior, the approximation of ω_{crit} up to a limiting value is also observed.

As shown quantitatively in Fig. 11 and Eqs. (2) and (3), the clockwise rotor movement (RS1) demands less deformation for producing the drop break-up than the counterclockwise rotor motion (RS2) due to the effectiveness of the guillotine effect. Consequently, less rotational speeds, and thus, less energy inputs are necessary in any condition of viscosity ratio for producing the breakup of the drops.

Conclusion

In this work, we have explored the performance of a homemade rotor-stator that models the geometry of a newly designed extruder, in order to study at laboratory scale its capabilities on multiphase flows. The deformation and breakup behavior of oily droplets immersed in a water phase and subjected to the action of the rotor-stator have been studied as a function of the rotor movement, angular velocity and drop initial insertion position.

Two types of drop deformation behaviors are observed: one periodic when the drop is close to the stator wall and the rotor moves clockwise and another one composed of a base line coupled with peaks of deformation, for the other dynamical conditions. In general, the deformation increases when increasing the angular velocity of the rotor up to a critical ω_{crit}, for which the drop breaksup. The mechanism of drop rupture depends on the rotor movement: when this is clockwise (RS1) the drop is engaged at one stator tooth which acts as a guillotine, provoking the drop break. When the rotor movement is counterclockwise (RS2), the drop develops a filament shape prior to its breakup. We also provide quantitative scaling-laws relating the critical deformation and the viscosity ratio, in order to predict the drop breakup. According to the smaller deformation values for drop break, the RS1 arrangement may be declared as more effective for breaking drops of any viscosity.

Acknowledgment

The authors thank Marc Lawrence (IfA, ETH-Zürich) for style corrections.

References

[1] Harper, J. M., and Clark, J. P., 1979, "Food Extrusion," Crit. Rev. Food Sci. Nutr., **11**, pp. 155–215.
[2] Ding, F., and Giacomin, A. J., 2000, "Die Lines in Plastics Extrusion," J. Polym. Eng., **20**, pp. 1–39.
[3] Kulikov, O., 2005, "Novel Processing Aids for Extrusion of Polyethylene," J. Vinyl Addit. Technol., **11**, pp. 127–131.
[4] Otsuka, M., Gao, J., and Matsuda, Y., 1994, "Effect of Amount of Added Water during Extrusion-spheronization Process on Pharmaceutical Properties of Granules," Drug Dev. Ind. Pharm., **20**, pp. 2977–2992.
[5] Remon, J. P., 2004, "Hot Melt Extrusion as a Pharmaceutical Manufacturing Process," Eur. J. Pharm. Sci., **23**, pp. 7–30.
[6] Grida, I., and Evans, J. R. G., 2003, "Extrusion Freeforming of Ceramics Through Fine Nozzles," J. Eur. Ceram. Soc., **23**, pp. 629–635.
[7] Lee, B. S., Joo, D. H., and Kim, M. H., 2005, "Extrusion Behavior of Al-Cu Alloys in the Semisolid State," Mater. Sci. Eng., A, **402**, pp. 170–176.
[8] Rossen, J. L., and Miller, R. C., 1973, "Food Extrusion," Food Technol. Aust., **27**, pp. 46–53.
[9] Bolliger, S., Kornbrust, B., Goff, H. D., Tharp, B. W., and Windhab, E. J., 2000, "Influence of Emulsifiers on Ice Cream Produced by Conventional Freezing and Low-Temperature Extrusion Processing," Int. Dairy J., **10**, pp. 497–504.
[10] Gregson, C. M., and Lee, T. C., 2004, "Quality Modification of Food by Extrusion Processing," Adv. Exp. Med. Biol., **542**, pp. 187–200.
[11] Schuler, W., 1995, *Der Doppelschnecken-Extruder*, VDI Verlag, Düsseldorf.
[12] Lindt, J. T., 1985, "Mathematical-Modeling of Melting of Polymers in a Single-Screw Extruder: A Critical-Review," Polym. Eng. Sci., **25**, pp. 585–588.
[13] Lai, E., and Yu, D. W., 2000, "Modeling of the Plasticating Process in a Single-Screw Extruder, A Fast-track Approach," Polym. Eng. Sci., **40**, pp. 1074–1084.
[14] Stranzinger, M., Bieder, A., Feigl, K., and Windhab, E., 2002, "Effects of Flow Incidence and Secondary Mass Flow Rate on Flow Structuring Contributions in Scraped Surface Heat Exchangers," J. Food Proc. Eng., **25**, pp. 159–187.
[15] Bostanci, T., Güner, F. S., and Ercives, T., 2005, "Production of Viscosity Improvers for PVC," Macromol. Symp., **228**, pp. 237–243.
[16] Li, Y., Chen, G., Guo, S., and Li, H., 2006, "Studies on Rheological Behavior and Structure Development of High-density Polyethylene in the Presence of Ultrasonic Oscillations during Extrusion," J. Macromol. Sci., Phys., **45**, pp. 39–52.
[17] Taylor, G. I., 1943, "The Viscosity of a Fluid Containing Small Drops of Another Fluid," Proc. R. Soc. London, Ser. A **438**, pp. 41–48.
[18] Megias-Alguacil, D., Fischer, P., and Windhab, E. J., 2006, "Determination of the Interfacial Tension of Low Density Difference Liquid-Liquid Systems Containing Surfactants by Droplet Deformation Methods," Chem. Eng. Sci. **61**, pp. 1386–1394.
[19] Kaufmann, S. F. M., 2002, Experimentelle und Numerische Untersuchen von Tropfendispergiervorgängen in Komplexen Laminaren Strömungsfeldern, Ph.D. thesis, Zürich.
[20] Windhab, E. J., Dressler, M., Feigl, K., Fischer, P., and Megias-Alguacil, D., 2005, "Emulsion Processing—from Single Drop Determination to Design of Complex Processes and Products," Chem. Eng. Sci., **60**, pp. 2101–2113.
[21] Grace, H. P., 1982, "Dispersion Phenomena in High Viscosity Immiscible Fluid Systems and Application of Static Mixers as Dispersion Devices in Such Systems," Chem. Eng. Commun., **14**, pp. 225–277.
[22] Stone, H. A., and Leal, L. G., 1989, "The Influence of Initial Deformation on Drop Breakup in Subcritical Time-dependent Flows at Low Reynolds-numbers," J. Fluid Mech., **206**, pp. 223–263.
[23] Rumscheidt, F. D., and Mason, S. G., 1961, "Deformation and Burst of Fluid Drops in Shear and Hyperbolic Flow," J. Colloid Sci., **16**, pp. 238–261.

John Borg
Department of Mechanical Engineering,
Marquette University,
1515 W. Wisconsin Ave.,
Milwaukee, WI 53233

Susan Bartyczak
Center-Dahlgren Division,
Naval Surface Warfare,
Dahlgren, VA 22448-5100

Nancy Swanson
Abacus Enterprises,
2582 Island View Ln.,
Lummi Island, WA 98262

John R. Cogar
CORVID Technologies,
149 Plantation Ridge Dr.,
Suite 170,
Mooresville, NC 28117

Impact and Dispersion of Liquid Filled Cylinders

The computational and experimental results of impact loading a thin wall liquid filled cylindrical target within a vacuum chamber are presented. The impact velocity ranges from 2.2 to 4.2 km/s. *Both experimental and computational results are presented. It will be shown that impact dynamics and the early time fluid expansion are well modeled and understood. This includes the mass distribution and resulting expansion velocity. However, the late time dynamics, which includes the liquid breakup and droplet formation process of impacted liquid filled cylinders, is not well understood.*
[DOI: 10.1115/1.2353270]

Keywords: impact, fluid impact, fluid dispersion, fluid-structure interaction

1 Introduction

In the experiments presented here, a projectile impacts a liquid filled thin skin steel target in a velocity range from 2.2 to 4.1 km/s. At this impact velocity, a shock wave is launched into the fluid target and expands spherically ahead of the penetrating projectile. Upon reaching the target free surface the resulting increase in pressure, i.e., the shock wave, ruptures the solid case and launches the fluid. The fluid is then free to expand inside of a vacuum chamber.

The underlying objective behind this work is to develop an understanding of the fluid breakup mechanisms and to predict the resulting drop size distribution and velocity distribution resulting from this impact event. Understanding and predicting the long time dynamic evolution process of an impact-loaded liquid system is a challenging hydrodynamic stability problem and will not be completely addressed here. However, as a first step towards understanding this complicated fluid breakup mechanism, developing an understanding of the fluid impact dynamics and the resulting fluid ejection process is a key component of the underlying objective and is the focus of the work presented in this paper. Towards this end the primary objective of this work is to characterize the fluid evolution as a result of being impacted by a fast moving projectile. This is accomplished through an experimental test series. A secondary objective is to assess the ability of hydrocodes and/or simple physics-based models to accurately predict the initial impact and fluid ejection. The computational results are validated by comparing the expansion geometry, including the expansion velocity and fluid thicknesses, as well as the pressure traces recorded in the target, to the experimental results.

There are several aspects of the fluid regime investigated here which are unique relative to classic shock-loaded hydrodynamic phenomenology and hydrodynamic stability. One aspect of the present work which causes theoretical and experimental difficulty is the mixed time scales. The impact loading and resultant shock event occur on a microsecond time scale, whereas the fluid expansion, evolution and eventual droplet breakup process occur on the millisecond time scale. As the ambient air pressure around the target is reduced the time scale of the droplet breakup process is increased. An order of magnitude difference in the time scales for these two related events, i.e., the shock loading and the hydrodynamic instability, are increased as the surrounding ambient air pressure is decreased.

The shock pressure and fluid bulk velocity resulting from impact can be accurately predicted using hydrodynamic calculations. Thus the early time evolution is well understood. However, the difficulty arises when predicting the long time fluid dynamics which includes the eventual liquid breakup and the formation of a resulting drop distribution. The fluid ejection process, which is the focus of the work presented here, represents the transition from the early or shock velocity time scale to the late time or expansion velocity time scale. In the context of a hydrodynamic stability investigation, a difficult aspect of the work presented here is that there are no pre-imposed disturbances. Disturbances are imposed by the fracture of the thin steel target membrane which initially contains the fluid. Thus predicting the final state time and length scales is more challenging. Another interesting feature of this work is that all of the experiments presented here were conducted in a vacuum tank held at approximately 1 Torr. This minimizes the effects of the ambient air, drives the Atwood number to unity and delays the onset of instability growth. Together the various aspects of this work: Impact-load, no initially imposed disturbances and Atwood number near unity, define the regime investigated here within the larger context of classical hydrodynamics.

2 Background

The evolution of a liquid-filled tank has been of interest to researchers trying to mitigate the damage by a high speed projectile or understand the hazards associated with sprays generated from impacted tanks. However, most researchers have either focused on the damage done to the tank as a result of impact or focused on more controlled hydrodynamic stability research were the initial conditions are better understood. The underlying objective of this research is to develop an understanding of the liquid breakup event as a continuous process from impact to drops.

Early work on liquid-filled tanks focused on evaluating damage to the target structure as a result of high velocity impact. This early work was focused on developing protection criteria for space bound liquid-holding tanks from micro-meteor impacts. A criterion which correlated the kinetic energy deposited onto the target to damage levels was developed. NASA conducted several

Contributed by the Fluids Engineering Division of ASME for publication in the JOURNAL OF FLUIDS ENGINEERING. Manuscript received April 4, 2005; final manuscript received April 7, 2006. Assoc. Editor: Georges L. Chahine.

test series in order to develop these criteria [1–4]. In addition, a tank damage classification system has been developed in order to establish standard levels of damage [5,6]. Most researchers have focused on the damage done to the target without regard to the liquid evolution within the tank or the liquid evolution after it is ejected from the tank [7,8]. In an effort to understand the damage mechanisms, some researchers have placed pressure gauges within the target tank in order to record the pressure time history [9,10]. In addition, in order to characterize the projectile penetration, several test programs have been conducted to investigate depth of penetration by a high speed projectile [11–13]. In most of these tests, the target tanks were larger than the projectile, thus the damage levels achieved in these tests were not catastrophic. In general a single hole was punched into the tank or possibly an end cap was destroyed. The damage observed in the test series present here exceeds all of NASA's standard damage levels and would rank as catastrophic on the NASA damage level criteria.

With regard to the late time evolution of the fluid contained within the target, it is speculated that the liquid will break-up as a result of hydrodynamic instabilities. However, this has not been observed directly in the tests presented here. Liquid breakup as a result of hydrodynamic instabilities is a large field of study. The evolution of shock-accelerated liquid sheets remains a fundamental area of research within the broader field of hydrodynamic stability. Taylor developed a generalized analytical two-dimensional planar theory that demonstrated the stability criterion for an accelerated interface between two fluids with a single wave number disturbance was simply the sign of the Atwood number [14,15]. This physical phenomenon has come to be known as Rayleigh-Taylor instability (RT). The Atwood number is defined as the ratio of density difference between the upper and lower fluids divided by the sum of the two densities, $A=(\rho_2-\rho_1)/(\rho_{2+}\rho_1)$. Richtmyer modified Taylor's original formulation so that the acceleration of the fluid interface was impulsive in time, i.e., a shock [16]. Meshkov experimentally verified Richtmyer's growth rate predictions for a gas-gas geometry with a single disturbance [17]. The growth of disturbances of impulsively driven fluid sheets has come to be known as Richtmyer-Meshkov (RM) instability. However, RM results are only valid during the short time initially linear growth stage. Including the nonlinear terms arising from the hydrodynamics suppresses the growth of RM waves as compared to the linear RM waves. In fact, as time goes to infinity the impulsively driven nonlinear disturbance growth rate approaches zero, not the constant growth put forth by Taylor and Richtmyer [18]. The suppression of growth as a result of late time nonlinear effects have been experimentally verified using high acceleration rates for gas-gas interfaces with a single wave number imposed disturbance [19,20]. The evolution of the shock accelerated fluid investigated in this paper is in the nonlinear growth regime and, therefore, the growth rates are suppressed, so much so that liquid breakup was not observed in this work. Additional considerations, such as surface tension and viscosity, for two semi-infinite fluids tend to have a stabilizing effect on the linear growth of RT instabilities [21–23]. Experimental work supports the analytic work and suggests that viscosity dampens short wave-length perturbations but not long wave-length perturbations[24].

Numerous variations in flow geometry and initial conditions affect the growth of RM instabilities. For example, all of the flow fields studied in this work are divergent. The effects of geometric variations on the RT instabilities, such as convergent or divergent flow, increase the complexity of the instability growth [25–27]. All of the fluids in this work are initially contained by a solid steel membrane. Various studies as to the effect of a solid membrane containing the fluid have concluded that the membrane suppressed the initial growth rate of the interface [28,29]. In typical RT or RM studies a known initial disturbance is placed on the fluid interface. In this study the surfaces are initially smooth. Therefore, the fluid perturbations arise from the rupturing of the steel membrane initially containing the fluid, which is a stochastic event. Several studies have investigated accelerated fluid sheets with no imposed disturbances [30,31]. It has been suggested that the onset of nonlinear disturbance growth behavior for fluid sheets without imposed disturbances begins whenever a collection of modes, over a specific small region of wave number space, becomes comparable in amplitude to the wavelength. The flow field for the fluids evolution investigated in this work contain two interfaces. The stability of thin multiple layer sheets, which contain multiple interfaces, is more complicated than two semi-infinite fluids separated by a single interface due to interface coupling via boundary conditions [14,32,30]. Systems with coupled interfaces lead to unconditionally unstable hydrodynamic instability growth [14]. This phenomenon can lead to linear excitation or freeze-out of modes, which is related to cancellation of growing modes by destructive shock interaction, depending upon geometrical and mechanical conditions [30]. Thus for a given geometry, different wave number perturbations can cause drastically different results. This is especially relevant in this work since the fluid perturbations are not known a priori. Bifurcations in the late time evolution of multi-layer thin sheets have also been demonstrated [33]. Multiple distinct flow patterns can emerge from near identical initial conditions [34,35].

To summarize, in this work a liquid-filled steel target is impacted with a high speed projectile. The target catastrophically ruptures and the fluid is ejected. The initial perturbations applied to the fluid result from the rupture of the steel casing. The fluid then expands in a multiple interface, i.e., upper and lower free surface, divergent flow configuration through a near vacuum environment. Together, the various aspects of this work: impact-loaded, no imposed disturbances and Atwood number near unity, define the work relative to classic hydrodynamic investigations.

3 Computational Approach

Two computational codes, CTH and CFDlib were used to model the experiments presented in this work. The following is a brief description of each code.

3.1 CTH Hydrocode. In order to model the projectile/target impact as well as the resulting liquid evolution and radial expansion velocity, the computational hydrocode, CTH, was used [36]. The CTH algorithm, developed by Sandia National Laboratory, is a finite volume numerical approach utilizing a combination Eulerian/Lagrangian formulation. The computational domain is discretized into an Eulerian structured grid and the conservation equations are advanced in time using a Lagrangian step, i.e., the grid is allowed to deform. At the end of the time step, the state variables are mapped back onto the fixed Eulerian grid. CTH is a fundamental physics solver in that it simultaneously solves conservation equations of mass, momentum and energy, Eqs. (1)–(3)

$$\text{Mass:} \quad \frac{\partial \rho}{\partial t} + \nabla \cdot (\rho \vec{V}) = 0 \tag{1}$$

$$\text{Momentum:} \quad \left(\frac{\partial \rho \vec{V}}{\partial t} + (\vec{V} \cdot \nabla) \cdot \rho \vec{V} \right) = \rho \mathbf{g} - \nabla P + \nabla \cdot \vec{\tau}_{ij} \tag{2}$$

$$\text{Energy:} \quad \left(\frac{\partial \rho \hat{u}}{\partial t} + (\vec{V} \cdot \nabla) \cdot \rho \hat{u} \right) + P(\nabla \cdot \vec{V}) = \nabla \cdot (k \nabla T) + \Phi \tag{3}$$

In order to obtain closure, several material equations of state (EOS) models and constitutive relations are available. For all of the tests presented here, unless otherwise specified, the following Mie-Gruneisen [37] equation of state was used

$$P(\rho, E) = P_H(\rho) + \Gamma(\rho)\rho[E - E_H(\rho)] \tag{4}$$

Table 1 Equation of state and constitutive input parameters

	TBP	Steel	Aluminum
Density, ρ (g/cm^3)	0.972	7.9	2.796
Sounds Speed, C_s (cm/s)	1.39×10^5	4.57×10^5	5.328×10^5
Gruneisen Parameter, Γ	1.6	1.93	2
U_s-u_p slope, s	1.0	1.49	1.338
Specific Heat, C_V (cm^2/s^2 eV)	2.1×10^{11}	5.180×10^{10}	1.07×10^{11}
Yield strength, (dynes/cm^2)	0	12.0e9	4.00e9
Poisson's ratio	0.5	.379	.330
Fracture strength, (dynes/cm^2)	-0.5×10^3	-17×10^9	-4.82×10^9

$$E(\rho,T) = E_H(\rho) + C_V(T)[T - T_H(\rho)] \tag{5}$$

where $\Gamma(\rho)$ is the Gruneisen parameter, C_V is the specific heat and T_H, E_H, and P_H, the temperature, internal energy and pressure, respectively, correspond to a reference state. For the Mie-Gruneisen equation of state, the reference state lies on the Hugoniot which is defined as follows:

$$\mu_\nu = 1 - \frac{\rho_0}{\rho} = \frac{u_P}{U_s}$$

$$P_H = P_0 + \rho_0 U_s u_P$$

$$E_H = E_0 + \frac{u_P^2}{2} = E_0 + (P_H + P_0)\frac{\mu_\nu}{2\rho_0}$$

Here the material particle velocity is u_p and the shock velocity is U_s. The initial state is denoted with a subscript zero.

The parameters which define the reference states for the calculations performed in this investigation are listed in Table 1. Where stated, a tabular equation of state was used to model the working fluid. This tabular equation of state was developed for this test series at Applied Research Associates Southwest Division (ARA/SWD) in conjunction with Sandia National Laboratory [38,39]. Tabular equations of state, often called sesame tables, are advantageous in that they can contain numerous models simultaneously for various phases of the material. Phase change or chemical reactions are difficult to model with analytic expressions such as the Mie-Gruneisen equation of state. The sesame table EOS utilized in these calculations includes an Arrhenius Reactive Burn (ARB) model which allows for chemical effects such as deflagration and disassociation.

Regardless of the equation of state selected, the material strength is modeled with an elastic, perfectly plastic, stress-strain relationship with a von Mises yield surface with thermal softening and density degradation.

The strengths of the CTH algorithm lie in its ability to simultaneously evolve dynamic phenomena involving multiple materials with various equations of state, to capture large scale material deformation, and to track shock wave propagation generated from impact phenomena. The weakness of CTH, especially notable for this class of problems, lies in its inability to model the constitutive relations necessary for viscous fluid flows or include the effects of surface tension and drop formation. The CTH code is a highly evolved code that has a long pedigree in this class of problems involving impacts and wave propagation [36].

3.2 CFDlib Hydrocode. In order to model the fluid-structure interactions the computational fluid dynamics code CFDlib was used [40]. CFDlib, i.e., computational fluid dynamics library, developed at Los Alamos National Laboratory was used to perform the late time fluid slit-plate iterations. CFDlib, an arbitrary Lagrangian-Eulerian (ALE) solver, is capable of solving a wide range of computational fluid dynamics (CFD) problems in two or three space dimensions. The CFD libraries are related to one another by virtue of a set of common features. These include the use of finite volume computational schemes in which all state variables are cell-centered; a multi-block data structure that enables highly efficient processing on modern supercomputers; and an ALE split computational cycle. All flow speed regimes are accessible within the library, ranging from fully incompressible to hypersonic; and code volumes exist that enable multi-fluid and multiphase computations with an arbitrary number of fluid fields, each with their own set of conservation equations, Eqs. (1)–(3). The property values used for the calculations presented here are listed in Table 2.

Table 2 Physical properties used in CFDlib calculations

Property[a]	TBP	Steel	Air
Modulus of elasticity (g/cm ms^2)	-	750000	-
Poisson's ratio	-	0.3587	-
Yield strength (g/cm ms^2)	-	3650	-
Hardening modulus (g/cm ms^2)	-	375000	-
Density (g/cm^3)	0.9982	2.785	0.001
Speed of sound (cm/ms)	148.5	532.8	34
Hugoniot slope	1.921	1.338	0
Gruneisen's gamma	0.35	2.0	0
Specific heat (cm^2/ms^2 K)	14.03	1.070	41.87
Kinematic hardening factor	-	0.5	-
Critical equivalent plastic strain	-	0.008	-
Softening modulus (g/cm ms^2)	-	1×10^{100}	-
Von Mises yield condition	-	0	-
Reference temperature (K)	300	300	300
Reference pressure (g/cm ms^2)	1.01325	1.01325	1.01325
Viscosity (cm^2/ms)	9.838×10^{-6}	-	-

[a]All properties are in centimeter-gram-millisecond-bar-K units.

Notice that some of the values listed for the TBP in Table 2 differ from those listed in Table 1. This was done in order to account for the various flow regimes in which these codes are used. CTH was used mostly in the initial impact and shock regime whereas CFDlib was used in the late time low pressure regime.

The strengths of the CFDlib algorithm lie in its ability to simultaneously evolve dynamic phenomena involving multiple materials with various equations of state and various constitutive relations, in order to capture large scale material deformation. The CFDlib code has the advantage over CTH in that constitutive relations for Newtonian fluids are incorporated. However, CFDlib is not especially adept at evolving shock driven flow fields with extremely high pressure such as those generated by high velocity impact.

3.3 Calculations Performed. All of the calculations presented here were three-dimensional simulations unless otherwise indicated. For the majority of the calculations presented in this paper, the Eulerian mesh spacing was $\Delta x = 0.1$ cm. Geometrically, the exact target and projectile geometries were modeled, see Fig. 1. Thus for the impact problem investigated here, the initial conditions are simply an aluminum sphere traveling at a given velocity impacting a steel cylinder containing a liquid. The boundary conditions for all of the calculations were input/output, meaning the pressure is zero in the ghost cell and all material is removed upon entering a ghost cell. No mass is allowed to enter the mesh but mass is allowed to leave the mesh.

4 Materials, Specimens, Fabrication, and Test Methods

4.1 Target and Projectile. The target was a right circular cylinder with a cap seam welded to one end. The other end of the cylinder had a removable air-tight seal cover, see Fig. 1. The removable cover was secured to the target via two flange rings; each ring was 0.5 mm thick. The target was 74.42 mm in diameter, 121.39 mm long, and held 530 ml of fluid which was filled under vacuum to minimized dissolved air. The entire target, except for the seal cover flanges, was made of 0.15 mm thick cold rolled 1010 low carbon steel shim stock that was laser seam

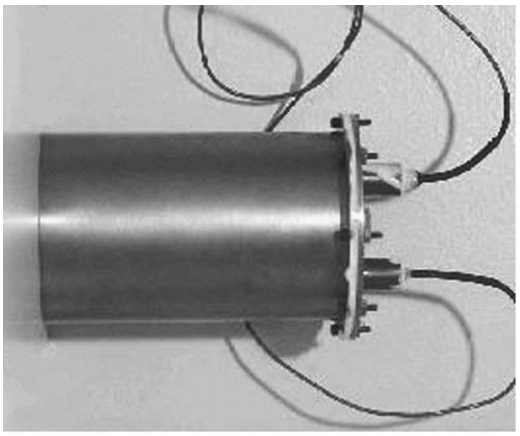

(*a*)

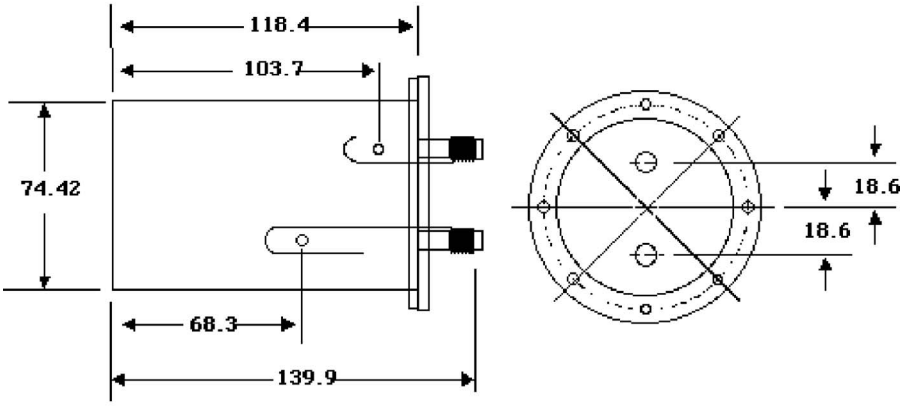

(*b*)

Fig. 1 (*a*) Target filled with 550 ml of TBP and (*b*) schematic of gauge locations

welded. The seal cover flange were made from mild steel. The projectile was a 23.8 mm 7075 aluminum sphere with a total mass of 19 g. The target was instrumented with either zero, one, or two PCB piezotronic tourmaline crystal pressure gauges model number 138M129 [41], as shown in the Fig. 1(*b*). These gauges record pressure-time histories within the fluid during the impact event. It should be noted that the target and the pressure instrumentation suite for each test shot was completely destroyed by the test. The projectile passed completely through the target and was caught by a stop at the rear of the target tank.

4.2 Fluid Fill. The targets were filled with tributyl phosphate (TBP), which has a density of 0.97 g/cc at 25°C and a viscosity of 3.3 centipoises (cp). By adding the copolymer, poly[styrene-butyl acrylate] (PSBA), the fluid viscosity can be increased. For tests using thickened TBP, the fluid is 4.5% PSBA by weight and has a total viscosity of 1100 cp. Both TBP and thickened TBP contained less than 1 percent Mordant Blue #1003 dye for visual contrast. TBP was chosen as the working fluid because of its low vapor pressure and, therefore, would not vaporize under the 1 Torr vacuum within the target tank.

4.3 Experimental Test Setup. Experimental results were obtained at the Aero Research Laboratory (ARL) within the University of Alabama at Huntsville (Fig. 2). The test series was conducted in the ARL's 108 mm two-stage gas gun [42–44]. An illustration of the gun is presented in Fig. 1. The operation of the gun is initiated by igniting the black powder charge, shown in the far left of Fig. 1. The increase in pressure drives the piston down the 108 mm diameter pump tube compressing the medium pressure helium and thereby greatly increasing the pressure in the transition breech. The burst diaphragm ruptures at a specified pressure thereby exposing the projectile to a high pressure driver gas. The transition breech is tapered so that the piston motion is arrested within the transition breech. The projectile then travels down the 30 mm diameter launch tube where it passes a high

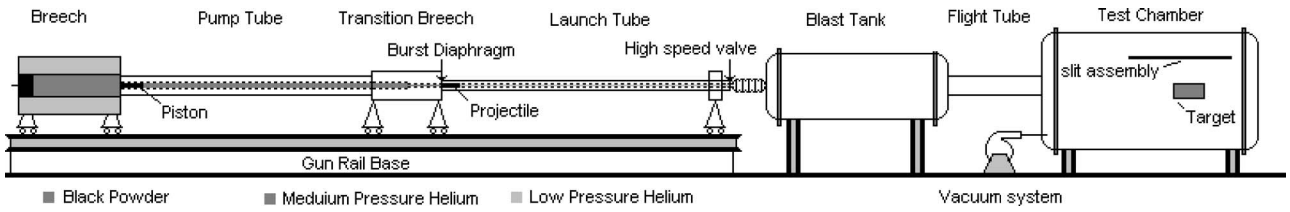

Fig. 2 Two stage gas gun facility at University of Alabama's Aero Research Laboratory

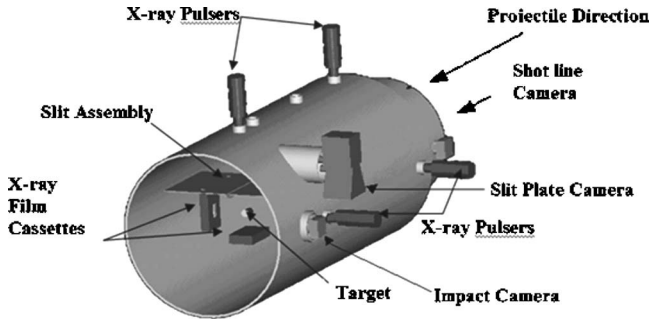

Fig. 3 Schematic of the target tank illustrating the location of the data acquisition equipment

speed valve used to maintain the vacuum pressure in the blast and target tank. The high speed valve is explosively driven to close within 15 ms of the projectile passing. Thus both the blast and target tanks are continuously held below 1 Torr pressure throughout the experiment. Once past the high speed valve, the projectile is then in free flight through the blast and target tank until it strikes the target. The blast tank, approximately 2.5 meters (m) long by 1.5 m in diameter, is used to mitigate any high pressure gas which escapes the high speed valve. In so doing the less than 1 Torr vacuum of the target tank is insured throughout the impact and fluid dispersion event. The two stage design can produce launch velocities of up to six kilometers per second (km/s).

An illustration of the target tank and data acquisition systems are presented in Fig. 3. The target tank is 1.83 m in diameter and 4.3 m long. The target tank can maintain an absolute pressure of less than 1 Torr of a specified gas. The target tank included a slit assembly placed immediately above the target. The slit assembly included a plate which was essentially a 1.27 cm thick 80 cm by 120 cm aluminum plate with a slit cut all the way along the plate aligned with the shot line direction. The slit assembly was in place so that a cross-sectional view of the expanding fluid system could be observed above the slit plate.

4.4 Data Acquisition. In most tests there was a camera looking down range, i.e., the shot line camera, and several cameras looking normal to the shot line, i.e., the slit plate camera and the impact camera. All of the cameras are located outside the target tank. The shot line camera was approximately 3 meters from the impact event and several centimeters from the shot line itself. The normal cameras included one looking directly at the impact event and two cameras placed above the slit plate. The camera looking directly at the impact event, i.e., the impact camera, was approximately 1.15 m from the impact event. The impact camera was placed at the same elevation as the target and perpendicular to the shot line. The slit plate cameras were placed at the same horizontal distance from the target as the impact camera. However, they were elevated vertically by approximately 0.75 m so that they had a view above the slit plate assembly.

All of the cameras were 10,000 frames per second (10 kfps full-frame) Model 3261 HYCAM II 16 mm film cameras, which had a shutter speed of approximately five microseconds. The film used was 7251 Ektachrome. At times the cameras were run in quarter-frame mode so that they could produce images at a rate of 40,000 FPS. All of the high speed photography was flash illuminated with 12 Mega-Flash PF300 slow peak flashbulbs. Once the film was developed it was digitally scanned in order to post-process the images. Accounting for magnification used in these experimental test, the film resolution was 40 μm. For all of the images presented here, except where stated, the camera setup including the digitization process was such that particles as small as 100 micrometer (μm) were visible.

In addition to the cameras, there were two x-ray stations; each station consisted of two orthogonal x-ray pulsers. By having two orthogonal x-ray heads and two separate x-ray stations, the free flight and impact orientation of the projectile and target could be measured. The orientation of the cameras, x-ray heads and x-ray film cassettes can be seen in Fig. 3. One station had a field of view which included the target so that the impact and penetration could be assessed. The second station had a field of view of the projectile before impact so that the pre-impact point could be assessed. Each station consisted of two 20 kV soft x-ray tubes (model HP 130-515300) exposing two film cassettes containing high green emulsion 400 speed film. For the first x-ray station, i.e., the one which included the target, the x-ray cassettes were located within the target tank approximately 0.75 m from the target. The x-ray heads were placed outside the target approximately 1.0 m from the target.

Table 3 Conditions for UAH Test series

Test	Impact velocity (km/s)	Impact point x,y[c] (mm) and orientation	Target tank pressure (Torr)	X-ray timing (μs) (top/side view)
18	2.32[a]	$\cong 0,-1.2$[d]	75 He	N/A
21	2.35[a]	$\cong 0$[d]	4 Air	57.6/61.8
22	2.30[b]	$-12.7,1.3$[d]	4 Air	8.3/12.22
24	2.30[a]	$-7.6,-8.9$[d]	1 Air	40.5/44.5
25	2.30[b]	$4.5,7.1$[d]	<1 Air	24.9/29.1
26	3.20[a]	$1.0,9.1$[d]	1 Air	1.4/5.5
27	2.46[a]	$-0.495,0.178$[d]	0.76 Air	33.6/37.8
28	3.20[a]	$0.6,8.6$[d]	0.65 Air	1.6/5.8
29	4.10[a]	$15.0,-0.9$[d]	0.67 Air	21.2/25.3
31	2.36[b]	$0.6,7.5$[d]	0.83 Air	129.2129.2
32	3.20[b]	$4.4,4.6$[d]	0.73 Air	38.3/38.3
33	2.37[a]	$14.1,11.6$[d]	60 He	106.1/106.1
35	2.33[a]	$1.6,9.8$[e]	0.82 Air	24.9/24.9
36	2.32[a]	$6.7,10.1$[f]	0.81 Air	4.0/4.0
37	3.17[a]	$-0.3,13.4$[f]	0.8 Air	74.9/74.9
40	4.03[b]	$5.6,12.1$[d]	0.75 Air	54.2/54.2
41	2.40[a]	$-5.3,-7.2$[g]	0.77 Air	76.4/76.4
42	2.33[a]	$1.6,5.7$[d]	700 N_2	68/68
43	2.39[a]	$6.7,8.5$[d]	0.18 Air	116.3/116.3
52	2.28[a]	$0.419,0.876$[d]	0.7 He	176/176

[a]Tributyl phosphate (TBP), viscosity ~3.3 cp.
[b]Thickened TBP, viscosity ~1100 cp using copolymer, poly[styrene-butyl acrylate] (PSBA).
[c]Distance from intended hit point. The hit point is the center of the projected area. Positive is up for vertical and right for horizontal.
[d]Axial, see Fig. 4(*a*).
[e]90 deg end up.
[f]90 deg side up.
[g]45 deg end up.

4.5 Test Matrix. The test matrix is presented in Table 3 which includes the impact velocity, target orientation, and the impact point. The test numbering system adheres to the UAH test numbering system [42]. The right handed coordinates for the impact are given in *x-y* space with the origin fixed to the target center and the *z* axis extending along the shot line pointing downrange, see Fig. 4.

5 Test Results

For brevity, only a select few of the test results will be presented here with a discussion of the relevant behavior. The data and analysis will be presented in two sections: Early time and late time fluid impact and expansion. Essentially all of the data collected to an expansion radius of about 12 cm from the shot line or likewise the first 100 μs is early time while any data collected after the fluid passes through the slit plate, at about expansion radius of 48 cm from the shot line, is considered late time. The demarcation is made to distinguish between shock driven phenomenology and hydrodynamic free flight phenomenology.

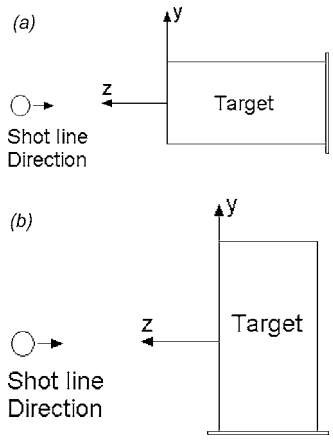

Fig. 4 Projectile and target orientation illustrating coordinate system for the impact point listed in Table 3. (*a*) Axial projectile target orientation. (*b*) 90 deg end down projectile target orientation.

5.1 Early Time: Expansion Geometry. After reviewing all of the film photography it was evident that the liquid did not immediately breakup into a wide distribution of drops with varying droplet velocity as anticipated. Instead, in early time, the liquid was contained in a relatively thin oblate spherical shell. The state of the liquid within the shell, including the porosity, is difficult to assess.

Figure 5 presents a series of photographs taken looking down the shot line for test #40 which was in the configuration illustrated in Fig. 4(*a*). The timing marks below each photograph are relative to impact at time zero. As was typical for all the test, the fluid expanded in a nearly symmetric radial pattern about the shot line when viewed looking down the shot line. In Fig. 5(*b*), a fluid jet or spike can be seen at approximately 12:30 along the outside of the expanding fluid shell. This fluid jetting is a result of the ullage in the target. The jet was offset from vertical due to the impact point error for this shot, see Table 3. The projectile completely penetrates the target and thus the expanding shell is left hollow. This conclusion is supported by hydrocode calculations presented in Sec. 5.2 and photographs presented in Sec. 5.5.

Figure 6 is a side on view of the same test presented in Fig. 5, although each frame is not necessarily at the same instant in time. In Fig. 6, the projectile traveling horizontally enters the target moving from right to left. The fluid body can be broken into two distinct sections: The main body and the splash back. The main body or bulk of the fluid expands in an oblate spheroid, while a portion of the fluid splashes back to the right, i.e., up the shot line. The splash back fluid appears to readily break up into stringers and then drops, much like one would expect from a Rayleigh crown. These stringers and drops moving back along the shot line can be seen in Fig. 5(*b*) as a ring of lighter colored fluid. One major difference between the main body and the splash back region is that, unlike the splash back region, the main body's free surface appears relatively smooth. There are no large scale discernable instability spikes growing on the fluid's main body. None of the early time photographic evidence from any test shot demonstrated stringer or drops emanating from the main body in the early time scale.

For tests in which the target axis was aligned with the shot line, i.e., Fig. 4(*a*), the steel target ruptures in long strips along the target shot line axis, much like one would peel a banana. Although the formation of these strips is not entirely visible in these photographs, these strips were recovered after each test, see Sec. 5.8. These metal strips, or more specifically the gaps between the strips, define the initial conditions for the expanding fluid sheet. The target debris is presented in Sec. 5.8.

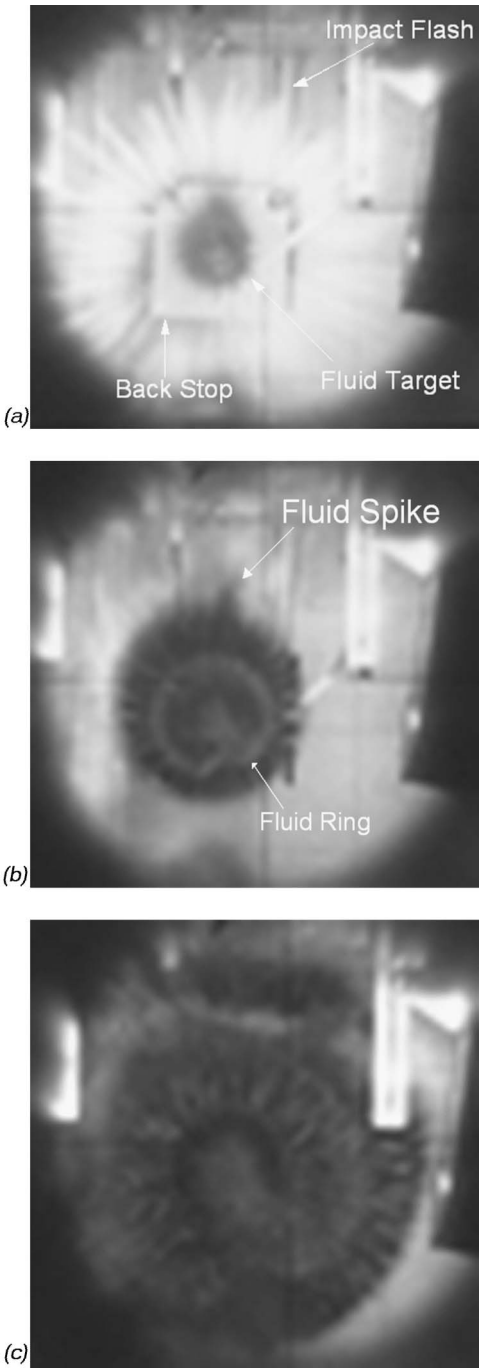

Fig. 5 Shot line view demonstrating radially symmetric fluid expansion, test #40; (*a*) time ≈70 μs, (*b*) time ≈200 μs, and (*c*) time ≈305 μs

5.2 Early Time: X-ray Photography. Figure 7 presents three x-ray images of the target from three separate tests as well as a corresponding CTH hydrocode simulation. In these x-ray images, the projectile, traveling horizontally, entered the target moving from left to right. The fragmentation of the solid target case, the penetration and fragmentation of the projectile and the early time shape of the expanding fluid can be identified in these x-rays images. In Fig. 7(*a*), the deformed projectile and the bow shock can be seen as well as a distinct division of material: Steel target membrane, aluminum projectile, TBP fluid. The darker material, i.e., higher density, is the steel container while the lighter material is fluid. Although some material is ejected rearward toward the

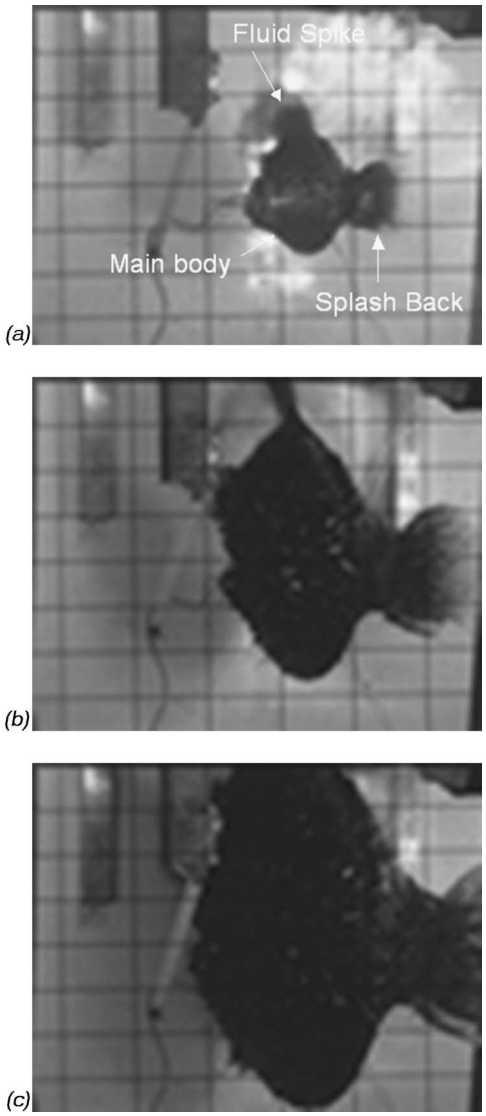

Fig. 6 Downrange view, projectile moving right to left, test #40; (*a*) time ≈70 μs, (*b*) time ≈200 μs, and (*c*) time ≈305 μs

direction of the shot, i.e., the splash back seen in Figs. 5 and 6, the majority of the fluid expands spherically/cylindrically, normal to the shot line and forms the main body of the oblique spheroid. In Fig. 7(*b*), the steel fragments from the target case can be discerned, thus a representative fragment size can be determined and compared with theoretical results [45,46]. In addition, one can identify the projectile although it has fractured. In Fig. 7(*c*), the maximum expansion radius presented, there is still no visible sign of fluid instabilities on the fluids main body. At this point, the fluid has expanded to a radius of 7.5 cm measured from the centerline of the target but yet the surface of the expanding cylinder remains smooth. The steel fragments can be identified as strips aligned with the shot line. The CTH calculations presented in Fig. 7 capture the main features of the flow: The depth of penetration, bow shock distance, expansion radius, etc. A more direct comparison of the CTH calculations and the experimental results is presented in Sec. 5.3.

5.3 Early Time: Expansion Geometry and Velocity. Dimensional measurements of the projectile penetration and target expansion were taken from all of the early time digitized x-rays in this test series. Figure 8 presents the nomenclature for the dimensional variables.

Dimensionless parameters were formed from the geometric variables presented in Fig. 8 so that all the test results could be compared simultaneously. Figure 9 presents the dimensionless parameters characterizing the target penetration and expansion. Figure 9(*a*) presents the dimensionless location of the maximum expansion diameter variable, l_d/D as a function of projectile penetration depth, $(L-l)/L$, where l_d is the location of the maximum expansion diameter, D is the maximum expansion diameter, l is the depth of penetration, and L is the original target length. The CTH calculations have been plotted alongside the experimental data for comparison. Aside from a qualitative comparison, these calculations demonstrate, in a quantitative way, the ability of CTH to predict the penetration and expansion of the engaugement in early time. The relationship between the penetration and expansion of the fluid does not appear linear but parabolic.

It is interesting to note that all of the test data appears to lie on one single curve. Thus, variations within the test series had minimal effect on the early time penetration/expansion relationship [47]. Namely, the viscous effects and external ambient pressure in this early stage of the engaugement are negligible and that nondimensional expansion velocity scales with nondimensional engaugement velocity. This implies that the underlying expansion of the target is hydrodynamic, self-similar and that the expansion can be collapsed onto a single growing shell.

5.4 Early Time: Pressure Trace Data. In order to capture the pressure time history, a maximum of two tourmaline pressure gauges, a long gauge and a short gauge, were inserted into some of the targets, see gauge description above. The pressure data was simulated with CTH via a computational Lagrangian tracer placed at the location of the tourmaline crystal. Thus the pressure calculated by CTH at the tourmaline sensors can be directly compared to the pressure traces recorded in the experiments. Two CTH simulations were performed for each test: One in which the entire gauge geometry was placed in the computational domain with the tracer and one in which only the tracer was placed in the computational domain. Thus the computational effects of the gauge presence (i.e., impedance mismatch, mixed cell effects, etc.) could be assessed. The results of both of these simulations are compared to the experimental pressure traces and are presented in Fig. 10. The calculations in Fig. 10 were performed using the Mie-Gruneisen equation of state described by Eqs. (4) and (5). Note that time zero corresponds to impact.

The initial pressure generated by an aluminum projectile striking a steel target, i.e., the Hugoniot pressure, is 697.5 kbar. By the time the shock has reached the long gauge the peak shock pressure has attenuated to approximately 10 kbar, see Fig. 10(*a*). For all of the calculations, CTH slightly under predicted the peak pressure. The CTH pressure trace waveform, i.e., the peak pressure, the shape of the shock as well as the decay, which did not include the gauge geometry more closely resembled the experimentally measured pressure waveform as compared to the calculated pressure trace waveform which did include the gauge geometry. The inclusion of the gauge geometry within the CTH calculations resulted in spurious pressure fluctuations. This is possibly due to the impedance mismatch of the various materials and/or mixed cell EOS errors.

The shock wave arrival time for all of the CTH calculation lagged the experimental results. The shock wave arrival time was measured at 2% of peak pressure. The error associated with the experimental measurement of arrival time is ±1 μs. The difference in arrival time between the CTH calculations with the long gauge and experiment, and short gauge and experiment was 2.1 and 2.5 μs, respectively. However these differences are rather arbitrary since the exact impact time for the experiments is unknown to ±1 μs. By calculating the difference between the arrival time between the two gauges as compared to the CTH calcula-

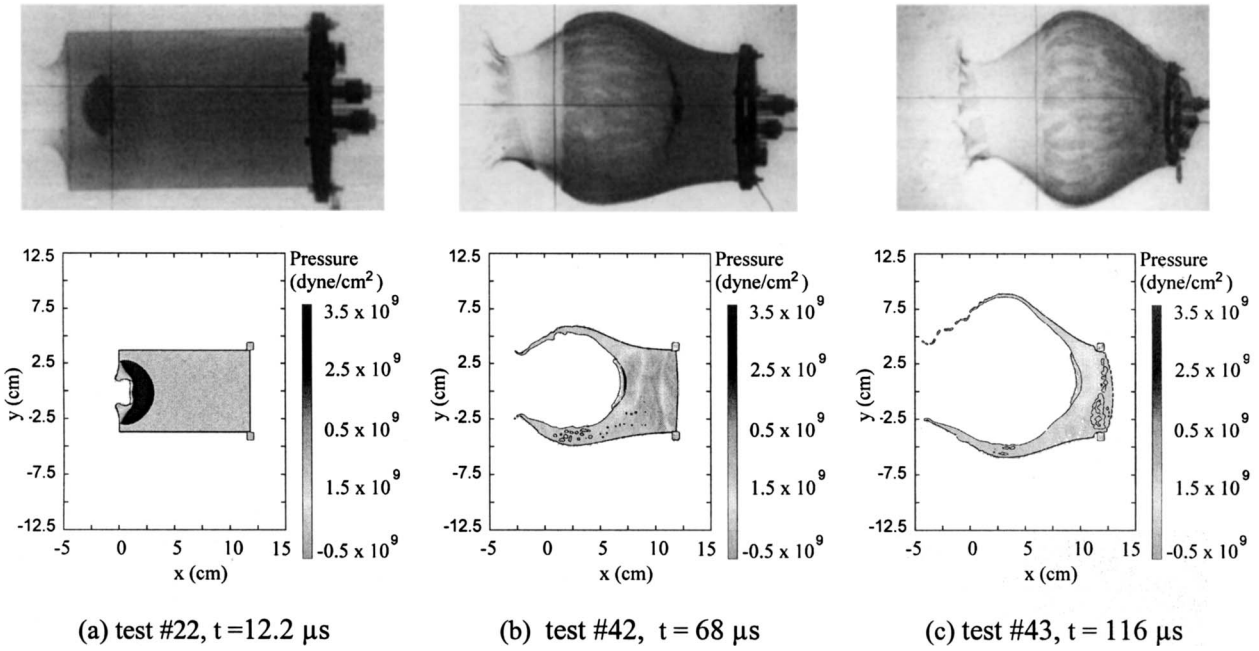

Fig. 7 X-ray images of target response as compared to CTH calculations. (*a*) test #22, *t*=12.2 μs, (*b*) test #42, *t*=68 μs, and (*c*) test #43, *t*=116 μs.

tions, the error associated with the measurement of the experimental impact time is eliminated. Essentially if we shifted the arrival time of the computational data such that it matched that of the experimental data then we would eliminate the experimental error associated with measuring the impact time. Thus the difference in the arrival times between the experimental and computational short gauge is a better indicator of the error associated with the computational shock propagation speed. The difference between the error in arrival time between the long gauge and the short gauge (i.e., $|2.1-2.5|$) was 0.4 μs; this is a relatively small error. Thus if one assumes the wave forms and their arrival times are accurately recorded in the experiment (i.e., neglecting dynamic effects of the gauges), the 0.4 μs error is a measure of the error associated in propagating the compressive wave through the material and is therefore a measure in the error of the EOS. This error could come from either an error in the magnitude of the measured sound speed of the TBP or an error in the Hugoniot slope used in the Mie-Gruneisen equation of state.

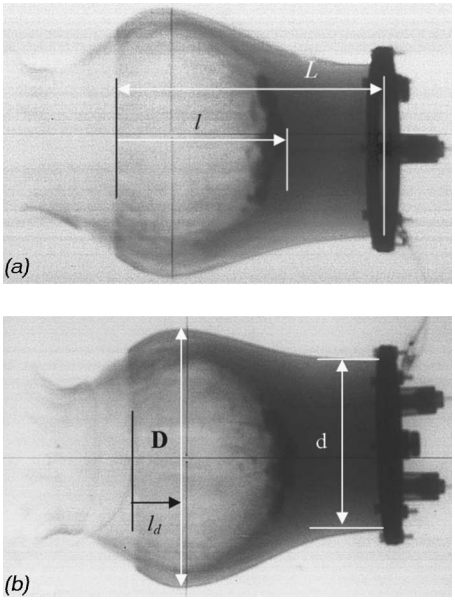

Fig. 8 Post impact x-rays illustrating dimensional variable nomenclature for test # 21 (*a*) Top view, *t*=57.6 μs; (*b*) Side view, *t*=61.8 μs

In addition to the Mie-Gruneisen equation of state, a tabular form of the equation of state, or sesame table, was used for the TBP in order to calculate the pressure time traces, see Sec. 3.1 for an explanation of tabular equations of state. The CTH pressure traces presented in Fig. 10 where recalculated using the reactive sesame EOS and the results are presented in Fig. 11. The sesame EOS slightly increased the computational peak pressure to be closer to that of the experimentally measured peak pressure. However the sesame EOS increased the lag in the arrival time as compared to the Mie-Gruneisen EOS. Since the general wave form, especially the slope in the release pressure for both computational EOS's, where not altered by including the chemical effects included in the Sesame EOS it is concluded that the pressures generated by this impact event where not sufficiently high to initiate deflagration or dissociation in the TBP fluid.

5.5 Late Time: Slit-Plate View. Within the target tank there was a slit-plate assembly positioned as shown in Fig. 3 along with a high speed camera to view the fluid after it passed through the slit. This plate was installed in order to view a cross-section of the expanding fluid shown in Figs. 5 and 6. The slit, which was 1.2 cm wide and approximately 120 cm long, was aligned with the shot line so that a longitudinal slice of the expanding fluid could be photographed. Thus the fluid leaves the top of the frame in Fig. 6(*c*), passes through the slit plate and is again photographed. Figure 11 is a collection of eight digitized photographs of the fluid directly above the slit plate filmed from the side (i.e., the same view in Fig. 6). The slit plate camera has a field of view (FOV) of 8 mm $\times$ 43 mm filmed at a rate of approximately 40,000 frames a second or 40 kfps. The effective resolution, after the film has been digitized, is 100 μm. At first glance, the structure moving from the bottom of the frame to the top of the film appears to be a continuous flow of fluid approximately 9 mm thick. At this resolution, digital analysis would be able to resolve 100 μm diameter drops should they exist. No distinguishable drops of this size or greater were observed. If the dark structure in the frames is

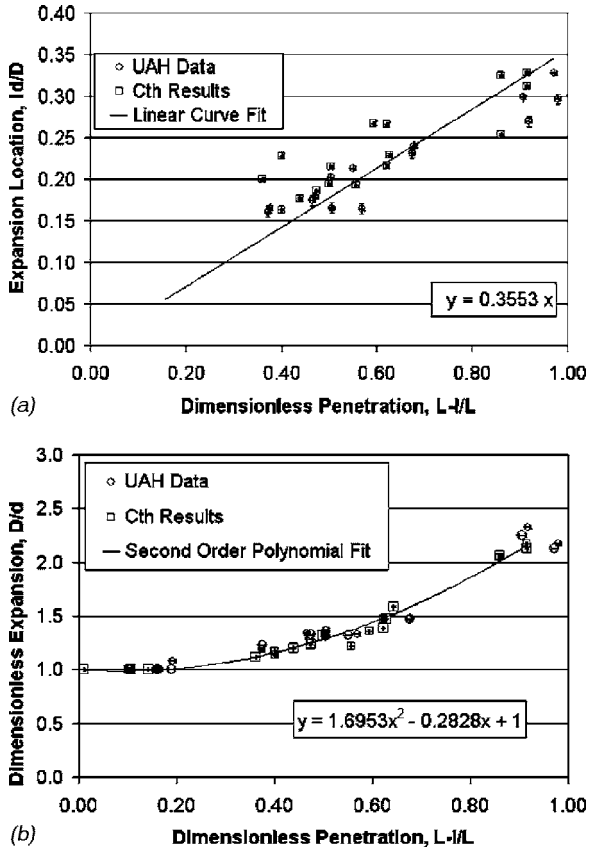

Fig. 9 Early time dimensionless parameterization for all the experimental test as compared to CTH calculations. (*a*) Dimensionless location of maximum expansion diameter. (*b*) Dimensionless radial expansion.

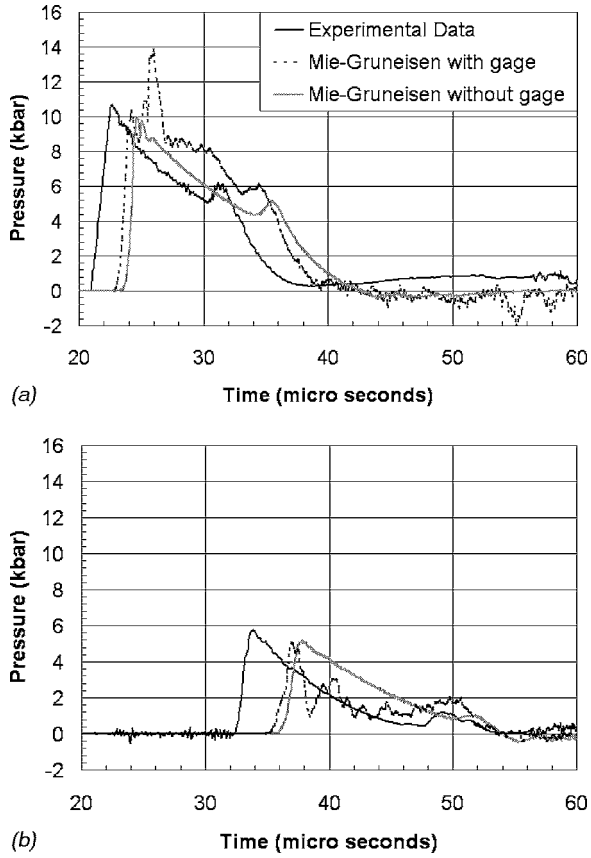

Fig. 10 Experimental and computational pressure traces, test #29; (*a*) long gauge and (*b*) short gauge

assumed to be a continuous fluid, it takes approximately 4.5 frames for the top of the fluid to traverse the frame from top to bottom. Thus the fluid expansion velocity above the slit plate is 372 m/s±50 m/s which resulted from an impact velocity of 2300 m/s. This assumes the measurement error to be 0.5 frames and the frame rate of the camera to be 39 kFPS for this specific section of film.

In order to obtain a more comprehensive image of the fluid dispersion, the FOV of the slit camera in Fig. 12 was increased to 245 mm×178 mm. The camera frame rate was changed to 10 kFPS and a resolution of 1 mm. The resulting images for four separate tests are presented in Fig. 13 for comparison; the parameters varied in each test are summarized below each image. The center point of the photographs presented in Fig. 13 was, on average, 52 cm above the shot line of the projectile. The target-slit plate alignment was such that the bulk of the fluid traveling up would impact the plate and come to rest, while a cross-section of the fluid would pass through the slit. In so doing a cross section of the expanding fluid in Figs. 5 and 6 could be viewed. This view allows one to assess the growth of the instabilities in the exterior and interior of the target. The effect of the slit plate on the fluid will be discussed in greater detail later in the paper.

It is evident from the photographs in Fig. 13 that a different phenomenology is at work in each test. In Fig. 13(*a*) the liquid remains intact; the shell is thin and continuous with slight long-wave varicose disturbances, as compared to the sheet thickness. In Fig. 13(*b*) there is a high amplitude shortwave or spike structure present, most prevalent on the underside, i.e., inside, the fluid spheroid. These spikes have grown quite large, orders of magnitude larger than the thickness of the fluid sheet. Thus if this flow is governed by a hydrodynamic instability such as Richmyer-Meshkov (RM) then this flow could be assumed to be well within the nonlinear growth regime. In Figs. 13(*c*) and 13(*d*) the atmospheric pressure within the target tank is increased, thus the Atwood number is decreased slightly, as compared to Fig. 13(*b*). The effects of increasing the ambient pressure are not conclusive. As the ambient pressure is increased, i.e., slight decrease in Atwood number, the length scale of the disturbances on the fluid spheroid changes dramatically. In Fig. 13(*c*), the spheroid exhibits longer wave, lower amplitude, disturbances as compared to Fig. 13(*b*). When the Atwood number is decreased again slightly, Fig. 13(*d*), a completely different disturbance structure dominates the flow. The fluid appears to have completely broken up; the fluid shell is no longer intact as compared to Fig. 13(*a*). In fact Fig. 13(*d*)

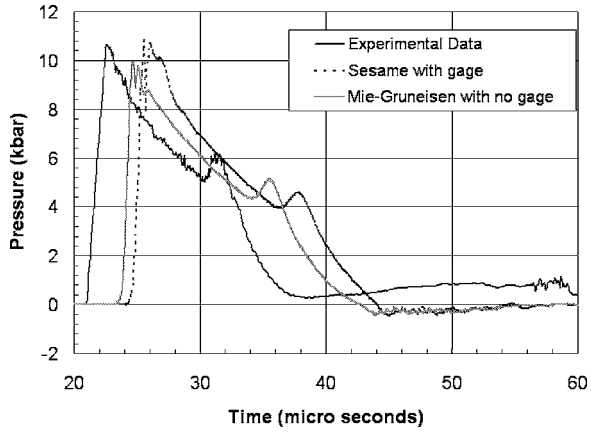

Fig. 11 Experimental and computational pressure traces with an Arrhenius Reactive Burn model: Long gauge test #29

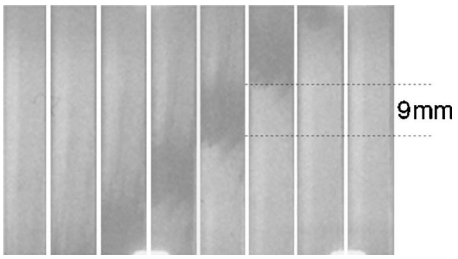

Fig. 12 Eight consecutive images of the fluid shell taken from above the slit plate for test #24. The fluid is traveling from the bottom of the frame to the top.

should not be classified alongside Figs. 13(*b*) and 13(*c*) because the fluid in Fig. 13(*d*) is no longer confined to a thin liquid sheet. Instead it is a near continuous spray of fluid.

All four images in Fig. 13 have the same initial conditions with the only variation being viscosity and ambient target tank pressure, i.e., Atwood number. Yet each image displays dramatically different phenomenology. Large changes in the evolution of the flow with no change in initial condition were also observed by Jacobs in similar fluid expansion type problems [34,35].

Consider Figs. 7 and 13 together. In Fig. 7, at an expansion radius of approximately 7.5 cm, the surface of the fluid main body remains smooth at early time. This is in great contrast to Fig. 13 at approximately 52 cm. Here clearly the surface is exhibiting disturbances which exceed the fluid thickness. Thus one would conclude that even though variations in initial conditions produces no dramatic effect on early time expansion, there is a dramatic difference in late time fluid evolution as a result of variations in initial conditions. At the end of the early time expansion process CTH demonstrates that the shock behavior has attenuated. Thus one could conclude that the mechanisms which lead to fluid breakup of impacted fluids in vacuum are long time hydrodynamic effects not short time shock effects.

5.6 Fluid-Slit Interactions. In order to better understand the physical geometry of the fluid in Fig. 13 and the effect of the interaction between the fluid and the slit plate, the following analysis was performed. Initially successive images from the film taken above the slit plate were digitized so that the fluid velocity and thickness could be measured. Figure 14 presents the measured shell thickness distribution as a function of original target length, i.e., in the negative z-direction see Fig. 4(*a*). At 4 cm along the target axial location, the conservation of mass predicts thickness of the fluid spheroid to be approximately 6.98 mm. From Fig. 12 the measured fluid thickness, was approximately 9 mm in Fig. 12, in Fig. 14 the measured fluid thickness is approximately 8 mm. Thus measured fluid thicknesses are larger than what is allowed via conservation of mass. In order to understand this discrepancy the fluid-slit interaction was numerically simulated CFDLib [40].

Figure 15 presents a CFDlib calculation simulating the fluid passing through the slit plate. In this figure the fluid is traveling from the bottom to the top of the frame. The fluid, represented by Lagrangian particles, is initially confined to the 4 mm Eulerian mesh as indicated in the figure. The fluid is then given a y-velocity of approximately 505 m/s and allowed to impact the slit blades and pass through the slit plate. Upon impact, the slit blades are bent outward and the fluid is elongated. As the fluid passes through the slit plate, it can be radially elongated approximately three times the original thickness as seen in Fig. 14(*b*). Thus the computational thickness of the shell appears to be 11.5 mm. In all of the tests, the fluid which is photographed above the plate appears to be slightly thicker than would be predicted by simple conservation of mass. It should be noted that it is exceedingly difficult to measure thickness from the digitized film to a high degree of accuracy owing to difficulty associated with locating the edge of the fluid. It is also difficult to assess the opaqueness of the fluid when it is elongated.

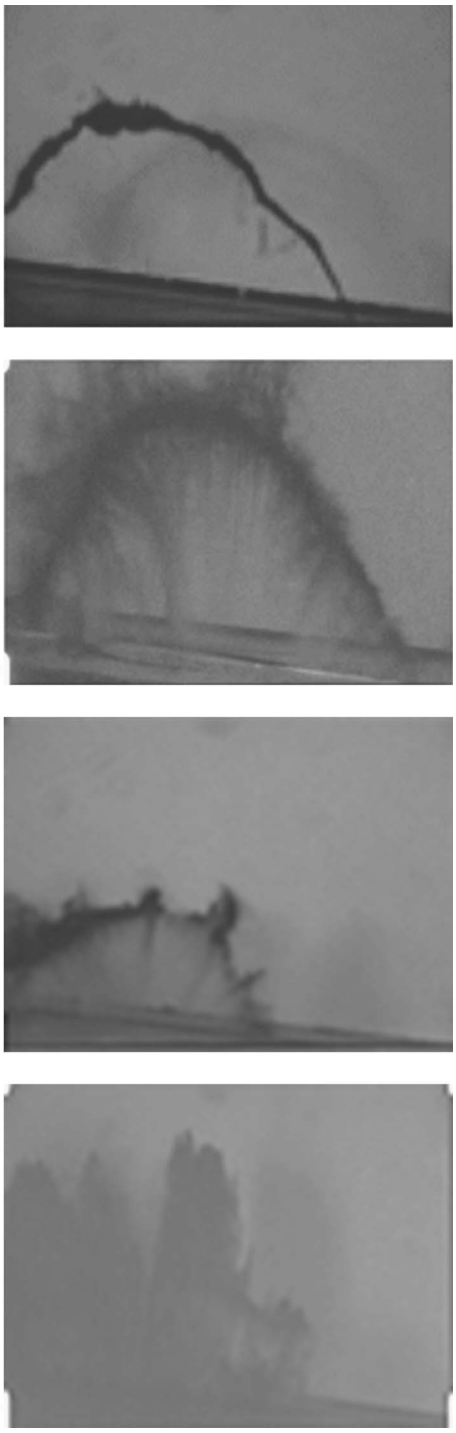

Fig. 13 Results of four test shots each represents different phenomenology for different fluid properties given identical initial conditions

5.7 Late Time: Expansion Velocity. The fluid expansion velocity after it passed through the slit plate was measured from the digitized film from the cameras placed above the slit plate. Not all tests had cameras above the slit plate, thus not all tests have late time expansion velocity data. Figure 16(*a*) compares the experimentally measured expansion velocity for several tests plotted against original target length, see Fig. 4(*a*) for nomenclature. Fig-

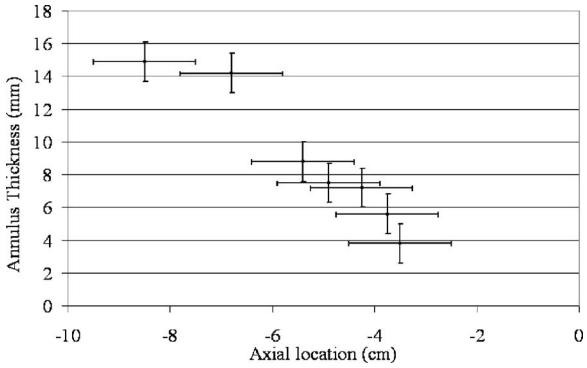

Fig. 14 Measured fluid thickness as seen in Fig. 13(*b*), test #27

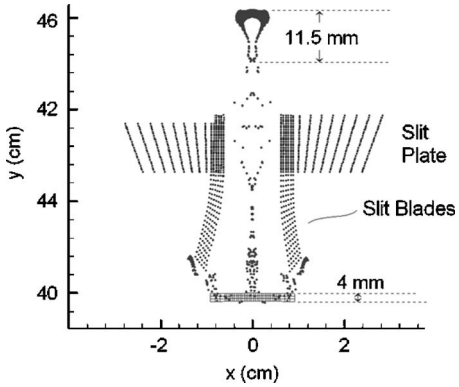

Fig. 15 Computational simulation of fluid passing through slit plate. The effect of the slit plate on the fluid, specifically an increase in apparent fluid thickness, is calculated for test #27.

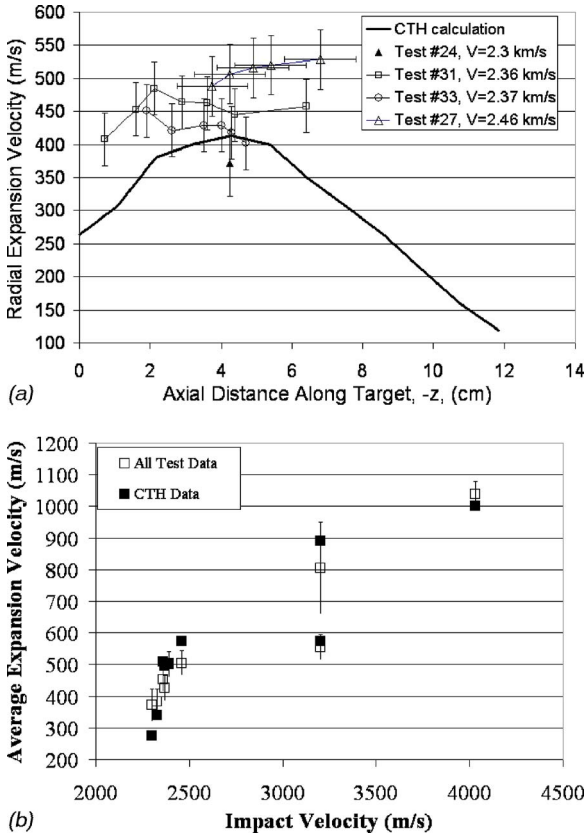

Fig. 16 Late time average fluid velocity after passing through slit plate; (*a*) axial velocity distribution and (*b*) Average expansion velocity

ure 16(*a*) includes all axial impact tests with above the slit plate velocity data with an impact velocity near 2.35 km/s. In addition, Fig. 16(*a*) includes a corresponding CTH calculation for an impact velocity of 2.35 km/s and zero impact error, i.e., the projectile impacted at location $(x,y)=(0,0)$. The CTH calculation under-predicts the experimentally measured expansion velocities for tests 27, 31, and 33 and over-predicts the expansion velocity for test 24. The reason for this discrepancy can be understood by considering the actual projectile impact point, see Table 3. Since the slit is located directly above the target in the *y*-direction, an offset in the projectile impact point in the *y*-direction would increase the fluid expansion velocity as compared to an impact point located at $(x,y)=(0,0)$. Thus for tests 27, 31 and 33, the impact point is offset in the positive *y*-direction causing an increase in the positive *y*-direction expansion velocity. For test 24, the impact point is offset in the negative *y*-direction which causes a decrease in the positive *y*-direction expansion velocity.

Figure 16(*b*) presents the average expansion velocity results for all of the tests in this test series. The average expansion velocity is obtained by averaging the radial expansion velocity, as presented in Fig. 16(*a*), along the target axis. Thus each test produced one average expansion velocity at late time. In addition to the experimental results, Fig. 16(*b*) presents the average expansion velocity as calculated with CTH. In these CTH calculations the impact point for each test was taken into account as an initial condition. Thus, CTH predicts the average radial expansion velocity within the experimental uncertainty when the impact point is considered.

As noted before, it is difficult to measure the shell thickness and velocity because of the diaphanous liquid above and below the fluid and selecting the proper level of intensity threshold for the digital images. Table 4 summarizes all of the axial impact test data which were suitable for velocity calculations.

5.8 Target Tank Damage. Before each test the target tank was marked with a grid. After each test, the projectile and target tank debris were collected. From post impact reconstructions of the target, it was evident that the target had ruptured in strips aligned to the target axis. Figure 17 is a photograph of the debris collected from the highest and lowest impact velocities in this test

Table 4 Summary of experimental determined expansion velocities

Test #	Impact velocity (km/s)	Impact orientation	Fluid viscosity (cp)	Test chamber pressure (Torr)	Expansion velocity (m/s)	Computational expansion velocity (m./s)
27	2.46	axial	3.3	0.76	505±40	575
28	3.2	axial	3.3	0.65	806±145	890
31	2.36	axial	1100	0.83	454±40	510
32	3.2	axial	1100	0.73	555±40	575
33	2.37	axial	3.3	60	425±40	495

Fig. 17 Post impact debris. In each image, the target debris is presented on the left and the projectile debris is presented on the right. (*a*) Test #22, Impact velocity 2.2 km/s. (*b*) Test #29, Impact velocity 4.1 km/s.

series, respectively. As can be seen, the target catastrophically failed as a result of the impact. In general, as the impact velocity increased, the average fragment size from the target decreased.

The surface of the target, i.e., the steel skin, is very thin as compared to the diameter and axial length of the target and the diameter of the spherical projectile. The skin of the target is constructed of 1010 steel, 0.15 mm thick. Typical shock pressures generated by impact were on the order of hundreds of kbar, specifically for test #29 with an impact velocity of 4.1 km/s the shock pressure generated by impact, i.e., the Hugoniot pressure is 365 kbar. The shock attenuates as it travels through the target and as the target ruptures and expands. Towards the rear of the target the shock pressure has reduced to approximately 6 kbar, see Fig. 10(*b*). Since the yield strength of the 1010 steel is approximately 3 kbar the entire target will rupture as the first shock wave passes through the target. Since the target skin is thin, the horizon time for the fracture event is very short; in other words, it will take approximately 22×10^{-9} s for the target to fracture. The relative effect of the target on the shock wave and on the initial fluid motion is therefore minimized. CTH calculations with and without the target skin produced the same average fluid expansion velocity, Fig. 16(*b*), and pressure time traces, Fig. 10.

6 Summary and Conclusions

From the data collected in this test series along with the computational analysis, the following conclusions can be made:

(1) From the data presented here it is concluded that the computational code CTH accurately predicts the early time (i.e., the first 100 μs) liquid impact event. The computational early time fluid expansion can accurately reproduce the experimental results by treating the fluid as an inviscid, elastic-perfectly plastic material with a simple Mie-Gruneisen equation of state. The computational simulations accurately predict the shock pressure, mass distribution and expansion velocity.
(2) The impact and expansion event produces a smooth fluid shell in early time. Rapidly growing disturbances are not observed within the first 100 μs after the impact event.
(3) In early time, variations in the EOS had little effect on the bulk fluid expansion process. Variations in viscosity and chamber pressure did not alter the early time expansion behavior. In fact all of the data could be collapsed onto a single self-similar curve.
(4) In early time, the bulk liquid TBP when impacted by a high speed projectile did not immediately fracture into a wide variety of droplets. Instead the liquid appeared to stay together, continuously or discontinuously, in an oblate spheroid expanding shell of fluid, although it is unclear as to the exact state of the post-impact liquid. The breakup mechanism and/or final state drop size is unclear.
(5) At late time, i.e., after 500 μs, CTH accurately predicts the average expansion velocity of the fluid shell. In addition, CTH accurately reproduces the mass distribution and the shell thickness.
(6) At late time, variations in the fluid viscosity and ambient target chamber pressure resulted in large variations in the fluid shell shape and the growth of disturbances. Much like hydrodynamic stability suggests, the growth of disturbances late time is sensitive to initial conditions and is suppressed by increases in viscosity.
(7) Decreasing the ambient target chamber pressure, i.e., increasing the Atwood number, and/or increasing the fluid viscosity decreased the disturbance wavelength.

Acknowledgment

The authors would like to thank the Naval Surface Warfare Center – Dahlgren Division (NSWC-DD) for funding this research in association with the Missile Defense Agency (MDA).

References

[1] Stepka, F. S., and Morse, C. R., 1963, "Preliminary Investigation of Catastrophic Fracture of Liquid-Filled Tanks Impacted by High-Velocity Particles," NASA TN D-1537 Nasa Leis Research Center.
[2] Stepka, F. S., Morse, C. R., and Dengler, R. P., 1965, "Investigation of Characteristics of Pressure Waves Generated in Water Filled Tanks Impacted by High-Velocity Projectiles," NASA TN D-3143 NASA Lewis Research Center, N66-1329.
[3] Morse, C. R., and Stepka, F. S., 1966, "Effect of Projectile Size and Material on Impact Fracture of Walls of Liquid-Filled Tanks," NASA TN D-3627 NASA Lewis Research Center.
[4] Ferguson, C. W., 1966, "Hypervelocity Impact Effects on Liquid Hydrogen Tanks," NASA CR-54852, NASA Lewis Research Center.
[5] Richardson, A. J., and Knepper, J. J., 1970, "Hypervelocity Particle Damage Limits for Pressure Vessels," Space Division North American Rockwell Corporation, SA 500, NAS 9-150.
[6] Whitney, J. P., 1993, "Hypervelocity Impact Tests of Shielded and Unshielded Pressure Vessels," NASA Report JSC 32294.
[7] Schafer, F. K., Schneider, E. E., and Lambert, 1997, "Hypervelocity Impacts on Cylindrical Pressure Vessels—Experimental Results and Damage Classification," Proceedings from ASME-PVP Conference, Orlando, FL, PVP-Vol. 351, pp. 235–244.
[8] Friesen, L. J., 1995, "Hypervelocity Impact Tests of Shielded and Unshielded Pressure Vessels, Part II," NASA Report JSC 27081.
[9] Lee, T. W., and Yatteau, J. D., 1976, "Hydraulic Ram Investigations," US Army Armament research and Development Command, ARBREL-CR-00365, Aberdeen Proving Ground.
[10] Lewis, M. W., and Wilson, T. L., 1997, "Response of water-filled spherical Vessel to an internal explosion," Los Alamos, LA-13240-MS.
[11] Wisotski, J., 1978, "Penetration of Water by Rod Type Fragments," Denver Research Institute, Report N00123-76-C0166.
[12] Yatteau, J. D., and Wisotski, J., 1978, "Penetration of Fluid by Rod Type Fragments," DRI No. 2710, Denver Research Institute.
[13] Yatteau, J. D., Zernow, R. H., Dunn, J. A., and Wisotski, J., 1989, "Fragment Penetration of Fluid-Backed Plates," AFATL R 89-59, Air Force Armament Laboratory, Eglin Air Force Base.
[14] Taylor, G. I., 1950, "The Instability of Liquid Surfaces when Accelerated in a Direction Perpendicular to their Planes I," Proc. R. Soc. London, Ser. A, **201**, pp. 192–196.

[15] Sharp, D. H., 1984, "An Overview of Rayleigh-Taylor Instability," Physica D, **12**, pp. 3–18.
[16] Richtmyer, R. D., 1960, "Taylor Instability in Shock Acceleration of Compressible Fluids," Commun. Pure Appl. Math., **XIII**, pp. 297–319.
[17] Meshkov, E. E., 1970, "Instability of the Interface of Two Gases Accelerated by a Shock Wave," NASA Tech. Trans. F-13, 074.
[18] Zhang, Q., and Sohn, S., 1996, "An Analytical Nonlinear Theory of Richtmyer-Meshkov Instability," Phys. Lett. A, **212**, pp. 149–155.
[19] Holmes, R. L., Dimonte, G., Fryxell, B., Gittings, M. L., Grove, J. W., Schneider, M., Sharp, D. H., Velikovich, A. L., Weaver, R. P., and Zhang, Q., 1999, "Richtmyer-Meshkov Instability Growth: Experiment, Simulation and Theory," J. Fluid Mech., **389**, pp. 55–79.
[20] Prasad, J. K., Rasheed, A., Kumar, S., and Sturtevant, B., 2000, "The Late-Time Development of the Richtmyer-Meshkov Instability," Phys. Fluids, **12**(8), pp. 2108–2115.
[21] Bellman, R., and Pennington, R. H., 1954, "Effects of Surface Tension and Viscosity on Taylor Instability," Q. Appl. Math., **12**, pp. 151–162.
[22] Chandrasekhar, S., 1961, *Hydrodynamic and Hydrodynamic Instability*, Oxford University Press, New York.
[23] Menikoff, R., Mjolsness, R. C., Sharp, D. H., and Zemach, C., 1977, "Unstable Normal Mode for Rayleigh-Taylor Instabilities in Viscous Fluids," Phys. Fluids, **20**(12), pp. 2000–2004.
[24] Mulser, P., 1987, "Reduction of Rayleigh-Taylor Growth due to Viscosity Effects," Laser Part. Beams, **6**(1), pp. 119–120.
[25] Plesset, M. S., 1954, "On the Stability of Fluid Flows with Spherical Symmetry," J. Appl. Phys., **25**(1), pp. 96–106.
[26] Berkoff, G., 1954, "Note on Taylor Instability," Q. Appl. Math., **12**(3), pp. 306–309.
[27] Zhang, Q., and Graham, M. J., 1998, "A Numerical Study of Richtmyer-Meshkov Instability Driven by Cylindrical Shocks," Phys. Fluids, **10**(4), pp. 974–992.
[28] Jones, M. A., and Jacobs, J. W., 1997, "A Membraneless Experiment for the Study of Richtmyer-Meshkov Instability of a Shock-Accelerated Gas Interface," Phys. Fluids, **9**, pp. 3078–3085.
[29] Vetter, M., and Sturtevant, B., 1994, "Experiments of the Richtmyer-Meshkov Instability of an air/SF_6 Interface," Shock Waves, **4**, pp. 247–252.
[30] Mikaelian, K. O., 1990, "Rayleigh-Taylor and Richtmyer-Meshkov Instabilities in Multilayer Fluids with Surface Tension," Phys. Rev. A, **42**(12), pp. 7211–7225.
[31] Hann, S. W., 1988, "Onset of Nonlinear Saturation for Rayleigh-Taylor Growth in the Presence of a Full Spectrum of Modes," Phys. Rev. A, **39**(11), pp. 5812–5825.
[32] Mikaelian, K. O., 1990, "Rayleigh-Taylor and Richtmyer-Meshkov Instabilities and Mixing in Stratified Spherical Shells," Phys. Rev. A, **42**(12), pp. 3400–3420.
[33] Zhang, Q., and Graham, M. J., 1997, "Scaling Laws for Unstable Interfaces Driven by Strong Shocks in Cylindrical Geometry," Phys. Rev. Lett., **79**(14), pp. 2674–2677.
[34] Jacobs, J. W., Jenkins, D. G., Klein, D. L., and Benjamin, R. F., 1995, "Nonlinear Growth of the Shock-Accelerated Instability of a Thin Fluid Layer," J. Fluid Mech., **295**, pp. 23–42.
[35] Jacobs, J. W., and Collins, B. D., 1999, "Experimental study of the Richtmyer-Meshkov instability of a diffuse interface," *Proceedings of the 22nd International Symposium on Shock Waves*, Imperical College, London.
[36] Hertel, E. S., Jr., Bell, R. L., Elrick, M. G., Farnsworth, A. V., Kerley, G. I., McGlaun, J. M., Petney, S. V., Silling, S. A., Taylor, P. A., and Yarrington, L., 1993, "CTH: A Software Family for Multi-Dimensional Shock Physics Analysis," *Proceedings of the 19th International Symposium on Shock Waves*, Vol. I, pp. 377–382, Marseille, France 26–30. July.
[37] Assay, J. R., and Shahinpoor, M., 1993, *High-Pressure Shock Compression of Solids*, Springer-Verlag, Berlin, ISBN 0-387-97964-6.
[38] Winfree, N. A., and Kerley, G. I., 1999, "Equation of State model for Tributyl Phosphate," *Proceedings of the 11th Biennial International Conference of the American Physical Society Topical Group on Shock Compression of Condensed Matter*, Snowbird, Utah.
[39] Reinhart, W. D., Chhabildas, L. C., Winfree, N. A., and Grady, D. E., 1999, "Dynamic Properties of Tributyl Phosphate," *Proceedings of the 11th Biennial International Conference of the American Physical Society Topical Group on Shock Compression of Condensed Matter*, Snowbird, Utah.
[40] Baumgardner, J. R., Cline, M. S., Johnson, N. L., and Kashiwa, B. A., 1990, "CFDLIB: A Library of Computer Codes for Problems in Computational Fluid Dynamics," Los Alamos National Laboratory, Los Alamos, NM. LA-UR-90-1361.
[41] Tussing, R. B., 1982, "Accuracy and Response of Tourmaline Gauges for Measurement of Underwater Explosion Phenomena," NSWC TR-82-294, Naval Surface Warfare Center, White Oak, MD.
[42] Hayami, R. A., 1999, "Liquid Dispersion Characterization Test," University of Alabama in Huntsville Aerophysics Research Center. UAH/ARC TR 98-01.
[43] Ference, S. L., Borg, J. P., and Cogar, J. R., "Source Term Investigation of TBM Bulk Chemical Target Intercepts: Phase 1 Test Report, (under review).
[44] Ference, S. L., Borg, J. P., and Cogar, J. R., "Source Term Investigation of TBM Bulk Chemical Target Intercepts: Phase I1 Test Report, (under review).
[45] Grady, D. E., 1988, "The Spall Strength of Condensed Matter," J. Mech. Phys. Solids, **36**(3), pp. 353–384.
[46] Grady, D. E., and Kipp, M. E., 1985, "Geometric Statistics and Dynamic Fragmentation," J. Appl. Phys., **58**(3), pp. 1210–12222.
[47] Borg, J. P., Grady, D., and Cogar, J. R., 2001, "Instability and Fragmentation of Expanding Liquid System," Int. J. Impact Eng., **26**, pp. 65–76.

Comparison of Computational Results Obtained From a Homogeneous Cavitation Model With Experimental Investigations of Three Inducers

Imene Mejri
Assistant Professor
e-mail: imen.mejri@paris.ensam.fr

Farid Bakir
Professor
e-mail: farid.bakir@paris.ensam.fr

Robert Rey
Professor
e-mail: robert.rey@paris.ensam.fr

Laboratoire d'Energétique et de Mécanique de Fluides Interne (LEMFI),
Site Paris UMR CNRS 7067,
Ecole Nationale Supérieure d'Arts et Métiers (ENSAM),
151 Boulevard de l'Hopital 75013 Paris,
France

Thabet Belamri
Doctor
ANSYS Canada,
554 Parkside Dr.,
Waterloo, Ontario,
Canada
e-mail: thabet.belamri@ansys.com

The paper presents full 3D numerical simulations and experimental investigations of the cavitating flow through three axial inducers. These inducers are identified by the tip blade angle at the leading edge β_{1T}=8, *10, and* 13 deg. *The numerical and experimental investigations were carried out at the* **LEMFI** *laboratory (***L***aboratoire d'***E***nergétique et de* **M***écanique de* **F***luides* **I***nterne) of the ENSAM-Paris center (***E***cole* **N***ationale* **S***upérieure d'***A***rts et* **M***étiers). A review of the cavitating regime modeling and the cavitation homogeneous model used for this paper's calculations is first presented. The numerical model is based on a combination of the multiphase flow equations with a truncated version of the Rayleigh-Plesset model predicting the complicated growth and collapse processes of bubbles. The mass transfers due to cavitation are source/sink terms in continuity equations of the liquid and vapor phases. The cavitation model also features a solution methodology which implicitly couples the continuity and momentum equations together. The main results are presented for the inducers at a range of flow rates and cavitation numbers: (1) Experimental results concerning: (i) the overall performances: Pressure head coefficient and efficiency versus flow rates; (ii) critical cavitation number (5% and 15% of drop) versus the flow rate; (2) Numerical results concerning: (i) the overall performances; (ii) the numerically investigated water vapor volume fraction distributions and other CFD results, which enable us to explain the cavitating behavior for these inducers; (iii) the location and sizes of the blade cavity and backflow vortex. Finally, the comparisons between experimental and simulated results on the overall performances, cavity sizes and cavity location are discussed. A qualitative agreement between experimental and predicted results was found for two inducers for a range of flow rates. The head breakdown in the simulations started at a different cavitation coefficient than that in the experiment.* [DOI: 10.1115/1.2353265]

Keywords: cavitation, inducer, CFD, experiment, head-drop

1 Introduction

The authors have been involved for several years in the development of design rules for axial inducers at **LEMFI**-Paris [1–8]. But rather than attempt a general treatise on inducers, we shall here focus attention on special cavitation problems and design issues associated with the flow of liquid through axial inducers. The appearance of the cavitating structures, their geometry and more generally their static and dynamic properties, depend on several parameters which include above all: The blade's profile, camber, thickness [9], incidence, stacking, and leading edge shape, as well as the walls roughness, the upstream turbulence, the existence of gas micro-bubbles in the flow, the fluid viscosity, etc. CFD has been extensively used to predict the flow through the inducers under noncavitating conditions. However, because of the physical and numerical challenges associated with cavitation, CFD has only recently started to be used to predict cavitating flows. We have already studied experimentally in cavitating and noncavitating regimes the influence of geometrical parameters [3,4] such as the shape of the blade leading edge and its sharpening [8], but since a few years, we are combining numerical and experimental approaches in order to achieve this goal [5–7].

The association inducer/centrifugal pump is utilized in various industrial fields due to the inducer's efficient way to achieve the high suction performance for the pump, since it is able to keep the high head-rise performance even in severe cavitating conditions. As a consequence, there is a strong demand to explore the limits of the inducer's performance when it is forced to operate at the conditions imposed by the centrifugal pump placed downstream.

In practice, these conditions do not match the optimal flow rate nor the angular speed for which the inducer was designed. The inducer may then operate at his nominal flow rate as well as at overload or part load conditions. Thus, for the diversity of operation processes, many inducers should be tested with the same pump. Since the flow rate and the cavitation number are imposed by the pump, it is important to analyze the inducers behavior in cavitating and noncavitating conditions at the three previous operation modes. In the present study, three inducers with different tip blade angles at their leading edges are compared at their respective nominal flow rates (Q/Q_n=1), at low flow rates (Q/Q_n =0.71), and at high flow rates (Q/Q_n=1.14).

Recently, numerical cavitating flow simulations have been applied to rotating machinery such as pumps, inducers, and water turbines [10–15]. Nakai et al. [14] studied the impellers with an

Contributed by the Fluids Engineering Division of ASME for publication in the JOURNAL OF FLUIDS ENGINEERING. Manuscript received February 28, 2005; final manuscript received February 20, 2006. Assoc. Editor: Joseph Katz.

even number of blades and established that the predicted alternate blade cavitation depends on the geometry of the impeller. Nohmi and Goto [16] validated a homogeneous numerical model with new experimental measures carried on in a centrifugal pump.

Over the last few years, numerical models have been developed to predict the cavitating flows through these devices [10–13]. These models are based on stability analyses of the total flow variations through a cavitating blade-to-blade channel [10,11], or through a 2D blade cascade that leads to neglect the peripheral cavitation in the inducer, or finally on calculating the flow around attached cavities [12].

Although there have been many researches for cavitation instabilities in axial inducers, no experimental nor numerical analysis has been made to illustrate some specific design parameters such as the tip blade angle effects on the performance in a cavitaing regime. The present study contributes to identify the best value of this design parameter relatively to the flow rate range.

2 Flow Modeling in a Regime of Cavitation

The cavitating pockets can be of several natures; some remain attached to the blades with more or less oscillating lengths and frequencies of release which can vary from a blade to another. They can also be rotating with different rotation frequencies; only steady sheet cavitation is considered in the present paper. Nevertheless, even with continuous cavitation, the flow is always unsteady because of the shedding of bubbles from the trailing edge of continuous cavitation. The prediction of steady cavitation and more specifically the steady cavity length is important for the cavitation instabilities prediction [10,14].

Some of the CFD models developed for cavitation were more adapted to the isolated 2D profiles for steady [17] and unsteady flows [18]. Recently, cavitation models were implemented in CFD codes using the 3D Reynolds averaged Navier-Stokes equations.

In reality, the dynamics of collapse are complex and depend on a variety of factors including surface tension, viscous effects, and noncondensable content. Not surprisingly, there are no cavitation models which attempt to account for all of these complexities. However, there are models which do account for nonequilibrium effects. Most of these models are based upon the Rayleigh-Plesset equation [1,19].

We can then distinguish four classes of cavitation models:

► The models used for the study of micro-bubbles dynamics, growth, and collapse in the flow. These models are generally related to the notion of cavitation inception by integrating empirical formulations accounting for drag, lift, pressure and inertial forces. The rate of cavitation events can be estimated based on phase averaged distributions of pressure, and bubbles [20].

► The cavity interface tracking method, which is a simplistic method where only the flow in the liquid phase is studied and is supposed to circumvent the cavity. The cavity is continuous and remains attached to the blade. The simulation of the interface shape and the cavity varies from authors to others [21].

► The single phase models with one set of classical conservation equation (for mass, momentum, and eventually energy) applied to one phase along with empirical state law defining the density and establishing the mixture conditions between the liquid and the vapor phases [22–24]. The main difference between these homogeneous models concerns the source terms ($\dot{m}^-$ and $\dot{m}^+$) considered to simulate mass transfer. These terms represent evaporation and condensation of the phases, respectively, and results in a variable density field. This approach considers a nonslip condition between vapor and liquid phases. Moreover, an equilibrium thermodynamic state is supposed to be instantaneously reached during condensation and vaporization. A simpler approach is based on the use of equations relating pressure and density such as:

The barotropic relation of Delannoy and Kueny [18]:

$$\rho = f(P) \tag{1}$$

the equation of Chen and Heister [25] relating the density derivative to time and pressure (C is a constant):

$$D\rho/Dt = C(P - P_v) \tag{2}$$

the polynomial equation of Song and He [23] (C_i are constants):

$$\rho = \sum_{i=1}^{5} C_i \mathrm{P}^i \tag{3}$$

or the use of assumptions regarding the thermodynamic path of the flow (for example, constant entropy or enthalpy).

► The two-phase models, based on solving two sets of conservation equations with simplifying assumptions for the calculation of the mass and momentum exchange terms [26–29]. Those models account for the nonequilibrium effects during vaporization and condensation. The source term in the mass equation of the vapor may be related to the condensation and evaporation empirical coefficients ($C_{\text{destruction}}$ and $C_{\text{production}}$) [27] or to the variation of the bubbles radius in the Rayleigh-Plesset equation for example [26].

3 Governing Equations and Phase Change Modeling

For this study, the CFD results are computed by the commercial code CFX-5.7 developed by CFX of Ansys Canada. The validation of the models was done on an inducer designed and tested at LEMFI - Paris [30]. A cavitation multiphase model is implemented in this code as an interphase mass transfer process. This has the numerical advantage of the usage of the volume fluxes (rather than mass fluxes) which are continuous at the interface and simplify the solution process.

The multiphase flow is treated as a homogenous mixture of two phases and three components, irrespectively whether the control volume contains one pure phase or a mixture. The model tracks the volume fraction of each fluid by solving only one set of momentum equation throughout the domain. Thus, no attempt is made to model a distinct liquid/vapor interface; the volume fraction field may vary continuously from 0 to 1 in the cavitation zone covering many grid elements.

The volume fraction scalar α_n is the variable associated to each phase n. In each control volume, the sum of the volume fractions of all the phases is equal to unity (Eq. (4)).

$$\sum \alpha_n = 1 \tag{4}$$

The volume fraction equation is written for each phase n in order to determine the interface (the phases are supposed to share the same velocity u_i)

$$\frac{\partial(\rho_{\mathrm{n}}\alpha_n)}{\partial t} + \frac{\partial(\rho_{\mathrm{n}}\alpha_n u_i)}{\partial x_i} = S_n \tag{5}$$

S_n is the source term for phase n (including vaporization and condensation in the case of cavitating flows) and satisfies the constraint:

$$\sum S_n = 0 \tag{6}$$

In the thermodynamic point of view, the flow is considered isothermal (T=300 K). Since the compressibility is important in a general cavitating flow, it is necessary to determine the densities of the three components. Equations of state are then used: The noncondensable gas and the vapor phase are considered to be ideal gases. The vapor density can also be calculated using the saturated vapor curve. For low speed flows, it can be assumed to be constant. If the compressibility is not important, the liquid density is supposed to remain constant. If not, it can be calculated via a liquid EOS.

The suffixes l, v, and d denote, respectively, the liquid, vapor, and dispersed phases. The noncondensable phase mass fraction y_d

is assumed to be constant and well mixed in the liquid so that they can be combined and form one fictive phase m with the associated volume scalar α_m and density ρ_m

$$\alpha_m = \alpha_l + \alpha_d \tag{7}$$

$$\rho_m = \frac{1}{(1-y_d)/\rho_l + y_d/\rho_d} \tag{8}$$

The *volume of fluid* equation is then applied to this phase

$$\frac{\partial(\rho_m \alpha_m)}{\partial t} + \frac{\partial(\rho_m \alpha_m u_i)}{\partial x_i} = S_l \tag{9}$$

The mass fractions satisfy the additional constraint

$$y_l + \mathbf{y_v} + \mathbf{y_d} = \mathbf{1} \tag{10}$$

Instead of attempting to distinguish components between liquid and vapor and to track their interface, an alternative strategy is to treat the cavitating flow as a homogeneous two-phase mixture, where the mixture density is defined as

$$\rho = \rho_m \alpha_m + \rho_v \alpha_v \tag{11}$$

The governing mixture equations for mass and momentum are

$$\frac{\partial(\rho)}{\partial t} + \frac{\partial(\rho u_i)}{\partial x_i} = 0 \tag{12}$$

$$\frac{\partial(\rho u_i)}{\partial t} + \frac{\partial(\rho u_i u_j)}{\partial x_i} = -\frac{\partial \tau_{ij}}{\partial x_j} - \frac{\partial P}{\partial x_i} \tag{13}$$

If we adopt the assumptions that bubble-bubble interactions and bubble coalescence are neglected and if we consider a spherical bubble of radius R, in an infinite domain of liquid whose pressure far from the bubble is P_∞, the generalized Rayleigh-Plesset equation describing its growth is

$$R\frac{d^2R}{dt^2} + \frac{3}{2}\left(\frac{dR}{dt}\right)^2 + \frac{2T}{\rho_l R} + \frac{4\mu_l}{\rho_l R}\frac{dR}{dt} = \frac{P_B(R,t) - P_\infty}{\rho_l} \tag{14}$$

where T is the surface tension coefficient. In this equation it is assumed that the liquid density ρ_l and the dynamic viscosity μ_l are constant. It is also assumed that the bubbles remain spherical. Their contents are supposed homogeneous and the temperature T_B, and pressure $P_B(R,t)$ within the bubble are always uniform ($P_B = P_v$, where P_v is the vapor pressure and T_B is assumed to be a simple constant equal to the temperature T_∞ far from the bubble). P_∞ is set equal to the cell pressure P. These assumptions may not be justified in some circumstances.

Equation (14) is rather used under its simplified form called "*Inertia controlled bubble growth equation*" where thermal and buoyancy effects are neglected considering the typical situation that Froude and Weber numbers are large

$$\frac{dR}{dt} = \sqrt{\frac{3}{2}\frac{P_v - P}{\rho_l}} \tag{15}$$

The number of bubbles per unit volume changes depending on the direction of the phase change. During vaporization (bubble growth), this number is given by

$$N_B = (1-\alpha_v)\frac{3\alpha_d}{4\pi R^3} \tag{16}$$

and during condensation

$$N_B = \frac{3\alpha_v}{4\pi R^3} \tag{17}$$

The transfer rate can be generalized to include condensation, using a calibration empirical coefficient F ($F = F_{\text{vaporization}}$ if $\text{sign}(P - P_v) = (+)$ and $F = F_{\text{condensation}}$ if $\text{sign}(P - P_v) = (-)$) as follows:

$$S_v = -S_l = F N_B \rho_v 4\pi R^2 \sqrt{\frac{2}{3}\frac{|P_v - P|}{\rho_l}}\ \text{sign}(P_v - P) \tag{18}$$

Though this interfacial cavitation model is not completely empiricism free, it certainly imparts physical understanding to the mass transfer rates ($F_{\text{condensation}}$, $F_{\text{vaporization}}$) in source terms. These empirical factors are designed to account for the fact that condensation and vaporization may occur at different rates since in practice, these processes have different time scales. Indeed, vaporization is an endothermic process that requires a certain amount of energy to overcome the liquid intermolecular forces; whereas condensation is an exothermic process that releases the same amount of energy but at a different time scale. Vaporization is a process that can be described by standard equations of chemical kinetics. It is a dynamic competition between water molecules in the liquid moving to the vapor phase (vaporization) and molecules of water vapor moving to the liquid phase (condensation). At any given temperature, the rate of vaporization is directly proportional to the concentration of water in the liquid phase, which is constant as long as there is some liquid water present. Whereas the rate of condensation at any given temperature is proportional to the concentration of water molecules in the vapor phase [31].

To allow for these constraints and to take into consideration the fact that condensation is usually much slower than vaporization, $F_{\text{condensation}}$ value is smaller than $F_{\text{vaporization}}$ value.

In their principal, $F_{\text{condensation}}$ and $F_{\text{vaporization}}$ factors are similar to the empirical coefficients $C_{\text{destruction}}$ and $C_{\text{production}}$ (for the destruction and production of vapor) introduced by Kunz et al. [32]. $C_{\text{destruction}}$ and $C_{\text{production}}$ are also obtained by sensitivity analysis. In fact, Kunz et al. followed the same idea as Merkle et al. [22] to detail the evaporation and condensation processes.

For these paper's calculations, we considered only the steady approach. In the case of cavitating flows, we used the concept of pseudo-time in order to make the iterative methods converge on the correct solution. Since we seek a steady solution through iteration in pseudo time domain, the discretization order in pseudo time will not affect the final solution when steady state is achieved.

In the case of unsteady calculations (not presented here), the cavitation pocket development is ruled by a different time constant than that of incompressible flow field.

The cavitation model used for the calculations features a control volume finite discretization and a solution methodology which implicitly couples the continuity and momentum equations together. The global continuity constraint is cast in volumetric form while remaining fully conservative. Detailed documentation of the numerical procedure can be readily obtained [33].

4 Inducers Design and Test Facility

4.1 Presentation of the Inducers. The design methodology we used to make up the inducers is a classical procedure equivalent to those found in the bibliography [2–8,34]. Each inducer was built from one piece of aluminium manufactured by a numerically controlled machine tool provided with five axes. In order to provide the inducers blade with better resistance to the erosion by cavitation, a sanding and an anodization of the hubs and blades were done.

The inducers are all of type C (also called helical type because of the radial distribution of the inducer blade angle) and differentiate by their tip blade angle at the leading edge $\beta_{1T} = 8$, 10, and 13 deg. The three inducers are thus noted as *Inducer* 8 deg, *Inducer* 10 deg, and *Inducer* 13 deg. As it can be seen in Fig. 1, the inducers outlet diameter is slightly increased to reach the diameter of the impeller assembled downstream of the inducer on the same driving shaft.

Each inducer has three blades with constant thickness and back swept leading edges. The inducers blades have the same axial length, tip diameter, leading edge cut, and leading edge sharpen-

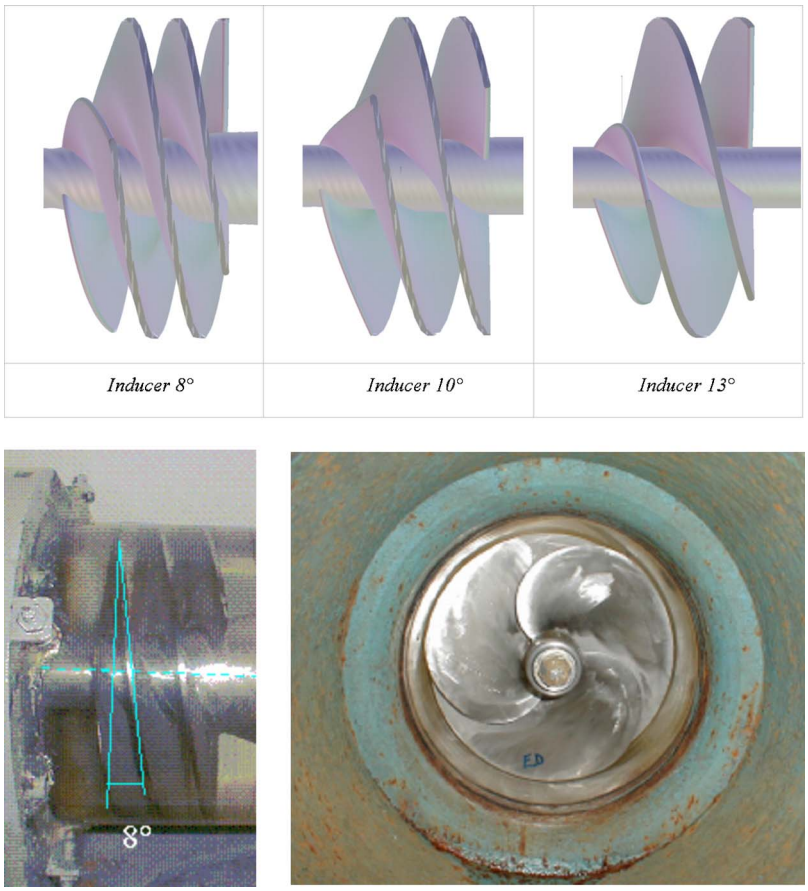

Fig. 1 Pictures of the studied inducers

ing. The stacking of the trailing edge is made radially. The main constructive parameters of the three machines are shown in Fig. 2 and Table 1.

The choice of β_{1T}=8, 10, and 13 deg is justified by the fact that the presence and the intensity of the backflow vortex depend on the angle β_{1T}, the hub to tip ratio and the flow coefficient. The recommended values for β_{1T} are between 7.5 and 15 deg. The consequence of a low β_{1T} value choice is an inducer with a large diameter. In this case, the inducer diameter is much higher than the inlet diameter of the centrifugal impeller placed downstream, therefore, a linking device must be set up. Due to its length, this linking device increases the inducer overhang which requires a complementary bearing. For the industrial pumps these devices are expensive and not very reliable, blade angles of 13 and 15 deg are then better adapted.

4.2 General Overview of the Test Rig and Pressure Measurements. The LEMFI-Paris axial and centrifugal pumps test rig is composed of two independent but interconnected loops. The axial pump loop used in this study provided a straight inducer inlet section and is composed with the following main elements (Fig. 3):

- Two storage tanks with a capacity of 4 m^3 each, connected by a 350 mm diameter pipe. They can be loaded and emptied using two electrical control valves.
- A liquid ring vacuum pump is used to control the pressure at the free surface inside the storage tanks.
- A 22 kW alternative motor powered by a variable frequency controller was used to drive the tested inducer. The manufacturer gives the electric efficiency η_{elec} of the motor. The rotational speed is measured using a magnetic tachometer (accuracy 0.1%).
- A motorized control valve serves to adjust the flow rate accurately.
- The inducer equipped with a transparent acrylic cover to enable direct observations of the flow.
- A centrifugal pump installed in series with the impeller in order to overcome the circuit losses.
- Various measurement instruments and devices:

  An ultrasonic flow meter ("A500 - Sparling Meter Flow," accuracy 1%), placed at the inlet of the inducer.
  Two piezo-resistive manometers (Kistler, type 601A, accuracy 1%). They are positioned at the inlet and outlet sections and measure the average tip pressure (at about 20 mm upstream of the leading edge and 150 mm downstream of the trailing edge of the blade). The signal resulting from these sensors is amplified then treated by a Lecroy spectrum analyzer (type 930 4A). Its connection with a computer enables us to store and to use these signals.
  A temperature probe (accuracy 1%): The average temperature during the tests presented below is 18 °C.

Air-water behavior in the inducers was observed through the transparent casing with video camera equipment and a stroboscopic light.

The hydraulic efficiency is defined as

$$\eta = \frac{P_{hydr}}{P_{shaft}} = \frac{\rho g H_{tot} Q}{\eta_{elec} P_{elec}}$$

where H_{tot} is the head based on the total pressure, P_{shaft} is the power transmitted to the shaft ($P_{shaft}=P_{elec}\times\eta_{elec}$) and P_{elec} is the electrical power provided to the engine. η_{elec} is the engine electrical efficiency determined by a calibration curve provided by the

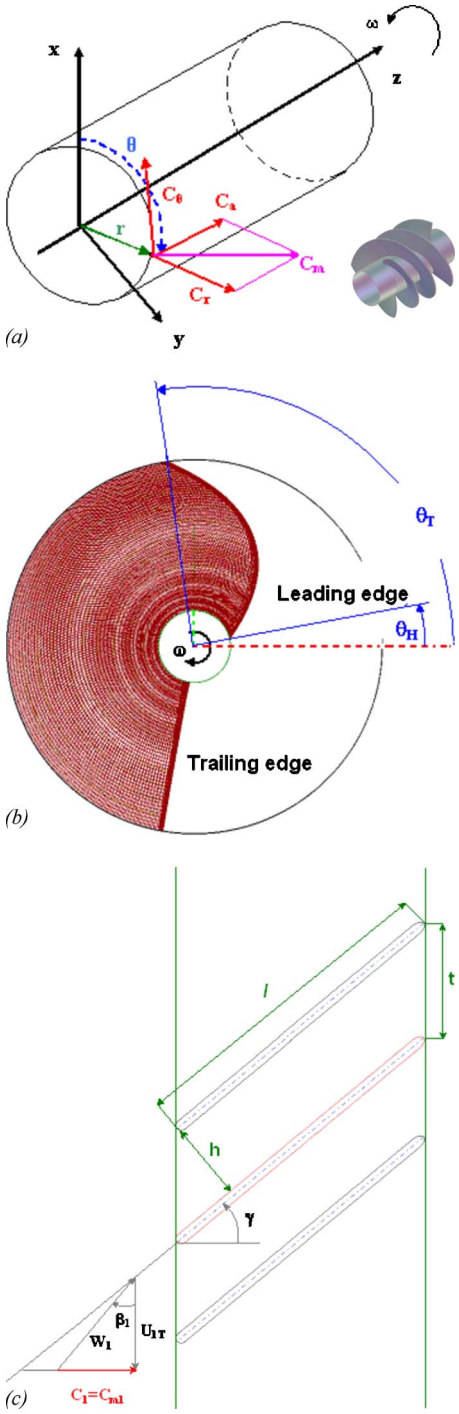

Fig. 2 (*a*) Velocity components in the 3D view. (*b*) Inducer face view. (*c*) Main definitions of the blade cascade.

engine manufacturer.

The experimental pressure coefficient ψ is evaluated based on tip pressure coefficient and the numerical one is calculated by mass averaging the static pressure at the inlet and the outlet. As shown in Fig. 3, the (static) pressure experimental measurements at inducers inlet and outlet are carried out at the cross sections "*S1 for measurements*" and "*S2 for measurements*," corresponding, respectively, to duct diameters of 340 and 275 mm.

The section "*S1 for measurements*" is preceded by the honeycomb shown at the plane *AA* of Fig. 3. This device insures the uniformity of the flow characteristics along a cross section. Moreover, there is no prerotation of the flow, so that the static pressure at the section "*S1 for measurements*" is approximately equal to the static pressure at the section "*S1 for calculations*" (if we neglect the kinetic energy and the very low head losses).

The kinetic energy is actually formed by three components:

A radial component whose value is very low;
a tangential component which is lost because of a cross-piece device (see Fig. 4) placed downstream of the inducer;
and finally an axial component. We indeed verified by calculations that this component is negligible.

For the experimental tests, the cross-piece device is placed at the inducer outlet (upstream of the divergent represented in Fig. 3) to "break" the tangential component of the velocity and guarantee that the pressure distribution becomes uniform in a cross section.

For the numerical simulations, the pressure is measured at the sections "*S1 for calculations*" and "*S2 for calculations*," respectively, located at about more than one diameter from the inducer inlet plane and more than a diameter from the inducer outlet plane for the reasons explained in the Sec. 5.2 (grid size, calculation time, etc.).

At the sections "*S1 for measurements*" and "*S2 for measurements*," the pressure over one section is almost constant, and its value on the external diameter of the pipe is the same as its value on the rest of the cross section (Fig. 4). The mean value of the pressure calculated at the section "*S2 for calculations*" is approximately equal to the mean value of the pressure measured at the section "*S2 for measurements*."

The experimental measurements are not carried out immediately in the vicinity of the inducer trailing edge, but at approximately 1 m downstream of the cross-piece (i.e., at the section "*S2 for measurements*"), to insure that the axial velocity is almost uniform ($\forall r$) and that the tangential velocity is very low so that the pressure distribution over the section is approximately constant and equal to its value at the external diameter (=275 mm).

5 Comparison of the Inducers Performances

5.1 Experimental Results. Although the use of inducers is frequent today, several aspects of their operation and their behavior still remain difficult to model. In order to elucidate some phenomena, affecting the reliability of these devices, their maximum performance and their operational limits, we still rely on experimentation. This section compares the performances of the three machines, namely: Overall performances (head, flow rate, efficiency) and the behavior with the critical cavitation characterized by the cavitation coefficient σ_C.

For the experimental cavitation procedure, the rotational speed is fixed to 1450 rpm; the flow rate is measured by the flow-meter and set to the operating value using the motorized control valve. The inlet pressure drop is realized by the liquid vacuum pump. Both calculations and experimental results correspond to an outlet flow rate which is equal to the inlet flow rate, even in the fall area of the head curve. For the experimental measures, after detecting the head drop, we stop the process when the outlet flow rate is no more equal the inlet flow rate.

According to our experience, the pressure drop starts when the cavitating pocket reaches the throat formed by two successive blades where it is quickly dragged to the trailing edge. While retaining this particular criterion for the calculated pocket, we obtain a good approach of the critical NPSH in a range of incidence close to the design point.

For certain operating values of flow rates and inlet pressure, some specified types of cavitation were observed. For all tested flow rates, a sudden head drop happens with very low inlet pressure values. For each inducer, at any flow rate, we observe first three clouds of cavitation (one on each blade) extending upstream from the inducer's inlet. They are generated in the backflow vortices at the tip. Thus, in the shear layer between the swirling backflow and axial main flow, we have an axial vorticity that rolls

Table 1 Main constructive parameters of the studied inducers

Rotational speed	1450 rpm		
Blades number	3		
Blade thickness	5 mm		
Tip diameter	234 mm		
Tip clearance	0.4 mm		
	Inducer 8 deg	*Inducer* 10 deg	*Inducer* 13 deg
Hub to tip ratio at inlet	0.2	0.2	0.2
Hub to tip ratio at outlet	0.29	0.24	0.2
Flow coefficient	0.057	0.087	0.107
Hub blade angle (radial definition, this angle is constant from inlet to outlet.)	54	42.8	50.2
Tip blade angle (radial definition, this angle is constant from inlet to outlet.)	8 deg	10 deg	13 deg
Hub solidity	3.63	3.98	3.21
Tip solidity	2.45	1.93	1.38
$NPSH_{5\%}$ (m)	0.45	1.19	1.18
Q_n (m^3/hr)	150	220	280
H_n(m)	3.6	4.3	4

up and forms a vortex structure surrounding the backflow region. Due to the centrifugal forces, the pressure at the center of these vortices is lowered and cavitation occurs there if inlet pressure is decreased. This mechanism of inlet backflow in inducers is dependant on the flow rate fluctuations [35]. It can also have profound effects on cavitation instabilities [35].

After the backflow cavitation, we observe a forward rotating cavitation propagating in the same direction and faster than the inducer. Since the blade-to-blade throat is located more downstream at the shroud, the cavity starts to develop much sooner at shroud than at hub before reaching the blade-to-blade throat. Indeed, the vapor accumulating region observed along the blade suction surface at the periphery is elongated downstream of the blade channel. This clouded string of vapor is sheared and suppressed by high circumferential flow in the tip clearance zone. The difference of vapor behavior might results in inducer head difference. When the cavity reaches the blade-to-blade throat, the head-drop begins.

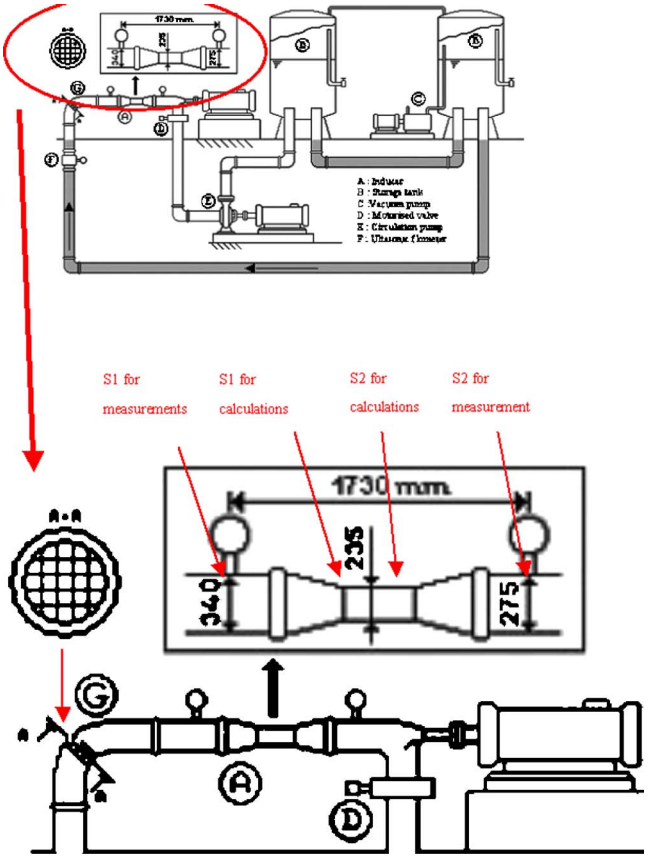

Fig. 3 Hydrodynamic test bench of the LEMFI - Paris

5.2 Overall Performance. The flow rate is characterized by the flow coefficient ϕ. The overall performance in noncavitating regime (Fig. 5) is the highest for Inducer 13 deg, with a hydraulic efficiency which increases with β_{1T} from 60 to 70%. Inducer 8 deg overall performances are the lowest ones, even if the pressure head coefficients ψ of the three inducers reach comparable levels at low flow rates. Inducer 8 deg efficiency does not exceed 56% and its nominal head is 3.6 m, while Inducer 10 deg has a better efficiency and nominal head. More specifically, those ψ-ϕ performances curves has a stable negative slope. For the values corresponding to the maximum efficiency, the flow coefficient and the angles of incidence are given in Table 2.

5.2.1 Behavior With Cavitation. The experimental head-drop curves are presented on Fig. 6 for the three inducers at many flow rates. The accuracy on the evaluation of ψ and σ_c is less than 10%. As shown on this figure, the head curve breakdown depends on the flow rate, as it would be expected (because of the specific speed). Around the nominal flow rate and especially for higher flow rates, the head-drop curves show a sudden drop. For low flow rates, the head curve drops smoothly with a significant increase in pressure. This local performances improvement is due to the blade attached cavity which increases the lift to the blade [36].

The examination of these values and other experimental results shows a general superiority for Inducer 8 deg concerning the behavior with cavitation.

The behavior in cavitating regime is characterized by the cavitation parameters σ_C corresponding to head drops of 5% and 15%. Those values of $\sigma_{C,5\%}$ and $\sigma_{C,15\%}$ are determined by the character of the head-drop curves (sudden, smooth,…). The test results concerning the comparison of the performances in cavitating regime are synthesized in Fig. 7. We note the important increase in the $\sigma_{C,5\%}$ and $\sigma_{C,15\%}$ for inducer 13 deg at ϕ=0.09 due to cavitation development in the blade passage. For inducer 8 deg, $\sigma_{C,5\%}$ increases at ϕ=0.07.

One also observes the σ_C rises in partial flow, this phenomenon is more significant when β_{1T} increases. The best σ_C value for a head drop of 5% is obtained, as envisaged, for inducer 8 deg. At high flow rates, the critical cavitation number increases for induc-

Inducer 13°.

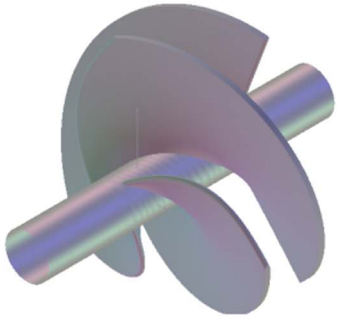

The cross-piece device placed downstream of the inducer.

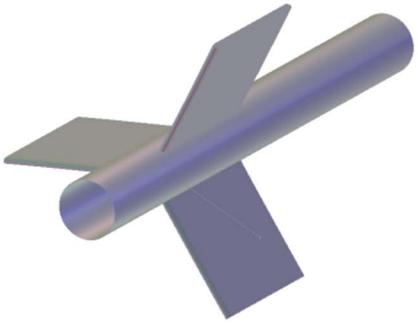

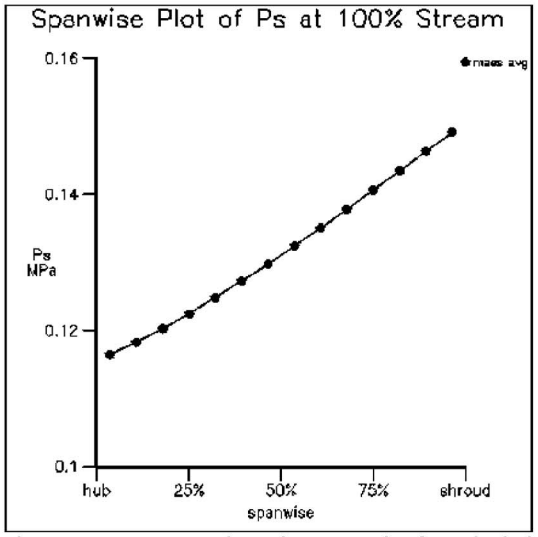

The static pressure at the inducer's outlet from the hub to the shroud.

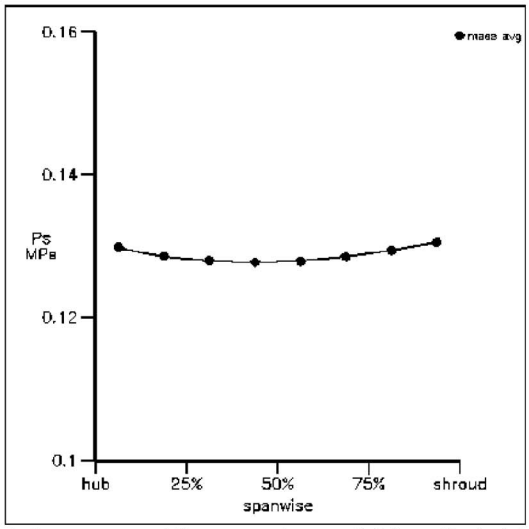

The static pressure at the cross-piece outlet from the hub to the shroud.

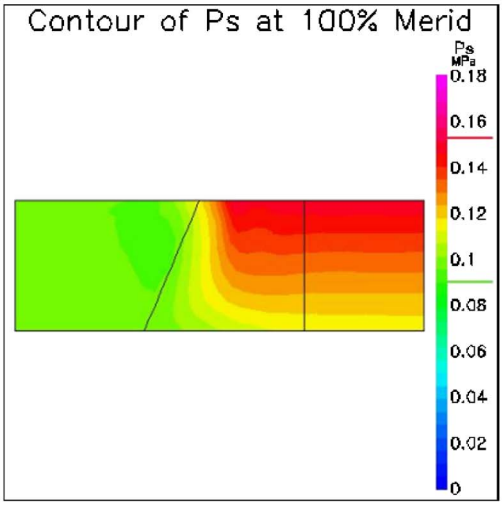

Static pressure in the meridional view.

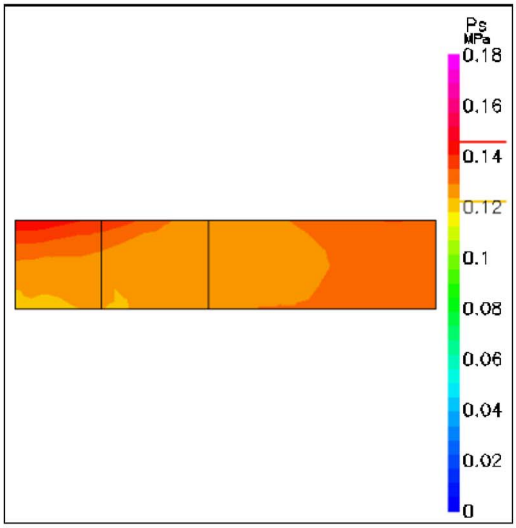

Uniform static pressure distribution at the end of the cross-piece meridional view.

Fig. 4 Inducer 13 deg (Q=83.3 kg/s and P_{inlet}=1 bar): Numerical results of the static pressure distribution without (on the left) and with (on the right) the cross-piece

ers 8 deg and 10 deg but not for inducer 13 deg. For a head drop of 15%, the resistance to the cavitation changes in a variable way: Very little for inducer 10 deg until very strongly for inducer 13 deg.

These results show that if we have to choose one of these three inducers to be placed upstream of an impeller with a flow rate that is equal or lower than Inducer 8 deg nominal flow rate, then Inducer 8 deg would be the optimal choice. Inducer 13 deg is more convenient for high flow rates and Inducer 10 deg behavior is intermediate between the two others.

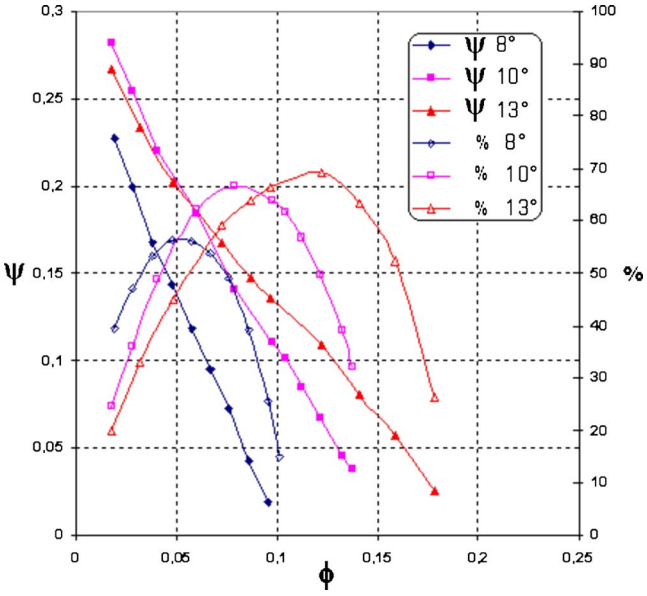

Fig. 5 The overall performances in noncavitating regime for the three inducers

In general, the best values of the suction specific speed are observed for flow rates higher than those corresponding to the maximum efficiency. Table 3 recapitulates the best values for the three inducers.

5.3 Numerical Results. It is clearly felt that there are many limitations of experimental measurements to describe the development of the flow fields. Then, an important role exists for fully three dimensional viscous flow analyses to fill in the details left by the experimentations. Nevertheless, these 3D analyses in the inducers previously tested may be made difficult by their low spiral angle and their long passages.

The real flow pattern within the rotating inducers is complex and three-dimensional. The long but tightly spiraled and high-solidity passages added to the vapor pockets seem to give rise to secondary flow fields strongly influenced by the blade walls and tip clearance.

To describe the irregular phenomena associated to the cavitating flows through the inducers, CFD computations have been performed on the three machines. The calculations presented here are carried on for isolated inducers, not taking into account their upstream and downstream components. The tip clearance effects are not incorporated in this first stage of investigation.

The flow is highly three-dimensional with tip leakage and backflow vortex cavitation. We cannot, therefore, expect quantitative agreement between observed and computed results, especially at low flow rates. Nevertheless, it is still interesting to compare general tendencies.

For cavitating flow situations in inducers—especially at part load conditions—the prediction of the correct swirl in the backflow and the pressure depression in the core is critical since it leads to vapor formation [37].

Table 2 Values of the flow coefficient and the angles of incidence corresponding to the maximum efficiency

β_{1T}	η_{MAX}	ϕ_N	i/β_{1T}
8 deg	0.56	0.057	0.057
10 deg	0.60	0.087	0.064
13 deg	0.68	0.107	0.09

5.3.1 Computational Mesh. The cavitating flow through a single blade passage is modeled at a range of flow rates and cavitation numbers. The domain consists of a region extending approximately more than one diameter upstream of the blade, a single inducer passage, and a corresponding region extending more than one diameter downstream of the blade (Fig. 8). It is common to make an extension of five diameters of the upstream and downstream regions. The length we chose for the upstream region may be insufficient to insure that the inflow boundary is not too close to the blade, but by increasing its length, one also increases the grid size and thus the computing time. Instead of increasing the upstream region, we chose to increase the blade passage grid size.

Due to extreme blade angles of the inducers, a special meshing strategy is required in order to prevent high mesh nonorthogonality. As illustrated by Figs. 8–10, the geometry of an inducer is particularly challenging for structured grid codes due to the fact that the blades angles at both inlet and outlet are quite close to the tangential direction.

The full mesh consists of approximately 300,000 active nodes (Fig. 10). It is composed of upstream and downstream grids added to a single-block H grid through the blade passage. The H grid type is more suited for blades with low to moderate solidity. Periodic connections are defined by the placement of periodic boundary control points (Fig. 9). More control points are added in the regions close to the blade leading and trailing edges (Fig. 9). They are restricted in their position by the periodic surface definitions. Grid elements inside the blade are "blocked off" to form the blade surface. The points placement is optimized to achieve a low grid skewness. Upstream and downstream blocks meshes (not represented in Fig. 9) are conventional in nature. The three grids are fully coupled and linked into one single mesh as show in Fig. 10. The meshes (generated by the mesh generator CFX-TurboGrid), consist of hexahedral elements.

5.3.2 Computational Methodology. After a grid dependence solution study for inducer 13 deg, an approximately 300,000-structured mesh for one blade passage was used for the computations. This study is time-consuming; we supposed then that this mesh size is sufficient for the two other inducers.

The total pressure is specified at the inlet, and the mass flow rate at the outlet. Appropriate stationary or rotating wall conditions are imposed on solid surfaces. A periodic boundary condition is used to connect the sides of the domain together. No-slip walls are used for all other boundaries. Turbulence in the flow is handled using a standard k-ε model with wall functions.

The nominal density ratio (ρ_l/ρ_v) is the ratio between thermodynamic values of density of liquid and vapor phases at the corresponding flow conditions. A value of 1000 is taken for this ratio in all computations in this study.

A very small noncondensable air fraction of 5.10^{-4} is used. The introduced nuclei mean diameter is 2.10^{-6} m. At LEMFI, we carried out cavitation tests with different water properties (water temperature, bubbles number, bubbles size, etc.) to investigate the influence of the liquid properties upon cavitation process. A special micro-bubbles generation system was developed at LEMFI and installed in the test loop. It consists of a high pressure pump with a bubble injector. Approximate bubbles characteristics were detected with an oxymeter.

In a first order of approximation, the values of condensation and vaporization factors F were, respectively, fixed to 0.1 and 50. The chosen values for F are derived from a sensibility study that we carried out for a simplified 2D geometry in a 8 deg Venturi, since the calculations in axial inducers are very time consuming processes. Experimental studies on this 8 deg Venturi were conducted by Stutz and Reboud [38], who used a double optical probe to measure the void fraction and velocity. The values which we chose for F_{vap} and F_{cond} were obtained by trial and error on the

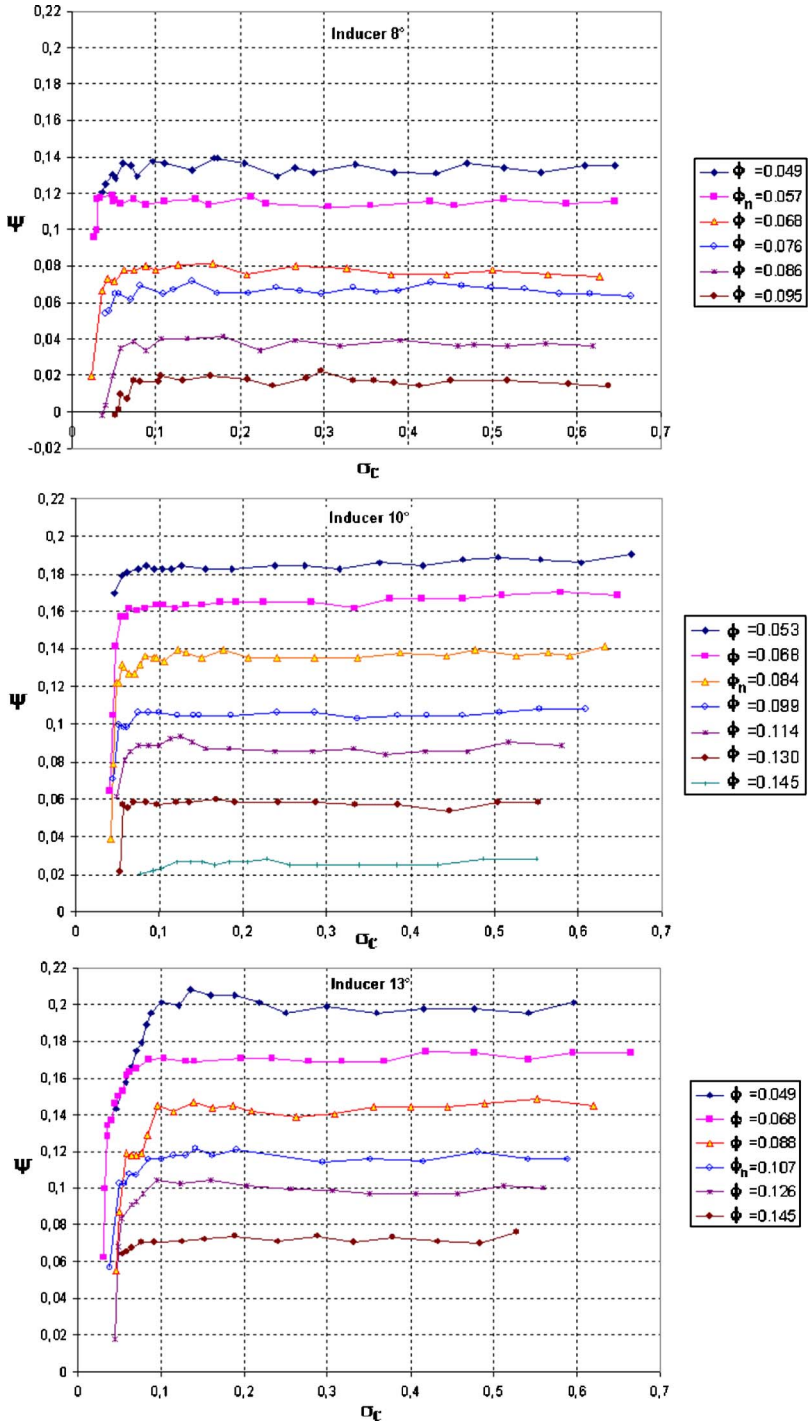

Fig. 6 Head-drop curves in cavitating regime for the three inducers—experimental results

8 deg Venturi until the predicted cavity length, the average frequency, and the corresponding average Strouhal number became equal to their experimental values. Coutier-Delgosha et al. [39] simulated by 2D computations, the viscous, compressible, and turbulent cavitation in the same Venturi.

Concerning our inducers, extensive studies are being carried out to investigate the influence of the condensation and vaporization coefficients F on the prediction of the overall performances and cavitation behavior of these axial machines.

The head-drop curves are created gradually. For each curve, a noncavitating solution was first obtained. The cavitation model was then activated and the inlet total pressure decreased by 10,000 [Pa] for each point on the curve. When the head-drop became significant, the inlet pressure was dropped in smaller increments of 1000 [Pa] and less, to overcome the high instability of the solution due to the strong nonlinear behavior of the cavitation.

The cavitation prediction for one flow rate and thus one head-drop curve is performed for approximately 15 operating points. The time consumed for the creation of one point is about 7 h (and more, especially for inducer 10 deg in one hand and near the head impairment zone in the other hand). In all the cases this required

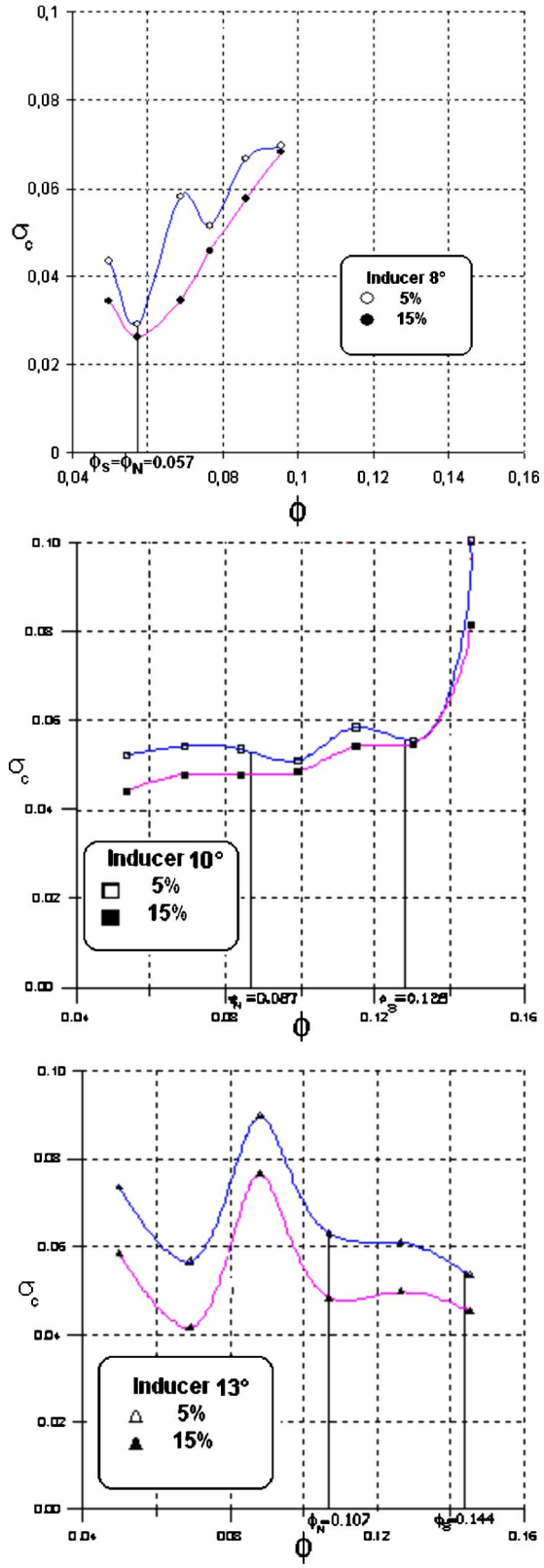

Fig. 7 Blade angle influence on the performance in a regime of cavitation

less than 900 iterations (except for Inducer 10 deg which requires 1200 iterations) on a standard machine (CPU 2.3 GHz, RAM 4 Go). Each calculation was declared converged when the maximum normalized residual dropped below 10^{-4}.

Table 3 The best values for the three inducers

β_{1T}	ϕ_N	$\sigma_{C,5\%}$	ϕ_S	$S_{\max,5\%}$
8 deg	0.057	0.030	0.057	534
10 deg	0.087	0.0520	0.128	482
13 deg	0.107	0.0608	0.144	509

5.3.3 Overall Performances and Pressure Plot. The pressure head coefficient is computed from the CFD simulation results by mass averaging the static pressure at the inlet and at the outlet. The calculated overall performances in noncavitating regime are presented in Fig. 11. In the same figure are also presented the experimental pressure head coefficient of Fig. 5. Compared to the experimental results, differences can be observed especially in low flow rates. Moreover, the experimental ψ-ϕ performance curve has a stable negative slope but the calculated curve has a locally positive slope in the case of low flow rates.

As it can be seen in Fig. 11, for inducer 8 deg and for the majority of Inducer 13 deg calculated flows, the predicted head slightly exceeds the measured one. This is a rather unusual result, since the tendency is to underestimate it.

This is partially due to the highly complicated geometry of the inducers (relatively low hub/tip ratio and high azimutal angle at the trailing edge) making the flow difficult to model especially at low flow rates. To this we can add:

The turbulence model which has to be improved for the cavitating flow simulation. It is not established that the k-ε model represents the optimum choice of turbulent model for cavitating flow in turbomachines. Moreover, the turbulence model was recently found to be also of first importance to predict accurately the cavitation phenomenon, and more specifically the unsteady process [39].

The tip clearance effects that were not taken into consideration in CFD calculations and that are actually characterized by the increase of the blade averaged drag coefficient.

For the head-drop curves, the calculations were made at many flow rates. As an example, only three values of Q/Q_n are presented here: 0.71, 1, and 1.14, which corresponds to part load, nominal flow rate and overload conditions (see Table 4 for the corresponding flow coefficients).

On Fig. 12(*a*) are presented only the numerical results (for clarity reasons) corresponding to the head-drop curves and on Fig. 12(*b*) the same results are presented with the experimental one. For the nominal conditions, the numerical flow coefficients for the three machines are exactly the same as the experimental ones. For the other flow rates, there is sometimes a small difference between ϕ_{num} and ϕ_{exp}. These slight differences are due to the fact that the calculations and the experimental tests were carried out separately.

As shown on Fig. 12(*a*), a qualitative agreement between the experimental and numerical results is obtained at nominal and relatively high flow rates: The head-drop occurs in the same way. At low flow rates, the numerical head-drop occurs as smoothly as the experimental one. At the nominal flow rate it occurs more rapidly. At high flow rates, the numerical curve falls as suddenly as the experimental one but at different inlet pressure: The blockage phenomenon has occurred experimentally and not yet numerically and reciprocally. The cavitation model does not predict with accuracy the blockage phenomenon. This can be attributed to the values chosen for the empirical coefficients of vaporization and condensation in the cavitation model. Moreover, the grid may need much refinement and a more elaborated stability analysis with respect to the different models used for the calculations.

For Inducer 10 deg, there is very little difference between the numerical head curves of the three flow rates. This suggests a

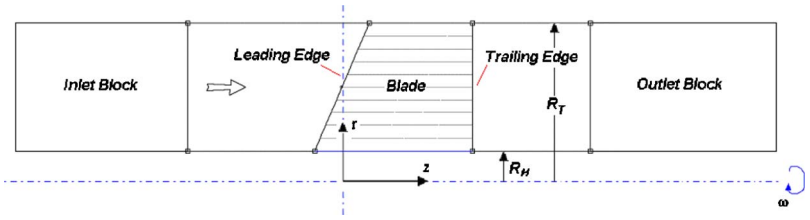

Fig. 8 Inducer 8 deg meridional view

larger than anticipated grid quality influence on the one hand and upstream region length on the other hand on the calculations quality.

5.3.4 Cavitation Figures. The predicted shapes of the cavitation pockets were compared to experimental visualizations at the three flow rates (nominal flow rate condition Q_n, part load conditions Q/Q_n=0.71, and overload conditions Q/Q_n=1.14).

Figure 13 shows as an example the numerical results for inducer 8 deg at nominal flow rate. The experimental pictures of cavitation and the associated predicted water vapor fraction are also represented in the same figure. The general development of cavitation in the inducer is illustrated at seven operating points, corresponding to decreasing cavitation numbers. The plot also illustrates the experimental head-drop curve. Evident correlation exists between the cavity development (length and wake) and the head fall. The cavity starts to develop much sooner at shroud than at hub (points 1–3). The predicted cavitation zones are located in the leading portion of the suction side as shown by the volume fraction plotted on the blade surface and in the inter-blade passage. Nevertheless, the pictures show that the simulated cavity is not as thick and long as the experimental one. As the inlet pressure decreases, the cavity lengthens and its thickness decreases (points 5 and 6): It is aspired forward in the blade-to-blade channel.

The CFD results show the three-dimensional character of the flow which is characterized by cavitation pocket that extends first forwards (σ_C=0.051, very unstable zone, Fig. 13(*a*)). In the same figure, 3D computations show, for the peripheral grid, the same phenomena. The pocket has the same orientation but experimentally, its extent is amplified by the presence of the tip clearance. When σ_C decreases, we observe the presence of attached pockets, which will lead the drop performance. It is a phenomenon of partial flow rate described in [40]. The large cavitation zone occurring at the suction side is transferred to the pressure side of the following blade (point 5).

Figure 14 shows for Inducers 8, 10, and 13 deg the magnitude and the streamlines of the water velocity $\mathbf{C}_l$. The considered value of σ_c is 0.28. The vector $\mathbf{C}_l$ is calculated on the blade surface and on the external vapor pocket surface, at three flow rates: Q/Q_n

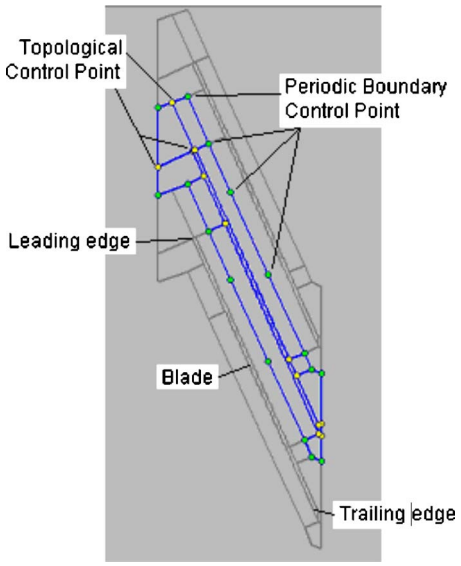

Fig. 9 Overall control point position in a blade-to-blade view

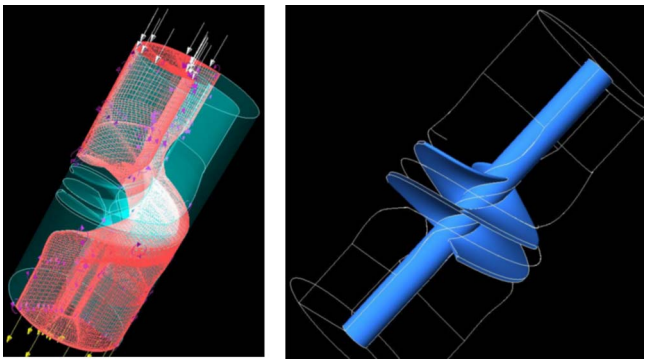

Fig. 10 Inducer 13 deg: Typical mesh used for the simulation, 320,000-structured mesh for one blade passage

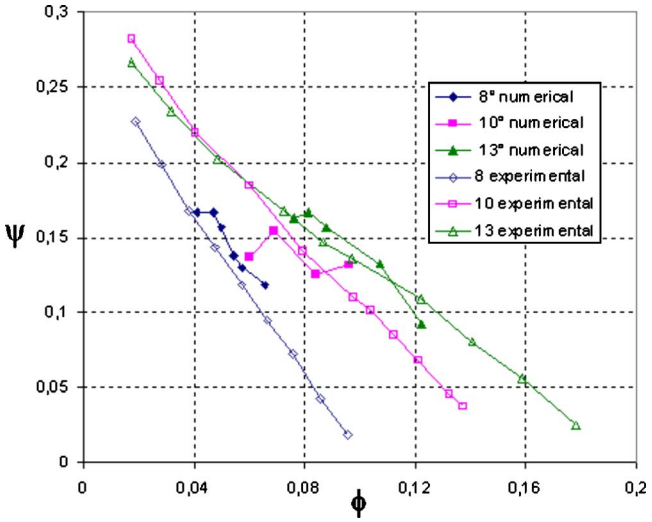

Fig. 11 Numerical and experimental pressure head coefficients in noncavitating regime for the three inducers

Table 4 Q/Q_n and the corresponding flow coefficients

	ϕ of Inducer 8 deg	ϕ of Inducer 10 deg	ϕ of Inducer 13 deg
Q/Q_n=0.71	0.041	0.060	0.076
Q/Q_n=1	0.057	0.0870	0.107
Q/Q_n=1.14	0.065	0.096	0.122

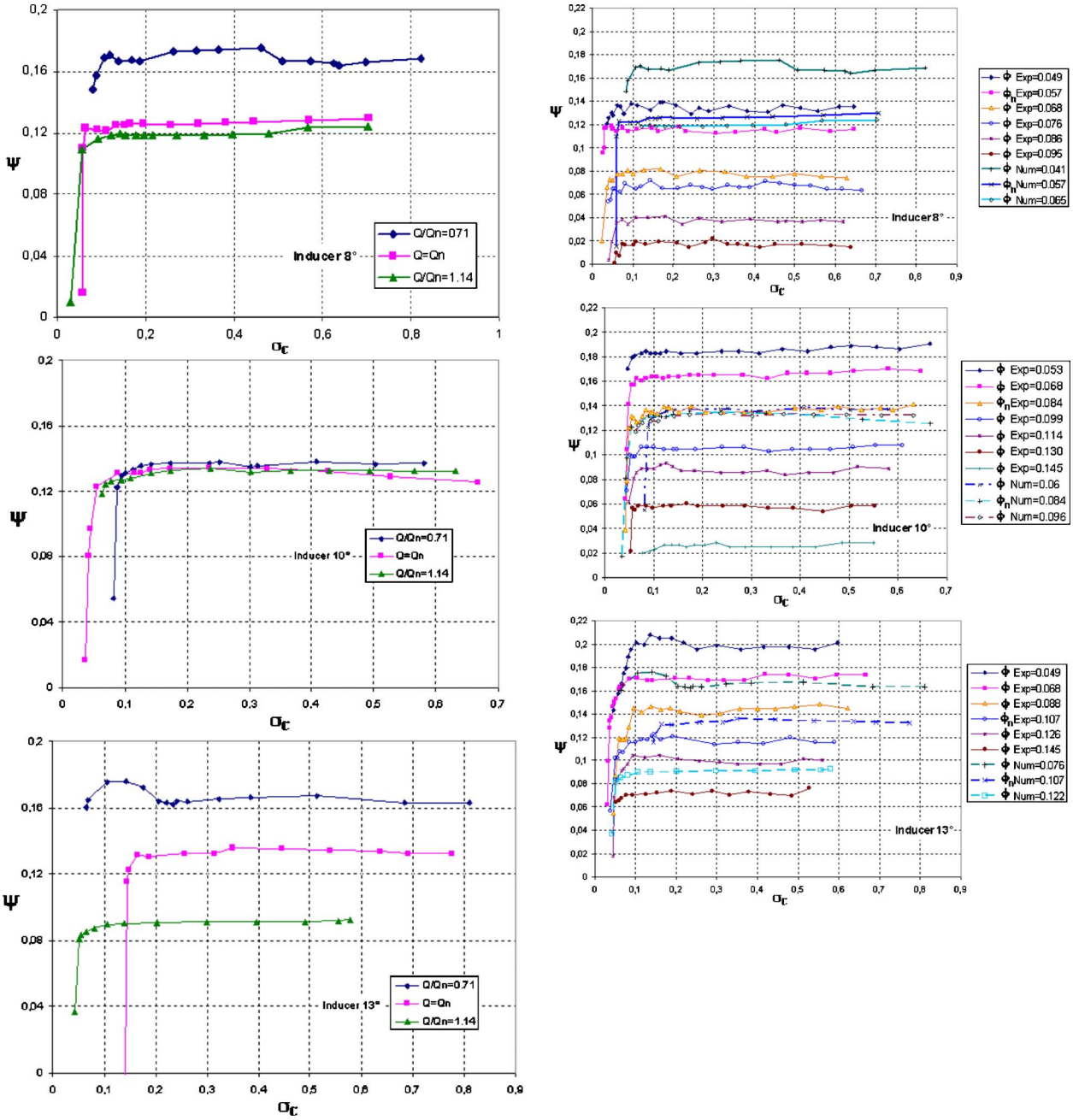

Fig. 12 (*a*) **Calculated head-drop curves for the three inducers.** (*b*) **Experimental and calculated head-drop curves for the three inducers.**

=0.71, 1, and 1.14. For the three inducers, the simulated pockets are first situated on the suction side of the blades. As it can be seen in this figure, inducer 8 deg has the best behavior with cavitation, then comes inducer 10 deg, and finally inducer 13 deg. Compared to the flow in the other inducers, the flow through Inducer 8 deg is well organized, with less extension of the vortex and gradient zones.

Those numerical simulations confirm the experimental results that the resistance to cavitation changes in a variable way from little (for inducer 10 deg) to strongly (for inducer 13 deg). In the same figure, 3D computations show for the three inducers that the flow is more organized at high flow rates than at lower flow rates. Thus, as Q/Q_n decreases from 1.14 to 0.71, the inducers become unstable and the meridional flow is less uniform. The backflow vortex is formed at the leading edge, on the suction side: It is the first cavitating structure that appears in the flow. It corresponds experimentally to the beginning of vibrations and pressure fluctuations. According to the experimental observations, this cavitation zone is unsteady and the flow is disturbed by the time-dependent bubble shedding.

At $Q/Q_n=1$ the vortex is amplified and a very high vibration level is observed experimentally. It is generated by the coupling between the backflow vortex and the cavitation.

6 Conclusion

The details of a homogeneous cavitation model are first presented and applied to analyze three axial inducers for the cavitating regime. The three machines are designed with the same methodology and are mainly differentiated by the value of the tip blade angle around the leading edge $\beta_{1T}=8$, 10, and 13 deg.

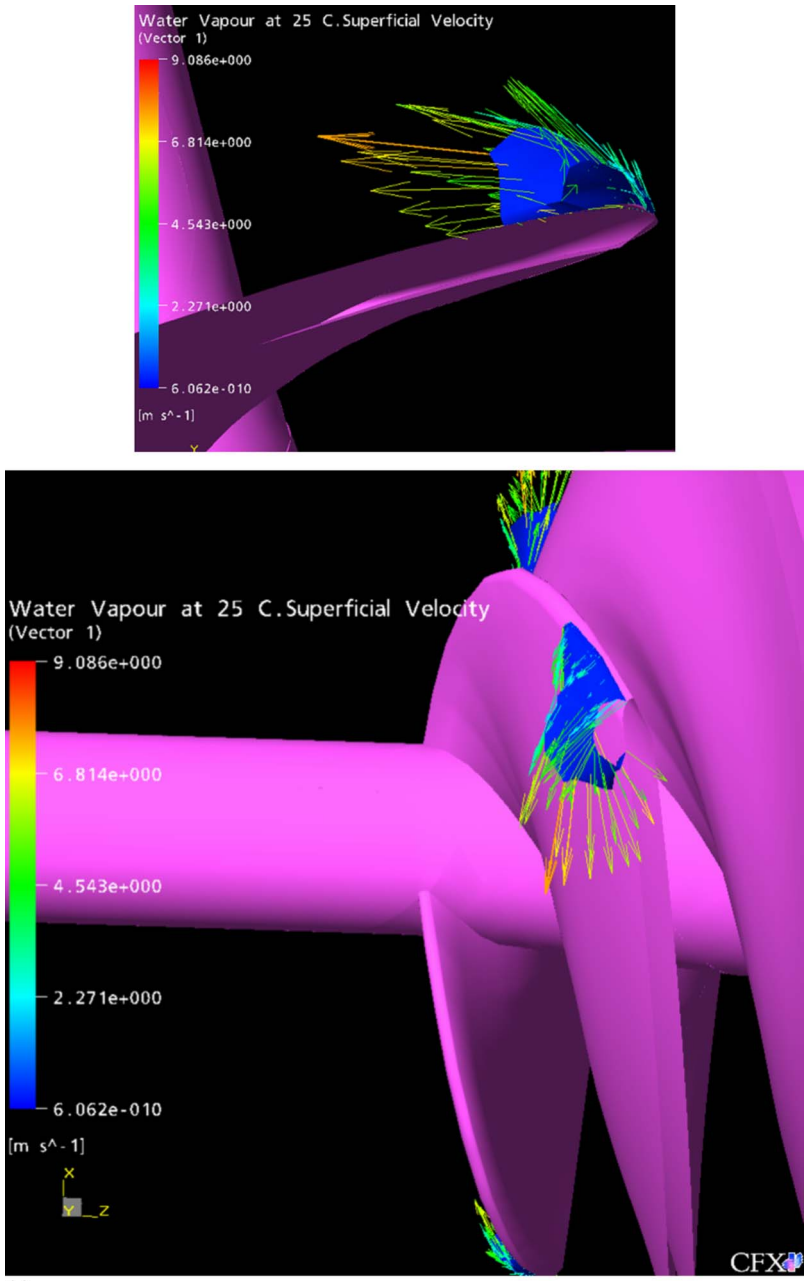

(a)

Fig. 13 Inducer 8 deg experimental and numerical cavitation figures (*a*) water vapor velocity vector at the leading edge, σ_C=0.051 corresponding to point (1) of the head-drop curve of part b; the first cavitation pocket extends forward; (*b*) experimental results of head-drop curve and cavitation figures at nominal flow rate and the associated numerically simulated flow visualization

The numerical and experimental results show the overall performances increase with β_{1T}. On the contrary, they confirm the relative superiority of Inducer 8 deg through the critical cavitation coefficient of 5%. For a 15% drop, the three inducers have quite the same performance. Contrary to Inducers 8 deg and 10 deg, we do not observe, for Inducer 13 deg, any increase of the critical cavitation number at high flow rates.

Internal flow analysis obtained from CFD, shows that this aspect is linked to the presence of the re-circulation vortex localized in periphery at the leading edge of the blade. This phenomenon can be associated to the vibrations in high and in partial flow rate, close to the design point and will be studied in future research.

The better cavitation performances of inducer 8 deg seems as well related to the longer wrap of the blade as to the inlet blade angle at the periphery.

Three criterions (among others) can be adopted separately or simultaneously to choose the best design for the three studied inducers: The critical cavitation coefficients corresponding to 5% and 15% of head drop, the head and efficiency produced in cavitating and noncavitating conditions, and the vibrations generated by the inducers operations. This study shows that the optimal inducer design depends on these criteria and on the pump flow rate.

The observation of the inducers performances and associated

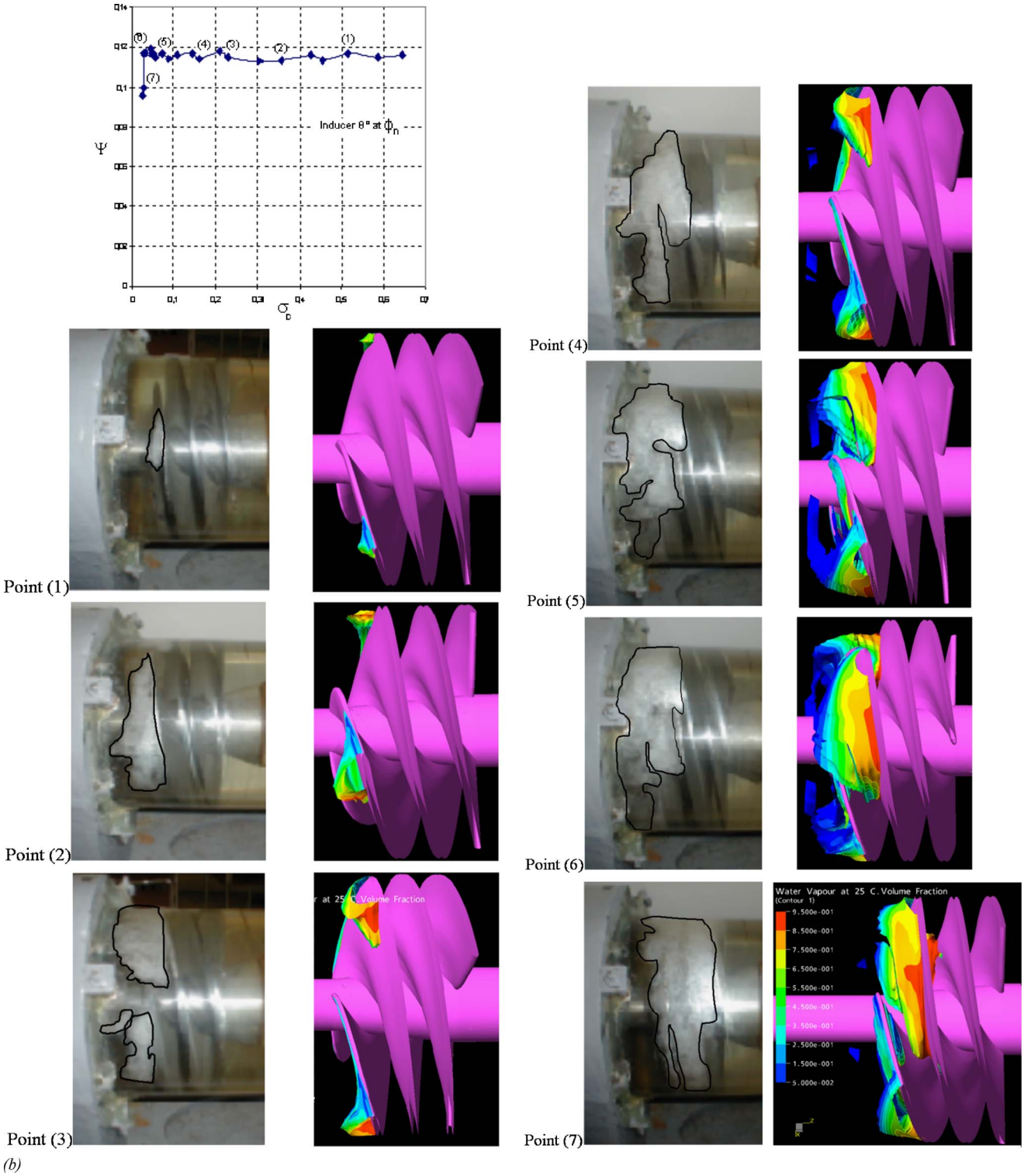

(b)

Fig. 13 (***Continued***).

flow fields lead us to conclude that if the flow rate through the pump placed downstream of one of these three inducers is Q then:

- if $Q \leq Q_{n \text{ of inducer 8 deg}}$, then inducer 8 deg is the most appropriate for the association inducer/pump;
- if $Q \geq Q_{n \text{ of inducer 13 deg}}$, then inducer 13 deg is the most appropriate for the association;
- from a cavitation point of view, inducer 10 deg behavior is intermediate between the two others: it is strongly affected by cavitation at high flow rates where it should not be used.

The CFD cavitation model implemented in the available code and used for the simulations overpredicts the cavitating flow in part load conditions. At overload where the blockage phenomenon occurs, the model underpredicts the head impairment location. At part load, there is a significant difference between experimental and numerical results partially due to the model itself but also to

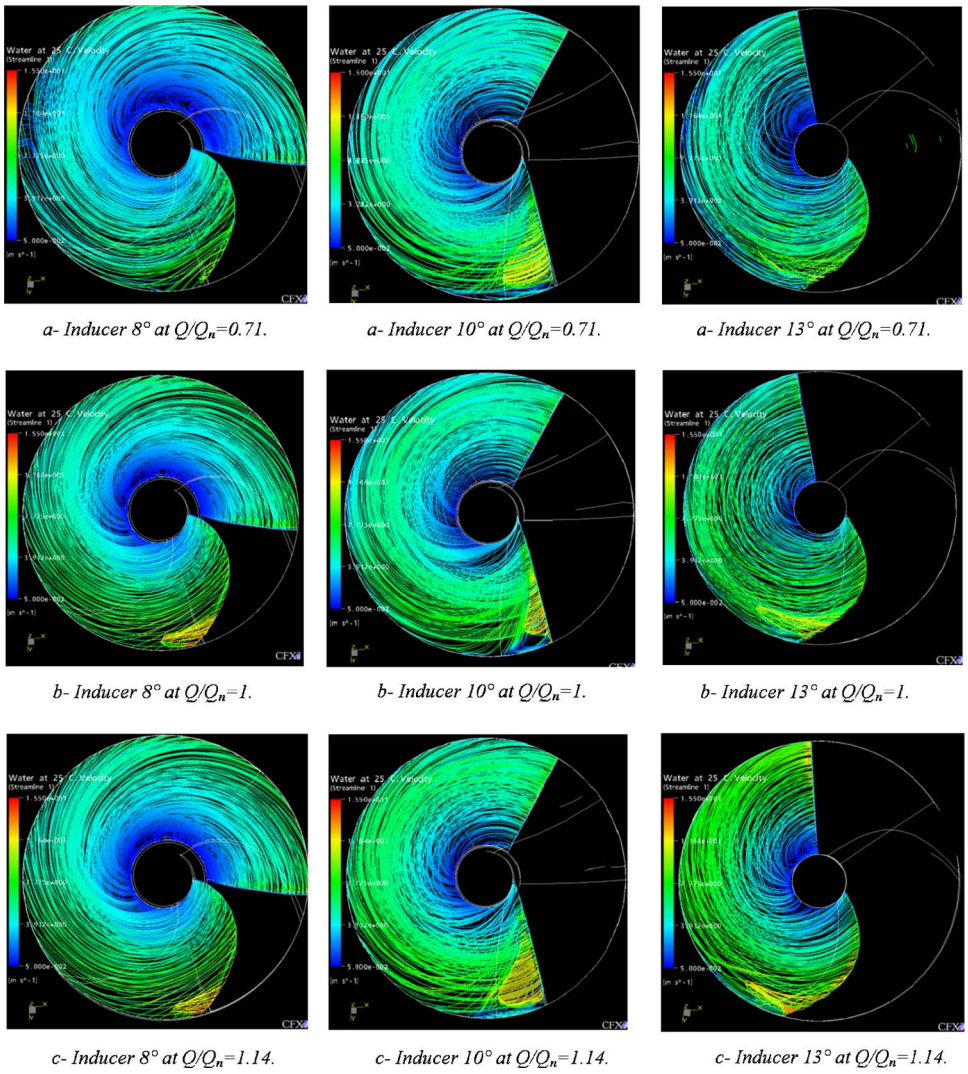

a- Inducer 8° at Q/Q_n=0.71. *a- Inducer 10° at Q/Q_n=0.71.* *a- Inducer 13° at Q/Q_n=0.71.*

b- Inducer 8° at Q/Q_n=1. *b- Inducer 10° at Q/Q_n=1.* *b- Inducer 13° at Q/Q_n=1.*

c- Inducer 8° at Q/Q_n=1.14. *c- Inducer 10° at Q/Q_n=1.14.* *c- Inducer 13° at Q/Q_n=1.14.*

Fig. 14 Computed magnitude and streamlines of C_l for three flow rates at $\sigma_c \sim 0.2$

the meshes quality, the upstream region length, and the tip clearance effects which were neglected for the numerical simulations.

Despite the fact that this cavitation model is powerful, it is a very time consuming process. One can also expect improvements in turbulence model of this commercial CFD code for the cavitating flows. Nevertheless, in the design and development of high-speed machinery, numerical analysis is expected for the acquisition of detailed information of the flow fields, which is not obtainable experimentally.

To obtain further improvement, a future development of cavitation research will include on the one hand the tip clearance effects and on the other hand the unsteady aspects of the pocket formation, transport, and implosion in the blade channel.

Acknowledgment

This study has been accomplished in relation and with the support of the ENSIVAL-MORET Company in Saint Quentin, France.

Nomenclature

C_m = meridional velocity [m/s]

$C_{m1}=Q/[\pi(R_{1T}^2-R_{1H}^2)]$ = inlet meridional velocity [m/s]

g = acceleration due to gravity [m/s^2]

$H=(P_{\text{static,outlet}}-P_{\text{static,inlet}})/\rho g$ = energy head based on the static pressure [m]

H_{tot} = energy head based on the total pressure [m]

$i=\beta_{1T}-\beta_1$ = incidence angle [rad]

NPSH = net positive suction head [m]

$\text{NPSH}_{5\%}$ = NPSH corresponding to 5% of head drop [m]

P_{elec} = electrical power (calculated by the formula $P_{\text{elec}}=\text{UI}$) [w]

Q = flow rate [m^3/s]

r = radial coordinate

R = radius [m]

R_T = tip radius [m]

R_H = hub radius [m]

$S=52.9326\ (\omega\sqrt{Q}/(g.NPSH_{5\%})^{0,75})$ = suction specific speed [-]

$T=R_H/R_T$ = hub to tip ratio [-]

$U_{1T}=\omega R_{1T}$ = peripheral speed of the impeller [m/s]

z = axial coordinate

β = angle of the relative velocity [rad]

β_{1T} = tip blade angle at inlet [rad]

$\eta = P_{hydr}/P_{shaft}$
$= \rho g H_{tot} Q/(\eta_{elec} P_{elec})$ = hydraulic efficiency [%]
η_{MAX} = best efficiency [%]
η_{elec} = electrical efficiency of the engine given by the manufacturer [%]
$\phi = C_{m1}/U_{1T} = tg\beta_1$ = flow coefficient [-]
ϕ_N = flow coefficient at design point [-]
ϕ_S = flow coefficient at S_{max} [-]
γ = stagger angle [rad]
$\psi = gH/\omega^2 R_T^2$ = pressure head coefficient [-]
θ = azimuthal angle [rad]
ρ = fluid density [kg/m^3]
$\sigma_c = gNPSH/1/2\omega^2 R_T^2$ = cavitation number [-]
$\sigma_{C,5\%}$ = critical cavitation number corresponding to 5% of head drop [-]
$\sigma_{C,15\%}$ = critical cavitation number corresponding to 15% of head drop [-]
ω = angular velocity [rad/s]

subscripts

max = maximum
n = nominal (design point)
T = tip
H = hub
S = Smax
1 = blade inlet
2 = blade outlet
l = liquid phase
v = vapor phase
d = dispersed (or noncondensable gas) phase

References

[1] Bakir, F., Rey, R., Gerber, A. G., Belamri, T., and Hutchinson, B., 2004, "Numerical and Experimental Investigations of the Cavitating Behavior of an Inducer," Int. J. Rotating Mach., **10**(1), pp. 15–25.

[2] Mejri, I., Bakir, F., Kouidri, S., and Rey, R., 2003, "Hub Shape Effects under Cavitation on the Inducers Performance," Fifth International Symposium on Cavitation (CAV 2003). OS-6-001, Osaka, Japan, November 1–4, 2003.

[3] Bakir, F., Kouidri, S., Noguera, R., and Rey, R., 1998, "Design and Analysis of Axial Inducers Performance," ASME Fluid Machinery Forum, Washington, D.C., paper FEDSM98 - 5118.

[4] Noguera, R., Rey, R., Massouh, F., Bakir, F., and Kouidri, S., 1993, "Design and Analysis of Axial Pumps," ASME Fluids Engineering, Second Pumping Machinery Symposium, pp. 95–111, Washington, USA.

[5] Mejri, I., Bakir, F., Kouidri, S., and Rey, R., 2005, "Influence of Peripheral Blade Angle on the Performance and the Stability of Axial Inducers," IMECH E Journal of Power and Energy, A04404, **219**, pp. 289–301.

[6] Mejri, I., Bakir, F., Rey, R., and Belamri, T., 2005, "Comparison of Computational Results Obtained from a VOF Cavitation Model with Experimental Investigations of three Inducers - Part I: Experimental Investigations," ASME Fluids Engineering Conference - Fifth Pumping Machinery Symposium. June 19–23, Houston, Texas.

[7] Mejri, I., Bakir, F., Rey, R., and Belamri, T., 2005, "Comparison of Computational Results Obtained from a VOF Cavitation Model with Experimental Investigations of Three Inducers - Part II: Numerical Approach," ASME Fluids Engineering Conference - Fifth Pumping Machinery Symposium. June 19–23, Houston, Texas.

[8] Bakir, F., Kouidri, S., Noguera, R., and Rey, R., 2003, "Experimental Analysis of an Axial Inducer: Influence of the Shape of the Blade Leading Edge on the Performance in a Regime of Cavitation," J. Fluids Eng., **125**, pp. 293–3001.

[9] Horiguchi, H., Semenov, Y., Nakano, M., and Tsujimoto, Y., 2003, "Linear Stability Analysis of the Effects of Camber and Blade Thickness on Cavitation Instabilities in Inducers," Fifth International Symposium on Cavitation (CAV 2003). OS-4-004, Osaka, Japan, November 1–4, 2003.

[10] Tsujimoto, Y., 2001, "Simple Rules for Cavitation Instabilities in Turbomachinery," Proceedings of the 4th International Symposium on Cavitation, CAV 2001. June 20–23, Pasadena, CA.

[11] Horiguchi, H., Watanabe, S., Tsujimoto, Y., and Aoki, M., 2000, "Theoretical Analysis of Alternate Blade Cavitation in Inducers," J. Fluids Eng., **122**(1), pp. 156–163.

[12] Watanabe, S., Sato, K., Tsujimoto, Y., and Kamijo, K., 1999, "Analysis of Rotating Cavitation in a Finite Pitch Cascade Using a Closed Cavity Model and a Singularity Method," J. Fluids Eng., **121**(4), pp. 834–840.

[13] Coutier-Delgosha, O., Perrin, J., Fortes-Patella, R., and Reboud, J. L., 2003, "A Numerical Model to Predict Unsteady Cavitating Flow Behavior in Inducer Blade Cascades," Fifth International Symposium on Cavitation (CAV 2003). OS-4-005, Osaka, Japan, November 1–4, 2003.

[14] Nakai, H., Horiguchi, H., Nakano, M., and Tsujimoto, Y., 2003, "Cavitating Flows in Centrifugal Impellers and their Stability Analysis," Fifth International Symposium on Cavitation (CAV 2003). OS-6-008, Osaka, Japan, November 1–4, 2003.

[15] Braun, O., Kueny, J. L., and Avellan, F., 2005, "Numerical Analysis of Flow Phenomena Related to the Unstable Energy-Discharge Characteristic of a Pump-Turbine in Pump Mode," ASME Fluids Engineering Conference - Fifth Pumping Machinery Symposium. June 19–23, Houston, Texas.

[16] Nohmi, M., and Goto, A., 2003, "Cavitation CFD in Centrifugal Pump," Fifth International Symposium on Cavitation (CAV 2003). OS-4-010, Osaka, Japan, November 1–4, 2003.

[17] Dupont, Ph., and Avellan, F., 1991, "Numerical Computation of Leading Edge Cavity," CAV 91 Symposium, 1st ASME - JSME Fluids Engineering Conference. June 23–27, Portland, Oregon.

[18] Delannoy, Y., and Kueny, J. L., 1990, "Cavity Flow Predictions Based on the Euler Equation," ASME Cavitation and Multiphase Flow Forum.

[19] Athavale, M., Li, H. Y., Jiang, Y., and Singhal, A. K., 2002, "Application of the Full Cavitation Model to Pumps and Inducers," Int. J. Rotating Mach., **8**(1), pp. 45–56.

[20] Gopalan, S., Katz, J., and Knio, O. M., 1999, "The Flow Structure in the Near Field of Jets and its Effect on Cavitation Inception," J. Fluid Mech., **398**, pp. 1–43.

[21] Hirschi, R., Dupont, P., Avellan, F., Favre, J. N., Guelich, J. F., Handsloser, W., and Parkinson, E., 1998, "Centrifugal Pump Performance Drop due to Leading Edge Cavitation: Numerical Predictions Compared With Model Tests," ASME J. Fluids Eng., **120**, pp. 705–711.

[22] Merkle, C. L., Feng, J., and Buelow, P. E. O., 1998, "Computational Modeling of the Dynamics of Sheet Cavitation," Proceedings of the 3rd International Symposium on Cavitation, CAV 98, April 7–10, Grenoble, France.

[23] Song, C. C. S., and He, J., 1998, "Numerical Simulation of Cavitating Flows by Single-Phase Flow Approach," Proceedings of the 3rd International Symposium on Cavitation, CAV 98, April 7–10, Grenoble, France.

[24] Kunz, R. F., Lindau, J. W., Kaday, T. A., and Peltier, L. J., 2003, "Unsteady RANS and Detached Eddy Simulations of Cavitating Flow Over a Hydrofoil," Fifth International Symposium on Cavitation, CAV 2003. OS-1-12, Osaka, Japan, November 1–4, 2003.

[25] Chen, Y., and Heister, S. D., 1996, "Modeling Hydrodynamic Nonequilibrium in Cavitating Flows," J. Fluids Eng., **118**, pp. 172–178.

[26] Sauer, J., and Schnerr, G. H., 2000, "Unsteady Cavitating Flow – A New Cavitation Model Based on a Modified Front Capturing Method and Bubble Dynamics," Proceedings of the 2000 ASME Fluids Engineering summer conference, Boston.

[27] Senocak, I., and Shyy, W., 2001, "Numerical Simulation of Turbulent Flows With Sheet Cavitation," Proceedings of the 4th International Symposium on Cavitation, CAV 2001, June 20–23, Pasadena, CA.

[28] Abgrall, R., and Saurel, R., 2003, "Discrete Equations for Physical and Numerical Compressible Multiphase Mixtures," J. Comput. Phys., **186**, pp. 361–396.

[29] Le Métayer, O., Massoni, J., and Saurel, R., 2004, "Elaborating Equations of State of a Liquid and its Vapor for Two-Phase Flow Models," Int. J. Therm. Sci., **43**, pp. 265–276 (in French).

[30] Mejri, I., Belamri, T., and Bakir, F., 2002, "CFX TascFlow^{TM}2.12: Validation of the VOF Model on the LEMFI Inducer," CFX European Conference, 16–18 September. Strasbourg, France.

[31] Sirignano, W. A., 1999, "*Fluid Dynamics and Transport of Droplets and Sprays*," Cambridge University Press, University of California, 313 pp.

[32] Kunz, R. F., Boger, D., Chyczewski, T., Stinebring, D., and Gibling, H., 1999, "Multi-phase CFD Analysis of Natural and Ventilated Cavitation about Submerged Bodies," 3rd ASME/JSME Joint Fluids Engineering Conference, San Francisco.

[33] Zwart, P. J., Gerber, A. G., and Belamri, T., 2004, "A Two-Phase Flow Model for Predicting Cavitation Dynamics," ICMF International Conference on Multiphase Flow, Yokohama, Japan, May 30–June 3, paper No. 152.

[34] Japikse, D., 2001, "Overview of Industrial and Rocket Turbopumps Inducer Design," Proceedings of the 4th International Symposium on Cavitation, CAV 2001, June 20–23, Pasadena, CA.

[35] Tsujimoto, Y., Horiguchi, H., and Qiao, X., 2005, "Backflow From Inducer and its Dynamics," ASME Fluids Engineering Conference - Fifth Pumping Machinery Symposium, June 19–23, Houston, Texas.

[36] Fiedrichs, J., and Kosyna, G., 2001, "Rotating Cavitation in a Centrifugal Pump Impeller of Low Specific Speed," ASME Fluids Engineering Division Summer Meeting, Louisiana, USA- paper FEDSM2001 – 18084.

[37] Hosangadi, A., Ahuja, V., and Ungewitter, R. J., 2005, "Simulations of Inducers at Low-Flow Off-Design Flow Conditions," ASME Fluids Engineering Conference - Fifth Pumping Machinery Symposium, June 19–23, Houston, Texas.

[38] Stutz, B., and Reboud, J. L., 1997, "Experiments on Unsteady Cavitation," Exp. Fluids, **22**, pp. 191–198.

[39] Coutier-Delgosha, O., Fortes-Patella, R., and Reboud, J. L., 2003, "Evaluation of the Turbulence Model Influence on the Numerical Simulations of Unsteady Cavitation," J. Fluids Eng., **125**, pp. 38–45.

[40] Tsujimoto, Y., Yoshida, Y., Maekawa, Y., Watanabe, S., and Hashimoto, T., 1997, "Observations of Oscillating Cavitation of an Inducer," J. Fluids Eng., **119**, pp. 775–781.

A Finite-volume Approach for Simulation of Liquid-column Separation in Pipelines

Mark A. Chaiko
Sr. Staff Scientist
PPL Corporation,
Two North Ninth Street,
GENPL5,
Allentown, PA 18101
e-mail: machaiko@pplweb.com

A finite-volume approach, based on the MUSCL-Hancock method, is presented and applied to liquid-column separation transients in pipelines. In the mathematical model, sudden closure of a valve on the downstream end of a pipeline initiates the hydraulic transient, while a head tank maintains constant upstream pressure. The two-phase fluid is treated as a homogeneous mixture, and changes in fluid pressure are assumed to occur at constant entropy. Effects of pipe elasticity on wave propagation speed are included in the model by coupling the circumferential stress-strain relation for the pipe wall to the local fluid pressure. In regions of the domain where the solution is smooth, second-order accuracy is achieved by means of data reconstruction based on sloping-difference formulas. Slope limiting prevents the development of spurious oscillations in the neighborhood of steep wave fronts. Data reconstruction leads to a piece-wise linear representation of the solution, which is discontinuous across cell boundaries. In order to advance the solution in time, a Riemann problem is solved on each cell junction to obtain mass and momentum flux contributions. A splitting technique, which separates flux terms from gravity and frictional effects, allows the compatibility equations for the Riemann problem to be expressed as total differentials of fluid velocity and an integral that depends only on the fluid pressure. Predictions for large-amplitude pressure pulses caused by liquid-column separation and rejoining are compared against experimental data available in the literature. Amplitude and timing of the predicted pressure response shows reasonably good agreement with experimental data even when as few as 20–40 computational cells are used to describe axial variations in fluid conditions along a pipeline of approximately 35 m *in length. An advantage of the current method is that it does not give rise to spurious oscillations when grid refinement is performed. The presence of nonphysical oscillations has been a drawback of a commonly used method based on discrete vapor cavities and characteristic treatment of wave propagation.* [DOI: 10.1115/1.2353271]

1 Introduction

It is well known that hydraulic transients in pipelines can cause localized and distributed vaporization within the fluid. Momentum effects, for example, can cause a liquid column to separate from the downstream side of a suddenly closed valve resulting in the formation of a localized vapor cavity. Transients of this type have been investigated analytically and experimentally by Li and Walsh [1], Safwat [2,3], and Barbero and Ciaponi [4]. In the experiments of Li and Walsh, water flow in a 2-in. horizontal plastic pipe was stopped suddenly by rapid closure of an air-operated valve. Photographs included in their paper show that a cloud of vapor and liberated gas bubbles first appears in the region immediately downstream of the valve. A growing cavity of pure vapor then begins to form between the valve and the departing water column. Shortly afterward, the bubbly liquid column reverses flow direction and advances toward the closed valve collapsing the cavity and generating a pulse of high pressure. The cycle repeats several times, but each time, viscous dissipation causes cavity size to be smaller than in the previous cycle.

Abrupt closure of a valve in a pipeline can result in liquid column separation on the upstream side of the valve as well as on the downstream side. At the instant of valve closure, liquid pressure on the upstream side of the valve rises sharply in accordance with the Joukowsky relation, which states that the rise in pressure is proportional to the fluid velocity just prior to valve closure, the constant of proportionality being the product of liquid density and wave speed [3]. If the flow path is such that the compression wave generated by valve closure can propagate upstream to a constant-pressure reservoir, the reflection from the reservoir will be in the form of a rarefaction wave. When this disturbance reaches the closed valve, pressure drops below that of the reservoir, and vaporization of the fluid in the neighborhood of the valve, and at considerable distances from the valve, can occur. Studies of liquid-column separation on the upstream side of a suddenly closed valve have been carried out experimentally and analytically by Baltzer [5], Simpson and Wylie [6,7], Martin [8], Weyler et al. [9], and Bergant and Simpson [10].

Pressure transients generated by liquid-column separation and rejoining can produce large force imbalances on segments within a piping network with potential to overstress pipe supports and damage piping components. Consequently, methods that can accurately predict the magnitude and frequency of pressure pulses associated with these phenomena have important application in the power and process industries where fluids are routinely transported though complex networks of piping. The most widely used approach for modeling liquid-column separation is the discrete vapor cavity model (DVCM) also referred to as CCM (concentrated cavity model) developed by Streeter and Wylie [11] in which the cavity is assumed to occupy the entire cross section of the pipe. A review of analytical methods for water hammer analysis performed by the Electric Power Research Institute [12] concluded that this approach was the most reliable method for simulating liquid-column separation transients. The model allows vapor cavities to form at fixed, predetermined locations corresponding to computational grid points within the solution domain. Cavity formation is initiated when the pressure at a grid point drops below the fluid saturation pressure. Liquid is assumed to

Contributed by the Fluids Engineering Division of ASME for publication in the JOURNAL OF FLUIDS ENGINEERING. Manuscript received May 20, 2005; final manuscript received March 26, 2006. Assoc. Editor: Georges L. Chahine.

always occupy regions between grid points. A method-of-characteristics (MOC) solution of the single-phase water hammer equations provides a description of wave transmission from grid point to grid point. In purely single-phase problems, the MOC yields velocity and pressure at each computation grid point in the domain; however, when vaporization is predicted to occur at a particular location, the pressure becomes a known quantity, i.e., it is equal to the saturation pressure. In this case, the MOC approach is modified to allow computation of two fluid velocities: one for each side of the vapor cavity (the vapor cavity is treated as an internal pressure boundary condition). From these two velocities and the pipe flow area, the volume of the cavity is determined as part of the solution. Vapor-cavity volume is monitored at each time step to check for cavity collapse that occurs when calculated cavity volume returns to zero. The magnitude of the pressure spike and the fluid velocity at the instant of cavity collapse are obtained by switching back to the single-phase water hammer equations at that location.

The major drawback of the DVCM is that solutions tend to become artificially spiky when a relatively fine mesh is used. Specifically, if vapor formation is allowed to initiate at all grid points where fluid pressure drops below vapor pressure, and mesh refinement is performed, the solution becomes corrupted with spikiness and high-frequency oscillations. As discussed in [12], there are a number of variations with regard to implementation of the DVCM that are designed to overcome this difficulty. One approach that has been used is to only allow vapor cavities to form at judiciously selected locations such as at high points in the system, while the minimum pressure at other grid points is limited to saturation pressure. The other alternative is to allow vapor formation at all grid points while restricting the number of reaches such that a relatively coarse grid is maintained. The discrete cavity approach can also become complicated when it is desired to incorporate vapor cavity formation adjacent to moving components such as valves and pumps, e.g., formation of a vapor cavity on the downstream side of a closing valve before the valve has completely closed. Other limitations include the inability of the cavity to propagate with the flow and a tendency of the model to overpredict the magnitude of pressure spikes generated by liquid-column rejoining [7,12]. With the purpose of limiting overshoot on pressure pulses and reducing excessive numerical oscillations, Wylie [13] has taken the approach of introducing a small amount of noncondensable gas into the vapor cavity to provide numerical damping. This method, which is referred to as the discrete gas cavity model (DGCM), shows better agreement with experimental data than does the DVCM. The gas cavity model contains an adjustable parameter, namely the initial void fraction α of the noncondensable gas. Numerical studies suggest that a value of $\alpha=10^{-7}$ provides sufficient damping to achieve reasonable agreement between calculations and column separation experiments [4,13]; however, the actual volumetric concentration of free gas is generally unknown in most practical problems. Moreover, calculation results are sensitive to the initial assumed void fraction [4]. In both the DVCM and the DGCM, vapor and gas volumes are usually computed using the backward-Euler method to introduce numerical dissipation into the solution (see, for example, [4,14]), and consequently, solutions obtained with these discrete models are restricted to first-order accuracy.

A number of system modeling codes that contain the physical models necessary for simulation of water hammer with liquid-column separation have been developed for nuclear power plant thermal-hydraulic analysis, e.g., RELAP [15] and TRAC [16]. These codes emphasize highly detailed, thermal-hydraulic models required for simulation of loss-of-coolant accidents in nuclear reactors. Both codes employ nonequilibrium, two-fluid models that consist of six balance equations. Solution techniques, based on finite-volume formulations, make use of semi-implicit numerical schemes that are designed to minimize computation times as much as practicable. Owing to the complexity of the field equations and closure relations, numerical solutions are, however, limited to first-order accuracy. Although this level of numerical accuracy has been found to be satisfactory for typical steam-liquid flow [17] and a wide range of reactor transients, it is not well suited for tracking the propagation of steep, large-amplitude pressure waves generated by liquid-column separation, as truncation errors can diffuse the sharpness of the wave front.

The purpose of the present work is to develop a numerically stable, second-order-accurate approach for solving hydraulic transients involving liquid-column separation and column rejoining in which cavitation is described by a continuum rather than discrete model. The approach adapts the high-resolution finite volume methods developed for the study of shock waves in gas flows [18] to the solution of the homogeneous, equilibrium, fluid model. The governing equations, which are solved in conservation form with second-order accuracy, incorporate pipe flow area variation with pressure as well as transient friction effects, and assume density change at constant entropy. Slope limiting is used to eliminate spurious oscillations that typically arise in the neighborhood of steep wave fronts when standard second-order solution methods such as Lax-Wendroff, MacCormack, and Beam-Warming are used [18,19]. For example, Kranenburg [20] found that the Lax-Wendroff method, when applied to cavitating pipe flows, produced solutions containing nonphysical oscillations and computational instabilities, and in order to obtain stable solutions, it was necessary to incorporate additional numerical viscosity into the computational scheme. A finite-volume technique was chosen for the present study because the wave speed is highly discontinuous across the phase boundary, and therefore, direct solution of the governing equations by the method of characteristics is not practicable. The strong discontinuity in wave speed precludes the use of interpolation in determining the origination point of a characteristic on a previous time level. The finite-volume method used in this work does, however, incorporate the method of characteristics, but only in the solution of an auxiliary Riemann problem in which the origination point associated with a characteristic is irrelevant. In addition, a variable transformation allows the Riemann problem to be solved in terms of a composite function of pressure that is continuous across the phase boundary.

Although the approach presented here is somewhat more complicated to implement than the DVCM, it has a number of advantages. First, solutions do not develop artificial spikiness when refined computational meshes are employed. This permits the use of successive grid refinement in evaluating whether sufficient resolution has been achieved in the solution of a column separation problem. The ability to examine the behavior of a solution on successively refined grids makes computations performed with the present finite-volume method more reliable than those computed with the DVCM in cases where experimental data are not available for comparison. Second, the method does not rely on the use of noncondensable gas to dampen nonphysical oscillations as in the DGCM. This later point is significant in light of the fact that noncondensable gas release should not play a significant role in the physics of the very rapid column separation transients investigated in the present work. As discussed in [4,14], gas release effects become important in transients occurring in long pipelines where the wave reflection time is on the order of seconds. Such pipelines are orders of magnitude longer than those considered in the present study. Other advantages are that predicted pressure amplitudes do not exhibit significant overshoot, and since the fluid is treated as homogeneous, no special considerations are required for the treatment of boundary conditions adjacent to dynamic components such as closing valves or pumps. Moreover, nonlinear convective terms are easily incorporated into the solution, whereas these terms are almost always neglected in characteristic-based water hammer analyses in order to obtain linear wave-propagation paths between discrete vapor cavities. Although inclusion of the convective terms does not have a significant influence on the solution to the fast hydraulic transients discussed

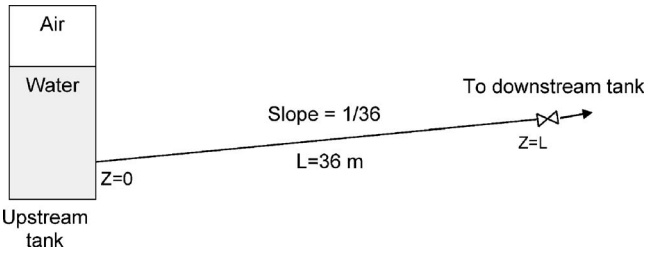

Fig. 1 Simplified schematic of experimental apparatus used by Simpson and Wylie for study of liquid-column separation and rejoining [6]

in this work, it does, however, extend the range of applicability of the model to include slower transients that occur on a time scale defined by the propagation of kinematic waves. Finally, a simple standard technique, dimensional splitting, exists for extending finite-volume calculations to multidimensions, if necessary [18]. The applicability of characteristic solution methods, on the other hand, is not easily extended to include multidimensional transient fluid problems.

Validation of the homogeneous, equilibrium, two-phase model and the finite-volume solution method is provided by comparing results against experimental data obtained from the water hammer experiments of Simpson and Wylie [6] and Bergant et al. [14,21]. Section 2 of this paper describes the experimental apparatus used by Simpson and Wylie to study liquid-column separation on the upstream side of a suddenly closed valve. This setup defines the physical model for the present analytical study. A similar experimental apparatus was developed by Bergant and Simpson [21], and physical characteristics are included in Sec. 2. Equations governing the dynamics of the flow and the finite-volume solution approach are presented in Secs. 3 and 4, respectively. Simulation results are compared against experimental records in Sec. 5, and conclusions are drawn in Sec. 6.

2 Physical Model

The physical model emulated in this study consists of the experimental apparatus designed and constructed by Simpson and Wylie [6] for investigation of liquid-column separation and rejoining. A simplified schematic of the apparatus is shown in Fig. 1. The system consists of a head tank that can be pressurized with air, and a copper pipe with a fast-closing ball valve on the downstream end of the line. The pipe inside diameter is 19.05 mm (0.06250 ft), and the wall thickness is 1.588 mm (0.005210 ft). Pipe length from the head tank to the valve is 36 m (118 ft). The 36-m copper pipe contains one 90 deg bend, and slopes upward with a rise of 1 m over the total length of 36 m. Water temperature was maintained at approximately 24°C (75°F). The wave speed for the liquid-filled line was determined, by spectral analysis, to be 1280 m/s (4,200 ft/s).

In the experiments, an initial steady-state flow was established to the downstream tank. The ball valve was then closed suddenly to create a rapid rise in pressure. Two experimental runs that generated vaporous cavitation zones upstream of the ball valve were selected to assess the ability of the model and numerical method to accurately predict the pressure response during transients that include column separation and rejoining. The experimental conditions associated with these two runs are summarized in Table 1.

A similar experimental apparatus was designed and constructed by Bergant and Simpson [21]. Pipeline length is 37.2 m, pipe inside diameter is 22.1 mm, wall thickness is 1.6 mm, and water temperature is 20°C. The copper pipeline rises 2.0 m with constant slope along the direction of initial flow. A downstream ball valve is closed rapidly (9 ms closure stroke) to initiate a water hammer transient. Two transients (Runs 3 and 4 in Table 2) were selected to validate the present model. In Runs 1–3, the initial velocity is high enough to cause cavitation in the vicinity of the closed downstream valve, while in Run 4, the fluid remains entirely in the liquid state.

Table 1 Conditions for Simpson and Wylie [6] Experiments

Run No.	Initial velocity	Pressure head at $z=0$ (gauge)
1	0.332 m/s	23.41 m
	(1.09 ft/s)	(76.80 ft)
2	1.125 m/s	21.74 m
	(3.691 ft/s)	(71.32 ft)

3 Governing Equations

The one-dimensional, homogeneous-fluid continuity and momentum equations

$$\frac{\partial}{\partial t}(\rho A)+\frac{\partial}{\partial z}(\rho u A)=0 \tag{1}$$

and

$$\frac{\partial}{\partial t}(\rho u A)+\frac{\partial}{\partial z}\left(\rho u u A+pA-\frac{1}{2}A' p^2\right)+\rho A g\sin\theta+\frac{1}{4}f\pi D\frac{\rho u|u|}{2}=0 \tag{2}$$

describe the dynamics of the flow in a circular pipe. Here $p(z,t)$ is the pressure, $\rho(p)$ is the fluid density, $u(z,t)$ is the fluid velocity, $A(p)$ is the pipe flow area, f is the Darcy friction factor, g is the acceleration due to gravity, θ is the angle of inclination, t is the time, z is the axial distance along the pipe, and $A'=dA/dp$. Note that the form of Eq. (2) applies only to the case where dA/dp is constant.

Since the pipe material is elastic, the flow area can vary with fluid pressure. When the fluid pressure is greater than ambient (atmospheric) pressure p_∞, a hoop stress is induced in the pipe wall, and there is an accompanying increase in flow area. Variation of flow area with pressure is described through the stress-strain relation [22]

$$A(p)=A_0\left[1+\frac{D_0(p-p_\infty)}{eE}\left(1+\frac{e}{D_0}\right)c_1\right] \tag{3}$$

where A_0 and D_0 denote the pipe flow area and the inside diameter for the unpressurized state, e refers to the thickness of the pipe wall, and E is the modulus of elasticity for the pipe material. For copper, the modulus of elasticity is 120 GPa (17×10^6 psi) [23]. The constant c_1 included in Eq. (3) is a piping restraint factor. For pipe anchored against longitudinal movement, and having $D_0/e<25$, the appropriate relation for c_1 is [13]

$$c_1=\frac{2e}{D_0}(1+\nu)+\frac{D_0(1-\nu^2)}{D_0+e} \tag{4}$$

where ν is Poisson's ratio, which for the copper pipe material, has a value of 0.35 [24]. Pipe stresses are assumed not to exceed the yield point.

Table 2 Conditions for experiments performed by Bergant et al. [14,21]

Run No.	Initial velocity	Pressure head at z=0 (gauge)
3	0.30 m/s	22 m
	(0.98 ft/s)	(72 ft)
4	0.20 m/s	32 m
	(0.66 ft/s)	(105 ft)

Since changes in fluid density are assumed to occur at constant entropy, the density depends only on the pressure. In the subcooled liquid region defined by $p > p_{sat}(T_0)$, the density is related to the pressure through

$$\rho(p) = \rho_f(T_0)\left[1 + \frac{p - p_{sat}(T_0)}{\kappa}\right] \tag{5}$$

where the constants T_0 and κ are the initial temperature and bulk modulus of the liquid. A typical value of $\kappa = 300{,}000$ psi (2.07 GPa) is used for water at ordinary temperatures [13]. Within the saturated region, $p \leq p_{sat}(T_0)$, the assumption of a homogeneous mixture at thermodynamic equilibrium and at constant entropy s leads to the following relation for the density as a function of pressure

$$\rho(p) = \left(v_f(p) + \frac{s - s_f(p)}{s_{fg}(p)} v_{fg}(p)\right)^{-1} \tag{6}$$

where v is the fluid specific volume, and the subscripts f and g refer to saturated liquid and vapor, respectively. The effect of surface tension on liquid-column separation is assumed negligible.

A head tank maintains pressure at the upstream end of the pipe; therefore, the pressure at $z=0$ is constant and equal to the tank pressure p_T applied during the experiments. On the downstream end ($z=L$), the fluid velocity is a specified function of time during the valve closure stroke and zero for the remaining part of the transient. The initial velocity of the fluid in the pipe is uniform and equal to u_0. Initial and boundary conditions for Eqs. (1) and (2) consist of

$$u(z,0) = u_0 \tag{7a}$$

$$p(z,0) = p_T - z\rho(p_T)\left(\frac{f u_0^2}{2D} + g \sin\theta\right) \tag{7b}$$

$$p(0,t) = p_T \tag{8a}$$

and

$$u(L,t) = \begin{cases} V(t) & \text{for } 0 \leq t \leq t_1 \\ 0 & \text{for } t > t_1 \end{cases} \tag{8b}$$

where $V(t)$ is a specified velocity boundary condition derived from the experimental data, and t_1 is the time interval during which the data are applied as a boundary condition. In developing the initial pressure distribution $p(z,0)$, the effect of the pressure gradient on liquid density is neglected.

In validating the proposed fluid-dynamics model and numerical solution method for simulation of liquid-column separation transients, it is important to accurately represent the velocity at $z=L$ during the closure stroke of the ball valve. A mathematical model for the flow resistance generated during closure of the valve could be employed, but this would introduce inaccuracies into the solution in addition to those attributable to the fluid model and the solution method. Therefore, in order to focus the validation on the fluid-dynamics model and the finite-volume numerical scheme, the velocity at the valve during closure is determined implicitly from the experimental data. For the first 30 ms of Runs 1 and 2, the velocity $V(t)$ at the valve is determined by matching the calculated pressure at the valve with the experimental record. After the first 30 ms, the fluid velocity at the valve is set to zero. Valve closure time for the Simpson and Wylie experiments ranged from 10 ms to 25 ms [6]. The time interval $t_1 = 30$ ms was chosen to bound the longest closure time for the valve. In the experiments performed by Bergant et al. (Runs 3 and 4), valve closure time was 9 ms; therefore, the velocity at the valve was derived from the experimental record for $t \leq t_1 = 10$ ms, and was specified as zero for $t > t_1$. Figure 2 shows a plot of the specified downstream fluid velocity $V(t)$ in Eq. (8*b*) derived from the experimental data for Run 1 defined in Table 1.

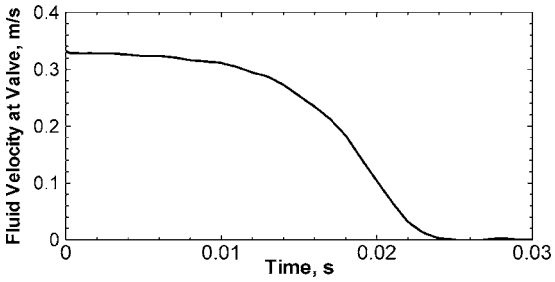

Fig. 2 Specified downstream fluid velocity $V(t)$ in Eq. (8) derived from experimental data for Run 1 defined in Table 1

As shown by Bergant and Tijsseling [14], accurate simulation of wave attenuation in single-phase water hammer transients requires consideration of unsteady friction effects. Following the approach used in [14,25], the friction factor f in Eq. (2) is expressed in terms of the Brunone model [26] as modified by Vítkovský [25]

$$f = f_q + \frac{kD}{u|u|}\left(\frac{\partial u}{\partial t} + a\ \text{sign}(u)\left|\frac{\partial u}{\partial z}\right|\right) \tag{9}$$

where f_q is the quasisteady Darcy friction factor, which is computed from the Swamee-Jain equation [24] for turbulent flow and as 64/Re for laminar flow. As suggested in [25,27], the Brunone friction coefficient k is evaluated as $k = \frac{1}{2}(C^*)^{1/2}$, where the shear decay coefficient C^* is defined by

$$C^* = \begin{cases} 0.00476 & \text{for laminar flow} \\ \dfrac{12.86}{\text{Re}^{\log_{10}(15.29/\text{Re}^{0.0567})}} & \text{for turbulent flow} \end{cases} \tag{10a}$$

In computing the Reynolds number for the homogeneous fluid, the viscosity μ in the two-phase region is expressed in terms of the fluid quality x according to [28]

$$\mu = \frac{\mu_f}{x\mu_f/\mu_g + (1 - x)} \tag{10b}$$

In Eq. (9), the wave speed a through the homogeneous fluid within the pipe is computed from Eq. (26).

4 Solution Method

A second-order-accurate, finite-volume numerical formulation with operator splitting is used to solve the governing continuity and momentum equations. Slope limiting is employed to prevent nonphysical oscillations in the neighborhood of steep pressure and velocity gradients. Selection of this approach for simulation of large-amplitude pressure pulses caused by liquid-column separation and rejoining is motivated by the excellent agreement achieved between numerical simulations and experiments obtained by Igra et al. [29,30] for propagation and reflection of intense pressure waves in gases and dust suspensions. The present study differs significantly, however, from the work of Igra et al. in the nature and complexity of the associated Riemann problem. For the predominately liquid medium considered here, the assumption of constant entropy greatly simplifies the Riemann problem and its solution as compared to the studies in [29,30]. In addition, the present analysis is limited to only one space dimension.

The domain is divided into N computational cells of equal length as shown in Fig. 3, and the solution is then computed on each grid point $j \in \{1, \ldots, N\}$, corresponding to the cell center. An operator splitting technique is used to decouple source term contributions associated with friction and gravity from mass and momentum flux effects, resulting in two subproblems. Splitting the problem in this manner allows the compatibility relations associ-

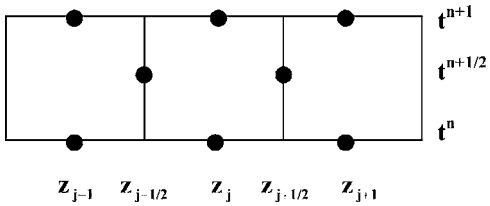

Fig. 3 Finite-volume representation of computational domain

ated with the auxiliary Riemann problem to be expressed as total differentials. Gravity and friction effects are captured by

$$\frac{\partial}{\partial t}(\rho A) = 0 \tag{11a}$$

and

$$\frac{\partial}{\partial t}(\rho u A) = -\rho A g \sin\theta - \frac{1}{4} f \pi D \frac{\rho u|u|}{2} \tag{11b}$$

while mass and momentum flux contributions are accounted for by

$$\frac{\partial}{\partial t}(\rho A) + \frac{\partial}{\partial z}(\rho u A) = 0 \tag{12a}$$

and

$$\frac{\partial}{\partial t}(\rho u A) + \frac{\partial}{\partial z}\left(\rho u u A + pA - \frac{1}{2}A' p^2\right) = 0 \tag{12b}$$

If $\Lambda_0(\Delta t)$ and $\Lambda_1(\Delta t)$ represent difference operators for the second-order accurate numerical integration of the split Eqs. (11) and (12), respectively, over one time step Δt, then according to the operator splitting theory of Strang [31,32], the sequential application of discrete solution schemes defined by

$$\Lambda(\Delta t) \equiv \Lambda_0\left(\frac{1}{2}\Delta t\right)\Lambda_1(\Delta t)\Lambda_0\left(\frac{1}{2}\Delta t\right) \tag{13}$$

provides a second-order accurate integration of the complete Eqs. (1) and (2) over Δt. In carrying out the numerical integration represented by $\Lambda(\Delta t)$, the results obtained from the first half-step integration $\Lambda_0(\Delta t/2)$ are used as initial data for the integration over Δt represented by $\Lambda_1(\Delta t)$. Results from the second integration step provide initial conditions for the third integration, which is carried out over $\Delta t/2$.

4.1 Integration Represented by $\Lambda_0(\Delta t/2)$. From Eq. (11*a*), the quantity ρA is constant in time for any fixed value of z. Equation (11*b*) can thus be simplified to

$$\frac{\partial u}{\partial t} = -g\sin\theta - f\frac{u|u|}{2D} \tag{14}$$

Expanding the derivative in Eq. (11*a*) leads to the restriction

$$\frac{\partial p}{\partial t}\left(\rho\frac{dA}{dp} + A\frac{d\rho}{dp}\right) = 0 \tag{15}$$

on the variation of pressure, flow area, and density for this part of the split problem. Since ρ, A, dA/dp, and $d\rho/dp$ are all greater than zero, relation (15) requires $\partial p/\partial t = 0$, and therefore, the only unknown in the Λ_0 problem is the velocity u. Note that the friction factor f depends on the fluid velocity u through Eq. (9). Substituting Eq. (9) into Eq. (14) and evaluating the resultant expression at $z = z_j$ leads to the set of ordinary differential equations

$$\left(1 + \frac{1}{2}k_j\right)\frac{du_j}{dt} = -g\sin\theta - \frac{f_{q,j}u_j|u_j|}{2D_0} - \frac{k_j a_j}{2}\mathrm{sign}(u_j)|m(u)_j| \tag{16}$$

where $m(u)_j$ denotes the slope of the velocity in cell j evaluated consistent with the form of Eqs. (18) and (19). A second-order Runge-Kutta method is used to integrate Eq. (16) explicitly on each grid point $j \in \{1, \ldots, N\}$ over the time interval $1/2\ \Delta t$, where $\Delta t = t^{n+1} - t^n$.

4.2 Integration Represented by $\Lambda_1(\Delta t)$. Conservation equations (12) are numerically integrated on a uniform grid of finite volumes as shown in Fig. 3. Central differences in both space and time are used to obtain the second-order accurate finite difference formulas,

$$(\rho A)_j^{n+1} = (\rho A)_j^n - \frac{\Delta t}{\Delta z}\left[(\rho u A)_{j+1/2}^{n+1/2} - (\rho u A)_{j-1/2}^{n+1/2}\right] \tag{17a}$$

and

$$(\rho u A)_j^{n+1} = (\rho u A)_j^n - \frac{\Delta t}{\Delta z}\left[\left(\rho u u A + pA - \frac{1}{2}A' p^2\right)_{j+1/2}^{n+1/2} - \left(\rho u u A + pA - \frac{1}{2}A' p^2\right)_{j-1/2}^{n+1/2}\right] \tag{17b}$$

which are used to carry out the integration represented by the numerical scheme $\Lambda_1(\Delta t)$. In Eq. (17), j is the finite-volume index, n refers to the time level, and $\Delta z = z_j - z_{j-1}$. Numerical flux terms defined on the cell boundaries at time $t^n + \Delta t/2$ are evaluated using the second-order accurate MUSCL-Hancock method (MHM), where MUSCL stands for monotone upstream-centered scheme for conservation laws. As described by Toro [33], the MHM consists of three sequential steps: piece-wise, linear reconstruction of data on the current time level, Taylor series expansion of the piece-wise linear solution at time t to obtain the fluid state adjacent to cell boundaries at $t + \Delta t/2$, and solution of the Riemann problem on each cell boundary at $t + \Delta t/2$ to obtain the required numerical fluxes in Eq. (17).

Slope limiting is used in the data reconstruction step to prevent the occurrence of spurious oscillations in the neighborhood of sharp gradients. For interior cells, $j \in \{2, \ldots, N-1\}$, slope limiting is accomplished through application of the minmod slope limiter. Specifically, the slope m of ρA on interior cell j at time t^n computed using the minmod limiter is [18]

$$m(\rho A)_j^n = \mathrm{minmod}\left\{\left(\frac{(\rho A)_j^n - (\rho A)_{j-1}^n}{\Delta z}\right), \left(\frac{(\rho A)_{j+1}^n - (\rho A)_j^n}{\Delta z}\right)\right\} \tag{18}$$

where definition of the minmod function is provided in Appendix A. Inward-sloping difference formulas

$$m(\rho A)_1^n = \frac{(\rho A)_2^n - (\rho A)_1^n}{\Delta z} \quad m(\rho A)_N^n = \frac{(\rho A)_N^n - (\rho A)_{N-1}^n}{\Delta z} \tag{19}$$

are employed to obtain slopes for the first and last cells, respectively. Slope limiting is not applied to these boundary cells. Using the slopes calculated from Eqs. (18) and (19), the quantity ρA is obtained on the left and right side, respectively, of each cell boundary according to

$$(\rho A)_{j+1/2}^{n,L} = (\rho A)_j^n + \frac{\Delta z}{2}m(\rho A)_j^n \quad (\rho A)_{j-1/2}^{n,R} = (\rho A)_j^n - \frac{\Delta z}{2}m(\rho A)_j^n \tag{20}$$

The same approach is followed for the mass flow rate $\rho u A$. Note that ρA and $\rho u A$, thus computed, are in general discontinuous across cell boundaries. With the use of slope limiting, second-order accuracy is obtained in regions where the solution varies

smoothly, but in the neighborhood of steep wave fronts, where derivatives are ill-behaved or not defined at all, the limiter gives a slope of zero [18]. The zero-slope solution is first-order accurate and corresponds to the classical Godunov method. Velocity, pressure, and flow area are computed from the values of ρA, ρuA, and Eqs. (3), (5), and (6). Fluid velocity is obtained directly, and in the subcooled liquid region direct calculation of pressure is accomplished by solution of a quadratic equation. In the saturated two-phase region, an iterative numerical procedure is used to calculate the pressure. A guess is made for the pressure, and then the flow area and density are computed from Eq. (3) and the known value of the product ρA. Newton's method is applied to Eq. (6) in order to recalculate pressure from the density. The calculated pressure is then compared against the guessed value to determine if convergence has been achieved, or if another iteration is required. In using Newton's method to calculate the fluid pressure from Eq. (6), thermodynamic property derivatives are approximated by analytic expressions obtained by differentiating simplified saturation curve fits of steam table data. The approximate representations of saturated property derivatives are provided in Appendix B. This approach significantly reduces the time associated with the numerical solution without loss of accuracy (roots obtained using Newton's method are independent of the values used to approximate the slopes). Thermodynamic state values are, however, obtained from highly accurate steam table subroutines.

The quantities ρA and ρuA adjacent to the cell boundaries at time t^n are expanded with respect to t in Taylor series to obtain these quantities on the left and right sides of the cell boundaries on time level $t^{n+1/2}$. Expansions including up to first-order terms are given by

$$(\rho A)_{j+1/2}^{n+1/2,L} = (\rho A)_{j+1/2}^{n,L} - \frac{\Delta t}{2} m (\rho uA)_j^n \tag{21a}$$

$$(\rho A)_{j-1/2}^{n+1/2,R} = (\rho A)_{j-1/2}^{n,R} - \frac{\Delta t}{2} m (\rho uA)_j^n \tag{21b}$$

$$(\rho uA)_{j+1/2}^{n+1/2,L} = (\rho uA)_{j+1/2}^{n,L} - \frac{\Delta t}{2} m \left(\rho uuA + pA - \frac{1}{2} A' p^2 \right)_j^n \tag{22a}$$

and

$$(\rho uA)_{j-1/2}^{n+1/2,R} = (\rho uA)_{j-1/2}^{n,R} - \frac{\Delta t}{2} m \left(\rho uuA + pA - \frac{1}{2} A' p^2 \right)_j^n \tag{22b}$$

where m is the slope defined consistent with Eqs. (18) and (19). In obtaining relations (21) and (22), the conservation equatons (12) were used to eliminate temporal derivatives from the Taylor series expansions in favor of spatial derivatives. The computed quantities in Eqs. (21) and (22) provide initial data for a Riemann problem at each cell boundary, the solution of which yields the flux terms in Eq. (17) for $t - t^{n+1/2} \to 0^+$.

In order to solve the Riemann problem, Eqs. (12*a*) and (12*b*) are reformulated by carrying out the indicated differentiation to obtain

$$\frac{\partial p}{\partial t} + u \frac{\partial p}{\partial z} + \frac{\rho A}{(\rho A)'} \frac{\partial u}{\partial z} = 0 \tag{23a}$$

and

$$\frac{\partial u}{\partial t} + u \frac{\partial u}{\partial z} + \frac{1}{\rho} \frac{\partial p}{\partial z} = 0 \tag{23b}$$

where the prime denotes differentiation with respect to pressure. The function $\rho'(p)$, which is discontinuous across phase boundaries is defined by the derivative of Eq. (5) for $p > p_{\text{sat}}(T_0)$ and the derivative of (6) for $p \leqslant p_{\text{sat}}(T_0)$.

For this system, compatibility equations and characteristics, respectively, are given by

$$\frac{d(F \pm u)}{dt} = 0 \quad \text{on} \quad \frac{dz}{dt} = u \pm a \tag{24}$$

where

$$F(p) \equiv \int_{p_{\text{sat}}(T_0)}^{p} \frac{dp}{\rho a} \tag{25}$$

and the wave speed a for the fluid within the pipe is given by the well-known expression

$$a = \sqrt{\frac{A}{(\rho A)'}} \tag{26}$$

Since $F(p)$ is a continuous and monotonic function of the pressure, the quantities p, $\rho(p)$, and $A(p)$ are completely determined by the value of F. Although in the two-phase region, the integral F appearing in the Riemann invariants $F \pm u$ is not a simple algebraic function of the pressure as it is in isentropic gas flow [34], it can be evaluated numerically in a computationally efficient manner. $F(p)$ depends only on the pressure and the initial fluid temperature T_0. For any given problem, the initial temperature is a system parameter that is specified. For saturated fluid, $p \leqslant p_{\text{sat}}(T_0)$, the function $F(p)$ is generated numerically using Simpson's rule and stored in a one-dimensional array for use during the transient part of the calculation. Quadratic interpolation is used within the one-dimensional array to determine F as a function of p and vice versa. In evaluating the integral $F(p)$ in the subcooled liquid region, $p > p_{\text{sat}}(T_0)$, the weak dependency of density and wave speed on pressure is neglected to obtain

$$F(p) \approx \frac{p - p_{\text{sat}}(T_0)}{\rho_f(T_0)} \left(\frac{\kappa/\rho_f(T_0)}{1 + \dfrac{\kappa/E}{e/D_0}(1 + e/D_0) c_1} \right)^{-1/2} \tag{27}$$

On interior cell boundaries ($j = 2, \ldots, N-1$), where rightward and leftward propagating characteristics intersect, the solution to Eq. (24), subject to initial conditions provided by Eqs. (21) and (22) is given by

$$F_{j+1/2}^{n+1/2} = \tfrac{1}{2} [(F+u)_{j+1/2}^{n+1/2,L} + (F-u)_{j+1/2}^{n+1/2,R}] \tag{28a}$$

and

$$u_{j+1/2}^{n+1/2} = \tfrac{1}{2} [(F+u)_{j+1/2}^{n+1/2,L} - (F-u)_{j+1/2}^{n+1/2,R}] \tag{28b}$$

As mentioned previously, the quantities p, ρ, and A are completely determined by the value of F. Note that the compatibility equations included in Eq. (24) have been integrated to obtain the result (28) without having to determine the characteristics. Because of the strong discontinuity in wave speed a across the phase boundary, construction of the characteristic paths on a fixed grid would be very challenging.

On the left boundary ($z = 0$), the pressure is equal to the tank pressure p_T; therefore, $p_{j-1/2}^{n+1/2} = p_T$ for $j = 1$. This boundary condition along with the compatibility equation for the leftward propagating characteristic leads to the result

$$u_{j-1/2}^{n+1/2} = -(F-u)_{j-1/2}^{n+1/2,R} + F(p_T) \quad \text{for } j = 1 \tag{29}$$

which gives the system inlet velocity at the intermediate time level. Similarly, the velocity of the fluid on the boundary at $z = L$ is specified by Eq. (8), and the fluid pressure is given implicitly by the relation

$$F_{N+1/2}^{n+1/2} = (F+u)_{N+1/2}^{n+1/2,L} - u(L, t^{n+1/2}) \tag{30}$$

Determination of F and u on the cell boundaries at the intermediate time level $t^{n+1/2}$ allows computation of the flux terms in Eq.

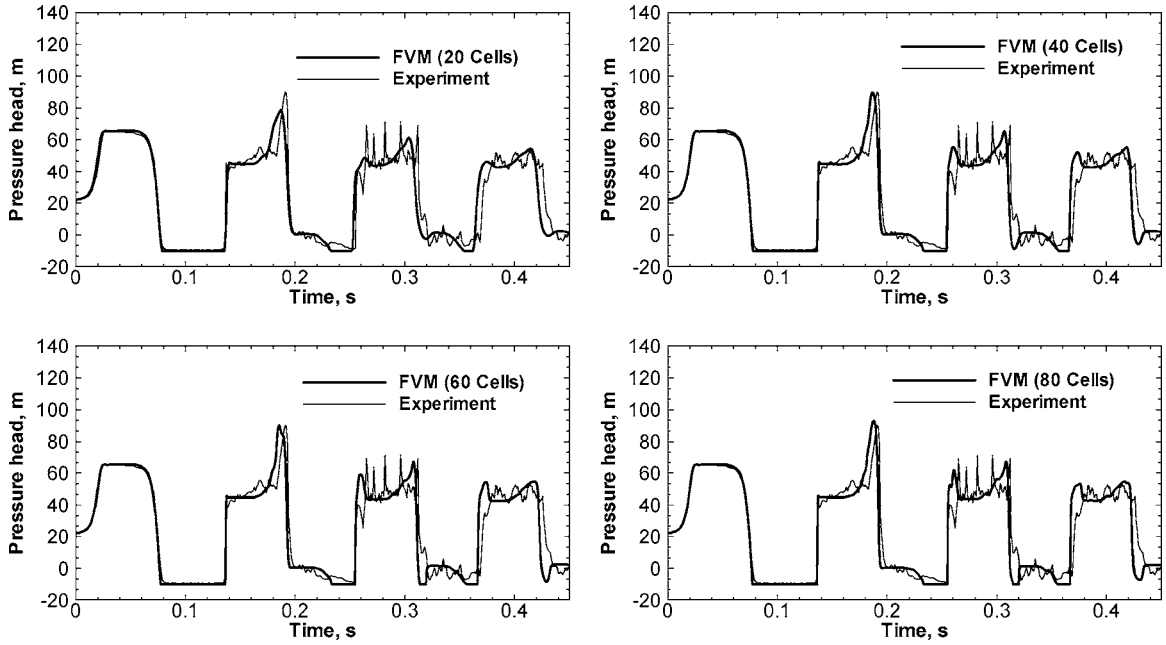

Fig. 4 Comparison of finite-volume calculation of pressure at valve ($z=L=36$ m) against experiment for initial fluid velocity of 0.332 m/s and reservoir pressure head of 23.41 m (Run 1)

(17) and completion of the second-order integration represented by $\Lambda_1(\Delta t)$. Using the results of this integration as initial conditions for an additional half-time-step integration $\Lambda_0(\Delta t/2)$ defined by Eq. (16) advances the solution to Eqs. (1) and (2) to t^{n+1} with second-order accuracy in regions where the solution is smooth.

5 Results

Figures 4–7 compare calculated fluid pressure against the experimental data of Simpson and Wylie (Runs 1 and 2 in Table 1). Pressure is calculated, and compared to data, at two axial locations: $z=L=36$ m (at the valve), and $z=L/4=9$ m. Calculations were carried out using 20, 40, 60, and 80 computational cells spanning the 36-m copper pipeline. As discussed in Sec. 3, the mathematical model is forced by imposing experimental data as the boundary condition at the valve ($z=L$) for the first 30 ms. After this time, the downstream ball valve is closed, and a zero-velocity boundary condition is specified. Using the experimental data in deriving the downstream boundary condition for the first 30 ms incorporates dynamics associated with rapid closure of the ball valve. All calculations were performed with a constant time step size equal to $0.8\Delta z/a_\ell$ where a_ℓ is the sound speed calculated from Eq. (26) for the initial subcooled liquid conditions. Basing

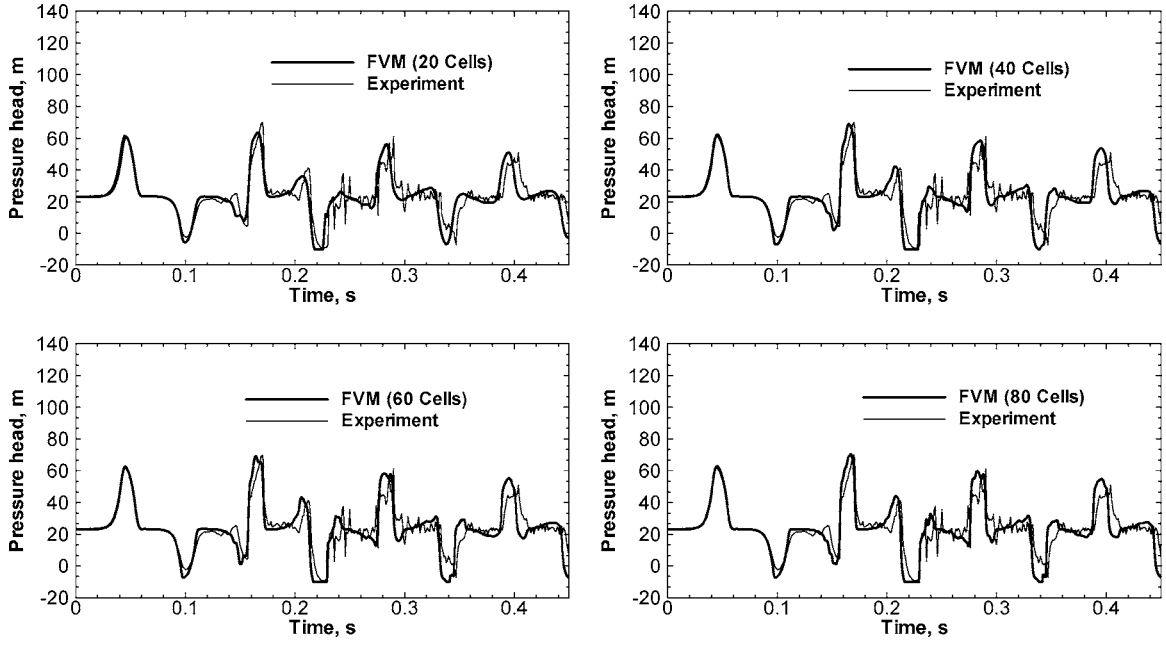

Fig. 5 Comparison of finite-volume calculation of pressure at $z=L/4=9$ m against experiment for initial fluid velocity of 0.332 m/s and reservoir pressure head of 23.41 m (Run 1)

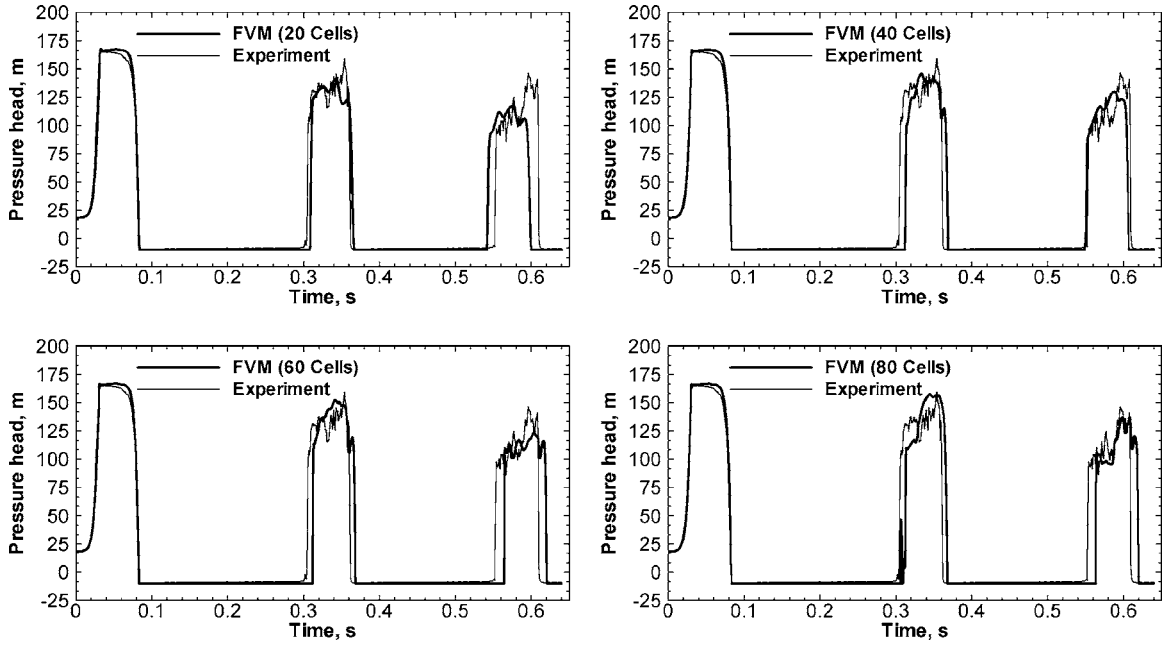

Fig. 6 Comparison of finite-volume calculation of pressure at valve ($z=L=36$ m) against experiment for initial fluid velocity of 1.125 m/s and reservoir pressure head of 21.74 m (Run 2)

time step size on liquid conditions ensures that the Courant limit is not violated for any computational cell. Using relations (3)–(5), the liquid-phase sound speed predicted by Eq. (26) is 1295 m/s. This result compares very well with the measured wave speed of 1280 m/s (see Sec. 2).

In Figs. 4 and 5, pressure traces determined by computation are compared against experimental data for the case of mild cavitation (Run 1 in Table 1). Both amplitude and timing of simulated pressure pulses display reasonably good agreement with experimental data even when as few as 20 computational cells are used to describe axial variations in fluid conditions along the 36-m pipeline. When the number of computational cells is increased, there is some increase in resolution of pressure pulses, but the basic predicted response remains essentially unchanged.

As shown in Figs. 6 and 7, pressure-pulse amplitudes for the case of moderate cavitation (Run 2) tend to approach those of the experimental record when 40 computational cells are used. Because of the more severe nature of this transient relative to Run 1, it is necessary to use a larger number of computational cells in order to achieve reasonably good agreement with data. From Fig. 6, it can be seen that the liquid column separates from the valve at 0.08 s, and the column rejoins to the valve at 0.3 s creating a

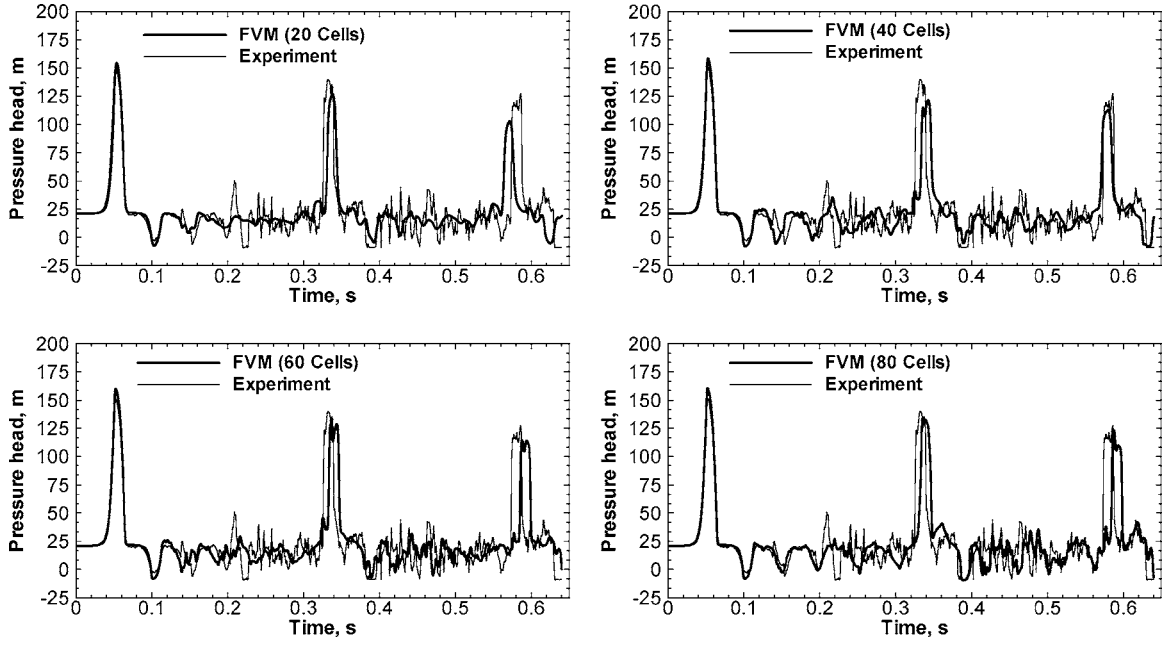

Fig. 7 Comparison of finite-volume calculation of pressure at $z=L/4=9$ m against experiment for initial fluid velocity of 1.125 m/s and reservoir pressure head of 21.74 m (Run 2)

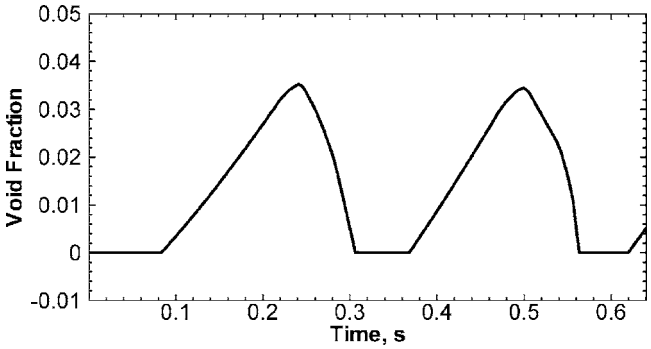

Fig. 8 Finite-volume calculation of void fraction at center of computational cell adjacent to downstream valve (Run 2 with 80 computational cells)

pressure pulse with magnitude of 160 m gauge. Frictional dissipation causes the subsequent pulse to be somewhat smaller in amplitude. As can be seen from the experimental record in Fig. 6, pressure at the valve begins to decline somewhat, immediately after valve closure. If the pipe were completely rigid, the pressure at the valve would remain flat until the rarefaction wave generated from the upstream head tank reached the closed end of the pipe. The observed decline in pressure is consistent with temporary elongation of the pipeline that occurs when an unbalanced force is generated by the sharp rise in fluid pressure on the downstream end immediately after valve closure. The model does not predict this decline in pressure on the first pulse because effects of pipe elongation are not included. No significant overshoot of predicted pressure pulses relative to data is observed nor is there any evidence of spurious oscillations in any of the numerical solutions.

Figure 8 displays the calculated fluid void fraction at the center of the computational cell adjacent to the valve in Run 2 using 80 cells to span the length of the pipeline. This location is 22.5 cm upstream of the valve. Comparing Figs. 6 and 8 shows the relationship between void formation and collapse and the generation of large-amplitude pressure pulses at the valve. The two-phase region that forms in the vicinity of the valve tends to behave as a constant pressure boundary condition with pressure equal to the fluid saturation pressure. Unless an advancing compression wave is strong enough to completely collapse the voids, it cannot create a significant pressure disturbance in the two-phase region as pressure must remain essentially fixed at the saturation pressure corresponding to the fluid temperature.

Run 1 was also simulated using the MOC with the DVCM described in Sec. 1 and compared against the experimental data. Results for the pressure response at the valve with 21, 41, 61, and 81 grid points are presented in Fig. 9 along with the experimental

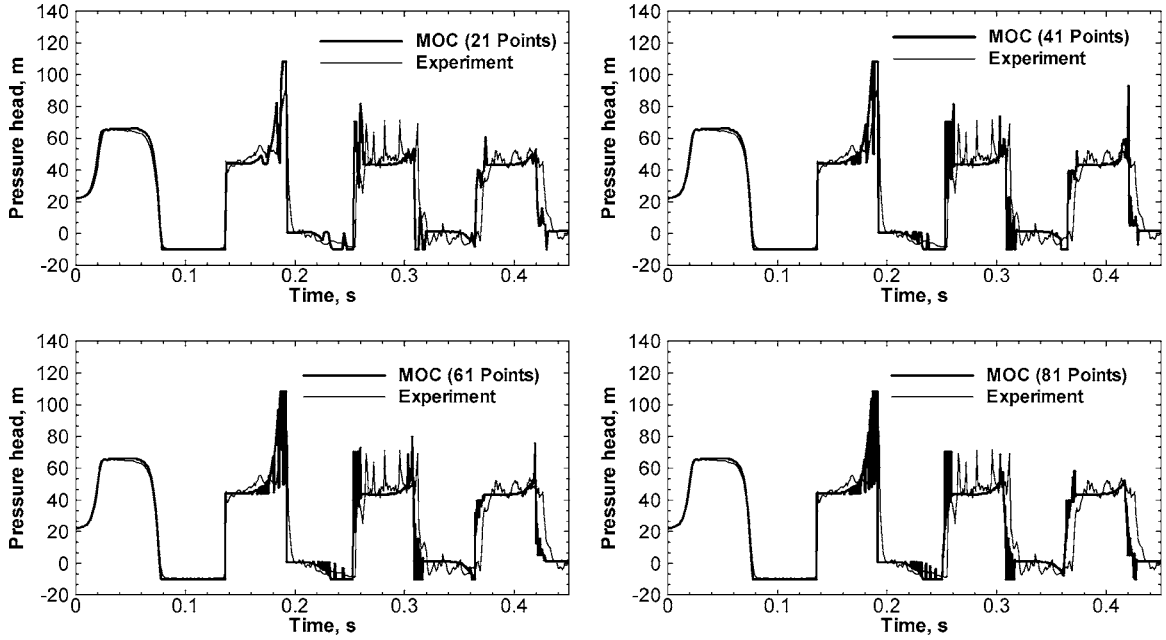

Fig. 9 Comparison of DVCM calculation of pressure at valve ($z=L=36$ m) against experiment for initial fluid velocity of 0.332 m/s and reservoir pressure head of 23.41 m (Run 1)

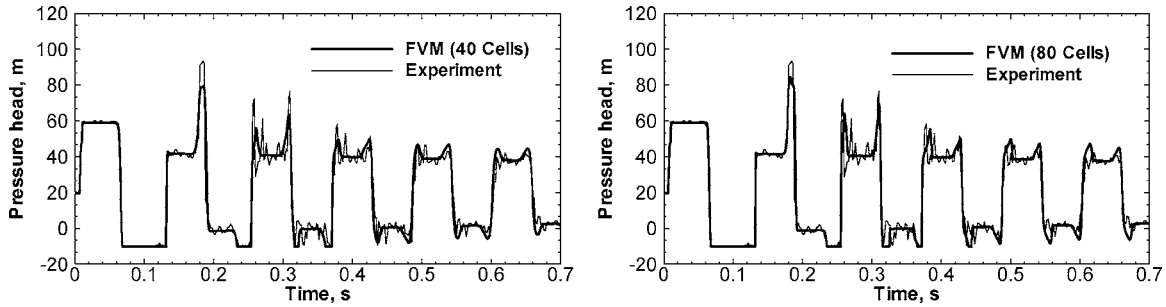

Fig. 10 Comparison of finite-volume calculation of pressure at $z=L=37.2$ m against experiment for initial fluid velocity of 0.30 m/s and reservoir pressure head of 22 m (Run 3)

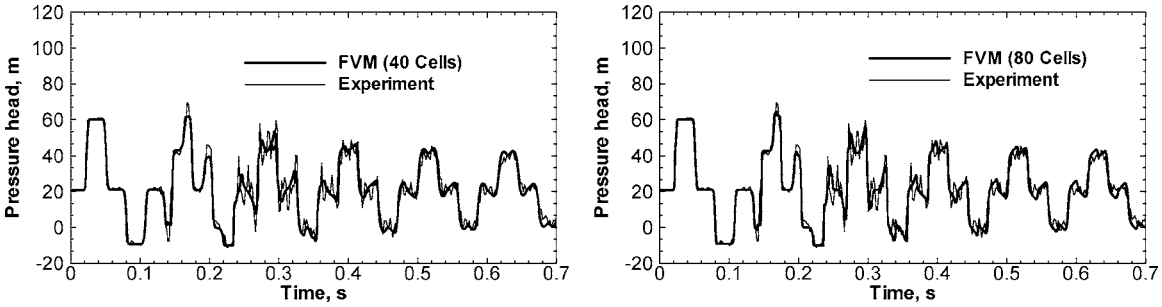

Fig. 11 Comparison of finite-volume calculation of pressure at $z=L/2=18.6$ m against experiment for initial fluid velocity of 0.30 m/s and reservoir pressure head of 22 m (Run 3)

record. For the case corresponding to 21 grid points, the numerical solution obtained with the DVCM model agrees reasonably well with experiment; however, nonphysical pressure spikes and high-frequency oscillations corrupt the solution when more refined grids are employed.

Figures 10 and 11 compare calculated pressure at the valve and at the pipeline midpoint against the experimental records for Run 3 in Table 2. The FVM shows very good agreement with the experiments, particularly with regard to the timing of the pressure oscillations. As in the simulations for Runs 1 and 2, the model is driven by imposing experimental data as the boundary condition at the valve ($z=L$) during the valve closure stroke (see Sec. 3). Figure 12 compares calculated pressure for Run 4, which is a single-phase water hammer transient, against experimental data. Again, good agreement is achieved with regard to the timing and amplitude of the pressure oscillations. As in previous work, [14,25], the present study found that incorporating the Brunone transient friction model significantly improved agreement with experimental data, particularly in the single-phase transient. Without transient friction, the predicted decay rate of pressure oscillations was found to be slow relative to data.

6 Conclusions

Based on comparison of computational predictions against experimental data, the HEM with isentropic equation of state, pressure-dependent pipe flow area, and unsteady friction accurately predicts the amplitude and frequency of pressure disturbances generated by sudden valve closure in pipelines. The second-order accurate MUSCL-Hancock method with minmod slope limiting provides an effective approach for solving the governing equations. For the case of water hammer with cavitation, solutions obtained with as few as 20–40 computational cells spanning a pipeline of ~35 m in length show good agreement with data. Use of a transient friction model with the finite-volume approach allows accurate prediction of pressure oscillation damping in single-phase water hammer transients. The Brunone transient friction model is easily incorporated into the fluid model through the use of operator splitting and a second-order Runge-Kutta method. Although the finite-volume method is somewhat more difficult to implement than characteristic-based approaches involving discrete vapor cavities, solutions do not exhibit artificial spikiness as grid refinement is performed, and no significant overshoot, relative to data, is observed in the results. Moreover, the FVM does not rely on the introduction of small concentrations of noncondensable gas to mitigate spurious oscillations as in the DGCM. This is a desirable feature because the initial concentration of free air in a water system is generally unknown, and computational predictions are sensitive to the volume fraction of air assumed in the analysis. The finite-volume approach used in this work for simulation of liquid-column separation and rejoining provides a useful alternative to the DVCM and the DGCM, and also provides a framework, through the use of operator splitting, for the modeling of multidimensional water hammer transients.

In the DVCM, vapor generated during cavitation is assumed to exist at the saturation pressure corresponding to the liquid temperature, just as in the HEM used in the present work. Thus, the major difference between the HEM and the classic DVCM is essentially formal; however, the difference in the form of the equations is crucial with regard to obtaining stable numerical solutions. The HEM provides a continuous rather than discrete treatment of the two-phase fluid, and consequently, the problem can be expressed compactly in terms of two conservation equations, and an equation of state. Expressing the problem in conservation-law form allows application of the high-resolution, finite-volume methods developed for the study of shock waves in gas flows to the problem of cavitating flow in pipelines. Since the flow is adiabatic and the mass fraction of vapor remains small in the hydraulic transients of interest, the mixture entropy can be treated as a constant. With this approximation, and with the use of operator splitting to separate friction and gravity terms from flux terms in the continuity and momentum equations, the two-phase Riemann problem for the numerical fluxes in the FVM can be solved by the MOC. Through this approach, upwinding inherent to the MOC is applied to the two-phase mass and momentum fluxes at the cell

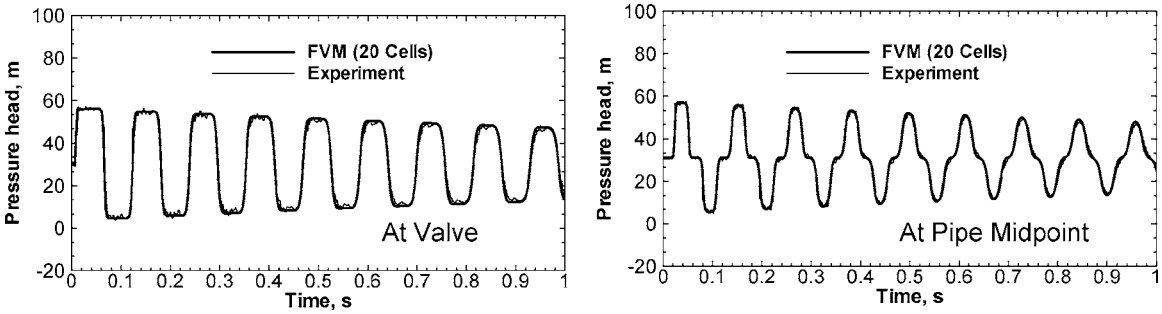

Fig. 12 Comparison of finite-volume calculation of pressure against experiment for initial fluid velocity of 0.20 m/s and reservoir pressure head of 32 m (Run 4)

boundaries, and thus provides a stable numerical solution as long as the Courant limit on time step size is not violated. The DVCM, on the other hand, applies upwinding through the MOC to the liquid portion of the cavitation problem only, which results in a less stable solution. This conclusion is supported by the fact that stability of the DVCM is highly dependent on the numerical method used to solve for the vapor cavity volume, with the most favorable approach being the backward Euler scheme because of its dissipative quality. It is also supported by the fact that the improved stability of the DGCM over the DVCM lies in the inclusion of noncondensable gas into the vapor cavity to provide additional damping of pressure disturbances.

Acknowledgment

The author is grateful to Professor Wylie and Professor Bergant for providing the experimental data used to validate the finite-volume model. In addition, the author would like to thank the reviewers for their insightful comments and helpful suggestions, which significantly improved the paper.

Nomenclature

A = pipe flow area (m^2)
A' = derivative of A with respect to pressure (m^2/Pa)
a = wave speed through homogeneous fluid contained in pipe (m/s)
c_1 = pipe restraint factor
D = pipe inside diameter (m)
DVCM = discrete vapor cavity model
DGCM = discrete gas cavity model
E = modulus of elasticity for the pipe material (Pa)
e = pipe wall thickness (m)
FVM = finite-volume method
f = Darcy friction factor
g = acceleration due to gravity (9.8 m/s^2)
HEM = homogeneous equilibrium model
k = Brunone friction coefficient
L = pipe length (m)
MHM = MUSCL-Hancock method
MOC = method of characteristics
MUSCL = monotone upstream-centered scheme for conservation laws
m = minmod-limited slope
N = number of computational cells
p = fluid pressure (Pa)
s = fluid specific entropy (J/kg K)
sign(u) = +1 if $u \geq 0$ and −1 if $u < 0$
T = fluid temperature (K)
t = time (s)
u = homogeneous fluid velocity (m/s)
z = pipe axial coordinate (m)
x = fluid quality
κ = bulk modulus of water (Pa)
μ = dynamic viscosity (Pa·s)
ν = Poisson's ratio
θ = pipe angle of inclination (deg)
ρ = fluid density (kg/m^3)
ρ' = derivative of ρ with respect to pressure
v = fluid specific volume (m^3/kg)
Δt = time step size (s)
V = fluid velocity at valve during closure stroke (m/s)
Δz = length of computation cell (m)

Subscripts

0 = initial state or unpressurized state
∞ = condition external to pipe
f = saturated liquid
g = vapor
fg = difference between vapor and liquid properties
j = cell number
ℓ = liquid
q = quasi-steady
sat = saturation condition
T = fluid conditions at head tank

Superscripts

n = time step number
L = left-hand side of cell boundary
R = right-hand side of cell boundary

Appendix A: Minmod Function

The minmod function of two real numbers a and b is defined by [18]

$$\text{minmod}(a,b) = \begin{cases} a & \text{if } |a| \leq |b| \text{ and } ab > 0 \\ b & \text{if } |b| < |a| \text{ and } ab > 0 \\ 0 & \text{if } ab \leq 0 \end{cases}$$

Appendix B: Simplified Curve Fits of Thermodynamic Property Derivatives for Saturated Water

The following simplified thermodynamic property derivatives are based on curve-fits of ASME Steam Table 5th Edition data for saturation temperatures from 32°F to 212°F.

Derivative of Saturated Liquid Specific Volume

$$\frac{dv_f(p)}{dp} = \frac{b_2 - b_1 b_3 - 2b_1 b_4 p - b_2 b_4 p^2}{(1 + b_3 p + b_4 p^2)^2}$$

where $b_1 = 0.015998104$, $b_2 = 0.0044345191$, $b_3 = 0.26677934$, and $b_4 = -0.00030725452$.

Derivative of Saturated Vapor Specific Volume

$$\frac{dv_g(p)}{dp} = \frac{-b_2 b_3 p^{b_3 - 1}}{(b_1 + b_2 p^{b_3})^2}$$

where $b_1 = -4.4255234 \times 10^{-6}$, $b_2 = 0.0029984187$, and $b_3 = 0.94048131$.

Derivative of Saturated Liquid Specific Entropy

$$\frac{ds_f(p)}{dp} = \frac{b_2 b_4 (b_3 - b_1) p^{b_4 - 1}}{(b_2 + p^{b_4})^2}$$

where $b_1 = -0.18743837$, $b_2 = 2.3447148$, $b_3 = 0.87897231$, and $b_4 = 0.26864489$.

Derivative of Saturated Vapor Specific Entropy

$$\frac{ds_g(p)}{dp} = \frac{-b_2 b_3 p^{b_3 - 1}}{(b_1 + b_2 p^{b_3})^2}$$

where $b_1 = 0.19002505$, $b_2 = 0.31547431$, and $b_3 = 0.068415043$.

References

[1] Li, W. H., and Walsh, J. P., 1964, "Pressure Generated by Cavitation in a Pipe," J. Engrg. Mech. Div., **90**, pp. 113–133.
[2] Safwat, H. H., 1972, "Transients in Cooling Water Systems of Thermal Power Plants," D. Sci. dissertation, Delft University of Technology, Delft, The Netherlands.
[3] Arastu, A. H., Chiu, C., Griffith, P., Rooney, J. W., Sabin, J. W., Safwat, H. H., and Van Duyne, D. A., 1996, "Water Hammer Handbook for Nuclear Plant Engineers and Operators," EPRI Report No. TR-106438, Electric Power Research Institute, Palo Alto, CA.
[4] Barbero, G., and Ciaponi, C., 1991, "Experimental Validation of a Discrete Free Gas Model for Numerical Simulation of Hydraulic Transients with Cavitation," Proceedings of the Ninth Round Table of IAHR Group on Hydraulic Transients with Water Column Separation, Valencia, Sept. 4–6, pp. 51–67.
[5] Baltzer, R. A., 1967, "Column Separation Accompanying Liquid Transients in Pipes," ASME J. Basic Eng., **89**, pp. 837–846.
[6] Simpson, A., and Wylie, E. B., 1987, "Column Separation Experiments with Large Pressure Pulses," ASME Paper 87-PVP-18, Pressure Vessel and Piping Conference, San Diego, June 28–July 2.
[7] Simpson, A. R., and Wylie, E. B., 1987, "Recent Advances in the Understand-

ing and Numerical Modelling of Column Separation in Pipelines," Conference on Hydraulics in Civil Engineering, Melbourne, October 12–14.
[8] Martin, C. S., 1983, "Experimental Investigation of Column Separation with Rapid Closure of Downstream Valve," Proceedings of the Fourth International Conference on Pressure Surges, BHRA, Bath, England, September.
[9] Weyler, M. E., Streeter, V. L., and Larsen, P. S., 1971, "An Investigation of the Effect of Cavitation Bubbles on the Momentum Loss in Transient Pipe Flow," ASME J. Basic Eng., **93**, pp. 1–10.
[10] Bergant, A., and Simpson, A. R., 1999, "Pipeline Column Separation Flow Regimes," J. Hydraul. Eng., **125**, pp. 835–848.
[11] Streeter, V. L., and Wylie, E. B., 1967, *Hydraulic Transients*, McGraw-Hill, New York.
[12] Arastu, A. H., Safwat, H. H., and Husaini, S. M., 1992, "Water Hammer Prevention, Mitigation, and Accommodation," Vol. 4, Part 2, EPRI NP-6766, Electric Power Research Institute, Palo Alto, CA.
[13] Wylie, E. B., and Streeter, V. L., 1993, *Fluid Transients in Systems*, Prentice Hall, Upper Saddle River, NJ.
[14] Bergant, A., and Tijsseling, A., 2001, "Parameters Affecting Water Hammer Wave Attenuation, Shape and Timing," Proceedings of the Tenth International Meeting of IAHR Group on The Behaviour of Hydraulic Machinery Under Steady Oscillatory Conditions," Trondheim, Norway, June 26–28.
[15] Carlson, K. E., Riemke, R. A., Rouhani, S. Z., Shumway, R. W., and Weaver, W. L., 1995, "RELAP5/MOD3 Code Manual Vol. I: Code Structure, Systems Models, and Solution Methods," INEL-95/0174, NUREG/CR-5535, Idaho National Engineering Laboratory.
[16] Borkowski, J. A., and Wade, N. L., (eds.), 1992, "TRAC-BF1-MOD1: An Advanced Best-Estimate Computer Program for BWR Accident Analysis," EGG-2626, NUREG/CR-4356, Idaho National Engineering Laboratory.
[17] Bilicki, Z., Kardas, D., and Michaelides, E. E., 1998, "Relaxation Models for Wave Phenomena in Liquid-Vapor Bubble Flow in Channels," ASME J. Fluids Eng., **120**, pp. 369–377.
[18] LeVeque, R. J., 2002, *Finite Volume Methods for Hyperbolic Problems*, Cambridge University Press, Cambridge, UK.
[19] Anderson, D. A., Tannehill, J. C., and Pletcher, R. H., 1984, *Computational Fluid Mechanics and Heat Transfer*, Hemisphere, New York, pp. 144–146.
[20] Kranenburg, C., 1974, "Gas Release during Transient Cavitation in Pipes," J. Hydr. Div., **100**, pp. 1383–1398.
[21] Bergant, A., and Simpson, A. R., 1995, "Water Hammer and Column Separation Measurements in an Experimental Apparatus," Research Report No. R128, Department of Civil and Environmental Engineering, University of Adelaide.
[22] Crandall, S. H., Dahl, N. C., and Lardner, T. J., 1972, *An Introduction to the Mechanics of Solids*, 2nd ed., McGraw-Hill, New York, p. 94.
[23] Perry, R. H., and Chilton, C. H. (eds.), 1973, *Chemical Engineers' Handbook*, 5th ed., McGraw-Hill, New York, p. 23-48.
[24] Lindeburg, M. R., 2001, *Mechanical Engineering Reference Manual*, 11th ed., Professional Publications, Belmont, CA.
[25] Bergant, A., Simpson, A. R., and Vítkovský, J., 2001, "Developments in Unsteady Pipe Flow Friction Modelling," J. Hydraul. Res., **39**(3), pp. 249–257.
[26] Brunone, B., Golia, U. M., and Greco, M., 1995, "Effects of Two-dimensionality on Pipe Transients Modeling," J. Hydraul. Eng., **121**(12), pp. 906–912.
[27] Vardy, A. E., and Brown, J. M. B., 2003, "Transient Turbulent Friction in Smooth Pipe Flows," J. Sound Vib., **259**(5), pp. 1011–1036.
[28] Lahey, R. T., and Moody, F. J., 1977, *The Thermal Hydraulics of a Boiling Water Nuclear Reactor*, American Nuclear Society, La Grange Park, IL, p. 228.
[29] Igra, O., Wu., X., Hu, G. Q., and Falcovitz, J., 2002, "Shock Wave Propagation Into a Dust-Gas Suspension Inside a Double-Bend Conduit," ASME J. Fluids Eng., **124**, pp. 483–491.
[30] Igra, O., Hu, G., Falcovitz, J., and Heilig, W., 2003, "Blast Wave Reflection from Wedges," ASME J. Fluids Eng., **125**, pp. 510–519.
[31] Strang, G., 1968, "On the Construction and Comparison of Difference Schemes," SIAM (Soc. Ind. Appl. Math.) J. Numer. Anal., **5**(3), pp. 506–517.
[32] Ben-Artzi, M., and Falcovitz, J., 2003, *Generalized Riemann Problems in Computational Fluid Dynamics*, Cambridge University Press, Cambridge, UK.
[33] Toro, E. F., 1999, *Riemann Solvers and Numerical Methods for Fluid Dynamics: A Practical Introduction*, 2nd ed., Springer-Verlag, New York.
[34] Thompson, P. A., 1988, *Compressible-Fluid Dynamics*, Rensselaer Polytechnic Institute, pp. 379–380.

A Comparative Study of DES and URANS for Flow Prediction in a Two-Pass Internal Cooling Duct

Aroon K. Viswanathan

Danesh K. Tafti
e-mail: dtafti@vt.edu

High Performance Computational Fluids—Thermal Sciences and Engineering Lab, Mechanical Engineering Department, Virginia Polytechnic Institute and State University, Blacksburg, VA 24060

The capabilities of the detached eddy simulation (DES) and the unsteady Reynolds averaged Navier-Stokes (URANS) versions of the 1988 k-ω model in predicting the turbulent flow field in a two-pass internal cooling duct with normal ribs is presented. The flow is dominated by the separation and reattachment of shear layers; unsteady vorticity induced secondary flows and strong streamline curvature. The techniques are evaluated in predicting the developing flow at the entrance to the duct and downstream of the 180 deg *bend, fully developed regime in the first pass, and in the* 180 deg *bend. Results of mean flow quantities, secondary flows, and the average friction factor are compared to experiments and large-eddy simulations (LES). DES predicts a slower flow development than LES, whereas URANS predicts it much earlier than LES computations and experiments. However, it is observed that as fully developed conditions are established, the capability of the base model in predicting the flow is enhanced by the DES formulation. DES accurately predicts the flow both in the fully developed region as well as the* 180 deg *bend of the duct. URANS fails to predict the secondary flows in the fully developed region of the duct and is clearly inferior to DES in the* 180 deg *bend.* [DOI: 10.1115/1.2353279]

Introduction

In order to keep up with increasing demand for higher efficiency and lower emissions, turbine inlet temperatures have continued to rise over the past several years. In fact, modern gas turbines have turbine inlet temperatures that are well above the melting-point temperature of the blades. Because of the harsh operating conditions in the first turbine stage of modern gas turbines, external and internal blade cooling is employed. Internal cooling involves forced convection inside the blades by means of serpentine flow passages. Since convection can be increased by inducing turbulence in the flow, the boundary layer is tripped using various kinds of turbulators (ribs). This increases the heat transfer in the passages, but also results in an increase in friction in the duct. The ultimate aim behind designing these passages is to obtain effective overall cooling of the components at the least penalty on the friction coefficient.

The efficient design of these internal cooling passages in gas turbine blades and nozzles requires a detailed knowledge of the flow and heat transfer phenomena. The flow and heat transfer in a ribbed internal cooling duct is a function of the flow Reynolds number and the geometric parameters, such as the rib-height-to-hydraulic diameter ratio, the rib pitch, the aspect ratio of the duct, the angle of the rib with respect to the flow, and the shape of the rib as shown by some studies [1–4]. The present work is motivated by the need to accurately predict the flow characteristics in such flows. The flow behind a rib, though geometrically simple, has some complex features: separation of the boundary layer, a curved shear layer, primary and secondary recirculation, reattachment of the boundary layer, recovery, etc. Additionally, the reattachment is followed by redevelopment of the downstream boundary layer. Using the current computational capabilities, it is possible to simulate the complex flow in these passages; however, one challenge that still persists is the modeling of the turbulence in the flow. The flows inside the cooling ducts are rich in turbulent physics, and thus, numerical prediction of these flows in not trivial. Numerical techniques range from the solution of the full flow field, such as in direct numerical simulations (DNS), to the modeling of all turbulent scales using Reynolds averaged Navier-Stokes equations (RANS).

In spite of the continual development of RANS models, it has been observed that these models often do not perform efficiently outside their calibration regime. Studies in massively separated flow regimes show that the turbulent viscosity and the turbulent shear stress are usually overpredicted by the two-equation eddy-viscosity models [5], resulting in the rapid spreading of the shear layer due to which reattachment is predicted early. Liou et al. [6] used a k-ε algebraic stress model to predict flow in a stationary two-dimensional (2D) ribbed duct with ribs on one wall. Their studies showed that the k-ε model failed to predict the flow accurately, whereas the k-ε-A model, which accounted for the anisotropy of turbulence, gave reasonable results. Periodic flow calculations on a rectangular ribbed duct were carried out by Prakash and Zerkle [7] for stationary and rotating ducts using k-ε model. It was observed that the heat transfer coefficient predictions for the stationary case are not consistent at the side walls for the stationary case. Saidi and Sunden [8] also used k-ε models in a periodic channel with inline orthogonal ribs, and the computations showed mixed results. Iacovides [9] carried out computations using k-ε and low-Re zonal differential stress models (DSM) in a periodic ribbed duct for stationary and rotating cases. Though reasonable flow behavior was predicted by the k-ε model, the thermal behavior was not predicted accurately. The low-Re DSM model gave better predictions than the k-ε model. Iacovides and Raisee [1] introduced a modified version of the Yap correction to the low-Re DSM models and obtained reasonable heat transfer results in a 180 deg bend channel. Lin et al. [10] studied the three-dimensional flow and heat transfer in a U-shaped duct under rotating and non-rotating conditions using Menter's shear stress model for closure. The studies showed that the average heat transfer augmentation showed only moderate agreement with experimental results. Ooi et al. [11] presented predictions using a v^2-f model on orthogonal in-line ribs and found that the model performed better than the k-ε and Spalart-Allmaras RANS models. Rigby [12] studied the heat and mass transfer in a two-pass ribbed channel with a 180 deg turn using a modified version of Menter's SST model [13,14]. Both stationary and rotating cases at low Rey-

Contributed by the Fluids Engineering Division of ASME for publication in the JOURNAL OF FLUIDS ENGINEERING. Manuscript received September 3, 2005; final manuscript received April 14, 2006. Assoc. Editor: Ugo Piomelli.

nolds numbers (5200–7900) were considered, and it was observed that the standard turbulence model failed to predict the reattachment accurately. Thus, modifications in the ω boundary conditions were required for the model to predict the flow attachment accurately.

Although RANS models are not always consistent in their prediction capability, large eddy simulations (LES) have been found to be more reliable. Murata and Mochizuki [15] studied the effect of the high-momentum turbulent flow on the heat transfer at the walls of a ribbed duct using LES and compared it to the heat transfer in a laminar flow. Murata and Mochizuki [16] also studied the effect of Coriolis force and the duct cross section on the heat transfer in smooth and ribbed channels. Watanabe and Takahashi [17] carried out LES computations and experimental studies on a rectangular channel with transverse ribs that were heated from one side and obtained good agreement with experiments. The studies also revealed the unsteady mechanism that enhanced the heat transfer in the ribbed channel. Tafti [18] used 96^3 and 128^3 grids to predict the fully developed flow and heat transfer in a channel with orthogonal ribs at Re=20,000. Mean and turbulent quantities compared very well to experiments. Abdel-Wahab [19] used LES to study the effect of rotation on fully developed flow and heat transfer in square ducts with normal ribs. Comprehensive flow and heat transfer studies in developing region and the bend region of an internal cooling duct were also carried out by Sewall [20], where the effects of Coriolis forces and centrifugal buoyancy on the heat transfer and the flow were successfully captured. LES computations by Sewall et al. [21] on a single-pass ribbed duct with nine ribs using 8.85×10^6 cells showed that the flow and the heat transfer were near fully developed by the fourth rib. The flow features and the heat transfer after the fifth rib showed good agreement with the fully developed profiles. Subsequently, Sewall and Tafti [22] used LES to compute the flow and heat transfer in a 180 deg degree bend with three ribs upstream and downstream of the bend. A total of 8.4×10^6 cells were used for the computation. The predicted flow and heat transfer showed good agreement with available experimental data.

Though LES is a viable alternative to RANS for accurate computations, the near-wall resolution required for LES makes it expensive. This is the rationale behind the continual development and application of hybrid RANS-LES methods, which combine the advantages of both the schemes. In order to exhibit both LES and RANS behavior, a simple modification of the Spalart-Allmaras model was proposed by Spalart [23] such that the computation behaves as RANS in the "attached" near-wall regions and as LES in the unsteady "detached" regions of the flow. This scheme, known as detached eddy simulations (DES), has been widely used for a plethora of external flows since its inception. The technique, initially proposed based on the Spalart-Allmaras turbulence model [23,24], treats the inner boundary layer in a RANS mode and by modifying the length scale in the destruction term the model switches to a sub-grid-type formulation. Although the RANS-LES switch in the SA model is tied to the distance from the wall, Strelets [25] defined a DES scheme for the Menter's shear stress transport model, which used the grid scale to affect the RANS-LES switch. Viswanathan and Tafti [26,27] successfully applied this method to predict fully developed flow and heat transfer in a duct with normal and skewed ribs. The computations showed good agreement with experiments and LES results at a much lower computational cost. Viswanathan and Tafti [28] further extended the fully developed computations to flow and heat transfer in rotating ducts from low to high rotation numbers. They found good agreement with experiments and LES [29] and found DES to be superior to unsteady RANS. Subsequently, the DES studies on fully developed stationary ducts were extended to a full two-pass duct [30]. The present study is an extension of the DES study on a two-pass duct and evaluates the prediction capabilities of URANS in comparison to LES and DES.

Objective of the Study. The objective of this work is to compare the prediction capability of the 1988 k-ω URANS to its equivalent DES model in predicting the turbulent flow in a two-pass internal cooling ribbed duct with a 180 deg turn. The ability of URANS and DES to predict the flow in the developing region of the duct, the fully developed region, and the 180 deg duct is compared to LES results and experiments. The LES calculations of Sewall et al. [21,22] and experiments of Rau et al. [31] are used for this purpose.

Computations are carried out for a ribbed channel with a rib pitch to rib height of 10 and rib height to hydraulic diameter of 0.1 for a bulk Reynolds number of 20,000. A complete analysis of a two pass channel with a 180 deg bend and 12 sets of ribs in the first and the second pass has been carried out. Around 262,000 cells are used in each rib section with a total of around 7.77×10^6 cells to discretize the whole channel with the 180 deg bend.

Computational Model and the Governing Equations. The computational domain consists of two passes of an internal cooling duct. The governing flow equations are nondimensionalized by a characteristic length scale, which is chosen to be the hydraulic diameter of the channel (D_h), and a characteristic velocity scale given by the inlet velocity (U_0).

The nondimensional time-dependent continuity and momentum equations for turbulent flow are

Continuity

$$\nabla\cdot\vec{u}=0$$

Momentum

$$\frac{D\vec{u}}{Dt}=-\nabla p+\nabla\cdot\left[\left(\frac{1}{\mathrm{Re}}+\frac{1}{\mathrm{Re}_t}\right)\nabla\vec{u}\right]$$

where $\vec{u}$ is the Cartesian velocity vector, p is the pressure, Re is the Reynolds number, and Re_t is the turbulence Reynolds number, which is defined as

$$\frac{1}{\mathrm{Re}_t}=\gamma^*\frac{k}{\omega}$$

The equations for the turbulent kinetic energy (k) and the rate of dissipation of energy per unit volume and time (ω) [32] are

$$\frac{\partial k}{\partial t}+\frac{\partial(u_j k)}{\partial x_j}=\tau_{ij}\frac{\partial u_i}{\partial x_j}-\frac{k^{3/2}}{l_{k-\omega}}+\frac{\partial}{\partial x_j}\left[\left(\frac{1}{\mathrm{Re}}+\frac{\sigma^*}{\mathrm{Re}_t}\right)\frac{\partial k}{\partial x_j}\right]$$

$$\frac{\partial\omega}{\partial t}+\frac{\partial(u_j\omega)}{\partial x_j}=\gamma\frac{\omega}{k}\tau_{ij}\frac{\partial u_i}{\partial x_j}-\beta\omega^2+\frac{\partial}{\partial x_j}\left[\left(\frac{1}{\mathrm{Re}}+\frac{\sigma}{\mathrm{Re}_t}\right)\frac{\partial\omega}{\partial x_j}\right]$$

The Boussinesq approximation is used to define the Reynolds stress tensor in terms of the mean strain rate tensor (S_{ij}) as

$$\tau_{ij}=\frac{2}{\mathrm{Re}_t}\left[S_{ij}-\frac{1}{3}\frac{\partial U_k}{\partial x_k}\delta_{ij}\right]-\frac{2}{3}k\delta_{ij}$$

where

$$S_{ij}=\frac{1}{2}\left(\frac{\partial u_j}{\partial x_i}+\frac{\partial u_i}{\partial x_j}\right)\text{ is the strain rate tensor.}$$

The closure coefficients and the auxiliary relations are defined as

$$\gamma=\frac{5}{9},\quad \beta=\frac{3}{40},\quad \beta^*=0.09$$

$$\gamma^*=1,\quad \sigma=\sigma^*=\frac{1}{2}$$

In the DES formulation, the RANS length scale $l_{k\text{-}\omega}$, which is defined as

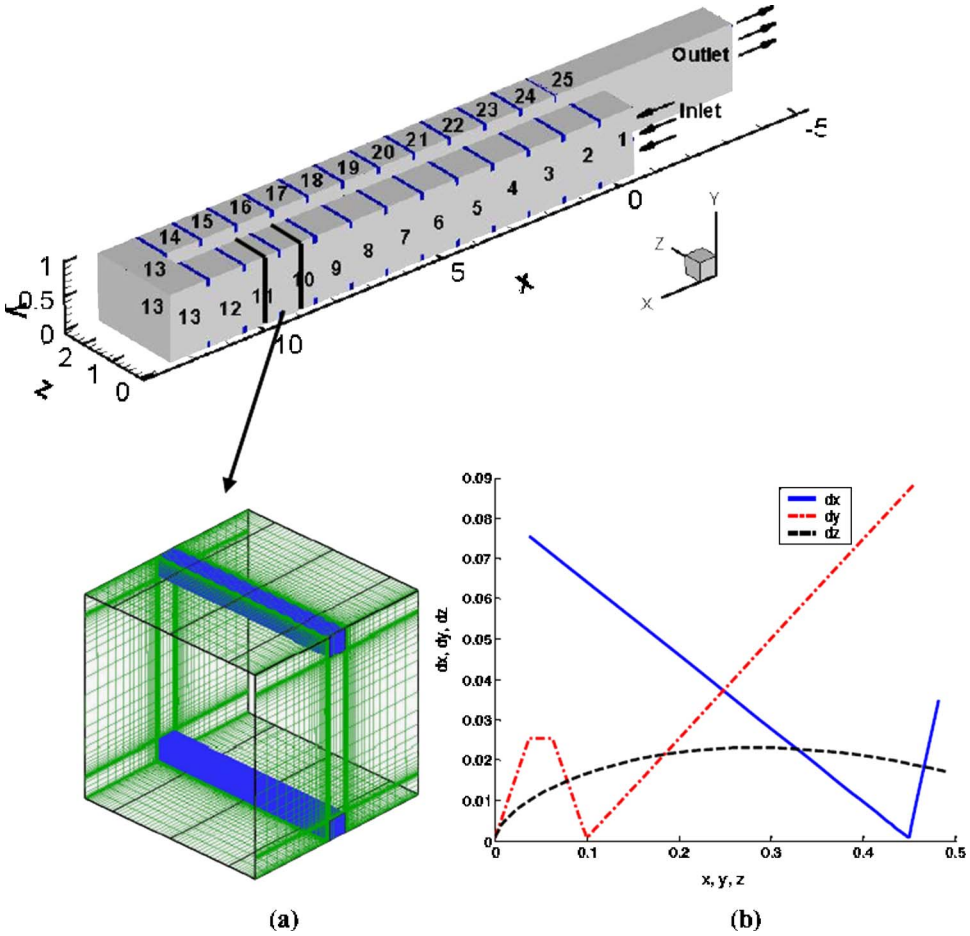

Fig. 1 (***a***) **Schematic diagram representing the two pass channel used in the study and the grid in a unit rib region. The numbers 1–25 represent the blocks used for spatial averaging.** (***b***) **Grid distribution in rib pitch.**

$$l_{k-\omega} = \frac{\sqrt{k}}{\beta^* \omega}$$

for the k-ω model is replaced by a DES length scale δ, where

$$\delta = \min(l_{k-\omega}, C_{\mathrm{DES}}\Delta)$$

and

$$\Delta = \max(\Delta_x, \Delta_y, \Delta_z)$$

Based on this, the dissipation term in the k-transport equation is reduced to

$$D^k = \frac{k^{3/2}}{\delta}$$

Hence, regions near solid boundaries and where the turbulent length scale is less than the local maximum grid dimension are assigned the RANS mode of solution. As the turbulent length scale exceeds the grid dimension, the regions are solved using the LES mode.

Numerical Method. The governing equations for momentum are discretized with a conservative finite-volume formulation using a non-staggered grid topology. The Cartesian velocities and pressure are calculated and stored at the cell center, whereas contravariant fluxes are stored and calculated at the cell faces. The discretized continuity and momentum equations are integrated in time using a projection method. The temporal advancement is performed in two steps, a predictor step, which calculates an intermediate velocity field, and a corrector step, which calculates the updated velocity at the new time step by satisfying discrete continuity. A second order central difference scheme is used to discretize the momentum and energy equations. The k-ω model (in URANS and DES forms) is used for closure and the standard boundary conditions, as prescribed by Wilcox [32], are used. The equations for the turbulent kinetic energy and the dissipation rate are solved using a second order central difference scheme subject to a TVD limiter.

The computer program GENIDLEST (generalized incompressible direct and large eddy simulations of turbulence) used for these simulations has been applied extensively to study air-side heat transfer augmentation in compact heat exchangers and internal cooling in gas turbines [19,20,27,33–37]. Details about the algorithm, functionality, and capabilities can be found in Tafti [38].

Computational Details. The calculations are carried out in a complete two-pass channel with 12 ribs in the first and the second passes, which are connected by a 180 deg bend. Each rib unit consists of two in-line ribs placed at the center of the channel at the top and the bottom. The grid and the coordinate system used are shown in Fig. 1. The grid in a rib pitch consists of 65 nodes in the streamwise direction, of which 13 nodes lie directly over the rib, with 53 nodes in the inter-rib space. In the cross-stream direction, the grid consists of 65×65 nodes with 13 nodes each in the regions of the rib, covering the rib height of e and 41 nodes in the middle of the channel and 65 nodes distributed using a monotonic spline distribution along the span (Fig. 1). The grid distribution is symmetric in the y and z directions.

A posteriori evaluation of the grid distributions were carried out

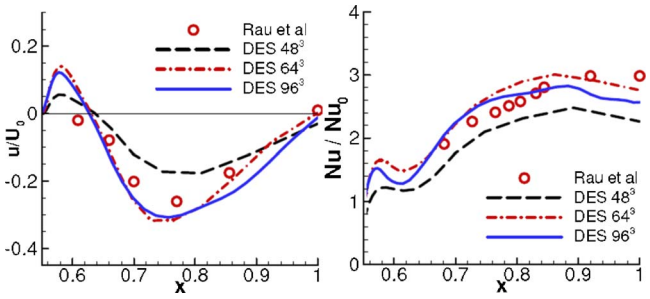

Fig. 2 Comparison of the fully developed flow and heat transfer characteristics downstream of the rib as predicted by DES for various grid densities. The *x*-axis correspond to the *x* locations from a previous study under fully developed condition [26] and is different from the notation used in the current study.

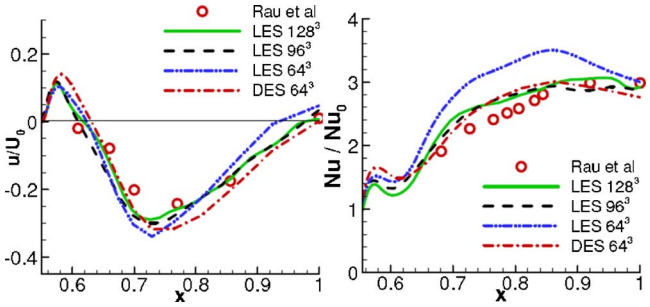

Fig. 3 Comparison of the fully developed flow and heat transfer characteristics downstream of the rib as predicted by LES [18] and DES [26]. The *x*-axis correspond to the *x* locations from previous studies under fully developed conditions [18,26] and is different from the notation used in the current study.

based on the local friction velocities in a fully developed rib unit. The streamwise grid distribution gives $\Delta^+ < 1$ near the ribs and $\Delta^+_{\max} \sim 150$ in the inter-rib space. The spanwise distribution yields $\Delta^+ < 1$ near the side walls and $\Delta^+_{\max} \sim 180$ in the center. Although the grid distribution in the wall normal direction ($\Delta^+ \sim 1-1.25$) was similar to the values obtained in the LES computation, the streamwise and spanwise grids for this grid are more relaxed than the LES computation in which $\Delta^{\parallel} < 30$. The grid spacing in the x, y, z directions, for a rib pitch, are shown in Fig. 1(*b*). This distribution allows a major part of the boundary layer to be treated in the RANS mode. In total, each period was discretized into $64 \times 64 \times 64$ cells and was divided into four equal blocks in the spanwise direction to facilitate parallel processing. The middle of the 180 deg bend was discretized into $64 \times 64 \times 32$ cells and divided into two blocks. The second leg of the duct had an outlet region that was around four hydraulic diameters long. All these total 7.7×10^6 cells, which are distributed in 110 blocks.

A nondimensional time step (based on the hydraulic diameter, D_h and bulk velocity, U_0) of 1×10^{-4} was used in all of the cases. Calculations are initiated by assuming a uniform flow velocity in the computational domain and imposing a uniform laminar flow inlet profile, approximating the flow exiting a plenum into the ribbed channel. Time evolution of bulk quantities such as friction factor is monitored as the solution is allowed to reach a statistically steady state for about 20 nondimensional time units. The mean characteristics of the flow are obtained by averaging the solution for an additional 20 time units.

The augmentation ratios for friction are calculated with reference to a smooth channel. The reference values for friction factor for a smooth duct are obtained from the correlation [39]

$$f_0 = 0.046 \mathrm{Re}^{-0.2}$$

Grid Sensitivity. In order to justify the selection of the grid used for the DES computation, some grid sensitivity studies were carried out on one periodic unit of a ribbed duct under fully developed flow and thermal conditions [26]. Figure 2 shows the streamwise velocity and the heat transfer augmentation downstream of the rib (x=0.55–1.0),[1] as predicted by DES on three grids—48^3, 64^3, and 96^3. The predicted values are compared to the experimental measurements by Rau et al. [31]. The plot shows the streamwise flow downstream of the rib at the center of the plane y=0.1e in the separated recirculation region. It is observed that although the predictions by the 64^3 and 96^3 grid are in good agreement with the measured values, the 48^3 grid underpredicts the magnitude of the velocities. It is also observed that the reattachment is overpredicted by the coarse grid, whereas the 64^3 and 96^3 grids predict the reattachment accurately. A plot of the heat transfer augmentation in the separation bubble reiterates the inability of the 48^3 grid to accurately predict the flow and heat transfer using DES. The coarse grid underpredicts the heat transfer, whereas the heat transfer augmentation predicted by the 64^3 and 96^3 grids is consistent with the experimental measurements. Since the 64^3 and the 96^3 grids predict the trends accurately, the 64^3 grid was considered to be sufficiently accurate to be used for one rib unit. Using the same argument, DES computations were carried out for stationary [26] and rotating [28] fully developed ribbed duct on the 64^3 grid. The results showed good agreement with the LES computations and the experiments.

Although a 64^3 grid is observed to be suitable for DES, it is necessary to justify that the same grid is not sufficient for LES. Figure 3 evaluates the performance of LES on three grids—128^3, 96^3, and 64^3. A comparison of the streamwise velocities predicted with the data obtained from experiments by Rau et al. [31] shows that the trends observed by the experiments in the separated region are captured well by all the LES grids and the DES on the 64^3 grid. However, the reattachment point is underpredicted by the 64^3 LES. The reattachment was observed to be located at a distance of 4.1–4.25e downstream of the rib by the experiments. Although the LES 128^3 and 96^3 grids and the DES 64^3 grid predict reattachment at a distance of around 4.1e downstream of the rib, the LES 64^3 grid predicts the value to be at 3.7e. Though the flow features were predicted reasonably well by LES on the 64^3 grid a comparison of the heat transfer augmentation clearly emphasizes the inability of the 64^3 grid to be used for LES. It is observed that the 64^3 grid overpredicts the heat transfer in the separated region of the flow, whereas the other LES grids and the DES case predicted the heat transfer with good accuracy. The underpredicted reattachment and the overprediction of the heat

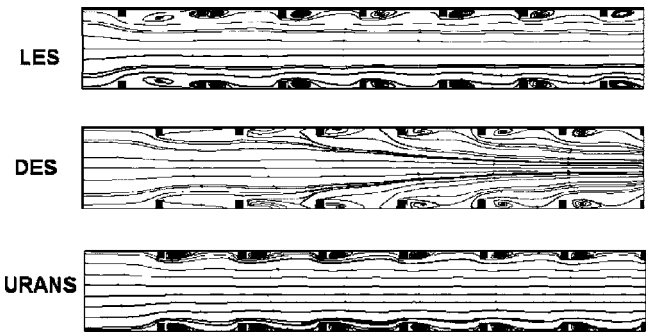

Fig. 4 Comparison of streamlines in the developing region through a plane passing through the center *z* plane

[1]The x value corresponds to the x locations from a previous study [26] and is different from the notation used in the current study.

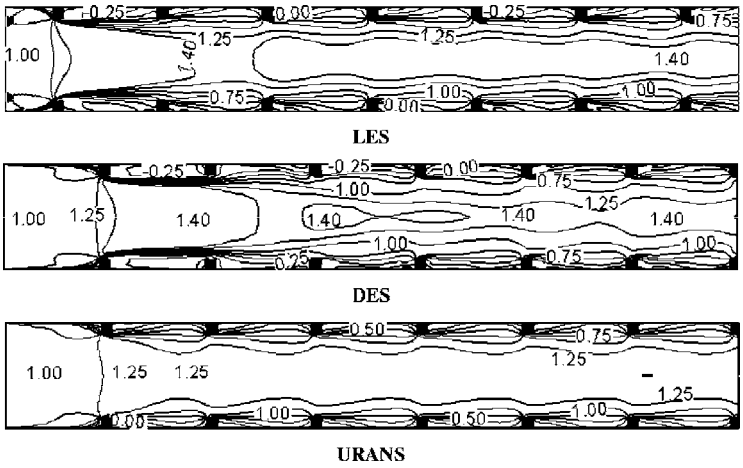

Fig. 5 Comparison of *u* velocities in the developing region through the center *z* plane. Flow is from left to right.

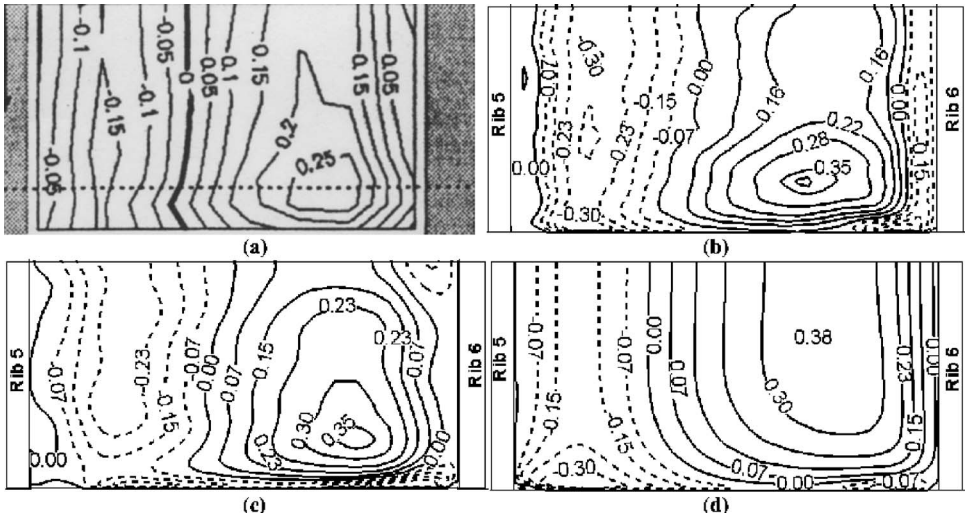

Fig. 6 *U* velocities at a plane passing through the rib: (*a*) experiments Rau et al. [31], *P*/*e*=9; (*b*) LES—fully developed region (rib 6); (*c*) DES—fully developed region (rib 6); and (*d*) URANS—fully developed region (rib 6)

transfer shows that the 64^3 grid used for DES is coarse for LES.

In addition, the plots shown in Figure 3 also show the convergence of the results as the grid is refined to 96^3 and 128^3. Earlier LES computations on fully developed flow in stationary [18] and rotating [29] ducts using the 128^3 and the 96^3 grids also show that the mean flow and heat transfer characteristics are captured well by both the grids. Thus, when the LES computations were extended to the single pass of a cooling duct consisting of 9 ribs [28] and the bend region [22], the grid consisting of $96\times96\times96$ cells for each rib unit was chosen. These computations have been used for comparison with the DES and URANS results in the current study.

Results

The DES and URANS results in the first pass of the duct are compared with LES computations by Sewall et al. [21]. The flow in the fully developed region is also compared to experiments by Rau et al. [31] and LES computations [18,21]. The flow in the 180 deg bend is compared to LES results in the bend by Sewall and Tafti [22] and experimental results by Sewall et al. [21]. The LES computations have been validated extensively with experiments in Sewall et al. [21], and except for some differences at the center of the duct and in the 180 deg bend, all physical phenomena characterized by mean and turbulent rms quantities are reproduced with excellent quantitative accuracy.

Streamwise Flow Development in First Pass. Figure 4 shows the development of the streamwise flow velocity. The LES calculation [21] shows that the separated shear layer at the first set of ribs immediately transitions to turbulence, which then starts dif-

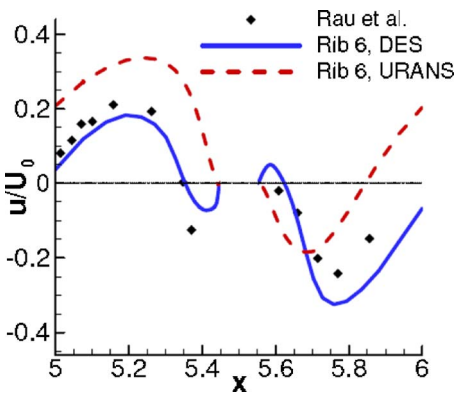

Fig. 7 Comparison of the streamwise velocities at *y*/*e*=0.1 with experimental data, rib location *x*=5.45–5.55 (blank space in the plot)

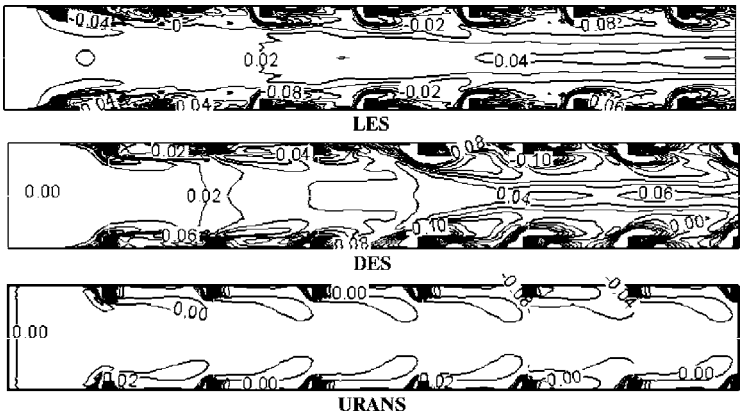

Fig. 8 Comparison of *w* velocities in the developing region through a plane near the side wall. Streamwise flow is from left to right.

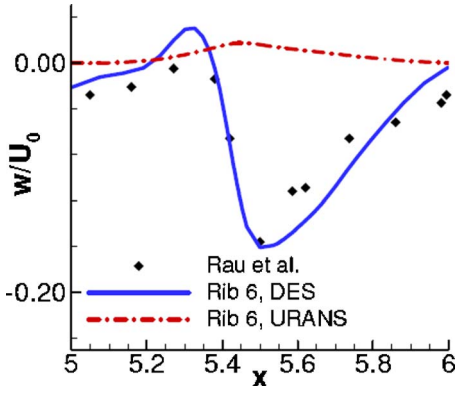

Fig. 9 Secondary flow in the duct measured at $y/e=1.5$ and $z/D_h=0.45$

fusing toward the duct wall and the duct centerline. The flow separates in the vicinity of the first set of ribs and reattaches just upstream of the second set of ribs. However, at the second rib, because of the increased mixing promoted by turbulence, reattachment occurs at around half the rib pitch, after which the flow quickly settles down to a near fully developed state by the third to fourth rib. After the first four ribs the reattachment is observed to occur at a distance of around $4.5e$ downstream of the rib in the first pass of the duct.

DES predicts a much larger region of flow separation after the first rib, which reattaches only after the second rib. However, as the flow progresses, fully developed conditions are observed after four to five ribs, where the reattachment is observed at a distance of $4.4-4.5e$ downstream of the rib. In the URANS case, the separated shear layer at the first rib reattaches much earlier than in LES and the flow immediately settles down to a fully developed turbulent state, where the reattachment is observed at a distance of $3.6-3.7e$ downstream of the rib. This can be clearly identified in Fig. 4. A comparison of the streamwise velocity contours in Fig. 5 shows that the DES results are different from that predicted by LES for the first three to four rib pairs. At the first three ribs, the separation zones are much larger than in LES and the streamwise velocity distribution in the cross section is less "pluglike," but shows a gradual increasing trend toward the center of the duct, both of which imply that DES is unable to predict the rapid transition to a turbulent state. Although LES reaches a quasiperiodic state after the third rib, DES reaches a similar state after the fourth to fifth rib pair. On the other hand, the flow predicted by URANS shows a flat turbulent profile immediately downstream of the first rib. The magnitudes of the centerline velocities observed with URANS is less than the velocity magnitudes observed in LES and DES.

Figure 6 compares the flow features in the vicinity of rib 6 (where the flow is fully developed) as predicted by DES and URANS to the flow predicted by LES [21] and experiments [31]. For $P/e=9$, at a plane passing through $y/e=0.15$, Rau et al. [31] observed the maximum velocity to lie at a distance of around $0.15D_h$ from the wall in the fully developed region. Although some differences in magnitude of the velocities are observed due to the different rib pitch in the experiments, LES and DES predict this feature in the fully developed region of the first pass of the duct. URANS fails to predict this offset and predicts a uniform high-velocity region spanning the channel.

Figure 7 shows the streamwise velocities measured at a plane

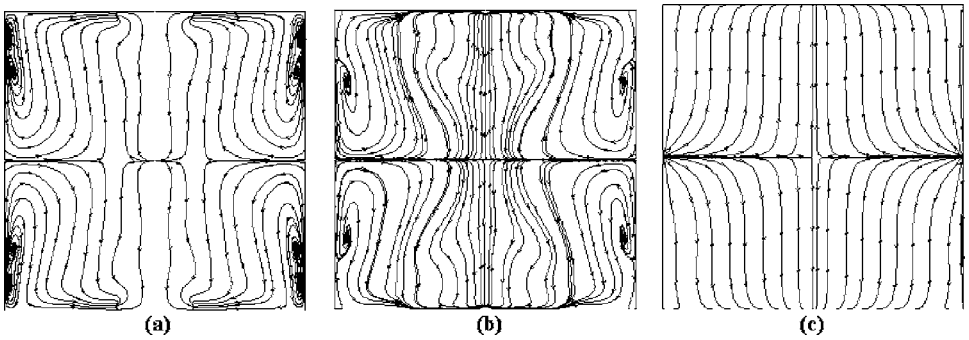

Fig. 10 Secondary flow in the fully developed region of the duct (between ribs 9 and 10): (*a*) LES, (*b*) DES, and (*c*) URANS. The horizontal axis represents the spanwise direction and the vertical axis represents the normal direction.

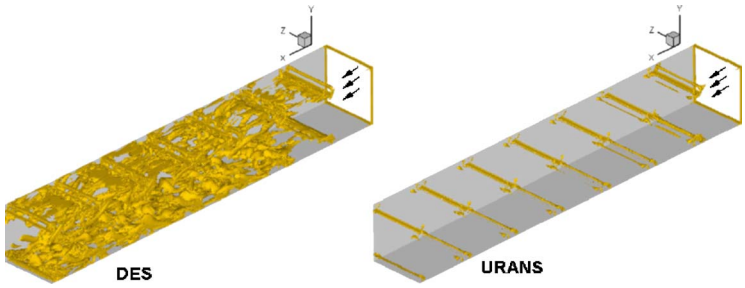

Fig. 11 Iso-surfaces of instantaneous coherent vorticity (vorticity magnitude=4.0) predicted by DES and URANS in the developing regions of the duct. Black arrows represent the flow at the inlet.

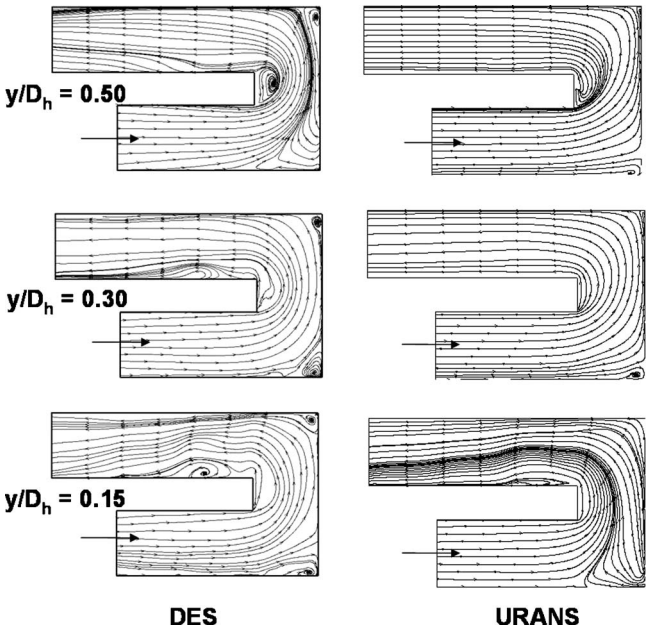

Fig. 12 Comparison of the flow predicted by DES and URANS in the 180 deg bend

passing through the center at $y/e=0.1$. As the flow passes over the ribs, a separated region is formed downstream of the ribs, where negative velocities are observed up to the reattachment region. The flow accelerates after reattachment and separates in front of the next rib as shown by the small negative velocities upstream of the rib ($x=5.35$). The separation in front of the rib and the secondary recirculation trapped behind the rib are predicted accurately by DES, and the velocity magnitudes are consistent with the fully developed experimental data. In the region considered, the reattachment length is slightly higher than the reattachment length in a fully developed case. URANS predicts early attachment of the flow and also fails to predict the recirculation regions immediately upstream and downstream of the rib.

Development of Secondary Flows. Unlike skewed or angled ribs, which exhibit strong secondary flow patterns, normal rib-induced secondary flows are comparatively weak but highly localized and strong near the junction of the rib with the side walls. The presence of the rib induces strong spanwise velocities at the junction. This physics is not captured by the standard eddy-viscosity RANS models [11,26]. Figure 8 shows the development of the spanwise velocity contours at a plane near the side wall ($z/D_h=0.05$). Although some changes in the secondary flow are observed even further downstream toward the core of the duct [30], the flow near the side wall is fairly established by the third rib in LES and by the fourth rib in DES. However after it is established, the magnitudes are consistent between the two methods. On the other hand, URANS fails to predict the secondary flow accurately. The w velocities predicted by URANS are of an order of magnitude less than that predicted by DES and LES.

The lateral w velocities (Fig. 9) measured above the rib along a line close to the smooth side wall ($y/e=1.5$, $z/D_h=0.45$), also emphasizes the inability of URANS to accurately predict the secondary flow. A comparison of the w velocities shows that the secondary flow predicted by DES in the vicinity of rib 6 is in good agreement with the fully developed experimental results, unlike the URANS predictions. Although DES predicts a strong secondary velocity toward the side walls (negative w velocities) in the vicinity of the ribs ($x=5.4-5.6$), the URANS model calculates a near-zero spanwise velocity at these locations.

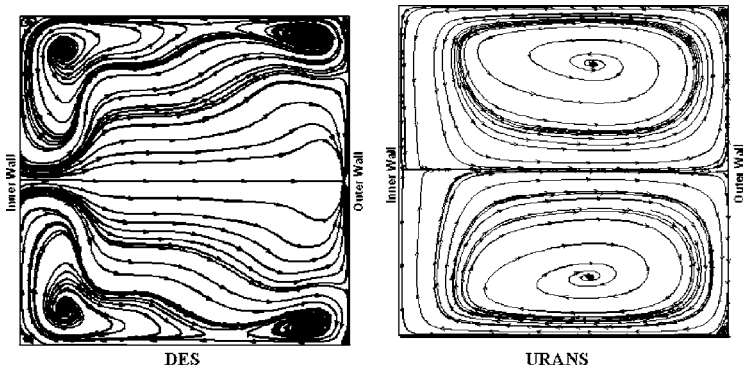

Fig. 13 Secondary flow at the center of the 180 deg bend. DES predicts Dean vortices impinging on the inner and outer walls, whereas URANS fails to predict these vortices.

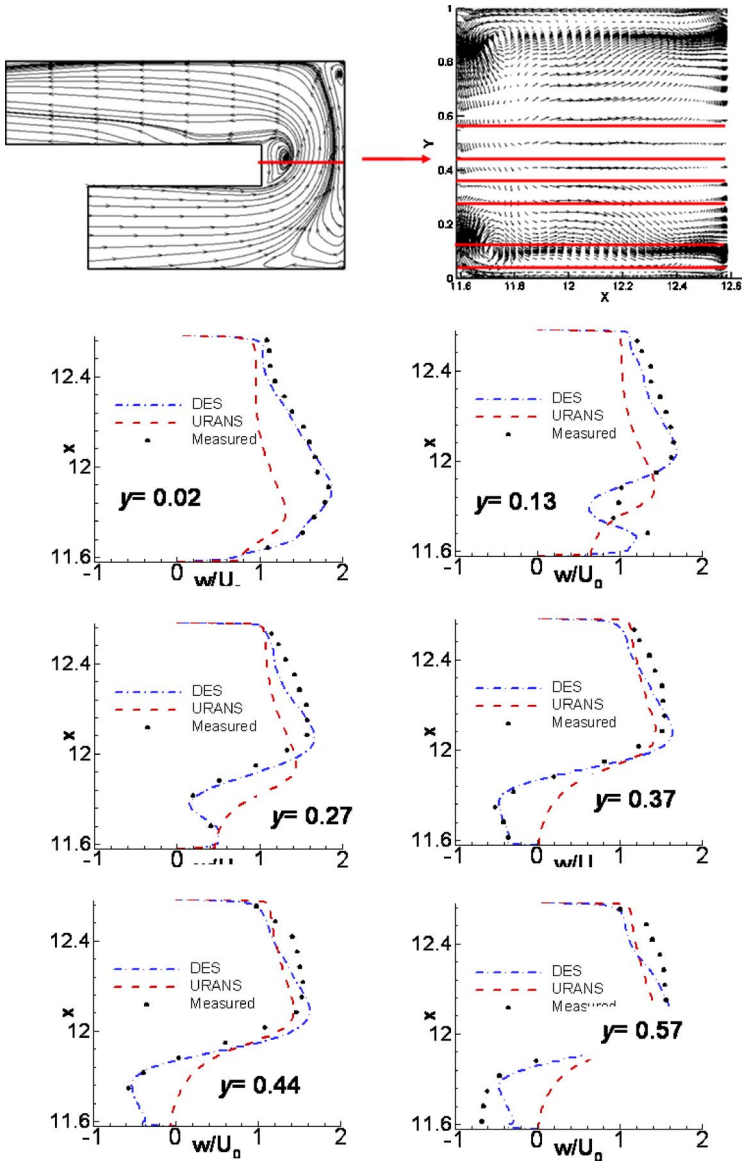

Fig. 14 Schematic diagram of the lines where the measurements have been presented (top). Velocities in the center of the 180 deg bend in comparison to experiments by Sewall et al. [21] (bottom).

Mean spanwise structures were studied experimentally by Liou et al. [40] using LDV techniques. These secondary flow structures are strongest in the vicinity of the ribs. Figure 10 shows that the flow causes core fluid in the center of the duct to be drawn toward the side walls. Near the center of the channel, there is a flow toward the ribbed walls. The flow turns near the corners and moves along the smooth walls toward the center of the channel. Small recirculating eddies are observed near the smooth wall. A comparison of the secondary flows between the ninth and tenth ribs (where the secondary flow was observed to be completely developed) shows that DES, like the earlier LES computations [21], predicts the secondary flows accurately. Earlier calculations [11,26] showed that two-equation RANS models are incapable of capturing the secondary flow. The k-ω URANS computation shows a similar discrepancy in predicting the secondary flow.

A comparison of the instantaneous coherent vorticity or swirl [41] as predicted by 64^3 DES and 64^3 URANS is shown in Fig. 11. These plots give an idea of the flow structures resolved by the two schemes. The structures with a swirl magnitude of 4.0 are plotted. It is observed that DES resolves more structures than the equivalent URANS model. Thus, the modification in the length scales in the URANS model, which converts it into an equivalent DES model, substantially improves the fidelity of the simulation.

Flow Features in 180 deg *Bend and Second Pass*. Figure 12 shows streamlines at three cross-stream locations $y=0.5$, 0.3, and 0.15 for the flow entering and exiting the 180 deg bend as predicted by DES and URANS. The flow predicted by DES shows that as the flow approaches the bend it separates at the outer corners almost through out the whole height of the duct. At the inner wall, the flow accelerates and separates as it encounters the sharp corner toward the center of the duct ($y/D_h=0.50$). This separated zone reattaches only after the flow turns the corner into the second pass of the duct. This separation is however not sustained through out the height of the duct as can be observed at $y/D_h=0.30$ and $y/D_h=0.15$. Another recirculation region downstream of the bend at the inner wall in the vicinity of the second rib is also predicted by DES. Furthermore, the flow is characterized by impingement on the back wall and outer downstream wall of the duct. LES computations [22] showed similar recirculation

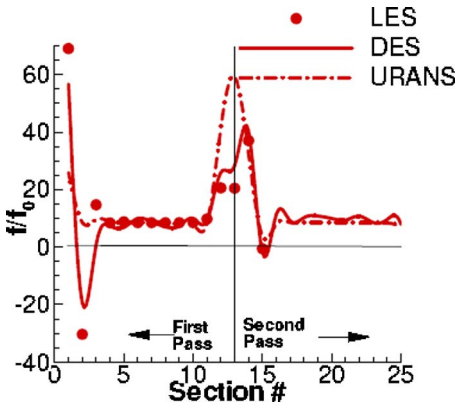

Fig. 15 Block-averaged friction factors in the complete channel

regions at the inner wall and the outer corners of the bend. Earlier studies [30] also showed reasonable agreement of the flow predicted by DES with that predicted by LES in the bend. URANS, on the other hand, does not show any separation downstream of the bend or at the inner wall of the bend. It also fails to predict the recirculation at the outer walls of the bend. However, URANS predicts a slight separation downstream of the bend on moving down the height of the duct.

Figure 13 shows the secondary flow in the center of the bend as predicted by DES and URANS. DES predicts a maximum cross-stream velocity of 0.7 at the inner wall and 0.2 at the outer wall with elongated Dean vortices in the cross section. URANS predicts a completely different structure of the flow in the center of the bend corresponding to a maximum cross-stream velocity of 0.4–0.5 at both the inner and outer walls.

To verify the accuracy of the flow predicted by URANS and DES, the streamwise velocities computed at the center of the 180 deg bend at different locations are compared to LDV data from Sewall et al. [21] (Fig. 14). At all y locations, the velocity in the outer half of the bend ($x=12.1-12.6$) is quite uniform at ~ 1.5 times the bulk velocity. However, at the inside of the bend, the streamwise velocity steadily decreases as y increases with a reversal in the flow direction occurring between $y=0.27$ and $y=0.37$. The profile at $y=0.27$ shows a velocity of nearly zero, indicating that the recirculation zone occupies $\sim 25\%$ of the height of the duct. It is observed that at all the six locations, DES predictions match well with experiments while URANS fails to predict some key features, such as the recirculating cells in the 180 degree bend, as observed in the profiles at $y=0.37$, 0.44, and 0.57.

Pitch Averaged Frictional Losses. Figure 15 shows the comparison of the friction factor values obtained from DES and URANS with the LES computations [20,21] across each rib. The LES data have been collected from two cases: stationary developing flow [21] for the first nine ribs in the first pass, and LES computations in a 180 deg bend [22], for the 180 deg bend and two ribs upstream and downstream of the bend. In the DES and URANS computations, the data are obtained by using the average pressure drop across one pitch ($f=-\Delta p/2\Delta l$) across a rib and are fitted to a spline. Slight differences from the LES are expected in the vicinity of the 180 deg bend since the LES computation was carried out assuming a fully developed turbulent flow two ribs upstream of the bend, whereas a complete channel is studied in this case.

A comparison of the friction factors shows that DES, like LES, predicts a negative friction factor due to pressure recovery downstream of the inlet, whereas URANS completely fails to predict this recovery. Further downstream as the flow reaches a fully developed state, the predictions by DES as well as URANS are consistent with the LES predictions. The average friction factor, as predicted by DES and URANS, from the fourth rib to tenth rib is observed to be around 8.15 times that in a smooth channel, which compares well to the LES value of 8.5.

The shear induced due to the turning of the flow upstream of the 180 deg bend results in a higher friction factor in the region. Based on the LES predictions, the friction factor immediately upstream of the bend is around three times that in a fully developed case. The friction factor in the bend is almost of similar magnitude, but as the flow turns the corner (block 14 in Fig. 1), it encounters a large drop in pressure. Pressure recovery results in a negative friction factor immediately downstream, which is similar to the entry region where an initial drop in pressure is followed by a pressure recovery. The pressure drop predicted in the vicinity of the 180 deg bend by DES compares well to the LES cases. URANS overpredicts the friction factor in the vicinity of the bend. As the flow settles down in the second pass, the average friction factor in the second pass of the duct is observed to be close to 9.5 as predicted by DES and URANS.

Conclusions

The capability of DES and URANS with a base k-ω model for predicting the flow in a complete two pass ribbed duct is evaluated. The results are compared to LES computations by Sewall et al. [21] and Sewall and Tafti [22] and experiments by Rau et al. [31] and Sewall et al. [21].

The following major conclusions are drawn from this study:

1. DES does not predict shear layer transition with accuracy and as a result predicts a greater development length than LES. However, once the flow is fully developed, DES predictions compare very well to LES and experiments. URANS, on the other hand, predicts near complete transition to turbulence immediately after the first rib and underpredicts the centerline velocities in the developing region. Comparisons to experiments show that although DES captures the detailed flow characteristics (Fig. 4), URANS does not.
2. DES is also able to capture the localized unsteady vorticity driven secondary flows at the junction of the rib with the side wall, whereas URANS completely fails in this regard (Figs. 6–8).
3. DES reproduces the flow in the 180 deg bend with much better accuracy than URANS (Figs. 10 and 11). URANS completely fails to predict the recirculating cells in the inner wall and the outer corners of the bend.

Although URANS does not show the fidelity of DES to capture detailed flow physics, it does reproduce the overall friction factor with reasonable accuracy in the fully developed region of the duct, and downstream of the bend (Fig. 12). However, it does not capture the variations at the first three ribs and grossly overpredicts the friction in the bend. DES agrees much better with LES predictions and experiments [21].

In conclusion, it is shown that by a small switch in the underlying model to a DES mode, the accuracy of the model can be improved to be consistent with the underlying physics leading to better prediction capability. It is also concluded that using eddy-viscosity models in the DES mode overcomes some of the inherent shortcomings of the base RANS model.

Acknowledgment

This research was supported by the US DOE, Office of Fossil Energy, and National Energy Technology Laboratory. Any opinions, findings, conclusions, or recommendations expressed herein are those of the authors and do not necessarily reflect the views of the DOE.

Nomenclature

D_h = hydraulic diameter (characteristic length)

e = rib height
f = fanning friction factor
f_0 = fanning friction factor in a smooth duct
k = turbulent kinetic energy
$l_{k\text{-}\omega}$ = RANS length scale
P = rib pitch
p = total pressure
Re = Reynolds number based on bulk velocity
Re_t = turbulent Reynolds number
$\vec{u}$ = Cartesian velocity vector
u, v, w = velocities in the x, y, and z directions
U_0 = bulk velocity or inlet velocity, characteristic velocity
W = width of the 180 deg bend=$0.5D_h$
Δ = grid (LES) length scale
δ = DES length scale
ω = rate of dissipation of k

References

[1] Iacovides, H., and Raisee, M., 1999, "Recent Progress in the Computation of Flow and Heat Transfer in Internal Cooling Passages of Turbine Blades," Int. J. Heat Fluid Flow, **20**, pp. 320–328.

[2] Jia, R., Saidi, A., and Sunden, B., 2002, "Heat Transfer Enhancements in Square Ducts with V-Shaped Ribs of Various Angles," *Proc. ASME Turbo Expo*, ASME, New York, ASME Paper No. GT-2002-30209.

[3] Johnson, B. V., Wagner, J. H., and Steuber, G. D., 1993, "Effect of Rotation on Coolant Passage Heat Transfer: Vol II—Coolant Passages With Trips Normal and Skew to Flow," NASA Contractor's Report No. 4396.

[4] Johnson, B. V., Wagner, J. H., Steuber, G. D., and Yeh, F. C., 1994, "Heat Transfer in Rotating Serpentine Passages With Selected Model Orientations for Smooth or Skewed Trip Walls," ASME J. Turbomach., **116**, pp. 738–744.

[5] Amano, R. S., and Goel, P., 1995, "Computation of Turbulent Flow Beyond Backward Steps Using Reynolds Stress Closure," AIAA J., **23**, pp. 1356–1361.

[6] Liou, T.-M., Hwang, J. J., and Chen, S. H., 1992, "Turbulent Transport Phenomena in a Channel With Periodic Rib Turbulators," J. Thermophys. Heat Transfer, **6**(3), pp. 513–521.

[7] Prakash, C., and Zerkle, R., 1995, "Prediction of Turbulent Flow and Heat Transfer in a Ribbed Rectangular Duct With and Without Rotation," ASME J. Turbomach., **117**, pp. 255–264.

[8] Saidi, A., and Sunden, B., 2001, "On Prediction of Thermal-Hydraulic Characteristics of Square-Sectioned Ribbed Cooling Ducts," ASME J. Turbomach., **123**, pp. 614–620.

[9] Iacovides, H., 1998, "Computation of Flow and Heat Transfer Through Rotating Ribbed Passages," Int. J. Heat Fluid Flow, **19**, pp. 393—400.

[10] Lin, Y. L., Shih, T. I.-P., Stephens, M. A., and Chyu, M. K., 2001, "A Numerical Study of Flow and Heat Transfer in a Smooth and a Ribbed U-Duct With and Without Rotation," ASME J. Heat Transfer, **123**, pp. 219–232.

[11] Ooi, A., Iaccarino, G., Durbin, P. A., and Behnia, M., 2002, "Reynolds Averaged Simulation of Flow and Heat Transfer in Ribbed Ducts," Inf. Sci. (N.Y.), **23**, pp. 750–757.

[12] Rigby, D. L., 1998, "Prediction of Heat and Mass Transfer in a Rotating Ribbed Coolant Passage with a 180 Degree Turn," International Gas Turbine and Aeroengine Congress and Exhibition, Stockholm, Sweden, June 2–5, ASME Paper No 98-GT-329.

[13] Menter, F. R., 1992, "Improved Two-Equation k-ω Turbulence Models for Aerodynamic Flows," NASA Technical Memorandum 103975.

[14] Menter, F. R., 1993, "Zonal Two Equation k-ω Turbulence Models for Aerodynamic Flows," AIAA No. Paper 93–2906.

[15] Murata, A., and Mochizuki, S., 2001, "Comparison Between Laminar and Turbulent Heat Transfer in Stationary Square Ducts With Transverse or Angled Rib Turbulators," Int. J. Heat Mass Transfer, **44**, pp. 1127–1141.

[16] Murata, A., and Mochizuki, S., 2000, "Large Eddy Simulation With a Dynamic Subgrid-Scale Model of Turbulent Heat Transfer in an Orthogonally Rotating Rectangular Duct With Transverse Rib Turbulators," Int. J. Heat Mass Transfer, **43**, pp. 1243–1259.

[17] Watanabe, K., and Takahashi, T., 2002, "LES Simulation and Experimental Measurement of Fully Developed Ribbed Channel Flow and Heat Transfer," *Proceedings of ASME Turbo Expo*, Amsterdam, June, Paper No. GT 2002-30203.

[18] Tafti, D. K., 2005, "Evaluating the Role of Subgrid Stress Modelling in a Ribbed Duct for the Internal Cooling of Turbine Blades," Inf. Sci. (N.Y.), **26**(1), pp. 92–104.

[19] Abdel-Wahab, S., 2003, "Large Eddy Simulation of Flow and Heat Transfer in a Staggered 45° Ribbed Duct and a Rotating 90° Ribbed Duct," M.S. thesis, Virginia Polytechnic Institute and State University.

[20] Sewall, E. A., 2005, "Large Eddy Simulations of Flow and Heat Transfer in the Developing and 180° Bend Regions of Ribbed Gas Turbine Blade Internal Cooling Ducts with Rotation: Effect of Coriolis and Centrifugal Buoyancy Forces," Ph.D. dissertation, Virginia Polytechnic Institute and State University.

[21] Sewall, E. A., and Tafti, D. K., 2006, "Large Eddy Simulation of Flow and Heat Transfer in the 180-Deg Bend Region of a Stationary Gas Turbine Blade Ribbed Internal Cooling Duct," J. Turbomach., **128**(4), pp. 763–771.

[22] Sewall, E. A., and Tafti, D. K., 2005, "Large Eddy Simulation of Flow and Heat Transfer in the 180° Bend Region of a Stationary Ribbed Gas Turbine Internal Cooling Duct," ASME Turbo Expo 2005, June 6–9, Reno-Tahoe, ASME Paper No. GT-2005-68518.

[23] Spalart, P. R., Jou, W. H., Streletes, M., and Allmaras, S. R., 1997, "Comments on the Feasibility of LES for Wings and a Hybrid RANS/LES Approach," *First AFSOR Int. Conf. on DNS/LES, Aug 4–8, 1997*, C. Liu and Z. Liun eds., Greyden Press, Columbus, Advances in DNS/LES.

[24] Spalart, P. R., 2001, "Young Person's Guide to Detached-Eddy Simulation Grids," NASA Contractor Report No. 2001-211032.

[25] Strelets, M., 2001, "Detached Eddy Simulation of Massively Separated Flows," AIAA Paper No. 2001-0879.

[26] Viswanathan, A. K., and Tafti, D. K., 2005, "Detached Eddy Simulation of Turbulent Flow and Heat Transfer in a Duct," ASME J. Fluids Eng., **127**(5), pp. 888–896.

[27] Viswanathan, A. K., and Tafti, D. K., 2005, "Detached Eddy Simulation of Flow and Heat Transfer in a Stationary Internal Cooling Duct With Skewed Ribs," ASME Turbo Expo 2005, June 6–9, Reno-Tahoe, ASME Paper No. GT-2005-68118.

[28] Viswanathan, A. K., and Tafti, D. K., 2006, "Detached Eddy Simulation of Flow and Heat Transfer in Fully Developed Rotating Internal Cooling Channel With Normal Ribs," Inf. Sci. (N.Y.), (accepted).

[29] Abdel-Wahab, S., and Tafti, D. K., 2004, "Large Eddy Simulations of Flow and Heat Transfer in a 90° Ribbed Duct With Rotation: Effect of Coriolis and Centrifugal Buoyancy Forces," ASME J. Turbomach., **126**(4), pp. 627–636.

[30] Viswanathan, A. K., and Tafti, D. K., 2006, "Detached Eddy Simulation of Turbulent Flow and Heat Transfer in a Two-Pass Internal Cooling Duct," Inf. Sci. (N.Y.), **27**(1), pp. 1—20.

[31] Rau, G., Cakan, M., Moeller, D., and Arts, T., 1978, "The Effect of Periodic Ribs on Local Aerodynamic and Heat Transfer Performance of a Straight Cooling Channel," ASME J. Turbomach., **120**, pp. 368–375.

[32] Wilcox, D. C., 1988, "Reassessment of the Scale-Determining Equation for Advanced Turbulence Models," AIAA J., **26**(11), pp. 1299–1310.

[33] Abdel-Wahab, S., and Tafti, D. K., 2004, "Large Eddy Simulation of Flow and Heat Transfer in a Staggered 45° Ribbed Duct," ASME Turbo Expo, Vienna, ASME Paper No. GT2004-53800.

[34] Patrick, W., and Tafti, D. K., 2004, "Computations of Flow Structure and Heat Transfer in a Dimpled Channel at Low to Moderate Reynolds Number," 2004 ASME Heat Transfer/Fluids Engineering Summer Conference, July 11–15, Charlotte, ASME Paper No. HT-FED2004-56171.

[35] Sewall, E. A., and Tafti, D. K., 2004, "Large Eddy Simulation of the Developing Region of a Stationary Ribbed Internal Turbine Blade Cooling Channel," ASME Turbo Expo, Vienna, ASME Paper No. GT2004-53832.

[36] Sewall, E. A., and Tafti, D. K., 2004, "Large Eddy Simulations of the Developing Region of a Rotating Ribbed Internal Turbine Blade Cooling Channel," ASME Turbo Expo, Vienna, ASME Paper No. GT2004-53833.

[37] Viswanathan, A. K., Tafti, D. K., and Abdel-Wahab, S., 2005, "Large Eddy Simulation of Flow and Heat Transfer in an Internal Cooling Duct With High-Blockage 45° Staggered Ribs," ASME Turbo Expo 2005, June 6–9, Reno-Tahoe, ASME Paper No. GT-2005-68086.

[38] Tafti, D. K., 2001, "GenIDLEST—A Scalable Parallel Computational Tool for Simulating Complex Turbulent Flows," *Proc. ASME Fluids Engineering Division, ASME-IMECE*, ASME, New York, FED—Vol. 256.

[39] Incropera, F. P., and Dewitt, D. P., 2002, *Fundamentals of Heat and Mass Transfer*, 5th ed., Wiley, New York.

[40] Liou, T.-M., Chen, M.-Y., and Tsai, M.-H., 2003, "Fluid Flow and Heat Transfer in a Rotating Two-Pass Square Duct With In-Line 90-Degree Ribs," ASME J. Turbomach., **125**, pp. 260–268.

[41] Chong, M. S., Perry, A. E., and Cantwell, B. J., 1990, "A General Classification of Three-Dimensional Flow Fields," Phys. Fluids A, **2**(5), pp. 765–777.

An Advanced Numerical Model for Single Straight Tube Coriolis Flowmeters

Tao Wang

Roger C. Baker

Department of Engineering,
University of Cambridge,
Cambridge, CB2 1RX UK

Yousif Hussain
Krohne Ltd.,
Wellingborough, NN8 6AE UK

A detailed numerical model has been developed to simulate the single straight tube Coriolis flowmeter, which includes all important practical features. The measuring tube is modeled as fluid-tube interaction elements characterized as mass, stiffness, and damping matrices based on the theories of fluid-structure interaction and finite element method. Other features, such as the inner and outer cases and the driver spring, are modeled as standard ANSYS beam and shell elements and coupled to the measuring tube. The modal frequency and sensitivity factor from experiments are used to validate the model. In particular, our results show that the modal behaviour of the meter can only be adequately modeled if these practical features are included. [DOI: 10.1115/1.2353266]

Keywords: Coriolis mass flowmeters, finite element, fluid structure interaction

1 Introduction

The Coriolis meter has been used commercially since the late 1970s, although designs based on the Coriolis principle have been reported since the early 1950s [1]. It measures mass flow rate, and is capable of use with most single phase fluids. Most commercial designs have used twin tubes bent into a "U" or other shape. In the U tube version, for instance, the fluid splits equally between the two parallel tubes. The tubes are caused to vibrate perpendicular to the plane of the U like a tuning fork. The amplitude of the motion is very small, typically a fraction of a millimeter. The motion of the fluid through the tubes creates Coriolis accelerations, and the forces applied by the tubes to counter this cause the tubes to distort. This small distortion, two orders of magnitude or so less than the applied vibration, is measured (normally as time delay between two sensing positions), and from it the mass flow through the tubes can be deduced.

Single straight tube Coriolis flowmeters were first introduced to the market in the late 1980s and early 1990s. Since then, various hardware or software technologies have been applied to improve the effects of external mounting conditions and temperature variations. With these improvements, together with the intrinsic advantages of the meter (such as compactness, low pressure drop, self-draining, etc.), single straight tube meters have become an important option.

Raszillier and Durst [2] provided an analytical solution based on perturbation theory assuming a relatively small flow velocity compared with the critical velocity. In their recent work, Kutin and Bajisic [3] gave an analytical solution with a higher order of flow velocity by using the Galerkin method. Although these analytical solutions reflect the fundamental principle of Coriolis meters, they are limited to modal analysis of the measuring tube with simple geometry and boundary conditions.

Numerical methods, especially the finite element (FE) method, have been applied to investigate more complicated geometry and boundary conditions, or to conduct forced-response analyses [4–9]. Where analysis of single straight tube meters has been reported in the literature, they have been treated as simple straight fluid-conveying tubes with two clamped ends. However, modern designs of industrial flowmeters normally include other important features such as vibration compensation and stiffness modification mechanisms. This paper, therefore, considers a more complete and realistic numerical model of the industrial flowmeter design.

2 A Practical Design for Single Straight Tube Coriolis Flowmeters

One of the major design criteria for single straight tube flowmeters is the minimization of external mounting effects. Besides the measuring tube, the inner housing cylinder [10,11] is an essential part of the flowmeter structure and has several requirements: It provides the rigid structure which clamps the ends of the fluid-conveying tube; it carries the driver and sensors to create and measure the vibration and Coriolis effect; it ensures that the tube is isolated from the neighboring pipework through its compensation capability.

In addition, a stiffness modification mechanism, such as a reinforcing spring [12], is important in improving the measurement performance. Such a spring acts on the measuring tube and modifies the frequency of the drive mode. Since the phase shift due to mass flow can be affected by the spectral distance between the drive mode and the nearby anti-symmetric mode, the sensitivity to mass flow rate can also be modified for a specific design purpose.

A schematic view of this design [10–12] is shown in Fig. 1. The measuring tube component is between points A_L and A_R. Although the principle of this practical design is similar to the situation assumed in previous work, where A_L and A_R were perfectly clamped, it is clear that the dynamic behavior of the whole system will be different.

It is the objective of this paper to identify the difference in a quantitative way. The aim is to use this practical model as a simulation tool to improve and enhance the performance of the flowmeter.

3 The Finite Element Model

3.1 The Formulation of the Fluid-Tube Interaction Element. In his book, Païdoussis [13] gave a detailed explanation and derivation of the governing equations of fluid-tube interaction. For single straight tube meters, as pointed out by Wang and Baker [9], the axial stress term is necessary. This term is included in the governing equations. In the plane of the driving motion, the equation of motion for the transverse deflection u and rotation θ at a specific point x and time t is given by

Contributed by the Fluids Engineering Division of ASME for publication in the JOURNAL OF FLUIDS ENGINEERING. Manuscript received March 29, 2005; final manuscript received April 5, 2006. Assoc. Editor: Malcolm J. Andrews. Paper presented at the FLOMEKO 2004.

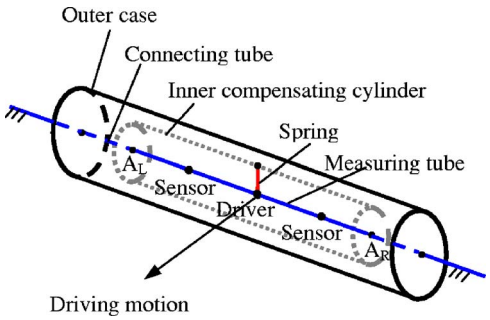

Fig. 1 A schematic view of a modern design

$$(\rho_f A_f + \rho_p A_p)\frac{\partial^2 u}{\partial t^2} + 2\rho_f A_f v_0 \frac{\partial^2 u}{\partial x\,\partial t} + (\rho_f A_f v_0^2 - \sigma_0 A_p)\frac{\partial^2 u}{\partial x^2} + kGA_p\left(\frac{\partial \theta}{\partial x} - \frac{\partial^2 u}{\partial x^2}\right) = 0$$

$$(\rho_f I_f + \rho_p I_p)\frac{\partial^2 \theta}{\partial t^2} - kGA_p\left(\frac{\partial u}{\partial x} - \theta\right) - (E + \sigma_0) I_p \frac{\partial^2 \theta}{\partial x^2} = 0 \quad (1)$$

where the fluid in the tube is assumed to move with uniform and constant velocity v_0, in a tube of area A_f, to have density ρ_f, and to have a rotary inertia I_f; and where the conveying tube has an initial stress of σ_0, density ρ_p, cross-sectional area of A_p, rotary inertia I_p, Young's modulus E, shear modulus G, and shear correction factor k. Equation (1) is also valid for the other transverse motion perpendicular to the drive motion. It is worth noting that Eq. (1) is essentially a Timoshenko beam formulation, because the measuring tube is not necessarily slender enough for the validity of an Euler-Bernoulli beam formulation [13]. In addition, the axial and torsional motions follow the normal structural analysis. Therefore, in a three-dimensional (3D) space each point has 6 degrees of freedom (DOF).

For the measuring tube alone, it is possible to solve Eq. (1) analytically. However, as shown in Fig. 1, there are other features coupled with the measuring tube. A finite element in its matrix form was developed to model the measuring tube so that it could be conveniently coupled with available finite elements. This fluid-tube interaction element uses a linear interpolation of displacement for axial and torsional DOFs separately, and a combined cubic interpolation for lateral and bending DOFs. This results in the matrix form of the partial differential equations. For a free vibration analysis

$$\mathbf{M}^{(e)}\ddot{\mathbf{d}} + \mathbf{C}^{(e)}\dot{\mathbf{d}} + \mathbf{K}^{(e)}\mathbf{d} = 0 \quad (2)$$

where $\mathbf{d}$ is the vector of the nodal displacement, and $\mathbf{M}^{(e)}$, $\mathbf{C}^{(e)}$, and $\mathbf{K}^{(e)}$ represent one particular element e ($e=1,\ldots,n$), which consists of two nodes (i and j) and has a total of 12 degrees of freedom in a 3D coordinate system as shown in Fig. 2. In a matrix form, the unknown displacement vector $\mathbf{d}$ for a finite element is $\mathbf{d}=[u_1^{(i)}, u_2^{(i)}, u_3^{(i)}, \theta_1^{(i)}, \theta_2^{(i)}, \theta_3^{(i)}, u_1^{(j)}, u_2^{(j)}, u_3^{(j)}, \theta_1^{(j)}, \theta_2^{(j)}, \theta_3^{(j)}]^T$. The derivation of these three elemental matrices $\mathbf{M}^{(e)}$, $\mathbf{C}^{(e)}$, and $\mathbf{K}^{(e)}$ is given in the Appendix.

Similarly, for a forced-response analysis

$$\mathbf{M}^{(e)}\ddot{\mathbf{d}} + \mathbf{C}^{(e)}\dot{\mathbf{d}} + \mathbf{K}^{(e)}\mathbf{d} = \mathbf{f}^{(e)} \quad (3)$$

where $\mathbf{f}^{(e)}$ is the driving force, for example, on the driver position.

3.2 The Implementation of the Model. For all fluid-conveying tubes (the measuring tube, connecting tubes, and process pipes) of the flowmeter, the above matrices were used to model their dynamics. Along these tubes, the added rings were simply modeled as different sections. Matrix elements are provided by some commercial FE packages, which make the implementation convenient. We used the ANSYS Matrix27 element and its parametric language to calculate these matrices according to the flow and design parameters. This matrix element can be used to represent the mass, stiffness, or damping matrix, where the individual component is calculated according to the formulation described in the Appendix.

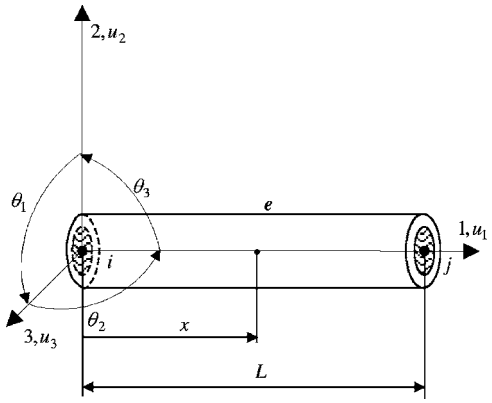

Fig. 2 A fluid-tube interaction element

For the driver spring, a normal beam element was used. However, since the hollow measuring tube was modeled, essentially, as a 1D beam element, the connection between the measuring tube and the driver spring had to be coupled approximately. This coupling was investigated by comparing a full 3D dynamic FE analysis and the beam model. It was found that a rigid coupling region between the end of the driver spring and the center of the tube gave a satisfactory result. With this coupling method, the agreement between 3D and beam models in terms of the resonant frequencies for the first three modes was better than 0.2%.

While it might be more accurate to model the inner compensating cylinder and outer case as 3D solid elements, this would involve more computation time. Shell elements are found to be sufficient since we are more interested in the behavior of the measuring tube. The coupling method used for the measuring tube and inner cylinder, and for the connecting tube and outer case was a rigid region similar to the coupling between driver spring and measuring tube.

A section view of a complete model is shown in Fig. 3. To solve Eq. (2), ANSYS complex eigensolver [14] is used. With the calculated amplitude and phase for each node at the drive mode, phase shift can be extracted as the difference between two sensor positions, while time delay is calculated as phase shift divided by

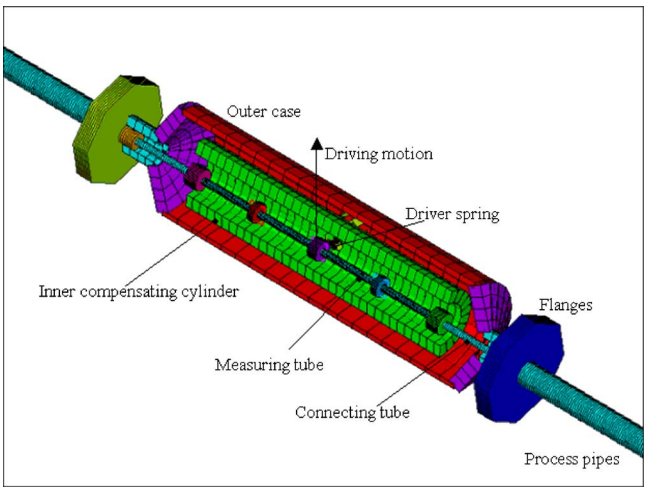

Fig. 3 A section view of the complete finite element model

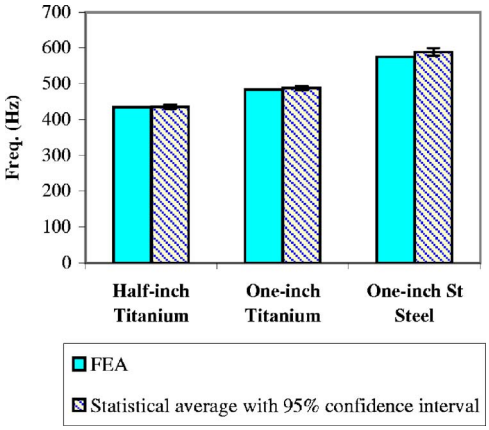

Fig. 4 Comparison of the drive frequency for water

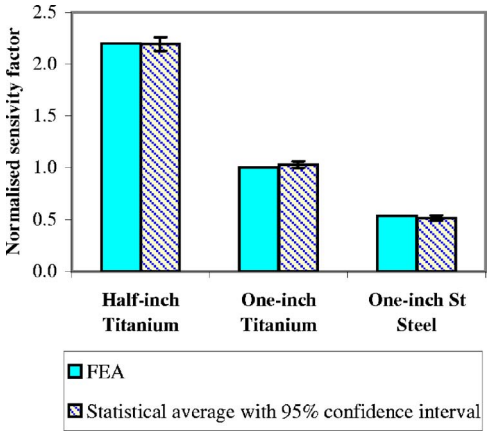

Fig. 5 Comparison of the sensitivity factor for full-scale water flow

angular frequency. It is worth noting that for each sensor the amplitude or phase is actually the relative movement between the corresponding points on the measuring tube and the inner cylinder. Because the meter is working under forced vibration, Eq. (3) is useful, especially for modeling zero shift due to small nonsymmetrical configurations. To solve Eq. (3), a harmonic response analysis [14] was used.

3.3 Material Damping. In the damping matrix of Eqs. (2) or (3), only the effects due to mass flow rate are included. Although material damping does exist in reality, it is rather difficult to model. Unlike stiffness and mass, which can be quantitatively specified according to material and geometric data, damping has to be determined experimentally. A modal test was conducted by using a hammer impact as input and the two sensor signals as output on a half-inch single straight titanium meter. Q factors were estimated by a circle-fitting method. It was estimated that the Q factor of the drive and nearby anti-symmetric modes is greater than 3000 (damping ratio less than 0.02%), while the Q factor of the modes which involve the inner cylinder or outer case is less than 200 (damping ratio greater than 0.25%).

With these data, global proportional damping and local material damping was added to the model so that the global damping matrix is

$$\mathbf{C} = \sum_{e} \mathbf{C}^{(e)} + \alpha\mathbf{M} + \beta\mathbf{K} + \sum_{i} \beta_i \mathbf{K_i} \tag{4}$$

where $\mathbf{C}^{(e)}$ is the individual damping matrix for each fluid-tube interaction element; $\mathbf{M}$ and $\mathbf{K}$ are the global mass and stiffness matrices, respectively, α and β are constant; and where β_i and $\mathbf{K_i}$ are proportional damping for a local region i $(i=1,\ldots,m)$. By varying α, β, and β_i, a best fit to experimental data can be obtained, and is used in the current model.

4 Typical Results and Discussion

4.1 The Validation of the Model. Two sizes (one-inch and half-inch) of Krohne Optimass meters were chosen for this study. For each size, meters of two different materials (titanium and stainless steel) were used. Nominal dimensions in the drawings and material properties from the suppliers were used in the current model. For the measuring tube, the density of the titanium alloy is 4510 kg/m^3 and stainless steel is 7800 kg/m^3; Young's modulus of the titanium alloy is 105 GPa and stainless steel is 200 GPa. Approximately, 400 fluid-tube interaction elements were used in the simulation. The comparison between FEA (finite element analysis) and the statistical data of a number of calibrated meters is shown below.

In Fig. 4, the frequencies of FEA are those resonant frequencies calculated from a free vibration analysis for the drive mode. In order to compare with practical data in normal calibrations, meters were simulated filled with water (998 kg/m^3) at room temperature. The error bars represent $\pm 2\sigma$, where σ is the standard deviation of about 200 calibrated meters. In the three simulated meters, the maximum difference between FEA and the statistical average is 14 Hz or 2.4%.

In Fig. 5, the comparison is given in terms of the sensitivity factor, which is defined as time delay between two sensors divided by mass flow rate (nanoseconds per kg/s). Again, the simulated fluid was water at its corresponding full scale. To compare various simulated meters together, the sensitivity factor is normalized to the simulated one-inch Titanium meter. In the three simulated meters, the maximum difference between FEA and the statistical average is 0.03 or 4%.

4.2 Minimizing the Effects of Mounting Conditions. To minimize the effect of mounting conditions, one of the objectives is to reduce the noise coming from or escaping to the outside environment. A possible solution is the optimization of the stiffness and mass of the connecting tube and inner cylinder. Hussain [11] gave a theoretical explanation and described the adaptive sensor technology (AST).

We modeled a typical titanium meter and used the ratio of the amplitude at the flanges to the amplitude at the driver to characterize the possible noise problem. The comparison between the current design and two modified cases is shown in Fig. 6. In this comparison, the process pipes are clamped at a distance of five times the pipe diameter away from the flanges, and full-scale wa-

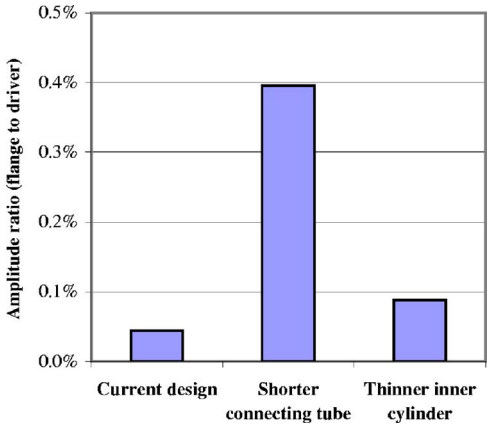

Fig. 6 Comparison of amplitude ratio of flange to driver for three simulated cases

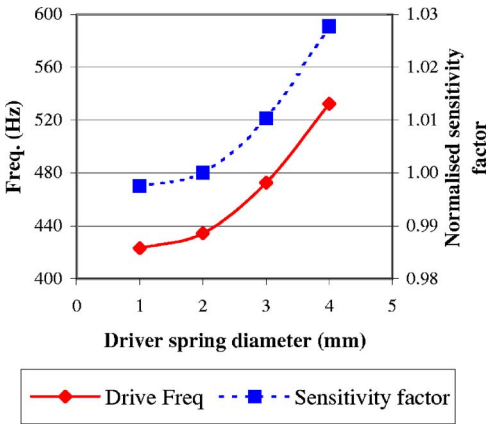

Fig. 7 The effects of a driver spring

ter flow was simulated. As reported by Hussain [11], the current design appears to provide an optimal combination of stiffness and mass and to achieve good decoupling from the outside world.

4.3 The Effects of a Driver Spring. The drive frequency and normalized sensitivity for variation in the diameter of the driver spring are shown in Fig. 7. It is clear that this is an efficient tool for changing the dynamic behavior of a meter.

5 Conclusions

Our study has shown that the formulated fluid-tube interaction element coupled with conventional structural finite elements can be used as a numerical simulation tool for single straight tube Coriolis flowmeters. The predicted drive frequency and phase shift agree with the statistical data obtained from calibration of 200 meters, which validates the application of this model for further work.

In particular, the function of the compensating cylinder and connecting tube to decouple the measuring tube from the outside world has been demonstrated in a quantitative way by using this model. It has been shown that an optimal combination of stiffness and mass can achieve a metering system relatively insensitive to mounting conditions.

Furthermore, other additional features, such as the driver spring, emphasize the benefit of using a more complete numerical model of the meter design, noting that the simpler theoretical models of single straight tube meters have omitted important features of the real meter.

Acknowledgment

The authors would like to thank Professor Ian Hutchings and Professor Jim Woodhouse of Cambridge University Engineering Department for helpful discussions. Thanks are also due to Jacques van den Bosch, Chris Rolf, and Edward Jukes of Krohne, Ltd. for their assistance with some of the experimental work. The authors also wish to acknowledge support for this work from Krohne Limited, from Knowledge Transfer Partnership funding, and from the Gatsby Charitable Foundation.

Appendix

Along the elemental axis 1 shown in Fig. 2, each point has six degrees of freedom, denoted by a vector, $\mathbf{u}=[u_1 \quad u_2 \quad u_3 \quad \theta_1 \quad \theta_2 \quad \theta_3]^T$. In plane (12), the displacement u_2 and rotation θ_3 can be expressed as

$$u_2 = \mathbf{N}_u^T\mathbf{q} \quad \text{and} \quad \theta_3 = \mathbf{N}_\theta^T\mathbf{q}$$

where the unknown displacement vector

$$\mathbf{q} = \begin{Bmatrix} u_2^{(i)} \\ \theta_3^{(i)} \\ u_2^{(j)} \\ \theta_3^{(j)} \end{Bmatrix}$$

and the shape functions

$$\mathbf{N}_u = \frac{1}{12g+L^2}\begin{Bmatrix} (12g+L^2) - \dfrac{12g}{L}x - 3x^2 + \dfrac{2}{L}x^3 \\ (6g+L^2)x - \dfrac{6g+2L^2}{L}x^2 + x^3 \\ \dfrac{12g}{L}x + 3x^2 - \dfrac{2}{L}x^3 \\ -6gx + \dfrac{6g-L^2}{L}x^2 + x^3 \end{Bmatrix}$$

and

$$\mathbf{N}_\theta = \frac{1}{12g+L^2}\begin{Bmatrix} -6x + \dfrac{6}{L}x^2 \\ (12g+L^2) - \dfrac{12g+4L^2}{L}x + 3x^2 \\ 6x - \dfrac{6}{L}x^2 \\ \dfrac{12g-2L^2}{L}x + 3x^2 \end{Bmatrix}$$

where

$$g = \frac{EI_p}{kGA_p}.$$

If, ignoring gravity, the Lagrangian of the element for free vibration [15] is

$$\mathcal{L} = T_p + T_f - U_p$$

where T_p is the kinetic energy of the pipe, T_f the kinetic energy of the conveyed fluid, and U_p is the potential energy of the pipe, which can be given as follows:

$$T_p = \tfrac{1}{2}\int_0^L (\rho_p A_p \dot{u}_2^2 + \rho_p I_p \dot{\theta}_3^2)dx$$

where the dot denotes differentiation with respect to t

$$T_f = \tfrac{1}{2}\int_0^L [\rho_f A_f v_0^2 + \rho_f A_f (v_0 u_2' + \dot{u}_2)^2 + \rho_f I_f \dot{\theta}_3^2]dx$$

where the prime denotes differentiation with respect to x, and

$$U_p = \tfrac{1}{2}\int_0^L [(E+\sigma_0)I_p(\theta_3')^2 + \sigma_0 A_p(u_2')^2 + kGA_p(u_2' - \theta_3)^2]dx$$

Using Hamilton's principle, $\delta\int_0^t \mathcal{L}\, dt = 0$, we have

$$\mathbf{M}^{(12)}\ddot{\mathbf{q}} + \mathbf{C}^{(12)}\dot{\mathbf{q}} + \mathbf{K}^{(12)}\mathbf{q} = 0$$

where

$$\mathbf{M}^{(12)} = \int_0^L [(\rho_f A_f + \rho_p A_p)\mathbf{N}_u\mathbf{N}_u^T + (\rho_f I_f + \rho_p A_p)\mathbf{N}_\theta\mathbf{N}_\theta^T]dx$$

$$\mathbf{C}^{(12)} = \int_0^L \rho_f A_f v_0 (\mathbf{N}_u\mathbf{N}_u'^T - \mathbf{N}_u'\mathbf{N}_u^T)dx$$

$$\mathbf{K}^{(12)} = \int_0^L [(\sigma_0 A_p + kGA_p - \rho_f A_f v_0^2)\mathbf{N}_u' \mathbf{N}_u'^T + (EI_p + \sigma_0 I_p)\mathbf{N}_\theta' \mathbf{N}_\theta'^T + kGA_p(\mathbf{N}_\theta \mathbf{N}_\theta^T - \mathbf{N}_u' \mathbf{N}_\theta^T - \mathbf{N}_\theta \mathbf{N}_u'^T)]dx$$

In plane (23) we can have the similar derivation for u_3 and θ_2. For the axial deformation u_1 and torsional deformation θ_1, a conventional finite element formulation procedure is followed, and will not be given here. By assembling matrices for bending, axial and torsional deformation, we can obtain the three elemental matrices, $\mathbf{M}^{(e)}$, $\mathbf{C}^{(e)}$, and $\mathbf{K}^{(e)}$. For the sake of brevity, the details of these matrices are not given here.

References

[1] Baker, R. C., 2000, *Flow Measurement Handbook*, Cambridge University Press, Cambridge, UK, Chap. 17.

[2] Raszillier, H., and Durst, F., 1991, "Coriolis-effect in Mass Flow Metering," Arch. Appl. Mech., **61**, pp. 192–214.

[3] Kutin, J., and Bajsic, I., 2001, "Stability-Boundary Effect in Coriolis Meters," Flow Meas. Instrum., **12**, pp. 65–73.

[4] Sultan, G., and Hemp, J., 1989, "Modelling of the Coriolis Mass Flowmeter," J. Sound Vib., **132**(3), pp. 473–489.

[5] Watt, R. M., 1990, "Computational Modeling of Coriolis Mass Flowmeters," North Sea Flow Measurement Workshop, East Kilbride, Scotland.

[6] Stack, C. P., Barnett, R. B., and Pawlas, G. E., 1993, "A Finite Element for the Vibration Analysis of a Fluid-Conveying Timoshenko Beam," AIAA Paper No. 93-1552-CP.

[7] Belhadj, A., Cheesewright, R., and Clark, C., 2000, "The Simulation of Coriolis Meter Response to Pulsating Flow Using a General Purpose FE Code," J. Fluids Struct., **14**, pp. 613–634.

[8] Cheesewright, R., Belhadj, A., and Clark, C., 2003, "Effect of Mechanical Vibrations on Coriolis Mass Flow Meters," ASME J. Dyn. Syst., Meas., Control, **125**, pp. 103–113.

[9] Wang, T., and Baker, R. C., 2004, "Manufacturing Variation of the Measuring Tube in a Coriolis Flowmeter," IEE Proc.: Sci., Meas. Technol., **151**(3), pp. 201–204.

[10] Hussain, Y. A., and Rolph, C. N., 1994, "Mass Flow Meter," U.S. Patent 5,365,794.

[11] Hussain, Y. A., 2003, "Single Straight Tube Mass flowmeters Using Adaptive Sensor Technology," IEE Seminar on Advanced Coriolis Mass Flow Metering, Oxford.

[12] Hussain, Y. A., and Rolph, C. N., 1994, "Mass Flow Meter," U.S. Patent 5,291,792.

[13] Païdoussis, M. P., 1998, *Fluid-Structure Interactions: Slender Structures and Axial Flow*, Academic, New York.

[14] ANSYS Inc., 2003, "ANSYS Theory Reference."

[15] Laithier, B. E., and Paidoussis, M. P., 1981, "The Equations of Motion of Initially Stressed Timoshenko Tubular Beams Conveying Fluid," J. Sound Vib., **79**(2), pp. 175–195.

Experimental Examination of Unsteady Friction Models for Transient Pipe Flow Simulation

Adam Adamkowski

Mariusz Lewandowski

Department of Hydraulic Machinery Tests and Diagnostics,
The Szewalski Institute of Fluid-Flow Machinery of the Polish Academy of Sciences,
Gdansk, Poland

The paper presents a comparative analysis of calculations performed basing on the selected unsteady friction models and their validation based on the results of own experimental tests. The computer code developed for predicting transient pipe flows includes the models of: Zielke, Trikha, Vardy and Brown, Zarzycki, and Brunone et al. Our own experiments have been conducted at a test rig designed and constructed at the Institute of Fluid-Flow Machinery of the Polish Academy of Sciences (IMP PAN) in Gdansk in order to test transient pipe flows in a wide range of Reynolds numbers. The results following from this analysis enable the quantitative and qualitative assessment of the models under consideration. [DOI: 10.1115/1.2354521]

1 Introduction

The assumption in accordance to which the unsteady liquid flow in a long closed conduit[1] (pipeline) may be treated as a one-dimensional flow is commonly accepted. In such an approach it is also common practice to assume the velocity profile during transient flows in a closed conduit to remain the same as under the steady-state flow conditions featured by the same mean velocity. However, it is generally known nowadays that the approach based on the quasi-steady friction losses hypothesis is one of the basic reasons for differences between experimental and computational results obtained according to the one-dimensional flow theory. Unsteady friction models and the relevant computational methods are the subject of various research projects at the research centers all over the world.

Multiyear effort of numerous researchers has resulted in developing miscellaneous models of hydraulic transients with the unsteady hydraulic resistance taken into account. The most widely used models consider extra friction losses to depend on a history of weighted accelerations during unsteady phenomena or on instantaneous flow acceleration.

Development of the first group of models was initiated in 1968 by Zielke [1]. In his model the instantaneous wall shear stress (which is directly proportional to friction losses) is the sum of the quasi-steady value plus a term in which certain weights are given to the past velocity changes. This approach is assigned for transient laminar flow cases. The model developed by Zielke is based on solid theoretical fundamentals and the multiple experimental validation tests have shown good conformity between calculated and measured results. It is, therefore, no wonder that numerous researchers have followed Zielke's scent, giving rise to a number of proposals for describing friction losses in unsteady turbulent flows. From among these proposals, known also as the multi-layer models, those of Vardy and Brown [2,3] (two-layer model) or Zarzycki [4,5] (four-layer model) may be distinguished. In general, the models mentioned are based on experimental data on the distribution of the turbulent viscosity coefficient in the assumed flow layers. The efforts aimed at enhancement of these models are still in progress—numerous papers emphasize the need to develop and validate experimentally the models that can be used in a wide range of frequencies and Reynolds numbers.

The second group of models mentioned assumes the wall shear stress due to flow unsteadiness is proportional to the variable flow acceleration. This approach has been introduced by a group of researchers headed by Daily [6]. The proportionality coefficient has been established based on the experimental measurements carried out by Cartens and Roller [7]. Modifications of this model have been the subject of numerous subsequent studies, including those of Brunone et al. [8]. Easy applicability to numerical computations is a significant advantage of this approach. However, the need to determine the empirical coefficient mentioned is an obvious demerit. There appeared suggestions that the friction coefficient in this model depends also on the velocity derivative of the second or even higher order.

It follows from this brief survey of unsteady friction models that the approaches mentioned require comparative analyses of both the models between each other and the computational results with experimental data. The comparative analysis of computational results based on selected friction models is presented in this paper. The authors have also validated these calculations with experimental data obtained at the special test rig erected in the IMP PAN—the experiments have covered a wide range of initial Reynolds numbers.

2 Theoretical Basis of Calculation Method

Based on the method described below, a computer code was developed in order to calculate the unsteady pipe flow phenomena.

2.1 Governing Equations Describing Unsteady Liquid Flow in Closed Conduits. The following assumptions were made to derive equations describing unsteady liquid flow in closed conduits (water hammer):

- The flow in closed conduits is one-dimensional, which means that the characteristic quantities are cross-section averaged;
- the flow velocity is small compared to the pressure wave celerity (speed);
- the liquid is a low-compressible fluid—it deforms elastically under pressure surges with insignificant changes of its density;
- the pipeline wall is deformed by pressure surges according to the elastic theory of deformation.

[1] A conduit may be considered as a *long conduit* when proportion between its length L and internal diameter D is greater than 10.

Contributed by the Fluids Engineering Division of ASME for publication in the JOURNAL OF FLUIDS ENGINEERING. Manuscript received April 6, 2005; final manuscript received March 18, 2006. Assoc. Editor: James A. Liburdy. Paper presented at the 9th International Conference on Pressure Surges, 24–26 March 2004, Chester, UK.

According to the above assumptions, the following equations are used for mathematical description of unsteady liquid flows in closed conduits [9]:

- Continuity equation:

$$\frac{\partial H}{\partial t} + \frac{a^2}{g} \cdot \frac{\partial V}{\partial x} = 0 \tag{1}$$

- Momentum equation:

$$\frac{\partial V}{\partial t} + g \cdot \frac{\partial H}{\partial x} + g \cdot J = 0 \tag{2}$$

Equations (1) and (2) form a closed system of partial differential equations of the hyperbolic type with unknown functions of the piezometric head, $H=H(x,t)$, and flow velocity, $V=V(x,t)$. Elasticity of pipe walls and liquid is represented by the pressure wave celerity (a in Eq. (1)). The J quantity in Eq. (2) stands for head loss per length unit of pipe and represents hydraulic resistance caused by internal friction in liquid and friction at the pipe wall. This quantity is a sum of the quasi-steady flow pipeline resistance J_q (active resistance resulting from viscous friction at the pipe wall) and pipeline inertance J_u (reactance accounting for liquid inertia)

$$J = J_q + J_u \tag{3}$$

There are several friction models differing between each other in definition of Eq. (3) terms.

2.2 Friction Models Used in Calculation Method. In the computer code algorithm the following friction models have been applied (see Appendix A for the detailed description):

- *Quasi-steady friction model*:
  In this approach the pipeline inertance J_u equal zero is assumed. The pipeline resistance J_q is usually described basing on the Darcy-Weisbach equation. The quasi-steady friction coefficient (the Darcy friction coefficient) is calculated basing on the Hagen-Poiseuille law used for laminar flows ($\mathbf{Re} \leqslant \mathbf{Re}_{c\text{-}s}$ where $\mathbf{Re}_{c\text{-}s}=2320$) or on the Colebrook-White formula used for turbulent flows ($\mathbf{Re} > \mathbf{Re}_{c\text{-}s}$));
- *Unsteady friction models developed by*:
  - Zielke [1]:
    This model describes pipeline inertance as a function of flow acceleration and weighted past velocity changes. According to assumptions, this solution is correct for laminar flows (for $\mathbf{Re} \leqslant \mathbf{Re}_{c-s}$);
  - Trikha [10]:
    This approach is based on an approximated form of inertance as proposed by Zielke. It presents an attempt to describe the unsteady losses in low Reynolds number turbulent flows;
  - Vardy and Brown [2,3]:
    This model follows from an analysis of axisymmetric flow separated into two layers according to the empirical distribution of turbulent viscosity coefficient (two-layer model). The inertance is described as in Zielke model but with **Re**-dependent weighting function;
  - Zarzycki [4,5]:
    The model belongs to the group of multi-layer models, including also the model proposed by Vardy and Brown. It follows from dividing the axisymmetric flow into four layers with given approximation of turbulent viscosity distribution in each of them;
  - Brunone et al. [8]:
    Description of friction losses is based on an assumption that the inertance is proportional to local and convectional derivative of the mean pipe flow velocity. The role of the proportionality coefficient, k_3, is crucial for this model. This coefficient may be assumed constant (with the value fitted to conform with computational and experimental results [11] or depending on the initial **Re** value—see Appendix A) or as a variable, depending on the instantaneous **Re** values during unsteady flow [2].

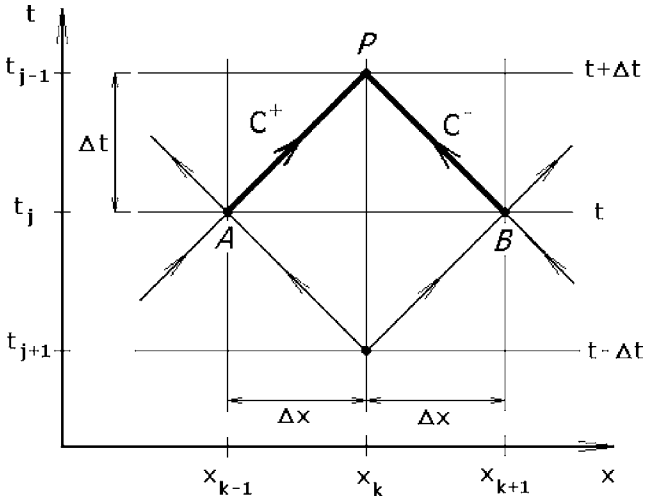

Fig. 1 Diamond grid of characteristics with notation used in the calculation method

3 Method of Solution

The method of characteristics has been applied in order to solve the system of Eqs. (1) and (2) [9,12]. According to this method, Eqs. (1) and (2) are transformed into the following two pairs of ordinary differential equations (for positive and negative characteristics $\mathbf{C}^+$ and $\mathbf{C}^-$):

$$\text{for } \mathbf{C}^+: \frac{\mathrm{d}x}{\mathrm{d}t} = +a \rightarrow \mathrm{d}V + \frac{g}{a}\mathrm{d}H + gJ \cdot \mathrm{d}t = 0 \tag{4}$$

$$\text{for } \mathbf{C}^-: \frac{\mathrm{d}x}{\mathrm{d}t} = -a \rightarrow \mathrm{d}V - \frac{g}{a}\mathrm{d}H + gJ \cdot \mathrm{d}t = 0 \tag{5}$$

The first-order finite-difference approximation is used in order to integrate Eqs. (4) and (5) along the characteristic lines relevant to each of them, respectively. This procedure leads to the following form of these equations:

$$\mathbf{C}^+: (V_P - V_A) + \frac{g}{a}(H_P - H_A) + (gJ)_A \Delta t = 0 \tag{6}$$

$$\mathbf{C}^-: (V_P - V_B) - \frac{g}{a}(H_P - H_B) + (gJ)_B \Delta t = 0 \tag{7}$$

In all selected unsteady friction models the values of V and H in node P are calculated using term (gJ) related to the velocity partial derivatives, which are determined at time levels t_{j-1} and t_j. Two types of numerical grids may be used in MOC — diamond (Fig. 1) and rectangular grid of characteristics (Fig. 2). From among all the differences between them a way of calculating the velocity partial derivatives necessary to determine quantity J is the most important. It follows from the fact that the rectangular grid is two times denser than the diamond grid. In both grids longitudinal step Δx is related to time step Δt as follows (stability condition):

$$\frac{\Delta x}{\Delta t} = a \tag{8}$$

Increasing density of the grid (of the same structure) has no significant effect on the computational results. This fact is already

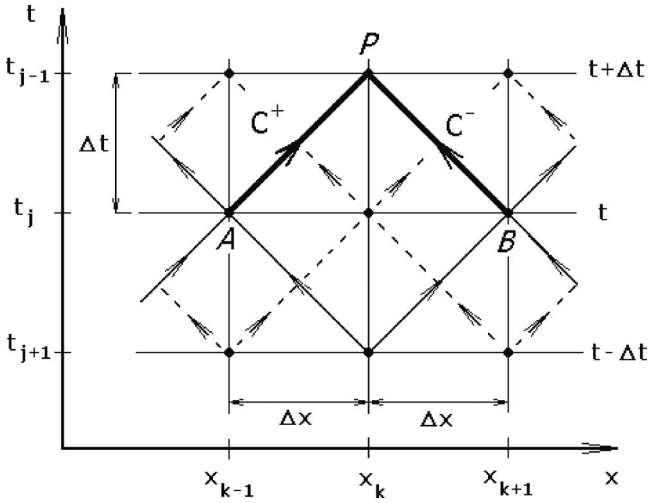

Fig. 2 Rectangular grid of characteristics with notation used in the calculation method

confirmed by many numerical tests published in the literature concerning this issue (in [13,14] the numerical grid with 8, 16, and 32 computational reaches were tested). However, there are much more differences between calculations obtained based on different grid structures, diamond and rectangular. It follows directly from basic feature of the rectangular grid which, in fact, consists of two diamond grids shifted in relation to each other. These two diamond grids are coupled only through the partial velocity derivatives in quantity J which are calculated using finite differences (see Appendix A). In order to get a clear-cut proof that the density of the grid has no significant influence on the results of calculations, appropriate comparisons were made using diamond grids of different density within the confines of testing the computer program. The results are presented in Appendix B.

4 Experimental Tests

Experiments were conducted at a test rig specially designed in order to investigate the water hammer phenomenon with schematic shown in Fig. 3. The rig was constructed at the laboratory of IMP PAN in Gdansk. Its main component is the $L=98.11$ m long copper pipe with an internal diameter of $D=0.016$ m and a wall thickness of $e=0.001$ m. The steel cylinder with diameter of about 1.6 m was used to spirally coil the pipe on it. The pipe is rigidly mounted to the cylinder coating in order to minimize its vibrations. The inclination angle of the pipe (β) is not larger than 0.5 deg. A quick-closing, spring driven ball valve is installed at one end of the pipe. The valve design enables an almost stepwise discharge variation up to a complete flow cut-off. This has been confirmed by the records of valve closure with a duration not exceeding 0.003 s, which is 2% of the half-period of pressure wave propagation along the pipe ($2L/a$).

The test rig is equipped with appropriate measuring instrumentation. Absolute pressure semiconductor transducers are mounted on the main components of the hydraulic circuit of the test rig, four of them positioned at equidistant (every $L/4$) sections along the pipeline and the last one—measuring pressure in the high pressure reservoir. The basic characteristics of these transducers are as follows:

- measuring range: (0–4) MPa
- transmitted frequency band: (0–2) kHz
- precision class: 0.2%

A turbine flowmeter with the range of 1.5 m^3/h ($\sim 4.2 \cdot 10^{-4}$ m^3/s) and precision class of 1% is used for indirect

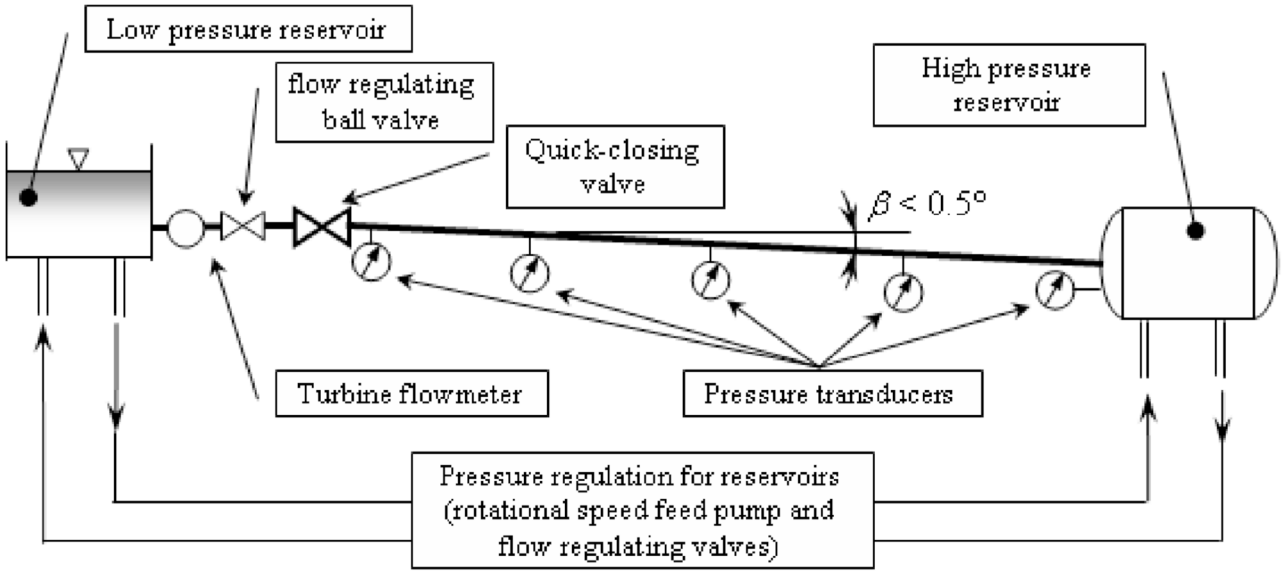

Fig. 3 Layout of the test rig

Table 1 Initial values of V_o and Re_o in the performed experimental runs

		1	2	3	4	5	6	7	8	9
Initial mean flow velocity	V_o [m/s]	0.066	0.162	0.340	0.467	0.559	0.631	0.705	0.806	0.940
Initial Reynolds number (approx. value)	$\mathbf{Re}_o$ [-]	1111	2737	5731	7871	9421	10634	11882	13590	15843

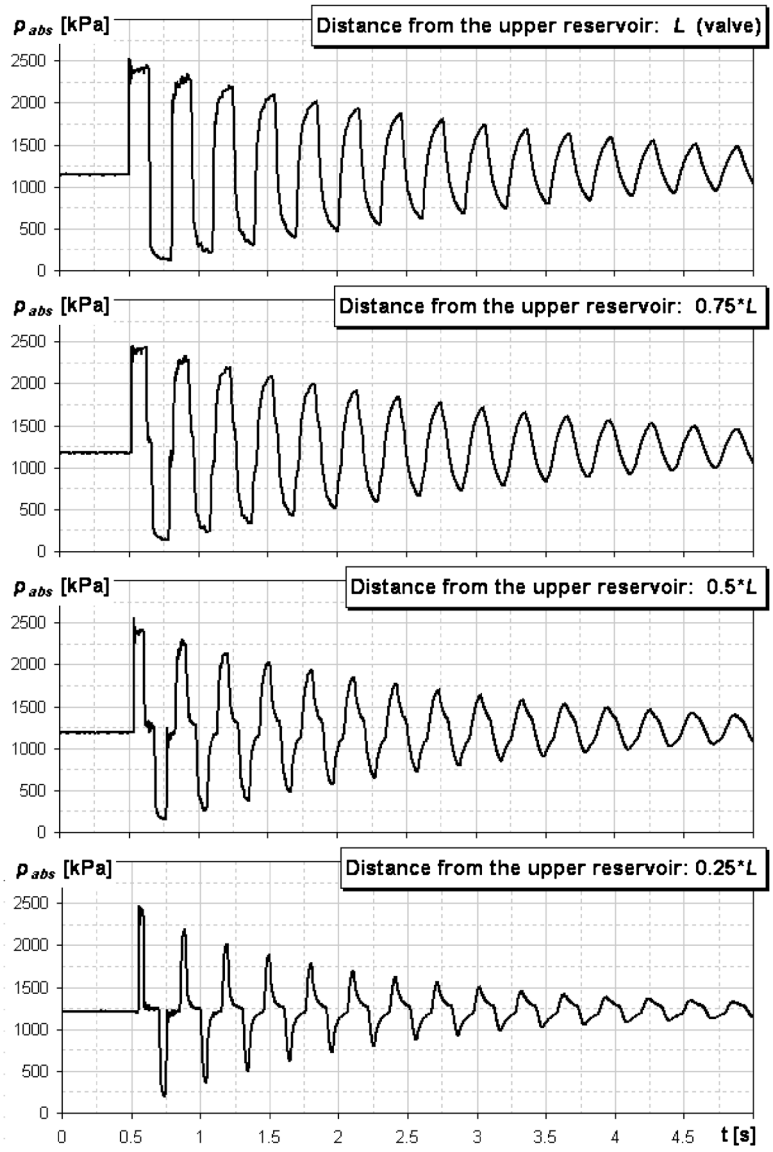

Fig. 4 Pressure changes measured in four pipe cross-sections—case of sudden flow cut-off with initial flow velocity V_o=0.94 m/s

measurement of average flow velocity in the pipeline. The flowmeter was checked using volumetric method before and after the measurements.

It is worthwhile to stress that the test rig described enables us to generate the water hammer without column separation phenomenon at the initial conditions of the Reynolds numbers up to $\mathbf{Re} \cong 16{,}000$.

Before starting the experiments, the hydraulic system was filled with water and left for a few days to remove undissolved air from the liquid in as much as possible. The intention was to minimize the influence of undissolved air bubbles on the analyzed phenomenon courses.

The tests consisted in several runs of unsteady flow after sudden closure of the valve from different initial flow conditions—velocity V_o ($\mathbf{Re}_o$)—Table 1. During the tests the steady head water level was kept up in the high-pressure reservoir ($H_o \cong 1250$ kPa), the temperature of water was 22.6°C, and the kinematic viscosity coefficient for these conditions was $\nu = 9.493 \cdot 10^{-7}$ m^2/s.

Every measurement, started by cutting-off the flow, was preceded by an adjustment of required stable initial conditions (initial velocity V_o and steady head water level H_o). The regulating ball-valve installed between the quick closing valve and flowmeter and also feed pump with adjustable rotational speed was used for this purpose (Fig. 3). After adjusting the initial conditions and after some time needed for stabilization of the flow conditions (not less than 180 s) the flow rate measurement was made. Recording of the pressure changes and the valve closure rate was started a few seconds before quickly cutting-off the flow (water hammer phenomenon). Flow cut-off causing water hammer was executed by releasing the spring in the driving mechanism of the quick closing valve.[2] After the recording was ended the test rig was prepared to execute the next experimental run—the quick closing valve was opened, the ball valve opening and/or pump rotational speed was appropriately adjusted in order to set another initial flow condition for the next run. Recording of the pressure changes and the valve closure rate[3] was carried out with a sampling frequency of 2.5 kHz using a computerized data acquisition system.

[2]Based on the comparison between many recorded courses of the quick closing valve closure, repeatability of these courses was affirmed so that repeatability of the manner of flow cut-off was also affirmed.

[3]For recording traces of closing the valve the potentiometer was used.

An example of measured pressure variations in case of initial flow velocity of $V_o=0.94$ m/s ($\mathbf{Re}\cong 15{,}800$) is shown in Fig. 4. Some other experimental results are presented together with computational results in the further sections of this paper. In the measured traces the pressure overshoot at the first pressure pulse retains attention. This effect is interpreted as the result of the fluid-structure interaction.

It is worthwhile to stress that the absolute systematic uncertainty of pressure measurements, ±8 kPa ($0.002 \cdot 4$ MPa), was decreased to the value of ±4 kPa due to calibration of pressure transducers carried out in thermal condition similar to those occurred during measurements at the test rig. Transmitted frequency band of transducers used, 0–2 kHz, indicates that the rise time of output signal for up to 4 MPa stepwise change of pressure (measuring range) is shorter than 0.0005 s (1/2000 Hz). This time is shorter than about 0.165% of the pressure wave period ($4L/a=\sim 0.3$ s) or, in other words, transmitted frequency band for each transducer is at least 600 times wider than the pressure wave frequency amounting to about 3.3 Hz ($a/(4L)$).

5 Comparison Between Calculation and Measurements

5.1 Calculations. All runs recorded at the water hammer test rig were used in order to verify the friction models considered in the calculation method. The initial conditions of the pipe flow for each tested run are shown in Table 1.

Calculations were carried out taking into account the following friction models:

- Quasi-steady friction model;
- Zielke model;
- Trikha model;
- Vardy and Brown model;
- Zarzycki model;[4]
- Brunone et al. model with constant k_3 coefficient (ver. 1);
- Brunone et al. model with varying k_3 coefficient (ver. 2).

Calculations for a frictionless flow were also carried out. Their results are shown below in order to illustrate the influence exerted by friction terms in Eq. (2) on computational results. The calculations were accomplished using the diamond grid (Fig. 1) (only calculations based on the Trikha model was made using the rectangular grid—it follows from the author's assumptions introduced into this model). The density of these grids was assumed by fixing 24 computational reaches along the pipe length. The pressure wave celerity was calculated from the recorded data based on the analysis in the time and frequency domain of all pressure courses taken into account. The mean value of this quantity was amounted to $a=1301.8$ m/s, and it differs from the exact value for each of the runs not more than 0.3%. It needs to be emphasized that the mean pressure wave celerity determined based on the experimental data is in comparison to the value calculated from the following formulas[5] [9]:

$$a=\frac{\sqrt{\frac{K_w}{\rho}}}{\sqrt{1+(1-\nu^2)\frac{K_w}{E}\frac{D}{e}}}=\frac{1449}{\sqrt{1.2457}}=1298.4 \text{ m/s} \qquad (9)$$

where:

- for water
  - at $\sim 20°$C:
  - bulk modulus: $K_w=2.1\cdot 10^9$ Pa,
  - density $\rho=1000$ kg/m^3,
- for copper
  - pipeline coating:
  - Poisson's coefficient: $\nu=0.35$,
  - density: $\rho_{\text{copper}}=8890$ kg/m^3,
  - Young's modulus: $E=120\cdot 109$ Pa,
  - internal pipe diameter: $D=0.016$ m,
  - pipe-wall thickness: $e=0.001$ m.

The difference between these two values (from the experiment and calculated value) is only about 0.26%. However, the experimental value of a determined for each considered run was taken into account in order to avoid discrepancy of the pressure wave period in compared courses.

A stepwise change of the flow velocity at the valve and the constant pressure head level in the high pressure reservoir were assumed as boundary conditions. Additionally it was assumed that the pipeline is straight and horizontal.

The full-convolution scheme was used for the models developed by Zielke, Vardy and Brown, and Zarzycki. Their application requires much more computation time and computer storage in comparison with other models. As it was mentioned earlier the Zielke model is applicable for transient laminar flow simulations (according to general assumptions). Vardy and Brown and the Zarzycki models are assigned also to transient turbulent flows. The fundamental difference between Vardy and Brown and Zarzycki turbulent models is not only the number of flow layers taken into a account (the Vardy and Brown model is a two-layer model and the Zarzycki model is a four-layer model). They also differ in assuming the critical value of **Re**, which separate laminar and turbulent flows. Vardy and Brown use the value equal to $\mathbf{Re}_{c-s}\cong 2320$ (the same as in steady flow cases). Zarzycki, based on Ohmi et al. investigations [15], uses so-called unsteady value of critical **Re** equal to $\mathbf{Re}_{c-u}$ given by Eq. (A13). The **Re**-dependant weighting function (A12) proposed by Zarzycki is used only when instantaneous **Re** reaches values higher than $\mathbf{Re}_{c-u}$. More detailed description of all models used is presented in the Appendix A.

Chosen results of the calculation (the relative pressure head variations at the valve for runs with initial Reynolds number equal to 1100, 5700, 10,600, and 15,800) are shown together with the experimental results enabling thus a visual assessment of applied models—Figs. 5–8.

5.2 Discussion of the Results. The comparative analysis of measured and calculated pressure head variations during unsteady pipe flow, presented in Figs. 5–8, indicates that the unsteady friction models show the unquestionable advantage over the quasi-steady friction modeling. This is another proof of the well-known fact that the analysis of attenuation of pressure waves in the closed conduits based on the quasi-steady friction losses hypothesis is a much simplified approach.

Unsteady friction models based on the inertance depending on the weighted past velocity changes (given by Zielke, Trikha, Vardy and Brown, and Zarzycki) deserve special attention. In distinction to all other methods applied, these models predict almost superbly the wave front shape. Moreover they preserve the frequency. The model developed by Trikha (as aforementioned, Trikha has proposed expression (A7), which in an efficient way approximates the weighting function in the model of Zielke) reveals different wave front shape. The increase of pressure near the wave top is a bit steeper and symmetrically the same situation is when the pressure decreases near the wave bottom. Additionally pressure oscillations are slightly shifted in relation to other calculated courses. This is not exactly the feature of this model but

[4] $\mathbf{Re}_{c-u}$ value in the turbulent case is about 30,000. It means that in this case (with initial conditions of $\mathbf{Re}_o=15{,}800$) calculations have to be carried out using the weighting function in (A9).

[5] It was assumed that the pipeline at the test rig is anchored against longitudinal movement.

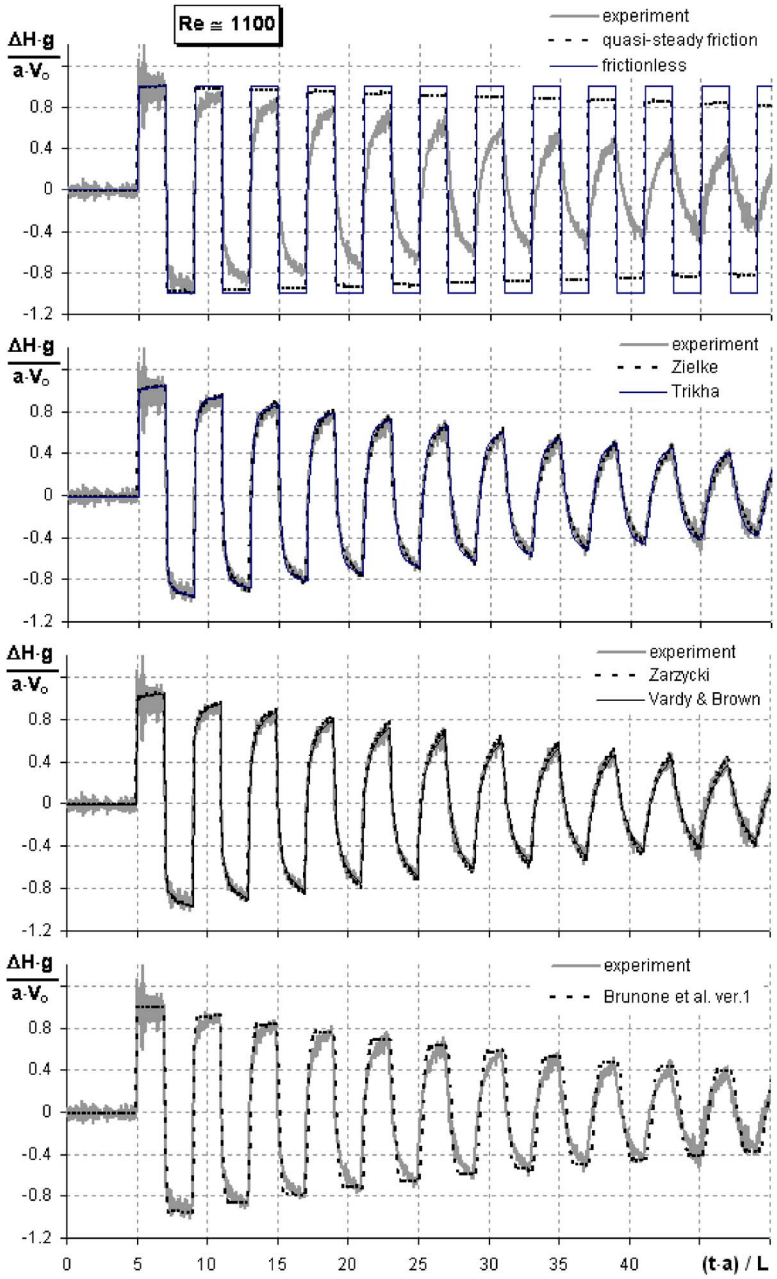

Fig. 5 Run with $Re_o \cong 1100$—comparison between calculated and measured pressure traces at the valve

rather the result of using the rectangular grid instead of the diamond one used with other friction models. Besides these insignificant facts, the results obtained using the Trikha model are acceptable and, moreover, they need much lesser computing power and time as it is in the case of using other multi-layer models with the full convolution scheme for the weighting function $W(\tau)$.

For multi-layer models it is symptomatic that the rise of $\mathbf{Re}_o$ results in an increase of the differences between calculation and measurement. In the case of runing with the highest $\mathbf{Re}_o$ (15,800), the computational damping effect is substantially more intense than in reality—Fig. 8. Much more detailed analysis is needed in order to clarify this phenomenon. However, it does not change the fact that the models developed by Zielke, Trikha, Vardy and Brown, and Zarzycki yield the closest results to the experimental ones both in the laminar and turbulent cases.

The shape of the pressure wave front predicted basing on the Brunone et al. model shows poorer conformity with the measurements than predicted by means of multi-layer models. The analysis shows a minor change in frequency of the pressure wave simulated by means of this model (in lower values direction). The results attained using version 2 of this model (with variable k_3 coefficient) are featured by more effective damping and insignificantly lower frequency than those following from version 1 (with constant k_3 coefficient). In both versions, an effect similar to that of the multi-layer models is observed—rising the Reynolds number results in rising differences between calculated and measured amplitudes of pressure head oscillations—see Figs. 5–8.

The authors of this paper have compared in [16] the experimental data published by Holmboe and Rouleau [17] with the computational results following from the unsteady friction models. Generally, the comparative analysis of Ref. [16] confirms conclusions quoted above. Both under laminar ($\mathbf{Re}_o \cong 82$) and turbulent ($\mathbf{Re}_o \cong 7200$) initial flow conditions, the multi-layer models reflect

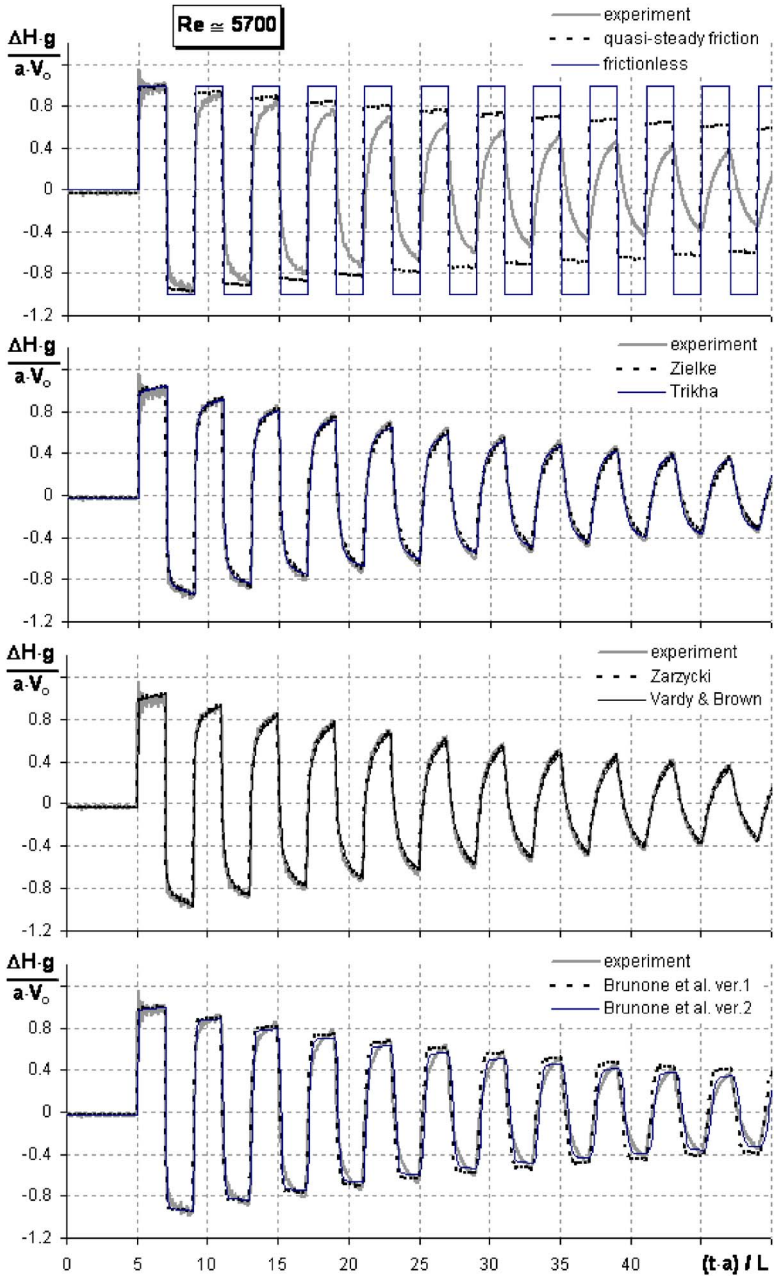

Fig. 6 Run with $Re_o \cong 5700$—comparison between calculated and measured pressure traces at the valve

properly the pressure traces following from the Holmboe and Rouleau tests. However, the abovementioned effect of damping overestimation is not observed. At the moment, it is difficult to give a clear explanation of this observation. Nevertheless, some significant differences between geometry of two rigs (e.g., the L/D ratios in hydraulic circuits are substantially different—around 1400 for the Holmboe-Rouleau's test rig and over 6100 for the IMP PAN rig) may be indicated. It is worthwhile to notice that the turbulent flow test described by Holmboe-Rouleau (the only one available) has covered only four pressure wave periods. Additionally, the test was featured by a relatively low Reynolds number, $\mathbf{Re}_o \cong 7200$ (the effect of computational damping exceeding the experimental one is not visible neither in run with $\mathbf{Re}_o \cong 5700$, nor in the runs with higher value of $\mathbf{Re}_o$).

In order to allow for a precise evaluation, the analysis of friction models was supplemented with the rate of pressure traces convergence, defined as follows:

$$I_{c-m} = \left(\int_{t_0}^{t_e} |\Delta H_c| dt - \int_{t_0}^{t_e} |\Delta H_m| dt \right) \Bigg/ \int_{t_a}^{t_e} |\Delta H_m| \mathrm{d}t \quad (10)$$

This coefficient shows the difference between areas enclosed in the pressure line and the center line of pressure oscillations for calculated (index c) and measured (index m) traces. As the value of I_{c-m} is closer to zero the convergence between compared traces is better. Additionally, it is worth paying attention to the calculated pressure course. ΔH_c is characterized by a more intense pressure wave damping than in a measured one ΔH_m. Therefore, the difference in brackets is less than 0 and the value of I_{c-m} is negative. Consequently, the positive value of I_{c-m} occur when the calculated pressure course is characterized by less attenuation than in a measured one.

The analysis of the I_{c-m} coefficient has been carried out for the

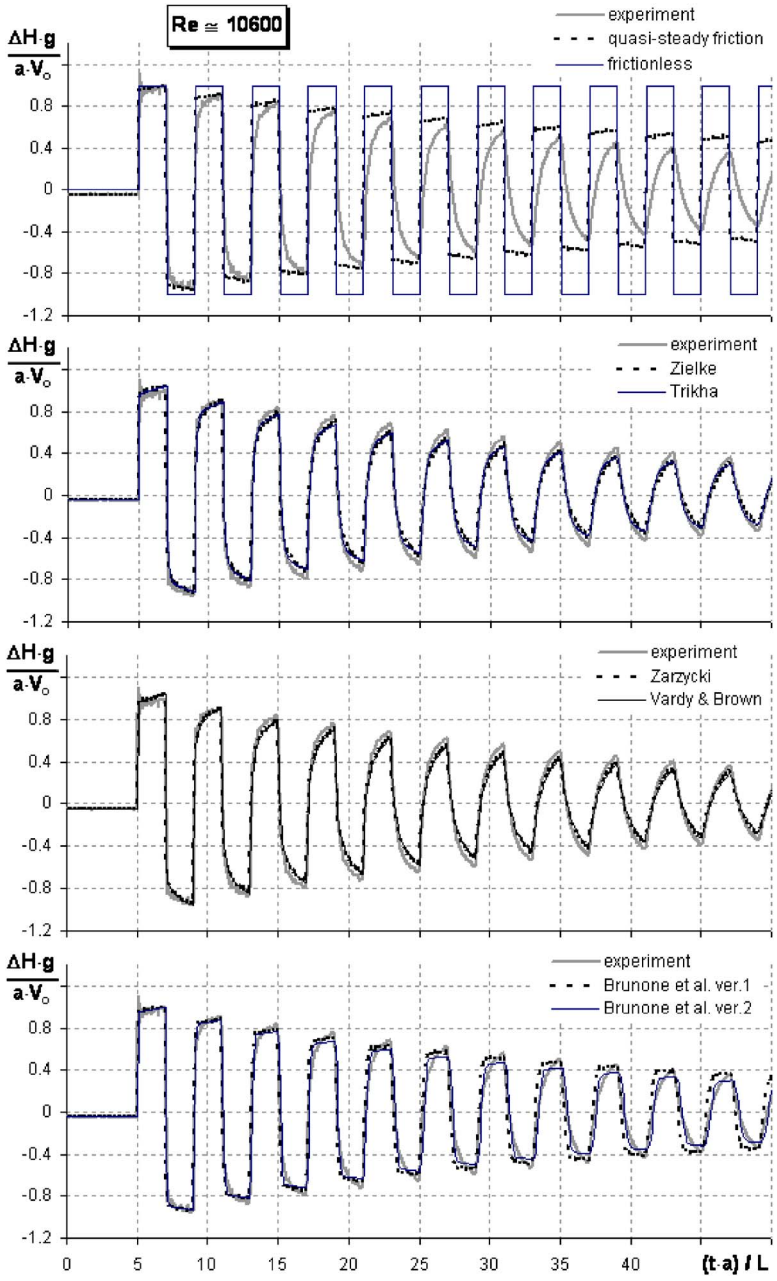

Fig. 7 Run with $Re_o \cong 10{,}600$—comparison between calculated and measured pressure traces at the valve

first 20 pressure wave periods.[6] It was assumed that amplitudes of waves beyond the first 20 are relatively small and, therefore, insignificant for purposes of the analysis. Measured and calculated pressure traces at the pipe cross-section next to the quick-closing valve have been applied for all runs presented in Table 1. The results of this analysis are shown in Fig. 9 as the relation $I_{c-m}=f(\mathbf{Re}_o)$ for $\mathbf{Re}_o \cong (1100-15{,}800)$.

Comparison between I_{c-m} coefficients for analyzed friction models reconfirms conclusions drown from the qualitative analysis carried out based on charts presented in Figs. 5–8. Firstly, this comparison shows that assuming frictionless processes is much simplified for simulating the water hammer (curve "I" on Fig. 9(*a*)). Secondly, the unsteady friction models give significantly better results than the quasi-steady friction model. In the case of the quasi-steady friction model (curve "II" on Fig. 9(*a*)) in the range of analyzed $\mathbf{Re}_o$ (initial Reynolds numbers) coefficient I_{c-m} have a positive value and it decreases from 150% to 60% as $\mathbf{Re}_o$ increases (higher values of I_{c-m} confirm significant discrepancies between the experimental and calculated pressure wave traces).

Analyses of values of I_{c-m} and their relation with $\mathbf{Re}_o$ for the unsteady friction models (curves on Fig. 9(*b*)) bring us to the following conclusions:

– Results obtained based on the second version of the Brunone et al. model with variable k_3 coefficient (depending on instantaneous **Re** according to (A14)—see Appendix A) are better than in the case of ver. 1 of the Brunone et al. model with constant k_3 coefficient (depending on the initial value of **Re** ($\mathbf{Re}_o$) according to (A14));

[6]The value of I_{c-m} depends on the number of wave periods taken into account.

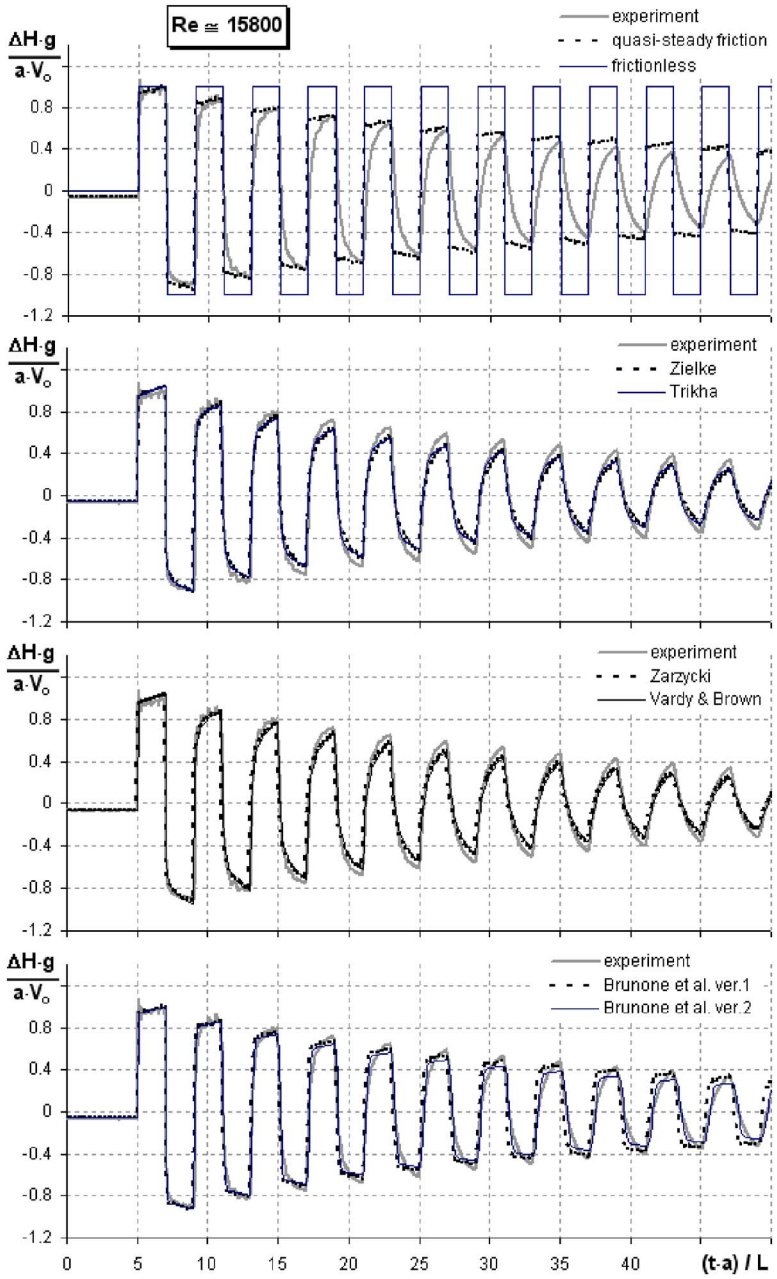

Fig. 8 Run with $Re_o \cong 15800$—comparison between calculated and measured pressure traces at the valve

– the multi-layer friction models give better results than ver. 1 of the Brunone et al. model in the whole analyzed range of $\mathbf{Re}_o$ and also than ver. 2 of the Brunone et al. model with $k_3 = f(\mathrm{Re})$ for $\mathbf{Re}_o$ values from laminar range and up to $\mathbf{Re}_o \cong 10{,}000$;
– in the case of high $\mathbf{Re}_o$ numbers, where the damping effect in the calculated pressure traces is greater than in the experimental ones, ver .2 of the Brunone et al. model gives better results of I_{c-m} values—this is mainly because in the calculated pressure traces the top of the waves are much wider in comparison to those from the experiment (and also from the multi-layer models) however, the amplitudes in the calculated courses reveal a similar damping effect to the one observed for the multi-layer models;
– the Zielke model (curve "3" on Fig. 9(*b*)) predict the realistic pressure variations with a high convergence rate in the case of the laminar Reynolds numbers (applicability range of this model) and low turbulent Reynolds numbers (up to 5000)—in this range the absolute value of I_{c-m} does not exceed 5%;
– the Zarzycki and Vardy and Brown models (curves "5" and "6" on Fig. 9(*b*), respectively) gives comparable results. It is worth paying attention to the Zarzycki model which gives the relation $I_{c-m} = f(\mathbf{Re}_o)$ parallel to this obtained for the Zielke model—it follows that in analyzed range of Re the weighting function in the Zarzycki model is independent from **Re** (likewise in the Zielke model). However, the Vardy and Brown model slightly represents a better trend in relation $I_{c-m} = f(\mathbf{Re}_o)$ (flatter) and this is due to the relation of the weighting function to the **Re** number (for $\mathbf{Re} > 2320$—see Appendix A);

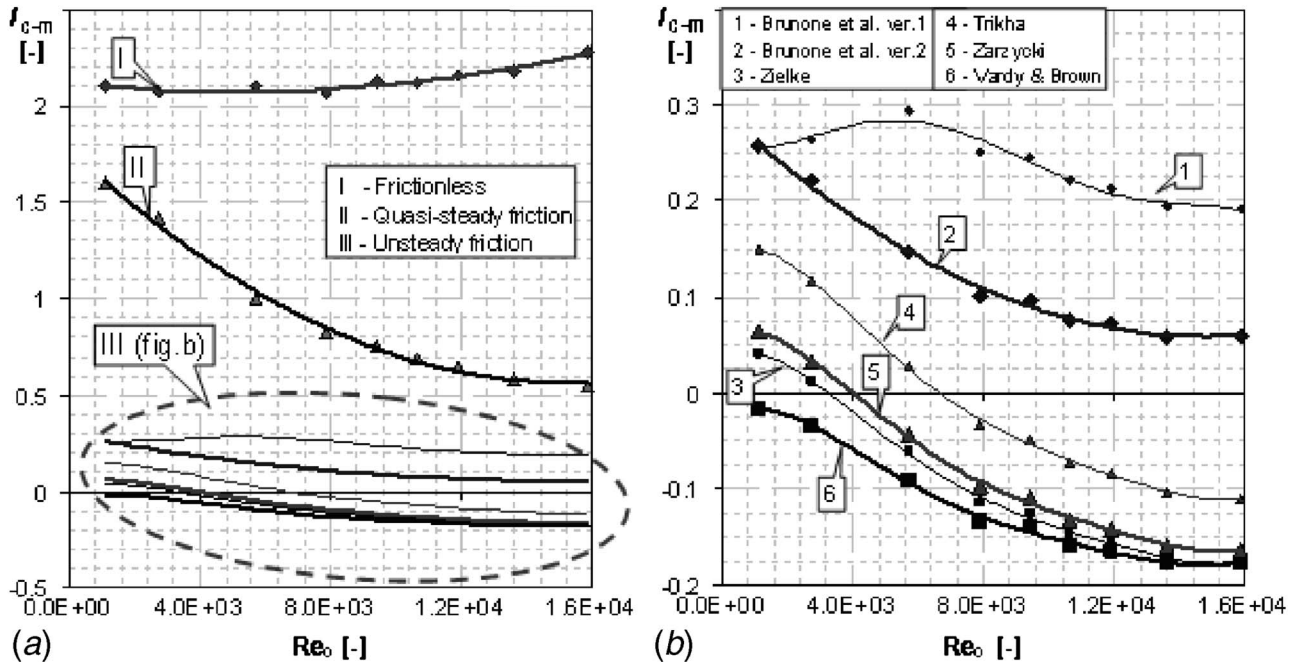

Fig. 9 Relation between the rate of pressure traces convergence and initial Reynolds number; $I_{c-m}=f(\mathrm{Re}_o)$

– all multi-layer models worsen their conformity with the experiment for $\mathbf{Re}_o > (6-10)\cdot 10^3$ — the value of I_{c-m} coefficient in this range of **Re** falls beneath (−10%);
– relatively good results obtained using the Trikha model are worth mentioning. This undoubtedly shows that the approach consisted in such an efficient approximation of the Zielke weighting functions is successful (it enables us to save time and computer storage nevertheless it gives comparable results to those obtained using the multi-layer models).

6 Conclusions

(i) Basing on the presented results of the theoretical and experimental investigations it was proved that predictions of the water hammer courses can be significantly improved using the unsteady friction models in comparison to the quasi-steady friction models, commonly used in practical analyses of this phenomenon so far.
(i) High conformity between the results of experiments and the results of calculations obtained using the Zielke model for unsteady laminar flows ($\mathrm{Re} < \sim 2320$), revealed also in other investigations, is confirmed.
(iii) From all analyzed unsteady friction models for turbulent flows the Trikha model and the multi-layer models (Vardy and Brown, Zarzycki) have to be singled out. These models predict almost superbly the wave front shape and preserve the frequency. However, it is symptomatic that for higher $\mathbf{Re}_o$ (over approx. 10,000) the damping effect observed in the calculated courses is greater than in the experimental ones. Eliminating this disadvantage requires an improvement of the analyzed models or working out alternative friction models.
(iv) In general, prediction of the pressure wave according to the Brunone et al. models (versions 1 and 2) gives slightly worse results than the multi-layer friction models. However, as it can be seen from the values of the rate of pressure traces convergence (Fig. 9), version 2 of the Brunone et al. model gives better results for high Reynolds numbers. This is mainly because the top of the calculated waves are much wider in comparison to those from the experiment but the amplitudes in the courses calculated according to this model still reveal a similar damping effect to this observed for the multi-layer models.
(v) It is required to broaden the assessment of the unsteady friction models for a wider range of the Reynolds numbers (higher than 16,000) and to include the cases of water column separation.

Acknowledgment

Some results of investigations published in this paper were presented on the 9th International Conference on Pressure Surges "The Practical Application of Surge Analysis for Design and Operation," 24–26 March 2004, Chester, UK.

Nomenclature

a = [m/s] pressure wave celerity
A_i, B_i = [-] coefficients in (A6)
A^*, C^*, κ = [-] coefficients in (A10)
C_1, C_2, m = [-] coefficients in (A11)
C, n = [-] coefficients in (A12)
D = [m] internal pipe diameter
e = [m] pipe wall thickness
f_q = [-] steady flow friction coefficient
g = [m/s^2] acceleration of gravity
H = [m] piezometric head
ΔH = [m] pressure head rise
I = [-] rate of pressure trace convergence
J = [-] head loss per pipe length unit
K = [m] equivalent sand roughness height
k_3 = [-] coefficient in (A14)
L = [m] penstock length
m_i, n_i = [-] coefficients in (A8)
Re = [-] Reynolds number VD/ν
t = [s] time
V = [m/s] average flow velocity in a pipe
W = [-] weighting function
x = [m] distance along pipe axis
y_i = [m/s] variables in (A7)
ν = [m^2/s] kinematic or eddy viscosity (distinguished by subscript)

ρ = [kg/m^3] fluid density
τ = [-] dimensionless time

Subscripts and Superscripts

app = approximation
c = calculated value
m = measured value
$c-s/c-u$ = critical value under steady/unsteady conditions
l/t = laminar/turbulent flow
o/e = initial conditions/end of simulation
q = according to the quasi-steady flow hypothesis
r = in radial co-ordinate direction
x = in axial co-ordinate direction
u = according to an unsteady flow model

APPENDIX A: Description of Friction Models Used in the Computer Code Algorithms

A.1 Quasi-Steady Friction Model

It is commonly assumed that the velocity profile during an unsteady flow is not deformed in comparison with the velocity profile during a steady flow with the same mean velocity. In this connection, the hydraulic losses for an unsteady flow are calculated using formulas correct for steady flows.

Friction modeling according to the quasi-steady flow hypothesis assumes that pipeline inertance J_u equals zero. The pipeline resistance J_q is usually described basing on the Darcy-Weisbach equation

$$J_q = \frac{f_q}{gD} \cdot \frac{V|V|}{2} \tag{A1}$$

Calculation of the quasi-steady friction coefficient (Darcy friction coefficient):

- For laminar flows ($\mathbf{Re} \leqslant \mathbf{Re}_{c-s}$ where $\mathbf{Re}_{c-s}=2320$) depends only on flow characteristics (**Re**) according to the Hagen-Poiseuille law:

$$f_{q-l} = 64/\mathbf{Re} \tag{A2}$$

- for turbulent flows ($\mathbf{Re} > \mathbf{Re}_{c-s}$) depends on flow characteristics (**Re**) and absolute pipe-wall roughness (K/D) according to the **Colebrook-White formula**

$$\frac{1}{\sqrt{f_{q-t}}} = -2\lg\left(\frac{2.51}{\mathbf{Re}\sqrt{f_{q-t}}} + \frac{K/D}{3.71}\right) \tag{A3}$$

A.2 Unsteady Friction Models

The models of the unsteady friction reject the assumptions of the quasi-steady hypothesis. They respect complexity of the unsteady flow which manifest in the deformed velocity profiles in comparison with the velocity profile during the steady flow with the same mean velocity. The intension of such an approach is to obtain the correct description of inertial and friction forces which are responsible for the velocity profile deformation in the pipe cross section.

Zielke (1968) [1] has developed the model of unsteady friction for laminar flows. For this purpose he used Laplace transform to the equation of motion for laminar axisymmetric flow of an incompressible fluid

$$\frac{\partial^2 V}{\partial r^2} + \frac{1}{r}\frac{\partial V}{\partial r} - \frac{1}{\nu}\frac{\partial V}{\partial t} = g\frac{1}{\nu}\frac{\partial H}{\partial x} \tag{A4}$$

(It was assumed that the pressure p and the density ρ are constant in the pipe cross section and the velocity V is related to time t and the distance from the pipe axis r). This method allowed him to achieve functional dependency between the transform of the wall shear stress and the acceleration of fluid. The inverse transformation led to the equation in which the pipeline inertance can be related to the local acceleration of flow by means of the weighting function $W(t)$ [1]

$$J_u = \frac{16\nu}{gD^2}\int_0^t \frac{\partial V}{\partial t}(u) \cdot W(t-u)du \tag{A5}$$

where:

$$W(\tau) = \sum_{i=1}^{5} e^{-A_i i} \quad \text{for} \quad \tau \geqslant 0.02$$

$$W(\tau) = \sum_{i=1}^{6} B_i \cdot \tau^{\frac{i-2}{2}} \quad \text{for} \quad \tau < 0.02 \tag{A6}$$

with

$$A_i = \{26.3744; 70.8493; 135.0198; 218.9216; 322.5544\}$$

$$B_i = \{0.282095; -1.25; 1.057855; 0.9375; 0.396696; -0.351563\}$$

Equation (A5) is based on solid theoretical fundamentals and remains valid in case of any law of mean velocity versus time variation. It is worthwhile to pay special attention to the weighting function W, in (A6), that should be interpreted as a function, which relates inertance at pipe cross-section to past flow velocity changes in this cross-section.

The simplified inertance expression in the Trikha model takes the following form [10]:

$$J_u = \frac{16\nu}{gD^2}(y_1 + y_2 + y_3) \tag{A7}$$

where

$$y_i^{t+\Delta t} = y_i^t \cdot e^{-n_i\left(\frac{4\nu}{D^2}\right)\Delta t} + m_i(V^{t+\Delta t} - V^t)$$

$$W_{\text{app}}(\tau) = \sum_{i=1}^{3} m_i e^{-n_i \tau} \quad \text{for} \quad \tau > 0.00005 \tag{A8}$$

with $m_i = \{40.0; 8.1; 1\}$ $n_i = \{8000; 200; 26.4\}$

The Trikha model presents a simplification of the Zielke model. Numerical codes based on this model, because of approximation of weighting function used, allow saving a lot of computing power and time needed for making the calculations. Such a solution initiated the development of models with efficient approximations of weighting functions [18–20]. However, the most important is that Trikha for the first time proposed to apply this approach to calculate turbulent unsteady flows.

One of the main groups of unsteady friction models for turbulent unsteady flows (the multi-layer models) bases mathematical description on the Reynolds-averaged Navier-Stokes equations applied to axisymmetric flow. In these equations the Reynolds averaging procedure is used for averaging the flow parameters [2,3]. Adoption of the Boussinesq hypothesis which relates to the turbulent Reynolds stress and averaged velocity field $\overline{V_x}$, as in (A9), the eddy viscosity coefficient is introduced into the mathematical description of the analyzed phenomenon ν_t

$$\rho \cdot \overline{V_x' V_r'} = -\rho \nu_t \frac{\partial \overline{V_x}}{\partial r} \tag{A9}$$

In models based on such an approach, experimental data concerning cross-sectional eddy viscosity distribution are used. The axisymmetric flow is divided into two, three, or even four regions as regards phenomena occurring in the flow.

The velocity profile analyses for turbulent unsteady flows allow Vardy et al. to state that the relation (A5) proposed by Zielke is correct for turbulent unsteady flows if only a weighting function

W would be related to the Reynolds number **Re**. In the Vardy and Brown model approximation of real eddy viscosity distribution is used and flow is divided into two regions—the outer annular region (near the wall) where the eddy viscosity is assumed to vary linearly with distance from the pipe wall and the inner core region (in the vicinity of the pipe axis) in which the eddy viscosity is assumed to be constant. Using such distribution of eddy viscosity and applying Laplace transform to equations describing analyzed phenomenon Vardy and Brown obtained **Re**-dependent weighting function W

$$W_{\text{app}} = \frac{A^* \cdot e^{-\pi/C^*}}{\sqrt{\tau}} \tag{A10}$$

$$\text{with} \quad A^* = \frac{1}{2\sqrt{\pi}} = 0.2821, \quad C^* = \frac{12.86}{\mathbf{Re}^{\kappa}}; \quad \kappa = \log_{10}\left(\frac{15.29}{\mathbf{Re}^{0.0567}}\right)$$

In the case of laminar flow ($\mathbf{Re} \leqslant \mathbf{Re}_{c-s}$) the value of the Reynolds number in (A10) is replaced by the critical value of **Re** ($\mathbf{Re}_{c-s} = 2320$) that separates laminar and turbulent flows (the critical value of **Re** for transient flows in this model remain the same as in the case of steady flows). According to the authors this model is valid for the initial Reynolds numbers $\mathbf{Re} < 10^8$ and for smooth pipes only.

The analysis of axisymmetric flow similar to this presented by Vardy and Brown but using a four-region ν_t distribution enabled us to define the weighting function in the Zarzycki model [4,5] by means of the following equations:

(a) For laminar flows ($\mathbf{Re} \leqslant \mathbf{Re}_{c-u}$)

$$W_{\text{app}} = C_1 \tau^{-0.5} + C_2 \cdot e^{-m\tau} \tag{A11}$$

$$\text{with} \quad C_1 = 0.2812; \quad C_2 = -1.5821; \quad m = 8.8553$$

(b) for turbulent flows ($\mathbf{Re} > \mathbf{Re}_{c-u}$)

$$W_{\text{app}} = C\frac{1}{\sqrt{\tau}} \cdot \mathbf{Re}^n \tag{A12}$$

$$\text{with} \quad C = 0.299635; \quad n = -0.005535; \quad \tau = \frac{4\nu \cdot t}{D^2}$$

Zarzycki, after Ohmi et al., assumed similarity between transient and oscillating flows. Therefore, for transient flows, he adopted the Re critical value separating laminar and turbulent oscillating flows. The $\mathbf{Re}_{c-u}$, so-called unsteady critical value of Reynolds number, is given as follows:

$$\mathbf{Re}_{c-u} = 800\sqrt{\Omega} \tag{A13}$$

$$\text{with:} \quad \Omega = \frac{\omega \cdot D^2}{4\nu}; \quad \omega = \frac{2\pi}{T}; \quad T = \frac{4L}{a}$$

The Brunone et al. model is related to the second trend in hydraulic resistance modeling.

The authors of this model had carefully analyzed the influence of the quasi-steady hypothesis on the results of calculations. On this basis they stated that observed discrepancies between calculations and experimental data are caused mainly by the inappropriate mathematical description of inertial forces and wall friction stress. It results directly from assuming the uniform velocity profile in calculations. Analyses based on experimental data concerning velocity profiles in different pipe cross sections and at a wide range of **Re** revealed clear correlation between the pipeline inertance and the acceleration (local and convective velocity derivative) defined as [8]

Table 2 Rates of pressure traces convergence for different grid densities

Friction model	$I_{c12-c24}$[-]	$I_{c36-c24}$[-]
Quasi-steady	−2.20%	0.74%
Zielke	−1.54%	0.49%

$$J_u = \frac{k_3}{g}\left(\frac{\partial V}{\partial t} - a\frac{\partial V}{\partial x}\right) \tag{A14}$$

Originally [8,11], the k_3 coefficient was established so as to match computational and experimental results on a sufficient level of conformity. Vardy and Brown proposed the following empirical relationship to derive this coefficient analytically [2,13]:

$$k_3 = \frac{\sqrt{C^*}}{2} \tag{A15}$$

The k_3 coefficient can be assumed constant (with the value depending on the initial value of **Re**) or as variable (depending on the instantaneous **Re** value in the hydraulic transient considered) [14].

APPENDIX B: Analysis of Grid Density Influence on Computational Results

Additional numerical tests were carried out in order to check how the grid density influences the results of calculations. The diamond grids (Fig. 1) with $m = 12$, 24, and 36 computational reaches along the pipe length were used. Calculations were made using the quasi-steady model and the Zielke model. The initial conditions of the pipe flow for this numerical test were the same as in the run with $\mathbf{Re}_o \cong 10{,}600$ (Table 1).

Pressure courses calculated at different m are stable and characterized by the same pressure wave period (therefore, different dimensions of the grid cells do not change the pressure wave frequency). All calculations derived using considered unsteady friction models at a different number of computational reaches m gave the same amplitudes of pressure changes, what proves that different density of the grid does not influence the pressure wave damping. In order to definitely confirm these observations, the comparison between calculated pressure courses were conducted using the coefficient defined in (10) and the results are presented in Table 2. Pressure courses calculated using 12 (index $c12$) and 36 (index $c36$) computational reaches was compared with one obtained using 24 reaches (index $c24$) and the analysis has included the first 20 pressure wave periods.

As it follows from Table 2 presented above, the differences between calculated results of I are at insignificant level—areas enclosed in the pressure line and the center line of pressure oscillations differ a bit more for courses calculated using the quasi-steady friction model than for those obtained using the unsteady friction model.[7] The sign of I coefficient for different grid density is worth mentioning. Negative values of $I_{c12-c24}$ show that areas limited by the pressure line and center line of oscillations calculated for $m = 12$ are smaller than for courses calculated for $m = 24$. A completely different situation for calculations with $m = 36$ compared to calculations with $m = 24$—the value of $I_{c36-c24}$ is positive. Presented analysis proved that it does not follows from intensity of the pressure wave damping but from differences between the shapes of pressure waves—as the grid density grows the wave front is filled more and the wave at the top is slightly wider (analyzed areas are then slightly bigger).

[7]The values of I for quasi-steady model are greater then for the Zielke model because of much lesser damping effect of pressure wave oscillations which cause that areas enclosed in pressure lines are bigger.

The results of grid independence proved that different grid densities (number of computational reaches) have no significant influence on the convergence and stability of calculated pressure courses.

References

[1] Zielke, W., 1968, "Frequency-Dependent Friction in Transient Pipe Flow," ASME J. Basic Eng., **90**(1), pp. 109–1.

[2] Vardy, A. E., and Brown, J. M., 1996, "On Turbulent Unsteady, Smooth-Pipe Friction," *Proc. of the 7th International. Conf. on Pressure Surges-BHR Group*, Harrogate, United Kingdom.

[3] Vardy, A. E., and Brown, J. M., 2003, "Transient Turbulent Friction in Smooth Pipe Flows," J. Sound Vib., **259**(5), pp. 1011–1036.

[4] Zarzycki, Z., 1994, "Hydraulic Resistance in Unsteady Liquid Flow in Closed Conduits," Research Reports of Tech. Univ. of Szczecin, No.516, Szczecin (in Polish).

[5] Zarzycki, Z., 2000, "On Weighing Function for Wall Shear Stress During Unsteady Turbulent Pipe Flow," *Proc. of the 8th International Conf. on Pressure Surges-BHR Group*, The Hague, The Netherlands.

[6] Daily, W. L., Hankey, W. L., Olive, R. W., and Jordan, J. M., 1956, "Resistance Coefficients for Accelerated and Decelerated Flows Through Smooth Tubes and Orifices," Trans. ASME, **78**, pp. 1071–1077.

[7] Cartens, M. R., and Roller, J. E., 1959, "Boundary-Shear Stress in Unsteady Turbulent Pipe flow," J. Hydr. Div., **85**(HY2), pp. 67–81.

[8] Brunone, B., Golia, U. M., and Greco, M., 1991, "Some Remarks on the Momentum Equations for Fast Transients," International Meeting on Hydraulic Transients with Column Separation, 9th Round Table, IAHR, Valencia, Spain.

[9] Wylie, E. B., and Streeter, V. L., 1993, *Fluid Transients in Systems*, Prentince-Hall, New Jersey.

[10] Trikha, A. K., 1975, "An Efficient Method for Simulating Frequency-Dependent Friction in Transient Liquid Flow," ASME J. Fluids Eng., **97**(1), pp. 97–105.

[11] Bergant, A., and Simpson, A., 1994, "Estimating Unsteady Friction in Transient Cavitating Pipe Flow," *Proc. of the 2nd International Conference on Water Pipeline Systems*, Edinburgh, Scotland.

[12] Almeida, A. B., and Koelle, E., 1992, "*Fluid Transients in Pipe Networks*," CMP Southampton Boston and Elsevier Applied Science, London, New York.

[13] Bergant, A., Simpson, A., and Vitkovsky, J., 2001, "Developments in Unsteady Pipe Flow Friction Modelling," J. Hydraul. Res., **39**(3), pp. 249–257.

[14] Vitkovsky, J., Lambert, M., Simpson, A., and Bergant, A., 2000, "Advances in Unsteady Friction Modeling in Transient Pipe Flow," *Proc. of the 8th International Conf. on Pressure Surges-BHR Group*, The Hague, The Netherlands.

[15] Ohmi, M., Kyonen, S., Usui, T., 1985, "Numerical Analysis of Transient Turbulent Flow in a Liquid Line," Bull. JSME, **28**(239), pp. 709–806.

[16] Adamkowski, A., and Lewandowski, M., 2004, "Unsteady Friction Modelling in Transient Pipe Flow Simulation," Transactions of the Institute of Fluid-Flow Machinery, No. 115, pp. 83–97.

[17] Holmboe, E. L., and Rouleau, W. T., 1967, "The Effect of Viscous Shear on Transient In Liquid Lines," ASME J. Basic Eng., **89**(1), pp. 174–180.

[18] Ghidaoui, M. S., and Mansour, S., 2002, "Efficient Treatment of the Vardy-Brown Unsteady Shear in Pipe Transients," J. Hydr. Div., **128**(1), pp. 102–112.

[19] Suzuki, K., Taketomi, T., and Sato, S., 1991, "Improving Zielke's Method of Simulating Frequency-Dependent Friction in Laminar Liquid Pipe Flow," ASME J. Fluids Eng., **113**, pp. 569–573.

[20] Schohl, G. A., 1993, "Improved Approximate Method for Simulating Frequency-Dependent Friction in Transient Laminar Flow," ASME J. Fluids Eng., **115**, pp. 420–424.

A Low-Reynolds Number Explicit Algebraic Stress Model

M. M. Rahman
e-mail: mizanur.rahman@hut.fi

T. Siikonen

Department of Mechanical Engineering,
Helsinki University of Technology,
Laboratory of Applied Thermodynamics,
Sähkömiehentie 4,
FIN-02015 HUT, Finland

A low-Reynolds number extension of the explicit algebraic stress model, developed by Gatski and Speziale (GS) is proposed. The turbulence anisotropy Π_b and production to dissipation ratio P/ϵ are modeled that recover the established equilibrium values for the homogeneous shear flows. The devised (Π_b, P/ϵ) combined with the model coefficients prevent the occurrence of nonphysical turbulence intensities in the context of a mild departure from equilibrium, and facilitate an avoidance of numerical instabilities, involved in the original GS model. A new near-wall damping function f_μ in the eddy viscosity relation is introduced. To enhance dissipation in near-wall regions, the model constants $C_{\epsilon(1,2)}$ are modified and an extra positive source term is included in the dissipation equation. A realizable time scale is incorporated to remove the wall singularity. The turbulent Prandtl numbers $\sigma_{(k,\epsilon)}$ are modeled to provide substantial turbulent diffusion in near-wall regions. The model is validated against a few flow cases, yielding predictions in good agreement with the direct numerical simulation and experimental data. [DOI: 10.1115/1.2354527]

1 Introduction

The explicit algebraic stress model (ASM) acknowledges the inclusion of stress anisotropies and can be developed from a rigorous mathematical basis, having the associated computational cost comparable to that of an isotropic eddy viscosity model. This approach provides a good approximation to the full Reynolds stress closure (i.e., provides algebraic equations without solving the differential equations for the Reynolds stresses), and is believed to be a compatible Reynolds-averaged Navier-Stokes (RANS) model devoted to representing the turbulence.

Second-order closure turbulence models, based on the Reynolds stress transport equation, entangle the history and nonlocal effects adhering to complex turbulent flows that depart significantly from equilibrium. Recourse to the hypothesis of homogeneous turbulence in the limit of equilibrium, Rodi [1] proposed an idea of obtaining the ASM from the second-order closures. Physically, two assumptions are made herein: The difference between the convection and diffusion terms in the Reynolds stress equation is proportional to the corresponding difference in the turbulent kinetic energy equation, and the Reynolds stress anisotropy b_{ij} is constant along a streamline. Despite this idealization, the artifact retains a factor of major physical relevance, featuring the distinction between the components of the Reynolds stress tensor with an exclusion of accounting their transport histories.

Evoking the same equilibrium hypothesis, Pope [2] developed a methodology to procure an explicit relation for the Reynolds stress tensor from the implicit algebraic stress model (which Rodi obtained from the model of Launder et al. [3]) by using a tensorial polynomial expansion in the integrity basis. Gatski and Speziale (GS) used this method to derive an explicit algebraic stress equation for two- and three-dimensional turbulent flows [4]. In order to generalize the results, the algebraic stress representation is applied to the general class of pressure-strain correlation models [5], which are linear in the anisotropic tensor. After regularization, an anisotropic eddy viscosity model with strain-dependent coefficients is achieved, which has been referred to as an explicit ASM. Unambiguously, the explicit model extends the ability of the two-equation models to account for nonequilibrium and anisotropic effects. However, the model shows evidence of numerical instability when the flow is far from equilibrium [6]. The reason is that the explicit ASM is more susceptible to the rotational strains.

In particular, the GS model utilizes the equilibrium value for P/ϵ (production to dissipation ratio) arising in the context of the selected pressure-strain model. This may lead the model to inconsistency with a departure from equilibrium. To circumvent the problem, Girimaji [7] has developed a fully explicit, self-consistent variant of the GS model, by solving the cubic equation for P/ϵ. Although this achievement yields a new model variant, the resulting solution for P/ϵ is unfortunately too cumbersome to be implemented. Jongen and Gatski [8] have extended the same GS model through a new approach to characterizing the equilibrium states of the Reynolds stress anisotropy in homogeneous turbulence. The model consists of a generalized relation for P/ϵ, integrating all planar homogeneous turbulent flows with/without rotation.

The present study advances with resorting to the GS model, a convenient reference point for developing an attractive and viable alternative for the Reynolds stress model. Compatible relations for the model coefficients $\Pi_b = b_{ij}b_{ij}$ and P/ϵ are devised that depend nonlinearly on both the rotational and irrotational strains. Sticking to the realizability constraints (i.e., the positivity of the normal Reynolds stresses and Schwarz' inequality between turbulent velocity correlations), the coefficients are calibrated by reference to direct numerical simulations (DNS) data for homogeneous shear flows. Consequently, the strain-dependent sensitivity of the model is mitigated and a notable improvement in the numerical stability is attained. In near-wall regions, the anisotropic production in the ϵ equation is accounted for substantially by modifying the model constants $C_{\epsilon(1,2)}$ and adding a secondary source term. Furthermore, the wall singularity is removed by using a physically appropriate time scale that never falls below the Kolmogorov time scale $\sqrt{\nu/\epsilon}$, representing the near-wall turbulent phenomena. A near-wall eddy viscosity damping function f_μ is introduced that reproduces the distinct effects of low-Reynolds number and wall proximity. It reaches the upper limit value of unity in the logarithmic layer. In addition, the turbulent Prandtl numbers $\sigma_{(k,\epsilon)}$ are adjusted such as to provide substantial turbulent diffusion in near-wall regions.

The performance of the new model is demonstrated through the comparison with experimental and DNS data of well-documented flows, consisting of fully developed channel flows, a flat plate boundary layer flow with zero pressure gradient, a contracting

Contributed by the Fluids Engineering Division of ASME for publication in the JOURNAL OF FLUIDS ENGINEERING. Manuscript received October 4, 2005; final manuscript received April 7, 2006. Assoc. Editor: Ugo Piomelli.

channel flow, an asymmetric plane diffuser flow, and a plane U-duct flow, respectively. A concrete analysis of the simulated results is provided.

2 Turbulence Modeling

In collaboration with the RANS equations, the turbulence model determines the turbulence kinetic energy k and its dissipation rate ϵ by the following transport relations:

$$\frac{\partial \rho k}{\partial t} + \frac{\partial \rho u_j k}{\partial x_j} = \frac{\partial}{\partial x_j}\left[\left(\mu + \frac{\mu_T}{\sigma_k}\right)\frac{\partial k}{\partial x_j}\right] + \rho P - \rho \epsilon \tag{1}$$

$$\frac{\partial \rho \epsilon}{\partial t} + \frac{\partial \rho u_j \epsilon}{\partial x_j} = \frac{\partial}{\partial x_j}\left[\left(\mu + \frac{\mu_T}{\sigma_\epsilon}\right)\frac{\partial \epsilon}{\partial x_j}\right] + (C_{\epsilon 1}\rho P - C_{\epsilon 2} f_{\epsilon 2}\rho \epsilon + E_\epsilon)/T_t \tag{2}$$

where ρ is the density, μ and μ_T are the laminar and turbulent viscosity coefficients, $\sigma_{(k,\epsilon)}$ represent the appropriate turbulent Prandtl numbers, and the turbulent production term $P = -\overline{u_i u_j}(\partial u_i/\partial x_j)$. The secondary source term E_ϵ is designed to increase the level of ϵ in nonequilibrium flow regions. The symbolized T_t is the characteristic (mixed or hybrid) time scale, having the asymptotic consistency in the near-wall region. The function $f_{\epsilon 2}$ multiplying the coefficient $C_{\epsilon 2}$ usually takes the free turbulence into account. However, the use of $f_{\epsilon 2}$ in the GS model serves additionally to remove the singularity of the dissipation equation at the wall. The modeling of the Reynolds stresses $\rho\overline{u_i u_j}$ in the explicit ASM and associated relevant aspects are discussed in some detail in subsequent sections.

2.1 GS Explicit ASM. The mathematical rationale provoking the development of the explicit ASM by Gatski and Speziale refers to the integrity basis analysis. The explicit solution to the Reynolds-stress tensor $\rho\overline{u_i u_j}$ constitutes an anisotropic eddy viscosity model with strain-dependent coefficients. For two-dimensional mean turbulent flows, the nonlinear constitutive equation takes a simplified form

$$\rho\overline{u_i u_j} = \frac{2}{3}\rho k \delta_{ij} - 2\mu_T\left[\left(S_{ij} - \frac{1}{3}S_{kk}\delta_{ij}\right) + \alpha_4\frac{k}{\epsilon}(S_{ik}W_{kj} + S_{jk}W_{ki}) - \alpha_5\frac{k}{\epsilon}\left(S_{ik}S_{kj} - \frac{1}{3}S_{kl}S_{kl}\delta_{ij}\right)\right] \tag{3}$$

with

$$\mu_T = C_\mu \rho T_t k, \quad C_\mu = \frac{3\alpha_1}{3 - 2\eta^2 + 6\xi^2} \tag{4}$$

$$\eta^2 = \alpha_2 (T_t S)^2, \quad \xi^2 = \alpha_3 (T_t W)^2 \tag{5}$$

where $T_t S$ and $T_t W$ represent the shear and vorticity parameters, respectively; $S = \sqrt{2S_{ij}S_{ij}}$ and $W = \sqrt{2W_{ij}W_{ij}}$. The mean strain rate S_{ij} and vorticity W_{ij} tensors are defined as

$$S_{ij} = \frac{1}{2}\left(\frac{\partial u_i}{\partial x_j} + \frac{\partial u_j}{\partial x_i}\right), \quad W_{ij} = \frac{1}{2}\left(\frac{\partial u_i}{\partial x_j} - \frac{\partial u_j}{\partial x_i}\right) \tag{6}$$

The coefficients $(\alpha_1 - \alpha_5)$ associated with Eqs. (3)–(5) are given by

$$\alpha_1 = \left(\frac{4}{3} - C_2\right)\frac{g}{2}, \quad \alpha_2 = (2 - C_3)^2\frac{g^2}{8}$$

$$\alpha_3 = (2 - C_4)^2\frac{g^2}{8}, \quad \alpha_4 = (2 - C_4)\frac{g}{2}$$

$$\alpha_5 = (2 - C_3)g, \quad g = \left(\frac{C_1}{2} + \frac{P}{\epsilon} - 1\right)^{-1} \tag{7}$$

The pressure-strain-correlation model of Abid [9] is considered herein so that $(C_1 - C_4)$ become

$$C_1 = 3.4 + 1.80\frac{P}{\epsilon}, \quad C_2 = \frac{4}{5} - 1.30\Pi_b^{1/2}$$

$$C_3 = 1.25, \quad C_4 = 0.40 \tag{8}$$

where the anisotropy of the Reynolds stress b_{ij} is defined as

$$b_{ij} = \frac{\overline{u_i u_j} - \frac{2}{3}k\delta_{ij}}{2k} \tag{9}$$

For homogeneous turbulent flows that are in equilibrium, Π_b and P/ϵ attain constant values, so that $\Pi_b \approx 0.11$ and $P/\epsilon = (C_{\epsilon 2} - 1)/(C_{\epsilon 1} - 1) \approx 1.88$. These values are set in Eqs. (7) and (8) to calculate inhomogeneous flows. However, the necessity to account for changes in Π_b and P/ϵ is acknowledgeable since their equilibrium values drive the model to inconsistency in the context of a mild departure from equilibrium.

It is evident from Eq. (4) that the coefficient C_μ indulges in singularities with sufficiently large strain rates η. As a remedy, Gatski and Speziale modify the coefficient using the Pade-type approximation as follows:

$$C_\mu = \frac{3\alpha_1}{3 - 2\eta^2 + 6\xi^2} \approx \frac{3(1 + \eta^2)\alpha_1}{3 + \eta^2 + 6\eta^2\xi^2 + 6\xi^2} \tag{10}$$

Hence, a regularized model is obtained that constitutes a good approximation to the original model within the equilibrium range. The function $f_{\epsilon 2}$ defined by

$$f_{\epsilon 2} = 1 - \exp(-0.09\,\mathrm{Re}_y), \quad \mathrm{Re}_y = \frac{\sqrt{k}y}{\nu} \tag{11}$$

removes the singularity of the dissipation equation at the wall, given that y is the normal distance to the wall and ν denotes the kinematic viscosity. In addition, it reduces the destruction term and thereby increases the absolute value of ϵ in near-wall regions. The model can be integrated to the wall without adding a damping to the eddy viscosity since the strain-dependent coefficient C_μ in the eddy viscosity equation provides natural damping as the wall is approached.

2.2 Modified Explicit ASM. The new model appears with recourse to the realizability constraints, reflecting physically necessary conditions for developing an attractive turbulence model, applicable to a broad range of practical flows. The realizability conditions are defined as [5]

$$\overline{u_i^2} \geq 0, \quad \frac{\overline{u_i u_j}^2}{\overline{u_i^2}\,\overline{u_j^2}} \leq 1 \tag{12}$$

Equation (12) also represents the minimal requirement to prevent a turbulence model from producing nonphysical results. With reference to the GS model, the coefficients $(\alpha_1 - \alpha_5)$ with $g = 0.233$ are reported to be constant. This can potentially lead to the prediction of negative normal stress components, and thereby violate the realizability principle.

To revive the mathematical relevancy (i.e., realizability constraints) adhering to the turbulence modeling, Π_b and P/ϵ associated with the coefficients $(\alpha_1 - \alpha_5)$ in Eq. (7) need to be modeled. Based on the homogeneous shear flow characteristic and the property $\lim_{S\to\infty} P/\epsilon \sim S$ [8], the following formulations for Π_b and P/ϵ are proposed:

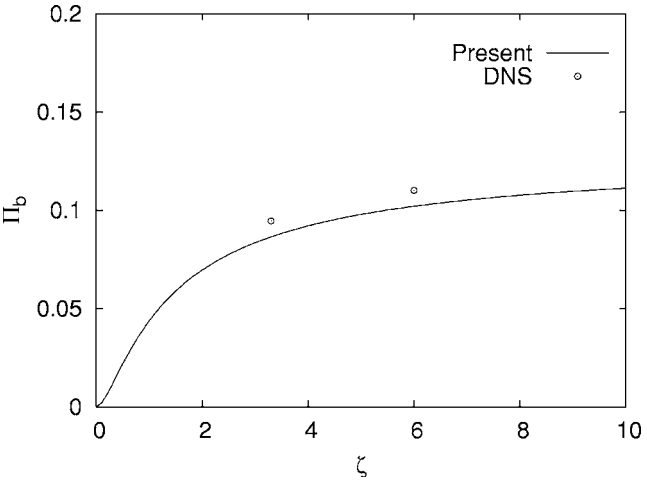

Fig. 1 Variation of modeled Π_b with shear parameter $\zeta(R=1)$

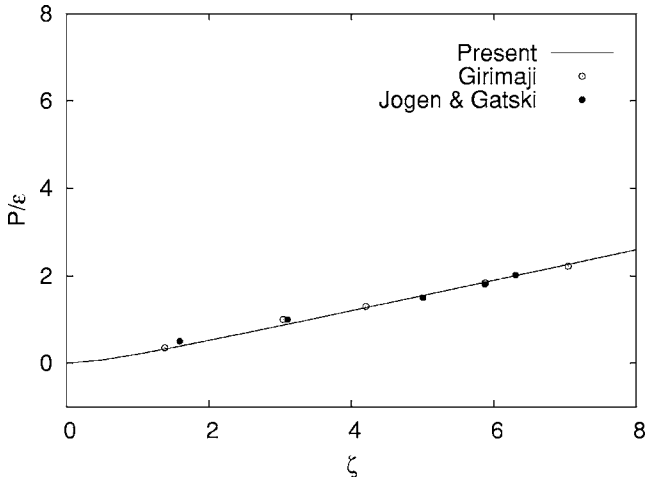

Fig. 2 Locus of solution points for state variable P/ϵ as a function of $\zeta(R=1)$

$$\Pi_b = C_\nu \frac{P}{\epsilon}, \quad \frac{P}{\epsilon} = C_\nu \zeta^2 \tag{13}$$

with

$$C_\nu = \frac{1}{2(1 + T_t S\sqrt{1+R^2})}$$

$$\zeta = T_t S \max(1, R) \tag{14}$$

where $R=|W/S|$ is a dimensionless parameter that is very useful to characterize the flow [10]. For instance, for a pure shear flow $R=1$, whereas for a plain strain flow $R=0$. It is appropriate to emphasize herein that introducing the auxiliary variables C_ν and ζ, the proposed relation is constructed so as to meet the requirements of the equilibrium state: $P/\epsilon \approx 1$ with $\Pi_b \approx 0.087$ for the logarithmic region in a turbulent channel flow at $\zeta(R=1) \approx 3.3$ [11], and $P/\epsilon \approx 1.9$ with $\Pi_b \approx 0.1$ for the homogeneous shear flow of Tavoularis and Corrsin [12] at $\zeta(R=1) \approx 6.0$, respectively. Note that the log layer of a channel flow is a region where the Reynolds stress equation has the same form as in the homogeneous case [13].

Figure 1 illustrates the distribution of Π_b as a function of shear parameter $\zeta(R=1)$. As is evident, the Π_b distribution is in good agreement with DNS data [11,12]. The profiles of P/ϵ are displayed in Fig. 2. Clearly, the relation (13) recovers the self-consistent models of Girimaji [7] and Jongen and Gatski [8] for the weak equilibrium condition. The new calibrated relations for Π_b and P/ϵ can assist the coefficients $(\alpha_1 - \alpha_5)$ in responding to both the shear and vorticity dominated flows that are far from equilibrium.

In particular, the modification by Eq. (10) having constant coefficients is inadequate to provide non-negative turbulent energy components, although it guarantees a positive value of the coefficient. As recognized from Eq. (10), improper behavior pertaining to turbulence intensities may exist when the flow field greatly deviates from pure shear flow (where, $S_{12}=S_{21}=W_{12}=-W_{21}=S/2$), because the normal strain rate is much larger than the shear strain rate, i.e., $\eta^2 \gg \xi^2$. To root this situation out, the following formulation is devised together with Eq. (13) as:

$$C_\mu = \frac{3\alpha_1}{3 - 2\eta^2 + 6\xi^2} \approx \frac{3\ \alpha_1}{3 - 2f_\eta \eta^2 + 6\xi^2} \tag{15}$$

where the model function f_η is introduced to assist the occurrence of reasonable turbulence intensities when $\eta^2 \gg \xi^2$ (i.e., $R \sim 0$). A rational approach to modeling f_η is that its effect essentially disappears in pure shear flows such as fully developed channel and homogeneous flows. To preserve the requirements, f_η is constructed as

$$f_\eta = 1 + C_\eta \eta^2 (R^2 - 1) \tag{16}$$

where $C_\eta=2$, so that the influence of f_η becomes as small as possible. The monitor function f_η provides insight into the manner by which the formulation is susceptible to controlling the degree of biasing the coefficient C_μ. Essentially, the outcome of f_η is compatible as R approaches toward zero.

The nonlinear constitutive equation, combined with the above-mentioned modifications is reconstructed as

$$\overline{\rho u_i u_j} = \frac{2}{3}\rho k \delta_{ij} - 2\mu_T \left[\left(S_{ij} - \frac{1}{3} S_{kk}\delta_{ij} \right) + \frac{\alpha_4 T_t}{f_\mu}(S_{ik}W_{kj} + S_{jk}W_{ki}) - \frac{\alpha_5 T_t}{f_\mu}\left(S_{ik}S_{kj} - \frac{1}{3}S_{kl}S_{kl}\delta_{ij} \right) \right] \tag{17}$$

Since the viscous dissipation presumably dominates near the wall, the eddy viscosity is evaluated from

$$\mu_T = C_\mu f_\mu \rho k T_t \tag{18}$$

Substituting Eq. (13) into Eq. (7) yields the coefficients $(\alpha_1 - \alpha_5)$ associated with the present ASM. Noteworthily, the eddy viscosity damping function f_μ is detached from the nonlinear part of the deviatoric Reynolds stress tensor. Consequently, the presence of f_μ partially alters the rationale (i.e., C_μ naturally damps out the eddy viscosity in near-wall regions) of the original ASM formulation.

Figure 3 shows the distribution of C_μ as a function of ζ. Conspicuously, the C_μ distribution is in excellent agreement with various DNS data [14–16] for pure shear flows (i.e., homogeneous shear flows with $R=1$). The coefficient C_μ is reduced significantly with increasing ζ and maintained at a level that could mimic the complex turbulent flows. On the contrary, the situation is different for plain strain flows (i.e., $R=0$), tending to return high C_μ values compared with the case of $R=1$. However, the invariant map confirms (shown afterward) that the model realizability is preserved in the case with $R=0$, substantiating the behavior of f_η embedded with C_μ worthily.

The Lumley triangle, i.e., the anisotropy invariant map [5] contains all physically realizable states of turbulence. Every realizable Reynolds stress adhering to a turbulent flow corresponds to a point in the Lumley triangle. Figure 4 shows the model behavior in the (III_b, II_b) phase space (where $II_b = b_{ip}b_{pi}$ and $III_b = b_{ip}b_{pq}b_{qi}$) for a wide range of the parameter ζ. As expected from the comparison with the DNS results, the present model yields predictions

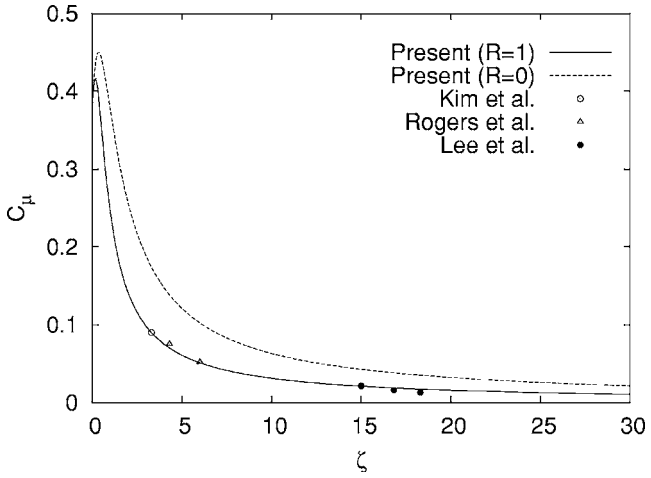

Fig. 3 Distribution of C_μ as a function of shear/strain parameter ζ

in close proximity to the invariant values from the DNS as well. Values of ζ in the range 0–200 are considered to be adequate to conduct the experiment. It is found that $\zeta > 100$ induces small changes in the invariants and ultimately, the model saturates within the invariant triangle for pure shear flows. This occurrence implies that even in a state with high shear rates, the modified formulation for C_μ in Eq. (15) is essentially just enough to maintain the physical consistency characterizing the realizability principle.

The model realizability is further contrasted with the accelerated flow where turbulence can be strongly attenuated [17]. The turbulence attenuation is characterized by plane straining (where $W_{ij}=0$ for all i and j), traditionally called stretching, rather than shear. Herein, the most pronounced attenuation of turbulence kinetic energy is the evolution of the component u_1u_1 in the direction of a primary strain S_{11}. The fundamental stretching field together with the continuity equation for incompressible flow suggests that the limiting states are [17]: the 2D stretching

$$S_{22} = -S_{11}(S_{33}=0), \quad S_{11} = S/2 \tag{19}$$

and the axisymmetric stretching

$$S_{22} = S_{33} = -S_{11}/2, \quad S_{11} = S/\sqrt{3} \tag{20}$$

The two cases in question are often associated with irrotational plane strain and axisymmetric contraction of the flow, having different implications on the model realizability. Both states are placed in the Lumley triangle as shown in Fig. 4. Evidently, each state remains in the allowed region of the invariant map. To this end, it must be stressed that the present model does not exhibit unrealizable features at moderate/severe strain rates.

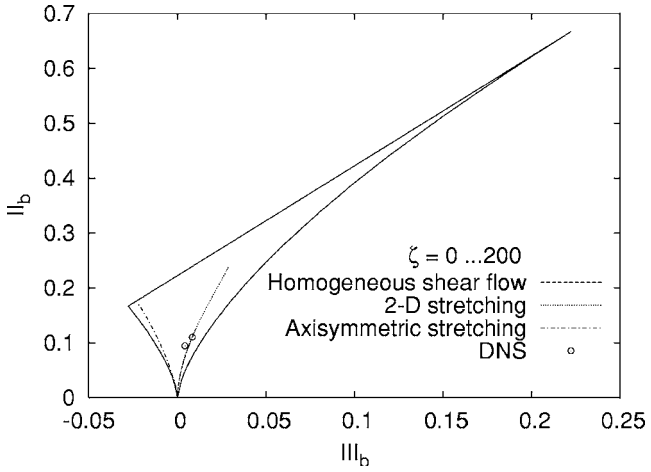

Fig. 4 Anisotropy invariant map at different shear/strain rates

Obviously, the explicit algebraic stress model augments the capacity of the two-equation models to account for nonequilibrium effects through the coefficient C_μ. Unfortunately, the GS model with the constant coefficients exhibits numerical instability in the context of the algebraic stress model when the flow is far from equilibrium. The reason is that the model responds more sensitively to the strain-dependent coefficients (i.e., rotational strains). To avoid numerical problems, modified forms of C_μ are proposed in Refs. [18,19] that reduce the strain-dependent sensitivity and numerical difficulties to a greater extent. An alternative regularized form of C_μ is used by Abid et al. [9] in aerodynamic flow computations. The formulation is synonymous to Eq. (10) to order η^6 and ξ^6, since it does not discernibly alter the value of C_μ near equilibrium conditions, but limits C_μ to a nonzero value $(0.2\alpha_1)$ for high values of η and ξ to preclude numerical instabilities. However, to maintain the relevant aspects of the ASM, the coefficient C_μ cannot be a constant. In principle, the robustness characteristics and predictive performance of the GS model are improved when the variation of P/ϵ is allowed [10]. Therefore, Eq. (13) is introduced with the GS model to gain, at least, some privilege over convergence. Consequently, the GS model reproduces the similar behaviors for C_μ and realizable states of turbulence (not shown) as plotted in Figs. 3 and 4. Nevertheless, the current formulation differs from the GS model by Eq. (15) that warrants rational turbulence intensities, and the near-wall turbulence modeling, discussed in the next section.

2.3 Near-Wall Modeling. In the vicinity of the wall, the molecular viscosity effect is superior to the turbulent mixing, reflecting a strong anisotropic condition. Consequently, an important criterion regarding the appropriateness of the turbulence model is to represent the near-wall behavior of turbulence quantities accompanied by a preferential damping of velocity fluctuations in the direction normal to the wall that reconciles the influence of wall proximity adequately.

The realizable time scale T_t associated with the new ASM can simply be defined as

$$T_t = \sqrt{\frac{k^2}{\epsilon^2} + C_T^2\frac{\nu}{\epsilon}} = \frac{k}{\epsilon}\sqrt{1 + \frac{C_T^2}{\mathrm{Re}_T}}$$

$$R_T = \frac{k^2}{\nu\epsilon} \tag{21}$$

where Re_T is the turbulence Reynolds number. Equation (21) warrants that the eddy time scale never falls below the Kolmogorov time scale $C_T\sqrt{\nu/\epsilon}$, dominant in the immediate neighborhood of the solid wall. It prevents the singularity in the dissipation equation down to the wall. Alternatively, the turbulence time scale is k/ϵ at large R_T but approaches the Kolmogorov limit $C_T\sqrt{\nu/\epsilon}$ for $\mathrm{Re}_T \ll 1$. The empirical constant $C_T = \sqrt{2}$ associated with the Kolmogorov time scale is estimated from the behavior of k in the viscous sublayer [19]. Articulately, the inclusion of T_t in the ϵ equation guarantees near-wall asymptotic consistency without resorting to ad hoc damping functions employed in many k-ϵ models [20].

The eddy viscosity damping function in Eq. (18) confronts the distinct effects of low-Reynolds number and wall proximity in near-wall regions, and is devised pragmatically as

$$f_\mu = 1 - \exp\left(-\frac{y}{L}\right)$$

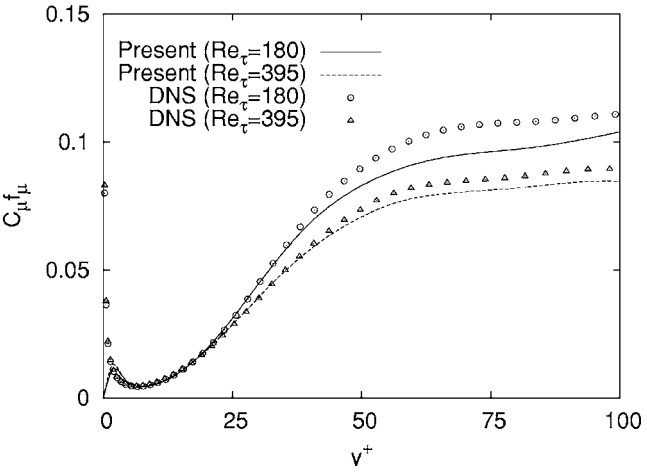

Fig. 5 Variations of eddy viscosity coefficients with wall distance in channel flow

$$L^2 = 2\zeta(6 + C_\mu \mathrm{Re}_T)\sqrt{\frac{\nu^3}{\epsilon}} \tag{22}$$

where $(\nu^3/\epsilon)^{1/4}$ signifies the Kolmogorov length scale. The empirical function f_μ is valid in the whole flow field, including the viscous sublayer and the logarithmic layer. In the region close to the wall, the Reynolds stress $-\overline{uv} \sim y^3$ and $k \sim y^2$. To preserve the correct cubic power-law behavior of $-\overline{uv}$, the damping function (herein the product $C_\mu f_\mu$) needs to increase proportionally to y^{-1} in the near-wall region. As evinced by Fig. 5 in comparison with the DNS data [21] for fully developed turbulent channel flows, the adopted form of $C_\mu f_\mu$ reproduces the asymptotic limit involving the distinct effects of low-Reynolds number and wall proximity. The product $C_\mu f_\mu \approx 0.09$ (the standard choice for $C_\mu = 0.09$, pertaining to the linear k-ϵmodel) remote from the wall to ensure that the model is compatible with the standard k-ϵ turbulence model. The use of $f_\mu = f_\mu(y, L)$ confronts the singularity at neither the separating nor the reattaching point in contrast to the adoption of $y^+ = u_\tau y/\nu$, where u_τ is the friction velocity. Consequently, the model is applicable to separated and reattaching flows. To this end, it must be emphasized that the wall distance from the surface is uniquely defined as being the shortest distance between the present point and all no-slip boundaries in a flow field. The distance does not have to be measured normal to a surface [22]. Even near the corner, it can be evaluated by introducing the limit of a wall with a very small curvature. The usual rationale of using the wall distance in the model functions is that the presence of the wall becomes very explicit to the turbulence model, and accordingly, the near-wall damping phenomenon is prosecuted.

It is appropriate to discuss the argument regarding the speed of the wall. As the wall speed approaches the main stream value the strain/vorticity rate goes to zero, and hence $C_\mu \approx 0.4$ and $f_\mu = 1$. Apparently, there is no damping. In this situation, the Reynolds stress as well as the turbulence production approaches toward zero. The turbulence kinetic energy (and therefore the eddy viscosity) becomes very small and consequently, the meaning of damping is ambiguous therein.

Near-wall flows show a tendency to underestimate the dissipation rate ϵ due to the local anisotropy of turbulence, adhering to the nondimensional parameter P/ϵ [23,24]. The formulation has been developed to enhance dissipation in such a situation using the relation: $C_{\epsilon 1} = C_{\epsilon 1}^*(a_1 + a_2 P/\epsilon)$, where $C_{\epsilon 1}^*$, a_1 and a_2 are model constants [25,26]. It is worth recalling that P/ϵ is practically always positive, but can under some conditions (for example, complex flows) temporarily and locally become negative. Therefore, alternative elements with relevance to P/ϵ may be used to counteract this adverse situation

$$C_{\epsilon 1} = 1 + \frac{\Pi_b^*}{C_T}, \quad C_{\epsilon 2} = C_T \tag{23}$$

where $\sqrt{\Pi_b^*} = C_\mu \zeta$ is essentially identical to Eq. (13), however, with the exception that C_ν is replaced by C_μ. It can be stressed that the rational subsistence Π_b^* to P/ϵ indubitably is conducive to allowing a compatible change in $C_{\epsilon 1}$ which accounts for the additional production of dissipation by the anisotropy of turbulence. Herein, one remarkable departure from the conventional modeling needs to be noted. The coefficient $C_{\epsilon 1}$ is made of a function of the invariants, while $C_{\epsilon 2}$ is reduced from its usual value of 1.92 to $C_T = \sqrt{2}$. However, $C_{\epsilon 2}/C_{\epsilon 1} \approx 1.33$ in the log layer of channel flow with $\zeta(R=1) \approx 3.3$, converging toward the standard $C_{\epsilon 2}$-to-$C_{\epsilon 1}$ ratio $(1.92/1.44 = 1.33)$.

The extra source term E_ϵ in Eq. (2) is constructed from the most extensive turbulent diffusion models for k and ϵ equations derived by Yoshizawa [27] with the two-scale direct-interaction approach using the inertial-range simplification. To receive positive benefits from the numerical reliability and to integrate the inertial-range condition directly to the solid wall, the cross-diffusion term is designed with the assistance of Ref. [28] as

$$E_\epsilon = C_T \frac{\mu_T}{T_t} \max\left[\frac{\partial(k/\epsilon)}{\partial x_i} \frac{\partial k}{\partial x_i}, 0 \right] \tag{24}$$

Obviously, the source term E_ϵ stimulates the energy dissipation in nonequilibrium flows, thereby reducing the departure of the turbulent length scale from its local equilibrium value and enabling improved prediction of adverse pressure gradient flows accompanied by flow separation and reattachment. At this stage, it appears necessary to identify that the quantity E_ϵ is characteristically beneficial in the vicinity of reattachment point and hence, it can be regarded as an attempt at replacing the Yap correction [29].

The budgets of k and ϵ from the DNS data approve that the role of turbulent diffusion in the near-wall region is substantial. Accordingly, the Prandtl numbers σ_k and σ_ϵ are modeled, rather than being assigned constant values (unlike the commonly adopted practice with $\sigma_k = 1.0$, and $\sigma_\epsilon = 1.3$)

$$\sigma_k = C_\mu + f_\mu, \quad \sigma_\epsilon = \sqrt{C_\mu} + f_\mu \tag{25}$$

The model coefficients σ_k and σ_ϵ are developed so that sufficient diffusion is obtained in the vicinity of the wall. This contrivance tends to successfully predict the kinetic energy and dissipation rate profiles [30]. The issue of the σ_ϵ formulation deserves further attention: the connection between the von Karman constant κ and the difference $(C_{\epsilon 2} - C_{\epsilon 1})$. The log-region analysis shows that κ is given by $\kappa^2 = \sigma_\epsilon (C_{\epsilon 2} - C_{\epsilon 1})\sqrt{C_\mu}$. The developed channel flow results in the validation section show that the log law is recovered and the von Karman constant thus determined is $\kappa \approx 0.4$.

3 Computations

To ascertain the generality and efficacy of the present model, a few applications to two-dimensional turbulent flows are considered. Tested flows consist of fully developed channel flows, a flat plate boundary layer flow with zero pressure gradient, a contracting channel flow, an asymmetric plane diffuser flow, and a plane U-duct flow. For a comparison purpose, calculations from the GS model are included. Table 1 summarizes functions and constants for different turbulence models.

A cell-centered finite-volume scheme together with an artificial compressibility approach [18,31] is employed to solve the flow equations. In the artificial compressibility method, the artificial compressibility is principally added to the derivative of density with respect to the pressure, influencing not only the continuity equation but also the other equations. A fully upwinded second-

Table 1 Functions and constants

Model	ϵ_w	C_μ	$C_{\epsilon 1}$	$C_{\epsilon 2}$	σ_k	σ_ϵ
GS	$2\nu(k/y_n^2)$	Eq. (10)	1.44	1.83	1.0	1.3
Present	$2\nu(k/y_n^2)$	Eq. (15)	Eq. (23)	Eq. (23)	Eq. (25)	Eq. (25)

Model	$f_{\epsilon 2}$	$\Pi_b, P/\epsilon$	T_t	f_μ	E_ϵ
GS	Eq. (11)	Eq. (13)	k/ϵ	1.0	0.0
Present	1.0	Eq. (13)	Eq. (21)	Eq. (22)	Eq. (24)

order spatial differencing is applied to approximate the convective terms. Roe's [32] damping term is used to calculate the flux on the cell face. A diagonally dominant alternating direction implicit (DDADI) time integration method [33] is applied for the iterative solution of the discretized equations. A multigrid method is utilized for the acceleration of convergence [34]. The basic implementation of the artificial compressibility method and associated features are described in Refs. [18,31,35].

A variable grid spacing is used to resolve the sharp gradient in near-wall regions. Grid densities are varied to ensure the grid independence of the numerical results. It is found that the solution is not very sensitive to the number of grid points as long as there are two points in $y^+ < 1.0$. In the computations that follow, convergence is judged by monitoring the root-mean-square residuals of flow variables. The solution is taken as having converged when all residuals are of the order 10^{-4} or less.

3.1 Channel Flow. Computations are carried out for fully developed turbulent channel flows at $\mathrm{Re}_\tau = 180$ and 395, for which turbulence quantities are attainable from the DNS data [21]. Calculations are conducted in the half-width of the channel, imposing periodic boundary conditions, except for the pressure, pertaining to the upstream and downstream boundaries. A 48×48 nonuniform grid refinement is considered to be sufficiently accurate to describe the flow characteristics. For both cases, the length of the computational domain is 32δ, where δ is the channel half-width. To ensure the resolution of the viscous sublayer, the first grid node near the wall is placed at $y^+ \approx 0.4$. Comparisons are made by plotting the results in the form of $u^+ = u/u_\tau$, $uv^+ = \overline{uv}/u_\tau^2$, $uu^+ = \sqrt{\overline{uu}}/u_\tau$, $vv^+ = \sqrt{\overline{vv}}/u_\tau$ and $ww^+ = \sqrt{\overline{ww}}/u_\tau$ versus y^+. To compute the $\overline{ww}$ component for this two-dimensional flow, the usual approximation $\overline{ww} = 2k - \overline{uu} - \overline{vv}$ is employed.

Figures 6 and 7 shows the mean velocity and shear stress profiles. As is evident, predictions of the present and GS models agree well with the DNS data. Profiles of the turbulent normal stress components are compared with the DNS data in Figs. 8 and 9, respectively. Both models yield good overall agreement with the turbulence quantities. However, the present model gives some improvement in the prediction of uu^+ compared with the GS model. It seems likely that the influence of the damping function f_μ is an important factor in predicting the energy components for the channel flow.

3.2 Flat Plate Boundary Layer Flow. The near-wall behavior of the turbulence model is checked by calculating the flow over a flat plate with a high free-stream turbulence intensity. The test case is taken from ERCOFTAC Fluid Dynamics Database WWW Services[1] reported by John Coupland. Measurements down to $x = 1.495$ m which corresponds to $\mathrm{Re}_x \approx 94{,}000$, are made by Roach and Brierly [36]. The inlet velocity is 9.4 m/s and the pressure gradient is zero. The upstream turbulence intensity Tu = 6.0%, defined as $\mathrm{Tu} = \sqrt{2/3k}/U_{\mathrm{ref}}$, where U_{ref} indicates the reference velocity. The dissipation is set so that the decay of free-stream turbulence is in balance [36].

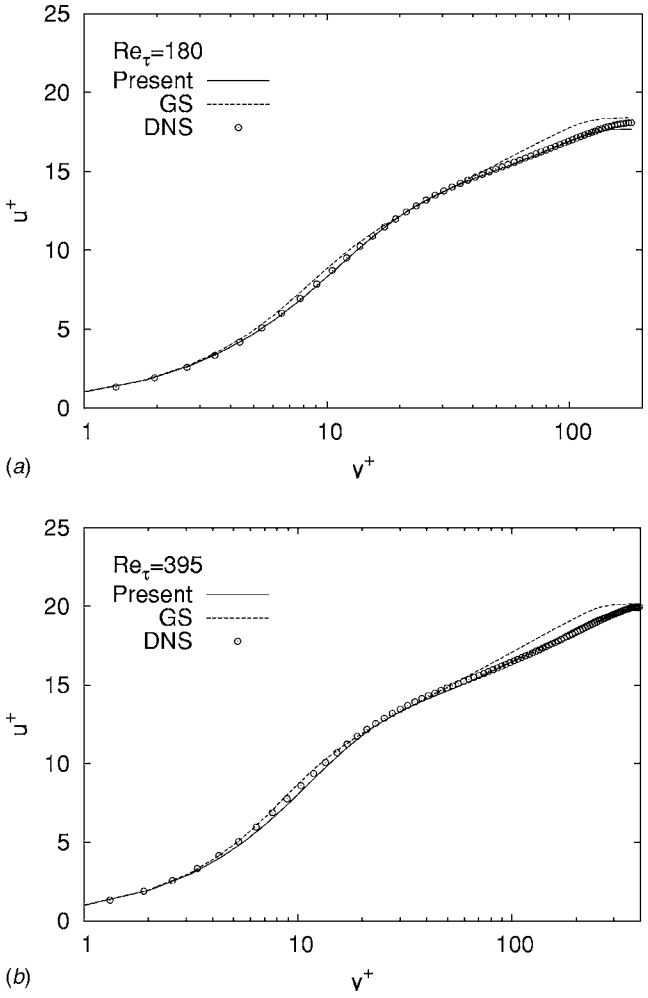

Fig. 6 Mean velocity profiles of channel flow

Computations begin 16 cm ahead of the leading edge and symmetric conditions are applied. The length and height of the grid are 1.6 m and 0.3 m, respectively. The near-wall node is located at $y^+ < 1.0$, except the point at the leading edge ($y^+ = 2.1$). The grid size is 96×64 and heavily clustered near the wall.

The predicted skin friction coefficients ($C_f = 2u_\tau^2/U_{\mathrm{ref}}^2$) are compared with the experimental data in Fig. 10. Note that the linear models, having the wall distance in the damping functions provide earlier transition than that seen in the experiment [37]. Although the present model uses the wall distance to characterize the near-wall viscous effects on turbulence, it returns the best skin friction in terms of its magnitude and trend. The physical reasoning is that the nonlinear eddy viscosity model resolves normal stress anisotropy and returns a substantially different response of turbulence to rotational and irrotational straining, in accord with reality [36].

3.3 Contracting Channel Flow. The model performance is then contrasted with the distributions of turbulent kinetic energy and Reynolds stress normal components along the contraction centerline of a plane converging channel flow. The experiment [38] claims that the grid is mounted about 18.7 mesh widths (i.e., 636 mm) upstream of the contraction inlet in order to achieve nearly isotropic turbulence at the inlet. Therefore, computations begin 636 mm ahead of the contraction inlet and a symmetric boundary condition is applied to the contraction centerline. The reference velocity is $U_{\mathrm{ref}} = 2.8$ m/s with an upstream turbulence intensity Tu = 10%. The boundary condition for the turbulent dis-

[1] http://ercoftac.mech.surrey.ac.uk/

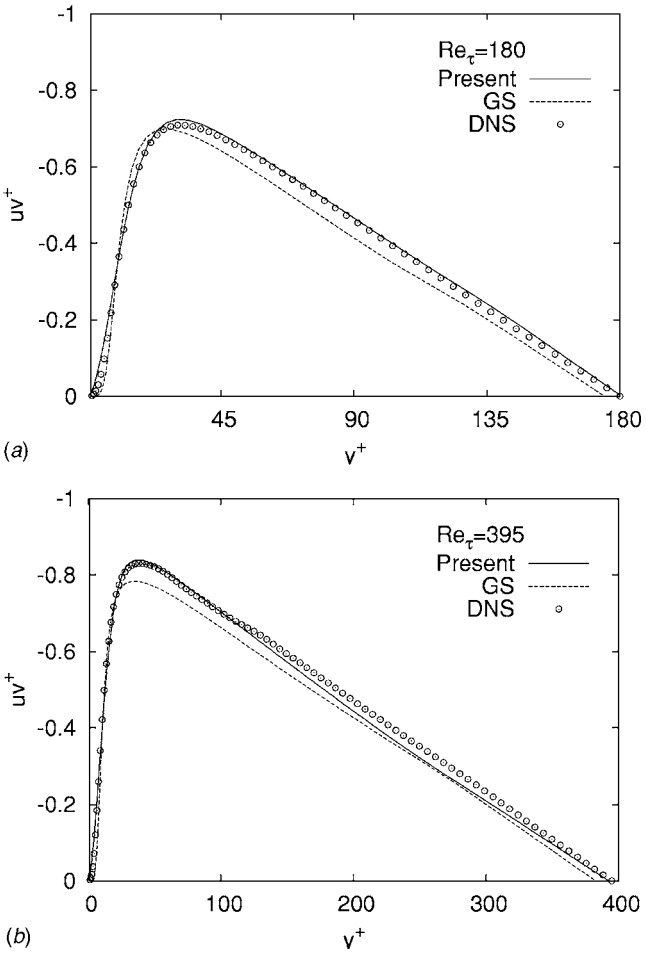

Fig. 7 Shear stress profiles of channel flow

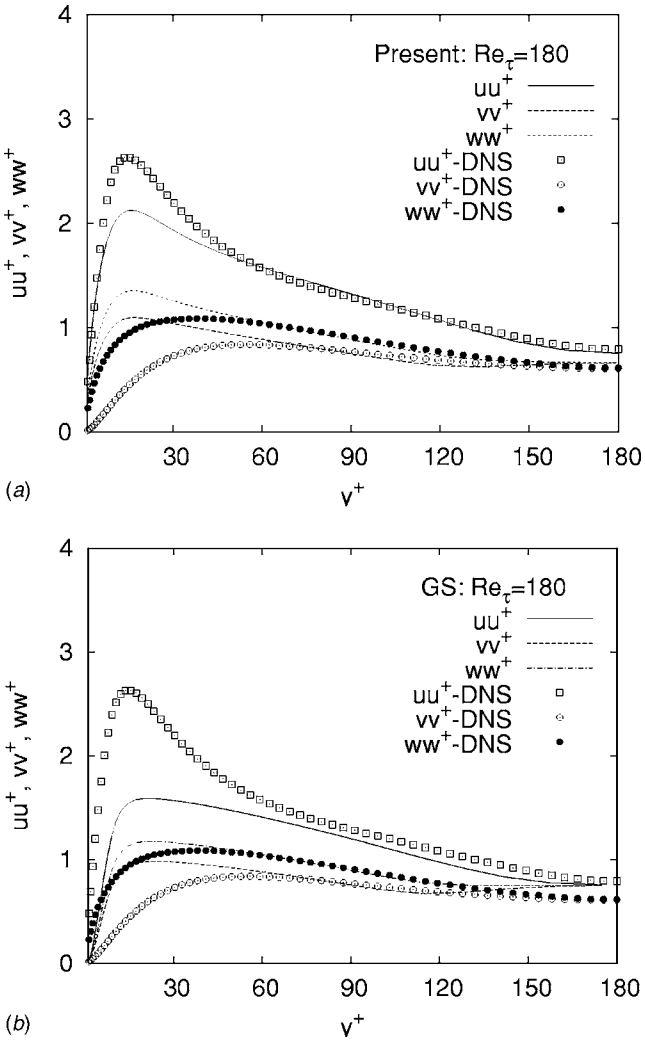

Fig. 8 Normal stress profiles in channel flow at Re$_\tau$=180

sipation at the inlet is evaluated from $\epsilon=0.09\rho k^2/(\mu R_\mu)$ with $R_\mu=\mu_T/\mu=30$, having the length scale $l_\epsilon=k^{1.5}/\epsilon\approx 15.45$ mm. At the contraction outlet the pressure is set to atmospheric pressure. The local contraction ratio $C=U/U_{\text{ref}}$ (where U is the local centerline velocity) with a half angle of 9.21 becomes approximately 13.8 at the outlet. A 352×96 nonuniform grid, heavily clustered near the solid wall, is used for the computations. The representative structured grid is displayed in Fig. 11.

Noteworthily, computations (for brevity, the results are not shown here) indicate that the specification of l_ϵ can have a profound effect on the predicted turbulent kinetic energy and Reynolds stresses. In other words, the computed results are considerably sensitive to the prescribed inlet dissipation length scale. This occurrence is coincident with Mehran's investigation [38]. Therefore, the choice of the inlet dissipation length scale $l_\epsilon=15.45$ mm is based on computational experiments.

Figure 12 shows the downstream development of the Reynolds stress normal components and the turbulent kinetic energy normalized by their contraction inlet values, respectively. As is observed, the experimental/computational intensities are characterized by the presence of a minimum at $C\approx 1.6$. The reason is that due to the nearly isotropic condition at the contraction inlet, the production of turbulent kinetic energy is almost zero. Close to $C\approx 1.6$, the rates of decay and turbulent production come to a balance. A closer inspection of the distribution indicates that the present model predictions are in broad agreement with the experimental data. Evidently, the applied boundary conditions are almost perfect for the present model. The GS model predicts $\overline{uu}$ on a reasonable level. However, it provides exaggerated k and $\overline{vv}$ at $C>1.8$. This unexpected behavior may be related to the eddy viscosity coefficient C_μ and $C_{\epsilon(1,2)}$. In principle, the contracting channel flow associated with a high rate of strain (i.e., the dominating term $S\approx \partial u/\partial x$) is characterized by strongly anisotropic turbulence. The inaccurately predicted energy components of the GS model are attributable to its inability in appropriately responding to strong anisotropy.

3.4 Asymmetric Plane Diffuser Flow. To validate the performance in complex separated and reattaching turbulent flows, the present model is applied to the flow in an asymmetric diffuser with an opening angle of 10 deg, for which measurements are available [39]. The expansion ratio of 4.7 is sufficient to produce a separation bubble on the deflected wall. Hence the configuration provides a test case for smooth, adverse pressure driven separation. The entrance to the diffuser consists of a plane channel to invoke fully developed flow with $\text{Re}=2.0\times 10^4$ based on the centerline velocity U_{ref} and the inlet channel height h. Computations involving a 120×72 nonuniform grid resolution are considered to be accurate to describe the flow characteristics. The length of the computational domain is 76 h. The thickness of the first cell remains below one in y^+ units on both the deflected and flat walls.

Figures 13(*a*) and 13(*b*) portray the predicted skin friction coefficients C_f. The performance of the present model evinces an encouraging qualitative agreement with measurements. As is observed, the GS model predicts C_f reasonably well along the deflected bottom wall. However, it gives the C_f distribution with a large overshoot along the straight top wall. Apparently, this am-

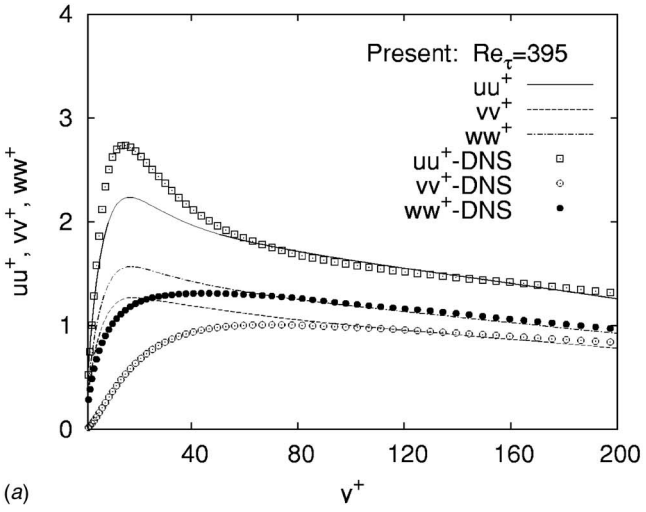

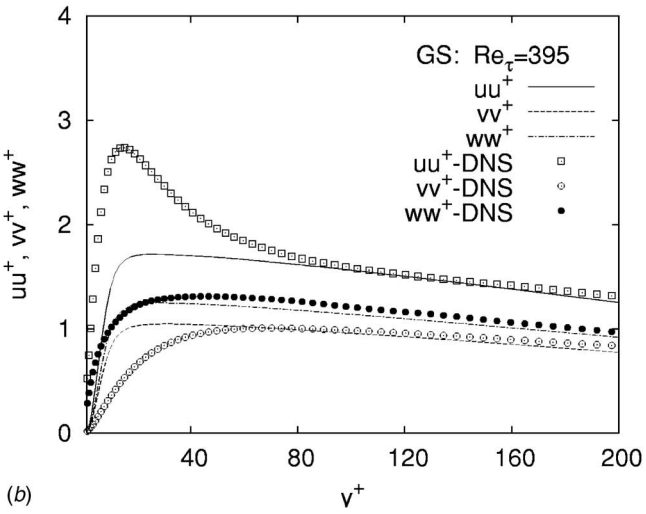

Fig. 9 Normal stress profiles in channel flow at Re$_\tau$=395

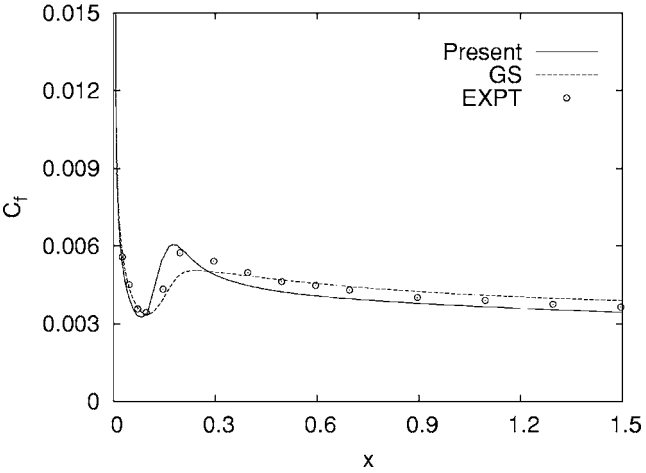

Fig. 10 Streamwise skin friction coefficient of boundary layer flow

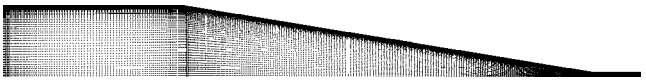

Fig. 11 Computational grid for contracting channel flow

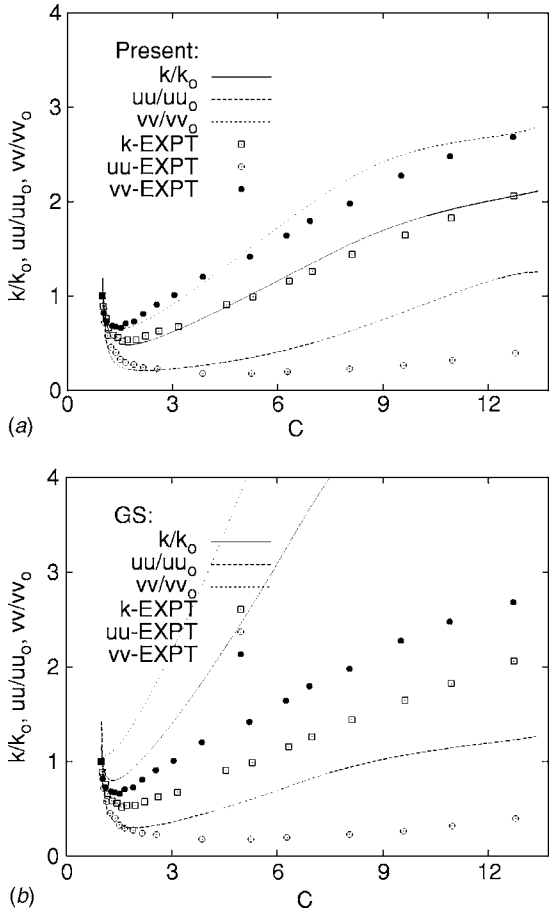

Fig. 12 Contracting channel flow: Reynolds normal stress and turbulent kinetic energy distributions along contraction centerline

biguous prediction regarding the GS model demands near-wall corrections in the ϵ equation to render the model results compatible with the experiment.

Figure 14 exhibits the mean velocity profiles at three representative positions. The performance of both the present and GS models in predicting the velocity profiles is indistinguishable and maintains good correspondence with the experimental data. It is a bit nebulous that the inaccurate prediction of the C_f distribution by the GS model has little effect on the u profiles. Comparisons are extended to the distributions of the Reynolds shear and normal stresses at different x/h locations, as displayed in Figs. 15 and 16. Overall, results indicate that although minor variations are evident between the two turbulence models, they generally produce very similar shear stress and energy components, having good agreement with the measured data.

3.5 Plane U-duct Flow. To further evaluate the performance, the model is applied to simulate the flow in a plane U duct with strong streamline curvature effects. The computations are conducted corresponding to the experimental case with Re=10^6, based on the channel height h=3.81 cm and reference velocity U_{ref}=31.8 m/s [40,41]. The turn has an inner radius of r_i =1.91 cm and an outer radius of r_o=5.72 cm. The finest grid employed is 288×160 and extends from $x/h=-4$ upstream of the bend to $x/h=12$ downstream. The maximum height of the first near-wall grid node is at $y^+<1.0$. The computational grid is shown in Fig. 17. The inlet boundary conditions are approximated from the experimental data, as depicted in Fig. 18. A coarser grid 144×80 is used to investigate grid sensitivity. However, no significant differences are found between the coarse and fine grid

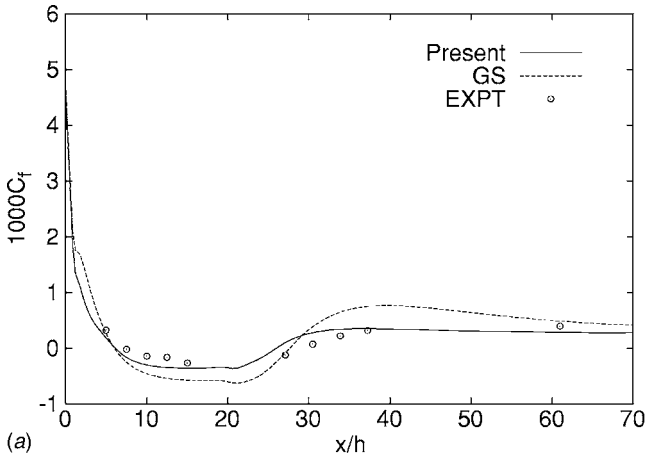

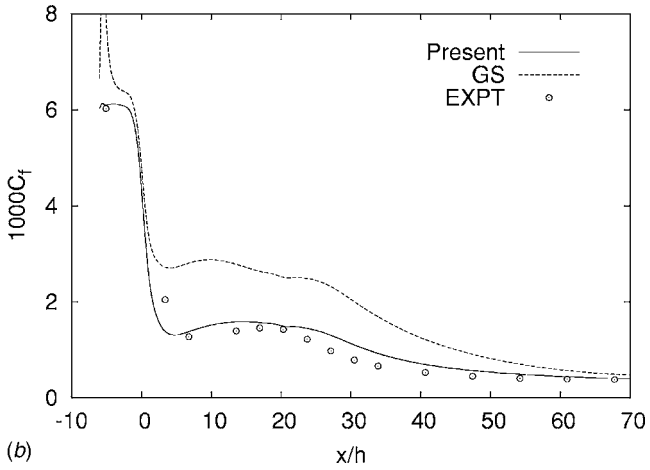

Fig. 13 Skin friction coefficients of diffuser flow: (*a*) along the deflected bottom wall and (*b*) along the straight top wall

results.

The predicted and experimental profiles of the streamwise velocity, shear stress and $500(\overline{uu}+\overline{vv})/U_{\text{ref}}^2$, referred to be as turbulent kinetic energy in the following for brevity, are shown in Figs. 19–21, respectively. At station $\theta=0$ deg ($x/h=0$, where the bend begins), both models predict the mean velocity in good agreement with each other and with experiment. The flow undergoes rapid acceleration near the inner wall and deceleration near the outer wall. The curvature effect on turbulence can be clearly observed from the experimental data. The convex curvature together with a large flow acceleration strongly attenuates the turbulence shear stress and kinetic energy near the inner wall. The present and GS models provide good predictions for $-\overline{uv}$ near the concave wall. However, they overpredict the magnitude significantly near the convex wall. For the kinetic energy profiles, both models yield similar results that agree with the measured data at the convex wall, but underpredict the magnitude of turbulence kinetic energy near the concave wall to a large extent.

As the flow reaches the $\theta=90$ deg position halfway around the bend, the curvature of the bend affects the turbulence significantly. The turbulence is damped near the convex wall, whereas turbulence enhancement occurs near the concave wall. Both models predict similar velocity profiles having reasonable agreement with experiment, although the velocity magnitude near the outer wall is underpredicted. None of the models is actively sensitive to the curvature effect, overpredicting/underpredicting the shear stress and kinetic energy levels at the convex/concave surface.

In fact, the flow envisages an adverse pressure gradient on the inner wall and a favorable pressure gradient on the outer wall downstream of $\theta=90$ deg [42]. Due to the severe adverse pressure gradient, as well as highly diminished turbulent shear stress, the boundary layer separates in the experiment around $\theta=150$ deg on the convex wall and extends to $x/h=1.0-1.5$ downstream of the end of bend. The velocity profiles predicted by the present and GS models at station $\theta=180$ deg agree well with the data. Nevertheless, there is a remarkable discrepancy between the numerical and experimental results in the turbulence quantities at the end of bend. The measured data show a very strong peak in the turbulent kinetic energy and shear stress profiles at the convex surface, which is not captured by any model. This large peak values probably result from large unsteadiness of the separation bubble, as reported in the experiment.

Computed and experimental friction coefficients C_f on the inner wall are plotted in Fig. 22. The s signifies the distance of the channel centerline from the U-duct inlet. As is observed, the present model result is close to that of experimental data. It nearly captures the separation and reattachment points, having comparable separation length in good agreement with the data. On the other hand, the GS model predicts the reattachment location somewhat too far downstream in comparison with experiment. As

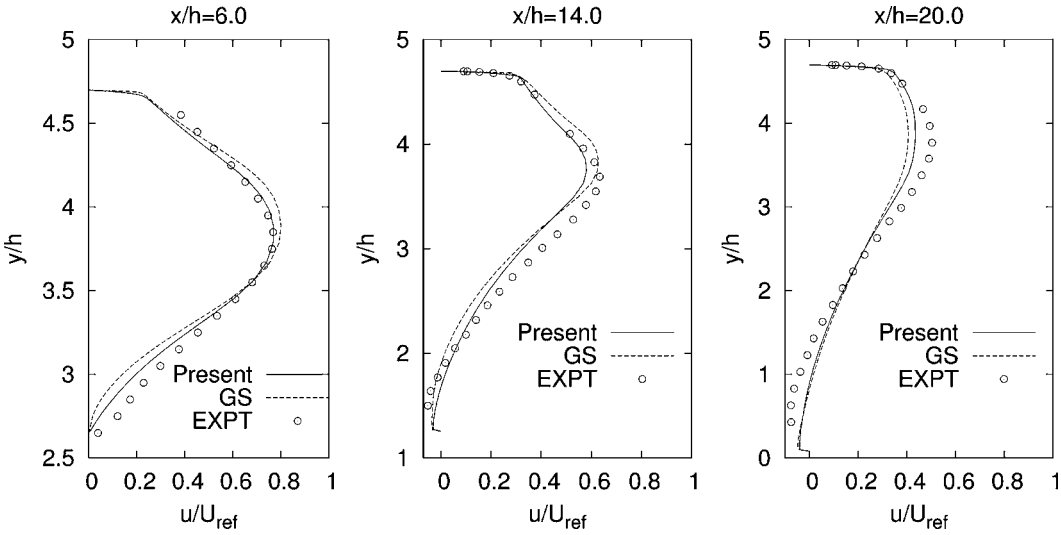

Fig. 14 Mean velocity profiles at selected locations for diffuser flow

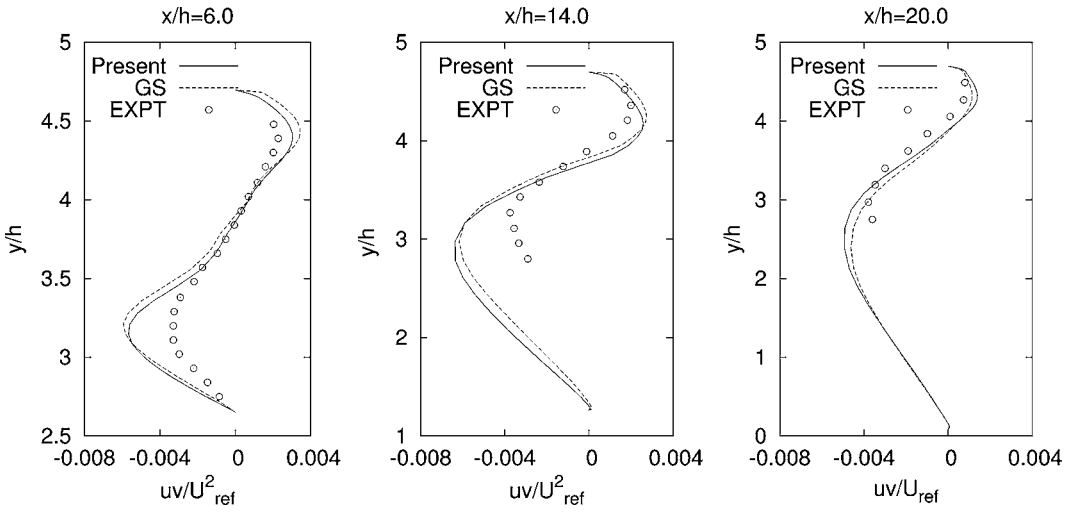

Fig. 15 Shear stress profiles at selected locations for diffuser flow

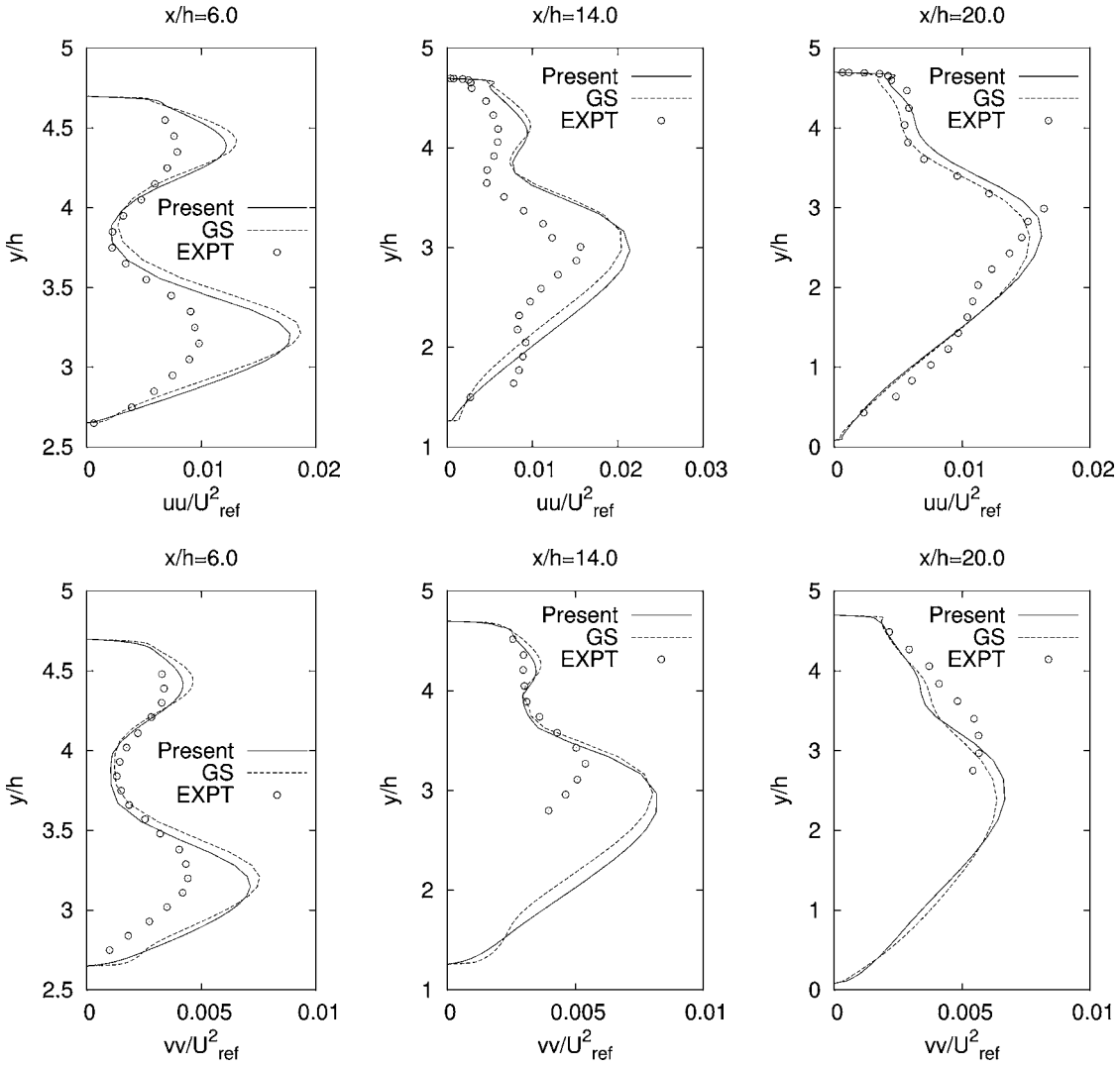

Fig. 16 Normal stress profiles at selected locations for diffuser flow

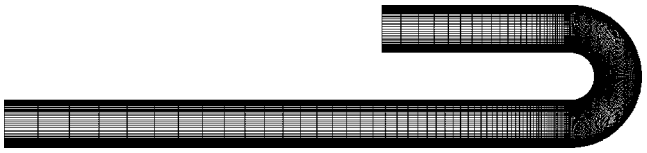

Fig. 17 Computational grid for U-duct flow

mentioned earlier, good agreement between the new model and data has been obtained in the flow separation and reattachment region, however, the glaring discrepancy is that the new model fails to recover the downstream experimental values in contrast to the GS model. This is probably because the model invokes a relatively small $(C_{\epsilon 2}-C_{\epsilon 1})$ compared with the GS model.

The static pressure coefficient C_p along the inner wall is shown in Fig. 23. On average, the GS model predicts the pressure level

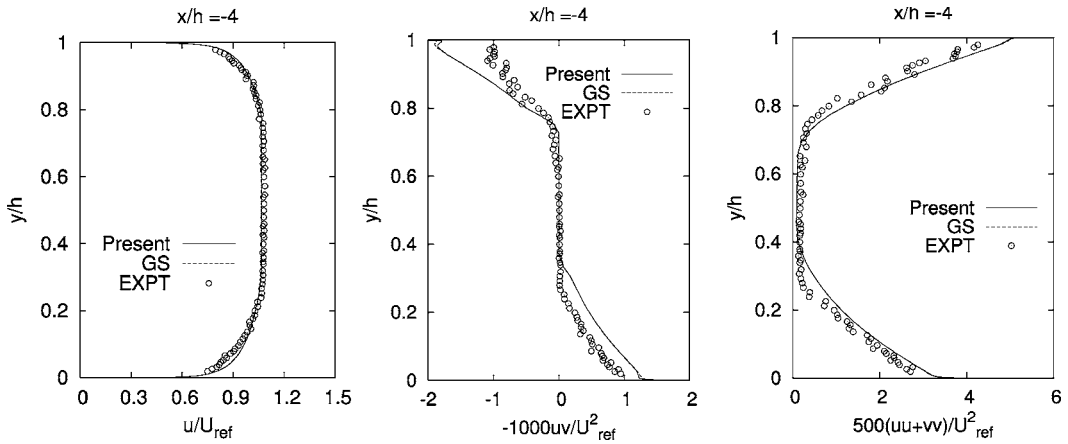

Fig. 18 Profiles at inlet for U-duct flow

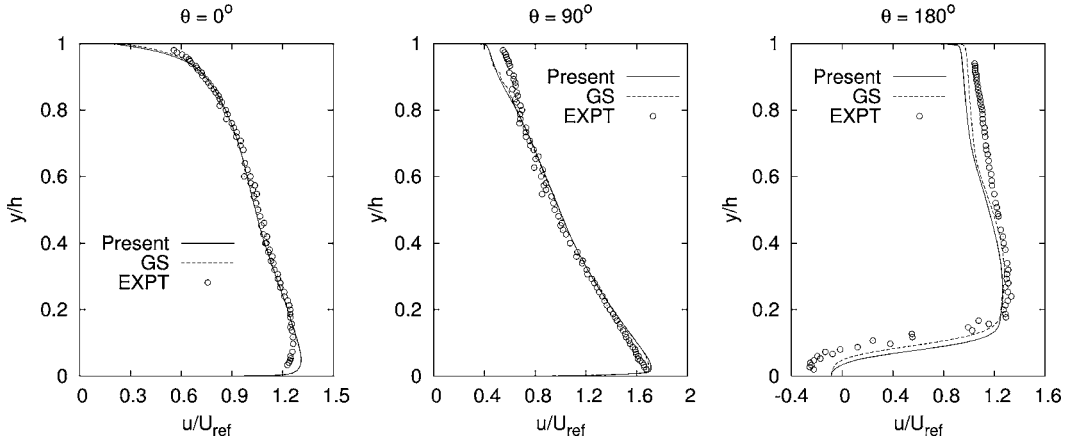

Fig. 19 Velocity profiles at selected locations for U-duct flow

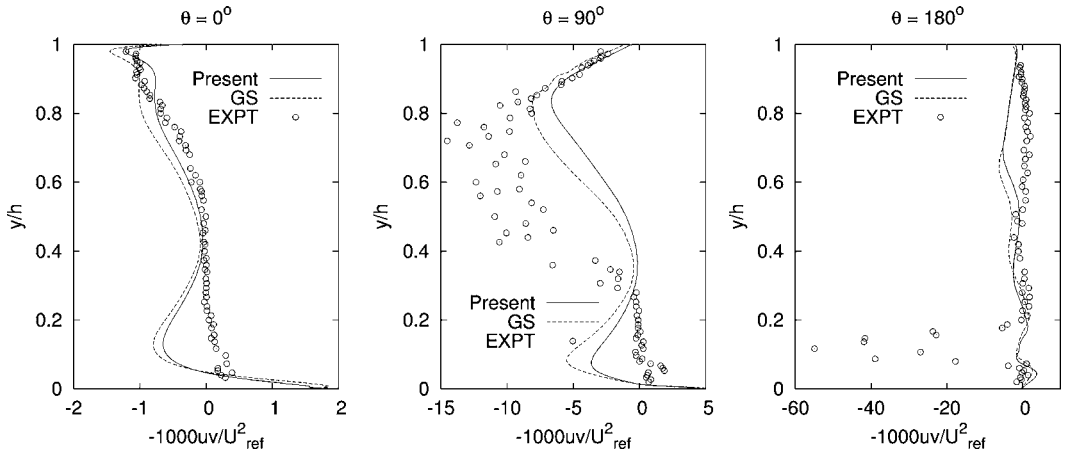

Fig. 20 Shear stress profiles at selected locations for U-duct flow

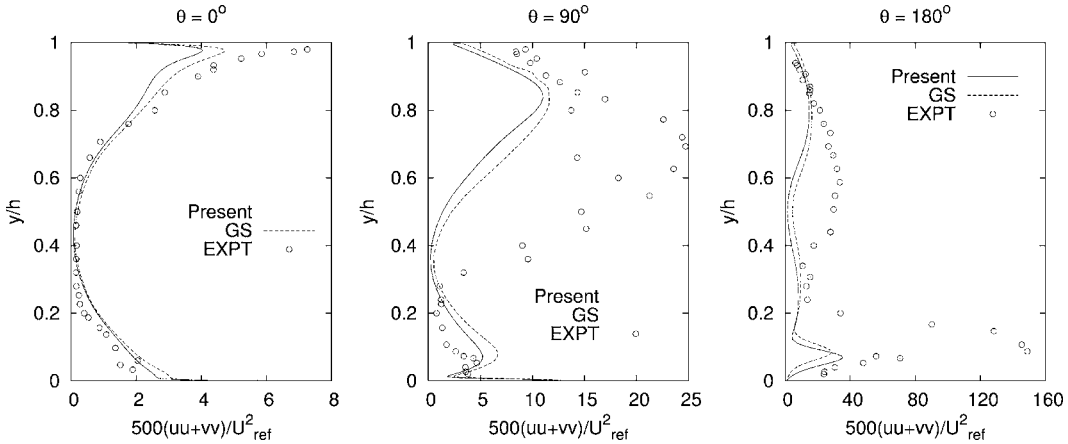

Fig. 21 Turbulence intensity profiles at selected locations for U-duct flow

downstream of the bend in slightly better agreement with experiment than that of the present model. However, the predicted C_p regarding the GS model near the bend exit is not accurate because it induces too slow a recovery after reattachment. The prediction by the present model seems to be a good compromise with the experiment.

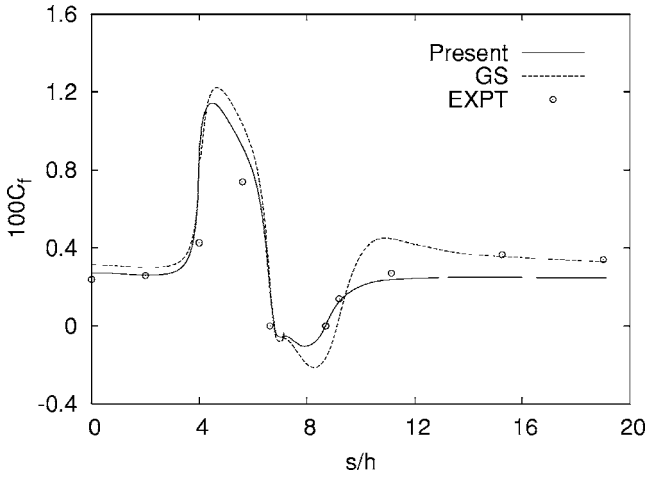

Fig. 22 Inner surface skin friction coefficient for U-duct flow

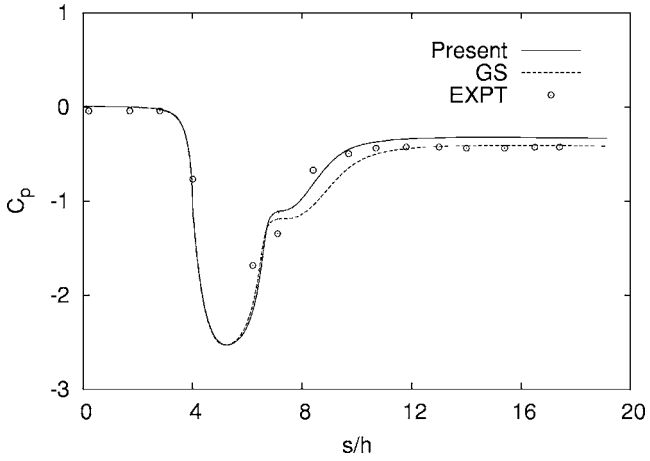

Fig. 23 Inner surface pressure coefficient for U-duct flow

4 Conclusions

The present model accounts for the near-wall and low-Reynolds number effects originating from the physical requirements. The model coefficient $C_{\epsilon 1}$ sensitized to both the mean strain rate and rotation rate fields, and a secondary positive source term in the dissipation equation enhance dissipation in near-wall regions. The newly calibrated relations for Π_b and P/ϵ serve to provide compatible changes with the coefficients $(\alpha_1 - \alpha_5)$. The combined effects of the anisotropic coefficients and the limiter function f_η associated with C_μ alleviate the numerical instabilities as is experienced by the original GS model and enforce the realizability constrains.

Contrasting the predicted results with measurements demonstrates that the present model reproduces successfully the skin-friction coefficients and turbulence quantities. The modeled Π_b and P/ϵ are deliberately included with the GS model to gain definitive advantages over convergence. Consequently, the present model differs from the GS model by a consistently formulated C_μ and the near-wall turbulence modeling. Nonetheless, model predictions compared with the experimental and DNS data for well-documented flows dictate that the present model offers considerable improvement over the GS model.

References

[1] Rodi, W., 1976, "A New Algebraic Relation for Calculating the Reynolds Stresses," Z. Angew. Math. Mech., **56**, pp. T219–221.

[2] Pope, S. B., 1975, "A More General Effective Viscosity Hypothesis," J. Fluid Mech., **72**, pp. 331–340.

[3] Launder, B. E., Reece, G., and Rodi, W., 1975, "Progress in the Development of a Reynolds Stress Closure," J. Fluid Mech., **68**, pp. 537–566.

[4] Gatski, T. B., and Speziale, C. G., 1993, "On the Explicit Algebraic Stress Models for Complex Turbulent Models," J. Fluid Mech., **254**, pp. 59–78.

[5] Lumley, J. L., 1978, "Computational Modeling of Turbulent Flows," Adv. Appl. Mech., **18**, pp. 124–176.

[6] Abid, R., Rumsey, C., and Gatski, T. B., 1995, "Prediction of Nonequilibrium Turbulent Flows With Explicit Algebraic Stress Models," AIAA J., **33**, pp. 2026–2031.

[7] Girimaji, S. S., 1996, "Fully Explicit and Self-Consistent Algebraic Reynolds Stress Model," Theor. Comput. Fluid Dyn., **8**, pp. 387–402.

[8] Jongen, T., and Gatski, T. B., 1998, "A New Approach to Characterizing the Equilibrium States of the Reynolds Stress Anisotropy in Homogeneous Turbulence," Theor. Comput. Fluid Dyn., **11**, pp. 31–47.

[9] Abid, R., Morrison, J. H., Gatski, T. B., and Speziale, C. G., 1997, "Prediction of Aerodynamic Flows With a New Explicit Algebraic Stress Model," J. Symb. Comput., **34**, pp. 2632–2635.

[10] Rumsey, C. L., Gatski, T. B., and Morrison, J. H., 2000, "Turbulence Model Predictions of Strongly Curved Flow in U-Duct," AIAA J., **38**, pp. 1394–1402.

[11] Kim, J., 1990, personal communication.

[12] Tavoularis, S., and Corrsin, A., 1981, "Experiments in Nearly Homogeneous Turbulent Shear Flow With a Uniform Mean Temperature Gradient, Part I," J. Fluid Mech., **104**, pp. 311–347.

[13] Abid, R., and Speziale, C. G., 1993, "Predicting Equilibrium States With Reynolds Stress Closures in Channel Flow and Homogeneous Shear Flow," Phys. Fluids A, **5**, pp. 1776–1782.
[14] Kim, J., Moin, P., and Moser, R., 1987, "Turbulence Statistics in Fully Developed Channel Flow at Low Reynolds Number," J. Fluid Mech., **177**, pp. 133–166.
[15] Lee, M. J., Kim, J., and Moin, P., 1990, "Structure of Turbulence at High Shear Rate," J. Fluid Mech., **216**, pp. 561–583.
[16] Rogers, M. M., and Moin, P., 1987, "The Structure of the Vorticity Field in Homogeneous Turbulent Flows," J. Fluid Mech., **176**, pp. 33–66.
[17] Rung, T., Thiele, F., and Fu, S., 1999, "On the Realizability of Nonlinear Stress-Strain Relationships for Reynolds Stress Closures," IAEA Bull., **60**, pp. 333–359.
[18] Rahman, M. M., Rautaheimo, P., and Siikonen, T., 1997, "Numerical Study of Turbulent Heat Transfer From a Confined Impinging Jet Using a Pseudo-Compressibility Method," 2nd Int. Sym. on Turbulence, Heat and Mass Transfer, edited by K. Hanjalic and T. W. J. Peeters, June 9-12, Delft University Press, The Netherlands, pp. 511–520.
[19] Rahman, M. M., and Siikonen, T., 2001, "Modifications for an Explicit Algebraic Stress Model," Int. J. Numer. Methods Fluids, **35**, pp. 221–245.
[20] Patel, V. C., Rodi, W., and Scheuerer, G., 1985, "Turbulence Models for Near-Wall and Low Reynolds Number Flow: A Review," AIAA J., **23**, pp. 1308–1319.
[21] Mansour, N. N., Kim, J., and Moin, P., 1988, "Reynolds-Stress and Dissipation-Rate Budgets in a Turbulent Channel Flow," J. Fluid Mech., **194**, pp. 15–44.
[22] Menter, F. R., 1994, "Two-Equation Eddy-Viscosity Turbulence Models for Engineering Applications," AIAA J., **32**, pp. 1598–1605.
[23] Mansour, N. N., Kim, J., and Moin, P., 1989, "Near-Wall k-ϵ Turbulence Modeling," AIAA J., **27**, pp. 1068–1073.
[24] Durbin, P. A., and Speziale, C. G., 1991, "Local Anisotropy in Strained at High Reynolds Numbers," J. Fluids Eng., **113**, pp. 707–709.
[25] Durbin, P. A., 1993, "A Reynolds-Stress Model for Near-Wall Turbulence," J. Fluid Mech., **249**, pp. 465–498.
[26] Ahn, J. W., Park, T. S., and Sung, H. J., 1997, "Application of a Near-Wall Turbulence Model to the Flows Over a Step With Inclined Wall," Int. J. Heat Fluid Flow, **18**, pp. 209–217.
[27] Yoshizawa, A., 1987, "Statistical Modeling of a Transport Equation for the Kinetic Energy Dissipation Rate," Phys. Fluids, **30**, pp. 628–631.
[28] Rahman, M. M., and Siikonen, T., 2000, "Improved Low-Reynolds-Number k-$\bar{\epsilon}$ Model," AIAA J., **38**, pp. 1298–1300.
[29] Yap, C. R., 1987, "Turbulent Heat and Momentum Transfer in Recirculating and Impinging Flows," Ph.D. thesis, Faculty of Technology, University of Manchester.
[30] Abe, K., Kondoh, T., and Nagano, Y., 1997, "On Reynolds-Stress Expressions and Near-Wall Scaling Parameters for Predicting Wall and Homogeneous Turbulent Shear Flows," Int. J. Heat Fluid Flow, **18**, pp. 266–282.
[31] Rahman, M. M., and Siikonen, T., 2001, "An Artificial Compressibility Method for Incompressible Flows," Numer. Heat Transfer, Part B, **40**, pp. 391–409.
[32] Roe, P. L., 1981, "Approximate Riemann Solvers, Parameter Vectors, and Difference Schemes," J. Comput. Phys., **43**, pp. 357–372S.
[33] Lombard, C., Bardina, J., Venkatapathy, E., and Oliger, J., 1983, "Multi-Dimensional Formulation of CSCM—An Upwind Flux Difference Eigenvector Split Method for the Compressible Navier-Stokes Equations," 6th AIAA Computational Fluid Dynamics Conference, AIAA Paper No. 83-1895-CP, pp. 649–664.
[34] Jameson, A., and Yoon, S., 1986, "Multigrid Solution of the Euler Equations Using Implicit Schemes," AIAA J., **24**, pp. 1737–1743.
[35] Siikonen, T., 1995, "An Application of Roe's Flux-Difference Splitting for $k-\epsilon$ Turbulence Model," Int. J. Numer. Methods Fluids, **21**, pp. 1017–1039.
[36] Chen, W. L., Lien, F. S., and Leschziner, M. A., 1998, "Nonlinear Eddy Viscosity Modelling of Transitional Boundary Layers Pertinent to Turbomachine Aerodynamics," Int. J. Heat Fluid Flow, **19**, pp. 297–306.
[37] Savill, A. M., 1993, "Some Recent Progress in the Turbulence Modeling of By-Pass Transition," in *Near-Wall Turbulent Flows*, R. M. C. So, C. G. Speziale, and B. E. Launder, eds., Elsevier, New York, pp. 829–848.
[38] Parsheh, M., 2001, "Flow in Contractions With Application to Headboxes," Ph.D. thesis, Royal Institute of Technology, Department of Mechanics, Faxenlaboratoriet, SE-100 44 Stockholm, Sweden.
[39] Buice, C., and Eaton, J. K., 1997, "Experimental Investigation of Flow Through an Asymmetric Plane Diffuser," Dept. of Mechanical Engineering, Thermoscience Div., Rept. TSD-107, Stanford University, CA.
[40] Monson, D. J., Seegmiller, H. L., McConnaughey, P. K., and Chen, Y. S., 1990, "Comparison of Experiment With Calculations Using Curvature-Corrected Zero and Two-Equation Turbulence Models for a Two-Dimensional U-Duct," AIAA Paper No. 90-1484.
[41] Monson, D. J., and Seegmiller, H. L., 1992, "An Experimental Investigation of Subsonic Flow in a Two-Dimensional U-Duct," NASA TM 103931.
[42] Luo, J., and Lakshminarayana, B., 1997, "Prediction of Strongly Curved Turbulent Duct Flows With Reynolds Stress Model," AIAA J., **35**, pp. 91–98.

Reynolds Stress Model in the Prediction of Confined Turbulent Swirling Flows

Ali M. Jawarneh
Assistant Professor
Department of Mechanical Engineering,
Hashemite University,
Zarqa 13115, Jordan
e-mail: jawarneh@hu.edu.jo

Georgios H. Vatistas
Professor
Department of Mechanical and Industrial Engineering,
Concordia University 1455 DeMaisonneuve Blvd. West,
Montreal, H3G 1M8 Canada
e-mail: vatistas@me.concordia.ca

Strongly swirling vortex chamber flows are examined experimentally and numerically using the Reynolds stress model (RSM). The predictions are compared against the experimental data in terms of the pressure drop across the chamber, the axial and tangential velocity components, and the radial pressure profiles. The overall agreement between the measurements and the predictions is reasonable. The predictions provided by the numerical model show clearly the forced and free vortex modes of the tangential velocity profile. The reverse flow (or back flow) inside the core and near the outlet, known from experiments, is captured by the numerical simulations. The swirl number has been found to have a measurable impact on the flow features. The vortex core size is shown to contract with the swirl number which leads to higher pressure drop, higher peak tangential velocity, and deeper radial pressure profiles near the axis of rotation. The adequate agreement between the experimental data and the simulations using RSM turbulence model provides a valid tool to study further these industrially important swirling flows. [DOI: 10.1115/1.2354530]

1 Introduction

Swirling flow occurs in many engineering applications, such as vortex separators, pumps, gas turbine combustors, furnaces, spray dryer, the vortex valve, the vortex combustor, and gas-core nuclear rocket. In modern combustors, swirl is used to produce good mixing and to improve the flame stability. In all confined vortex applications, it is important to understand adequately the overall flow field evolution as a function of both the geometrical and flow parameters. A good knowledge of these flows will improve the design and performance of a variety of vortex devices.

It is well known that the tangential velocity of the confined fluid changes from free to forced vortex as the flow approaches the axis of rotation. The static pressure in an attempt to balance the centrifugal force will reduce from a maximum value near the cylindrical wall of the chamber to a minimum on the axis of rotation. Depending on the inlet swirl intensity, the pressure inside the core might drop below the outside ambient, thus inducing a reverse flow. Escudier et al. [1] demonstrated experimentally the axial and swirl velocities distributions using Laser Doppler Anemomerty (LDA) measurements. The experiments were performed with water for a range of exit diameters. The observation revealed a remarkable change in the vortex structure as the exit diameter is reduced, where the vortex core size changes from a thick core to a thin core. In addition, the axial velocity was found able to develop profiles ranging from jetlike to wakelike shapes, thus revealing the evolution of the reverse flow. Vatistas [2] reported a model for single- or double-celled intense vortices, depending on the values of scaling constants. It was shown that the axial velocity component may attain profiles ranging from jetlike to wakelike. The last was an attempt to mathematically simulate the reverse flow conditions. Sullivan's [3] two-celled vortex model can also approximately simulate the direction reversal of the radial and axial velocity components near the axis of rotation.

The major obstacle in numerical modeling of complex turbulent swirling flows is the selection of appropriate turbulence closure models. In simple flow cases, the $k-\epsilon$ model performs well. However, for strongly swirling flows that involves severe streamline bending it fails. The last conclusion is clearly evident in a variety of studies; see for example the work of Nallasamy [4], Nejad et al. [5], and Weber [6]. A review of second-moment computations for engineering flows has been provided by Launder [7], Leschziner [8], and Ferziger and Peric [9]. The results of these computations demonstrate the superiority of RSM over eddy-viscosity models for curved flows, swirling flows and recirculating flows. Jones et al. [10] have studied the performance of second moment closure turbulence models for swirling flow in a cylindrical combustion chamber. The models are found to predict mean and turbulent flow quantities well. German and Mahmud [11] have shown that the overall agreement between the measurements and the predictions obtained with both the $k-\epsilon$ and Reynolds-stress turbulence models are reasonably good. However, some features of the isothermal and combusting flow fields are better predicted by the Reynolds-stress model. Jakirlic et al. [12] have shown numerically using three versions of the second-momentum closure and two eddy-viscosity models that the second-momentum models are superior. However, difficulties in predicting accurately the transformation from free- to forced-vortex modes or the determination of the normal stress components inside the core still remain. Vortex chamber flows at low Reynolds number via direct numerical simulations were investigated by Orland and Fatica [13]. Jones and Pascau [14] and Hoekstra et al. [15] used the $k-\epsilon$ turbulent model and a Reynolds stress transport equation model of a strong confined swirling flow. Once more, comparisons of the results with measurements show the superiority of the transport equation model, where $k-\epsilon$ gave large discrepancies between the measured and predicted velocity fields.

Since a Reynolds stress model (RSM) takes into consideration the effects of severe streamline bending due to swirl in a more appropriate way than the one- and two-equation models, it is best suited for the present study. The aim of this paper is to study the flow features in a vortex chamber experimentally and numerically using FLUENT (Fluent Inc.), and to compare the results obtained using a Reynolds stress model to available experimental data of vortex chambers operating under different swirl numbers. Performance assessment of the RSM in the predicting turbulent, strongly swirling vortex chamber flows will also be one of the objectives.

Contributed by the Fluids Engineering Division of ASME for publication in the JOURNAL OF FLUIDS ENGINEERING. Manuscript received February 9, 2005; final manuscript received March 22, 2006. Assoc. Editor: Ugo Piomelli.

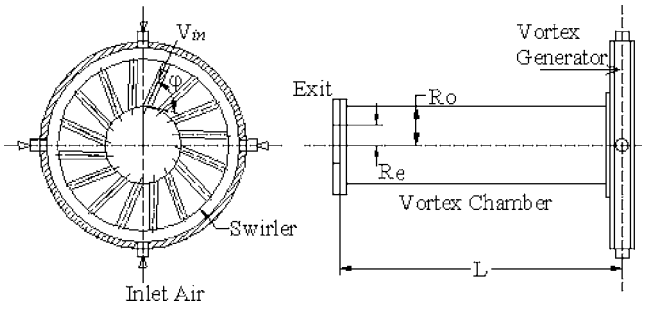

Fig. 1 Schematic of the vortex chamber

2 Experimental Setup

The experiments have been conducted using a jet-driven vortex chamber similar to the one utilized by Vatistas et al. [16]. The main difference between the two is that in the latest version, shown schematically in Fig. 1. It has a cylindrical configuration with constant cross-sectional area (R_o=7 cm) and a central axis outlet and circumferential inlets. Swirl is imparted to the fluid via the vortex generator shown in Figs. 1 and 2. It has four perpendicular air inlets where the compressed air is induced. The required set of inlet conditions is obtained by the insertion of the appropriate vortex generator blocks (swirler) into the vortex generator assembly a long the periphery of the vortex generator. A number of openings of a circular cross section (d_{in}) are drilled at a specified angle φ=30 deg. When the air flow passes through the swirlers, it is guided to enter the vortex chamber in the radial and tangential directions so that swirl is formed inside the vortex chamber. The swirler has 16 holes with diameter d_{in}=1.267 cm and inlet area (A_{in}=20.177 cm^2). Chamber diameter ratio (ξ), which is defined as the ratio of the diameter of a vortex chamber (D_o) to the diameter of the exit hole (D_e), was varied from ξ =2.5, 3.33, 3.67, 4.0, 5.01, 5.29, 5.80, 6.47, 7.08 to 7.45. Chamber aspect ratio (ζ), which is defined as the ratio of the chamber length L to the diameter of a vortex chamber (D_o) was fixed at ζ=3.00. Area ratio (α), which is defined as the ratio of the total inlet area (A_{in}) to the cross-sectional area of the vortex chamber A_o was fixed at α=0.131.

The measurements were made at inlet air flow rate Q_{in} =0.0187 m^3/s, which is corresponding to Reynolds number Re$_o$ =11,592, which is defined based on the average velocity as

$$\text{Re}_o = \frac{4\text{Q}_{\text{in}}}{\nu\pi\text{D}_o}$$

The static pressure is measured by a series of taps located ahead of the tangential ports and is averaged by connecting in parallel all the pressure pickup tubes into a common tube. The measurements of the mean gage pressure ($\Delta p = p_{in} - p_a$) were obtained using a U-tube filled with Meriam oil, having a specific gravity equal to 1.00. The estimated uncertainty is less than ±8% for the pressure drop measurements. A rotameter was used to measure the volumetric flow rate of the inlet air. This was carefully calibrated in standard conditions (1 atm and 20±0.5 % °C). For the flow rate used, the uncertainty was estimated to be ±2%.

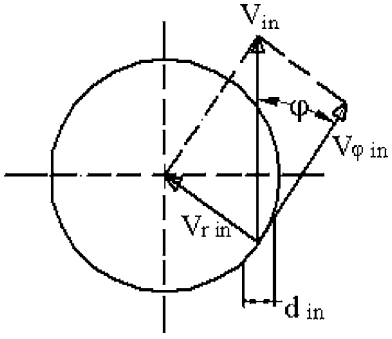

Fig. 2 Inlet flow boundary condition

3 Computational Details

Governing Equations. In Reynolds averaging, the solution variables in the instantaneous Navier-Stokes equations are decomposed into the mean and fluctuating components. For the velocity components: $u_i = \bar{u}_i + u_i'$ where $\bar{u}_i$ and u_i' are the mean and fluctuating velocity components. Likewise, for pressure and other scalar quantities: $\phi = \bar{\phi} + \phi'$ where ϕ denotes a scalar such as pressure. Substituting expressions of this form for the flow variables into the instantaneous continuity and momentum equations and dropping the over-bar on the mean velocity $\bar{u}$ yields the momentum equations. They can be written in Cartesian tensor form as

$$\frac{\partial}{\partial x_i}(\rho u_i) = 0 \tag{1}$$

$$\frac{\partial}{\partial x_j}(\rho u_i u_j) = -\frac{\partial P}{\partial x_i} + \frac{\partial}{\partial x_j}\left[\mu\left(\frac{\partial u_i}{\partial x_j} + \frac{\partial u_j}{\partial x_i} - \frac{2}{3}\delta_{ij}\frac{\partial u_l}{\partial x_l}\right)\right] + \frac{\partial}{\partial x_j}(-\rho\overline{u_i' u_j'}) \tag{2}$$

Equations (1) and (2) are called Reynolds-averaged Navier-Stokes (RANS) equations. Additional terms now appear that represent the effects of turbulence. These Reynolds stresses, $-\rho\overline{u_i' u_j'}$, must be modeled in order to close Eq. (2).

Reynolds Stress Transport Equations. The Reynolds stress model [17] involves calculation of the individual Reynolds stresses, $\overline{u_i' u_j'}$, using differential transport equations. The individual Reynolds stresses are then used to obtain closure of the Reynolds-averaged momentum (Eq. (2)). The transport equations for the transport of the Reynolds stresses, $-\rho\overline{u_i' u_j'}$, can be written as follows:

$$\underbrace{\frac{\partial}{\partial x_k}(\rho u_k \overline{u_i' u_j'})}_{C_{ij}} = \frac{\partial}{\partial x_k}\left(\frac{\mu_t}{\sigma_k}\frac{\partial \overline{u_i' u_j'}}{\partial x_k}\right) + \frac{\partial}{\partial x_k}\left[\mu\frac{\partial}{\partial x_k}(\overline{u_i' u_j'})\right] - \underbrace{\rho\left(\overline{u_i' u_k'}\frac{\partial u_j}{\partial x_k} + \overline{u_j' u_k'}\frac{\partial u_i}{\partial x_k}\right)}_{P_{ij}} + \Phi_{ij} - \frac{2}{3}\delta_{ij}\rho\epsilon \tag{3}$$

The term on the left-hand side of Eq. (3) represents the convection, the terms on the right-hand side represent the turbulent diffusion as proposed by Lien and Leschziner [18], molecular diffusion, stress production, pressure strain, and the dissipation, respectively. The pressure strain term Φ_{ij} is simplified according to the proposal by Gibson and Launder [19]:

$$\Phi_{ij} = \Phi_{ij,1} + \Phi_{ij,2} + \Phi_{ij,w} \tag{4}$$

$$\Phi_{ij,1} = -C_1\rho\frac{\epsilon}{k}\left(\overline{u_i' u_j'} - \frac{2}{3}\delta_{ij}k\right) \tag{5}$$

$$\Phi_{ij,2} = -C_2\left[(P_{ij} - C_{ij}) - \frac{1}{3}\delta_{ij}(P_{kk} - C_{kk})\right] \tag{6}$$

$$\Phi_{ij,w} = C_1'\frac{\epsilon}{k}\left(\overline{u_k'u_m'}n_k n_m\delta_{ij} - \frac{3}{2}\overline{u_i'u_k'}n_j n_k - \frac{3}{2}\overline{u_i'u_k'}n_i n_k\right)\frac{k^{3/2}}{C_l\epsilon d} + C_2'\left(\phi_{km,2}n_k n_m\delta_{ij} - \frac{3}{2}\phi_{ik,2}n_j n_k - \frac{3}{2}\phi_{jk,2}n_j n_k\right)\frac{k^{3/2}}{C_l\epsilon d} \quad (7)$$

where $C_1=1.8$, $C_1'=0.5$, $C_2'=0.3$, n_k is the x_k component of the unit normal to the wall, d is the normal distance to the wall, and $C_l=C_\mu^{3/4}/\kappa$, where $C_\mu=0.09$ and κ is the von Kármán constant (=0.4187). The scalar dissipation rate ϵ is computed with a model transport equation similar to that used in the standard $k-\epsilon$ model

$$\frac{\partial}{\partial x_i}(\rho\epsilon u_i) = \frac{\partial}{\partial x_j}\left[\left(\mu + \frac{\mu_t}{\sigma_\epsilon}\right)\frac{\partial\epsilon}{\partial x_j}\right] C_{\epsilon 1}\frac{1}{2}P_{ii}\frac{\epsilon}{k} - C_{\epsilon 2}\rho\frac{\epsilon^2}{k} \quad (8)$$

where $\sigma_k=1.0$, $C_{\epsilon 1}=1.44$, and $C_{\epsilon 2}=1.92$ are constants taken from Launder and Spalding [20]. When the turbulence kinetic energy is needed for modeling a specific term, it is obtained by taking the trace of the Reynolds stress tensor

$$k = \frac{1}{2}\overline{u_i'u_i'} \quad (9)$$

The turbulent viscosity μ_t is computed similarly to the $k-\epsilon$ model

$$\mu_t = \rho C_\mu\frac{k^2}{\epsilon} \quad (10)$$

where $C_\mu=0.09$. Because of severe pressure gradients, the nonequilibrium wall functions were used near wall as proposed by Kim and Choudhury [21].

Inlet Conditions for the Reynolds Stresses. Whenever flow enters the domain, the values for individual Reynolds stresses, $\overline{u_i'u_j'}$, and for the turbulence dissipation rate (ϵ) can be input directly or derived from the turbulence intensity and characteristic length. The turbulence intensity I can be estimated from the following formula derived from an empirical correlation for pipe flows

$$I = \frac{u'}{V_{\text{avg}}} = 0.16(\text{Re}_o)^{-1/8} \quad (11)$$

The turbulence length scale l is a physical quantity related to the size of the large eddies that contain the energy in turbulent flows. An approximate relationship between l and the physical size of the vortex chamber diameter D_o is

$$l = 0.07D_o \quad (12)$$

The relationship between the turbulent kinetic energy k and turbulence intensity I is

$$k = \frac{3}{2}(V_{\text{avg}}I)^2 \quad (13)$$

where V_{avg} is the average axial velocity. The turbulence dissipation rate ϵ can be determined as

$$\epsilon = C_\mu^{3/4}\frac{k^{3/2}}{l} \quad (14)$$

The values of the Reynolds stresses explicitly at the inlet are given by

$$\overline{u_i'u_j'} = 0 \quad \text{and} \quad \overline{u_i'^2} = \frac{2}{3}k \quad (15)$$

4 Turbulence Modeling in Swirling Flows

The problem is considered to be an incompressible, steady, axisymmetric, and turbulent swirling flow. In this case, we can model the flow in two-dimensional (2D) (i.e., solve the axisymmetric swirl problem) and incorporate the prediction of the swirl velocity; see Fig. 3.

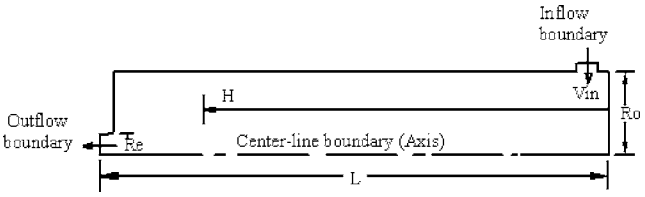

Fig. 3 Computational domain

The difficulties associated with the solution of strongly swirling flows can be attributed to high degree of coupling in the momentum equations. High fluid rotation gives rise to large radial pressure gradient, which drives the flow in the meridional plane. This, in turn, determines the distribution of the swirl in the field. Numerical instabilities that are attributed to momentum coupling require special solution techniques in order to obtain a converged solution. Hence, a segregated, implicit solver, which is wellsuited for the sharp pressure, and velocity gradients are more appropriate for the flow under consideration. The mesh is sufficiently must be also sufficiently refined in order to resolve the expected large flow parameter gradients. The under-relaxation parameters on the velocities were selected 0.3–0.5 for the radial and axial, and 0.9 for the azimuthal velocity components.

There is a significant amount of swirl in the chamber. The appropriate choice depends on the strength of the swirl, which can be gaged by the swirl number. To characterize the degree of swirling flow in a vortex chamber, a swirl number S is introduced. Based on Gupta et al. [22] definition,

$$S = \frac{G_\theta}{G_z\text{Re}} \quad (16)$$

where G_θ is the axial flux of swirl momentum,

$$G_\theta = \int_0^{R_o}\rho V_z V_\varphi r^2 dr \quad (17)$$

G_z is the axial flux of axial momentum,

$$G_z = \int_0^{R_o}\rho V_z^2 r dr \quad (18)$$

To simplify the calculation of swirl number, the free-swirl velocity profile and the average axial velocity are assumed inside the vortex chamber.

$$V_\varphi = \frac{V_{\varphi\text{in}}R_o}{r}, \quad V_z = V_{\text{avg}} \quad (19)$$

The ultimate form of the swirl number (S) can be determined as

$$S = \frac{V_{\varphi\text{in}}}{V_{\text{avg}}}\zeta \quad (20)$$

Then, the simulations were performed for different swirl numbers varied from $S=12.5-20$.

Grid Generation. A major challenge in calculating the flow inside the vortex chamber is providing an adequate description of the geometry. Because of the complex geometry of the vortex generator, control over the grid is limited, making it difficult to reduce the size of mesh without losing accuracy in the results. Also, the grid size is limited by the computer memory available. This leads to use axisymmetric problem, the formulation of 2D grid generation are shown in Fig. 4. Triangular mesh elements and an unstructured grid were used. A grid independent solution study was made by performing the simulations for three different grids consisting of 30,000, 43,000, and 50,000 nodes. The mean swirl velocity for the three different grid sizes is shown in the Fig. 5.

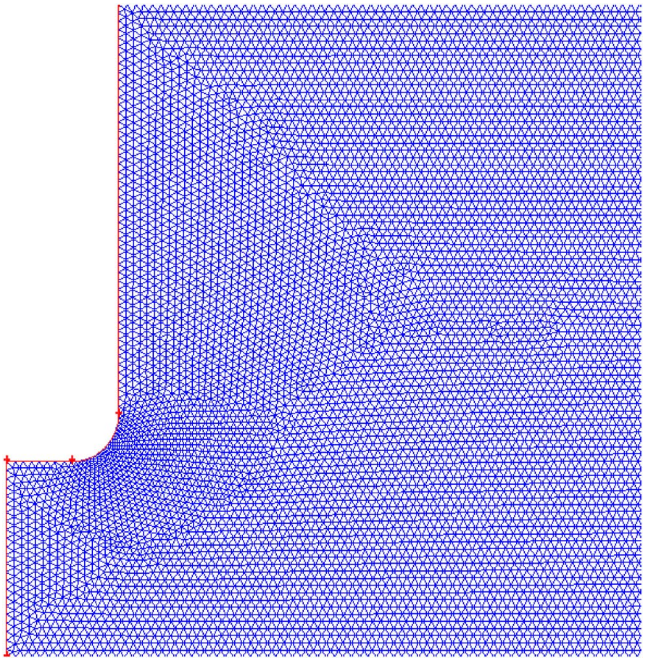

Fig. 4 Computational grid near the exit

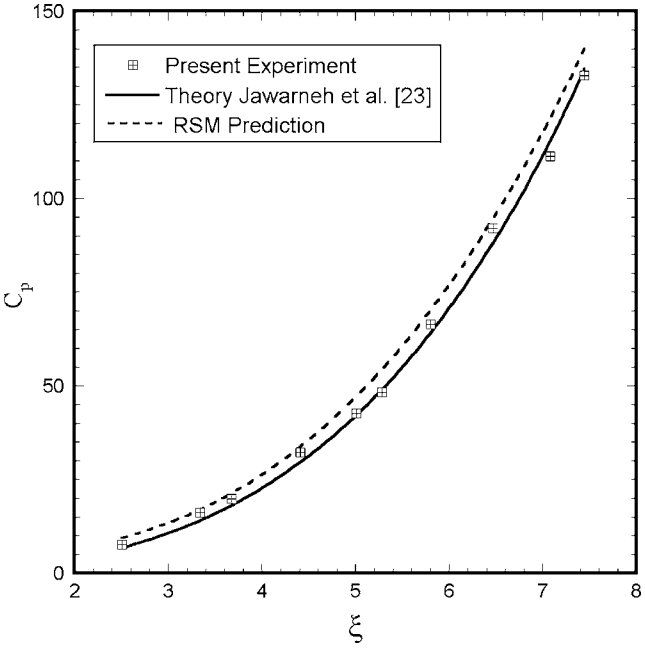

Fig. 6 Pressure drop coefficient

Boundary Conditions. Boundary conditions have to be specified in order to solve the governing equations; see Fig. 3. At the inlet, the values can be calculated from the given conditions at the inlet, boundary; see Fig. 2. The total inlet velocity vector (V_{in}) has two components $V_{r,in}$ and $V_{\varphi,in}$ and they are related to each other by:

$$V_{\varphi,in} = V_{in}\cos\varphi, \quad V_{r,in} = V_{in}\sin\varphi, \quad V_{in} = \frac{Q_{in}}{A_{in}} \tag{21}$$

However, at the outlet boundary there is no information about the variables and some assumptions have to be made. The diffusion fluxes in the direction normal to the exit plane are assumed to be zero. The pressure at the outlet boundary is calculated from the assumption that radial velocity at the exit is neglected since it does not have the space to develop, so that the pressure gradient from r momentum is given by

$$\frac{\partial p}{\partial r} = \frac{\rho V_\varphi^2}{r} \tag{22}$$

At the solids walls, the no-slip condition was applied where the velocities at the walls were specified to be zero. The centerline boundary was considered axis of symmetry.

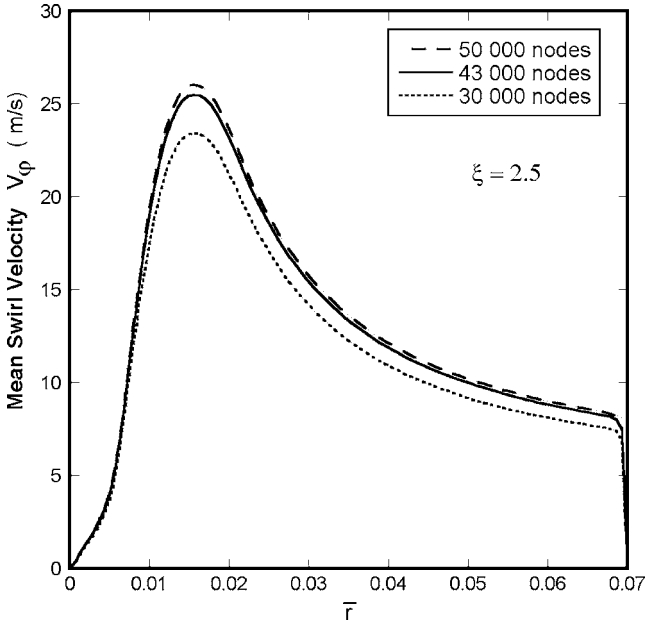

Fig. 5 Grid independent solution study

Discretization Scheme. The pressure-velocity coupling is handled by using the SIMPLE-algorithm, the pressure staggering option scheme was used for the pressure interpolation, the first order upwind schemes were used for momentum, swirl velocity, turbulence kinetic energy, turbulence dissipation rate, and Reynolds stresses. Convergence was assumed when the residual of the equations dropped more than 3 orders of magnitude.

5 Results and Discussion

Pressure Drop Coefficient. Pressure drop or loss can be regarded as energy loss from the point of view of energy conservation. In the vortex chamber, pressure drop occurs mainly through the dissipation of the swirl velocity as proposed by Jawarneh et al. [23]. The pressure drop coefficient is defined as

$$C_p = \frac{2\Delta p}{\rho V_{in}^2}$$

The estimated uncertainty for the pressure drop coefficient (C_p) has appeared at the maximum of ±9%. Figure 6 compares the present experimental data to the RSM prediction of the pressure drop coefficient (C_p) for aspect ratio ζ=3.0 and inlet angle φ =30 deg. It is clear that as the diameter ratio (ξ) increases, the pressure coefficient (C_p) increases. Stronger vortices will be produced by increasing the diameter ratio, resulting in a higher tangential velocity and hence a higher pressure drop. It can be seen that the Reynolds stress model gives good agreement with the experimental data and the percentage difference error between the predicted and experiments is $<$10%.

Mean Swirl Velocities Profiles. The predicted and measured radial profiles of mean tangential, axial velocities and radial pres-

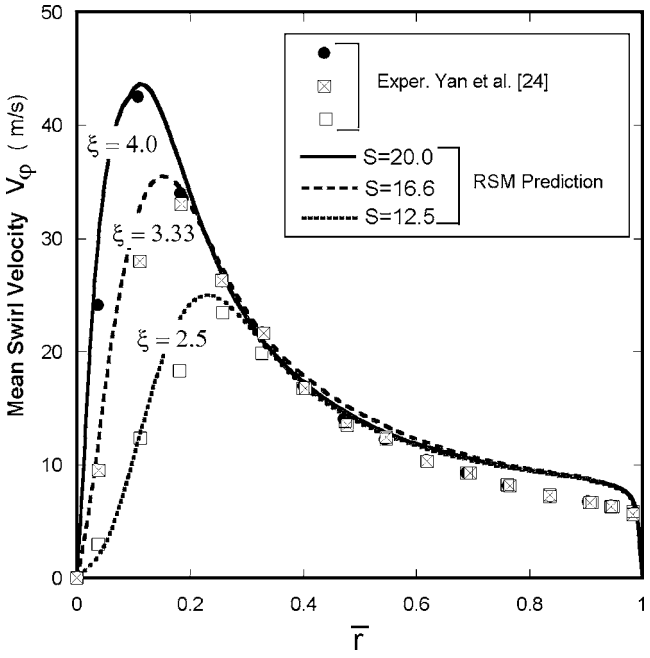

Fig. 7 Mean swirl velocity

sure for the chamber at station $H=0.8L$ are shown in Fig. 7, 8, and 10, respectively. Figure 7 shows the mean swirl velocities profiles for the configuration ($\varphi=30$ deg, $\zeta=3.0$, $\alpha=0.131$) at Reynolds number ($\mathrm{Re}_o=11{,}592$) and the predicted swirl velocity results are compared with available experiments data (LDA) from Yan et al. [24] at three diameter ratios ($\xi=2.5,3.33,4.0$). It is shown the ability of RSM to capture the free-vortex and forced-vortex regions. Because of the intense swirl by increasing the swirl number (S), a high level of swirl momentum is transported around the centreline and the consequence is the formation of the intense swirling vortex along the center-line. In the latter figure, the peak tangential velocity increases with increasing the diameter ratio or the swirl number, and the location where the tangential velocity is a maximum moves towards the vortex chamber center.

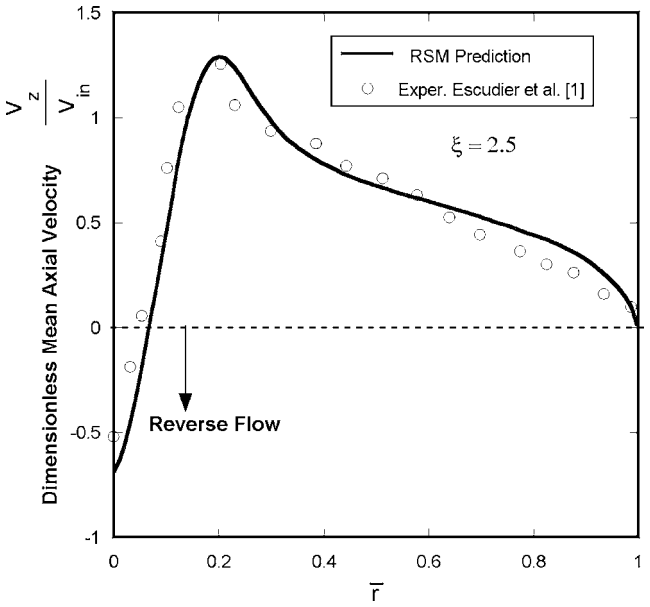

Fig. 8 Dimensionless mean axial velocity

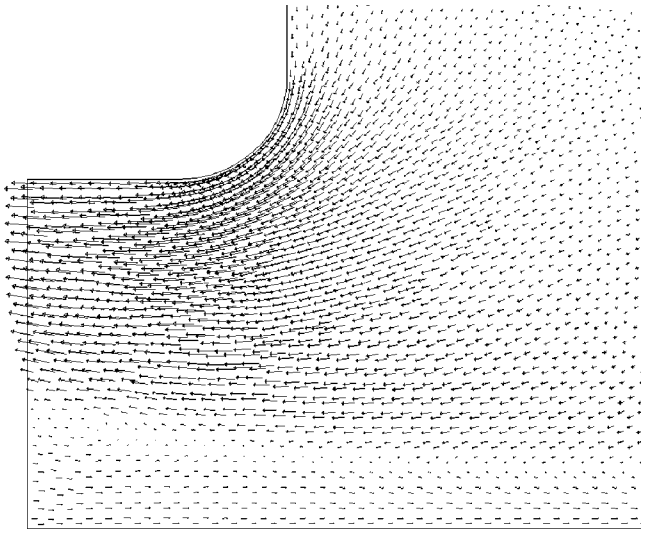

Fig. 9 Predicted axial velocity vectors near the exit

Mean Axial Velocity Profile. The mean axial velocity component is able to develop profile ranging from jetlike to wakelike shape as shown in Fig. 8. The predicted axial velocity results are compared with available experiments data (LDA) from Escudier et al. [1]. The reverse flow (backflow) in the vortex core is due to the reduction of static pressure to values that are below the ambient and the stagnation point is appeared clearly in Fig. 8. Figure 9 shows the predicted axial velocities vectors near the chamber exit, a flow-reversal region is found in the vortex core.

Mean Radial Pressure Profiles. The following analysis illustrates the mean pressure distribution profiles (Π), and the predicted radial pressure will be compared to available experimental data. The mean pressure distribution profiles (Π) is defined according to the following equation:

$$\Pi(\bar{r}) = \frac{2[p(\bar{r}) - p(\bar{r}=1)]}{\rho V_{\mathrm{in}}^2}, \quad \text{where } \bar{r} = \frac{r}{R_o}$$

Figure 10 compares the predicted radial pressure coefficient (Π) to the experimental results [25,26] at three diameter ratios ($\xi=2.5,3.33,4.0$). A good agreement with the experiments is observed especially with high-diameter ratios (i.e., $\xi=4.0$), where the flow field is under strong swirling condition. Increasing the swirl number (S) leads to deeper pressure profiles.

6 Conclusions

Confined vortex flow inside the vortex chamber was investigated both experimentally and computationally at different swirl ratio. The RSM model is able to predict the flow features, such as the press drop, tangential, axial velocities, and the radial pressure profiles. The prediction shows the behavior of the mean tangential velocity distribution where a forced-vortex inside the core and a free-vortex outside the core are existed and agree with the experimental data. The reverse-flow, which is associated with the axial velocity profile, is captured inside the core region and close to the chamber exit. The swirl number has sufficient impact of the flow features, the vortex core size contracts with increasing the swirl number leads to more pressure drop (energy loss), the peak tangential velocity grows up, and deeper radial pressure profiles. A comparison of the results with measurement shows clearly the superiority of the Reynolds-stress turbulence model in capturing the major features of a confined, strongly swirling flow.

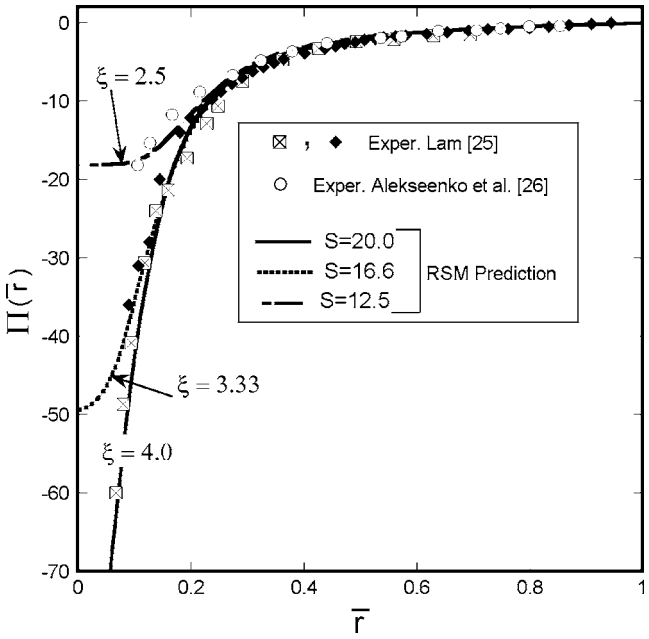

Fig. 10 Mean radial pressure

Nomenclature

A_o = cross-sectional area of the vortex chamber
A_{in} = total inlet area
C_p = pressure coefficient $(2\Delta p/\rho V_{\text{in}}^2)$
D_e = diameter of the exit port (2Re)
D_{in} = diameter of the inlet port
D_o = chamber diameter $(2R_o)$
k = turbulent kinetic energy
L = chamber length
p = static pressure
p_a = ambient static pressure
p_{in} = static pressure at the inlet
Q_{in} = inlet volumetric flow rate
r, φ, z = radial, tangential and axial coordinate respectively
$\bar{r}$ = normalized radius (r/R_o)
R_e = radius of exit port
Re_o = Reynolds number $(\text{Re}_o = 4Q_{\text{in}}/\nu\pi D_o)$
R_o = radius of the chamber
S = swirl number
u_i, u_j, u_k = velocity components in Cartesian coordinates
V_φ, V_z = mean tangential and axial velocity components
V_{in} = total velocity vector at the inlet
V_{avg} = average axial velocity
$V_{\varphi,\text{in}}$ = inlet tangential velocity component
$V_{\text{r,in}}$ = inlet radial velocity component

Greek Symbols

α = area ratio (A_{in}/A_o)
Δp = static pressure difference $(P_{\text{in}} - P_a)$
Π = radial pressure $(2[p(\bar{r}) - p(\bar{r}=1)]/\rho V_{\text{in}}^2)$
δ_{ij} = Kronecker delta
ϵ = turbulence dissipation rate
ν = kinematics viscosity
μ = dynamic viscosity
μ_t = eddy or turbulent viscosity
ρ = density of the fluid
φ = inlet angle
ζ = aspect ratio (L/D_o)
ξ = diameter ratio (D_o/D_e)

References

[1] Escudier, M. P., Bornstein, J., and Zehender, N., 1980, "Observations and LDA Measurements of Confined Turbulent Vortex Flow," J. Fluid Mech., **98**, pp. 49–63.
[2] Vatistas, G. H., 1998, "New Model for Intense Self-Similar Vortices," J. Propul. Power, **14**(4), pp. 462–469.
[3] Sullivan, R. D., 1959, "A Two-Cell Vortex Solution of the Navier-Stokes Equations," J. Aerosp. Sci., **26**(11), pp. 767–768.
[4] Nallasamy, M., 1987, "Turbulence Models and Their Applications to the Prediction of Internal Flows," Comput. Fluids, **15**(2), pp. 151–194.
[5] Nejad, A. S., Vanka, S. P., Favaloro, S. C., Samimy, M., and Langenfeld, C., 1989, "Application of Laser Velocimetry for Characterization of Confined Swirling Flow," Trans. ASME: J. Eng. Gas Turbines Power, **111**, pp. 36–45.
[6] Weber, R., 1990, "Assessment of Turbulence Modeling for Engineering Prediction of Swirling Vortices in the Near Burner Zone," Int. J. Heat Fluid Flow, **11**(3), pp. 225–235.
[7] Launder, B. E., 1989, "Second-Moment Closure and Its Use in Modelling Turbulent Industrial Flows," Int. J. Numer. Methods Fluids, **9**(8), pp. 963–985.
[8] Leschziner, M. A., 1990, "Modelling Engineering Flows With Reynolds Stress Turbulence Closure," J. Wind. Eng. Ind. Aerodyn., **35**(1), pp. 21–47.
[9] Ferziger, J. H., and Peric, M., 1999, *Computational Methods for Fluid Dynamics*, 2nd ed., Springer-Verlag, Berlin.
[10] Jones, L. N., Gaskell, P. H., Thompson, H. M., Gu, X. J., and Emerson, D. R., 2005, "Anisotropic, Isothermal, Turbulent Swirling Flow in a Complex Combustor Geometry," Int. J. Numer. Methods Fluids, **47**, pp. 1053–1059.
[11] German, A. E., and Mahmud, T., 2005, "Modelling of Non-Premixed Swirl Burner Flows Using a Reynolds-Stress Turbulence Closure," Fuel, **84**(5), pp. 583–594.
[12] Jakirlic, S., Hanjalic, K., and Tropea, C., 2002, "Modeling Rotating and Swirling Turbulent Flows: A Perpetual Challenge," AIAA J., **40**(10), pp. 1984–1996.
[13] Orland, P., and Fatica, M., 1997, "Direct Simulation of Turbulent Flow in a Pipe Rotating About Its Axis," J. Fluid Mech., **343**, pp. 43–72.
[14] Jones, W. P., and Pascau, A., 1989, "Calculation of Confined Swirling Flows With a Second Momentum Closure," ASME Trans. J. Fluids Eng., **111**, pp. 248–255.
[15] Hoekstra, A. J., Derksen, H. E. A., and Akker, V. D., 1999, "An Experimental and Numerical Study of Turbulent Swirling Flow in Gas Cyclones," Chem. Eng. Sci., **54**, pp. 2055–2065.
[16] Vatistas, G. H., Lam, C., and Lin, S., 1989, "Similarity Relationship for the Core Radius and the Pressure Drop in Vortex Chambers," Can. J. Chem. Eng., **67**, pp. 540–544.
[17] Launder, B. E., Reece, G. J., and Rodi, W., 1975, "Progress in the Development of a Reynolds-Stress Turbulence Closure," J. Fluid Mech., **68**(3), pp. 537–566.
[18] Lien, F. S., and Leschziner, M. A., 1994, "Assessment of Turbulent Transport Models Including Nonlinear RNG Eddy-Viscosity Formulation and Second-Moment Closure," Comput. Fluids, **23**(8), pp. 983–1004.
[19] Gibson, M., and Launder, B. E., 1978, "Ground Effects on Pressure Fluctuations in the Atmospheric Boundary Layer," J. Fluid Mech., **86**, pp. 491–511.
[20] Launder, B. E., and Spalding, D. B., 1974, "Numerical Computation of Turbulent Flows," Comput. Methods Appl. Mech. Eng., **3**(2), pp. 269–289.
[21] Kim, S. E., and Choudhury, D., 1995, "A Near-Wall Treatment Using Wall Functions Sensitized to Pressure Gradient," ASME FED, 217, Separated and Complex Flows, pp. 273–280.
[22] Gupta, A. K., Lilly, D. G., and Syred, N., 1984, *Swirl Flows*, Abacus, Tunbridge Wells, England, UK.
[23] Jawarneh, M. A., Vatistas, G. H., and Hong, H., 2005, "On the Flow Development in Jet-Driven Vortex Chambers," J. Propul. Power, **21**(3), pp. 564–570.
[24] Yan, L., Vatistas, G. H., and Lin, S., 2000, "Experimental Studies on Turbulence Kinetic Energy in Confined Vortex Flows," J. Therm. Sci., **9**(1), pp. 10–22.
[25] Lam, H. C., 1993, "An Experimental Investigation and Dimensional Analysis of Confined Vortex Flows," Ph.D. thesis, Department of Mechanical and industrial Engineering, Concordia University, Montreal.
[26] Alekseenko, S. V., Kuibin, P. A., Okulov, V. L., and Shtork, S. I., 1999, "Helical Vortices in Swirl Flow," J. Fluid Mech., **383**, pp. 195–243.

Journal of Fluids Engineering

Technical Briefs

Study of Drag Forces on a Designed Surface in Bubbly Water Lubrication Using Electrolysis

Haosheng Chen
State Key Laboratory of Tribology,
Tsinghua University,
Beijing, 100084 China
e-mail: chenhs@mail.tsinghua.edu.cn

Jiang Li
Department of Mechanology,
University of Science and Technology,
Beijing, 100083 China

Darong Chen
State Key Laboratory of Tribology,
Tsinghua University,
Beijing, 100084 China

To study the drag reduction effect of a bubbly fluid, a pin-disk experiment is performed on the Universal Micro Tribotester system. Bubbles are generated by water electrolysis in holes that are specially designed on the disk surface. Experiment result shows that the drag force experiences a dynamic process, both drag reduction and drag increment effects appear in the process depending on the bubble behavior. This process is numerically simulated using computational fluid dynamics (CFD), and the explanations for the drag variation are given based on the analysis of drag forces on each wall of the disk surface. The drag reduction occurs when the bubble fills the hole, as the viscous drag on the air-liquid surface is small, and the pressure drag is reduced as the side wall of the hole is covered by the bubble. The drag increment is thought to be caused by the increment of the fluid viscosity when the bubble leaves the hole and flows in the fluid.
[DOI: 10.1115/1.2354531]

Keywords: bubble, drag reduction, lubrication, surface roughness

1 Introduction

Water and water-based lubricants, such as emulsions, are widely used in metalworking lubrication and journal bearing lubrication [1–5]. The good lubricating properties of water-based lubricants have been studied for many years [1]. In most of the studies, the lubricant is seen as single phase or is treated as a discontinuous oil phase dispersed in a continuous water phase. But bubbles cannot be avoided in journal bearing lubrication as a previous study result [2] has pointed out. It is known that the effective viscosity of the bubbly mixture may decrease [3], but at times, the bubbly mixture show a negative effect on lubrication. Results in journal bearing lubrication provided by An et al. [2] and Nikolajsen [6] indicate that the viscosity of the bubbly oil increases and the friction force also increases. Studies on drag reduction give the same conclusion: the bubbles do not cause the drag reduction in laminar flow as they do in a turbulent boundary layer [7,8]; lubricants are often in laminar flow in journal bearing lubrication.

However, some conditions of the studies need to be noted here. First, the surface is considered to be smooth in such studies and the surface roughness is not included. Nevertheless, the surface roughness, such as the grooves and holes on the surface, has been shown to have important effects in journal bearing lubrication [9,10]. Second, since the bubbles are injected into the water in most of the drag reduction experiments [11,12], the condition that the bubbles are in the holes or grooves is not considered.

The goal of this ongoing study is to explore whether drag reduction can occur in laminar flow under the effect of designed surface roughness and controlled bubbles. A pin-disk friction experiment is designed using water lubricants; the Universal Micro Tribotester (UMT) system is used to measure the friction force at the pin-disk interface. Water electrolysis is used to generate bubbles in the lubrication, which is also adopted in the pioneering experiment done by McCormich and Bhattacharyya [13]. A board with holes on the surface is designed as the disk, and the bubbles are generated in the holes. In the experiment, both the bubbles' generation speed and the bubble size can be controlled, so the drag force in laminar flow with different bubble characteristics is investigated. Four models are established and the bubbly lubrication process is numerically simulated. The explanation for the drag variation is also given based on the analysis of the forces on the different walls. According to the instrument used in this experiment, the results are restricted in the oscillating machinery, and the laminar flow condition is satisfied as the fluid film thickness is usually considered very small.

2 Experimental

2.1 Bubble Generation. Here, water electrolysis is adopted to generate bubbles, and the bubble generation speed is controlled by the supply voltage; a special board is designed to control the size and position of the bubbles. The specially designed board is a kind of two-layer printed circuit board. Its structure and shape are shown in Fig. 1, where the unit of the dimension is millimeter.

The board is made of PTFE (polytetrafluoroethylene); the completed board is shown in Fig. 1(*c*), which is 37 mm wide and 46 mm long. The structure of the board with holes is shown as the cross section A-A in Fig. 1(*a*). The top surface of the board is covered by a thin gold layer, whose thickness is <10 μm, and the

Contributed by the Fluids Engineering Division of ASME for publication in the JOURNAL OF FLUIDS ENGINEERING. Manuscript received November 15, 2005; final manuscript received May 8, 2006. Assoc. Editor: Theodore Heindel.

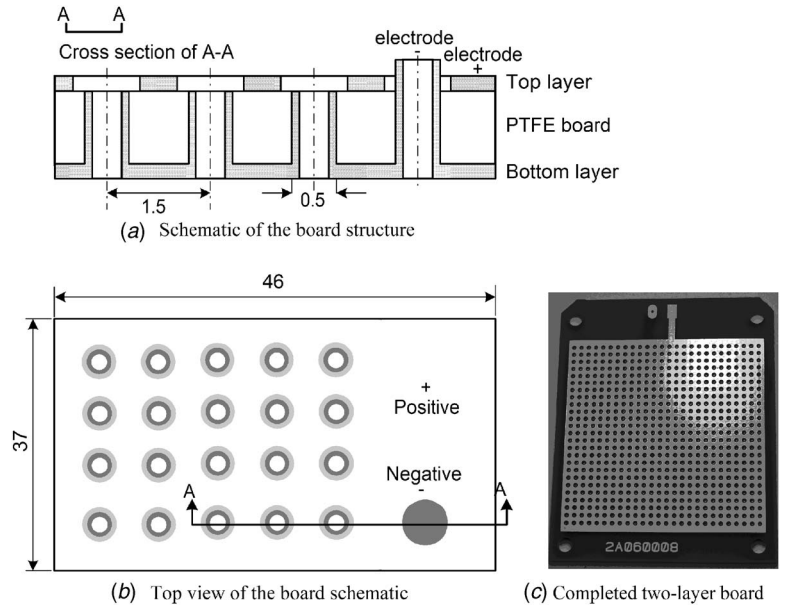

Fig. 1 Structure of the two-layer printed circuit board

layer is connected to the positive pole of the power supply; thus, the whole top layer acts as the positive electrode. In the same way, the whole bottom layer is connected to the negative pole of the power supply.

There is an array of holes through the board. Each hole's diameter is 500 μm, and the interval between two holes is 1.5 mm. The inner surface of each hole is also covered by a thin gold layer, and the layers inside the holes are connected with each other through the bottom layer. Because there is an insulation layer outside the bottom layer, all the inner surfaces of the holes act as the negative electrodes. In the experiment, the board will be dipped into the electrolyte, and a supply voltage will be added on the two electrodes to begin the water electrolysis. The water is electrolyzed and the bubble is generated in the hole. The position and the size of the bubble are controlled by the position and the diameter of the designed hole, whereas the speed of generation is controlled by the supply voltage.

2.2 Experimental Schematic. The schematic of the pin-disk friction force test setup is shown in Fig. 2. The pin is installed on a UMT system; the friction force and normal force on the pin surface are tested by the two-dimensional sensor of the system. The pin's position can be adjusted in the system, and the load of the pin on the disk can be controlled from 0 to 500 g. The printed circuit board is used as the disk; it is installed in the electrolyzing cell which is fixed on the carriage of the UMT system. As the carriage performs a reciprocating movement, whose speed is controlled by the UMT system, the top layer of the circuit board is considered as a moving surface, while the pin can be considered as the stationary surface in the pin-disk interface lubrication.

The electrolyzing cell is filled with the water lubricant. The water lubricant is a saturated salt (NaCl) solution. 0.25% HEC (hydroxyethylcellulose) is added into the solution to increase the solution's viscosity, in case that the friction force variation is too

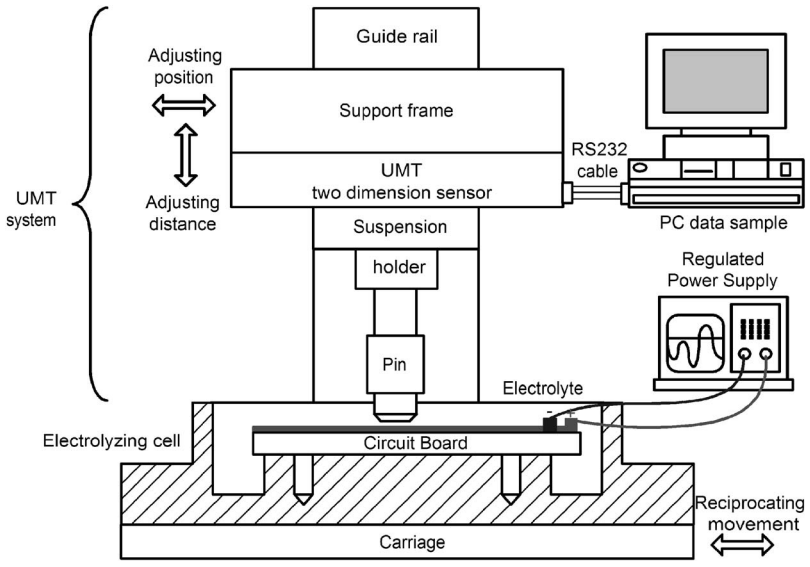

Fig. 2 Experimental system schematics

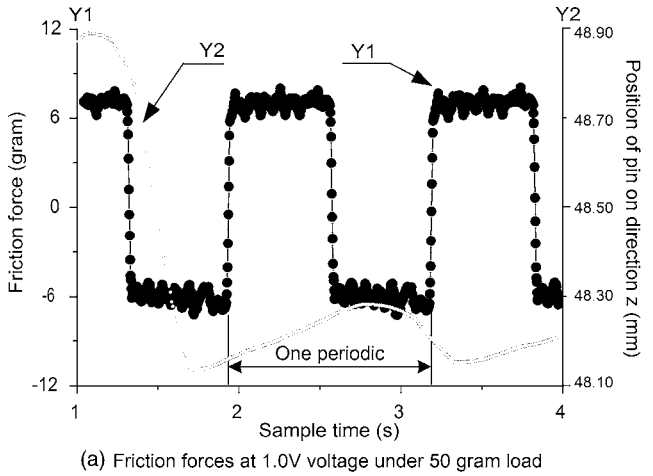

(a) Friction forces at 1.0V voltage under 50 gram load

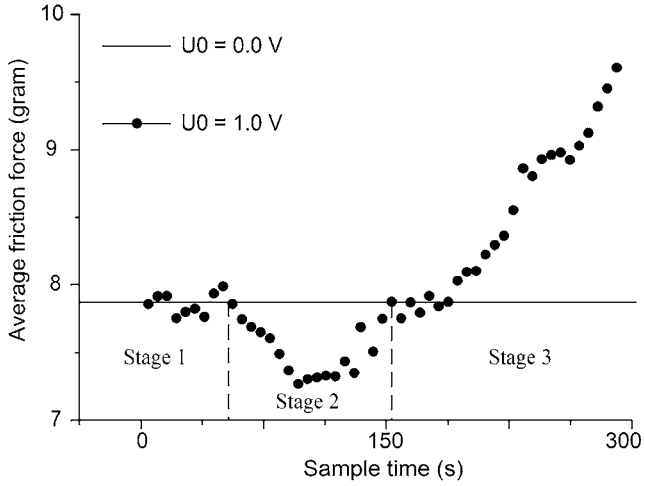

(*b*) Average friction forces at 1.0V voltage under 50 gram load in 300 seconds

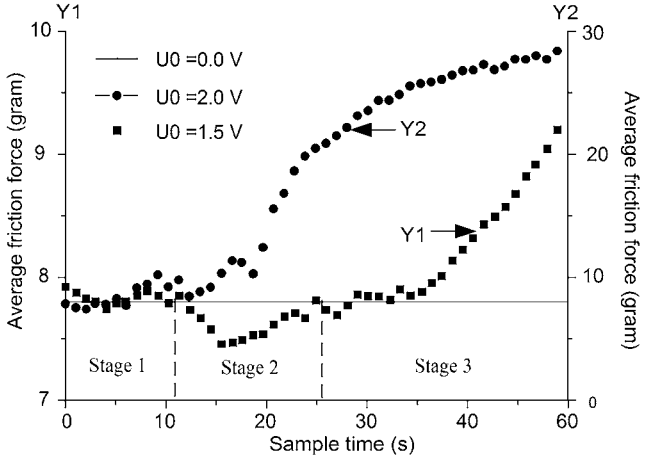

(*c*) Average friction forces under 50 gram load in 60 seconds

Fig. 3 Drag forces on the designed surface under difference supply voltages: (*a*) Friction forces at 1.0 V voltage under 50 g load, (*b*) average friction forces at 1.0 V voltage under 50 g load in 300 s, and (*c*) average friction forces under 50 g load in 60 s

small to be tested by the sensor. Two electrodes are connected to the power supply through two enamel wires. Once the voltage is supplied to the board, the water electrolysis begins in the cell. The gas in the bubbles are considered to be hydrogen because the bubbles are observed firstly in the holes with the negative electrode on the wall, then the bubbles are rising from the holes to the water surface and form a bubble array according to the positions of the holes. During this process, the bubbles' effect on the friction force in pin-disk interface lubrication is investigated.

2.3 Experimental Results. The air originally remaining in the holes is driven out using an ultrasonic cleaner before the experiment. Then the load of the pin is adjusted to 50 g, and the supply voltage is adjusted to 1.0 V. The carriage of the UMT system performs a reciprocating movement at the speed of 1 cm/s, as soon as the voltage is supplied on the electrodes of the disk. The testing lasts 300 s, and a trace of the friction forces on the pin surface at the beginning of the test is shown in Fig. 3(*a*). In the figure, the time for completing a whole reciprocating movement is called one periodic. Because the friction force is always opposite to the pin's moving direction, half of the data have positive values while the others have negative values in one period.

It should be noted here that the lubricating regime is thought to be in hydrodynamic condition because of two reasons. One is the friction coefficient. According to the experiment data, the friction coefficient calculated is lower than 0.2; the other is the position variation of the pin on direction z (perpendicular to the disk surface). At the beginning of the test, the pin contacts the disk surface under the load of 50 g. When the reciprocating movement is performed, the pin is automatically adjusted according to the pressure on the pin surface. The data of the position shown in Fig. 3(*a*) suggest that the pressure on the pin surface increases and the pin moves upward, which indicates that hydrodynamic lubricating occurs in the pin-disk interface.

The whole process of the friction force variation during the testing is shown in Fig. 3(*b*). In the figure, each point on the curve represents the average value of the positive friction forces in a half period; U0 represents the supply voltage for the water electrolysis. It is found from the result that the force variation is not monotonic, and it can be divided into three stages shown in Fig. 3(*b*). In stage 1, the friction forces on the pin surface almost keep constant, and no bubble is observed on the board surface. It is considered that the reaction time of the water electrolysis is not long enough for the bubbles to have an effect on the friction force. In the next few minutes of stage 2, the friction force on the surface decreases, and the forces are lower than the drag force at the beginning of the electrolysis. It indicates that the drag reduction

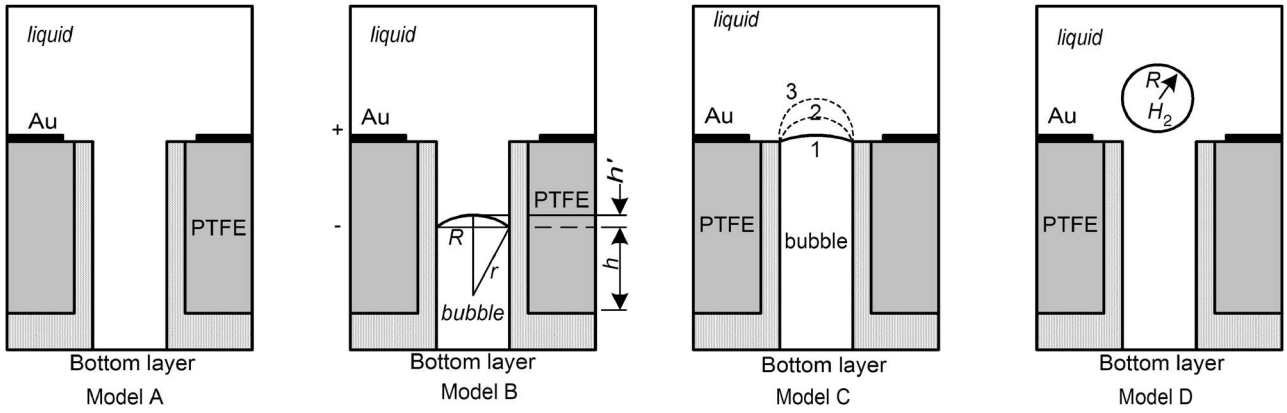

Fig. 4 Models for the bubbly lubrication in different stages

effect occurs under the experimental condition; thus, stage 2 may be called drag reduction stage. In this stage, a few bubbles appear on the board surface. In the last minutes of stage 3, the friction force increases rapidly as the water electrolysis continues, and it exceeds the drag force at the beginning of the electrolysis. It is predicted that the drag force increment cannot be avoided in the lubrication at last. In this stage, a lot of bubbles are observed to leave the holes and aggregate in the solution.

The expected drag reduction effect that occurred in the experiment lasts about 100 s under the voltage of 1.0 V. However, the continuous time of the effect depends on the electrolysis supply voltage. The continuous time of the drag force reduction effect under different voltages is shown in Fig. 3(*c*). The continuous time is shortened obviously when the supply voltage increases to 1.5 V. Moreover, when the supply voltage is high enough, for example, reaching 2.0 V in this experiment, the continuous time decreases, or even disappears as shown in Fig. 3(*c*). In such condition, the water electrolysis becomes strenuous, and the bubbles grow so fast that they leave the holes as soon as they are generated.

From the results, it is determined that the drag reduction effect can be realized even in laminar flow under the effect of bubbles, and the bubble behavior at different stages plays an important role in the drag force variation. Numerical analysis is provided as follows to give the explanations for the bubbly lubrication process.

The experimental error and uncertainty are discussed here. Take the data shown in Fig. 3(*b*) for example, each point in Fig. 3(*b*) represents the average value of the positive friction forces in a half period shown in Fig. 3(*a*). The bias limit is about ±0.364 at 95% confidence, and the uncertainty in the experiment result is ±0.217 using the sequential perturbation method [14]. The experiment has been performed three times and the uncertainty is ±0.254. Since the UMT is a kind standard tester machine and it is calibrated before the experiment, it is believed that the system error has been compensated already.

3 Numerical Analysis on Experimental Results

3.1 Models and Method. It is considered that the status of the bubble in the hole changes at different stages of the experiment. According to the dynamic process of drag force variation in the experiment, four models are established for calculating the drag forces at different stages. The schematics of the four models A, B, C, and D are shown in Fig. 4.

For model A, the water electrolysis begins or just lasts for a short time; no bubble is generated in the hole and the hole is filled with water. For model B, a bubble appears in the hole as the water electrolysis continues, and an air-liquid surface is formed. Because the contact angle of the water on the gold surface is <90 deg, a concave meniscus is formed. Two parameters are used to describe the shape of the bubble, one is called the bubble height h and the other is the curvature radius r of the air-liquid surface. The bubble height is increasing as the water electrolysis continues, while the curvature radius remains almost constant when the bubble is in the hole. In such condition, the hole is small enough to be seen as a capillary and the surface is considered as a part of a sphere. The simplified Laplace equation (1) [15] is used to calculated the curvature radius r.

$$\Delta P = \frac{2\sigma}{r} \tag{1}$$

where ΔP is the pressure difference in and outside of the bubble, σ is the surface tension force, g is the gravity acceleration. With the two parameters, the shape of the air-liquid surface is determined. As the electrolysis continues, the bubble height will reaches the hole depth, then model C is used. In this model, the bubble's height stays constant and equal to the hole's depth, but the curvature radius continues to decrease until it reaches the hole's radius. This process is shown as the dashed lines in model C; it is like the traditional maximum bubble pressure testing process. The curvature radius of the bubble will continues to increase after it reaches the hole's radius. However, such a bubble is unstable under shearing force and such status is not considered in this paper. As the electrolysis continues, the bubble will eventually leave the hole and go into the water solution. Thus, the bubbly lubricant is formed, and model D is adopted to calculate the drag force on the surface. For model D, the viscosity of the fluid is changed because there are a lot of bubbles in the solution. Here, the viscosity is calculated as the modified viscosity equation (2) provided by Sugden [15]. Where η_b is the bubbly lubricant's viscosity, η_0 is the water's viscosity, and β is the bubble content.

$$\eta_b = \eta_0(1 + 0.015\beta) \tag{2}$$

It should be noted that the four models take effect periodically and sequentially during the electrolysis. For example, when the bubble goes into water in model D, the water fills the hole and it is electrolyzed again. Then, a few bubbles are formed and the bubble will experience the next three models sequentially again. As the result, more and more bubbles aggregate in the lubrication.

With these models, the drag force on the surface in different stages can be calculated. However, the calculation is based on some conditions and assumptions stated as follows:

1. The fluid is in the laminar flow condition. This condition can be satisfied because the moving speed is adjusted to be small enough.
2. The real 3D experiment is represented by the 2D models shown in Fig. 4 in the calculation. This substitution affects the model precision, but it makes the calculation easy to be realized with current computers.
3. Although some polymer additives are added into the salt

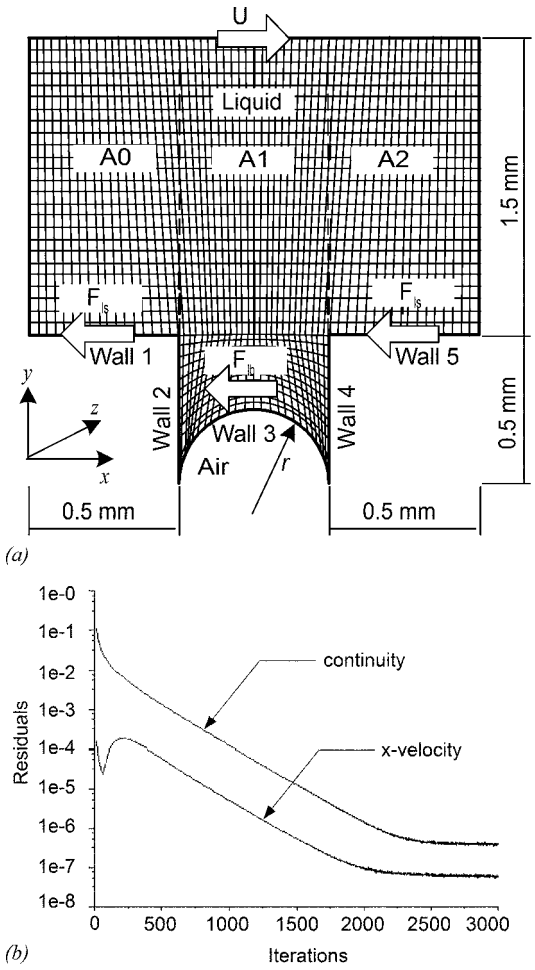

Fig. 5 Preprocessing and residuals for numerical simulation: (*a*) mesh and walls of model B and (*b*) residuals of the numerical results

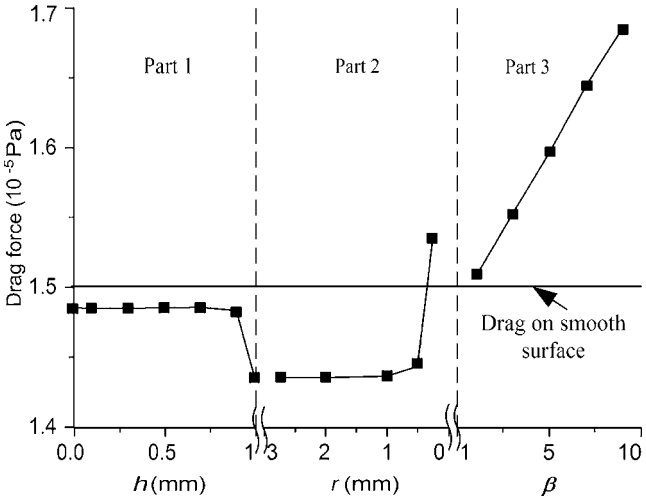

Fig. 6 Numerical simulation on drag force variation process

water to increase the viscosity, the solution is still treated to have a constant viscosity because the shear rate is kept constant.

4. It is considered that the hole is a kind of capillary, and the air-liquid surface is a part of spherical surface. Eq. (1) is established on the basis of this condition.
5. It is assumed that the curvature of the air-liquid surface keeps unchanged as the bubble height grows. When the bubble height is equal to hole depth, the curvature reduces until it reaches the hole's radius.
6. It is assumed that the radius of the bubble is equal to the hole's radius after it leaves the hole and stays in the solution. It is a simplification method to make the calculation easy.

Usually, the Reynolds equation is used in hydrodynamic lubrication calculations, but the models provided here have steep-walled roughness, and the depth of the hole is in the same order of the fluid thickness, so the traditional Reynolds equation is not applicable [16,17]. In this paper, the CFD software FLUENT is used to calculate the drag force on the surface. As a common method, FLUENT uses a control-volume-based technique to convert the governing equations to algebraic equations that can be solved numerically, which is called finite volume method. The continuity equation and momentum equation are adopted in the calculation, which are applicable for any continuous medium. The forces and pressures on different walls under the effect of bubbles are shown in Fig. 5(*a*). The bottom surface has been divided into five walls. The viscous force F_{ls} exists on solid-liquid surfaces (wall 1 and wall 5), while the viscous force F_{lb} exists on air-liquid surface (wall 3); pressure drag appears on the side wall 2 and 4. The total drag force on the surface consists of forces on different walls of the bottom surface.

The boundary conditions are defined as follows: the upper surface is a moving wall with the speed of 1 cm/s; the bottom surface consists of five stationary walls; the left side is a pressure inlet and the right side is a pressure outlet. However, some special conditions need to be added for different models. For models B and C, the air-liquid surfaces are treated as a "slip" wall, which means that there is a tangential velocity component in terms of the translational motion of the wall boundary. Nevertheless, the shear stress on the surface is considered to be zero. For model D, the viscosity of the fluid is calculated according to Eq. (2). Here, the lubricant is considered to perform a stable laminar flow, and the laminar model is adopted here.

Here, the residual definitions are used for judging convergence. This criterion requires that the residuals decrease to 10^{-6} for the continuity equation and velocity equation. The variations of the residuals are shown in Fig. 5(*b*). The residuals both reach the convergence criteria and almost keep constant after 2500 iteration steps, which indicate that the numerical process is converged. To show the pressure and fluid flow near the air-liquid surface more obviously, the mesh number is increased from the center to the wall and the grow factor is 1.1, which is also shown in Fig. 5(*a*). The grid size is about 20×20 μm^2, which is small enough in laminar flow compared to the size of hole marked in Fig. 5(*a*).

3.2 Lubrication Process Simulation. The calculated drag force on the pin surface during the whole process is shown in Fig. 6. It is found that the one simulated process is very like the real drag force variation process in the experiment, but what should be noted here is that the simulated process consists of three parts using different models, each part is numbered according to stages of the drag force variation in experiment that has been described in Fig. 3.

In Part 1, the drag force variation under different bubble heights has been shown, it corresponds with the experimental data in stage 1. When the bubble height is zero, model A is used to calculate the drag force, otherwise, model B is used in this part. It is found in Part 1 that the bubble's size does not show obvious effect on the drag force as the bubble is growing in the hole until the height is near the hole depth. At the end of Part 1, the bubble's height is very close to the hole depth, and model C is adopted. According to Eq. (1), the curvature radius is 2.73 mm. As the electrolysis continues, the curvature radius reduces until it reaches the hole radius 0.25 mm. The drag forces under different curva-

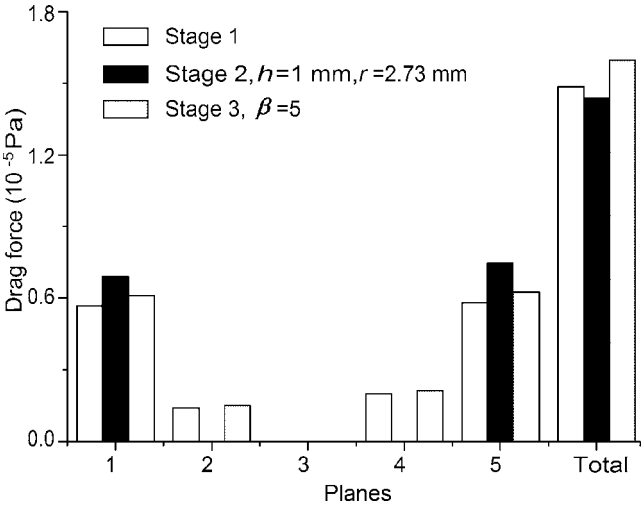

Fig. 7 Drag forces on different walls of the surface

ture radius are shown in Part 2. Only in this part, the drag reduction effect can be obviously observed. However, the drag reduction does not last the whole part. The drag force is increasing as the bubble curvature radius reduces, and it gets a correspondingly high value when it is equal to the hole's radius. This result corresponds with the experiment data in stage 2, and it indicates that only model C can produce the drag reduction effect in laminar flow. Model D is adopted in part 3, and the drag force increases as the bubble content β increases in the bubbly lubrication. The drag force seems to have a linear relationship with the bubble content in Fig. 6. In the calculation, the bubble content changes from 1 to 9; but in fact, the bubble content changes in a more complex manner, because some bubbles are generated in the hole while other bubbles are disappearing in the water. Thus, such a result exists only under a simplified condition.

It should be noted here that, although the process is periodic, the drag reduction effect only can be observed in the first period, because the water will be filled with bubbles after stage 3 of the first period, and the rapidly increased drag force will overcome the drag reduction effect that occurs in stages 1 and 2, which has been shown by the experiment results.

3.3 Analysis of Forces on Walls. Forces on different walls are analyzed to investigate the variation of drag force during the different stages. As shown in Fig. 5, walls 1, 3, and 5 are parallel to the $x-z$ wall, and are called parallel walls; wall 2 and wall 4 are perpendicular to the $x-z$ wall and are called perpendicular walls. On perpendicular walls, there are pressure drags, whereas on parallel walls, there are viscous drags. Here, the force on each wall is obtained using the finite volume method as discussed above, and the forces on each wall in different stages are compared in Fig. 7. Because the drag forces in model A and B are almost the same, model A is omitted and model B is used in stage 1. Models C and D with determined parameters are used in stage 2 and 3, respectively.

It can be seen that the drag force on bottom plane (plane 3) of the hole in all the three stages are very small because the flow velocity is rapidly decreased in the hole (i.e., the shear force is decreased, which leads to the decrement of viscous drag on the bottom plane). Although the loss of the forces on the bottom wall of the hole is compensated by the pressure drag on the perpendicular walls, the loss of the viscous force is higher than the acquired pressure drag. Compared to a smooth surface, a little drag reduction is acquired in stage 1 under this surface roughness.

In stage 2, there is small or even no pressure drag on perpendicular planes, because the perpendicular planes are almost covered by the bubble. Although the viscous drags on the parallel planes (walls 1 and 5) in stage 2 are higher than those in stage 1 and 3, the increment of the viscous drag cannot compensate for the loss of pressure drag, so there is a lower drag force in stage 2 than in stage 1. Compared to a smooth surface, the surface with holes seems to have less contact area with fluid because the shear stress on wall 3 is omitted, so there is less viscous drag on the surface. Also, there is no pressure drag to compensate for the loss of viscous drag. Thus the drag reduction appears. However, the arc height of the air-liquid surface increases when the curvature radius reduces, which causes the increment of the pressure drag on the surface. As a result, the drag force on the bottom surface increases, which corresponds with the drag increment part in stage 2 of the experiment.

In stage 3, forces on every wall are higher than those in stage 1, because the viscosity of the bubbly lubricant is higher than that of lubricant without bubbles. According to Eq. (2), the viscosity of the lubricant increases as the bubble content increases, which leads to the increment of the drag force. This numerical result also corresponds with the experimental data in stage 3.

From what has been discussed above, we can conclude that in stage 1, surface roughness is the reason of a little drag reduction effect; in stage 2, the bubble's shape is the dominant factor that causes an obvious drag reduction; in stage 3, the increment of the fluid's viscosity causes the drag increment.

4 Discussion

It is found that the drag reduction effect appears when the liquid-solid surface is partly substituted by the air-liquid surface. However, there is the question of whether the air-liquid surface has enough load capacity to bear the pressure generated in the hydrodynamic lubrication. In Sec. 3.1, the curvature radius of the air-liquid surface is calculated under the condition that there is only the stationary fluid pressure on the surface. In fact, the pressure on the surface will be higher when the hydrodynamic pressure is formed. An iteration process of the pressure and the surface shape are needed to calculate the curvature radius considering the hydrodynamic pressure. It is a really complex process, and it is not realized in this paper. However, we still have a choice to use the bubbly lubrication technology, even when the air-liquid surface cannot support the hydrodynamic pressure because we can design a surface with smaller holes. The pressure on one air-liquid surface will be afforded by more surfaces with smaller radius. It is an attractive study to investigate the relationship between the lubrication and bubble size; but, it is also another problem that is not discussed here.

5 Conclusions

In this experiment, bubbles are generated by water electrolysis, and the bubble's size and position are controlled by the specially designed surface. The bubbly lubrication is seen as a periodic and dynamic process, as the bubble changes status from staying in the hole to staying in the fluid film. During the process, a drag reduction effect appears even in laminar flow. After the drag reduction stage, the drag force on the surface increases rapidly. Based on the calculated forces on the walls, some conclusions are drawn as follows:

1. The bubbles have little effect on the drag force at the beginning of the water electrolysis, and the surface roughness causes a little drag reduction.
2. An obvious drag reduction can be acquired when the bubble height is close to the hole's depth. The reason is that the viscous drag on the air-liquid surface is omitted due to the slip wall effect, while the pressure drag on the side wall is also avoided because the side wall is almost totally covered by the bubble. However, the drag force will increase as the air-liquid surface grows, because the pressure drag appears and it increases as the surface arc height increases.
3. When the bubble leaves the hole and goes into the lubricat-

ing film, the bubbly lubricant is formed. Because the viscosity of the bubbly lubricant is higher than liquid, the drag force on the surface increases. The increment of the drag force in this stage will cover the drag reduction effect in the experiment as the electrolysis continues.

Acknowledgment

The authors would like to thank Han Zhonglin (Tsinghua University) for his contributions toward this work. This work is supported by the Research Fund for the Doctoral Program of Higher Education (Grant No. 20030003026), NSFC Project (No. 50505020), and NSFC Project (No. 50475018).

Nomenclature

g = gravity acceleration
h = height of the bubble
r = bubble's curvature radius
U = velocity of the moving wall
$U0$ = supply voltage
R = radius of the hole on circuit board

Greek Letters

σ = surface tension force
η_b = bubbly lubricant's viscosity
η_0 = water viscosity
β = bubble content in the fluid
ΔP = pressure difference in and outside of the bubble

References

[1] Boure, P., Mazuyer, D., and Georges, J. M., 2002, "Formation of Boundary Lubricating Layers With Water-Based Lubricant in a Concentrated Elastohydrodynamic Contact," ASME J. Tribol., **124**, pp. 91–102.
[2] An, Q., Zhou, Y. S., and Quan, Y. X., 1997, "Study on the Viscosity Properties of Bubbly Oil and the Static Characteristics of Journal Bearing Lubricated With Bubbly Oil," Wear, **213**, pp. 159–161.
[3] Hayward, A. T. J., 1962, "The Viscosity of Bubbly Oil," J. Inst. Pet., **48**, pp. 156–164.
[4] Kimura, Y., and Okada, K., 1989, "Lubricating Properties of Oil In Water Emulsions," Tribol. Trans., **32**, pp. 524–532.
[5] Schmid, S. R., and Wilson, R. D., 1996, "Lubrication Mechanisms for Oil-In-Water Emulsions," Lubr. Eng., **52**, pp. 168–175.
[6] Nikolajsen, J. L., 1999, "The Effect of Aerated Oil on the Load Capacity of a Plain Journal Bearing," Tribol. Trans., **42**, pp. 58–62.
[7] Madavan, N. K., Deutsch, S., and Merkle, C. L., 1985, "Numerical Investigation Into the Mechanisms of Micro Bubbles Drag Reduction," ASME J. Fluids Eng., **107**, pp. 370–377.
[8] Deutsch, S., Money, M., and Fontaine, A. A., 2003, "Microbubble Drag Reduction in Rough Walled Turbulent Boundary Layers With Comparison Against Polymer Drag Reduction," *Proceedings of 4th ASME/JSME Joint Fluids Engineering Conference*, ASME, New York, Vol. 2, Part A, pp. 665–673.
[9] Wang, L. L., and Cheng, I. W., 1997, "An Average Reynolds Equation for Non-Newtonian Fluid With Application to the Lubrication of the Magnetic Head-Disk Interface," Tribol. Trans., **40**(1), pp. 111–119.
[10] Chiang, H. L., and Hsu, C. H., 2004, "Lubrication Performance of Finite Journal Bearings Considering Effects of Couple Stresses and Surface Roughness," Tribol. Int., **37**, pp. 297–307.
[11] Kato, H., Miyanaga, M., and Haramoto, Y., 1994, "Friction Drag Reduction by Injecting Bubbly Water Into Turbulent Boundary Layer," *Cavitation and Gas-Liquid Flow in Fluid Machinery and Devices*, Fluids Engineering Division, ASME, New York, Vol. 190, pp. 185–194.
[12] Yoon, H. S., Kim, W. J., and Kim, H. T., 2003, "Experimental Study on the Drag Reduction by Injection of Microbubble and Polymer Solution in a Water Tunnel for Water-borne Vehicles," *Proceedings of 4th ASME/JSME Joint Fluids Engineering Conference*, ASME, New York, Vol. 2, Part A, pp. 705–712.
[13] McCormick, M. E., and Bhattacharyya, R., 1973, "Drag Reduction of a Submersible Hull by Electrolysis," Nav. Eng. J., **85**, pp. 11–16.
[14] Figliola, R. S., 2000, *Theory and Design for Mechanical Measurements*, Wiley, New York.
[15] Sugden, S., 1922, "Determination of Surface Tension from the Maximum Pressure in Bubbles," J. Chem. Soc., **121**, pp. 858–859.
[16] Elrod, H. G., 1979, "A General Theory for Laminar Lubrication With Reynolds Roughness," ASME J. Tribol., **101**, pp. 8–14.
[17] Almqvist, T., and Larsson, R., 2004, "Some Remarks on the Validity of Reynolds Equation in the Modeling of Lubricant Film Flows on the Surface Roughness Scale," ASME J. Tribol., **126**, pp. 703–709.

Numerical Simulation of the Fuel Oil Cooling Process in a Wrecked Ship

Jesús Manuel Fernández Oro

Carlos Santolaria Morros

Katia María Argüelles Díaz

Area de Mecánica de Fluidos,
Universidad de Oviedo,
Campus de Viesques,
33271, Gijón (Asturias), Spain

Pedro Luis García Ybarra
Departamento de Física, Matemáticas y Fluidos,
Facultad de Ciencias, UNED,
Senda del Rey, 9,
28040, Madrid, Spain

This work deals with a numerical simulation developed to predict the characteristic cooling times of a low-thermal diffusivity fuel oil confined in the tanks of a wrecked ship. A typical scenario has been introduced through the definition of tank geometries, physical boundary conditions (deep sea temperatures), and rheological properties of the fuel oil. The fluid dynamic behavior of the oil (free convection) inside the tanks, as well as the heat exchange with surrounding sea water has been simulated using a commercial code, FLUENT, which directly solves the Navier-Stokes set of equations, including energy. The purpose is focused on the prediction of both spatial and temporal evolution of the fuel oil characteristic temperature inside the tanks. The objective is to determine the deadline in which the asymptotic temperature curve of the fuel oil converges with deep sea thermal conditions. Inspectional analysis is also outlined, as a powerful tool to predict an order of magnitude in the cooling process.
[DOI: 10.1115/1.2354532]

1 Introduction

The supertanker *Prestige* sank off the northern coast of Spain on November 19, 2002, with more than 37,500 Tm of heavy fuel oil inside the tanks. Thus, the possibility of a massive oil spill emerging from the tanks was a critical issue to be addressed. As part of special actions taken by the Spanish authorities, a case study was defined in order to predict the fuel oil evolution inside the tanks of the sunken ship. It was necessary to know if the fuel oil would be frozen due to the low thermal conditions of the Atlantic Ocean (2.6 °C) at the sinking location and, if this were the case, how long it would take to reach this state. Therefore, the main goal was to determine whether the cooling process would produce a pasty, high-viscous resinous state of extremely low fluidity. For that purpose, a two-dimensional (2D) numerical simulation was carried out in order to understand the midrange and long-term behavior of the confined fuel oil. The accuracy and validation of two-dimensional models is discussed, and the evolution of the temperature and heat fluxes inside the tanks is analyzed. Finally, basic conclusions and recommended actions are outlined briefly.

Contributed by the Fluids Engineering Division of ASME for publication in the JOURNAL OF FLUIDS ENGINEERING. Manuscript received November 3, 2005; final manuscript received May 18, 2006. Assoc. Editor: Malcom J. Andrews. Paper presented at the 2005 ASME Fluids Engineering Division Summer Meeting and Exhibition (FEDSM2005), June 19–23, 2005, Houston, TX.

2 General Considerations

2.1 Fuel Oil No. 6 Physical Properties. Since the wreck of the *Prestige* is resting in the deep ocean (3820 m and 3545 m for each part of the wreckage), it was necessary to determine the fuel oil properties at high pressure ranges. Also, the evolution of thermal and physical properties of the fuel (density, viscosity, thermal conductivity, specific heat) as a function of the temperature was required. Thus, density and viscosity diagrams of *Prestige*'s fuel oil were obtained experimentally [1].

The fuel in the *Prestige*'s tanks is a Fuel Oil No. 2 (French designation) or a Fuel No. 6 or bunker oil "C" in the English designation. The viscosity of this kind of fuel oil largely depends on thermal conditions. In fact, because of its exponential evolution with the temperature (Fig. 1), the prediction of the temperature inside the tanks becomes a critical issue for an accurate estimation of the fuel oil fluidity (Table 1).

2.2 Conduction Versus Free Convection. The heat exchange of the fuel oil presents two associated mechanisms. On the one hand, there is a classical conduction problem, which is mainly governed by the low thermal diffusivity of the fuel. This kind of phenomena, well reported in the literature [2], gives a precise solution of the time necessary to cool the three-dimensional (3D) tanks of the wreck: a dozen years. On the other hand, a mechanism of natural convection is generated due to convective currents of cooled fuel oil that come from the cold zones beside the walls and go down to the bottom of the tank, establishing vortical structures and enhancing the heat transfer. In the case of the cool vertical wall, the convection generates global currents and stratifies the cooled fuel at the bottom of the tanks. This phenomenon, governed by Grashof and Prandtl numbers, appears in the lateral tanks from the outset and is established later in the central tank, when there are several degrees of difference between both tanks. Additionally, at the top of the tanks, a Rayleigh-Bénard (RB) convection is initiated when the thermal boundary layer becomes unstable as a consequence of the major contribution of the buoyancy terms, in comparison to viscous dissipative effects. The beginning of the RB convection is developed when the Rayleigh number exceeds a critical value, $\sim 10^3$. This kind of convection is quite periodic and creates small vortices, which generate a mixing effect between the hot fuel below the thermal layer and the cold fuel at the wall.

2.3 Case Study: On the Validity of 2D Approach. The definition of the problem considers a two-dimensional geometry that represents a transversal section of the ship. Figure 2 shows a sketch of the *Prestige*, with a front view of the transversal section. The total length of the ship was 243.5 m. Central and lateral tanks can be observed in the detailed front view. Transversal areas are 15×19 m^2 for the central tanks and 10×19 m^2 for the lateral ones. This configuration has a plane of symmetry, which simplifies the numerical domain.

The reason for this two-dimensional choice is based on the weak heat exchange that is established between two consecutive inner tanks in the longitudinal direction. Therefore, thermal boundary layers are expected to generate convective currents aligned with transversal planes. However, the inherent three-dimensionality of large eddies and the instabilities of the Rayleigh-Bénard convection (discussed below) could be quite representative, compromising the previous 2D hypothesis. Recent studies [3] have shown that in the case of high values of the Prandtl number ($\mathrm{Pr} \gg 1$), the flow structure and global quantities, such as the Nusselt or Reynolds number present similar behavior in 3D and 2D simulations for flows with a Rayleigh number of

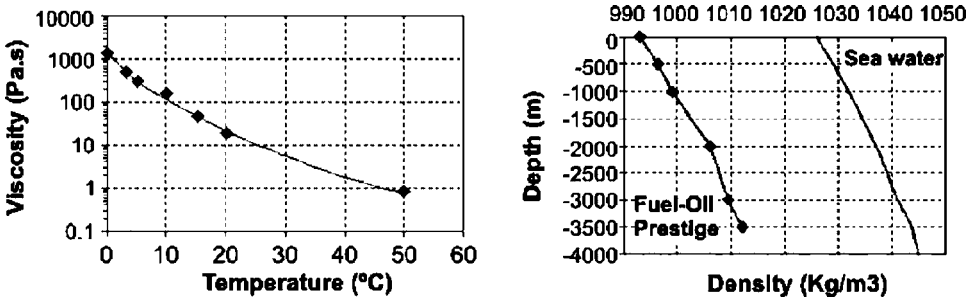

Fig. 1 Physical properties of Fuel No. 6

10^6. Table 2 summarizes the nondimensional parameters involved in the problem, pointing out the laminar characteristic of the flow ($Ra < 10^9$) and the high value of the Prandtl number. In addition, the Rayleigh number is quite close to those referenced in [3]. Since the present study basically predicts the global heat exchange in the tanks (the goal is not a detailed description of RB convection), a two-dimensional approach seems to be accurate to describe the global thermal process.

3 Inspectional Analysis

3.1 Vertical Wall. A balance between the temporal variation of temperature and the heat conduction gives an idea of the characteristic temporal thickness of the thermal boundary layer [4]: $l_T \sim \sqrt{\chi t}$. Thus, the increased density near the wall produces a thermal contraction and the generation of buoyancy forces. The cold fuel descends along the wall, transmitting this motion to the rest of the tank because of viscous transport. A balance between both features (buoyancy and viscous stresses) gives an order of magnitude for the induced velocities in the fuel currents: $u \sim (l_T^2 g \Delta\rho)/(\rho\nu)$. Combining these expressions, it is shown that at the initial transient state, the current's velocity increases linearly over time, while the thermal boundary layer thickens. However, this state lasts just a few hours (from 1 to 10 h, depending on Pr values), ending when the unsteady term of the momentum equation equals the heat convection. That is $t \sim \sqrt{(\rho h \mathrm{Pr})/(g\Delta\rho)}$, where h is the tank height. Therefore, a few hours after the sinking, a quasisteady flow structure had been established, with a thermal boundary layer of 3 cm, and vertical velocity values with an order of millimeters per second (taking values of the problem data).

Table 1 Fuel No. 6 thermophysical properties (at 350 atm, 2.6°C)

Specific heat	C_p (J/Kg K)	1700
Thermal conductivity	λ (W/m K)	0.13
Thermal diffusivity	χ (m^2/s)	7.56×10^{-8}
Dilatation coefficient	β (1/K)	7.40×10^{-4}

Complementarily, these velocities are transmitted by viscous dissipation over a distance l_v which can be evaluated by means of a convection-diffusion balance, giving $u^2/h \sim \nu u/l_v^2$. Introducing the previous expression for the velocity, u, it finally yields: $l_v \sim \mathrm{Pr}^{1/2} l_T$. Because of the high values of the Prandtl numbers (10^4 at the inner hot regions of the tanks), this means that the thermal boundary layer is extremely thin, compared to the viscous one (a hundred times less).

Thus, once the stationary state is reached, the averaged heat exchange is directly proportional to the temperature differences and inversely proportional to the thermal boundary layer thickness, through the thermal conductivity of the fuel oil. This can be expressed as

$$hl\rho C_p \frac{dT}{dt} = -C\lambda \frac{T - T_w}{l_T} h \tag{1}$$

where C is a constant of order unity and T_w is the temperature of the surrounding water. The integration of (1), using an oil temperature of $T_i = 50°\mathrm{C}$ at $t = 0$, gives

$$\frac{T - T_w}{T_i - T_w} = \left[1 + C \frac{\chi (\mathrm{GrPr})^{1/4}}{4hl} t \right]^{-4} \tag{2}$$

Consequently, (2) predicts an evolution of the cooling process according to a power law, with a temperature decrease ruled by time to the minus four.

3.2 Top of the Tanks. The previous heat exchange description is modified by the presence of top and bottom walls. Particularly, the cooled fuel oil beneath the top creates a heavy layer over a hotter, lighter fuel. Since this stratification is unstable, the RB convection dominates, thus increasing the heat transfer. Introducing $l_T \sim \sqrt{\chi t}$ into the definition of the Rayleigh number, the characteristic thickness of the thermal layer beneath the top wall is obtained. In addition, the time in which this convection is beginning to appear can be deduced according to (3), resulting in approximately 10^3 s.

$$l_T \sim \left(\frac{\nu\chi}{g\beta\Delta T} Ra_c \right)^{1/3} \quad t \sim \left(\frac{\nu}{\chi^{1/2} g\beta\Delta T} Ra_c \right)^{2/3} \tag{3}$$

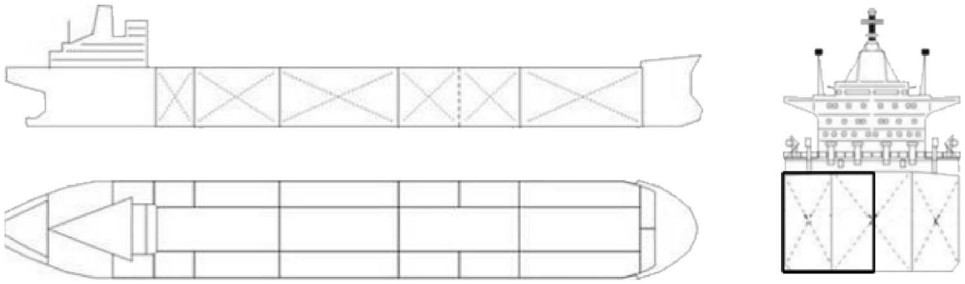

Fig. 2 Sketch of *Prestige* supertanker

Table 2 Nondimensional numbers for $\Delta T = 50°C - 2.6°C$

t (h)	υ (m^2/s)	l_T (mm)	Pr	Gr	Ra
1	8.40×10^{-4}	1.65×10^{-2}	1.11×10^{4}	2.19×10	2.44×10^{4}
3	8.40×10^{-4}	2.86×10^{-2}	1.11×10^{4}	1.14×10	1.27×10^{5}
5	8.40×10^{-4}	4.95×10^{-2}	1.11×10^{4}	5.92×10	6.58×10^{5}
24	8.40×10^{-4}	8.08×10^{-2}	1.11×10^{4}	2.58×10^{2}	2.86×10^{6}

3.3 Bottom Walls. The heat flux across that bottom wall is less critical due to the stable characteristics of the stratification. In this case, the Richardson number is greater than unity; thus, the buoyancy terms are larger than the inertial forces of the returning currents [5]. Thus, there are no possible instabilities and the stratification is guaranteed.

4 Numerical Simulation

4.1 Basic Assumptions. This numerical modeling considers the fuel oil as a Newtonian fluid, satisfying the Boussinesq approximation [6]. The DNS set of equations, including that of energy, are resolved unsteadily. The walls present no thickness (heat fluxes are instantaneous) with no slip condition for the velocity. External walls are taken to be at 2.6°C, and the initial temperature of the fuel oil is set to 50°C.

4.2 Spatial and Temporal Discretizations. Three different spatial discretizations were used in the modeling. The long-term behavior of the cooling curve was determined using coarse ($[124\times64]$ cells) and refined grids ($[240\times68]$ cells). In addition, a high-dense mesh ($[385\times195]$ cells) was used to capture the flow instabilities at initial stages of the simulation (Fig. 3).

The computational time step was adjusted according to the predominant mechanisms (time scale) of the time-marching solution (adaptative time-step strategy). Thus, time step ranged from 1 and 2 seconds (refined mesh at the beginning of the calculations) to 120, 600, and 900 s (coarse mesh at quasisteady stratified final state).

The commercial code FLUENT v6.0 was used for the simulation; executing parallel computations over a 4 PC cluster 1.8 GHz, 512 Mb RAM. In the case of coarse meshes, 200 hr of CPU time were required to solve the six-month cooling process.

4.3 Numerical Results. Figure 4 shows the numerical prediction of the average temperature inside the lateral tanks. Particularly, the influence of spatial and temporal discretizations is analyzed and compared to theoretical predictions. It is pointed out that the spatial discretization results are more critical than the temporal one. In fact, if the mesh is coarser, the cooling process is overestimated (temperature decreases faster). On the contrary, a reduced time step does not affect significantly the overall prediction, as can be observed in the marked lines.

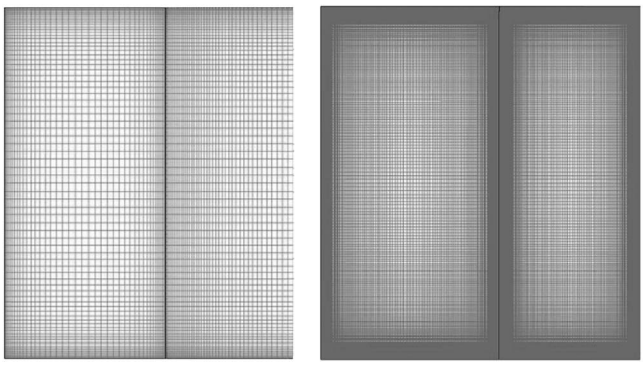

Fig. 3 Two-dimensional grid. Coarse and fine meshes.

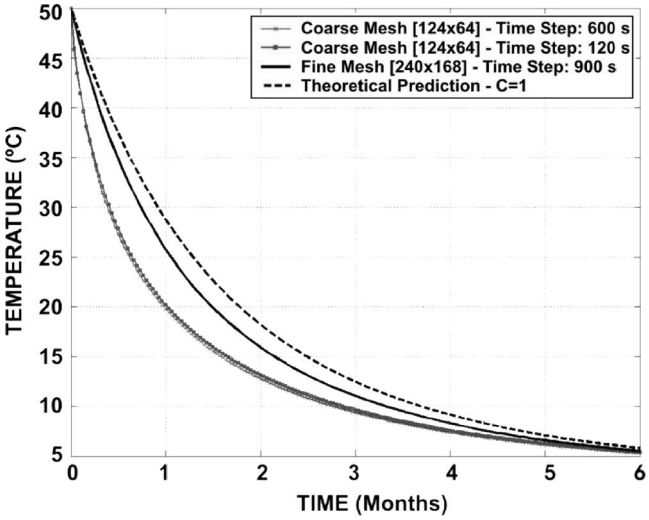

Fig. 4 Evolution of average temperature in the lateral tanks. Comparison of spatial and temporal discretizations.

Figure 5 analyzes results from both lateral and central tanks. This plot is derived from the fine mesh with a time step of 900 s. As expected, the fuel oil cooling is slower in the central tank than in the lateral one. These results predict a maximum difference of temperature between both tanks of 8°C (1.25 months after the sinking). In addition, the temperature in the tanks is reduced to 10°C after three (lateral tank) and five months (central tank), respectively. Considering this temperature as a critical condition for the fuel oil fluidity (*cloud point*), any pumping operation would be practically unfeasible just three months after the sinking. The global thermal flux transferred from both tanks to the surrounding sea water is also plotted in Fig. 5 using a logarithmic scale. Negative values indicate outgoing thermal flux. Because of the RB convection in the top walls, the heat flux presents a noisy evolution.

The study of the scales associated to the RB convection requires a high-dense grid for a better description of both thermal and viscous boundary layers (first grid point at 0.1 mm). In this case, just the first 5 hr after the sinking are analyzed in Fig. 6, due to the extremely high computational cost. The wall thermal fluxes have been represented separately in a logarithmic scale. Major

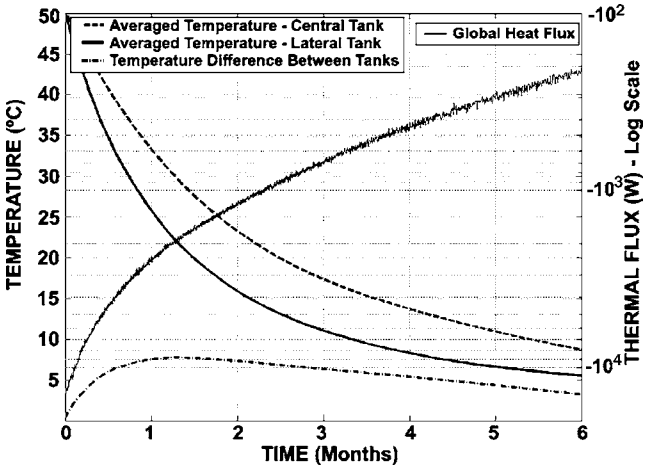

Fig. 5 Thermal flux and average temperature evolution. Comparison between lateral and central tanks.

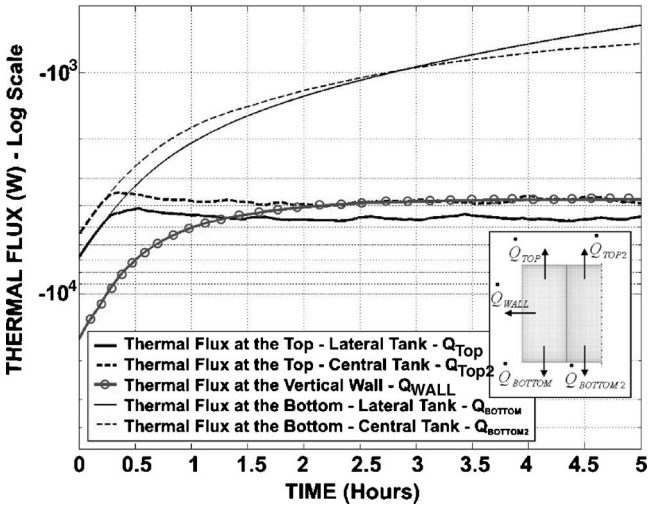

Fig. 6 Analysis of the first hours of the cooling process

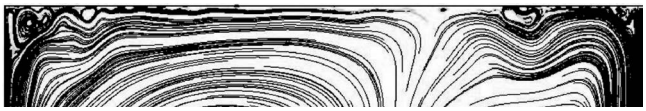

Fig. 7 Unstable vortices related to Rayleigh-Bénard convection

flux values on lateral tanks (dashed lines) are due to the larger size of the tank. Following the theoretical predictions, at 0.5 hr (1800 s), the top thermal fluxes become unstable ($\dot{Q}_{\mathrm{TOP}}$ and $\dot{Q}_{\mathrm{TOP2}}$ in the Fig. 6), due to the establishment of the RB convection. Since these instabilities enhance the thermal exchange, the heat flux at the top wall decelerates. Therefore, the thermal flux evolution becomes flat with the same order of magnitude of the heat flux across the main vertical wall.

Figure 7 shows unstable vortices generated by the RB convection beneath the top wall, 5 hr after the sinking. These instabilities interact with global flow patterns, generating small eddies that are progressively dissipated in the tank corners.

The numerical simulation predicts the stratification of the fuel oil inside the tanks. Thus, the temperature distribution is not uniform in the vertical direction. Figure 8 shows the evolution of convective currents in the tanks. At 15 days, low-velocity eddies are settled at the lower zones of the tanks, while global currents are active just in the upper zone. These structures will finally cause the stagnation of the fuel oil at the bottom (no convective eddies) when the fuel oil fluidity is compromised ($T<10^{\circ}\mathrm{C}$) three months after the sinking.

5 Conclusions

A numerical simulation to predict the characteristic cooling time of a low-thermal diffusivity fuel oil confined inside the tanks of a wrecked ship has been carried out. Basic mechanisms of heat exchange in the tanks (free and RB convection) have been described, in both theoretical and numerical analysis. Particularly, a two-dimensional unsteady case has been modeled for a typical transversal plane of the tanks. Although large eddies are inherently three-dimensional and RB convection is unstable, this 2D approach has provided good results due to the geometry and the

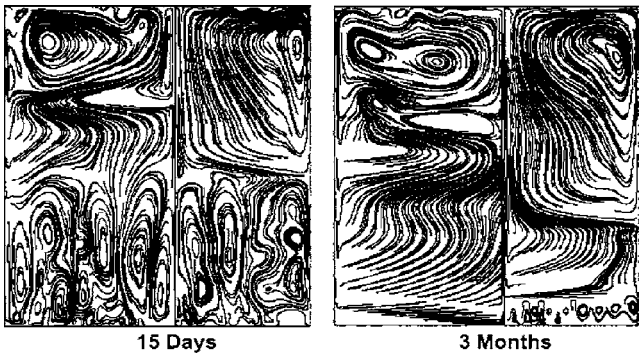

Fig. 8 Stratification in path lines distributions

heat transfer characteristics (laminar flow with a high Prandtl number). Consequently, stable and unstable flow patterns, and the characteristic scales of these mechanisms, have been well captured and studied, in detail. Finally, basic conclusions can be outlined as follows:

- The first stage of the cooling process lasts a few hours and is mainly ruled by heat conduction.
- Afterwards, RB and free convections are established, with time scales of about 10 s and 100 s, respectively. In addition, a stable stratification is developed from the bottom to the top.
- The *cloud-point* temperature ($10^{\circ}\mathrm{C}$) is reached three months after the sinking in the lateral tank. For the central tanks, this period is prolonged to five months.
- The inclusion of ribs enhances the cooling process in the early stages (the temperature decreases five additional degrees during the first month), but later on (i.e., from the third month) there are no appreciable differences in the temperature curves.

Acknowledgment

This work was supported by the General Direction of Investigation, Spanish Ministry of Science and Technology, under the Program of Scientific Intervention against Accidental Oil Spilling, 2004. Special Actions: "Modeling of the evolution of the fuel oil confined in the *Prestige* wreckage and the determination of its physical-chemical properties;" coordinated by the CIEMAT (Technological, Environmental and Energetic Investigations Center).

References

[1] "Archives du Prestige, Naufrage d'un pétrolier au large du cap Finisterre (Galice). 13 Novembre 2002," Documentation des opérations POLMAR, Archives de pollution, Cedre: Septembre 2004, version 1.1, Centre de Documentation de Recherche et d'Experimentations sur les Pollutions Accidentelles des Eaux, (CEDRE)-France.
[2] Carslaw, H. S., and Jaeger, J. C., 1954, *Conduction of Heat in Solids*, Clarendon, Oxford, p. 184.
[3] Schmalzl, J., Breuer, M., and Hansen, U., 2004, "On the Validity of Two-Dimensional Numerical Approaches to Time-Dependent Thermal Convection," Europhys. Lett., **67**(3), pp. 390–396.
[4] Landau, and Lifchitz, 1971. *Mécanique des Fluides*, MIR, Moscow, Chaps. 2, 5.
[5] Rosenhead, L., 1988, *Laminar Boundary Layers*, Dover, New York, Chap. 9.
[6] Ybarra, P. L., Dopazo, C. et al., 2004, "Informe final sobre Acciones Especiales," Acción especial "Modelización de la evolución del fuel-oil retenido en el pecio del buque Prestige y determinación de sus propiedades fisicoquímicas," Ministerio de Ciencia y Tecnología. Dirección General de Investigación. Ciemat.

A Quasi-Generalized-Coordinate Approach for Numerical Simulation of Complex Flows

Donghyun You[1]
Center for Turbulence Research,
Stanford University,
Stanford, CA 94305
e-mail: dyou@stanford.edu

Meng Wang
Department of Mechanical and Aerospace Engineering,
George Washington University,
Washington, DC 20052 and
Department of Aerospace and Mechanical Engineering,
University of Notre Dame,
Notre Dame, IN 46556

Rajat Mittal
Department of Mechanical and Aerospace Engineering,
George Washington University,
Washington, DC 20052

Parviz Moin
Center for Turbulence Research,
Stanford University,
Stanford, CA 94305

A novel structured grid approach which provides an efficient way of treating a class of complex geometries is proposed. The incompressible Navier-Stokes equations are formulated in a two-dimensional, generalized curvilinear coordinate system complemented by a third quasi-curvilinear coordinate. By keeping all two-dimensional planes defined by constant third coordinate values parallel to one another, the proposed approach significantly reduces the memory requirement in fully three-dimensional geometries, and makes the computation more cost effective. The formulation can be easily adapted to an existing flow solver based on a two-dimensional generalized coordinate system coupled with a Cartesian third direction, with only a small increase in computational cost. The feasibility and efficiency of the present method have been assessed in a simulation of flow over a tapered cylinder.
[DOI: 10.1115/1.2354533]

1 Introduction

In large-eddy simulation (LES) of flows in complex geometries, the generation of a high-quality mesh and the large memory requirement for the metric quantities of coordinate transformation are often major obstacles, when a three-dimensional structured, body-fitted mesh is employed. The problem is particularly severe for flow solvers employing the staggered mesh arrangement, which is strongly preferred in nondissipative LES codes for stability and discrete energy conservation (e.g. [1,2]). For instance, at least 80 (eight positions with ten variables (metric coefficients plus Jacobian) per mesh element) three-dimensional arrays are required, compared to ten three-dimensional arrays for collocated meshes. This makes LES employing a staggered grid impractical on large grids. In addition, the increase of partial derivative terms in the transformed governing equations cause a significant increase in computational cost.

On the other hand, many geometries in engineering and scientific applications can be handled using a two-dimensional curvilinear mesh with mild variations along the remaining third direction. Frequently observed variations are shift, rotation, magnification/contraction, and skewing of the curvilinear plane along a direction perpendicular to that plane. The airplane wing is an example of the shift and contraction of the airfoil section, and the blades in an axial compressor or turbine are observed to be twisted along the radial direction while maintaining the blade section profile.

The objective of this study is to exploit these geometric simplifications in the design of a numerical method, which can be applicable to a wide class of problems while minimizing the memory requirement and computational cost. To this end, a formulation of incompressible Navier-Stokes equations based on a "quasi-generalized" coordinate system is proposed. This coordinate system consists of two generalized curvilinear coordinates and a third quasi-curvilinear coordinate. By keeping all two-dimensional planes defined by constant third coordinate values parallel to one another, one can efficiently treat a wide class of fully three-dimensional geometries, and, at the same time, avoid the large memory requirement and high-computational cost associated with a fully generalized coordinate transformation, especially when a staggered grid is used for stability of nondissipative large-eddy simulation. In nondissipative LES, aliasing errors are controlled by enforcing kinetic energy conservation in contrast to the LES techniques employing dissipative upwind-biased schemes or to the implicit LES [3] which relies on a high-order spatial filter in lieu of a subgrid-scale model. The nondissipative feature was proven to be important for successful LES of turbulent flows [1,4] and it has been shown that better stability of the nondissipative algorithm is achievable by utilizing a staggered mesh [5,6].

A number of structured grid approaches have been proposed to handle mildly three-dimensional flow configurations. For instance, You et al. [5] and Tang et al. [7] proposed methods employing a three-dimensional grid which is generated by either merely translating or rotating a whole two-dimensional curvilinear grid along the remaining third coordinate. The present method significantly differs from the previous methods [5,7] in that it allows more general variations of a two-dimensional base grid along the remaining third coordinate, and therefore, can be utilized to confront problems involving a step further complex geometries.

The incompressible Navier-Stokes equations are transformed to a quasi-generalized coordinate system in Sec. 2. Then, in Sec. 3, formulas for some examples of geometric variations and their applicability are given. In Sec. 4, an implementation of the present formulation is evaluated by considering the flow over a tapered circular cylinder, and this is followed by a brief summary in Sec. 5.

2 Transformation of Governing Equations

The incompressible Navier-Stokes equations based on Cartesian coordinates are as follows:

$$\frac{\partial u_i}{\partial t} + \frac{\partial}{\partial x_j} u_i u_j = -\frac{\partial p}{\partial x_i} + \frac{1}{\mathrm{Re}} \frac{\partial}{\partial x_j} \frac{\partial u_i}{\partial x_j} \tag{1}$$

$$\frac{\partial u_i}{\partial x_i} = 0 \tag{2}$$

All the coordinate variables, velocity components, and pressure are nondimensionalized by a length scale L, reference velocity U_{ref}, and ρU_{ref}^2, respectively. The time is normalized by L/U_{ref}.

Equations (1) and (2) can be rewritten in the conservative form in a generalized coordinate system as

[1]Corresponding author.

Contributed by the Fluids Engineering Division of ASME for publication in the JOURNAL OF FLUIDS ENGINEERING. Manuscript received October 11, 2005; final manuscript received April 11, 2006. Assoc. Editor: Surya P. Vanka.

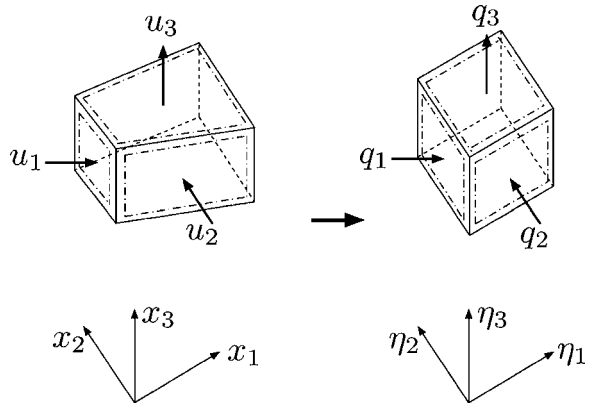

Fig. 1 Schematic diagram of coordinate transformation from Cartesian coordinates to curvilinear coordinates. Planes perpendicular to η^3 are required to be parallel in the quasi-generalized coordinates.

$$\frac{\partial q^i}{\partial t} = -N^i(\mathbf{q}) - G^i(p) + L^i(\mathbf{q}) \tag{3}$$

$$D^i q^i = 0 \tag{4}$$

where $\mathbf{q}=(q^1,q^2,q^3)$, N^i is the nonlinear convection term, $G^i(p)$ is the pressure gradient term, and L^i represents the diffusion term. D^i denotes the divergence operator. A transformation to generalized coordinates is introduced in Fig. 1 as

$$(x_1,x_2,x_3;u_1,u_2,u_3) \rightarrow (\eta^1,\eta^2,\eta^3;q^1,q^2,q^3) \tag{5}$$

The variable q^i is the volume flux across the faces of the cells, which is equivalent to the contravariant velocity components on a staggered grid multiplied by the Jacobian of the coordinate transformation. Then, the terms in Eq. (3) are expressed in generalized coordinates as

$$N^i(\mathbf{q}) = \frac{1}{J}\gamma_m^j \frac{\partial}{\partial \eta^j}\frac{1}{J}c_k^m q^k q^j \tag{6}$$

$$G^i(p) = \alpha^{ij}\frac{\partial p}{\partial \eta^j} \tag{7}$$

$$L^i(\mathbf{q}) = \frac{1}{J}\gamma_m^j \frac{\partial}{\partial \eta^k}\alpha^{kj}\frac{1}{\mathrm{Re}}\frac{\partial}{\partial \eta^j}\frac{1}{J}c_l^m q^l \tag{8}$$

where

$$q^j = \gamma_k^j u_k, \quad c_k^j = \partial x_j/\partial \eta^k, \quad \gamma_k^j = J(c_j^k)^{-1}, \quad \alpha^{jk} = J(c_j^m c_k^m)^{-1}$$
$$\text{and} \quad J = (\|c_j^m c_k^m\|)^{1/2} \quad \text{for } j,k,l,m,n = 1,2,3$$

When the fully three-dimensional curvilinear coordinate system is used, the large number of partial derivative terms in the transformed governing equations and the required memory for three-dimensional metric coefficients and Jacobians severely limit the computation to a relatively small number of mesh points. Here, we propose an approach which drastically reduces the memory requirement and computational cost. This is done by imposing a constraint which requires the planes defined by constant values of one coordinate (η^3 in the present formulation) to be parallel to one another. This results in $c_1^3=c_2^3=\gamma_1^3=\gamma_2^3=0$. With these vanishing metric quantities, a significant reduction of derivative terms in the transformed Navier-Stokes equations, compared to the equations in a fully three-dimensional generalized curvilinear coordinate system, is obtained:

$$\begin{aligned}\frac{\partial q^i}{\partial t} = &-\frac{1}{J}\gamma_1^j\frac{\partial}{\partial \eta^j}\frac{1}{J}c_k^1 q^k q^j - \frac{1}{J}\gamma_2^j\frac{\partial}{\partial \eta^j}\frac{1}{J}c_k^2 q^k q^j \\ &-\frac{1}{J}\gamma_3^j\frac{\partial}{\partial \eta^j}\frac{1}{J}\Big(\underbrace{c_1^3 q^1 + c_2^3 q^2}_{=0} + c_3^3 q^3\Big)q^j + \alpha^{ij}\frac{\partial p}{\partial \eta^j} \\ &+\frac{1}{J}\gamma_1^j\frac{\partial}{\partial \eta^k}\alpha^{kj}\frac{1}{\mathrm{Re}}\frac{\partial}{\partial \eta^j}\frac{1}{J}c_l^1 q^l + \frac{1}{J}\gamma_2^j\frac{\partial}{\partial \eta^k}\alpha^{kj}\frac{1}{\mathrm{Re}}\frac{\partial}{\partial \eta^j}\frac{1}{J}c_l^2 q^l \\ &+\frac{1}{J}\gamma_3^j\frac{\partial}{\partial \eta^k}\alpha^{kj}\frac{1}{\mathrm{Re}}\frac{\partial}{\partial \eta^j}\frac{1}{J}\Big(\underbrace{c_1^3 q^1 + c_2^3 q^2}_{=0} + c_3^3 q^3\Big)\end{aligned} \tag{9}$$

for $i=1,2$, and $j,k,l=1,2,3$, and

$$\begin{aligned}\frac{\partial q^3}{\partial t} = &\underbrace{-\frac{1}{J}\gamma_1^3\frac{\partial}{\partial \eta^j}\frac{1}{J}c_k^1 q^k q^j}_{=0} \underbrace{-\frac{1}{J}\gamma_2^3\frac{\partial}{\partial \eta^j}\frac{1}{J}c_k^2 q^k q^j}_{=0} \\ &-\frac{1}{J}\gamma_3^3\frac{\partial}{\partial \eta^j}\frac{1}{J}\Big(\underbrace{c_1^3 q^1 + c_2^3 q^2}_{=0} + c_3^3 q^3\Big)q^j + \alpha^{3j}\frac{\partial p}{\partial \eta^j} \\ &+\underbrace{\frac{1}{J}\gamma_1^3\frac{\partial}{\partial \eta^k}\alpha^{kj}\frac{1}{\mathrm{Re}}\frac{\partial}{\partial \eta^j}\frac{1}{J}c_l^1 q^l}_{=0} + \underbrace{\frac{1}{J}\gamma_2^3\frac{\partial}{\partial \eta^k}\alpha^{kj}\frac{1}{\mathrm{Re}}\frac{\partial}{\partial \eta^j}\frac{1}{J}c_l^2 q^l}_{=0} \\ &+\frac{1}{J}\gamma_3^3\frac{\partial}{\partial \eta^k}\alpha^{kj}\frac{1}{\mathrm{Re}}\frac{\partial}{\partial \eta^j}\frac{1}{J}\Big(\underbrace{c_1^3 q^1 + c_2^3 q^2}_{=0} + c_3^3 q^3\Big),\end{aligned}$$
$$\text{for } j,k,l = 1,2,3 \tag{10}$$

The total number of surviving derivative terms is only about one half of that in the fully generalized curvilinear coordinate system.

Compared to the formulation with two-dimensional generalized curvilinear coordinates and a nonuniform Cartesian third direction (e.g. [5]), the above formulation which allows the third coordinate to be curvilinear does not change the computational cost significantly. For a numerical algorithm based on a fractional-step method [8], the computational cost is dominated by the inversions of factored matrices and multigrid operations for solving the pressure Poisson equation, which are not much altered by this generalization.

The three-dimensional metric coefficients in the quasi-generalized coordinates can be expressed as products of metric coefficients in a two-dimensional plane and one-dimensional functions along the third direction, with decoupled Jacobians $J=(c_1^1c_2^2-c_2^1c_1^2)^{1/2}c_3^3$. These decoupled metric coefficients and Jacobians, with variations of the plane mesh along the perpendicular third direction as exemplified in the following section, result in a significant reduction of required memory.

3 Plane Variations and Metric Coefficients

In this section, we present several examples of grid topology in which variations along one direction are given by an algebraic relationship. Note that nonalgebraic variations are also allowed in the present formulation, as long as the mesh planes perpendicular to that direction are parallel to one another. In addition, more flexibility in the geometry can be achieved using a combination of these variations.

(*a*) Shift (Fig. 2(*a*))

$$\begin{cases} x_{1_{i,j,k}} = x_{1_{i,j,1}} + x_{1_k}^s \\ x_{2_{i,j,k}} = x_{2_{i,j,1}} + x_{2_k}^s \end{cases}$$

(*b*) Magnification/Contraction (Fig. 2(*b*))

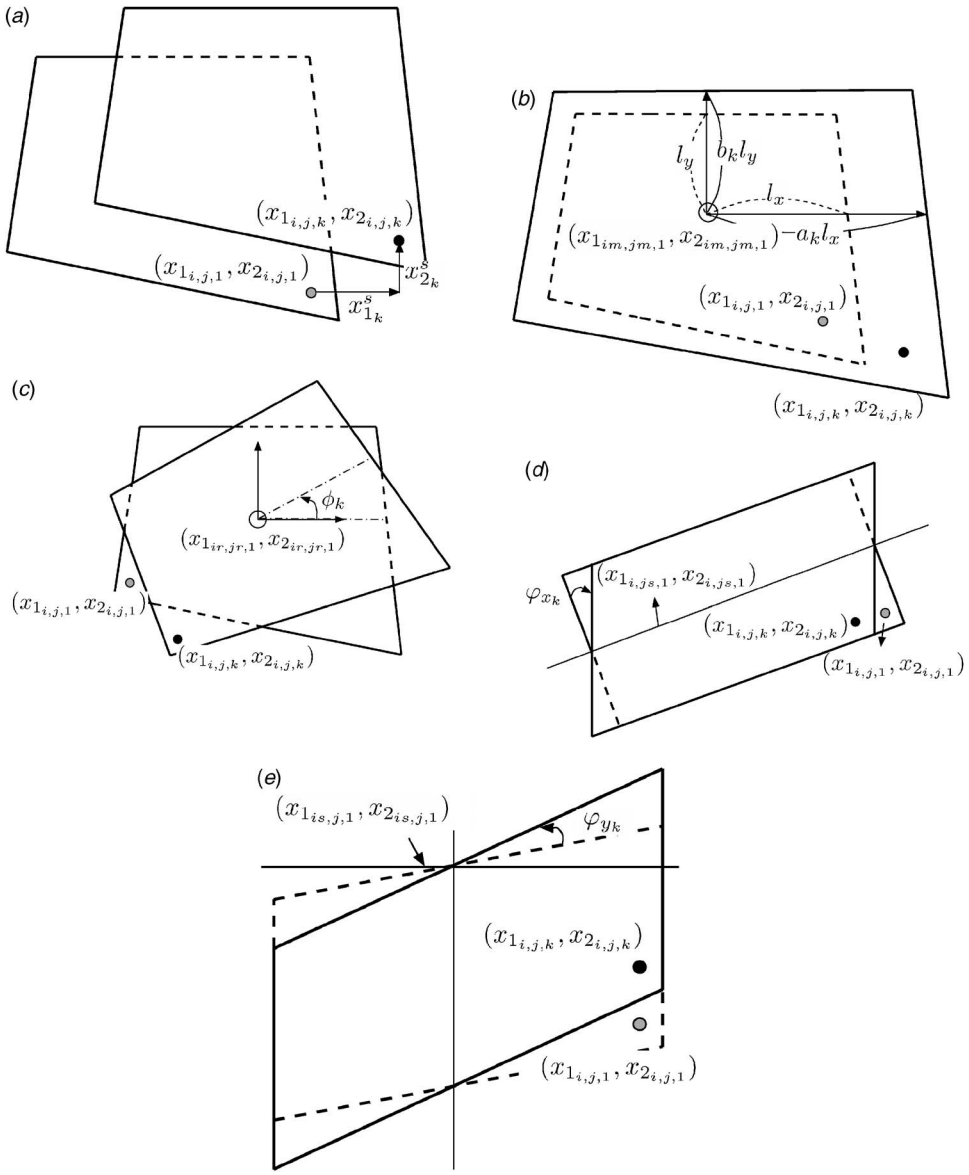

Fig. 2 Examples of algebraic functions used in the proposed transformation: (*a*) shift; (*b*) magnification/contraction; (*c*) rotation; (*d*) skewing to x_1 direction; (*e*) skewing to x_2 direction

$$\begin{cases} x1_{i,j,k} = a_k(x1_{i,j,1} - x1_{im,jm,1}) + x1_{im,jm,1} \\ x2_{i,j,k} = b_k(x2_{i,j,1} - x2_{im,jm,1}) + x2_{im,jm,1} \end{cases}$$

(*c*) Rotation (Fig. 2(*c*))

$$\begin{cases} x1_{i,j,k} = \cos\phi_k(x1_{i,j,1} - x1_{ir,jr,1}) - \sin\phi_k(x2_{i,j,1} - x2_{ir,jr,1}) + x1_{ir,jr,1} \\ x2_{i,j,k} = \sin\phi_k(x1_{i,j,1} - x1_{ir,jr,1}) + \cos\phi_k(x2_{i,j,1} - x2_{ir,jr,1}) + x2_{ir,jr,1} \end{cases}$$

(*d*) Skewing to x_1 direction (Fig. 2(*d*))

$$\begin{cases} x1_{i,j,k} = (x2_{i,j,1} - x2_{i,js,1})\tan^2\varphi_{x_k} + x1_{i,j,1} \\ x2_{i,j,k} = (x2_{i,j,1} - x2_{i,js,1})(1 + \tan^2\varphi_{x_k}) + x2_{i,js,1} \end{cases}$$

(*e*) Skewing to x_2 direction (Fig. 2(*e*))

$$\begin{cases} x1_{i,j,k} = x1_{i,j,1} \\ x2_{i,j,k} = (x1_{i,j,1} - x1_{is,j,1})\tan\varphi_{y_k} + x2_{i,j,1} \end{cases}$$

In the formulas (*a*)–(*e*), $x^s_{1(2)_k}$ is the amount of shift in the $x_1(x_2)$ direction. $x1(2)_{im,jm,1}$, $x1(2)_{ir,jr,1}$, $x2_{i,js,1}$, and $x1_{is,j,1}$ denote reference points for magnification, rotation, and skewing variations in x_1 and x_2 directions, respectively. a_k and b_k are the magnification/contraction factors in x_1 and x_2 directions, while ϕ_k, φ_{x_k}, and φ_{y_k} are the rotation and skewing angles. Additional formulas can be derived to meet other geometric need.

These algebraic variations, as well as combinations of the variations, result in not only geometric flexibility but also decoupled metric coefficients. Any metric coefficients and Jacobians can be expressed as products of those for the base grid at $k=1$ and variational functions along the k direction. This results in a great reduction of computational memory requirements with a negligible increase in computational operations.

Figures 3 and 4 are examples of the geometries which can be represented using the present formulation. Figure 3 shows a compressor blade which is twisted along the blade span while the blade cross-sectional profile is maintained. For this geometry, the base mesh is rotated and skewed along the blade wall normal direction with angles of up to 30 deg, and the skewing allows a periodic boundary condition to be applied in that direction in a

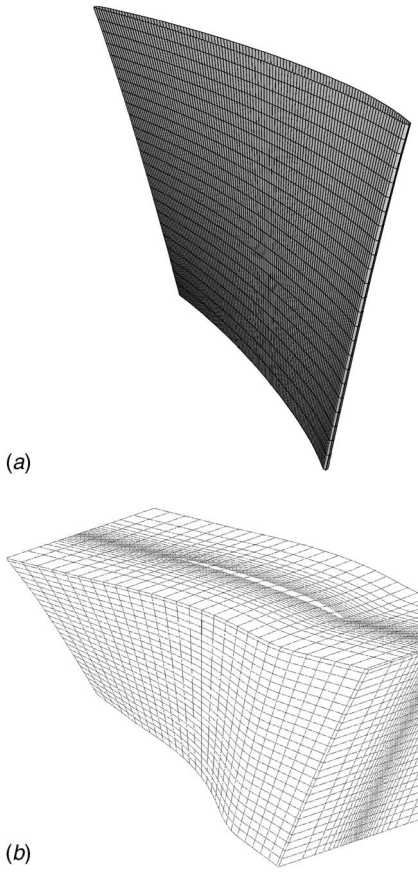

Fig. 3 A twisted compressor blade generated by mesh rotation and skewing: (*a*) compressor blade; (*b*) mesh around the blade

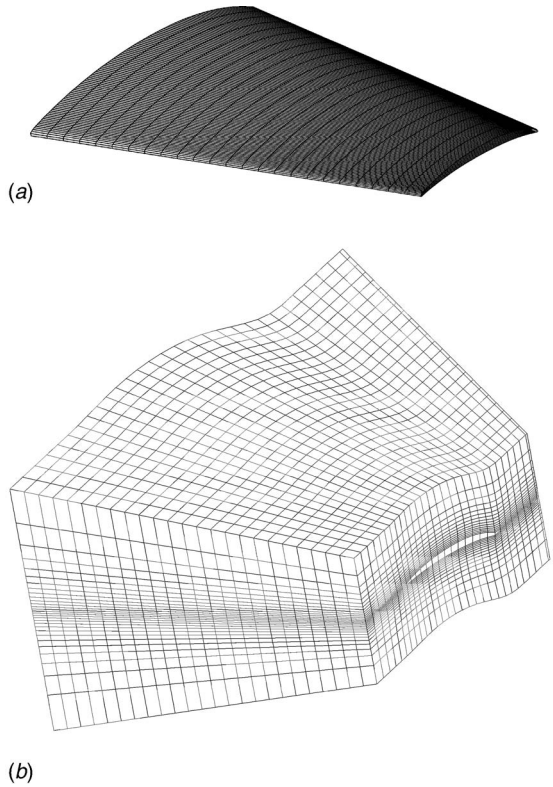

Fig. 4 An airplane wing generated by contraction and shift: (*a*) airplane wing; (*b*) mesh around the wing

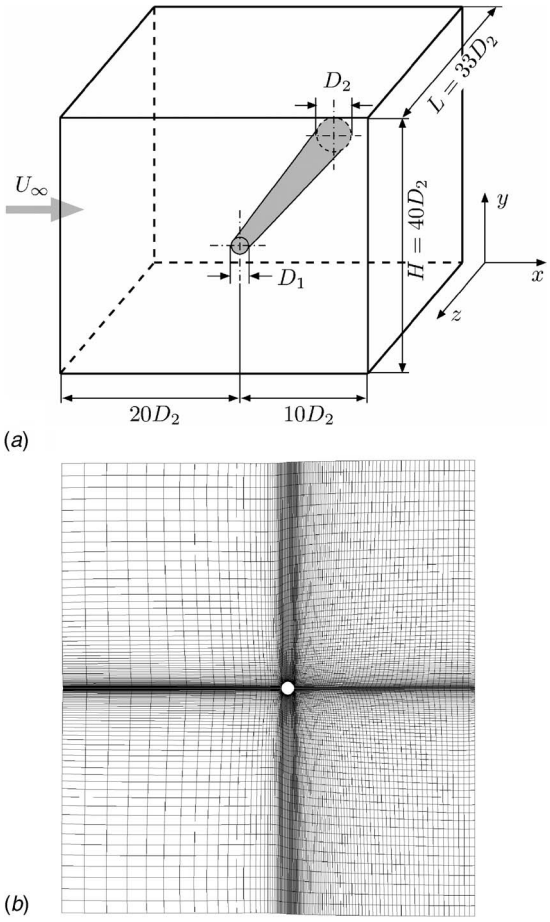

Fig. 5 (*a*) Flow configuration and computational domain, and (*b*) computational grid in a base *x-y* plane used for numerical simulation of flow over a tapered circular cylinder

simulation of flow in a blade passage. An airplane wing can be meshed by contraction and shift operations of the base grid, as shown in Fig. 4. The present approach can also be employed for internal flow configurations such as a pipe and a diffuser whose cross sections vary along the streamwise direction.

Enhanced geometric flexibility can be achieved by combining partially or approximately body-fitted meshes with an immersed boundary method [9,10]. This method has been successfully applied to the rotor tip-clearance flow found in axial turbomachines [5].

4 Implementation and Evaluation

Numerical simulation of vortex shedding behind a linearly tapered cylinder is performed to evaluate the present methodology and implementation. The configuration, shown in Fig. 5(*a*), is the same as that studied experimentally by Piccirillo and Van Atta [11]. The taper ratio, $R_T = L/(D_2 - D_1)$, is set to 50, where L is the cylinder length, and D_1 and D_2 are the diameters of the small and large ends of the cylinder, respectively. The Reynolds numbers based on the diameters and freestream velocity are 60 and 180 at the small and large ends, respectively.

A staggered grid arrangement is employed with the base grid of 257×257 mesh points which is shown in Fig. 5(*b*), and parallel mesh planes are generated along the perpendicular spanwise direction by contraction and expansion operations. Thirty three points are allocated uniformly along the span. A uniform laminar inflow is used and convective and no-stress boundary conditions are employed at the exit and each side wall, respectively. The use

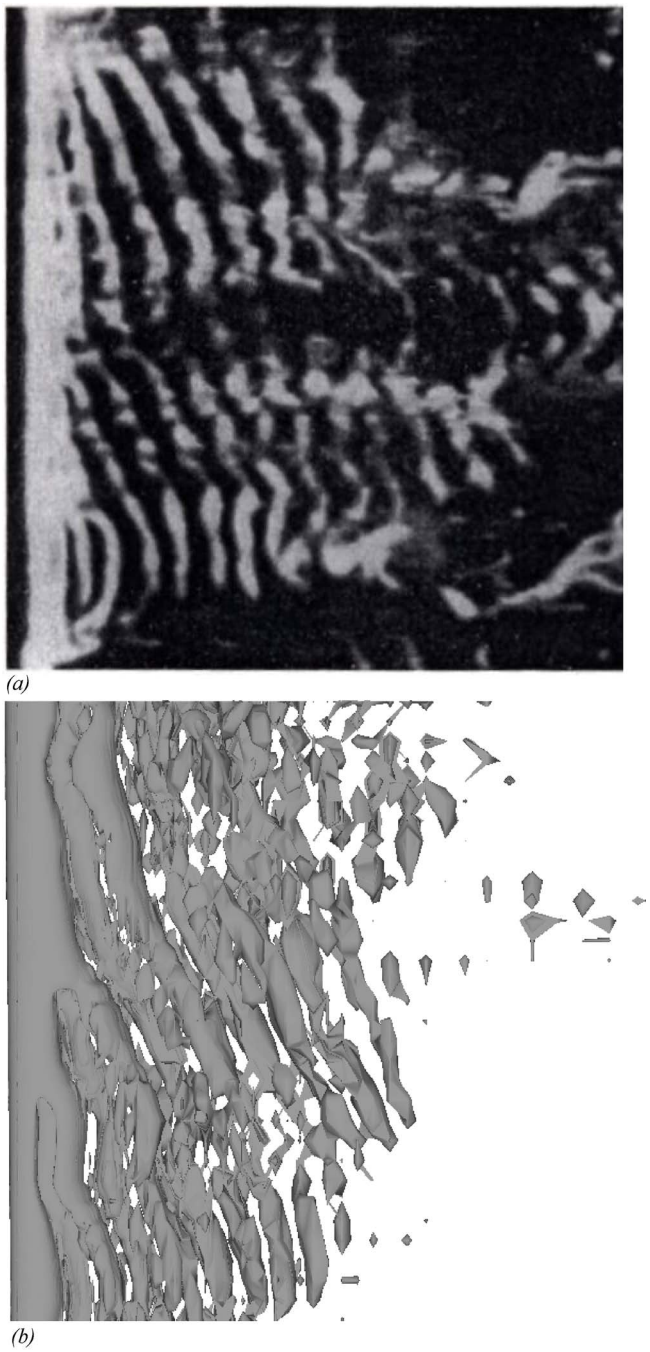

Fig. 6 Instantaneous vortical structures behind a tapered circular cylinder: (*a*) water tunnel flow visualization [11]; (*b*) λ_2 vortex identification from computational results

of a no-stress boundary condition at each side wall can be justified from the experimental observation that the vortex shedding of the flow is largely unaffected by end conditions [11]. About 110 s on 4 CPUs of SGI Origin 300 are used per time step, and this is only about 10% more than that measured by the solver based on the two-dimensional generalized curvilinear coordinate coupled with a straight third direction and with the same number of mesh points.

Figure 6 shows snapshots of instantaneous vortical structures behind the tapered cylinder observed in both the experiment [11] and the present numerical simulation. The oblique vortex shedding is a hallmark of this flow observed experimentally, and the present numerical approach is shown to capture this phenomenon.

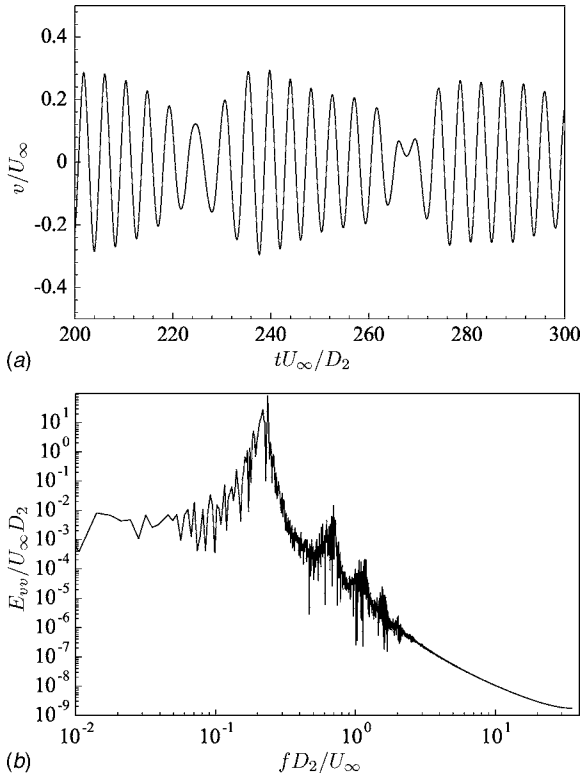

Fig. 7 (*a*) Time history and (*b*) frequency energy spectrum of the vertical velocity at $x/D_2=1$, $y/D_2=0$, $z/D_2=13.5$

In contrast to the laminar vortex shedding observed behind a straight cylinder, phase differences of the vortex shedding along the spanwise direction is clearly observed, and this complicates the downstream vortical structures. This phase difference accelerates the decay of downstream vortices due to enhanced mixing.

Figure 7 shows a typical velocity time history and its autospectrum as a function of nondimensional frequency. The signal represents the velocity at a near-wake position $x/D_2=1$, $y/D_2=0$, and $z/D_2=13.5$. The Strouhal number of vortex shedding at this location is 0.203, which in good agreement with the experimental result ($fD_2/U_\infty=0.204$) of Piccirillo and Van Atta [11].

5 Summary

The incompressible Navier-Stokes equations have been formulated in a two-dimensional, generalized curvilinear coordinate system complemented by a third quasi-curvilinear coordinate. By requiring all the two-dimensional planes to be parallel in the perpendicular direction, the proposed approach makes structured-mesh computation more affordable in fully three-dimensional geometries, in terms of both memory and CPU cost. In particular, it alleviates the huge memory requirement for metric coefficients and Jacobians by eliminating the need to save them as three-dimensional quantities. This feature is especially important when a staggered grid is used for stability of nondissipative large-eddy simulation. The formulation can be easily adapted to an existing solver based on a two-dimensional generalized coordinate system coupled with a Cartesian third direction, with only a small increase in computational cost. Furthermore, the present formulation can be extended to cylindrical (spherical) based coordinates by keeping the axial-circumferential (azimuthal-zenithal) planes parallel to one another in the radial direction.

Acknowledgment

The authors acknowledge the support of the Office of Naval Research under Grant No. N00014-99-1-0389 with Ki-Han Kim

as program manager. Computer time was provided by the Challenge Project Grant C82 from the U.S. Department of Defense High-Performance Computing Modernization Program (HPCMP) through Army Research Laboratory (ARL) Major Shared Resource Center.

References

[1] Mittal, R., and Moin, P., 1997, "Suitability of Upwind-Biased Schemes for Large-Eddy Simulation of Turbulent Flows," AIAA J., **35**(8), pp. 1415–1417.
[2] Nagarajan, S., Lele, S. K., and Ferziger, J. H., 2003, "A Robust High-Order Compact Method for Large-Eddy Simulation," J. Comput. Phys., **191**(2), pp. 392–419.
[3] Morgan, P. E., Rizzetta, D. P., and Visbal, M. R., 2005, "Large-Eddy Simulation of Separation Control for Flow Over a Wall-Mounted Hump," AIAA Paper No. 2005-5017, June.
[4] Beaudan, P., and Moin, P., 1994, "Numerical Experiments on the Flow Past a Circular Cylinder at Sub-Critical Reynolds Number," Report TF-62, Department of Mechanical Engineering, Stanford University, Stanford, CA.
[5] You, D., Mittal, R., Wang, M., and Moin, P., 2004, "Computational Methodology for Large-Eddy Simulation of Tip-Clearance Flows," AIAA J., **42**(2), pp. 271–279.
[6] Choi, H., Moin, P., and Kim, J., 1992, "Turbulent Drag Reduction: Studies of Feedback Control and Flow Over Riblets," Report TF-55, Department of Mechanical Engineering, Stanford University, Stanford, CA.
[7] Tang, G., Yang, Z., and McGuirk, J. J., 2004, "Numerical Methods for Large-Eddy Simulation in General Co-Ordinates," Int. J. Numer. Methods Fluids, **46**(1), pp. 1–18.
[8] Kim, J., and Moin, P., 1985, "Application of a Fractional-Step Method to Incompressible Navier-Stokes Equations," J. Comput. Phys., **59**(2), pp. 308–323.
[9] Fadlun, E. A., Verzicco, R., Orlandi, P., and Mohd-Yusof, J., 2000, "Combined Immersed-Boundary Finite-Difference Methods for Three-Dimensional Complex Flow Simulations," J. Comput. Phys., **161**(1), pp. 35–60.
[10] Kim, J., Kim, D., and Choi, H., 2001, "An Immersed-Boundary Finite-Volume Method for Simulations of Flow in Complex Geometries," J. Comput. Phys., **171**(1), pp. 132–150.
[11] Piccirillo, P. S., and Van Atta, C. W., 1993, "An Experimental Study of Vortex Shedding Behind Linearly Tapered Cylinders at Low Reynolds Number," J. Fluid Mech., **246**, pp. 163–195.

Journal of Fluids Engineering

Erratum

Erratum: "Experimental Investigation on the Onset of Gas Entrainment from a Stratified Two-Phase Region Through Multiple Branches Mounted on a Curved Surface" [Journal of Fluids Engineering, 2006, 128(4), pp. 726–733]

Tariq Ahmad and Ibrahim Hassan

The caption for Table 2 on p. 729 should read "Experimental data for dual discharge".

The caption for Table 3 on p. 729 should read "Experimental data for single discharge".

